Greater than the Sum of Its Parts:
Tuning Nickel for Uncommon Small Molecule Reactivity and Catalysis via Dative Bonds with Group 13 Lewis Acidic Metalloligands

A DISSERTATION

SUBMITTED TO THE FACULTY OF
UNIVERSITY OF MINNESOTA
BY

Ryan C. Cammarota

IN PARTIAL FULFILLMENT OF THE REQUIREMENTS
FOR THE DEGREE OF
DOCTOR OF PHILOSOPHY

Connie C. Lu, advisor

June 2018

© Ryan C. Cammarota

2018

Acknowledgements

I would like to thank everyone who has helped me throughout my time in graduate school at Minnesota, both with learning how to become a graduate student and an independent scientist, as well as with growing as a person. This thesis is the result of over five and a half years of work (let's round down to the nearest half year, shall we?). I don't think I have ever worked harder on anything in my life, and I have learned a lot about chemistry and myself in the process. Hopefully, in this final product of all that work, I managed to stumble upon at least a few things that are interesting enough that a future student in the lab will have to dig this up at some point.

First, I would like to thank my advisor Connie Lu. She has been very supportive of me throughout my time in her group, and many of the professional development opportunities I had, including conducting my research in collaboration with staff scientists at two different national labs and attending several academic conferences and workshops, would not have been possible without her efforts on my behalf. While we didn't always see eye to eye on a lot of things, I definitely learned a lot from her about how to be a scientist and design a research project.

I would also like to thank the members of the Lu Lab, past and present, that helped me along the way. I learned most of what I know about being a successful graduate student and working in the lab from Dr. Reed Eisenhart, Dr. Laura Clouston, and Dr. Steve Tereniak, who put up with me when I had no idea what I was doing. More recently, I have had the opportunity to work closely with Matt Vollmer, and I thank him for his efforts in advancing our research project and keeping me excited about it longer than I probably should have been. I have also had some amazing collaborators, including Dr. Samantha Burgess at PNNL, and Dr. Jing Xie, Dr. Jingyun Ye, and Dr. Kostas Vogiatzis in the Gagliardi group. I've enjoyed working them these past few years, as well as with Matt, James Moore, Bianca Ramirez, Sai Desai, and Dr. Anthony Thompson, and I have learned a lot from related research that they have pursued. Long story still kind of long, I'm grateful for all these folks, their company, insightful discussions, and for making these past five (and three-quarters) years a lot of fun.

Lastly, I'd like to thank my family and friends for their support and encouragement throughout this process. When I look back at these graduate school years someday, I'm

sure that a lot of it will be a bit of a blur, but I’m sure the good times I had with them will come to mind first.

Abstract

In transitioning to an energy infrastructure which is less reliant on fossil fuels and less deleterious to the environment, it will be critical to couple renewable energy sources to chemical reactions, like the multi-electron conversions of water to dihydrogen (H_2) and of carbon dioxide (CO_2) to liquid fuels, to allow for efficient energy storage and transport. Many of these essential chemical reactions require expensive metal catalysts to proceed; catalysts featuring multiple Earth-abundant metals are utilized in biological enzymes to facilitate these reactions, and offer underexplored possibilities in synthetic and industrial settings for replacing precious metals. Although inexpensive metals are often poor catalysts for challenging multi-electron processes, there are a multitude of possible metal-metal combinations, which may exhibit more desirable properties when paired together compared to those of their constituent metals. In this vein, an isostructural series of bimetallic complexes which feature a dative bond between Ni and a varied group 13 supporting metal has been systematically studied. The steric and electronic effects of larger group 13 supporting metals were found to poise Ni for the binding and activation of H_2, with the Ni center rendered more electron-deficient due to stronger Ni→M dative bonds and more favorably positioned geometrically for small molecule binding. Pairing Ni with Ga was found to be optimal for catalyzing the hydrogenations of olefins to alkanes and of CO_2 to formate, both of which often require precious metal catalysts and are challenging two-electron processes that a similarly-ligated mononuclear Ni center without a supporting metal is unable to mediate. By quantitatively comparing structure, redox properties, and the reactivity of key catalytic intermediates, the effects of the supporting metal on the properties of Ni and the catalytic activity of the Ni−M bimetallic complexes have been elucidated. Collectively, experimental and computational results demonstrate that modulating an active transition metal center via a direct interaction with a Lewis acidic supporting metal can be a powerful strategy for favorably altering the properties of inexpensive metals and promoting new reactivity paradigms in base-metal catalysis.

Table of Contents

List of Tables

Chapter 2

Chapter 3

Chapter 5

List of Figures

Chapter 1

Chapter 2

List of Abbreviations

*	antibonding (in MO context)
Å	Angstroms
A	hyperfine coupling constant
A_L	ligand acidity constant (Morris)
aq	aqueous state
Ar	aryl group (or argon)
atm	atmosphere(s)
avg or ave	average
$[BArF]^-$	tetrakis[3,5-bis(trifluoromethyl)phenyl]borate
BDE	bond dissociation energy
BDFE	bond dissociation free energy
br	broad
bs	basis set
°C	degrees Celsius
C or [ ]	concentration
c. or ca.	approximately (*circa*)
cal	calorie(s)
calc'd	calculated
CASSCF	complete active space self-consistent field
C_6D_6	deuterated benzene
c.f.	compare (*conferatur*)
C_2H_4	ethylene
C_6H_6	benzene
CH_3CN	acetonitrile
CH_3OH	methanol
COD	1,5-cyclooctadiene
cm^{-1}	wavenumber
Cp	cyclopentadienyl
crypt	2,2,2-cryptand
cryst syst	crystal system

CSD	Cambridge Structural Database
CV	cyclic voltammetry or cyclic voltammogram
Cy	cyclohexyl
d	doublet
DBU	1,8-diazabicyclo[5.4.0]undec-7-ene
dcpe	bis(dicyclohexylphosphino)ethane
dd	doublet of doublets
dedpe	(diethyldiphenylphosphino)ethane
depe	bis(diethylphosphino)ethane
DFT	density functional theory
d_{HH}	H−H distance
dmpe	bis(dimethylphosphino)ethane
dmpp	bis(dimethylphosphino)propane
dppe	bis(diphenylphosphino)ethane
dppv	bis(diphenylphosphino)ethylene
ΔE_p	peak-to-peak separation for a redox couple
$E°_{1/2}$	standard redox potential
E	*trans* isomer or Group 13 element
e^-	electron(s)
ECE	electron transfer/chemical transfer/electron transfer mechanism
EDA	energy decomposition analysis
eg	for example (*exempli gratia*)
E_{pa}	peak anodic potential
E_{pa}	peak cathodic potential
EPR	electron paramagnetic resonance
Eqn	equation
equiv	equivalent(s)
Et	ethyl
Et_2O	diethyl ether
ETS-NOCV	Extended Transition State—Natural Orbitals for Chemical Valence
ex	exchange

F	Faraday's constant
Fc or $FeCp_2$	ferrocene
$FeCp_2^{0/+}$	ferrocene/ferrocenium redox couple (reference in CV)
FeMo-co	FeMo-cofactor
Fp	$FeCp(CO)_2$
FSR	formal-shortness-ratio
Fw	formula weight
$\Delta G°$	Gibbs free energy
$\Delta G°_{H-}$	thermodynamic hydricity (Gibbs free energy of hydride transfer)
$\Delta G°_{H\bullet}$	Gibbs free energy of hydrogen atom transfer (=BDFE)
$\Delta G°_{H+}$	Gibbs free energy of proton transfer ($1.364 \cdot pK_a$)
$\Delta G^{‡}$	Gibbs free energy of activation
$\Delta G^{‡}_{MC}$	Gibbs free energy of activation for methylene coalescence
G	gauss
g	grams or gaseous state
g	g-factor (in EPR)
GC-MS	gas chromatography-mass spectrometry
$\Delta H°$	Enthalpy change for a reaction
h	hour(s)
H^+	proton(s)
$H:^-$	hydride ion
H•	hydrogen atom
HAT	hydrogen atom transfer
HBpin	pinacolborane
HCO_2^-	formate
HSAB	Hard Soft Acid Base Theory
Hz	hertz
I	nuclear spin quantum number
i-Bu	iso-butyl
ie	in other words (*id est*)
ip	1:1 ion-pair

i_{pa}	peak anodic current
i_{pc}	peak cathodic current
i_{pa}/i_{pc}	ratio of peak anodic current to peak cathodic current
IPr	N,N'-bis(2,6-diisopropylphenyl)imidazole-2-ylidene)
^{i}Pr or *i*Pr	isopropyl
IR	infrared
J	coupling constant
K	Kelvin
K	equilibrium constant
k	rate constant
k_B	Boltzmann's constant
K_d	dissociation constant
KC_8	potassium graphite
kcal	kilocalories
KIE	kinetic isotope effect
L	primary ligand, $[N(o\text{-}(NCH_2P^iPr_2)C_6H_4)_3]^{3-}$
L^*_3	L ligand with capping amine donor removed
LH_3	protonated ligand, $H_3N(o\text{-}(NCH_2P^iPr_2)C_6H_4)_3$
LN_2	liquid nitrogen
LUMO	lowest unoccupied molecular orbital
L^*_3	L ligand with capping amine donor removed
M	supporting metal or molarity = moles per liter
m	multiplet
Me	methyl
MeCN	acetonitrile
Mes	mesityl
mg	milligram
MHz	megahertz
min	minute(s)
mL	milliliter
mM	millimoles per liter

mmol	millimoles
MO	molecular orbital
mol	moles
mol%	(moles catalyst/moles substrate) x 100
ms	milliseconds
mT	millitesla
mV	millivolts
N_3	triamide binding pocket or plane of L
N_A	Avagadro's number
N_{eq}	equatorial amide nitrogen donors of L
NBO	Natural Bond Orbital
^{n}Bu	*n*-butyl
*n*BuLi	*n*-butyl lithium
NEt_3	triethylamine
NHE	Normal Hydrogen Electrode
$Ni(COD)_2$	bis(1,5-cyclooctadiene)nickel(0)
nm	nanometers
NMR	nuclear magnetic resonance
o	ortho
OEC	Oxygen-Evolving Complex
OTf	trifluoromethanesulfonate
P_3	triphosphine binding pocket or plane of L
P(X)	pressure of gas X
PEEK	polyether ether ketone
PEP	6,6"-bis(diphenylphosphino)-2,2':6',2"-terpyridine ligand
pF^-	fluoride ion affinity
Ph	phenyl
pK_a	p*K* for association
PNNL	Pacific Northwest National Laboratory
ppm	parts-per-million
$[PPN]^+$	bis(triphenylphosphoranylidene)ammonium cation

q	quartet
R	alkyl group or ideal gas constant
R’	alkyl group unless denoted as an aryl group
R^2	statistical coefficient of determination
r	distance or radius
r	covalent ratio
r^+, r^-	Fuoss ion-pair radius
r_x	covalent radius of atom X
RDS	rate-determining step
ref(s)	reference(s)
reflns	reflections
rel	relative
rt	room temperature
$\Delta S°$	Entropy change for a reaction
S	spin state
s	second(s) or singlet
s^{-1}	frequency
SCE	Saturated Calomel Electrode
sh	peak shoulder
SOMO	singly-occupied molecular orbital
std	standard
T	temperature
T_1	spin-lattice relaxation time
T_1(min)	minimum spin-lattice relaxation time
t	triplet
$t_{1/2}$	half-life for a reaction
TBA	tetrabutylammonium cation
^{t}Bu	*tert*-butyl
tBuTMG	*tert*-butyl tetramethylguanidine base
td	triplet of doublets
TD-DFT	time-dependent density functional theory

THF	tetrahydrofuran
THF-d_8	deuterated tetrahydrofuran
TMG	tetramethylguanidine base
TOF	turnover frequency
toluene-d_8	deuterated toluene
TON	turnover number
TPB	tris-(*o*-diisopropylphosphinophenyl)borane ligand
TS	transition state
UV-vis	ultraviolet-visible
V	volts or volume
Vkd or Vkd_iPr	2,8,9-triisopropyl-2,5,8,9-tetraaza-1-phosphabicyclo[3,3,3]undecane
Vkd_Me	2,8,9-trimethyl-2,5,8,9-tetraaza-1-phosphabicyclo[3,3,3]undecane
vs	versus
VT	variable temperature
W	linewidth (for NMR resonance)
wt%	percent by weight
Z	*cis* isomer or number of independent structures in unit cell
μ	absorption coefficient
*	antibonding (in MO context)
μ	bridging
δ	chemical shift
°	degrees
θ	degrees of data collection
ϵ	dielectric constant
α	electron transfer coefficient
η	hapticity
μL	microliter
μmol	micromoles
ε	molar absorptivity
ν	scan rate (in CV) or frequency (in IR)
λ	wavelength

λ_{max}	wavelength of maximum absorption
π	pi
σ	sigma

Chapter 1

Biologically Inspired Strategies for Small Molecule Activation: Design Principles for Mediating Multi-Electron Catalysis Using Earth-Abundant Transition Metals

In part from:

Cammarota, R. C.*; Clouston, L. J.; Lu, C. C.* "Leveraging Molecular Metal-Support Interactions for H_2 and N_2 activation." *Coord. Chem. Rev.* **2017**, *334*, 100-111.

1.1 Overview of Energy-Related Challenges and Relevant Multi-Electron Processes

Two of the major challenges we face as a society in the next century pertain to our reliance on fossil fuels to meet the ever-increasing global demand for energy. Namely, renewable energy sources must be developed which can eventually serve as cost-effective alternatives to fossil fuels, which will ultimately become depleted.[1] In the meantime, fossil fuel combustion generates enormous quantities of carbon dioxide (CO_2), and has contributed significantly to the drastic increase in atmospheric CO_2 from a pre-industrial level of 280 ppm to over 400 ppm in 2015.[2-5] This increase in atmospheric CO_2 levels has undoubtedly contributed to global warming through the greenhouse effect, and global climate will continue to be adversely affected in the years to come if changes are not made to alter the current trajectory.[6-7]

In addressing the problem of developing renewable energy alternatives to fossil fuels, wind energy and solar energy are two promising sources. However, both of these are intermittent sources of energy, in that they only are sources of energy when the wind is blowing and when the sun is shining.[8] Thus, efficient methods for energy storage and transport must be developed, such that renewable energy can be used when and where it is needed. By coupling solar and/or wind energy to chemical reactions, renewable energy can be stored in chemical bonds until it is needed.[8-9] Photosynthesis in plants is an example of this, as sunlight, water (H_2O), and CO_2 are used to generate energy-rich, organic sugar molecules.[1, 10-11] Likewise, many research efforts have focused on using solar energy to drive the splitting of H_2O into dioxygen (O_2) and dihydrogen (H_2), as H_2 is an energy-rich molecule that can be utilized in other processes (Equation 1.1).[11-12] Currently, 95% of H_2 in the U.S. is produced via energy-intensive steam-reforming of

methane (CH_4; Equation 1.2), with the subsequent water-gas shift reaction resulting in the formation of additional H_2 from the CO initially generated (Equation 1.3).[13-14] However, producing H_2 in this way results in about the same net CO_2 emissions as simply burning CH_4 in the first place (Equations 1.2-1.3), and so ideally H_2 could be produced sustainably by using solar energy to drive the splitting of water (Equation 1.1).[10, 14]

$$H_2O + h\nu \leftrightarrow \tfrac{1}{2}\, O_2 + H_2 \qquad \text{(Eqn 1.1)}$$

$$CH_4 + H_2O + \text{heat} \leftrightarrow 3\, H_2 + CO \qquad \text{(Eqn 1.2)}$$

$$CO + H_2O \leftrightarrow H_2 + \text{heat} + CO_2 \qquad \text{(Eqn 1.3)}$$

A sustainable source of H_2 would have far-reaching implications because H_2 serves as a reactant in many large-scale processes that are energetically relevant to society.[1, 11] Among them, H_2 is utilized to convert CO to longer-chain hydrocarbon fuels which power our vehicles via the Fischer-Tropsch process (Equation 1.4, n=10-20).[15] Additionally, H_2 and N_2 are combined to form ammonia (NH_3), the basis for fertilizer, in the Haber-Bosch process, which has been critical to the ability of our agricultural infrastructure to sustain rapid global population growth over the last few centuries (Equation 1.5).[16] Both of these processes require metal catalysts and high temperatures and pressures, and a large percentage of the annual global energy supply is used to generate the H_2 gas used in these important processes.[15-17]

$$(2n + 1)\, H_2 + n\, CO + \text{heat} \leftrightarrow C_nH_{2n+2} + n\, H_2O \qquad \text{(Eqn 1.4)}$$

$$3\, H_2 + N_2 + \text{heat} \leftrightarrow 2\, NH_3 \qquad \text{(Eqn 1.5)}$$

A third desirable process involving H_2 is one that converts CO_2 into hydrocarbon fuels; this has been the target of many recent research efforts because such a process would potentially be helpful in regard to both of the major societal challenges mentioned

at the outset. Specifically, large-scale conversion of CO_2 and solar-derived H_2 into liquid fuels could allow for a means of efficiently storing renewable energy, while also helping to mitigate the detrimental climate effects associated with rising atmospheric CO_2 levels.[1, 10-11] Furthermore, using H_2 in combination with CO_2 to form liquid fuels would also allow for more facile energy transport, as liquids such as formic acid (HCO_2H) and methanol (CH_3OH) have much higher energy density than gaseous H_2.[18] Formic acid (4.4 wt% H_2) and formate (HCO_2^-) derivatives could potentially serve as reversible H_2 storage mediums, whereas methanol (12.6 wt% H_2) is a useful fuel in its own right, and other hydrocarbon fuels like gasoline, ethylene, and propylene can all be readily synthesized from methanol via established industrial processes.[11, 18-19] The potential products of multi-electron reduction of CO_2 are shown in Figure 1.1a, with the relative favorability of forming each product and the number of electrons required to do so shown in the plot in Figure 1.1b.[1, 10]

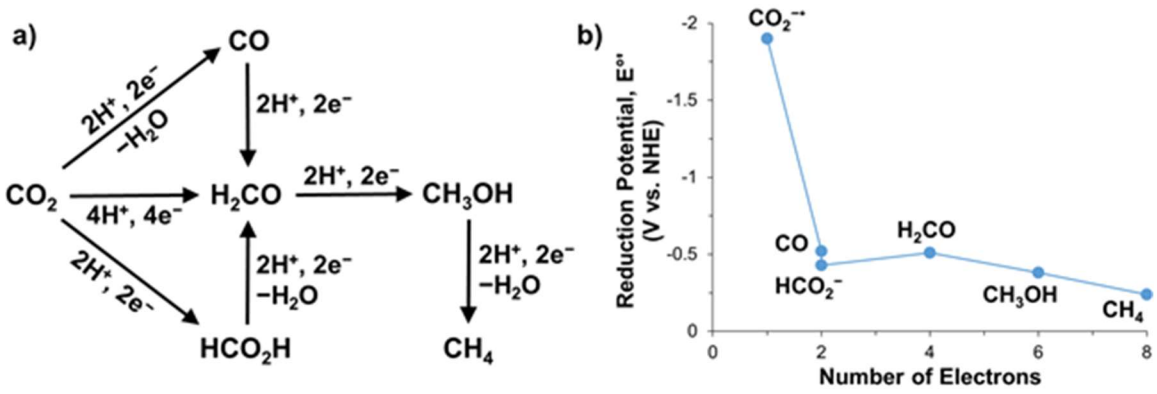

Figure 1.1. (a) Scheme showing products of multi-electron CO_2 reduction. (b) Plot of CO_2 reduction potentials, $E°'$ (V vs. NHE at pH = 7), for Equations 1.6-1.11 vs. the number of electrons by which CO_2 is being reduced.[1, 10]

The reduction potentials for various CO_2 reduction half-reactions, at pH = 7 vs. NHE, are shown in Equations 1.6-1.11, and displayed visually in a plot against the number of electrons involved in the reduction reaction in Figure 1.1b.[1, 10]

$$CO_2\ (g) + e^- \rightarrow CO_2^{-\bullet}\ (aq) \qquad E^{\circ\prime} = -1.9\ V \qquad \text{(Eqn 1.6)}$$

$$CO_2\ (g) + 2H^+ + 2e^- \rightarrow CO\ (g) + H_2O \qquad E^{\circ\prime} = -0.52\ V \qquad \text{(Eqn 1.7)}$$

$$CO_2\ (g) + H^+ + 2e^- \rightarrow HCO_2^-\ (aq) \qquad E^{\circ\prime} = -0.43\ V \qquad \text{(Eqn 1.8)}$$

$$CO_2\ (g) + 4H^+ + 4e^- \rightarrow H_2CO\ (aq) + H_2O \qquad E^{\circ\prime} = -0.51\ V \qquad \text{(Eqn 1.9)}$$

$$CO_2\ (g) + 6H^+ + 6e^- \rightarrow CH_3OH\ (aq) + H_2O \qquad E^{\circ\prime} = -0.38\ V \qquad \text{(Eqn 1.10)}$$

$$CO_2\ (g) + 8H^+ + 8e^- \rightarrow CH_4\ (g) + 2H_2O \qquad E^{\circ\prime} = -0.24\ V \qquad \text{(Eqn 1.11)}$$

As seen in Figure 1.1b and Equations 1.6-1.11, it is generally more thermodynamically favorable for multiple electrons to be transferred to CO_2 at once, as well as for the transfer of electrons to be coupled with the transfer of protons (H^+) to avoid the accumulation of charge.[1] For instance, the transfer of a single electron to form the $CO_2^{-\bullet}$ radical anion requires a much harsher reduction potential (−1.9 V vs. NHE) than does the two-electron reduction to either CO (−0.52 V vs. NHE) or HCO_2^- (−0.43 V vs. NHE).[1, 10] Furthermore, the most thermodynamically favorable of the CO_2 transformations are those that involve the transfer of the greatest amount of electrons: the six-electron reduction to methanol and the eight-electron reduction to methane (Figure 1.1b). That said, these multi-electron reductions are still slightly endergonic at pH = 7, though these reactions can be made to be more favorable in many cases by altering the pH, the choice of solvent, and/or the presence of an exogenous base.[10] That multi-electron reduction reactions are more thermodynamically favorable than stepwise reduction is a general trend that also holds true in the six-electron reduction of N_2 to NH_3

(Equation 1.5), with the overall process being thermodynamically favorable under standard state conditions.[20]

Despite multi-electron reductions being more thermodynamically favorable than single-electron reductions, they remain inherently more difficult to catalytically mediate due to the kinetic challenge of directing the simultaneous transfer of multiple electron and/or proton equivalents, so as to bypass high energy intermediates during catalysis. According to a Bell/Department of Energy 2008 report, "the major obstacle preventing efficient conversion of CO_2 into energy-bearing products is the lack of catalysts";[1] indeed, the development of catalysts for multi-electron transformations of CO_2 (Equations 1.7-1.11), and that of other small molecule feedstocks (Equations 1.1-1.5), is an overarching goal in the field of inorganic chemistry. In order to facilitate these challenging multi-electron processes, transition metal catalysts capable of undergoing multiple reversible redox events at relatively mild potentials could prove useful. Ideally, such catalysts would utilize earth-abundant first-row metals, but unfortunately first-row metals are prone to undergoing unproductive one-electron redox chemistry and often are incompetent in mediating key two-electron reaction steps which are necessary to complete many catalytic cycles (eg. oxidative addition, reductive elimination).[21-22] On the other hand, precious second-row and third-row transition metals typically undergo more facile multi-electron redox changes. For example, nearly all of the limited number of homogeneous catalysts which have been developed for performing the six-electron reduction of CO_2 to methanol utilize precious metals (Ru, Ir).[23-29]

One strategy to replace precious metal catalysts while maintaining multi-electron redox capability is to couple multiple first-row transition metals in a single catalyst or

active site. Multiple first-row metals working in concert could serve as an electron reservoir from which electrons could more easily be transferred to reduce substrate, thereby providing the required multi-electron redox versatility needed for catalysis. In this way, each first-row metal could undergo its preferred one-electron redox process, but still allow the multi-metallic catalyst to mediate net multi-electron redox processes. Furthermore, there are a large number of possible combinations of two first-row metals and an extensive array of different ways in which they could interact and cooperate to facilitate multi-electron processes.[30-31] Nature provides a good model to emulate, as the cooperative interactions of multiple first-row metals are utilized to perform numerous essential biological processes, including the reduction of N_2 to ammonia (NH_3) by the FeMo-cofactor of nitrogenase, the oxidation of water to O_2 by the oxygen-evolving complex (OEC) in Photosystem II, and the reversible activation of dihydrogen (H_2) by [NiFe]-hydrogenase. These three examples, as they pertain to informing the design of multi-metallic catalysts, are briefly discussed below.

1.2 Biological Design Principles: Harnessing Multiple First-Row Metals for Multi-Electron Processes

The FeMo-cofactor of the nitrogenase enzyme (FeMo-co) consists of a cluster of seven Fe centers and one Mo supported by nine bridging sulfides and an unusual carbide moiety which is positioned centrally between six of the Fe centers.[32-35] FeMo-co has evolved such an intricate architecture in order to facilitate the storage and directed transfer of the eight protons (H^+) and eight electrons (e^-) needed to reduce N_2 to two equivalents of NH_3 and release one equivalent of H_2. The presence of multiple proximal Fe centers has been proposed by Hoffman and co-workers to allow for the storage of four

electrons and two protons in the E_4 state, also known as the Janus intermediate, with two hydrides each bridging two Fe centers and another two protons residing on nearby bridging sulfur atoms (Figure 1.2a).[32, 36]

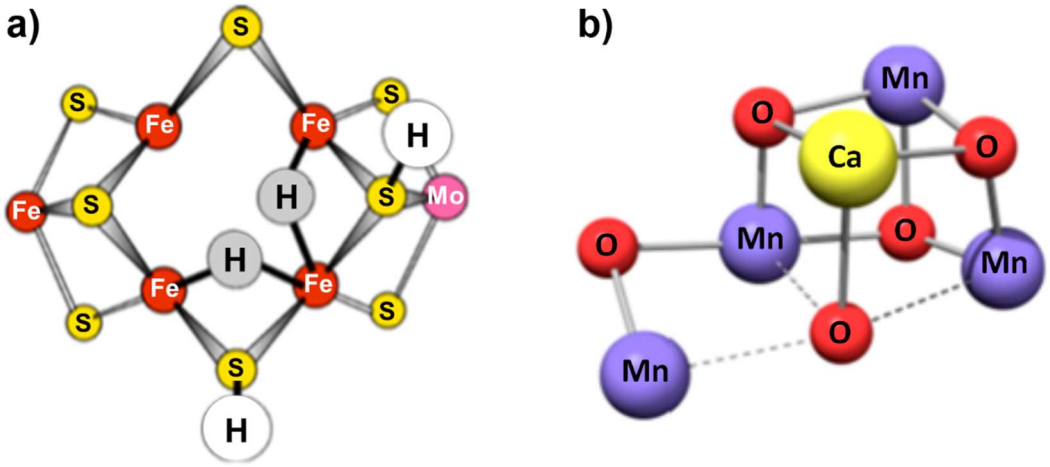

Figure 1.2. (a) Structure of E_4 state of FeMo-co active site, also known as the Janus intermediate. (b) Mn_4O_5Ca cubane cluster of the oxygen-evolving complex (OEC) in Photosystem II. Diagrams adapted from refs. 32 and 38.

Thus, positioning several Fe centers in close proximity serves two main purposes in FeMo-co that permit multi-electron reduction of N_2: (1) to allow the substantial buildup and storage of electron equivalents beyond that which would be attainable for single metal center, and (2) to accomplish the storage of reducing equivalents via the cooperative interaction of multiple Fe centers to stabilize bridging hydride moieties.[32, 36]

The oxygen-evolving complex (OEC) in Photosystem II also utilizes an active site featuring a cluster of first-row transition metals, Mn_4O_5Ca, which mediates the oxidation of water to O_2 by accumulating four electron holes at relatively mild potentials and with minimal potential separation between successive Mn-based oxidations (Figure 1.2b).[37-41] Though the Ca^{2+} ion in the cluster is redox-inactive and does not participate directly in the multi-electron redox chemistry, its substitution for Sr^{2+} results in diminished enzymatic activity, and alternative substitutions result in the loss of all activity. Studies of

the enzyme and model complexes thereof have proposed that the Ca^{2+} ion may play two important roles in promoting water oxidation: (1) to inductively modulate the electronic environment of the Mn_4 cluster for optimal water oxidation, and (2) to bind water and stabilize a reactive Ca−OH nucleophile that directly participates in O−O bond formation with a Mn-based oxo or oxyl moiety.[38, 42-43] Just as was seen in FeMo-co, the function of the Mn_4O_5Ca cluster of OEC again shows that a supporting metal can favorably impact the reactivity of a nearby active metal or metal cluster by tuning the redox properties of the system to allow for the storage of multiple electrons (FeMo-co) or electron holes (OEC), and by direct participation of multiple metals in interactions with substrate.

Lastly, a bimetallic active site rather than a metal cluster is responsible for the remarkable activity of [NiFe]-hydrogenase, which reversibly activates H_2. Breaking the H−H bond of H_2 is a challenging step that typically requires precious metals or metal-ligand cooperativity to complete a synthetic hydrogenation catalytic cycle; in fact, a mononuclear Ni center in isolation has never been reported to mediate the oxidative addition of H_2 to give a Ni dihdyride species.[44-45] Nevertheless, [NiFe]-hydrogenase reversibly activates H_2 via the cooperation of Ni with a coordinated cysteine residue and a proximal Fe center, to which it has formed a flexible metal-metal bond (Figure 1.3).[46-50]

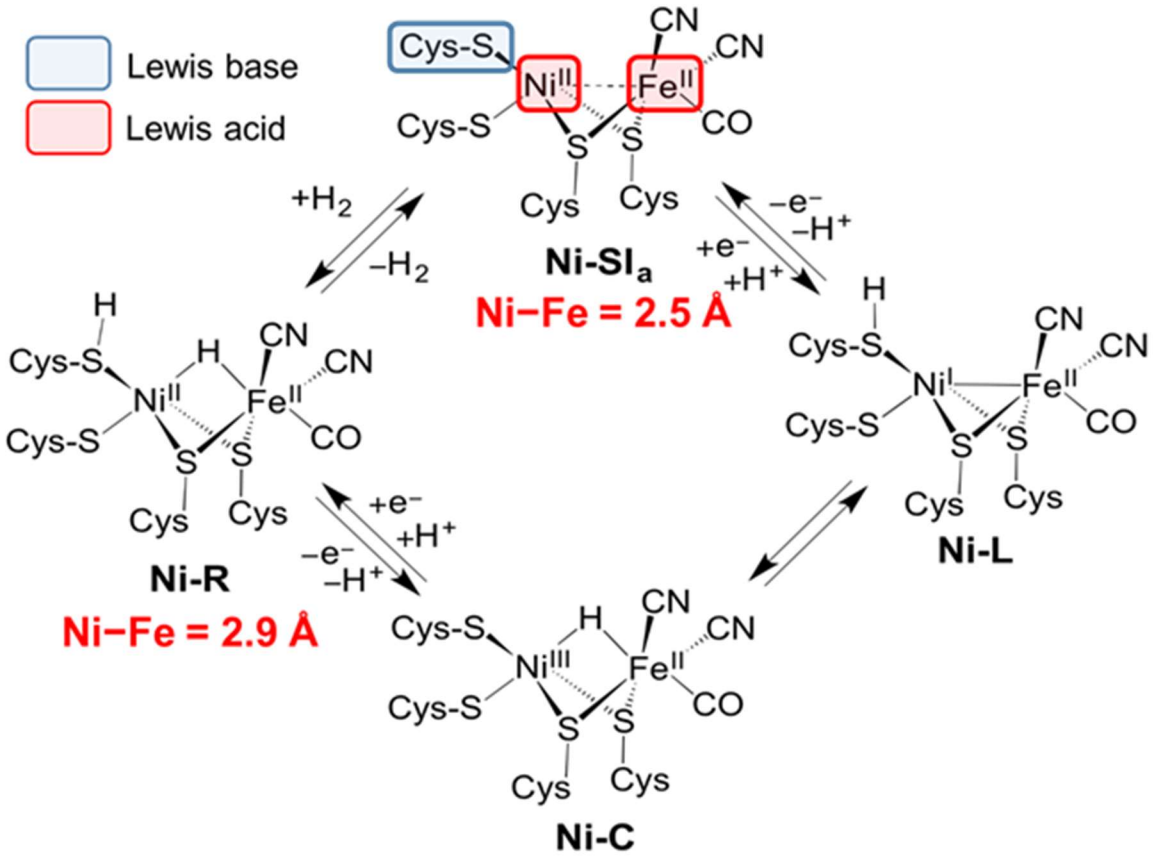

Figure 1.3. Catalytic cycle for the reversible conversion between H_2 and protons and electrons mediated by [NiFe]-hydrogenase. The oxidation states of Ni and Fe are labeled in each catalytic intermediate, as are the Ni−Fe bond lengths in the Ni-R and Ni-SI_a states. The roles of Ni, Fe, and the coordinated cysteine residue are classified as acting as either a Lewis acid (red) or a Lewis base (blue). Figure adapted from ref. 46 and Dr. Reed Eisenhart.

H_2 activation occurs via the cooperative interaction of Ni, Fe, and a coordinated cysteine residue in the Ni-SI_a state. Namely, the coordinated cysteine residue acts as a Lewis base and becomes protonated, with Ni(II) and Fe(II) acting as Lewis acids to cooperatively stabilize a bridging hydride, Ni−(μ-H)−Fe (Figure 1.3). The supporting Fe center maintains an invariant Fe(II) oxidation state throughout the catalytic cycle, and serves to accommodate the changing electronic requirements of the active Ni center, which traverses Ni(I), Ni(II), and Ni(III) oxidation states in various catalytic intermediates. For example, Fe acts as a Lewis acidic metalloligand in forming a dative

bond to Ni to stabilize an electron-rich Ni(I) species in the Ni-L state, but this direct dative interaction is broken in the Ni-C state to allow Ni(III) to be accessed (Figure 1.3). The flexibility of this Ni−Fe interaction is highlighted by the dramatic difference in the Ni−Fe bond distance between the Ni-SI_a (~2.5 Å) and Ni-R states (~2.9 Å).[46] In addition to tuning Ni through a flexible dative interaction, Fe also assists in substrate activation by stabilizing the bridging hydride moiety.

Inorganic chemists have long sought to apply the design principles underlying the function of biological enzymes to develop multi-metallic catalysts capable of functionalizing of small molecules. As illustrated by enzyme active sites, coupling multiple metal centers in close proximity can allow for maximal storage of electrons or electron holes, poising the metal centers to facilitate multi-electron transformations. However, large metal clusters, which are difficult to synthetically assemble, are not prerequisites for rich redox profiles; indeed, among other examples in the literature which will be discussed further in section 1.3, our group has reported a bimetallic Co−Cr complex which allows access to five redox states via four reversible one-electron processes.[51] Notably, the rich redox profile of a metal-metal bonded species may be synergistic in that it can be greater than the sum of its parts: electronic coupling of the metal centers may give rise to more accessible redox states than those of the individual constituent metals. Two metals in a metal-metal bonded unit are also in close enough proximity to engage in cooperative interactions with substrate, as was critical to stabilizing bridging hydride intermediates in both the nitrogenase and [NiFe]-hydrogenase enzymes. In short, while enzymatic active sites undoubtedly rely upon all metals and the surrounding residues to function, the key design principles of redox

versatility and cooperative substrate activation by multiple proximal metal centers may be retained in a bimetallic complex featuring two metals engaged in a metal-metal bond.[30]

The next section will focus on the applications of these biological design principles in synthetic systems. To begin with, the propensity of redox-inactive metals to modulate the redox properties of proximal transition metals in model complexes of OEC will be examined, with the rest of the section focusing on how adherence to the principles of multi-electron redox capability, cooperative activation involving multiple metals, and flexible bonding can allow for multi-electron reactivity and catalysis to be achieved with metal-metal bonded complexes.

1.3 Applications of Biological Design Principles in Synthetic Systems

1.3.1 Utilizing Redox-Invariant Supporting Metals to Optimize the Electronic Environment of Transition Metals for Desired Reactivity

As illustrated by the active sites of both OEC and [Ni−Fe]-hydrogenase, redox-invariant supporting metals can modulate the redox properties of proximal transition metals to allow for optimal reactivity. This redox modulation effect has been proposed to be one of the primary functions of the redox inactive Ca^{2+} ion in the Mn_4O_5Ca cluster of OEC, as substitution for any other metal ion was found to decrease or eliminate catalytic water oxidation activity. The only substitution for which catalytic activity was found to be preserved, albeit still decreased, was with Sr^{2+}, which has a similar Lewis acidity to Ca^{2+}, as defined by the pK_a of their respective $M(H_2O)_6^{n+}$ complexes.[38, 42, 52-53] In light of this, one hypothesis is that the Lewis acidity of Ca^{2+} is optimal for tuning the redox

potentials of the Mn cluster to allow for water oxidation, with this tuning occurring inductively through the bridging oxygen moieties.

This hypothesis has been tested systematically in a series synthetic Mn cluster model complexes reported by Agapie and co-workers. Two different isostructural series of Mn cluster complexes were reported, which have the general forms of Mn_3O_4M and Mn_3O_2M, where "M" is a variable redox-inactive metal ion which was systematically varied to several Groups 1, 2, and 3 ions, among others (Figure 1.4). In these model complexes, the Lewis acidity of the metal ion (Mn^{3+}, Zn^{2+}, Sc^{3+}, Y^{3+}, Ca^{2+}, Na^{+}) was found to linearly modulate the potential of the Mn-based reduction event for its respective cluster. A similar relationship between reduction potential and Lewis acidity, as defined by the pK_a of the $M(H_2O)_6^{n+}$ complexes, was seen in both series, with each pK_a unit shifting the reduction potential by approximately 100 mV (Figure 1.4).[42, 52]

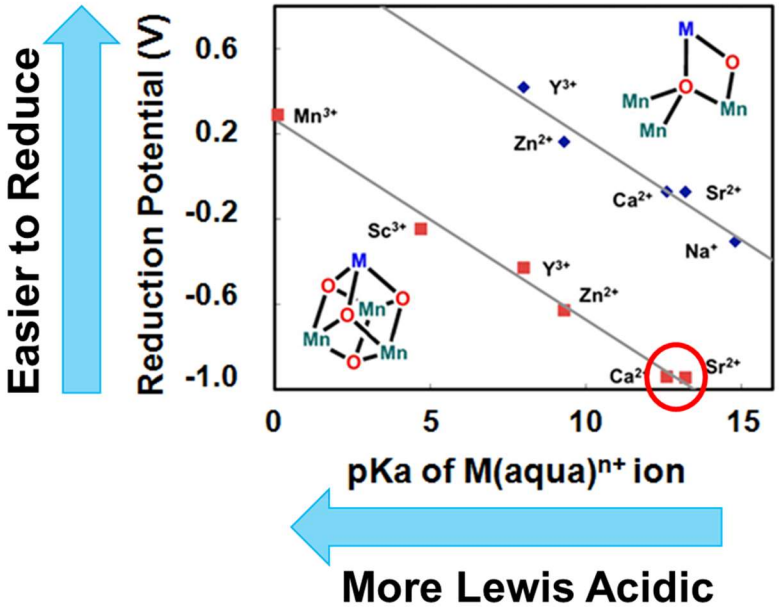

Figure 1.4. Correlation of the reduction potential of the Mn-oxido cubane cluster with the pK_a of the corresponding $M(H_2O)^{n+}$ complex, a proxy for the Lewis acidity of M^{n+}. The two structural motifs in which the Lewis acidic metal ion, M^{n+}, was varied are displayed next to the correlation found for that series of complexes. Figure adapted from refs. 42 and 52.

It makes intuitive sense that a more Lewis acidic metal ion (ie. lower pK_a of $M(H_2O)^{n+}$) will withdraw more electron density from the bridging oxygen atom, which will in turn withdraw more electron density from the adjacent manganese metal centers. This will result in more electron-poor Mn metal centers in the cluster which will be more easily reduced, as seen in the more positive reduction potentials for the more Lewis acidic metal ions. The Mn-based reduction events for the Mn_3O_2M and Mn_3O_4M clusters correspond to the $Mn^{IV}Mn^{III}_2/Mn^{III}_3$ and $Mn^{IV}_3/Mn^{IV}_2Mn^{III}$ redox couples, respectively (Figure 1.4).[42, 52]

In these complexes, the Lewis acidic metal ion is only indirectly interacting with the Mn metal centers through the bridging oxygen atoms. It remains to be seen exactly what role Lewis acidity plays in modulating reduction potentials in instances in which the transition metal and Lewis acidic moiety are directly interacting. One might expect that other factors may come into play, such as the relative energies and overlap of the donor and acceptor molecular orbitals, and this open question will be investigated during the course of this thesis. Although the active site of OEC and the cluster complexes prepared by Agapie and co-workers do not bear structural similarity to those synthesized in our research group, the possibility of tuning the redox properties of a transition metal through the choice of a supporting metal with the appropriate Lewis acidity is a theme that will be utilized and explored throughout this thesis. Specifically, it is hoped that the optimization of the electronic environment of a transition metal for desired reactivity with small molecule substrates may be achievable via a direct interaction with Lewis acidic metal ion.

1.3.2 Metal-Metal Bonded Species as Potential Reservoirs for Multi-Electron Reactivity

As discussed in the context of the OEC and FeMo-co active sites, multiple metal centers in close proximity can give rise to strong electronic coupling and rich redox profiles which allow for the accumulation of multiple electrons or electron holes delocalized over multiple metal centers, which is potentially useful for mediating challenging multi-electron catalytic processes. This section will highlight synthetic examples in which this strategy has allowed for multi-electron reactivity with small molecule substrates, as well as a few examples where catalytic reactions were achieved. As shown in Figure 1.5, Betley and co-workers have reported the synthesis of a trinuclear Fe cluster, (^{tbs}L)Fe$_3$(THF), in which three Fe centers are ligated in relatively close proximity within a flexible, hexadentate ligand platform (^{tbs}L, [1,3,5-C$_6$H$_9$(NPh-*o*-NSiMe$_2$^{t}Bu)$_3$]$^{6-}$) consisting of *o*-phenylenedianilide-based subunits.[54-55]

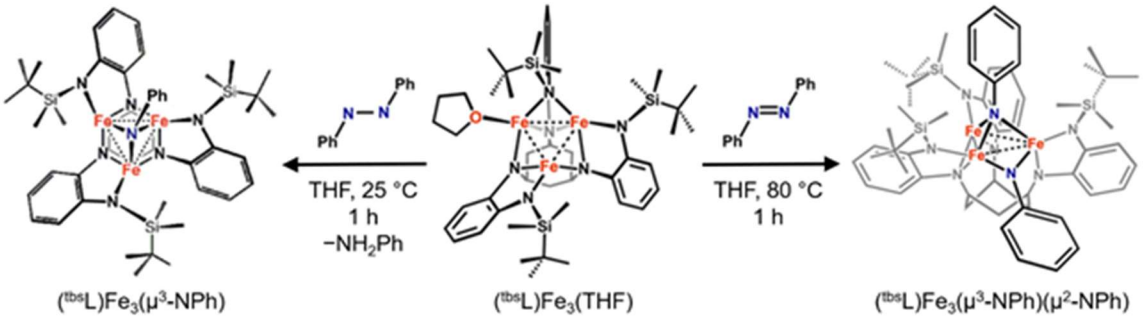

Figure 1.5. Multi-electron reactivity of a trinuclear Fe cluster, (^{tbs}L)Fe$_3$(THF), with azobenzene (right) and diphenylhydrazine (left), as reported by Betley and co-workers. Figure adapted from ref. 54 and Dr. Reed Eisenhart.

This cluster features interactions between three Fe(II) centers which give rise to a high-spin ground state of S=6, with an average Fe−Fe distance of 2.577(6) Å that is slightly longer than the Pauling single-bond radii for two Fe centers (2.33 Å). The addition of diphenylhydrazine to (^{tbs}L)Fe$_3$(THF) in THF results in the formation of (^{tbs}L)Fe$_3$(μ^3-NPh) with concomitant loss of 1 equiv aniline (Figure 1.5). This represents a

net two-electron reduction of diphenylhydrazine facilitated by a two-electron oxidation of the originally all-ferrous trinuclear cluster to $(Fe^{III})_2(Fe^{II})$, with the average Fe−Fe distance contracting slightly to 2.530(1) Å.[54] The cluster was also observed to exhibit even further multi-electron redox capability, with the cleavage of the N=N bond of azobenzene occurring upon heating to 80 °C in THF for 1 h, yielding $(^{tbs}L)Fe_3(\mu^3\text{-}NPh)(\mu^2\text{-}NPh)$, where a net four-electron oxidation of the trinuclear iron core to $(Fe^{III})_2(Fe^{IV})$ is consistent with both ^{57}Fe Mössbauer spectroscopy and charge balance (Figure 1.5).[54] The remarkable reactivity of these trinuclear iron clusters also underscores the inherent challenge of incorporating these multi-electron steps into a catalytic cycle: the strong bonds formed between the μ^3-NPh moieties and the iron cluster which facilitated the cleavage of the strong N=N bond of azobenzene in the first place will also limit the ability to liberate functionalized products and allow turnover to occur in a catalytic cycle.

Multi-electron redox chemistry via the cooperative interaction of multiple metals was also reported by Thomas and co-workers for a heterobimetallic Co−Zr complex, $Co(^{i}Pr_2PNMes)_3Zr(THF)$, which features a polarized metal-metal bond (Figure 1.6). The addition of CO_2 to $Co(^{i}Pr_2PNMes)_3Zr(THF)$ resulted in the formation of $(OC)Co(^{i}Pr_2PNMes)_2(\mu\text{-}O)Zr(^{i}Pr_2PNMes)$, where one of the C=O bonds of CO_2 has been oxidatively added across the metal-metal bond to give a terminal carbonyl ligand bound to Co and a μ-oxo moiety which bridges between the Co and Zr centers (Figure 1.6).[56]

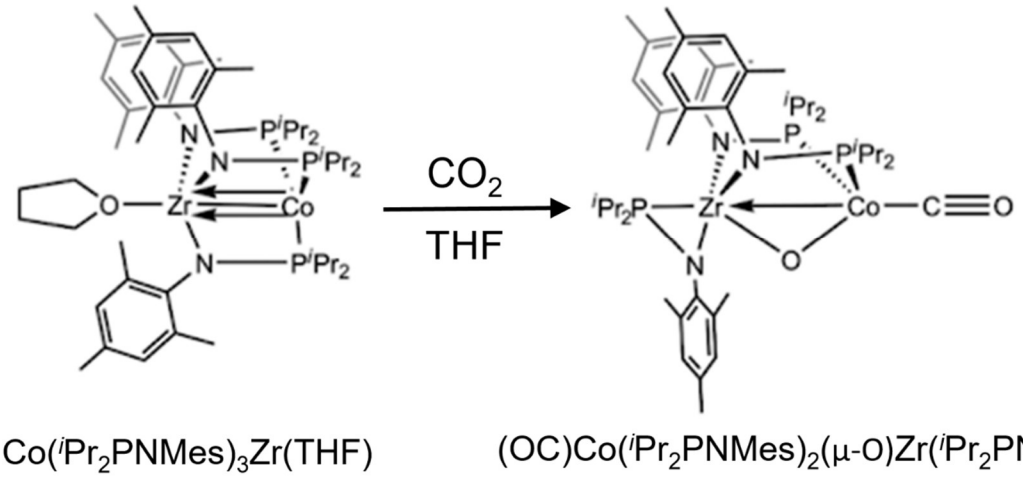

Figure 1.6. C−O bond cleavage of CO_2 by a Co−Zr bimetallic complex, as reported by Thomas and co-workers. Figure adapted from ref. 56.

This reaction showcases that two metals bonded together can serve as the source of multiple electrons for the reduction of small molecules, as CO_2 has been effectively reduced by two electrons to CO. Unfortunately, the high oxophilicity of Zr and the strong binding of CO to Co, both of which allow this exciting multi-electron transformation to occur in the first place, also renders catalytic liberation of CO_2-derived products challenging. Indeed, while the bridging μ-oxo moiety was found to be reactive in a stoichiometric fashion with silyl and alkyl electrophiles, as well as with additional CO_2 upon reduction to form a carbonate unit, its inherent stability, along with the difficulty of liberating CO from Co, precludes a catalytic cycle for CO_2 reduction in this system.[56-57] Nevertheless, this and other closely related heterobimetallic platforms reported by Thomas and co-workers have proven capable of activating a multitude of small molecules across the metal-metal bond, including alcohols, thiols, ketones, sulfones, imines, hydrazines, alkyl halides, azides, and silanes.[58-63] While in many cases this reactivity is limited to stoichiometric transformations for similar reasons to those outlined here for CO_2 reduction, the metal-metal bonded unit in this and related systems has enabled

catalytic ketone hydrosilylation, hydrazine functionalization, Kumada coupling of alkyl halides and Grignard reagents.[64-66]

These examples from Thomas, Betley, and their respective co-workers are meant to illustrate both the promise and challenges of utilizing the redox synergy of multiple metal centers to carry out multi-electron reactivity and catalysis.[67-68] Leveraging the redox capability of multiple metal centers allows for the transfer of multiple electrons to substrate, as well as for cooperative interactions between multiple metals to stabilize the products of substrate activation. However, the inherent challenge lies in the fact that in order to break strong metal-metal interactions to activate substrate, strong metal-substrate interactions must be formed that often preclude the catalytic liberation of functionalized products. That said, several examples from these labs and others have shown that multinuclear metal complexes can serve as efficient catalysts for a variety of transformations.

For example, a pentanuclear iron catalyst for water oxidation which exhibits remarkable redox versatility in the form of six accessible redox states was recently reported by Masaoka and co-workers, including four successive, reversible one-electron oxidations within a potential range of approximately 1 V (Figure 1.7).[69] Additionally, a bimetallic Ni complex reported by Uyeda and co-workers also affords access to five different redox states, with $Ni^{0}Ni^{I}$ to $Ni^{I}Ni^{I}$ oxidation states accessible and up to two electrons able to be stored by the redox-active napthyridine-diimine (NDI) ligand (Figure 1.7).[70]

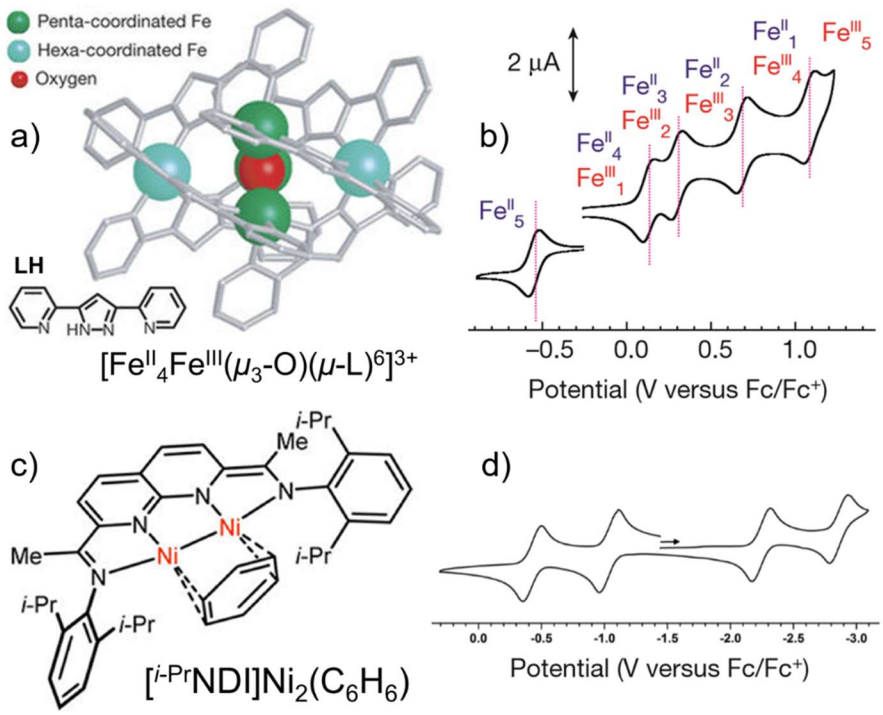

Figure 1.7. (a) Structure of the pentanuclear Fe cluster catalyst for water oxidation reported by Masaoka and co-workers, which exhibits five reversible redox events which are closely separated in potential in its CV (b). (c) Structure of a bimetallic Ni complex, [$^{i\text{Pr}}$NDI]Ni$_2$(C_6H_6), reported by Uyeda and co-workers, which exhibits two metal-based and two ligand-based reversible redox events and often binds substrate across the Ni−Ni bond. Figure reproduced with modifications from refs. 69-70.

The rich redox profiles of these multinuclear metal complexes stand in stark contrast to those typically observed for mononuclear Fe or Ni complexes, where successive one-electron redox events are usually less numerous and often separated by close to 1 V each. Furthermore, both of these complexes have desirable catalytic properties, as the pentanuclear Fe cluster catalyzes water oxidation with a turnover frequency (TOF) that is 1000 times greater than that of other Fe-based catalysts,[69] and Uyeda's Ni−Ni bimetallic platform has also proven remarkably versatile for catalysis, with catalytic alkyne cyclotrimerization and hydrosilylation, reductive vinylidene transfer, conversion of aryl azides to azoarenes, and carbonylative rearrangement via C−C bond oxidative addition all reported to be facilitated the same complex.[71-75]

1.3.3 Flexible Metal-Metal Dative Interactions in Catalysis

While multiple metals in close proximity stabilizing the maximal buildup of electrons or electron holes is a viable strategy for affecting multi-electron reactivity, the mechanism by which [Ni−Fe]-hydrogenase reversibly activates H_2 illustrates the power of a supporting metal which does not change in oxidation state, and instead simply acts as an electronic tuner that accommodates the electronic requirements of the active metal throughout catalysis by engaging in a flexible metal-metal dative interaction (Figure 1.3). Dative metal-metal bonds are typically polarized bonds between two disparate metal centers, and often take the form of a late transition metal donating electron density to an earlier, Lewis acidic metal. These metal-metal bonds are often much weaker than those considered in the previous section, where strong bonds and strong electronic coupling between metals was targeted to engender multi-electron redox capability. Furthermore, it stands to reason that breaking a typical dative metal-metal bond will not require the formation of as prohibitively strong metal-substrate bonds as will the rupture of a stronger and/or more covalent metal-metal bond; this was seen in the previous section to be one major challenge in utilizing strongly metal-metal bonded complexes as catalysts. As such, dative bonds can sometimes be more flexible and adaptable within the context of stabilizing various intermediates in a catalytic cycle.

Figure 1.8 shows an example reported by Mankad and co-workers of a complex featuring a flexible dative Fe→Cu bond which catalyzes C−H borylation of arenes, a two-electron process which had previously required precious metal catalysts.[76]

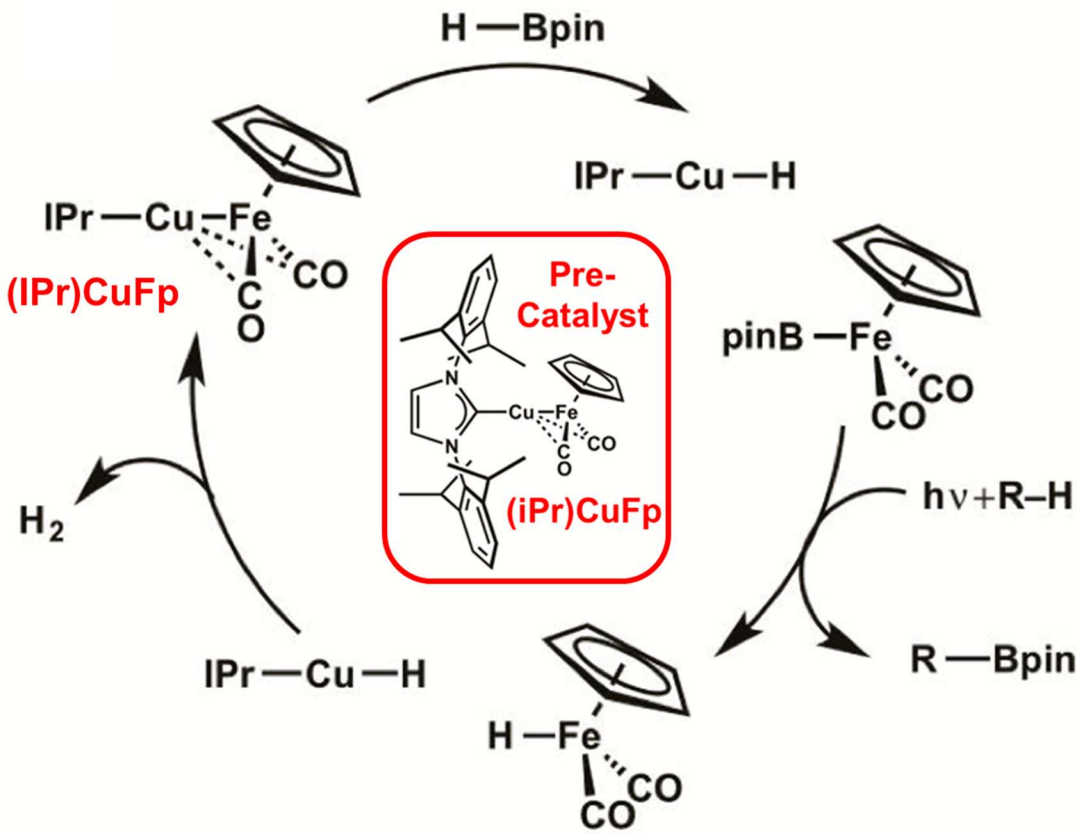

Figure 1.8. Catalytic cycle for photochemical C−H borylation catalyzed by a pre-catalyst featuring an Fe→Cu dative metal-metal interaction, as reported by Mankad and co-workers. Figure adapted from ref. 76 and Dr. Reed Eisenhart.

This complex, (IPr)Cu−FeCp(CO)$_2$ (abbreviated as (IPr)CuFp), where IPr = N,N'-bis(2,6-diisopropylphenyl)imidazole-2-ylidene), initiates the catalytic cycle by reacting with HBpin in a bimetallic oxidative addition reaction, which results in the complete rupture of the Fe→Cu bond and the formation of (IPr)CuH and Fe(Bpin)Cp(CO)$_2$ (Fp−Bpin). Under photolytic conditions, subsequent σ-bond metathesis of Fp−Bpin with the aryl C−H bond of substrate generates HFeCp(CO)$_2$ (Fp−H), which proceeds to react with (IPr)CuH in the bimetallic reductive elimination of H_2, with concomitant re-formation of the Fe→Cu bond and regeneration of the bimetallic pre-catalyst (Figure 1.8).[76] Highlighting the importance of metal-metal cooperativity to catalysis, no reactivity with close analogues of the mononuclear constituent fragments,

(Ipr)CuCl and [K][FeCp(CO)$_2$], was observed. This system showcases an extreme case of a flexible dative bond between two metals, as the metal-metal bond is completely broken and then re-formed over the course of the catalytic cycle. Additionally, this system realizes the desired cooperation of two first-row metals to perform a net two-electron processes that has often been envisioned as a strategy for replacing precious metal catalysts.

Another example of catalysis which is promoted by a metal-metal dative interaction is the Pd→Ti interaction in the Cl$_2$Ti(N^{t}BuPPh$_2$)$_2$Pd(η^3-methallyl) complex, which was reported by Michaelis and co-workers to enhance catalytic performance in allylic amination reactions (Figure 1.9).[77] Specifically, the Pd→Ti interaction was concluded to accelerate catalytic rates by a factor of 10^3 to 10^5 based on computational studies in which a flat conformer without a Pd→Ti dative interaction was considered. Catalytic experiments confirmed this dramatic rate enhancement, as a similar Pd complexes without a Ti supporting metal, [(PR$_3$)$_2$Pd(η^3-methallyl)]$^+$, gave much more sluggish catalysis with 2,2,6,6-tetramethylpiperidine as the substrate, with TOF of 0.2 to 0.7 h^{-1} at 90 °C compared with a TOF of 340 h^{-1} at rt for the Cl$_2$Ti(N^{t}BuPPh$_2$)$_2$Pd(η^3-methallyl) complex. The acceleration of catalysis is proposed to be the result of the Pd→Ti interaction stabilizing the rate-limiting transition state, TS1, with the barrier found to be approximately ~8 kcal/mol lower for the heterobimetallic complex than for monometallic Pd complexes (Figure 1.9).[77]

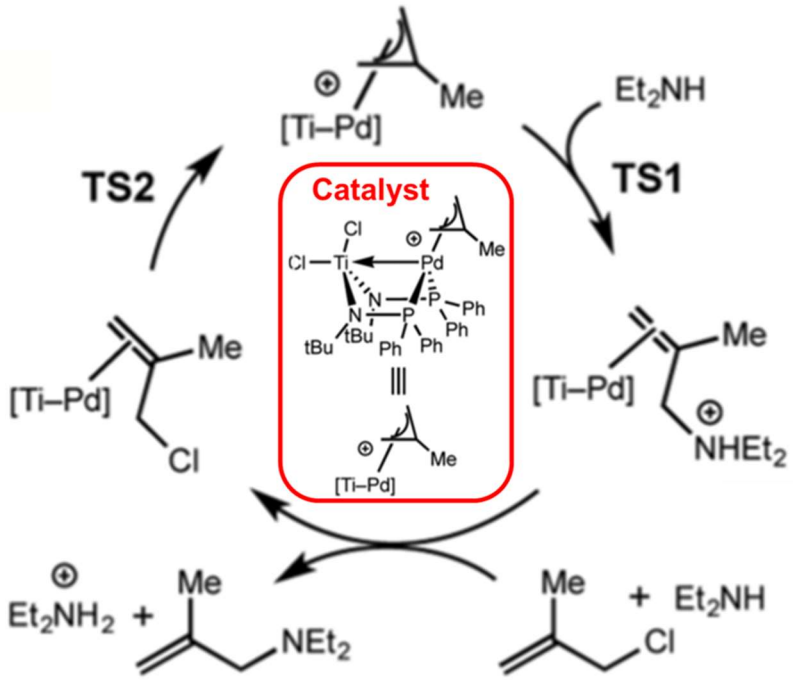

Figure 1.9. Catalytic cycle for allylic amination, where dramatically improved catalytic rates and yields were concluded by Michaelis and co-workers to be attributable to a Pd→Ti dative metal-metal interaction. Figure adapted from ref. 77.

The authors propose that electron-withdrawal by Ti from Pd via the dative interaction aides in stabilizing the developing Pd(0) oxidation state which is formed in the product of the first step of the reaction via TS1. In other words, the dative bond with Ti results in the Pd(methallyl) fragment being a better electrophile which can more readily interact with the incoming $NHEt_2$ nucleophile, which occurs via the stabilization of the Pd−C π^* orbitals from a molecular orbital perspective.[77] This example illustrates that subtle electronic modulation of an active metal center by a supporting metal through a dative interaction can serve to dramatically influence catalytic activity in a favorable way relative to that of the active metal alone without a supporting metal.

1.4 From Strong Metal-Metal Bonding to Dative Bonding: Using Our Phosphinoamide Ligand Framework as an Example to Illustrate Differences in Reactivity

As illustrated by the examples in the previous sections, both strong metal-metal bonding and weaker, more flexible dative interactions can allow for multi-electron reactivity with small molecule substrates to be realized. Our group's previously reported heptadentate tris(phosphinoamido)amine ligand, ($[N(o\text{-}(NCH_2P^iPr_2)C_6H_4)_3]^{3-}$, abbreviated as L), has afforded us the opportunity to compare the reactivity of bimetallic complexes featuring a multitude of different metal-metal pairings ($M_1{-}M_2$) with varying degrees of bonding interactions between the two metals, ranging from a dative bond to a quintuple bond (Figure 1.10).[31, 51, 78] While metal-metal bonds can allow for multi-electron redox capability and help facilitate desirable reactivity in many cases, as illustrated by our report of a bimetallic CoCoL complex which catalyzes the six-electron reduction of N_2 to trimethylsilyl amine,[30, 79] the propensity of stronger metal-metal bonds to limit reactivity with substrate has often been observed. This tendancy for strongly metal-metal bonded species within our ligand framework to limit reactivity with substrate is illustrated nicely by comparing the reactivity with N_2 of anionic $[M_1CrL]^-$ complexes for the case where M_1=Fe and Co (Figure 1.10).[30]

In this instructive comparison, the $[FeCrL]^-$ complex does not bind N_2,[80] whereas substitution of Fe in $[FeCrL]^-$ for Co, which is generally worse than Fe at π-back-bonding to N_2,[81] results in N_2 binding to form $[(N_2)CoCrL]^-$.[82] To understand this dichotomy in N_2 binding, it is instructive to note that the linear configuration of $N_2{-}M_1{-}M_2$ bonding requires that N_2 π-back-bonding competes with $M_1{-}M_2$ π-bonding

for electron density from M_1, which is typically a more electronegative late transition-metal bound to the phosphine donor set of the ligand (Figure 1.10).

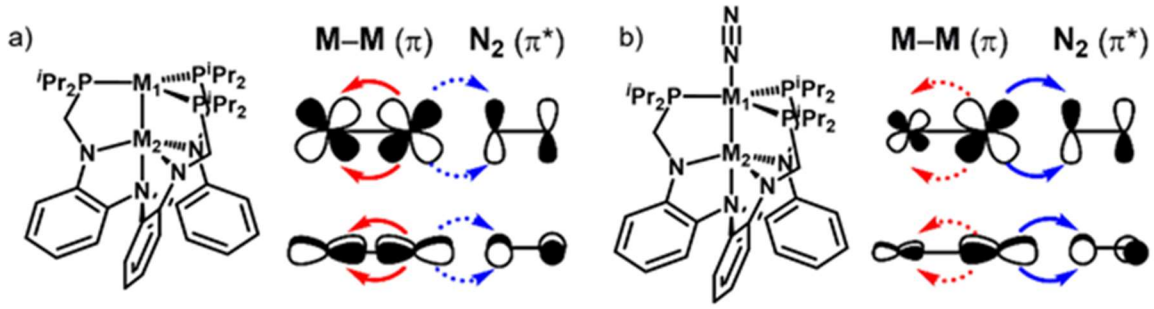

Figure 1.10. (a) Structure of a generic bimetallic complex, M_1M_2L within our phosphinoamide ligand framework (L), which has an apical binding site at M_1 to which N_2 can bind to form $(N_2)M_1M_2L$ (b). Visual illustrations of the competition between $M_1{-}M_2$ π-bonding and $M_1{\rightarrow}N_2$ π-back-bonding for $M_1{-}M_2$ bonds of varying strength and polarization are shown, with solid lines indicating which type of bonding has outcompeted the other (dashed lines) in each case. Figure adapted from ref. 30.

This competition between metal-metal bonding and metal-substrate bonding is evidenced by an excessively large increase of ~0.5 Å in the $Co{-}M_2$ distance in moving from CoM_2L to $[(N_2)CoM_2L]^-$ (M_2 = V, Cr, and Co), which indicates substantial weakening and/or cleavage of the $Co{-}M_2$ bond, though the addition of an electron to a $Co{-}M_2$ π* anti-bonding orbital also typically gives rise to a ~0.1 Å increase in the $Co{-}M_2$ bond.[82] The necessity of cleaving the $M_1{-}M_2$ bond to bind N_2 further underscores the differences between $[FeCrL]^-$ and $[(N_2)CoCrL]^-$. Fe and Cr have more similar *d*-orbital energies than do Co and Cr, which results in the formation of stronger and more delocalized π-bonds in $[FeCrL]^-$, as shown by the more covalent M−M π-bonding in Figure 1.10a. Thus, breaking the strong, delocalized Fe−Cr triple bond (σ + 2π) in order to bind N_2 is not as favorable as breaking the weaker, more polarized Co−Cr π-bonds (Figure 1.10b), thereby explaining the differences in N_2 binding between the two complexes.[30]

The requirement of cleaving or substantially weakening the M_1−M_2 bond in order to bind N_2 was not observed to as drastic of an extent for complexes with weaker M_1−M_2 bonds and polarized dative bonds (M_1→M_2) by previous research in our group. For example, the Co→Al dative bond in $[(N_2)CoAlL]^-$ remains intact even with N_2 bound, as evidenced by the Co−Al bond distance of 2.507(2) Å remaining similar to the sum of the Pauling single-bond radii for Co and Al (2.41 Å).[30, 83] In contrast, the Co−M bonds in $[(N_2)CoM_2L]^-$ complexes (M_2 = V, Cr, and Co) are significantly longer than the sum of the single-bond radii, with the strongest interaction of the trio being that in CoCrL, where the Co−Cr bond distance of 2.538(1) Å is still substantially longer than the sum of the single-bond radii of Co and Cr (2.33 Å).[82] Thus, it would seem that weaker M_1→M_2 dative bonds within our ligand framework may allow for a greater degree of flexibility, in that they allow for the binding of substrates like N_2 without requiring substantial weakening or breaking of the M−M bond. And while utilizing a supporting metal like Al, which is redox-inactive, may not readily allow for a similarly rich redox profile as a bimetallic complex featuring multiple redox-active transition metals, the multi-electron redox capability of the latter is rendered ineffective if small molecules are unable to bind and be activated toward multi-electron reactivity in the first place due to prohibitively strong metal-metal bonding.

1.5 Introduction to the NiML System and Synthetic Examples Which Outline Cooperative Strategies for Affecting Multi-Electron Reactivity with Ni Catalysts

The phosphinoamide ligand, L (Figure 1.10), is the ligand that will be used in nearly all of the chemistry that will be discussed in this thesis. Specifically, the use of this ligand to facilitate the synthesis of bimetallic Ni complexes featuring a dative bond

between Ni and a group 13 metal ion (M_1=Ni and M_2=Al, Ga, In in Figure 1.10) will be considered further in the ensuing chapters. The primary goal of this work is to enable challenging catalytic reactions using these Ni complexes that typically requires precious metal catalysts, which is an attractive prerogative due to the earth-abundance and low cost of Ni relative to precious metals. While mononuclear Ni complexes are not typically able to homogeneously catalyze multi-electron processes such as hydrogenation, the reactivity of [Ni−Fe]-hydrogenase lends insight into how supporting metals and ligands might cooperate to facilitate such reactivity at Ni. Namely, the cooperation of Lewis basic and Lewis acidic functionalities with Ni facilitate the heterolytic activation of H_2 in the enzyme active site, with the coordinated cysteine residue acting as a Lewis base and the adjacent Fe metal center acting as a complementary Lewis acidic moiety.

Figure 1.11 shows two synthetic examples which follow this paradigm, with the assistance of either a coordinated or pendant Lewis basic functionality facilitating heterolytic H_2 activation at Ni.

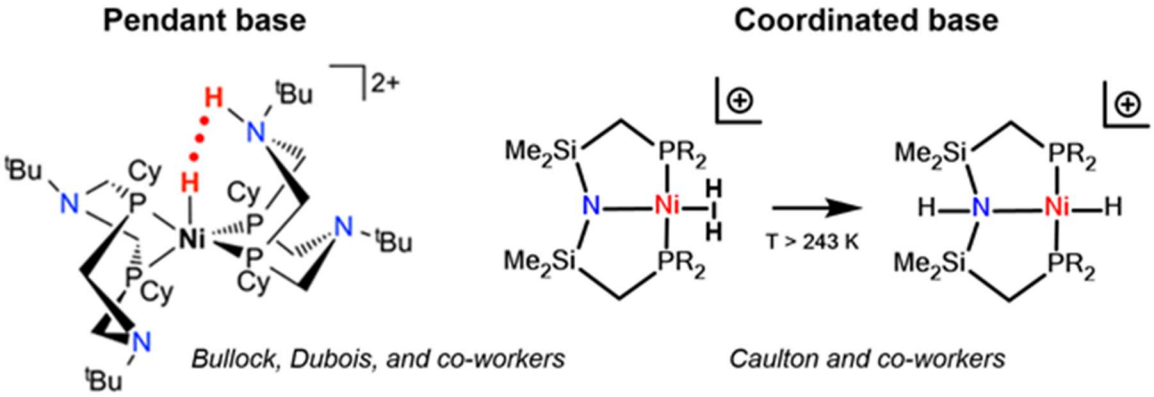

Figure 1.11. (a) Cooperative activation of H_2 by a pendant amine in $[Ni(PR_2NR'_2)_2]^{2+}$ complexes reported by Bullock, DuBois, and co-workers. (b) Heterolytic cleavage of H_2 across a Ni−N_{amide} bond to give a coordinated amine and a Ni−H at ambient T, as reported by Caulton and co-workers. Figure adapted from refs. 84-89.

Bullock, DuBois, and co-workers have reported a series of $[Ni(PR_2NR'_2)_2]^{2+}$ complexes, where R and R' are varied to modify the steric and electronic properties of the ligand.[84-87] These complexes were designed with pendant amine bases which are able to assist Ni in the heterolytic activation of H_2, with the basic amine moiety accepting a proton and the Lewis acidic, cationic Ni(II) center accepting a hydride (Figure 1.11a). This cooperation between the metal and the ligand where the pendant amines serve as proton relays allows the $[Ni(PR_2NR'_2)_2]^{2+}$ complex with R = R' = Ph to be a remarkably efficient electrocatalyst for the two-electron reduction of protons to H_2, with a reported turnover frequency (TOF) of 106,000 s^{-1} in acetonitrile with 1.2 M water and protonated dimethylformamide as the proton source.[85] Amazingly, this bifunctional Ni catalyst is substantially more active than the [FeFe]-hydrogenase enzyme itself, which has a turnover frequency (TOF) of 9,000 s^{-1} at 30 °C and also utilizes a pendant amine moiety to assist in H_2 activation.[88] The reductions of protons to H_2 is a process for which Pt catalysts are typically utilized, and so this system elegantly illustrates that excellent catalytic performance can also be achieved with an Earth-abundant metal like Ni with optimal ligand cooperation.

Alternatively, the basic moiety which assists the metal in substrate activation can be coordinated to the metal center, as was seen in the case of the cysteine residue in the active site of [NiFe]-hydrogenase and in the case of a coordinated amide in work by Caulton and co-workers (Figure 1.11b). Initial binding of H_2 to the $[(PNP)Ni]^+$ complex, where PNP is $N(SiMe_2CH_2P^tBu_2)_2$, occurs at low T, with heterolytic cleavage to form $[(PN(H)P)NiH]^+$ occurring via the addition of H_2 across the $Ni{-}N_{amide}$ bond upon warming to > 243 K.[89] Apart from these selected examples, Hansen and co-workers have

also studied similar metal-ligand cooperativity for Ni and Co complexes with coordinated amides,[90-92] and pioneering work in the area of utilizing metal-ligand cooperativity for H_2 activation and catalytic hydrogenation was conducted by Noyori, Milstein, Morris, and their respective co-workers, among others.[93-95]

Metal-ligand cooperativity is especially important for H_2 activation at Ni, since a mononuclear Ni center has not been reported to facilitate the oxidative addition of H_2 to give a Ni dihydride species.[44] Oxidative addition of H_2 requires M $d_\pi \rightarrow H_2$ σ^* back-donation to cleave the H−H bond and represents a net two-electron oxidation of the metal center, which precious metals are able to carry out readily.[45] Even among late first-row metals, Ni is a poor π-back-donor, as it is more electronegative and less π-basic than Fe and Co, which in the context of H_2 activation results in worse energetic overlap between the Ni d_π and H_2 σ^* orbitals.[30, 81] Future chapters of this thesis will further explore the inherent limitations of Ni in H_2 activation and hydrogenation catalysis, with the strategies discussed in this chapter applied to varying extents to circumvent these limitations where possible.

While metal-ligand cooperativity is essential to enabling multi-electron reactivity at Ni, it need not take the form of assistance by a Lewis basic functionality. Although transition metals are typically thought of as Lewis acids which bind Lewis basic ligands, a late transition metal paired with a Lewis acidic ligand could also allow for cooperative heterolytic cleavage of H_2. This strategy is exemplified by the (^{Mes}DPB^{Ph})Ni complex (where ^{Mes}DPB^{Ph} is ArB(*o*-$PPh_2C_6H_4)_2$ with Ar = mesityl) reported by Peters and co-workers, which features a dative bond between a low-valent Ni(0) center and a Lewis acidic borane moiety, which acts as an σ-acceptor, or Z-type, ligand (Figure 1.12a).[44]

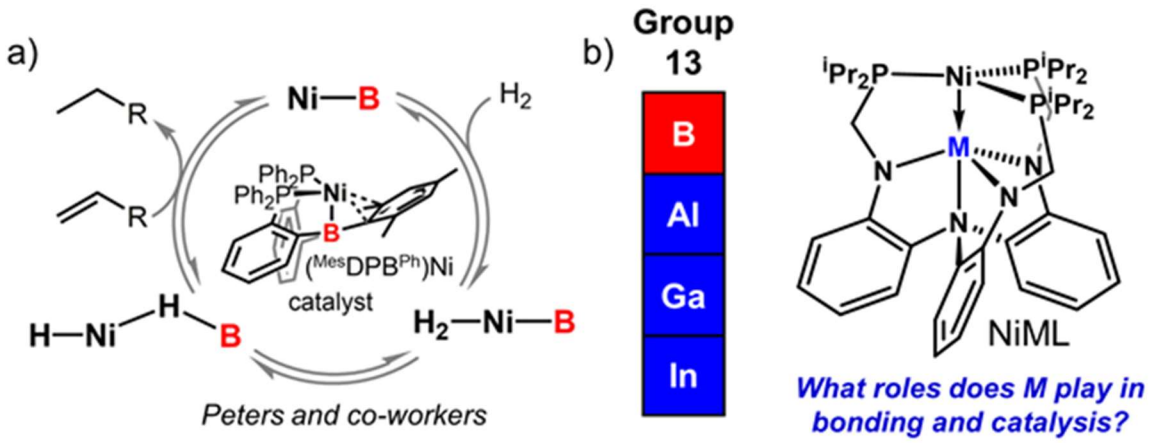

Figure 1.12. (a) Cooperative H_2 activation by the (^{Mes}DPB^{Ph})Ni complex reported by Peters and co-workers, which catalyzes olefin hydrogenation. (b) Comparison to NiML complexes which will be discussed in this thesis, where the supporting metal has been varied down group 13 (Al, Ga, In). Figure adapted from refs. 44 and 97.

Exposure of (^{Mes}DPB^{Ph})Ni to 1 atm H_2 generates (^{Mes}DPB^{Ph})(μ-H)NiH, which has a terminal Ni−H and a hydride bridging between Ni and B. In this reaction, Ni acts as a Lewis base to facilitate the heterolytic activation of H_2, with the Lewis acidic borane moiety serving to stabilize a hydride as a bridging hydride. This transformation represents a net oxidative addition of H_2 across the Ni→B bond, where the resulting Ni dihydride species which is typically unstable to H_2 loss is stabilized by the Lewis acidic borane (Figure 1.12a). The transition metal acting as a Lewis base is a role reversal from the heterolytic activation reported by Caulton and co-workers (Figure 1.11b). Ni is best described as Ni(0) in the neutral (^{Mes}DPB^{Ph})Ni complex, as compared with cationic Ni(II) in the Caulton system, rendering the metal centers well-suited for their roles as a Lewis base and Lewis acid, respectively. Upon heterolytically activating H_2, the (^{Mes}DPB^{Ph})Ni complex catalyzes the hydrogenation of terminal olefins to alkanes, with a 5 mol% catalyst loading in benzene giving full conversion of styrene to ethylbenzene in 1 h (TOF = 20 h^{-1}; Figure 1.12a).[44] This complex was also reported to catalyze the hydrosilylation of ketones.[96] Both olefin hydrogenation and ketone hydrosilylation are two-electron

process for which few homogeneous Ni catalysts have been reported, and so this system shows that a direct dative bond between a transition metal and a Lewis acidic, Z-type ligand can be an effective strategy for promoting multi-electron reactivity at a first-row metal center.

Figure 1.12b shows a comparison of the (^{Mes}DPB^{Ph})Ni complex with the NiML complexes that will be discussed in this thesis. We reasoned that varying the supporting group 13 metal ion might be a powerful lever by which to tune reactivity at Ni.[97] Such an approach has seldom been realized, owing in part to the synthetic challenge of incorporating main group elements into ligand scaffolds.[98-101] Our double-decker, phosphinoamide ligand, L, allows for facile formation of different M(III) metalloligands, obviating the need for *de novo* ligand synthesis.[51, 78] Like the (^{Mes}DPB^{Ph})Ni complex, the NiML complexes feature dative bonds between a Ni(0) metal center and a supporting group 13 M(III) ion, which acts as a Z-type metalloligand to Ni.[78, 97] As highlighted in the caption of Figure 1.12b, the roles of the supporting metal in bonding with Ni, as well as in reactivity and catalysis at the active Ni metal, are key questions that this thesis will explore. Before further outlining the studies of the NiML complexes that will be presented in this thesis, the next sections will discuss the nature of bonding between transition metals and group 13 M(III) ions acting as Z-type ligands, as well as examples of catalytic reactivity mediated by these complexes.

1.6 Bonding Between Transition Metals and Group 13 Z-type σ-Acceptor Ligands

The notion that Lewis acidic moieties such as boron trihalides could serve as σ-acceptor ligands and form dative bonds with transition metals was originally proposed in the early 1960s.[102-103] In addition to boranes, the propensity of other electron-deficient

Group 13 molecules, such as alanes, to act as Lewis acids was also recognized.[104] The first structurally characterized examples of bonding between transition metals and Lewis acidic boranes and alanes are shown below (Figure 1.13).[104-107]

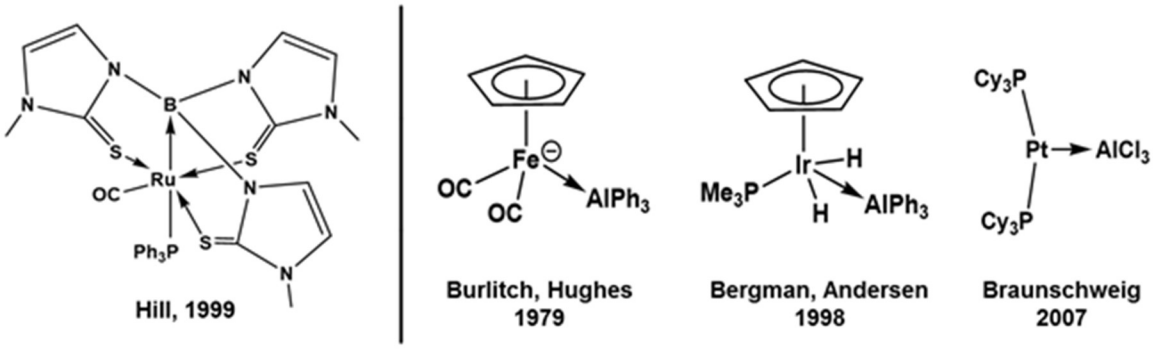

Figure 1.13. First structurally characterized examples of bonding between transition metals and boranes (left) and alanes (right). Adapted from refs. 78 and 104-107.

Hill and co-workers utilized a Lewis acidic borate ligand with additional sulfur donor moieties, allowing for the transition metal to bind in close proximity to the Lewis acidic site (Figure 1.13).[106] Unlike the metal-boranes reported by Hill and co-workers, the first metal-alanes to be structurally characterized featured unsupported M→Al interactions (Figure 1.13). The use of multidentate ligand scaffolds with multiple donors adjacent to a Lewis acidic site has become a widely employed strategy for the synthesis of complexes with transition metal-Lewis acid interactions.[99, 108]

Transition metal-Lewis acid bonding represents a role reversal from traditional metal-ligand interactions. Transition metals typically serve as electron-acceptors, with ligands donating two electrons (L-type) or one electron (X-type). Interactions with L-type and X-type donor ligands destabilize the metal-based *d*-orbitals, with stabilization of the bonding electrons in predominately ligand-based orbitals to form dative covalent and covalent bonds, respectively (Figure 1.14).[109] Lewis acidic ligands that do not donate any electrons, and instead accept two electrons from the transition metal, are called Z-type

ligands. Transition metal bonding to Z-type ligands is an unusual case in that the transition metal serves as only an electron-donor, or Lewis base. Electron donation from metal to ligand in the form of π-back-bonding also contributes substantially to the bonding of CO, N_2, and isocyanide ligands with transition metals, but in those cases σ-donation from ligand to metal also contributes significantly.[109-110]

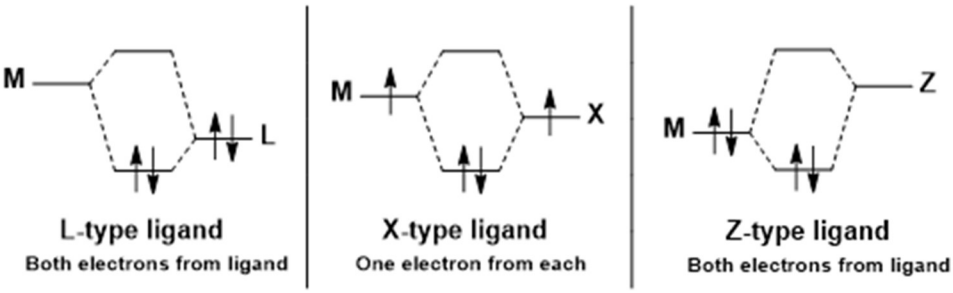

Figure 1.14. Molecular orbital diagrams depicting the fundamental interactions of L-, X-, and Z-type ligands with a transition metal, M. Figure adapted from refs. 109-111.

The extent of electron transfer from a transition metal to a Z-type ligand and the resulting effect on the oxidation state and *d*-electron count at the transition metal center can be somewhat ambiguous.[111] Based on the ubiquitous MLX formalism, an L-type ligand donates both bonding electrons and does not alter the *d*-electron count of the metal to which it binds. An X-type ligand and the metal each provide one electron to form a covalent bond, thereby reducing the *d*-electron count of the metal by one electron (Figure 1.14).[109] Following this logic, Parkin proposed that a Z-type ligand should oxidize the metal center by two *d*-electrons, as both the electrons in the dative bond formed are from the metal center.[112] This formulation represents one extreme in what can be thought of as a continuum of electron transfer from the transition metal to the Lewis acid. Alternatively, the other end of the continuum would be characterized by a dative interaction with more minimal electron transfer from metal to ligand that does not result in a formal change in the *d*-electron count of the metal. Representative examples of

complexes that are best described as approaching each limiting case have been selected to provide insight into the best description of the oxidation state of a transition-metal bonded to a Z-type ligand (Figure 1.15).

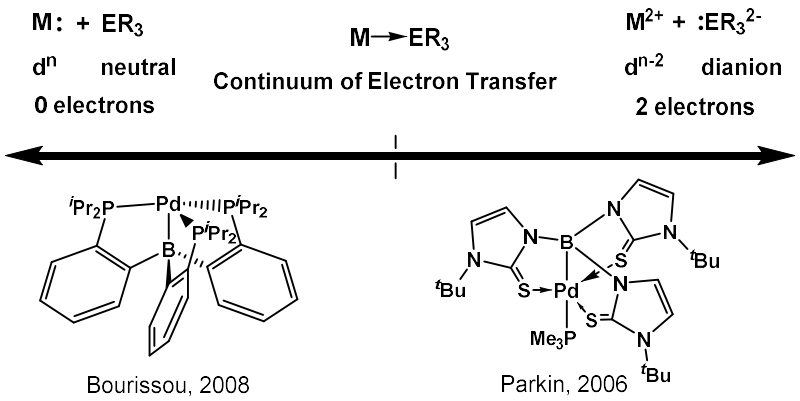

Figure 1.15. Continuum of electron transfer in transition metal bonding to Z-type ligands, ER_3, where E is a Group 13 atom. Examples of complexes that have been assigned by their respective authors to be closer to each limiting case are displayed above. Adapted from refs. 101 and 113.

Parkin and co-workers proposed a Pd(II) oxidation state for a palladaboratrane supported by a similar ligand framework to that used by Hill and co-workers (Figure 1.15).[113] On the contrary, Bourissou and co-workers reported a palladaboratrane that is best described as containing zero-valent palladium (Figure 1.15).[101] While a greater degree of electron transfer can be inferred by a shorter Pd−B distance of 2.050 Å in Parkin's palladaboratrane, compared with a distance of 2.254 Å in the case of Bourissou's complex, the potential redox non-innocence of the borate ligand in Parkin's complex is another confounding factor.[101, 112-113] The Pd(0) formulation in Bourissou's palladaboratrane is supported by characteristic Pd(0)−P bond distances and natural bond orbital (NBO) calculations, which were performed in order to estimate the natural charge on each atom. Such an analysis predicts approximately 0.3 additional units of negative

charge buildup on the B atom upon installation of Pd, consistent with only minimal formal electron transfer.[101, 114]

Recognizing the ambiguity in assigning oxidation states to transition metals that are interacting with Z-type ligands, Hill and co-workers proposed the adoption of the metal-nitrosyl notation of Enemark and Feltham.[111, 115-116] This notation would denote each of the two examples as $\{PdB\}^{10}$, indicating that the 10 electrons are distributed between Pd and B in both cases (Figure 1.15). In any case, it is clear that the extent of electron transfer from transition metal to Z-type ligand is complex-dependent and lies somewhere in between the two aforementioned extremes. However, computational studies like that of Bourissou have generally favored a description in which there is only limited electron transfer to the Z-type ligand, leaving the formal oxidation state of the transition metal unchanged.[101] Likewise, a zero-valent oxidation state for Ni was also concluded to be the best description for the (^{Mes}DPB^{Ph})Ni complex of Peters and co-workers, as well as the closely related (^{Ph}DPB^{iPr})Ni(H_2) complex.[44, 117] Computational studies of the NiML complexes which will be discussed in this thesis also favor a Ni(0)/M(III) formulation, indicating minimal formal electron transfer from Ni to M. However, it should be noted that this is simply a formal oxidation state assignment, and that the true oxidation state of Ni in the NiML complexes lies somewhere in between Ni(0) and Ni(II). Although the oxidation state is closer to Ni(0) based on experimental and computational studies that will be presented in this thesis, much of the reactivity that was observed for the NiML complexes is predicated on the Lewis acidic group 13 supporting metal rendering Ni more electron-deficient than a typical Ni(0) metal center.

1.7 Multi-electron Processes Catalyzed by Complexes with Dative Bonds between a Transition Metal and a Group 13 σ-Acceptor Ligand

Apart from the previously discussed (^{Mes}DPB^{Ph})Ni complex which catalyzes olefin hydrogenation and hydrosilylation, group 13 σ-acceptor ligands have been shown to be adept at stabilizing low-valent metals which are reactive toward H_2 and N_2, among other small molecule substrates.[78, 83, 118-124] Figure 1.16 shows two different examples of multi-electron reactivity catalyzed by complexes featuring dative bonds between a transition metal and a group 13 σ-acceptor ligand.

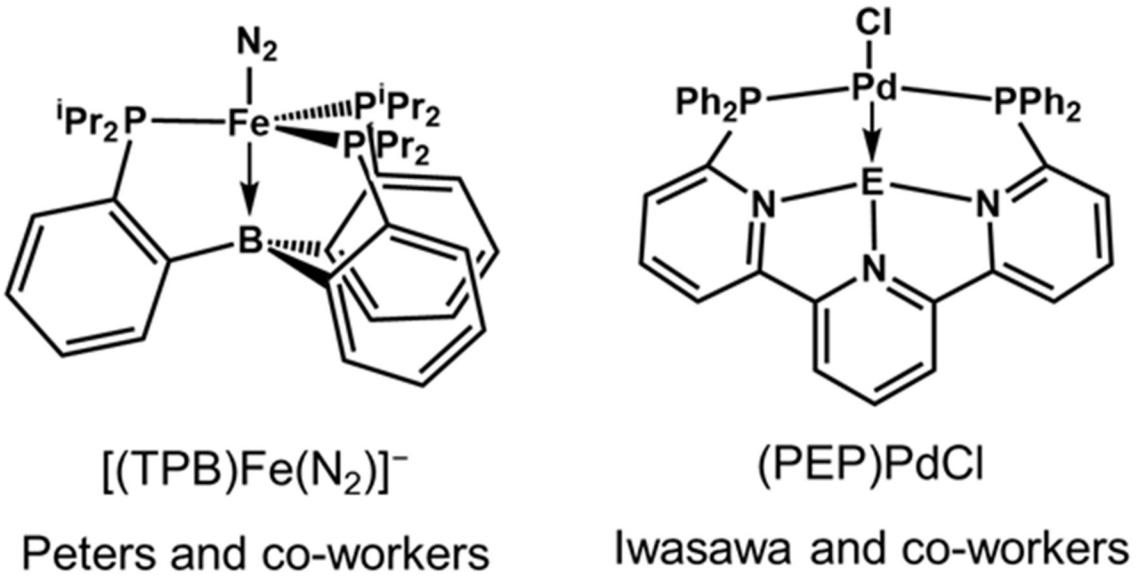

Figure 1.16. Two examples of transition metal-group 13 complexes which catalyze multi-electron transformations. Peters and co-workers reported catalytic conversion of N_2 to NH_3 with $[(TPB)Fe(N_2)]^-$ (left), and Iwasawa and co-workers reported (PEP)PdCl (right; E=Al, Ga, In) to be a highly active pre-catalyst for CO_2 hydrosilylation. Figure adapted from refs. 125-127.

Peters and co-workers have reported an anionic Fe−N_2 complex, $[(TPB)Fe(N_2)]^-$, where TPB = tris-(*o*-diisopropylphosphinophenyl)borane, which catalyzes the six-electron reduction of N_2 to NH_3 with a turnover number (TON) of 59 (±6) that surpasses the state-of-the-art Mo catalysts for this reaction (Figure 1.16).[125-126] The catalytic

activity of $[(TPB)Fe(N_2)]^-$ is made possible by the borane forming a flexible dative bond to Fe that allows for the stabilization of both π-acidic (N_2) and π-basic ($[NH_2]^-$) fragments in various catalytic intermediates, many of which have proven isolable. Another example of the employment of group 13 σ-acceptor ligands to facilitate catalysis at a proximal transition metal center is the isostructural series of (PEP)PdCl complexes reported by Iwasawa and co-workers, where PEP is 6,6"-bis(diphenylphosphino)-2,2':6',2"-terpyridine and the group 13 metal (E) is bonded to two chlorides (Figure 1.16).[127] At low catalyst loadings (0.1 mol%) of the Pd→Al analogue and using Cs-pivalate to activate the Pd−Cl bond and initiate catalysis, CO_2 hydrosilylation to give $OC(H)OSiMe_2Ph$ was catalyzed with the highest reported activity to date (TOF =19,300 h^{-1}). Additionally, a significant tuning effect of the supporting group 13 metal was observed, with catalysis proceeding in quantitative yield in 3 h in the case of E=Al, but only reaching 10% and 7% yield after 24 h for the catalysts with E=Ga and E=In, respectively.

These examples show the potential utility of group 13 σ-acceptor ligands in promoting catalysis at transition metals to which they are directly bonded. Other relevant literature complexes featuring dative bonds between transition metals and group 13 σ-acceptor ligands, as well as their reactivity and catalytic applications, will be discussed within each chapter where appropriate to inform and provide context for the investigation of the NiML complexes.

1.8 Our Strategy for Enabling Uncommon Reactivity and Catalysis at Ni: Overview of an Isostructural Series of NiML Complexes (M=Al, Ga, In)

As alluded to in Figure 1.12b and discussed briefly in section 1.5, this thesis will focus on an isostructural series of bimetallic complexes featuring dative bonding between Ni and various group 13 metalloligands (Al, Ga, In). One of the objectives of this work is to understand the effect of the dative bond with the supporting group 13 metal on the properties and reactivity of Ni, with the ultimate goal to rationally identify the optimal supporting metal(s) that allows the NiML complexes to catalyze challenging multi-electron transformations which mononuclear Ni complexes are unable to mediate.

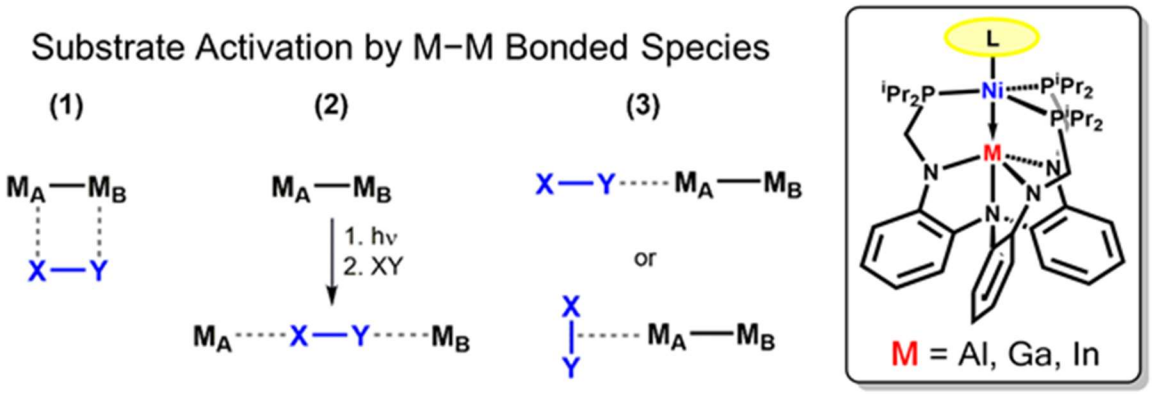

Figure 1.17. Three modes of X−Y bond activation at a metal-metal bonded unit (M_A−M_B), along with the structure of the NiML complexes, which feature an open binding site at Ni where substrate binding and activation can occur. Figure adapted from ref. 30.

Figure 1.17 shows three different types of substrate activation for metal-metal bonded species, which have been discussed through the lens of the literature examples presented in this chapter. For example, cooperative activation across the M_A−M_B bond in which both metals directly interact with substrate (type 1, Figure 1.17) was observed in the cases of H_2 activation by the (^{Mes}DPB^{Ph})Ni catalyst of Peters, alkyne activation by the [^{iPr}NDI]Ni$_2$(C_6H_6) catalyst of Uyeda, CO_2 activation by the Co(^{i}Pr$_2$PNMes)$_3$Zr(THF)

complex of Thomas, and azobenzene activation by the (^{tbs}L)Fe_3(THF) cluster of Betley. As has been illustrate by these examples, cooperative activation of the substrate X−Y bond across the M_A−M_B bond can occur in either a homolytic or heterolytic fashion, a distinction which typically depends on the polarity of both the M_A−M_B and X−Y bonds. The breaking of the metal-metal bond to allow both fragments to interact separately with substrate (type 2, which may or may not involve photolysis, Figure 1.17) was observed in the C−H borylation chemistry mediated by the (IPr)Cu−$FeCp(CO)_2$ catalyst reported by Mankad and co-workers. Lastly, the binding and activation of substrate at a single active metal that is interacting with a supporting metal (type 3) describes the allylic amination catalysis mediated by the $Cl_2Ti(N^tBuPPh_2)_2Pd(\eta^3$-methallyl) complex reported by Michaelis and co-workers, as well as the (PEP)PdCl catalyst for CO_2 hydrosilylation reported by Iwasawa and co-workers.

As the diagram of the NiML complexes shows in Figure 1.17, Ni has an open coordination site to which substrate can bind, but the supporting metal is not readily accessible for direct interactions with substrate. Thus, our system is classified as the third type of substrate activation, where a single active metal binds and activates substrate, with the supporting metal serving to tune the electronic environment of the active metal via the metal-metal interaction.[30] Relegating the second metal, M_B (Al, Ga, In), to a supporting role in which it primarily only serves to modulate the electronic environment of the active metal, M_A (Ni), was a key concept of our strategy. Coupling this paradigm with systematic variation of the supporting metal further streamlines understanding by isolating the effect of the supporting metal on substrate binding and catalysis at the active metal. Although Ni is often a poor catalyst relative to precious metals for multi-electron

processes, we hope to address these inherent shortcomings by favorably altering its properties via dative bonding to group 13 metalloligands (Figure 1.17).

The next chapter of this thesis (chapter 2) will discuss the synthesis and characterization of the isostructural series of NiML complexes.[97] Both steric and electronic effects of the supporting group 13 metal on Ni will be proposed based on x-ray crystallography and cyclic voltammetry (CV) studies, and the perturbations of the supporting metal on the electronic structure will be identified via UV-vis spectroscopy in conjunction with time-dependent density functional theory (TD-DFT) calculations. Comparisons to a similarly-ligated mononuclear Ni complex without a supporting metal, $NiLH_3$, will also be made where appropriate to more definitively elucidate the effect of the supporting metal.[51] The extent to which our findings are generalizable for other systems with direct dative bonding between transition metals and group 13 metalloligands will also be considered.

Chapter 3 will examine the propensity of the NiML complexes to bind small molecule substrates, including H_2, N_2, CO, CO_2, and C_2H_4, at the open coordination site at Ni. Experimental studies on the thermodynamics and kinetics of H_2 and N_2 binding to the NiML complexes, as well as qualitative observations regarding the binding of CO, CO_2, and C_2H_4, will be presented, thereby allowing for the relative order of binding strength as a function of the supporting metal to be elucidated. The specific molecular orbital interactions between the small molecules, Ni, and the supporting metal which facilitate small molecule binding were identified via a combination of UV-vis spectroscopy, theoretical calculations, and thermodynamic binding studies. Rare, nonclassical dihydrogen complexes were characterized by NMR spectroscopy, isotopic

labelling experiments, and single-crystal neutron diffraction studies, and these (η^2-H_2)NiML complexes were found to be the initial intermediate formed in the catalytic hydrogenation reactivity which will be discussed in chapters 4 and 5.

Chapter 4 will discuss the propensity of NiML complexes to mediate the catalytic hydrogenation of olefins to alkanes, a two-electron process for which few homogeneous Ni catalysts have been developed.[97] A dramatic tuning effect of the supporting metal was observed (Ga >> In), with an Al supporting metal or no supporting metal ($NiLH_3$) not resulting in any catalytic activity. The catalytic mechanism was examined by a combination of experimental and computational studies in order to understand the relative catalytic performance of the various bimetallic complexes and the roles played by the supporting metal in catalysis.[30]

Chapter 5 focuses on the catalytic hydrogenation of CO_2 to formate mediated by the NiML complexes in the presence of base, which represents an energetically-relevant two-electron reduction of CO_2 for which Ni complexes have previously been poor catalysts relative to both precious metals and other first-row metals (Fe, Co). Anionic Ni(0) hydride species which are potent hydride donors were found to be key intermediates in catalysis which spontaneously react with CO_2 to generate anionic formate adduct intermediates. These two species, along with the NiML and (η^2-H_2)NiML complexes, are the primary intermediates in proposed the catalytic cycle, and all four have been isolated and thoroughly characterized.[128] Computational studies allowed for an appreciation of subtler nuances in the catalytic mechanistic,[129] and experimental studies of the thermodynamic and kinetic favorability of each fundamental step in the catalytic mechanism as a function of the supporting metal allowed for the relative catalytic

performance of the NiML complexes (Ga > In > Al > no support) to be understood. Lastly, a comprehensive thermodynamic scheme was constructed which helps to illustrate the reactivity of the NiML complexes with protons, electrons, and H_2.

Collectively, the results that will be presented in this thesis demonstrate that modulating a transition metal center via a direct interaction with a group 13 Lewis acidic supporting metal can be a powerful strategy for promoting new reactivity paradigms in base metal catalysis.

Chapter 2

Synthesis and Characterization of an Isostructural Series of Ni Bimetallic Complexes Featuring Dative Ni→M Bonds to Lewis Acidic Group 13 Metalloligands

In part from:

Cammarota, R. C.; Lu, C. C.* "Tuning Nickel with Lewis Acidic Group 13 Metalloligands for Catalytic Olefin Hydrogenation." *J. Am. Chem. Soc.* **2015**, *137,* 12486-12489.

Cammarota, R. C.[‡]; Xie, J.[‡]; Vollmer, M. V.; Linehan, J. C.; Burgess, S. A.; Gagliardi, L.; Wang, X. P.; Hoffmann, C.; Young, V. G., Jr.; Lu, C. C.* "Lewis Acidic Group 13 Metalloligands Poise a Proximal Nickel Center for Small Molecule Binding: Thermodynamic and Kinetic Binding Studies and Neutron Diffraction Structure for an Isostructural Series of Ni(η^2-H_2) Adducts." **2018**, *manuscript in preparation*.

Vollmer, M. V.; Xie, J.; **Cammarota, R. C.**; Gagliardi, L. Bill, E.; Lu, C. C.* "Formel Nickelate(−I) Complexes Supported by Group 13 Ions: Where are the Valence Electrons?" *Ang. Chemie Int. Ed.* **2018**, *accepted*.

2.1 Overview and Introduction

Two new NiML bimetallic complexes featuring dative Ni→M bonds to Lewis acidic group 13 supporting metals (M=Ga, In) have been synthesized, utilizing the previously reported heptadentate tris(phosphinoamido)amine ligand ([N(*o*-($NCH_2P^iPr_2$)C_6H_4)$_3$]$^{3-}$, abbreviated as L).[78] The double-decker ligand allows for step-wise metalation to install group 13 M(III) ions in the amide (N_3) binding pocket, followed by subsequent metalation of Ni(0) into the phosphine (P_3) binding pocket.[97] In conjunction with the previously reported NiAlL complex[78], these three NiML bimetallic complexes represent an isostructural series in which the supporting metal has been varied down group 13, from Al to Ga to In. This series was targeted to assess the influence of the interaction with the supporting metal on the electronic environment of Ni, as well as on the propensity of Ni to react with substrates and mediate catalysis. Additionally, the previously reported $NiLH_3$ complex, a similarly ligated Ni(0) metal center without a supporting metal, serves as a convenient control complex for the effect of the supporting metal.[51]

In addition to allowing for a better understanding of the properties of the supporting metal which dictate bonding with Ni, it was hoped that the reactivity of Ni could be favorably modified through this metal-support interaction, such that NiML complexes might be capable of catalyzing challenging reactions not typically mediated by Ni complexes. The NiML series of bimetallic complexes is unique from most bimetallic series investigated previously in the Lu group because it consists of a constant active transition metal (Ni) and a varied supporting metal, whereas most previous series, including MCrL[51, 80], MVL[130], and MAlL complexes[78], featured the same supporting

metal and a varied active metal site across the first-row 3*d* transition metals (M=Fe, Co, and Ni, as well as M=Mn and Cr for MCrL). These early series were studied in this way with the primary goal of understanding metal-metal bonding in heterobimetallic complexes, but also in part due to the synthetic ease of generating a series of bimetallic complexes from the same metalloligand, ML. In contrast, a series of $[(N_2)CoML]^-$ complexes and their N_2 functionalization reactivity were studied with a constant active metal (Co) and a varied supporting metal across the first-row 3*d* transition metals (M=Ti, V, Cr, Co, plus Al).[30, 79, 82] Since the supporting metal serves primarily to tune the electronics of the active metal via a metal-metal bond and is essentially not accessible for direct interactions substrate in bimetallic M'ML complexes, the latter concept of a series of bimetallic complexes with a constant active metal and a varied supporting metal is more logical from the standpoint of investigating how to favorably alter the properties of the active metal for desired reactivity and catalysis. Hence, this strategy of varying the supporting metal was implemented in studying the NiML series of complexes, with the difference being that this variation was down a periodic group in the *p*-block, rather than across a periodic row in the *d*-block as was carried out for the series of $[(N_2)CoML]^-$ complexes.[30]

The isostructural series of NiML complexes was characterized by NMR spectroscopy, x-ray crystallography, cyclic voltammetry (CV), and UV-vis spectroscopy, in conjunction with time-dependent density functional theory (TD-DFT) calculations. Collectively, solid-state structures and CV studies showed that larger group 13 supporting metal ions (In > Ga > Al) withdraw more electron density from Ni via shorter normalized Ni→M dative bonds, relative to the size of the constituent metals. Steric effects of larger

group 13 supporting metals on the positions of both M and Ni relative to their respective binding pockets were revealed by the solid-state structures, with larger metals "forcing" Ni further above its preferred position of coplanar with the phosphine donor (P_3) plane.[97] The deconvolution of steric and electronic factors which combine to allow larger group 13 M(III) ions to act as stronger Lewis acids toward Ni in the NiML complexes is discussed, drawing upon related literature systems and work by other researchers in the Lu group where appropriate to inform this dichotomy. Lastly, the perturbations of the supporting metal on the electronic structure of the resulting NiML complexes was also elucidated by UV-vis spectroscopy, in conjunction with TD-DFT calculations. Overall, the steric and electronic effects of larger M(III) supporting metals render Ni more electron-poor and better geometrically positioned to bind substrates via σ-donation into a vacant, Lewis acid-stabilized molecular orbital (LUMO). This chapter will cover the characterization of the series of NiML complexes and discuss how the supporting metal influences the properties of Ni, with the rest of this thesis investigating how these effects of the supporting metal promote desirable reactivity with small molecule substrates that is uncommon for Ni complexes.

2.2 Results and Discussion

2.2.1 Synthetic Overview for New NiML Bimetallic Complexes with Group 13 Supporting Metals

The new Ni-M bimetallics, NiGaL (**2**) and NiInL **(3**), were prepared via a step-wise metalation route, analogous to the previously reported NiAlL (**1**) complex (Figure 2.1).[78]

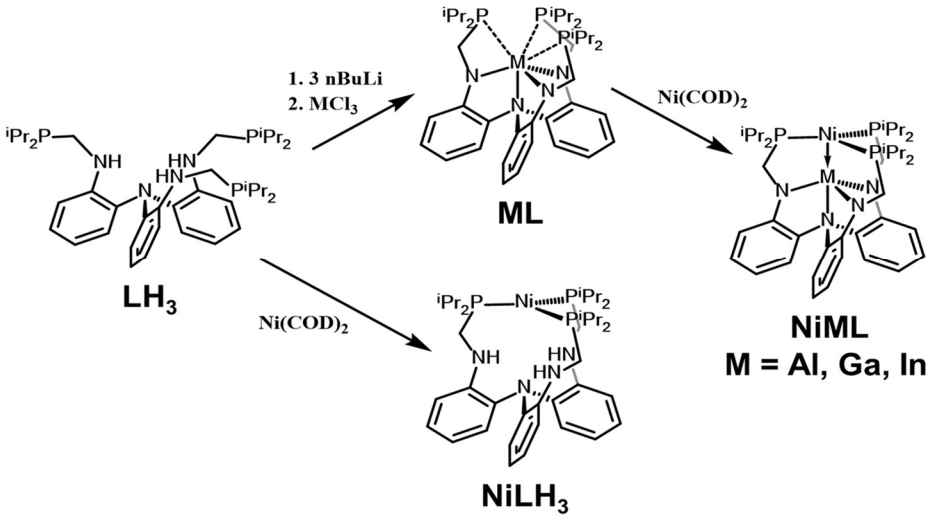

Figure 2.1. Synthetic scheme showing two-step metalation to form NiML bimetallic complexes by way of isolable monometallic ML complexes (M = Al, Ga, In). The synthesis of $NiLH_3$ is also shown,[51] and the synthesis of AlL and NiAlL was previously reported.[78]

2.2.2 Synthesis and Characterization of Monometallic ML Complexes by NMR Spectroscopy

First, deprotonation of LH_3 with 3 equiv *n*BuLi and subsequent addition of $GaCl_3$ or $InCl_3$ affords the GaL ($\mathbf{2}^{mono}$) and InL ($\mathbf{3}^{mono}$) metalloligands, respectively. Just as reported previously for AlL ($\mathbf{1}^{mono}$),[78] $\mathbf{2}^{mono}$ and $\mathbf{3}^{mono}$ were typically isolated as solids after the removal of the LiCl salt by-product via extraction into benzene and drying under vacuum. A single resonance is observed by ^{31}P NMR spectroscopy in C_6D_6 for both $\mathbf{2}^{mono}$ (15 ppm) and $\mathbf{3}^{mono}$ (39 ppm), consistent with solution-state three-fold symmetry where the three phosphine arms of the ligand are chemically equivalent. Likewise, C_{3v} symmetry is apparent from the ^{1}H NMR spectra, which clearly show the expected number of resonances for three equivalent ligand arms in both $\mathbf{2}^{mono}$ and $\mathbf{3}^{mono}$: four aryl resonances, one methylene CH_2 resonance, and one methine CH resonance, along with a large resonance for the methyl groups (Figure 2.2). It should be noted that depending on the fluxionality with which the ligand, L, binds metals, the methylene and methine

protons may either give rise to one or two resonances in the ^{1}H NMR spectrum, as will be discussed further in both this chapter and future chapters (*vide infra*).

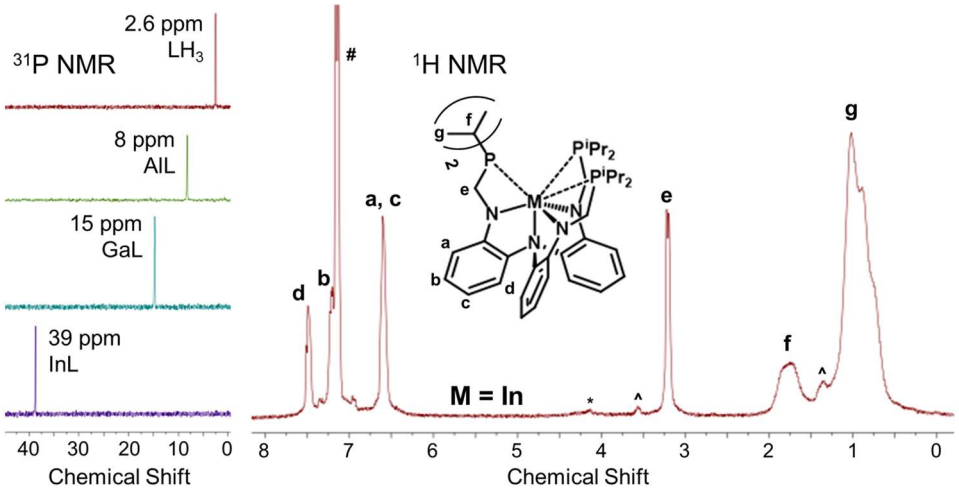

Figure 2.2. Stacked ^{31}P NMR spectra in C_6D_6 (left) comparing LH_3, AlL (**1**^{mono}), GaL (**2**^{mono}), and InL (**3**^{mono}), and the ^{1}H NMR spectrum of **3**^{mono} in C_6D_6 (right). The ^{31}P resonances shift downfield upon the installation and variation of metals down group 13. The proton resonances are assigned with labels, and solvent peaks for benzene (#) and THF (^), along with trace amounts of LH_3 as an impurity (*), are denoted.

It should be noted that in the case of **2**^{mono}, it is a distinct possibility that LiCl can remain after extraction due to the formation of a salt adduct with **2**^{mono}, which would be formulated as $(THF)_3LiCl{-}GaL$. Indeed, initial attempts to crystallize **2**^{mono} carried out by a previous graduate student provided structural evidence for this salt adduct, a testament to the Lewis acidity and affinity for halide interactions of Ga(III). To promote the separation of **2**^{mono} from LiCl, extractions were performed using even more nonpolar solvents than benzene, including pentane and hexane. In any case, essentially identical ^{31}P NMRs for **2**^{mono} were obtained regardless of whether pentane, hexane, or benzene was used as the solvent for extraction. Benzene extraction is preferable to allow more facile dissolution of large amounts of **2**^{mono} and **3**^{mono}, as well as because any residual salt that

remains can be more easily removed via later-stage purification of the resulting bimetallic NiML complexes (*vide infra*).

In thinking about the propensity of a monometallic ML complex to react with a second metal precursor to form a bimetallic complex, the degree to which the phosphine donors are coordinated to the metal (M) in ML is important. Intuitively, if a single metal coordinates the three phosphine donors too strongly and adopts an octahedral geometry by coordinating the three amide donors in addition to the phosphines, then the resulting ML complex may be too stable to react to form desired bimetallic complexes. One gauge of the degree to which the phosphines are coordinating to M in ML is to examine the chemical shift of the phosphorus nuclei by ^{31}P NMR spectroscopy. A significantly more downfield ^{31}P chemical shift is observed for **3**^{mono} (39 ppm) relative to both **2**^{mono} (15 ppm) and **1**^{mono} (8 ppm), which is indicative of relatively more de-shielded phosphorus nuclei in **3**^{mono}, presumably as a result of increased electron-donation from the phosphine donors to In relative to the other group 13 metals (Figure 2.2). Additionally, the equivalence of the methylene CH_2 protons by ^{1}H NMR spectroscopy provides another gauge of the rigidity with which the phosphines are coordinated to M in ML. In the limit of strong, rigid coordination of the phosphines to M in ML, the methylene CH_2 protons would be expected to be "locked" in chemically different environments and give rise to two distinct ^{1}H NMR resonances, one for each of the two diastereotopic methylene protons. Thus, the fact that the methylene CH_2 protons are observed to be chemically equivalent and give rise to a single peak in all ML complexes implies that the phosphines are coordinated with some degree of fluxionally to Al, Ga and In (Figure 2.2). The notion that the chemical equivalence, or lack thereof, of the methylene protons can be used to

gauge the extent to which the ligand is "locked" into place upon binding metals will be revisited in the characterization of the bimetallic NiML complexes.

2.2.3 Solid-State Structures of the ML Complexes (M=Al, Ga, In)

A more definitive means of assessing the degree of phosphine coordination in ML is to analyze the solid-state structures (Figure 2.3, Table 2.1).

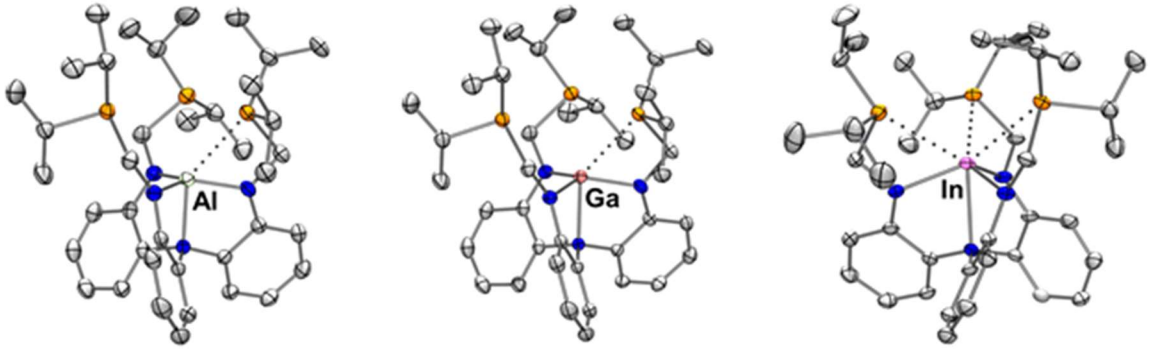

Figure 2.3. Solid-state structures of AlL (**1**^{mono}), GaL (**2**^{mono}), and InL (**3**^{mono}), with thermal ellipsoids shown at the 50% probability level. H atoms and lattice solvent molecules were omitted for clarity. Crystal structures were obtained by other researchers in our group: James T. Moore (**1**^{mono}, **2**^{mono}) and Dr. P. Alex Rudd (**3**^{mono}).

The M−P distances in ML are all relatively long and indicative of weak interactions, suggesting that the phosphine binding pocket of ML is poised for the installation of a second metal to form bimetallic complexes, as desired. **1**^{mono} and **2**^{mono} have one M−P interaction that is significantly shorter than the other two, indicating weak coordination of one phosphine in the solid-state, whereas in **3**^{mono} the three M−P distances are more similar to one another (~0.1 Å difference in shortest to longest M−P bond). Even the shortest M−P interaction in each ML complex are all significantly longer than the sum of the Pauling single-bond radii of phosphorus and the respective M atoms[131], consistent with weak M−P interactions (Table 2.1).

Table 2.1. Comparison of solid-state structures for monometallic ML complexes.

Metric	AlL[a] (**1**^{mono})	GaL[a] (**2**^{mono})	InL[b] (**3**^{mono})
M to N_3-plane (Å)	0.18	0.27	0.67
M−P (Å)	2.8283(8) 3.363(1) 3.476(1)	2.7851(7) 3.346(1) 3.465(1)	3.027(1) 3.087(1) 3.133(1)
M−P (Å)[c]	3.22	3.20	3.08
$r_M + r_P$ (Å)[d]	2.35	2.35	2.60
M−N_{eq} (Å)[c,e]	1.850(1)	1.905(1)	2.127(2)
M−N_{apical} (Å)	2.066(2)	2.163(2)	2.474(3)

[a]Crystal structures obtained by James T. Moore. [b]Crystal structure obtained by Dr. P. Alex Rudd. [c]Average value. [d]Sum of the Pauling single-bond radii for M and P.[131] [e]All three M-N_{eq} bond lengths are within 0.02 Å of each other for all ML.

The weak M−P interactions in the solid-state are consistent with the fluxionality observed in solution by ^{1}H NMR spectroscopy, which results in the equivalence of all three phosphine arms in solution for all ML (*vide supra*). Taking into account the significantly larger single-bond radius of In (1.497) relative to Al (1.248) and Ga (1.245), the In−P interactions are actually likely the strongest of the series, both on average and when considering only the shortest M−P interaction for each complex.[131] This is consistent with the aforementioned more downfield ^{31}P NMR chemical shift for InL (**3**^{mono}). Despite the long M−P distances, the phosphines are still positioned inward toward the metal in all ML complexes, rather than being "splayed" open and completely non-coordinating to the metal, as was observed in the solid-state upon the coordination of CH_3CN to AlL (**1**^{mono}) to form (CH_3CN)AlL.[78]

Lastly, another striking metric to compare across the trio of ML complexes are the M to N_3-plane distances. The In atom in **3**^{mono} sits significantly further above the N_3-plane than do Ga and Al in their respective ML complexes, with the M to N_3-plane distances found to be 0.67, 0.27, and 0.18 Å for In, Ga, and Al, respectively. An

interesting question to consider, which will be reconsidered for the bimetallic NiML complexes later in this chapter as well, is whether the positioning of the large In(III) ion relative to the N_3-plane is dictated by the steric constraints imposed by the capping NR_3 amine donor of the ligand, or by the relatively greater propensity of In(III) to interact with the phosphine donors than Al(III) and Ga(III). It should be noted that it is spatially feasible for the In atom to be positioned closer to the N_3-plane than it is in $\mathbf{3}^{mono}$, as will be seen in the solid-state structures of NiInL (**3**) and other related structures of small molecule adducts of **3**, which have In to N_3-plane distances ranging from 0.48 to 0.54 Å.[97] Thus, it seems fair to conclude that In sits an additional ~0.13 to 0.19 Å further above the N_3-plane in $\mathbf{3}^{mono}$ compared with these bimetallic complexes to interact with the phosphine donors. Likewise, the positioning of the smaller Ga(III) and Al(III) ions closer to the N_3-plane may be attributable to a preference for interacting more with the "harder" amide donors than with the "softer" phosphine donors, which is consistent with the more upfield ^{31}P NMR shifts for $\mathbf{1}^{mono}$ and $\mathbf{2}^{mono}$.

2.2.4 Synthesis and Characterization of Bimetallic NiML Complexes by NMR Spectroscopy

Addition of 1 equiv of bis(1,5-cyclooctadiene)nickel(0), abbreviated as $Ni(COD)_2$, to ML at rt in THF afforded the bimetallic NiML complexes in good yields after purification via washing with cold pentane and extraction into benzene.[97] Both rigorous drying and the pentane wash help to remove free COD from the NiML products. Although the NiML complexes are sparingly soluble in pentane, using cold pentane only resulted in a slight depression in the overall yields with a significant improvement in purity. Additionally, the benzene extraction removes any remaining salts leftover from

the synthesis of ML, as well as helps to purify NiML of $NiLH_3$ (**4**), a common impurity formed in the synthesis which is slightly less soluble in benzene than the desired NiML complexes. The resulting NiML complexes, NiAlL (**1**), NiGaL (**2**), and NiInL (**3**), are diamagnetic and possess solution-state three-fold symmetry, as evidenced by a single ^{31}P NMR resonance for all species. The lone ^{31}P resonance in toluene for complexes **1** (30.7 ppm), **2** (37.8 ppm), and **3** (44.4 ppm) shifts downfield upon introduction of the group 13 metal ion (relative to 30.1 ppm for **4**) and variation down the group (Figure A.1.4). Three-fold symmetry is also apparent from examination of the ^{1}H NMR spectra, which feature four distinct aryl proton resonances, as expected for three equivalent ligand arms of the tripodal ligand (Figure 2.4).[97] Either C_3 or C_{3v} symmetry, depending on T, is observed by ^{1}H NMR spectroscopy for complexes **1**-**4**, with the differences lying in whether the methylene and methine protons are diastereotopic or equivalent, respectively.

It should be noted that to prepare **3**, an argon atmosphere is necessary. Initial attempts to prepare **3** in a glovebox under N_2 instead resulted in the formation of a dinitrogen adduct species, (N_2)NiInL (**3**$-N_2$), which does not revert to **3** even after multiple freeze-pump-thaw cycles. However, it was found that **3** could be re-formed by dissolving **3**$-N_2$ in benzene in an argon glovebox followed by subsequent drying under vacuum. The end-on binding mode of N_2 to **3** was confirmed by an intense IR band at 2144 cm^{-1} (KBr pellet, Figure A.1.5) and x-ray crystallography (*vide infra*).[97] The relatively high ν(N−N) and short N−N bond distance of 1.103(5) Å suggest a weakly activated N_2 ligand, consistent with the poor π-basicity of Ni. Notably, the other Ni complexes, **1**, **2**, and **4**, do not bind N_2 under ambient conditions.[51, 78, 97]

^{1}H NMR spectra of complexes **1** and **3** are shown in Figure 2.4. In addition to indicating solution-state C_3 symmetry, important differences in fluxionality between the two complexes can be observed by closely examining the methylene CH_2 proton resonances (labeled "e"). In complex **3** (M=In), the methylene protons give rise to a single peak, whereas two peaks which are coupled to one another as leaning doublets are observed for the methylene protons in complex **1** (M=Al). This subtle difference in the ^{1}H NMR spectra arises due to differences in the flexibility and fluxionality of the bimetallic complexes in solution.

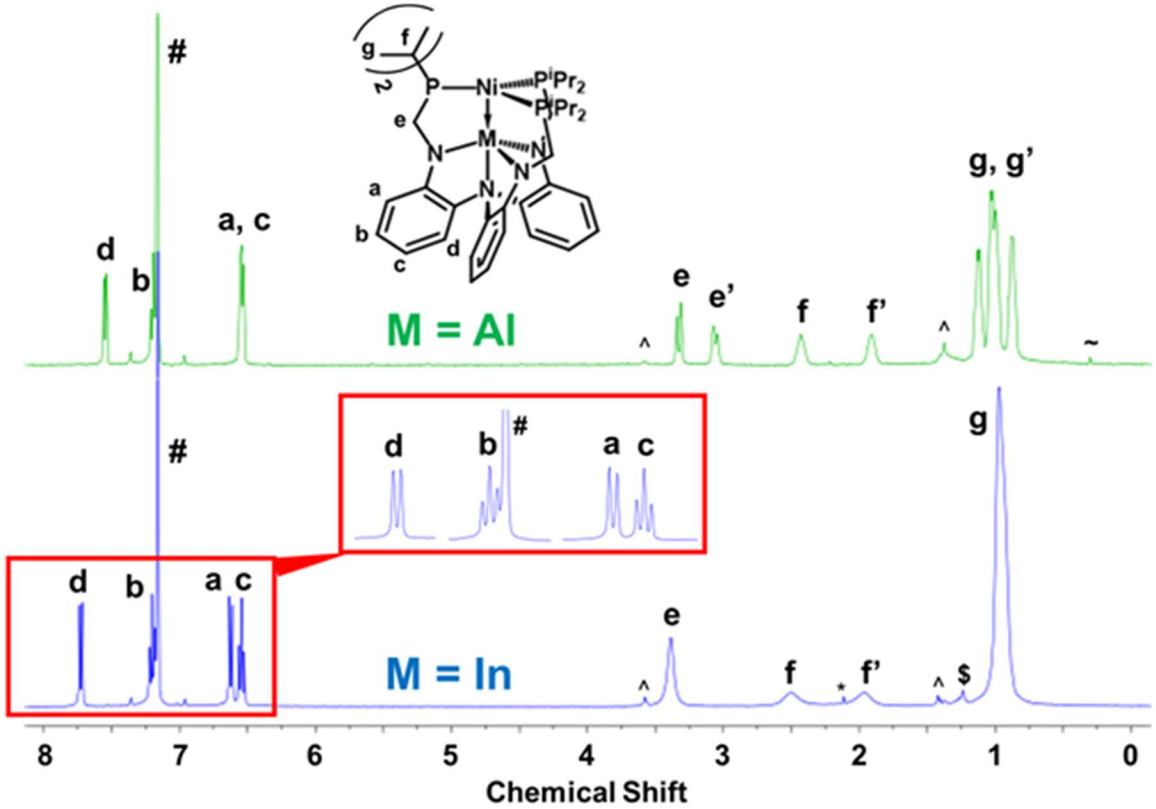

Figure 2.4. ^{1}H NMR (C_6D_6, 400 MHz) spectra of complexes **1** (M=Al, top) and **3** (M=In, bottom). The proton resonances are assigned with labels, with a close-up of the aryl region with resolved coupling shown for complex **3**. Residual solvent peaks for benzene (#), THF (^), toluene (*), pentane ($), as well as that for grease (~), are denoted.

If the ligand arms of L are completely and rigidly locked into position upon the binding of the two metals in a bimetallic M'ML complex, then the two methylene protons

will be chemically inequivalent, and give rise to two peaks (e and e'). In order for the methylene protons to coalesce and resonate as a single peak, they must be rendered chemically equivalent on the ^{1}H NMR timescale by a fluxional process. An analogous fluxional process has been previously observed by Bourissou and co-workers for similar C_3-symmetric "propeller"-type complexes[101], as well as by previous researchers in our laboratory for M'ML complexes[31, 132], and this process has been hypothesized to involve increased ligand flexibility via M−P bond weakening and/or cleavage. More details and quantitative evidence for this hypothesis on the fluxionality of the Ni−P bonds, as well as specific mechanistic proposals for this fluxional process which equates the two methylene protons, will be presented in chapter 4.

For now, suffice it to say that complex **1** exhibits less fluxionality and the ligand is more rigid and locked into place than is the case for complex **3**, as evidenced by the observation of two methylene proton peaks in **1** which are coalesced into a single peak in **3** (Figure 2.4). Thus, complex **1** exhibits C_3 symmetry at rt, and while the equivalence of the methylene protons of complex **3** would typically suggest C_{3v} symmetry, the inequivalence of the methine protons (f and f') limits complex **3** to solution-state C_3 symmetry at rt as well. The observation of the fluxional process which allows for methylene coalescence, which NMR spectroscopy is uniquely able to capture, will have important implications on the reactivity of the bimetallic NiML complexes that will be discussed further in chapter 4. Specifically, quantitative comparisons of the fluxionality of the Ni−P bonds in NiML and (L')NiML species in which a small molecule (L') binds to Ni will be made, which are of relevance to the mechanism of NiML-mediated olefin hydrogenation catalysis.[30, 97]

2.2.5 Solid-State Structures of NiML and $NiLH_3$ Complexes

Single crystals of **2** and **3**−N_2 suitable for x-ray diffraction studies were grown from vapor diffusion of concentrated pentane solutions into toluene. The growth of single crystals of **3** was achieved by allowing a concentrated benzene solution to sit under an Ar atmosphere at rt for several days. Figure 2.5 shows the solid-state structures of **2**, **3**, and **3**−N_2, along with those previously obtained for the two closely related complexes, **1** and **4**, which will be discussed throughout this thesis.[51, 78, 97]

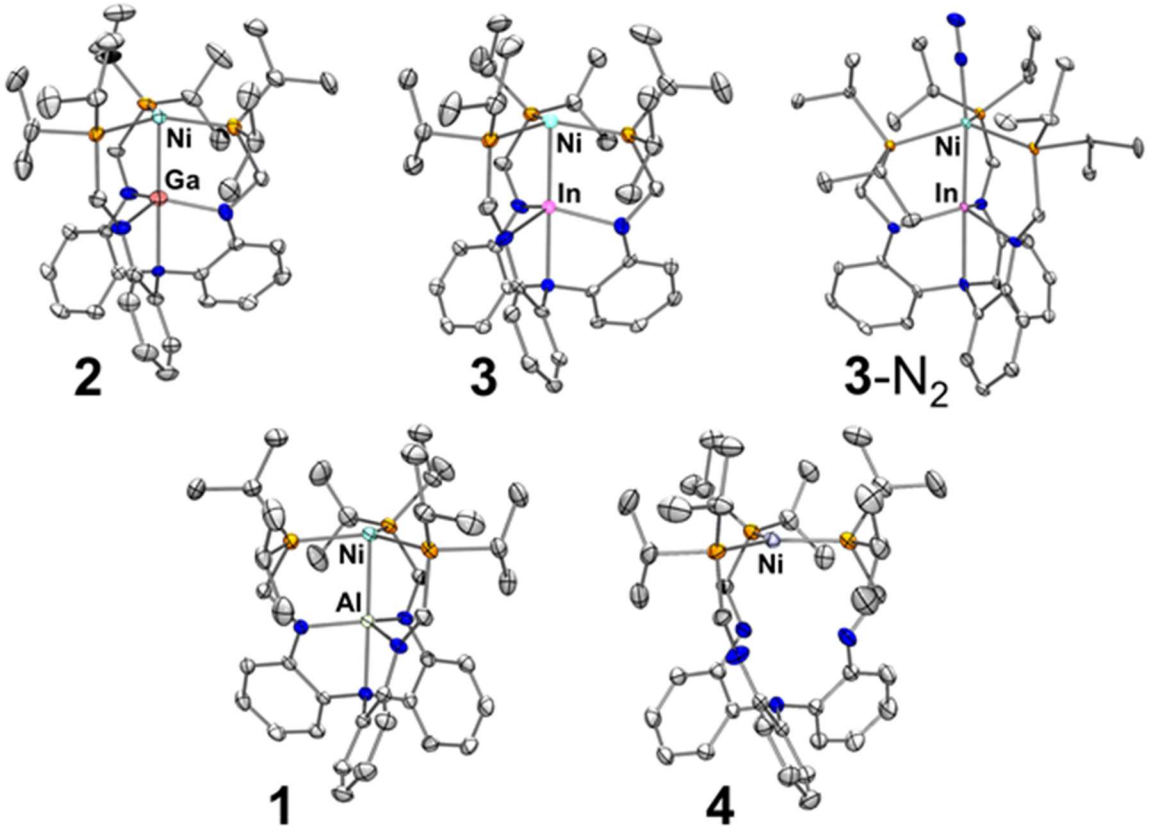

Figure 2.5. Solid-state structures of NiGaL (**2**), NiInL (**3**), (N_2)NiInL (**3**−N_2), NiAlL (**1**), and $NiLH_3$ (**4**), with thermal ellipsoids shown at the 50% probability level. H atoms and lattice solvent molecules were omitted for clarity. Carbon (gray), nitrogen (blue), and phosphorus (orange) atoms are color-coded, and the metal atoms are labeled in each structure. Crystal structures of **1** and **4** (bottom row) were obtained by Dr. P. Alex Rudd and Dr. Laura J. Clouston, respectively.[51, 78] Note that although it is not explicitly shown, the amide nitrogen atoms are protonated in complex **4**.[51]

Table 2.2 shows a comparison of selected bond lengths and other parameters for the isostructural NiML species in comparison to $NiLH_3$, which will serve as a useful control complex in that Ni is similarly ligated but is not interacting with a supporting metal. The solid-state structural parameters for **3**−N_2 will be considered and compared to those for other small molecule adducts of NiML in the next chapter, where small molecule binding will be considered in more detail.

In comparing the structures of complexes **2**-**4**, the M−N_{eq} bond length was found to increase linearly with the size of the M(III) ion, as given by the Shannon ionic radii[133] (R^2=1.000, Figure 2.6).

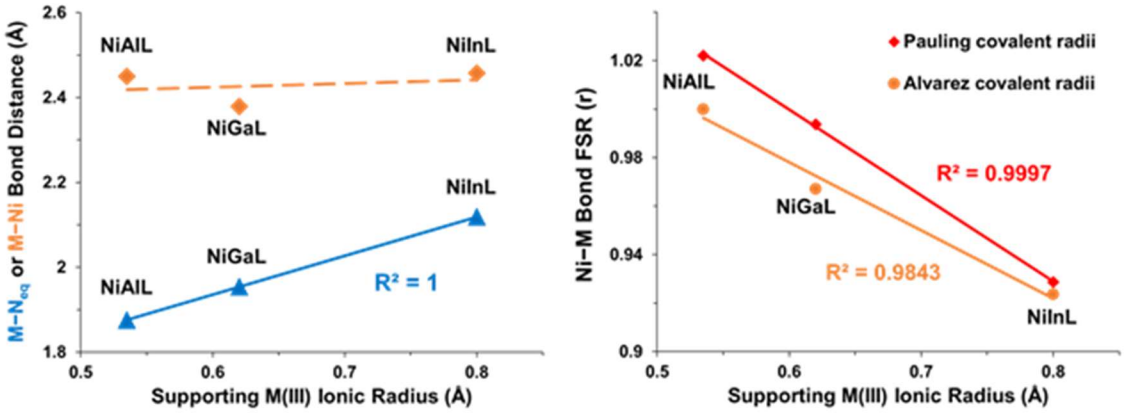

Figure 2.6. Plots of the M−N_{eq} and M−Ni bond distances (left) and of the Ni−M formal-shortness-ratio (FSR; right) vs. the ionic radius of the supporting metal for complexes **2**, **3**, and **4**. FSR, or the covalent ratio (*r*), is the ratio of the Ni−M bond distance to the sum of the radii of Ni and M, as given by both Pauling[131] (red diamonds) and Alvarez[134] (orange circles).

In contrast, the Ni−M bond lengths of 2.45, 2.38, and 2.46 Å in complexes **2** – **4**, respectively, are surprisingly similar, especially since the supporting metal size increases considerably in moving down group 13. This increase in size in moving down group 13 from Al to In is substantial regardless of whether it is measured in terms of the difference in Shannon ionic radii (~0.27 Å)[133], Alvarez covalent radii (~0.21 Å)[134], or Pauling

single-bond radii (~0.25 Å).[131] One would expect that for a given dative bond strength, the Ni−M bond distance would lengthen as the size of the supporting metal, M, increased, *ceteris paribus*. Thus, the fact that the Ni−M bond distance remains approximately the same even as the supporting metal size increases dramatically suggests a stronger Ni−M bond is formed with larger group 13 metals (In > Ga > Al).[97]

To illustrate this relative shortening of the Ni−M bond for larger supporting metals (M) more clearly and quantitatively, a comparison of the formal-shortness-ratio (FSR) values of the Ni−M bonds is instructive. FSR, as defined by Cotton, is given by the Ni−M bond distance divided by the sum of the Pauling single-bond radii of the constituent metals.[135] A related concept is the covalent ratio (*r*), where *r* is the ratio of the Ni−M bond distance to the sum of the radii of the constituent metals, which can be defined in alternative ways but are typically taken to be those defined by either Alvarez or Pauling.[131, 134-135] An *r* value of 1 is typically taken to correspond to a single bond, while values greater than 1 are indicative of weaker interactions than a single bond. Likewise, *r* values that are significantly less than 1 are indicative of multiple bonding. For the radii of transition metals, Alvarez covalent radii values were determined based on bond distances between each element and N, C, and O for complexes in the Cambridge Structural Database (CSD), whereas Pauling single-bond radii were determined based on metal-metal interatomic distances in bulk metal and intermetallic compounds (hence they are also referred to as metallic radii).[131, 134] Typically, main group chemists use the Alvarez covalent radii and inorganic chemists use the Pauling single-bond radii; since we are bridging both areas in examining dative bonds between Ni and group 13 elements, both sets of radii will be examined where appropriate. Another consideration for whether

to use Alvarez or Pauling radii is that Alvarez radii have different designations that reflect the different radii for low-spin or high-spin metal ions in some cases, where Pauling single-bond radii are more appropriate for zero-valent metals. In cases where just *r* is denoted, this will be taken to indicate the $r_{Alvarez}$ value; $r_{Alvarez}$ and $r_{Pauling}$ values often show similar correlations with experimental observables in our NiML system (Figure 2.6; *vide infra*).

Table 2.2. Selected solid-state structural parameters for complexes **1**-**4**.

Metric	**1**	**2**	**3**	**4**
Ni−M	2.450(1)	2.3789(8)	2.457(1)	−
r [b]	1.00	0.97	0.92	−
Ni−P [c]	2.204(1)	2.210(1)	2.252(1)	2.183(1)
$M-N_{apical}$	2.099(2)	2.216(3)	2.309(6)	−
$M-N_{eq}$ [c]	1.876(1)	1.954(2)	2.119(4)	−
$\sum N-M-N_{amide}$	354.5(1)	349.5(3)	345.3(1)	−
Ni to P_3-plane	0.13	0.13	0.23	0.03
M to N_3-plane	0.26	0.37	0.48	−

[b]Ratio of the Ni−M bond length to the sum of the covalent radii, as given by Alvarez and co-workers.[134]
[c]Average value.

As could be inferred from the constant Ni−M bond length in NiML complexes with various supporting metal sizes, comparison of the *r* values indeed shows that larger supporting metals result in smaller *r* values that are indicative of stronger Ni−M dative bonds. Specifically, the Ni−M *r* value in NiML complexes contracts as the supporting metal is varied down Group 13, from 1.00 (Al, **1)** to 0.97 (Ga, **2**) to 0.92 (In, **3**).[78, 97] An excellent correlation is observed between Ni−M *r* values and the Shannon M(III) ionic radii of the supporting metal[133], using either Pauling[131] (R^2=0.9997) or Alvarez[134] covalent radii values (R^2=0.9843) to tabulate *r* values (Figure 2.6). This correlation shows that larger supporting metals exhibit relatively shorter normalized crystallographic bond

distances with Ni, which is presumably reflective of stronger bonding with Ni. The range of *r* values for complexes **1**-**3** (0.92 to 1.00) is consistent with a dative single bond between Ni and M that becomes slightly stronger in varying the supporting metal down group 13. Whether the shorter relative Ni−M solid-state bond distances manifest in greater dative electron-withdrawal from Ni by the Lewis acidic supporting metal, M, will be examined in more detail in the next section on electrochemical studies of the NiML complexes.

In addition to dictating bonding with Ni, the geometric implications of M(III) size can be seen by scrutinizing the geometric positions of Ni and M relative to their respective binding pockets. Larger M(III) ions adopt positions higher above the N_3-plane in NiML complexes, from 0.26 Å for Al in **1,** to 0.37 Å for Ga in **2**, to 0.48 Å for In in **3** (Table 2.2).[78, 97] Furthermore, a good correlation is observed between the M(III) ionic radius of the supporting metal and its position above the N_3-plane in NiML complexes (R^2=0.95, Figure A.1.7). As the supporting M(III) ion becomes positioned further and further above the N_3-plane, one can envision that at some point it will begin to "force" Ni to be positioned further above the P_3-plane for steric reasons. From an electronic perspective alone, Ni would be expected to prefer to adopt a trigonal planar geometry with respect to the three phosphine donors to maximize the spatial orbital overlap of the phosphines with the Ni $3d_{xy}$ and $3d_{x^2-y^2}$ orbitals. This is seen to be the case for the Ni center in $NiLH_3$ (**4**) in the absence of a supporting metal, where the Ni center is positioned essentially coplanar with the phosphine donors (Ni to P_3-plane = 0.03 Å).[51] In the presence of supporting M(III) ions, Ni rises further above the P_3-plane by 0.10 Å in both **1** and **2** relative to its position in **4**, and by 0.20 Å in **3** relative to **4**, suggesting that

larger M(III) ions result in Ni adopting positions further above the P_3-plane (Figure A.1.6).[51, 78, 97] Presumably, steric pressure from the M(III) ion is counteracted by an electronic preference of Ni(0) for a trigonal planar coordination geometry, with the interplay of the two effects determining the resulting position of Ni relative to the P_3-plane in the NiML complexes. This interplay of the steric and electronic effects of larger supporting M(III) ions on Ni will be re-visited in discussing the electrochemistry of NiML complexes (section 2.2.6) and the reactivity of Ni toward added small molecule donor substrates (chapter 3).

Another structural trend to note is that the Ni−P bonds elongate modestly with the introduction and increasing size of the M(III) ion, from 2.18 Å in **4** to 2.25 in **3**, while the corresponding ^{31}P NMR resonance shifts downfield, from 30.1 ppm for **4** to 44.4 ppm for **3** (in toluene).[51, 78, 97] This dual trend of Ni−P bond elongation and de-shielding of the ^{31}P nuclei strongly suggests that the degree of Ni→P π-back-bonding is decreasing as M is varied down group 13. We propose that this decrease in Ni→P π-back-bonding is linked to the opposing gain in Ni→M dative bonding upon moving down group 13, since the Lewis acidic M(III) ion competes with the phosphines for Ni(0) electron density.[97] Another set of inversely related bonding interactions within the NiML complexes are the M−N_{apical} and Ni−M bonds. This has been reported previously for many bimetallic complexes within our ligand framework, and simply reflects the fact that as the supporting metal moves higher above the N_3-plane to interact with Ni, it is necessarily further from the apical amine donor (N_{apical}−M−Ni angles are ~179° to 180° in all complexes).[31]

2.2.6 Cyclic Voltammetry (CV) Studies of NiML and $NiLH_3$ Complexes

2.2.6.1 CVs of NiML and $NiLH_3$ in THF: Ni(I/0) Potential as an Indirect Gauge of Lewis Acidity

Cyclic voltammetry (CV) studies were conducted to probe the influence of the Lewis acidic group 13 metal ion on the electronic environment of Ni in the series of NiML complexes. Oxidation events observed for the NiML complexes were anticipated to be directly attributable to changes in oxidation state at Ni, since Al, Ga, and In all strongly prefer the +3 oxidation state and are generally considered to be redox-inactive, and the ligand shows no reversible oxidation events at readily accessible potentials.[78, 136] Notably, the notion of unambiguously assigned oxidation events was a unique feature of the NiML series of complexes compared with other bimetallic complexes prepared in our lab at that point, as bimetallic complexes featuring strong bonds between redox-active transition metals often exhibit redox events that are best described as delocalized to varying degrees across both metal centers.[31, 80, 130, 137-141] Thus, in light of the redox-inactivity of the group 13 supporting metals, we sought to quantitatively assess the relative extent of dative electron-withdrawal by the Lewis acidic group 13 metal ion from Ni by comparing the relative potentials for unambiguously assigned Ni-based oxidation events across the series of NiML complexes.

The CVs for complexes **1**-**4** under 1 atm N_2 in [TBA][PF_6] electrolyte solution in THF are shown in Figure 2.7, with separate plots showing the oxidation events observed in THF and those observed in CH_3CN. Note that reduction events were also observed for all NiML species, but not for $NiLH_3$ (Figure 2.9). Full CVs for all NiML complexes in both THF and CH_3CN are shown in the Appendix (Figures A.1.8-A.1.10). The interpretation of the reduction events is less straightforward, and so the Ni(0/I) oxidation

events will be discussed first. For each species, one oxidative feature is observed which corresponds to the Ni(I/0) redox couple (Figure 2.7). Upon introduction of an Al(III) supporting metal, the reversible Ni(I/0) redox couple shifts to harsher potential in **1** (−0.74 V vs. $FeCp_2^{0/+}$) relative to **4** (−1.02 V vs. $FeCp_2^{0/+}$).[51, 78, 97] This shift to more positive potential by 280 mV reflects that the Ni center is rendered more electron-deficient upon the installation of a Lewis acidic supporting metal, consistent with the description of a dative bond between Ni and Al in which Ni acts as a Lewis base and donates electron density to Al. Further shifts in the Ni(I/0) potential to less negative values are observed upon varying the supporting metal further down group 13 to Ga and In, indicating increasing electron-deficiency of the Ni center. A reversible oxidation event is observed with $E°_{1/2}$ = −0.57 V vs. $FeCp_2^{0/+}$ for **2**, whereas an irreversible oxidation is observed for **3**−N_2 with E_{pa} = 0.39 V vs. $FeCp_2^{0/+}$ (Table 2.3).[97]

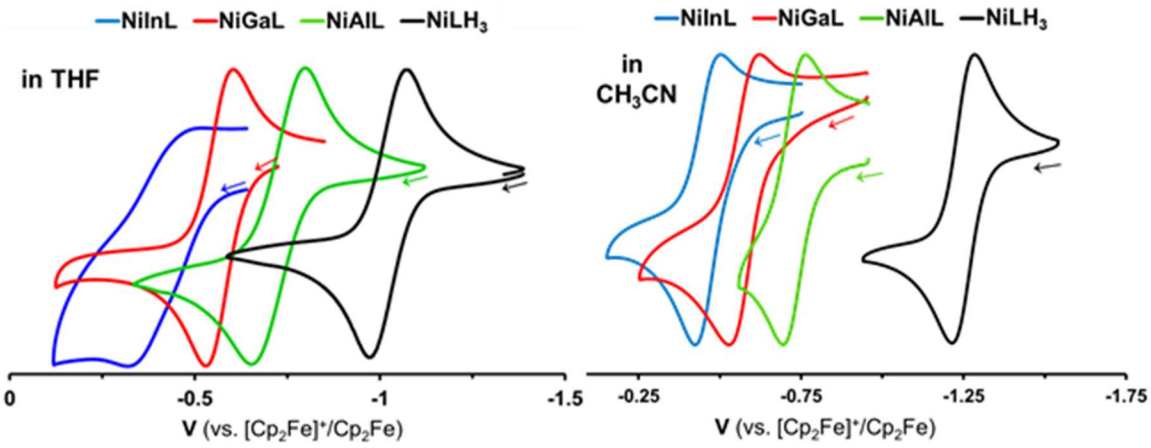

Figure 2.7. Cyclic voltammograms (CVs) of NiAlL (**1**), NiGaL (**2**), NiInL (**3**), and $NiLH_3$ (**4**) showing the Ni(I/0) redox couples in THF (left) and in CH_3CN (right). All CVs were collected under 1 atm N_2 with [TBA][PF_6] as the electrolyte (0.1 M or 0.4 M in THF, 0.4 M in CH_3CN). All CVs in CH_3CN were collected with a scan rate of 50 mV/s, whereas CVs in THF were obtained at either 25 or 50 mV/s. All redox potentials are given relative to the $FeCp_2^{+/0}$ redox couple.

Table 2.3. Comparison of Ni(I/0) redox couple for NiML complexes and **4** in CH_3CN and THF.

	Ni(I/0) couple in CH_3CN					Ni(I/0) couple in THF[a 51, 78, 97]				
Complex	E_{pa}	E_{pc}	$\boldsymbol{E°_{1/2}}$	ΔE_p	i_{pa}/i_{pc}	E_{pa}	E_{pc}	$\boldsymbol{E°_{1/2}}$	ΔE_p	i_{pa}/i_{pc}
4	−1.22	−1.28	**−1.25**	69	1.00	−0.97	−1.07	**−1.02**	100	1.09
1	−0.70	−0.77	**−0.73**	71	1.11	−0.68	−0.79	**−0.74**	108	1.04
2	−0.53	−0.62	**−0.57**	89	1.17	−0.53	−0.61	**−0.57**	73	1.01
3	−0.42	−0.50	**−0.46**	83	1.46	−0.39	–	–	–	–

Note: E_{pa}, E_{pc}, and $E°_{1/2}$ are given in V, and ΔE_p is given in mV. ΔE_p = 57 mV and i_{pa}/i_{pc} = 1.00 for a perfectly reversible redox event. All CVs were collected at a scan rate of 50 mV/s unless otherwise noted. All redox potentials are given relative to the $FeCp_2^{+/0}$ redox couple. [a] CVs of **2** and **3** in THF were collected at a scan rate of 25 mV/s.

The irreversibility of the Ni(I/0) couple for **3** in THF prevents straightforward comparison of its potential to that of the other NiML complexes, which was desired as a quantitative gauge of the Lewis acidic influence of the supporting metal on the relative electron-richness of the Ni centers in NiML complexes. It should be noted that faster scan rates up to 1.5 V/s did not result in any improvement in the reversibility of the Ni(I/0) couple for **3**, as no return current was observed for all scan rates examined. The irreversibility of the Ni(I/0) couple for **3** is most likely due to the instability of the $[NiInL]^+$ ($[\mathbf{3}]^+$) species, which likely undergoes rapid decomposition prior to the return cathodic scan. That $[\mathbf{3}]^+$ would be more prone to decomposition than the other $[NiML]^+$ species upon electrochemical generation is consistent with the less negative Ni(I/0) E_{pa} potential for **3**.

Additionally, it should be noted that unlike the other NiML complexes, **3** binds N_2 relatively strongly such that N_2 is not labile upon the application of vacuum, and so the CV of **3** under an atmosphere of N_2 is better described as that of (N_2)NiInL (**3**−N_2).[97] As such, an alternative explanation for the irreversibility would be that it involves N_2

dissociation from **3** upon oxidation. To test whether N_2 dissociation plays a role in the irreversibility of the Ni(I/0) redox couple, the CV of **3** was collected under 1 atm Ar. However, this control experiment was inconclusive and stymied by the decomposition of **3** after a few anodic scans to an unidentified species that was hypothesized to be a Ni−F species. The decomposition likely occurs via fluoride abstraction upon oxidation, likely from a trace impurity in the [TBA][PF_6] electrolyte. In the initial scans prior to decomposition, the Ni(I/0) wave remained irreversible and at essentially the same potential as that observed under 1 atm N_2. If N_2 dissociates from **3** after initial oxidation, then a return reduction wave would still be expected to be observed if [**3**]$^+$ is stable and does not decompose, albeit potentially with a large peak-to-peak separation for an electron transfer/chemical reaction/electron transfer (ECE) mechanism with "C" involving N_2 dissociation.[142] Therefore, because no return reduction current is observed, the irreversibility of the Ni(0/I) oxidation for **3** is proposed to be the result of the instability of the [**3**]$^+$ species that is generated via electrochemical oxidation.

2.2.6.2 CVs of NiML and $NiLH_3$ in CH_3CN: Improved Ni(I/0) reversibility via CH_3CN binding

CVs for all complexes were also collected in CH_3CN, with the hope that the presence of a coordinating solvent may help stabilize the extremely electron-deficient [**3**]$^+$ species such that the Ni(I/0) redox couple for **3** becomes reversible, thereby allowing for a more legitimate comparison of Ni(I/0) $E°_{1/2}$ potentials for the NiML complexes. Despite the relatively poor solubility of all complexes in CH_3CN compared with THF, reversible Ni(I/0) redox couples were observed for all species including **3**, which exhibited a quasi-reversible oxidation at −0.46 V (Figure 2.7, Table 2.3). One caveat to

the CVs in CH_3CN is that the neutral NiML complexes all bind CH_3CN to some degree, and so the Ni(I/0) redox couple in CH_3CN technically represents the oxidation of (CH_3CN)NiML to $[(CH_3CN)NiML]^+$. Complexes **2** and **3** appear to bind CH_3CN particularly strongly, with vibrant color changes observed from deep red in THF to orange-brown and yellow, respectively, upon dissolution in CH_3CN. This apparent strong binding of CH_3CN to **2** and **3** was confirmed by quantitative measurements of equilibria between H_2 and CH_3CN binding, which are detailed in chapter 5. For now, suffice it to state that all NiML complexes exist in solution with CH_3CN bound when CH_3CN is employed as the solvent and present in large excess. The possible exception to this statement is complex **4**, which exhibits only a very slight shift in its ^{31}P NMR spectrum between THF and CH_3CN (< 0.2 ppm) and does not exhibit a color change from its characteristic purple upon dissolution in CH_3CN.

Nevertheless, whether considering the Ni(I/0) redox couple for (CH_3CN)NiML to $[(CH_3CN)NiML]^+$ in CH_3CN or that for NiML to $[NiML]^+$ in THF, it should be appreciated that either case represents an isostructural series of complexes in which the only variable is the supporting metal identity. In accord with this notion that both sets of measurements should allow for elucidation of the electronic influence of the supporting metal, essentially identical potentials were observed for both **1** and **2** in CH_3CN and THF (Table 2.3). The Ni(I/0) $E°_{1/2}$ potential difference between solvents cannot be readily compared for **3**, since the Ni(I/0) wave is quasi-reversible in CH_3CN and irreversible in THF; however, it should be noted that the E_{pa} potentials are comparable between the two solvents (−0.39 in THF vs. −0.42 V in CH_3CN, both relative to the $FeCp_2^{0/+}$ redox couple). The only complex for which a large shift in the Ni(I/0) redox couple was

observed upon changing the solvent from THF to CH_3CN is **4**, with the $E°_{1/2}$ potential shifting more negative by about 230 mV from −1.02 V in THF to −1.25 V in CH_3CN (vs. $FeCp_2^{0/+}$ redox couple in both solvents). The solvent-dependent potential shift of **4** is somewhat puzzling: because it is the most electron-rich complex and does not seem to bind CH_3CN as readily as more electron-deficient NiML complexes, the solvent effect would not be expected to be so dramatic.

Furthermore, even if CH_3CN did not bind at all to $NiLH_3$ (**4**), it would almost certainly be expected to bind to the more electron-poor, 15-electron $[NiLH_3]^+$ ($[\mathbf{4}]^+$) complex upon its formation via electrochemical oxidation of **4**. If CH_3CN binds to $[\mathbf{4}]^+$ but not to **4**, this would likely manifest in a larger than normal peak-to-peak separation in the CV due to the return cathodic peak shifting to more negative potential for the more difficult reduction of the $[(CH_3CN)NiLH_3]^+$ species compared with that of $[\mathbf{4}]^+$.[142] However, no such increased peak-to-peak separation or quasi-reversibility due to CH_3CN binding in one of the two redox states was observed for **4**; in fact, its Ni(I/0) redox couple is closer to exhibiting perfect reversibility (ΔE_p = 69 mV, i_{pa}/i_{pc} = 1.00) than any of the other NiML complexes (Table 2.3).[142] Therefore, while the peak potential shift is difficult to explain, the full reversibility of the Ni(I/0) couple likely indicates that CH_3CN is either bound or unbound in both redox states; the former seems more likely due to the propensity of CH_3CN to bind to cationic metal complexes within our ligand framework, especially those which are electronically unsaturated (ie. ≤16-electron complexes).[31]

Just as the Ni(I/0) redox events at the harsher potentials in THF became less reversible, with the Ni(I/0) redox couple for **3** becoming fully irreversible, the Ni(I/0) redox couples in CH_3CN also become less reversible at harsher, more positive oxidation

potentials (Table 2.3, Figure A.1.11). This can be seen by noting the generally increasing ΔE_p and i_{pa}/i_{pc} values for the Ni(I/0) redox couples at more positive potentials: In > Ga > Al > $NiLH_3$ for i_{pa}/i_{pc}, and Ga ~ In > Al ~ $NiLH_3$ for ΔE_p (Table 2.3). Most importantly, by switching the solvent to CH_3CN, the Ni(I/0) redox couple becomes reversible or quasi-reversible for all complexes, allowing for a more robust comparison of Ni(I/0) $E°_{1/2}$ redox potentials.

2.2.6.3 Understanding Trends in Ni(I/0) Redox Couple: What Dictates the Lewis Acidity of M(III) Ions Toward Ni in NiML Complexes?

In comparing the Ni(I/0) redox potentials across the trio of NiML complexes in comparison to $NiLH_3$, the introduction of a Lewis acidic group 13 supporting metal ion and its variation from Al to Ga to In modulates the electronic environment of Ni such that the Ni(I/0) redox couple shifts by ~800 mV in CH_3CN and ~600 mV in THF.[97] This dramatic tuning effect illustrates the strong and variable Lewis acidity of group 13 metal ions when positioned in close bonding proximity to a transition metal center. Furthermore, this large range of Ni(I/0) redox potentials was encouraging in that it suggested that the electronic environments of the Ni centers were very different upon variation of the supporting metal, and so perhaps they may also display divergent reactivity with small molecule substrates from each other and from that of typical Ni complexes.

Since only the supporting metal was varied to give rise to such large differences in electron-richness at Ni in the resulting NiML complexes, the logical next step was to determine which, if any, fundamental properties of the group 13 supporting metal dictate its Lewis acidity toward Ni. Such an understanding would be invaluable toward the *a*

priori design of bimetallic complexes with desirable properties and reactivity. Table 2.4 shows selected properties of group 13 elements that were considered in assessing their respective Lewis acidities toward Ni in the NiML complexes, many of which have been considered relevant to Lewis acidity in other systems in the literature.[42, 52, 136, 143-144]

Table 2.4. Selected properties of group 13 elements of relevance to Lewis acidity.[136, 144]

Element	Ionic Radius[a]	Charge Density[b]	M(III/0) $E°_{1/2}$	pK_a $M(H_2O)_6^{3+}$	Electro-negativity	pF^- MF_3[144]
Al	0.535	4.68	−1.66	4.95	1.61	11.50
Ga	0.620	3.01	−0.56	2.6	1.81	10.70
In	0.800	1.40	−0.34	3.9	1.78	10.75

Note: Ionic radius is given in Å, charge density in elementary charge units per Å^3 (e/Å^3), M(III/0) $E°_{1/2}$ in V vs. $FeCp_2^{0/+}$, and electronegativity in Pauling units.[136] [a]Shannon 6-coordinate ionic radius values.[133] [b]Based on spherical ion with volume = $(4/3)\pi r^3$, with r = Shannon ionic radius.

The Ni(I/0) redox potentials were found to correlate reasonably well with the size of the supporting metal ion (R^2=0.907), as given by their respective Shannon M(III) 6-coordinate ionic radii values (Table 2.4, Figure 2.8).[78, 97, 133] A far better correlation was observed between the Ni(I/0) redox potentials and the charge densities of the group 13 metal ions (R^2=0.991). Charge densities were tabulated using the respective ionic radii to determine the volume of an idealized spherical +3 ion, and so it is expected that a similar correlation would be observed for both ionic radii and charge density, as the latter is a function of the former. The Ni(I/0) redox potentials were also found to correlate well with the normalized Ni→M bond distances, as given by the *r* values (R^2=0.966), consistent with the notion that shorter Ni→M bonds facilitate greater electron withdrawal from Ni by the supporting metal (Figure A.1.12).[97] Additionally, the standard M(III/0) reduction potentials were also found to correlate reasonably well with the Ni(I/0) redox potentials in the NiML complexes (R^2=0.934, Figure A.1.13). Perhaps just as informative

were which properties did not correlate: namely, electronegativity (R^2=0.72), pK_a of the corresponding $M(H_2O)_6^{3+}$ complexes (R^2=0.29), and pF^- of MF_3 complexes (R^2=0.79) were not found to be particularly useful parameters for explaining the trends in the Ni(I/0) redox potentials of the trio of NiML complexes (Figures A.1.14-A.1.15).[97]

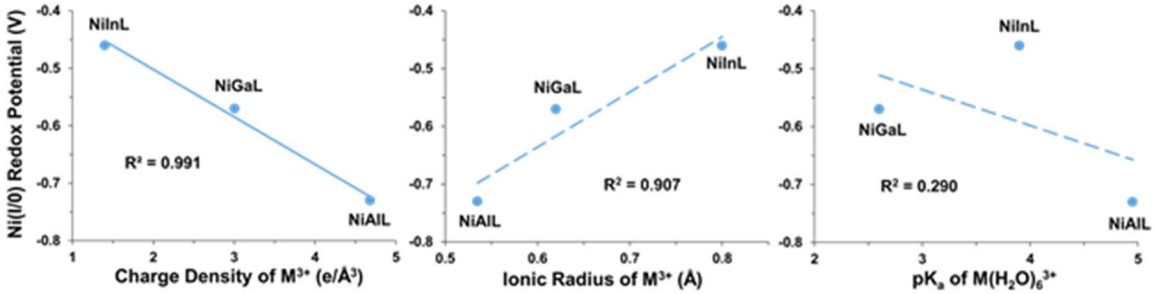

Figure 2.8. Plots of Ni(I/0) redox potential of the NiML complexes in CH_3CN vs. charge density (left), ionic radius (center), and pKa of $M(H_2O)_6^{3+}$ for the supporting metal (M).

It is particularly noteworthy that the Ni(I/0) redox potentials were not observed to correlate with the pK_a of $M(H_2O)_6^{3+}$ complexes (R^2=0.29), as this parameter has previously been found to serve as a proxy for the Lewis acidity of metal ions in other systems.[42, 52, 143, 145-147] For example, the redox potentials of mixed-metal oxide clusters (e.g. Mn_3O_2M) with a variable redox-inactive metal site (M) were found to be linearly modulated by the pK_a of the corresponding $M(H_2O)_6^{3+}$ complexes for a wide range of metal ions across multiple charge states, including group 13, group 3, group 2, and lanthanide metal ions.[42, 52, 146] One rationale for the differing Lewis acidity in systems like Mn_3O_2M compared with the NiML system is that the nature of the interactions between the Lewis acidic metal ion and the transition metal(s) is distinctly different.[97] In Mn_3O_2M, bridging oxygen moieties facilitate indirect interactions between the Mn cluster and the Lewis acidic metal ion. Thus, the Lewis acidic ion indirectly modulates the electronic environment of the metal cluster through inductive effects, whereas direct dative bonding between Ni and the Lewis acidic metal ion facilitates electron withdrawal

from Ni in NiML complexes. In a direct dative bond between a Lewis acidic metal ion and a transition metal, such as Ni→M, considerations such as spatial and energetic orbital overlap between Ni and M likely come into play in determining the Lewis acidity of the supporting metal towards Ni and the extent of electron withdrawal. Such orbital interaction considerations only come into play for the direct interaction between the Lewis acidic ions and the bridging oxygen atoms, but not with Mn, in the case of the Mn_3O_2M cluster. Therefore, it seems logical that since oxygen and a low-valent, late transition metal are very different Lewis bases, the relative Lewis acidity displayed towards them may not follow the same ordering for both cases.[136] Further discussion, drawing upon CV and x-ray crystallographic data, of why group 13 M(III) size dictates Lewis acidity toward Ni will be undertaken in section 2.2.7, along with assessment of whether the trends observed for the NiML complexes are generalizable for other ligand systems in which a transition metal interacts with a group 13 metal ion.

2.2.6.4 Unusual Reduction Observed for NiML by CV: Ni(0/−I) or M(III/II) redox couple?

In addition to the Ni(0/I) oxidation event, an unexpected reduction event was observed for all three NiML complexes (Figure 2.9). In THF, the $E°_{1/2}$ potentials for this reduction event were −2.82 V, −2.48 V, and −2.34 V for **1**, **2**, and **3**, respectively, relative to the $FeCp_2^{0/+}$ redox couple.[97] The reduction of **1** is fully reversible ($i_{pa}/i_{pc} \sim 1$), and the reduction of **2** is nearly fully reversible, with a relatively small peak-to-peak separation (ΔE_p = 85 mV), but an anodic to cathodic current ratio which deviates slightly from unity (i_{pa}/i_{pc} = 0.88). The reduction of **3**−N_2 is quasi-reversible, as the return anodic current is visibly diminished (i_{pa}/i_{pc} = 0.70), and reversibility does not appreciably improve with

faster scan rates up to 1 V/s. It is possible that this quasi-reversibility is due to the dissociation of N_2 upon reduction to $[NiInL]^-$, as "$[(N_2)NiInL]^-$" would be a 19-electron complex. Interestingly, the reductions all become irreversible in CH_3CN except for that of **1**, which could be generously described as quasi-reversible on the basis of a small but discernable anodic return current (Figure 2.9). potential by ~200 mV in CH_3CN relative to that in THF (Table 2.5).

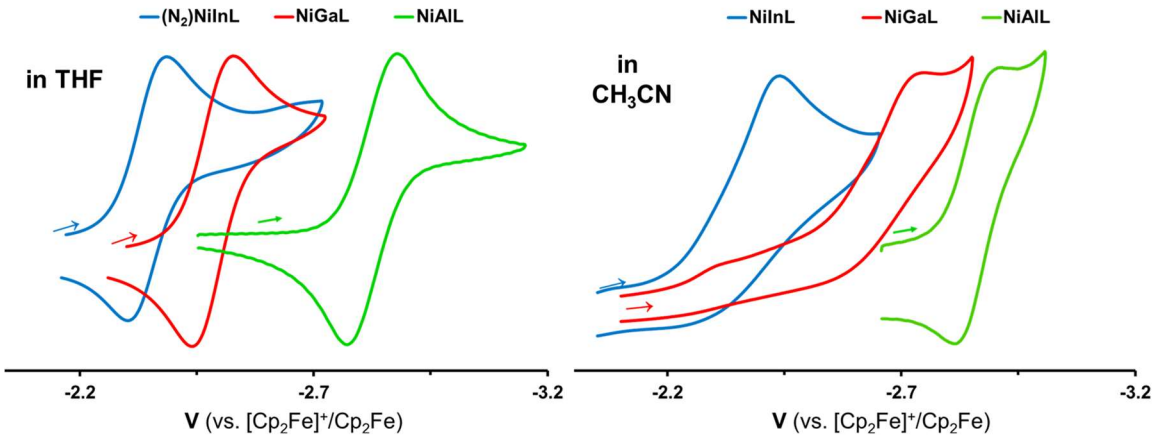

Figure 2.9. Cyclic voltammograms (CVs) of NiAlL (**1**), NiGaL (**2**), and NiInL (**3**) showing reduction event in THF[97] (left) and in CH_3CN (right). All CVs were collected under 1 atm N_2 with [TBA][PF_6] as the electrolyte (0.1 M or 0.4 M). All CVs in CH_3CN were collected with a scan rate of 50 mV/S, whereas CVs in THF were obtained at either 25 or 50 mV/s. All redox potentials are given relative to the $FeCp_2^{+/0}$ redox couple. No reduction event was observed for $NiLH_3$ within the solvent window in THF or CH_3CN.

Table 2.5. Comparison of NiML reduction events in THF and CH_3CN.

	Reduction in THF[a]					Reduction in CH_3CN[b]				
Complex	E_{pa}	E_{pc}	$\boldsymbol{E°_{1/2}}$	ΔE_p	i_{pa}/i_{pc}	E_{pa}	E_{pc}	$\boldsymbol{E°_{1/2}}$	ΔE_p	i_{pa}/i_{pc}
NiAlL (**1**)	−2.77	−2.88	**−2.82**	109	1.01	−2.81	−2.91	**−2.86**	99	–
NiGaL (**2**)	−2.44	−2.52	**−2.48**	85	0.88	–	−2.73	–	–	–
NiInL (**3**)[c]	−2.30	−2.38	**−2.34**	84	0.70	–	−2.44	–	–	–

Note: E_{pa}, E_{pc}, and $E°_{1/2}$ are given in V, and ΔE_p is given in mV. ΔE_p = 57 mV and i_{pa}/i_{pc} = 1.00 for a perfectly reversible wave. All CVs were collected at a scan rate of 50 mV/s unless otherwise noted. All redox potentials are given relative to the $FeCp_2^{+/0}$ redox couple. [a]CVs of **2** and **3** in THF were collected at a scan rate of 25 mV/s. [b]All species bind CH_3CN when it is present as the solvent (very large excess), and so the reduction events in CH_3CN are best described as the reduction of $(CH_3CN)NiML$ complexes. [c]**3** binds N_2, and so the reduction of **3** in THF is more precisely described as the reduction of **3**−N_2.

No improvement in the reversibility of the reductions of **2** or **3** in CH_3CN was observed at faster scan rates up to 1 V/s. The E_{pc} and $E°_{1/2}$ potentials are nearly identical for **1** in both THF and CH_3CN (within ~40 mV), and the E_{pc} potentials for **3** only differ by 60 mV at comparable scan rates (Table 2.5). A larger difference was observed for **2**, as its E_{pc} value shifts to harsher potential by ~200 mV in CH_3CN relative to that in THF (Table 2.5).

2.2.6.5 An Intriguing Detour: Examining the Unexpected Reduction of NiML to [NiML]$^-$

A few questions arise regarding the nature of this reduction event, and so these will be discussed briefly as part of a short detour from this chapter's focus on the characterization of the neutral NiML complexes. The first of these questions is whether the added electron in these highly-reduced species is better described as localized on Ni, M, the ligand, or delocalized over some combination of these. Second, given the relatively harsh reduction potentials, it was an open question as to whether these reduced [NiML]$^-$ species would be stable, as well as to why the reduction event becomes irreversible upon switching the solvent from THF to CH_3CN.

The last question regarding the solvent effect on the reversibility of the reduction event will be addressed first, as it does not require extensive knowledge of the nature of the reduced [NiML]$^-$ species. In THF, NiML complexes are formally Ni(0), 16-electron complexes, though they are fairly electron-deficient for formally Ni(0) complexes as a result of the dative bond to the Lewis acidic group 13 metal ion. The electron-deficiency of the formally Ni(0) center in NiML complexes manifests in the facile binding of σ-donor substrates that are present, including CH_3CN. Indeed, in the next chapter, the binding of small molecule substrates at Ni as a function of the supporting metal will be

discussed in depth. Of relevance to the CV interpretation, CH_3CN binds to NiML complexes (*vide supra*), but THF has not been observed to bind, presumably because THF is a worse σ-donor than CH_3CN. Therefore, the complexes exist as 18-electron (CH_3CN)NiML complexes in CH_3CN solution, as opposed to 16-electron NiML complexes in THF. Thus, upon reduction in CH_3CN, a highly-reduced 19-electron anionic $[(CH_3CN)NiML]^-$ complex would be formed, which likely results in rapid CH_3CN dissociation.

While CH_3CN dissociation alone could disrupt the reversibility of the reduction wave, a return oxidation peak would still be expected to be observed, albeit likely with a large peak-to-peak separation for an ECE mechanism, if the resulting naked $[NiML]^-$ species was stable to decomposition.[142] Thus, it seems clear that the highly reduced $[NiML]^-$ species decompose in CH_3CN, possibly by way of deprotonation of CH_3CN since $[NiML]^-$ would be expected to be highly basic. However, it should be noted that explaining the irreversibility of the reduction events in CH_3CN by decomposition alone is inconsistent with the observation that the reduction of **1** is the only one in the NiML series which exhibits any degree of reversibility; it would be expected that the harsher potential required to generate $[NiAlL]^-$ would result in it being the most unstable and prone to decomposition (and also the most basic if considering the propensity to deprotonate CH_3CN). Therefore, although the exact mechanism of decomposition remains unknown, it seems likely that rapid CH_3CN dissociation and decomposition upon reduction both may contribute to the irreversibility of reduction events in CH_3CN.

The first question regarding where the added electron "resides" is interesting from the perspective that neither Ni(0) or M(III) in the neutral NiML complexes would be

anticipated to be amenable to being reduced. Ni(0) already has a full 3*d* shell of electrons and would not typically be expected to have a high affinity for another electron to generate a formally Ni(−I) species. To this point, only a few examples of formally sub-valent Ni complexes are known, with a few others known to be isolable only under extreme conditions (gas matrices, etc.).[148-153] Likewise, the group 13 metal ions strongly prefer the +3 oxidation state[136]; in fact, bona fide group 13 M(II) radicals which do not form dimers via M−M bonds are extremely rare.[154-157] The phosphinoamide ligand is also not capable of redox activity at accessible potentials, as evidenced by control experiments which show only an irreversible oxidation at harsh potentials near that of the $FeCp_2^{0/+}$ redox couple. Thus, it is not clear where the additional electron would be added to form the highly reduced $[NiML]^-$ complexes. To further re-iterate the point that both Ni(0) and M(III) ions are not typically able to be reduced by one electron, neither $NiLH_3$ or ML, formally Ni(0) and M(III) complexes without a Ni→M interaction, has an accessible reduction event which is observable by CV.[158] Thus, there is something inherently important about the Ni→M dative bond that enables highly reduced $[NiML]^-$ complexes to be stable.

To assess whether the reduction was localized at Ni, as a Ni(0/−I) reduction, or at M, as a M(III/II) reduction, the extent to which the NiML reduction potentials correlate with both the Ni(I/0) redox couples and the standard M(III/0) reduction potentials of the supporting metal were examined (Figure 2.10).

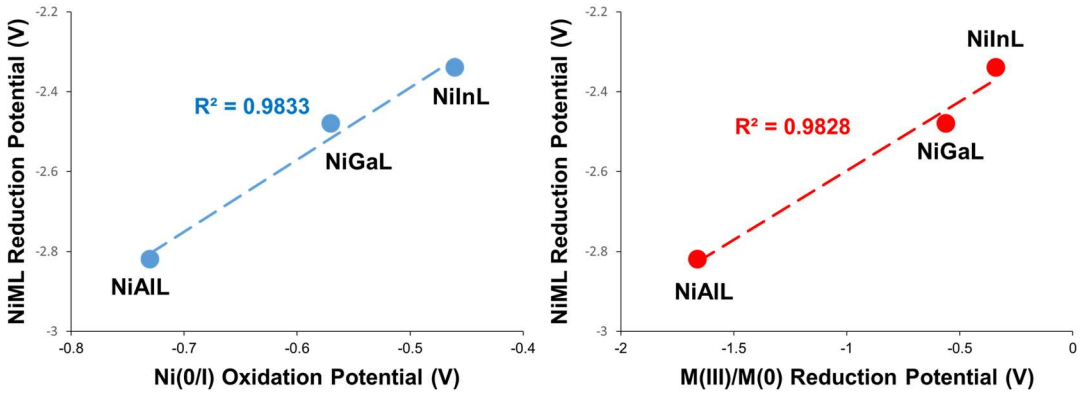

Figure 2.10. Plots of the NiML reduction $E°_{1/2}$ potential in THF vs. the Ni(0/I) oxidation $E°_{1/2}$ potential in CH_3CN (left) and the standard M(III/0) reduction potentials for the supporting group 13 metals (right). Ideally $E°_{1/2}$ potentials for both the oxidation and reduction events would be obtainable in the same solvent for the plot on the left, but it should be noted that the Ni(I/0) potentials are essentially identical in THF and CH_3CN, with improved reversibility for the NiInL oxidation event in CH_3CN.

If the reduction were truly a localized Ni(0/−I) reduction, then one would expect to see an excellent correlation with the unambiguously assigned Ni(0/I) oxidation potential; in other words, more electron-rich Ni(0) centers in the NiML series would be expected to be easier to oxidize to Ni(I) but more difficult to reduce to Ni(−I). Indeed, the Ni(I/0) redox potentials correlate well with the NiML reduction potentials (R^2=0.9833, Figure 2.10), consistent with a Ni-based reduction. However, an excellent correlation is also observed between the NiML reduction potentials and the standard M(III/0) reduction potentials of the supporting metal, as might be expected for a localized M(III/II) reduction (Figure 2.10).[158]

In order to determine the best way to describe the unusual, highly-reduced $[NiML]^-$ species that appeared to be stable in THF based on CV, further studies were conducted, to which I contributed preliminary results which were explored in much greater detail by two other researchers, Matt Vollmer and Dr. Jing Xie. Namely, the reduced $[NiML]^-$ species for M=Al ($[\mathbf{1}]^-$) and M=Ga ($[\mathbf{2}]^-$) were isolated and

characterized by electron paramagnetic resonance (EPR) spectroscopy and x-ray crystallography, as well as interrogated computationally using density functional theory (DFT) and complete active space self-consistent field (CASSCF) calculations.[158] [**1**]$^{-}$ and [**2**]$^{-}$, which are highly air- and water-sensitive owing to their highly reduced nature, could be generated chemically in good yields by either filtration of a THF solution of NiML through a plug of excess KC_8, or by addition of a slight excess (1 to 1.5 equiv) of KC_8, with 1 equiv 2,2,2-cryptand (crypt) added in both cases as an encapsulating agent. In short, the added electron appears to be delocalized to some extent across the Ni→M unit, suggesting that the formal oxidation states for the [NiML]$^{-}$ species lie somewhere in between Ni(−I)/M(III) and Ni(0)/M(II). That said, both theory and experiment support the notion that the [NiML]$^{-}$ complexes are better described by the Ni(−I)/M(III) formalism, making these rare examples of Ni complexes with sub-valent Ni character.[158]

Particularly supportive of a predominantly Ni-based reduction were CASSCF calculations, which predict the singly-occupied molecular orbital (SOMO) of [NiML]$^{-}$ to have ~70% Ni character with minor contributions from the supporting metal (14% for Al, 21% for Ga) and phosphorus (10-15%; Figure 2.11b).[158] Consistent with this, DFT calculations found that the relative Mulliken spin densities on Ni in [NiML]$^{-}$ were about twice as large as those on the supporting metals, with Ni:M spin density ratios of 1.8:1.0 and 2.1:1.0 for [**1**]$^{-}$ and [**2**]$^{-}$, respectively (Figure 2.11b).[158] Experimentally, the EPR signals for the S=1/2 radicals exhibited hyperfine coupling to the supporting metals for both [**1**]$^{-}$ and [**2**]$^{-}$, consistent with the computationally predicted delocalization of the radical to the Al/Ga atoms. The EPR spectra for both [**1**]$^{-}$ and [**2**]$^{-}$ were also well-modelled with hyperfine coupling to three equivalent P atoms, consistent with unpaired

spin density on Ni, which does not show hyperfine coupling due to the lack of spin-active Ni nuclei of appreciable natural abundance. The EPR spectra of [**1**]$^{-}$ at 61 K and rt are shown in Figure 2.11; at rt, the EPR signal becomes isotropic and hyperfine coupling to the ^{31}P nuclei becomes resolved (see Figure 2.11 caption for EPR parameters from best-fit simulation).[158]

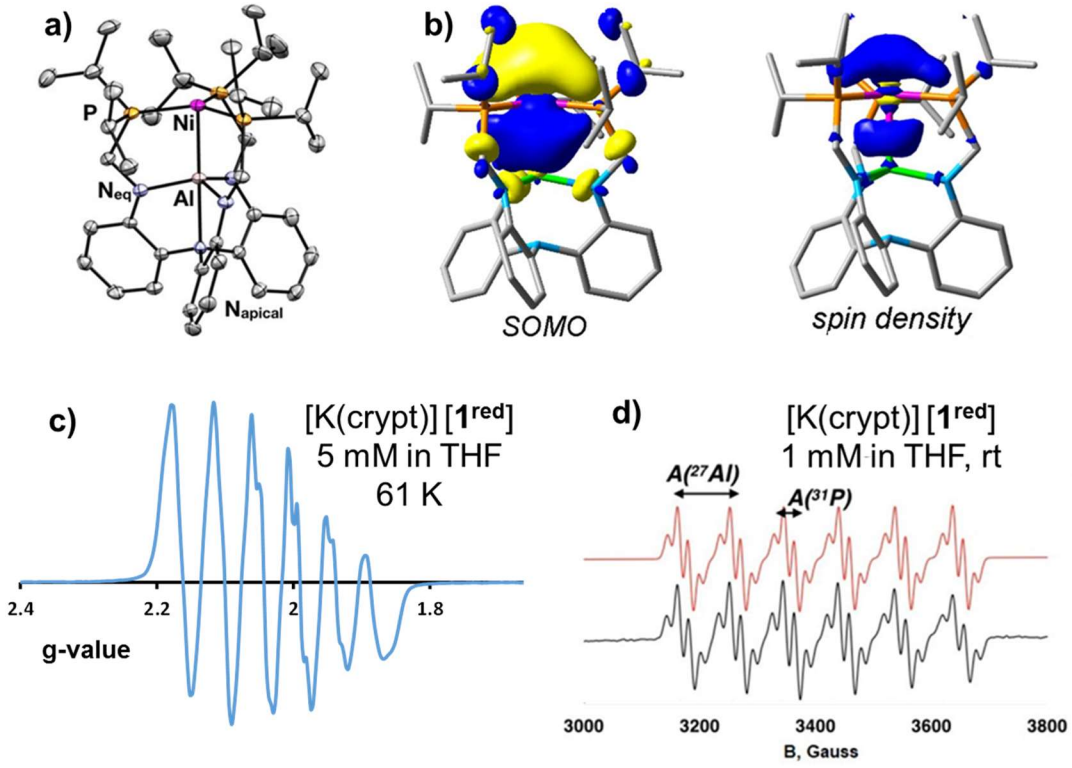

Figure 2.11. (a) Solid-state structure of [K(crypt)][**1**] obtained by Matt Vollmer (denoted as [K(crypt)][**1**^{red}] in this figure to avoid confusion with **1**), with ellipsoids shown at 50% probability and countercations, non-coordinating solvent molecules, and H atoms omitted for clarity. (b) Contour plots for SOMO of [**1**]$^{-}$ (*left*) and the Mulliken spin density (*right*), as calculated by DFT at the PBE/TZ2P level by Dr. Jing Xie. (c) X-band EPR spectrum of [K(crypt)][**1**] generated *in situ* (~5 mM in THF), which was modelled adequately as a nearly-axial signal with the following parameters: g_x=g_y=2.009, g_z=2.025, with A_x=11.5 mT, A_y=9.2 mT, and A_z=7.9 mT for coupling to ^{27}Al (I=5/2, 100% abundant). (d) X-band EPR spectra at rt of isolated [K(crypt)][**1**] (1 mM in THF, obtained and modelled by Matt Vollmer). The experimental spectra (black trace) is shown along with the simulated spectra (red trace), with isotropic parameters of g=2.0267, A_{Al}=7.6 mT, and A_P=1.3 mT. Note that DFT-calculated EPR spectra also match well with the experimental spectra. Figure adapted from that provided by Matt Vollmer.[158]

That the reduction is somewhat delocalized across the Ni→M interaction is also supported by the fact that the SOMO qualitatively depicts a σ-bonding interaction between Ni (mainly $4p_z$) and the supporting metal (*s* and *p* orbitals), albeit a highly polarized bonding interaction towards Ni as mentioned. Consistent with the added electron occupying a Ni→M bonding molecular orbital, the solid-state structure of [**1**]$^-$ shows a significant contraction in the Ni−Al bond distance relative to that of complex **1**, from 2.450(1) to 2.389(1) Å.[78, 158] Intriguingly, this represents an atypical bonding motif; in most cases where three valence electrons are shared between two atoms, one of the electrons occupies an antibonding orbital, which results in a formal bond order of 0.5 (ie. He_2^+).[159-162] In general, the propensity of the Lewis acidic group 13 supporting metal ion to aide in stabilizing highly-reduced Ni complexes will be a reoccurring theme that is revisited in the stabilization of unusual anionic Ni hydride complexes in chapter 5.

2.2.7 Why Does M(III) Size Dictate Lewis Acidity Toward Ni in NiML: Utilizing CV and X-ray Crystallographic Data to Attempt to Disentangle Electronic and Steric Effects of M(III) Size

In considering why M(III) size correlates well with the Lewis acidity of M(III) toward Ni, as measured in terms of the ionic radii and the Ni(I/0) redox potential, one subtlety that is important to understand is whether M(III) size serving as a proxy for Lewis acidity is a generalizable principle that can be expected to hold true for group 13 metals acting as Lewis acids toward Lewis basic transition metals in other systems. Alternatively, M(III) size could be dictating Lewis acidity toward Ni for steric or geometric reasons that are a consequence of the constraints of our ligand framework. This is an important distinction, and it will be dissected here by drawing upon insights from

other systems to inform the extent to which M(III) size dictating the Lewis acidity of group 13 metal ions toward transition metals is a generalizable principle.

It is important to recognize that Lewis acidity is not a concrete property that holds true for all chemical interactions involving a particular Lewis acid. That is, Lewis acidity is dependent on the particular Lewis base, or more broadly the type of Lewis base, from which the Lewis acid is withdrawing electron density. Thus, the relative strength of Lewis acids cannot be fully generalized, as different relative orderings of Lewis acidity can result depending on the characteristics of the Lewis base donor.[136] As Downs described this notion for group 13 Lewis acidity in particular, "attempts to assess relative Lewis acidities have emphasized the variety of factors contributing to the strength of the coordinate link."[136] To rationalize differing relative Lewis acidities toward different Lewis bases, Pearson proposed the Hard Soft Acid Base (HSAB) theory.[163] The fundamental principle of HSAB theory is that Lewis acids and bases can be classified on a continuum of "hardness" and "softness", and that Lewis acids and bases within the same hard/soft class form stronger dative bonds, or Lewis acid-base adducts, with each other. Soft Lewis acids are classified as such based on their larger radii, lower charge density, and greater degree of polarizability compared with hard Lewis acids.[163]

In applying HSAB theory to the relative Lewis acidities of group 13 metal ions, Ga(III) and In(III) would generally be expected to act as stronger Lewis acids toward "softer" Lewis base donors, while the smaller and more densely charged Al(III) and B(III) ions would generally be stronger Lewis acids toward "harder" donors.[136, 163-164] Late transition metals like Ni(0) are soft Lewis base donors, so based on HSAB theory, it would be expected that Ga(III) and In(III) moieties would be stronger Lewis acids toward

Ni than Al(III), in accord with the collective results of structural and electrochemical studies (*vide supra*). It is widely accepted that HSAB theory indirectly accounts for the need for a good match in Lewis donor and acceptor orbital energies to allow for strong dative bond formation.[163, 165-166] Applying this notion to NiML complexes, the M(III) ions withdraw electron density from both Ni(0) and from the three amide nitrogen donors. So, perhaps the poor energetic match of the N 2*p* orbitals of the amide donors with both the Ga $4p_z/5s$ and In $5p_z/6s$ orbitals, in comparison to that with the Al $3p_z/4s$ orbitals, results in preferential interaction of Ga(III) and In(III) with the soft Ni(0) Lewis base rather than with the harder amide donors.[97, 163]

This principle of larger group 13 M(III) ions acting as stronger Lewis acids toward transition metals via direct bonding interactions has not been extensively studied in the literature. One can imagine that a series of complexes in which the transition metal was held constant and the Lewis acidic moiety was varied may provide insight into the factors that dictate Lewis acidity toward transition metals. Such a series with more than two such complexes for group 13 Lewis acidic ions had not been prepared prior to our series of NiML complexes. To the best of my knowledge, prior to our report of NiML complexes, the only isostructural comparisons that could be made to gauge the relative Lewis acidity of group 13 metal ions involved in direct bonding interactions with transition metals were between Pd(TPE) (E=B, In) and ClAu(TPE) (E=B, Ga), complexes prepared by Bourissou and co-workers, where TPE is tris-(*o*-diisopropylphosphino-phenyl)E (Figure 2.12).[98, 100-101] Since our report of the NiML complexes, Iwasawa and co-workers reported an isostructural bimetallic series of PdCl(PEP) complexes, with the supporting metal varied down group 13 (E=Al, Ga,

In).[127] Our laboratory also recently reported two other isostructural series of M→E interactions between late transition metals (M=Rh, Co) and group 13 elements (E=Al, Ga, In).[132, 167] Notably, in all of the isostructural series in which only the group 13 supporting metal identity was varied, the normalized M−E bond distance between the transition metal (M) and the group 13 element (E), as given by *r*, was found to decrease in moving down group 13 to larger supporting metals (Figure 2.12).

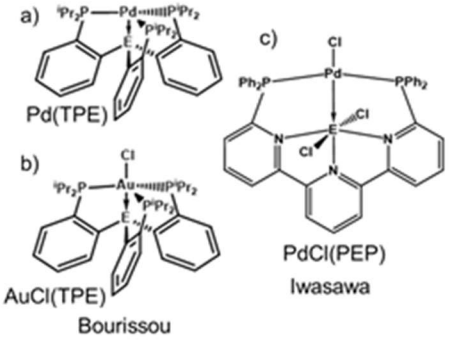

		M−E FSR (*r*) for Group 13 ("E")			
Isostructural Complexes		B	Al	Ga	In
other systems	Pd(TPE)	1.01	–	–	0.93
	AuCl(TPE)	1.05	–	1.00	–
	PdCl(PEP)	–	1.00	0.97	0.93
within our ligand (L)	NiEL	–	1.00	0.97	0.92
	(H_2)CoEL$^-$	–	1.00	0.96	0.92
	(Cl)RhEL	–	0.97	0.95	–

Figure 2.12. Isostructural series in which the effect of varying the group 13 Lewis acidic metal ion on direct bonding interactions with transition metals can be studied. Other systems in the literature include: (a) Pd triphosphinoborane[101] (TPB) and triphosphinoindane[98] (TPI) complexes, (b) Au(TPB)[101] and triphosphinogallane[100] (TPG) complexes, and (c) Pd−E complexes buttressed by the 6,6”-bis(diphenylphosphino)-2,2’:6’,2”-terpyridine (PEP) ligand.[127] Complexes (a) and (b) were reported by Bourissou and co-workers, while complexes (c) were reported by Iwasawa and co-workers. Our group has reported systems featuring Rh→E and Co→E dative bonds,[132, 167] ligated by the same ligand, L.[97] A comparison of M→E *r* values has been compiled for these sets of isostructural complexes in the chart on the right.

Strikingly, *r* values which decrease from 1.00 to 0.96-0.97 to 0.92-93 upon moving from Al to Ga to In, respectively, were observed for all three systems for which analogous Al, Ga, and In complexes have been characterized.[97, 127, 167] Likewise, among the systems in which two isostructural bimetallics with a varied group 13 element have been reported, the larger supporting group 13 metal has always been found to have a smaller M−E *r* value, consistent with a stronger interaction with the transition metal (Figure 2.12).[98, 100-101] In the case of the comparison of the Pd−In and Pd−B bonds in

Pd(TPE) complexes, the shorter normalized bond for Pd−In is predicted by natural bond orbital (NBO) analysis to be stronger by ~30 kcal/mol than the Pd−B interaction.[98, 101] It seems reasonable to conclude that the smaller $r_{alvarez}$ value and greater calculated bond energy for Pd−In is at least in part the result of the Pd $4d_z^2$ having a better orbital energy match with the $5p_z/6s$ orbitals of indium than with the $2p_z/3s$ orbitals of boron, in accordance with HSAB theory.[163, 165] On the contrary, B(III) is more Lewis acidic than In(III) based on the pK_a $M(H_2O)_6^{3+}$ scale for Lewis acidity.[136, 164] This discrepancy between the Lewis acidity toward oxygen donors in a water ligand and toward transition metals suggests that the relative orbital energies of the donor and acceptor likely play a prominent role in the strength of direct Lewis acid-base interactions.

All of this is collectively consistent with the fact that larger, softer group 13 Lewis acids form stronger dative bonds with a soft transition metal Lewis bases. Notably, just as was the case for NiML, greater electron-deficiency of the transition metal was observed by CV for shorter M→E bonds in the series of RhEL and CoEL complexes reported by our group.[132, 167] However, electrochemical data to gauge the relative electron-richness of the transition metal engaging in dative bonding to different group 13 metals was not reported for any of the three literature systems highlighted in Figure 2.12, so while it seems likely that the shorter dative bonds upon varying the supporting metal down group 13 translate into greater electron withdrawal from the transition metal in those systems as well, this has not been confirmed.[98, 100-101, 127]

2.2.8 Larger, Softer Group 13 M(III) Ions as Stronger Lewis Acids Toward Transition Metals: A Generalizable Principle?

The fact that the trend in decreasing M→E *r* values in moving down group 13 to larger supporting metals holds true for a few different ligand systems in the literature suggests that perhaps M(III) size serving as a proxy for the Lewis acidity of group 13 metals towards transition metal Lewis bases is a generalizable principle that follows from HSAB theory. However, the similarity of the ligands utilized to generate these series of isostructural M→E complexes cannot be overlooked, as all of them feature similar multi-dentate ligand buttresses designed to place the transition metal and group 13 moiety in close enough proximity to engage in dative bonding.[98, 100-101, 127] In doing so, the specific steric constraints of the ligand can also play a role in dictating the relative bond distances and Lewis acidities. Therefore, it is important to realize that the strength of M→E interactions and the relative Lewis acidity of "E" within these chelating ligand frameworks may be different from what might be found for an isostructural series of unsupported M→E bonds, where M and E are allowed to adopt an optimal bond distance independently from the steric constraints of the ligand donor sets. For example, in the lone example of unsupported isostructural M→E bonds with varying group 13 M(III) ions, $(PCy_3)_2Pt{\rightarrow}ECl_3$, a slightly shorter Pt→Al bond (2.3857 Å, *r*=0.928) was formed compared with Pt→Ga (2.4019 Å, *r*=0.931), illustrating that the larger group 13 M(III) ion does not always act as a stronger Lewis acid in unsupported bonds with relaxed steric constraints.[105, 108, 168]

Furthermore, both our ligand "L" and the terpyridine ligand of Iwasawa and co-workers feature capping donors, which tether the multidentate ligands together and are

positioned apically to the group 13 metal along the M→E bond vector (ie. M and the capping donor are *trans* to each other about E).[78, 97, 127] Thus, the group 13 metal position may not reflect its intrinsic propensity to bond with and act as a Lewis acid toward the transition metal, but instead may be a composite of that intrinsic propensity, its affinity for the ligand donor sets, and the spatial requirements imposed by the capping donor and the rest of the ligand framework. To this point, larger M(III) ions were found to be positioned higher above the N_3-plane in the solid-state structures of NiML complexes, with a good correlation between the M to N_3-plane distances and the Shannon M(III) ionic radii (R^2=0.95, Figure A.1.7).[78, 97] It is somewhat ambiguous whether the supporting metal sits further above the N_3-plane to promote stronger bonding with Ni for electronic reasons (ie. soft acid/soft base), or whether its position is dictated primarily by steric effects, where larger M(III) are sterically forced to be positioned further above the N_3 binding pocket and into closer proximity with Ni. Regardless of whether larger group 13 metals are "forced" into close proximity with Ni as an artifact of the ligand framework, once positioned there, larger group 13 metal ions do act as stronger Lewis acids and withdraw more electron density from Ni, as judged by the Ni(I/0) redox potentials from CV.[78, 97]

Key insights into the generalizability of the principle of size-controlled Lewis acidity of group 13 M(III) ions toward transition metals, as well as into the deconvolution of the steric and electronic effects of M(III) size, were recently provided by unpublished work by Bianca Ramirez, a graduate student in our group.[169] Figure 2.13 shows an analogous series of Ni−M bimetallic complexes (M=Al, Ga, In) synthesized and characterized by Bianca, with the key difference being that the capping amine donor

which tethers the three arms of the parent "L" ligand has been removed, such that the bimetallic pairing is now ligated by three individual phosphinoamide ligands ("L*$_3$").[169]

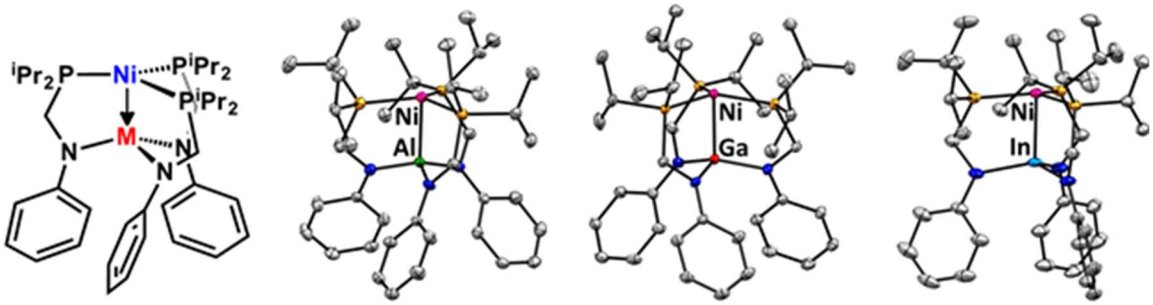

Figure 2.13. Solid-state structures of NiML*$_3$ complexes (M=Al, Ga, In) obtained by Bianca Ramirez.[169] Thermal ellipsoids are shown at the 50% probability level, and H atoms and lattice solvent molecules were omitted for clarity. Carbon (gray), nitrogen (blue), and phosphorus (orange) atoms are color-coded and the two metal atoms are labeled in each structure, with a Chemdraw structure also shown for clarity (left).

Because there are no longer any donor atoms along the Ni→M bond vector to impose any steric or electronic constraints on the positions of Ni and M, perhaps the intrinsic Lewis acidity of group 13 M(III) ions toward Ni can be more easily gleaned from comparing this series of NiML*$_3$ complexes to the parent NiML complexes. Nevertheless, the chelating ligand buttress will still dictate the positions of Ni and M to some extent, just as in the parent ligand, so perhaps the Lewis acidities toward Ni observed for the NiML*$_3$ complexes will still differ from those that might be observed in an isostructural series of unsupported dative bonds. The solid-state structural metrics of the NiML*$_3$ complexes are particularly informative in comparison to those of the NiML complexes of the parent ligand, as shown in Table 2.6.

Unlike the NiML complexes, in which the Ni−M *r* value decreases continuously as M is varied down group 13, the Ni−M *r* values are similar for Al, Ga, and In supporting metals in the trio of NiML*$_3$ complexes. Only a slight decrease in *r* value from 0.95 to 0.94 is seen in substituting In for Al in NiML*$_3$, compared with a much

more drastic decrease from 1.00 to 0.92 for that analogous substitution in the parent NiML series.[78, 97, 169] Even more strikingly, the Ni to P_3-plane and M to N_3-plane values for the NiML*$_3$ complexes are essentially invariant as the supporting metal was varied down group 13, with the former changing by <0.03 Å and the latter by <0.01 Å (Table 2.6).[169] This is in stark contrast to the NiML complexes, where the M to N_3-plane and Ni to P_3-plane distances varied by 0.22 Å and 0.10 Å, respectively, upon variation of the supporting metal down group 13.[78, 97, 170] Interestingly, the Ni→M bond distance changes significantly (~0.17 Å from M=Al to M=In) despite the aforementioned minimal changes in the Ni to P_3-plane and M to N_3-plane distances; this illustrates the greater flexibility of the individual phosphinoamide ligands (L*$_3$), relative to the parent ligand (L), to distort and twist so as to allow for the optimal Ni→M interaction in each case without necessitating significant changes in the positioning of Ni and M relative to their respective binding pockets.[169]

Table 2.6. Solid-state structural comparison of NiML*$_3$ and NiML complexes.[78, 97, 169]

Metric	**NiAlL*$_3$** [c]	**NiGaL*$_3$** [c]	**NiInL*$_3$**
Ni−M	2.3294(15)	2.340(1)	2.4927(5)
r [a]	0.95	0.95	0.94
Ni−P [b]	2.187(1)	2.203(1)	2.2293(5)
M−N_{eq} [b]	1.868(1)	1.918(1)	2.118(2)
Ni to P_3-plane	0.205	0.199	0.181
M to N_3-plane	0.421	0.424	0.423
	NiAlL	**NiGaL**	**NiInL**
Ni−M	2.450(1)	2.3789(8)	2.457(1)
r [a]	1.00	0.97	0.92
Ni−P [b]	2.204(1)	2.210(1)	2.252(1)
M−N_{eq} [b]	1.876(1)	1.954(2)	2.119(4)
Ni to P_3-plane	0.13	0.13	0.23
M to N_3-plane	0.26	0.37	0.48

[a]Ratio of the Ni−M bond length to the sum of the covalent radii, as given by Alvarez and co-workers.[134] [b]Average value. [c]Average values for two independent molecules in unit cell.

These dramatic differences upon the removal of the capping amine donor suggest that the steric effect of larger M(III) ions is more dramatic than was initially recognized in the parent NiML complexes, and plays a large role in dictating not only the positions of M and Ni relative to their respective binding pocket planes, but also in determining the extent of Ni→M dative bonding. The steric effect of larger M(III) is clearly seen when comparing Ni−Ga and Ni−In bimetallic complexes. For NiML, the larger In(III) ion sits 0.11 Å further above the N_3-plane compared with Ga(III), which "forces" Ni an additional 0.10 Å further above the P_3-plane relative to its position in **2**, and further from its preferred coplanar position with no supporting metal in **4** (Figure 2.14).[51, 97, 171]

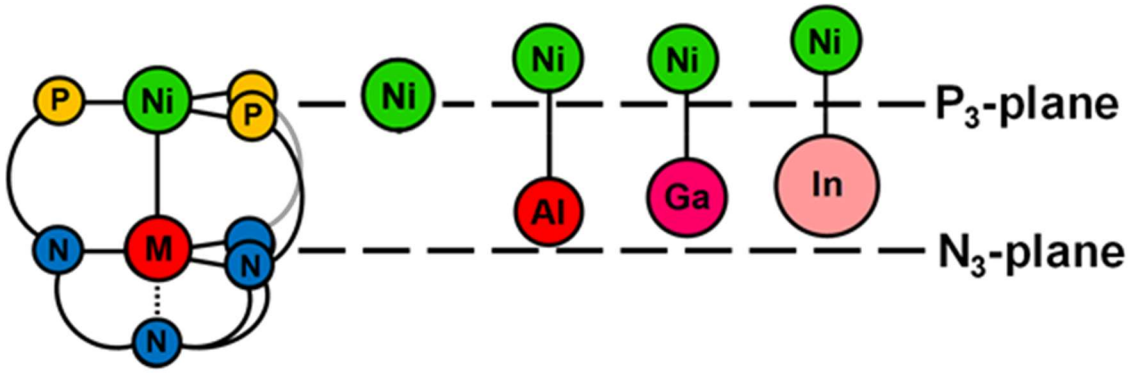

Figure 2.14. Diagram showing the effect of M(III) size on the positioning of both Ni(0) and M(III) relative to their respective binding pockets. Essentially no changes in the M to N_3-plane and Ni to P_3-plane distances were observed in the related NiML*$_3$ system.

In contrast, essentially no change in the positioning of Ga(III) and In(III) relative to the N_3-plane is observed for NiML*$_3$, and essentially no influence of the M(III) size on the positioning of Ni is observed either (Table 2.6).[169] Furthermore, it would appear that the large M to N_3-plane distance of In(III) in NiML complexes has more to do with steric effects imposed by the capping amine donor than with the preference of In(III) for facilitating greater interaction with Ni, as a similar propensity to interact with Ni to form

a short crystallographic bond as seen for NiInL is not observed in the analogous NiInL*$_3$ complex.

Preliminary CV results obtained by Bianca also show that the Ni center is more electron-deficient in NiGaL*$_3$ than in NiAlL*$_3$, with Ni(0/I) E_{pa} potentials in THF of −0.34 V and −0.45 V vs. $FeCp_2^{0/+}$, respectively.[169] Both of these potentials are harsher than those observed for the parent NiGaL and NiAlL complexes, which had Ni(0/I) E_{pa} potentials of −0.53 V and −0.68 V vs. $FeCp_2^{0/+}$, respectively.[97] Thus, the shorter Ni→M bonds observed in the solid-state structures of the NiGaL*$_3$ and NiAlL*$_3$ complexes do manifest in a greater degree of electron withdrawal from Ni and harsher Ni(I/0) redox potentials than in the analogous NiAlL and NiGaL complexes, though the removal of the capping amine donor may also slightly shift the Ni(I/0) redox potentials for all complexes to harsher potentials. An important preliminary conclusion from Bianca's work in looking at NiML*$_3$ complexes of group 13 (M=Al, Ga, In), group 3 (M=Y) and lanthanide (M=Lu) M(III) ions, is that the Ni(I/0) redox potentials seem to correlate well with the pK_a of the corresponding $M(H_2O)_6^{3+}$ complexes, just as was observed by Agapie and co-workers for the redox potentials in mixed metal-oxide clusters.[42, 52, 143, 146, 169]

Thus, it seems that by removing the capping amine donor, the steric constraints of the ligand are relaxed and the Lewis acidity of the supporting group 13 metal ion toward Ni is adequately described by similar parameters as that toward oxygen atoms in either water ligands ($M(H_2O)_6^{3+}$) or bridging oxide moieties (Mn_3O_2M).[42, 52, 146, 169] While it is clear that application of the HSAB theory holds some merit in dictating the degree of electron withdrawal by Lewis acidic group 13 M(III) ions from Ni in the NiML complexes based on spatial and energetic orbital overlap considerations,[97, 163, 165] in light

of the dramatic changes observed by removing the capping amine donor, it would appear that the steric effects imposed by the ligand framework in NiML complexes are much more dramatic than initially appreciated. Thus, it follows that M(III) size dictating the Lewis acidity of group 13 M(III) ions toward transition metals will be generalizable only in other similar chelating ligand frameworks, as seen in Figure 2.12, but need not hold true in the absence of the steric constraints imposed by capping donors along the M→E bond vector in these ligand buttresses.[98-101, 127] Indeed, as was seen from the elimination of the capping donor in the series of NiML*$_3$ complexes and from the examination of the limited number of unsupported M→E bonds, M(III) size alone does not generally predict Lewis acidity of group 13 M(III) ions toward transition metals.[108, 169]

2.2.9 UV-vis Spectroscopy and Electronic Structure of NiML Complexes

Based on analyzing the solid-state structures and CVs of the NiML complexes, it has been proposed that group 13 metal ions withdraw more electron density from Ni via shorter normalized Ni→M bonds. To understand the nature of the Ni→M dative bonding interactions and the perturbations of the Lewis acidic supporting metal on the electronic structure of Ni in the resulting NiML complexes, UV-vis spectroscopy studies were performed in conjunction with time-dependent density function theory calculations (TD-DFT, performed by our collaborator Dr. Jing Xie). Visually, complexes **1**, **2**, **3**, and **4** appear brown-yellow, deep red, red-purple, and purple, respectively; these color differences suggested that discernable differences would be observed in the UV-vis spectra of these complexes.

Figure 2.15 shows an overall comparison between the experimental UV-vis spectra and the TD-DFT (M06-D3) predicted spectra for the NiML and NiLH$_3$

complexes. Each peak is assigned to the excitation of one electron from an occupied orbital, either one of the Ni 3*d* orbitals or a ligand-based orbital, to the lowest unoccupied molecular orbital (LUMO), which is best described as an empty Ni-based $4p_z/s$ orbital, albeit with significant contributions from Ni (4*d*), M (*s*, *p*) and P (*p*) orbitals (Figures 2.17, A.1.17, Table A.1.2). Notably, the LUMO of NiML and the SOMO of the previously described $[NiML]^-$ complexes are essentially identical in terms of their composition, supporting the notion that the LUMO of NiML complexes are low-lying and energetically accessible to the point that they can be populated by an added electron in isolable complexes.[158]

The UV-vis spectra of complexes **1**, **2**, and **3** share the same three distinct peaks (labeled 1-3 in Figure 2.15) in the visible region of 400 – 700 nm, with all three peaks observed to red-shift upon varying the supporting metal down group 13 from Al to Ga to In.[78, 97] Calculated spectra (TD-DFT/M06-D3) predict the same features, with these three peaks assigned to the transitions from the $d_{xy}/d_{x^2-y^2}$ (1), d_{yz}/d_{xz} (2), and ligand π (major) plus minor d_{z^2} (3) orbitals to the LUMO (Figure 2.15, Table 2.7). The TD-DFT calculated transition energies are in moderately good agreement with experiment for **1** and **2**, though differentiation between the electronic structures of **2** and **3** proved problematic with all computational methods examined. We note that most predicted excitations are slightly blue-shifted from the experimentally observed peaks (Table 2.7). Additionally, it should be noted that the assignments of peaks 2 and 3 are reversed from the originally reported assignments; we feel confident that these updated assignments are correct based on the fact that four of the five functionals tested for TD-DFT agreed with one another and contradicted the original results reported for B3LYP (Table 2.9).[78]

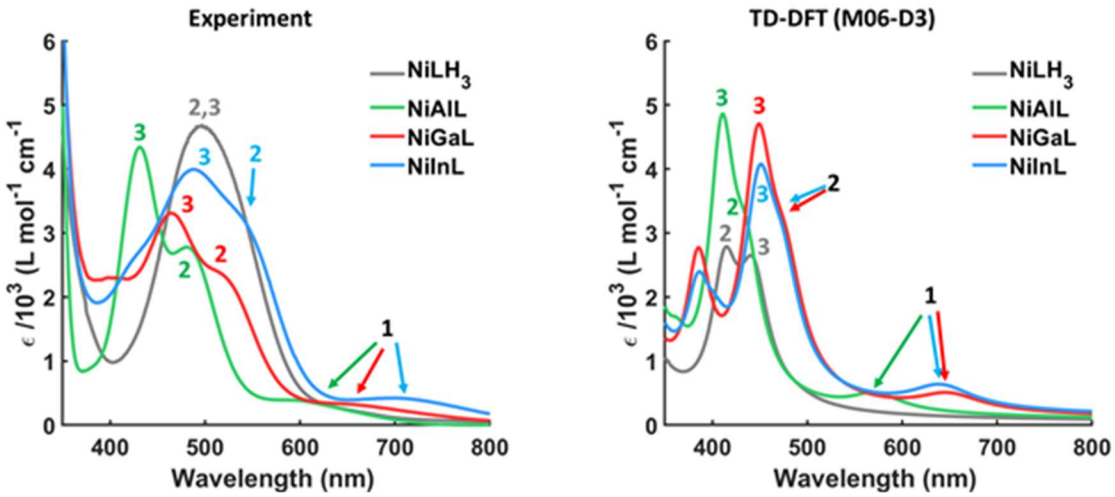

Figure 2.15. Experimental UV-vis spectra (left) and TD-DFT (M06-D3) predicted spectra (right) of $NiLH_3$ (gray), NiAlL (green), and NiGaL (red), and NiInL (blue) in THF. The assignments for the labeled peaks (1, 2, and 3) are listed in Table 2.7, with full assignments of simulated spectra shown in Figure A.1.16 and given in Table A.1.1.[78, 97]

An important comparison to make is the difference in electronic structure between $NiLH_3$ and NiML complexes, which should lend insight into the effect of introducing a supporting metal on the electronic structure of Ni. For $NiLH_3$, the experimentally observed broad peak at 497 nm is assigned to transitions from the d_z^2 (3) and d_{yz}/d_{xz} (2) orbitals to the LUMO, with an additional $d_{xy}/d_{x^2-y^2} \rightarrow$ LUMO transition with rather weak intensity predicted at 490 nm by TD-DFT (M06-D3). Relative to $NiLH_3$, the presence of the supporting metal in the bimetallic NiML species affects the Ni 3*d* orbital energy levels by stabilizing the $3d_z^2$ orbital and destabilizing the other four Ni 3*d* orbitals, such that the $3d_z^2$ orbital becomes the most stable of the five Ni 3d orbitals (Figures 2.15-2.16). The Ni $3d_z^2$ orbital is stabilized in NiML via dative Ni→M electron donation into the M $np_z/(n+1)s$ orbitals, in accordance with the blue shift in the predicted pure $3d_z^2 \rightarrow$ LUMO transitions from $NiLH_3$ (443 nm) to NiML (363-385 nm for complexes **1**, **2**, and **3**, respectively). The description of the Ni→M dative interaction as occurring via electron donation from the Ni $3d_z^2$ to M $np_z/(n+1)s$ orbitals was also corroborated by preliminary

natural bond orbital (NBO) calculations, and is in accord with the descriptions of other M→E interactions between transition metals and group 13 M(III) ions in the literature.[44, 101, 111-112]

Table 2.7. UV-vis transition assignments based on TD-DFT (M06-D3) calculations.[a]

No.	Transitions (nm)	$NiLH_3$	NiAlL	NiGaL	NiInL
1	$d_{xy}/d_{x^2-y^2}$ → LUMO	(490)	600 (573)	638 (650)	699 (642)
2	d_{yz}/d_{xz} → LUMO	497 (413)	490 (437)	508[b] (478)	530[b] (475)
3	Ligands + d_{z^2} → LUMO	497 (443[c])	430 (410)	464 (448)	488 (449)

[a]Experimental values with TD-DFT (M06-D3) calculated values in parenthesis. Table A.1.1 lists all other transition assignments based on TD-DFT. [b]Estimated value for peak shoulder; spectral deconvolution would be needed to confirm this as a precise value. [c]Pure Ni $3d_{z^2}$ → LUMO transition.

Besides its direct interaction with Ni, other indirect perturbations of the supporting metal on the Ni 3*d* orbitals are also important to consider. The predicted energy of the Ni $3d_{xz/}d_{yz}$ orbitals increases continuously upon installing a supporting metal ion and varying it down group 13 (no support < Al < Ga < In; Figure 2.16). This destabilization of the Ni $3d_{xz/}d_{yz}$ orbitals is attributable to weaker π-back-bonding (Ni $3d_{xz/}d_{yz}$ → P−C σ*) as the Ni center becomes more electron-deficient. This has been supported experimentally, as the Ni−P solid state bonds elongate with increasing Ni electron deficiency (In > Ga > Al > no support), with concomitant electronic de-shielding of the phosphorus nuclei manifesting in the ^{31}P NMR resonances shifting increasingly downfield.[51, 78, 97] Additionally, since transitions are observed from both the Ni $3d_{xy/}d_{x^2-y^2}$ and $3d_{xz/}d_{yz}$ orbitals to the LUMO, the difference in these transition energies can be evaluated to determine the energy gap between the Ni $3d_{xz/}d_{yz}$ and $3d_{xy/}d_{x^2-y^2}$ orbitals.[78] This analysis reveals that the energy gap between the Ni $3d_{xz/}d_{yz}$ and $3d_{xy/}d_{x^2-y^2}$ orbitals

increases from 0.46 to 0.50 to 0.57 eV upon variation of the supporting metal down group 13 (Figure 2.16).[78, 97]

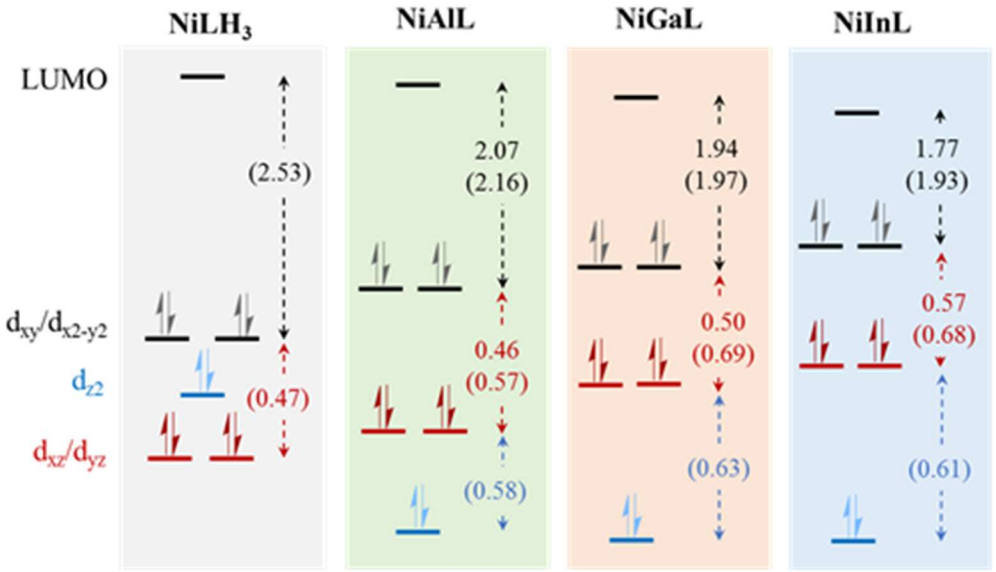

Figure 2.16. Molecular orbital diagrams of complexes **1**-**4** based on UV/Vis-spectra and TD-DFT calculations. Orbital energy differences (in eV) are shown as extracted from experimental UV-Vis spectra, with the corresponding calculated values from TD-DFT shown in parentheses. Figure provided by Dr. Jing Xie, with minor alterations.

Since the Ni $3d_{xz/}d_{yz}$ orbitals are destabilized in varying the supporting metal down group 13, as discussed, the Ni $3d_{xy/}d_{x}^{2}{}_{-y}^{2}$ orbitals must also be destabilized by a greater amount as the supporting metal is varied down group 13 in order for the energy gap between the two orbital sets to increase. However, destabilization of the Ni $3d_{xy/}d_{x}^{2}{}_{-y}^{2}$ orbitals seems somewhat counterintuitive since the solid-state Ni−P bonds elongate for NiML as the supporting metal is varied down group 13, which would typically result in less destabilization stemming from decreased spatial orbital overlap through which to facilitate P→Ni σ-donation. Perhaps the increasing electron-deficiency of Ni (In > Ga > Al > no support) results in compensating P→Ni σ-donation despite the elongation of the solid-state Ni−P bond distances. Though this nuance is admittedly not entirely understood, it should be noted that greater P→Ni σ-donation could also contribute to the

de-shielding of the phosphorus nuclei observed by ^{31}P NMR as the supporting metal was varied down group 13. Suffice it to say that the changes in P→Ni σ-donation across the trio of NiML complexes are somewhat difficult to interpret, but both experiment and theory agree that the Ni $3d_{xy}/d_{x^2-y^2}$ orbitals become increasingly destabilized upon variation of the supporting metal down group 13. Figure 2.17 shows the five Ni 3*d* molecular orbitals and the LUMO, as calculated for complex **2** by TD-DFT (M06-D3).

One last important trend to note is that the calculated HOMO-LUMO energy gap (ie. Ni $3d_{xy}/d_{x^2-y^2}$ → LUMO transition energy, labeled as peak 1 in Figure 2.15) decreases from 2.53 to 2.16 to 1.97 to 1.93 eV in moving from $NiLH_3$ to **1** to **2** to **3** (Figure 2.16). These HOMO-LUMO energy gaps agree well with the experimental values, which are 2.07, 1.94, and 1.77 eV for **1**, **2**, and **3**, respectively, with the biggest discrepancy stemming from the aforementioned inability of the computational methods to capture the electronic structure differences upon substitution of Ga for In.[78, 97] It is postulated that the decreasing HOMO-LUMO gap upon introduction of the supporting metal and varying it from Al to Ga to In results from both the aforementioned destabilization of HOMO (Ni $3d_{xy}/d_{x^2-y^2}$) and the stabilization of LUMO. The hypothesis that the LUMO is decreasing in energy upon introduction and variation of the supporting metal down group 13 is partially based on the empirical observation, detailed in the next chapter, that small molecule σ-donor substrates bind more readily to NiML complexes with smaller HOMO-LUMO gaps. Such a trend would not be expected if the decreasing HOMO-LUMO energy gap (Al > Ga > In) was only due to destabilization of the HOMO, while the LUMO, with which substrates interact with to bind, remained invariant in energy. Therefore, a decreasing LUMO energy upon introduction and variation of the supporting

metal down group 13 is proposed, such that the LUMO becomes more energetically accessible to accept σ-donation from small molecule substrates (further details in chapter 3).

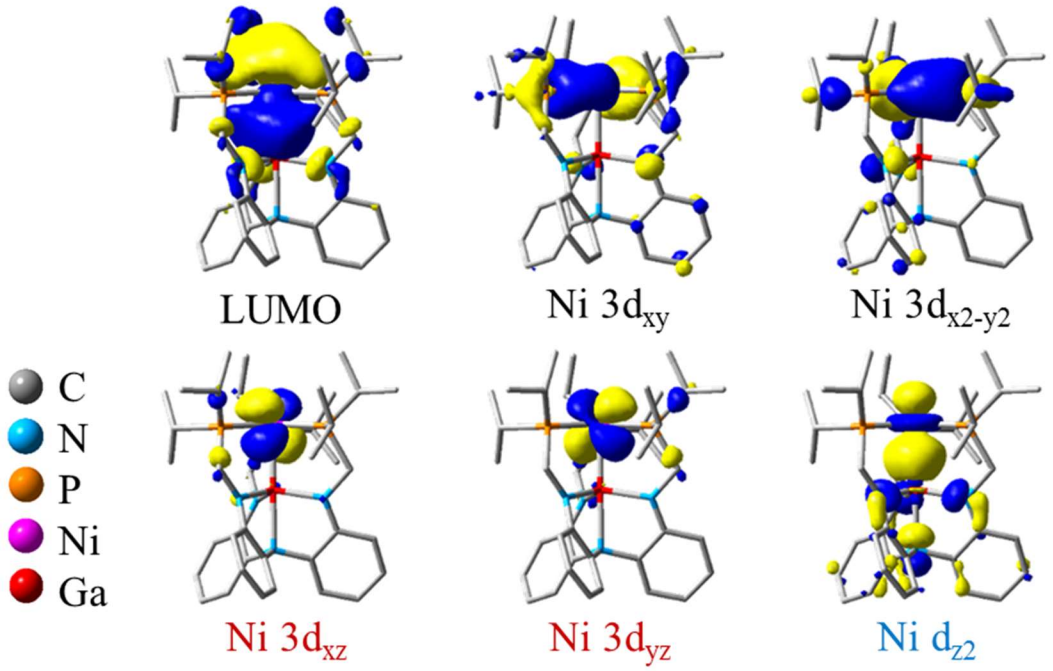

Figure 2.17. Selected molecular orbitals for complex **2**, as calculated by TD-DFT (M06-D3) by Dr. Jing Xie. All five Ni 3*d* orbitals are shown, and were found to be doubly occupied, consistent with the Ni(0), d^{10} formulation for the NiML complexes. The LUMO is also shown, which looks qualitatively like Ni 4p_z, but also consists of contributions from other Ni (4*s*, 4*d*), M (np_z/*s*) and P (*p*) orbitals (Table A.1.2). Similar molecular orbitals were calculated for complexes **1** and **3**.

The presence of a low-lying vacant orbital in NiML is not common for formally d^{10} transition metal centers, and this anomaly has been attributed to stabilizing interactions between the supporting metal np_z/(n+1)*s* orbitals with the Ni 4d_z^2/4p_z/4*s* orbitals which comprise the LUMO.[30, 158] In a simplified molecular orbital picture, one can think of the mixing of the Ni 3d_z^2, 4p_z/4*s*/4d_z^2 and M np_z/(n+1)*s* orbitals, all of which have the appropriate symmetry to mix or overlap. As a result, the Ni 3d_z^2 is stabilized as a bonding orbital, the M np_z/(n+1)*s* orbital set is greatly destabilized as antibonding, and

the Ni $4p_z/4s/4d_z^2$ orbitals which comprise the LUMO are formally non-bonding orbitals, but empirically the "non-bonding" orbitals seem to be stabilized by the M $np_z/(n+1)s$ orbitals to a greater extent for stronger Ni→M dative interactions (Ni $3d_z^2$ → M p_z/s).[30] That the HOMO-LUMO gap and the stabilization of the LUMO is directly related to the strength of the Ni→M dative interaction is supported by an excellent correlation between the HOMO-LUMO energy gap and the normalized Ni→M dative bonding interaction, as defined by the Ni−M $r_{Alvarez}$ value (R^2=0.9998; Figure 2.18).

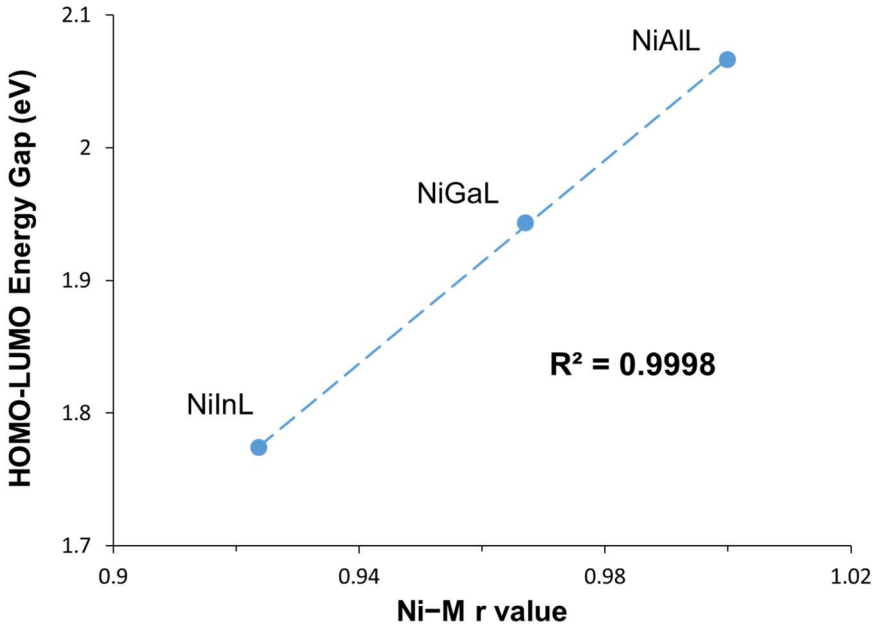

Figure 2.18. Plot of HOMO-LUMO energy gaps, as measured via experimental UV-vis studies, vs. normalized Ni→M dative interaction $r_{Alvarez}$ values from the solid-state structures.

Based on TD-DFT calculations, the bonding picture is more complicated than this simplified explanation, as the LUMO also has contributions from P (*p*) orbitals (Table A.1.2). The bottom line is that stronger Ni→M dative interactions result in greater stabilization of the LUMO of the NiML complexes, poising Ni to bind small molecule σ-

donors and react in ways that are not typical for Ni complexes without a supporting metal, as will be discussed in detail in the remaining chapters of this thesis.

2.3 Conclusions

An isostructural series of NiML bimetallic complexes featuring dative Ni→M bonds to Lewis acidic group 13 supporting metals (M=Al, Ga, In) has been synthesized via a step-wise metalation procedure.[78, 97] ^{1}H and ^{31}P NMR spectroscopy revealed that both the monometallic ML precursor complexes and the resulting NiML bimetallic complexes both retain solution-state C_3 symmetry, as well as lent insight into the relative degree of fluxionality of the M−P and Ni−P bonds. Solid-state structures of the monometallic ML complexes revealed weak M−P bonds poised to ligate a second metal, which was indeed seen to be the case upon successful installation of Ni(0) into the phosphine binding pocket. For the NiML bimetallic complexes, structural and electrochemical data showed that larger group 13 supporting metal ions (In > Ga > Al) withdraw more electron density from Ni via shorter normalized Ni→M dative bonds. Specifically, a dramatic electronic tuning effect was observed upon introduction and variation of the group 13 supporting metal down group 13, with Ni(I/0) redox potentials modulated by ~800 mV in CH_3CN and ~600 mV in THF. The spatial requirements of larger group 13 supporting metals were observed to influence the positions of both M and Ni relative to their respective binding pockets in the solid-state structures, with larger metals imposing steric pressure on Ni and "forcing" it further above its preferred position of coplanar with the phosphine donors (eg. in $NiLH_3$). Likewise, M(III) size and charge density, in terms of Shannon ionic radii, were also found to correlate well with the tuning

of the Ni electronic environment, as quantified by the Ni(I/0) redox potentials from CV studies.[97]

The disentanglement of the steric and electronic effects for why larger group 13 M(III) ions act as stronger Lewis acids toward Ni in NiML complexes is difficult. It is notable that the softness of the group 13 M(III) ions, as defined by HSAB theory and quantified by the estimated charge densities of the M(III) ions,[97, 163, 165] does seem to correlate well with the dative bond *r* values, not only in NiML complexes but also in the few other isostructural series of complexes with direct transition metal-group 13 interactions.[98, 100-101, 127, 132, 167] This similarity of the influence of M(III) size on Lewis acidity across several M→E systems, as well as the fact that typical descriptors of Lewis acidity such as the pK_a of $M(H_2O)_6^{3+}$ complexes fail to accurately reflect the trends in electron-richness and dative bonding in the NiML series, could be taken to suggest that the relative Lewis acidities of group 13 M(III) ions is fundamentally different for transition metal Lewis bases relative to those exerted toward typical Lewis bases like amines or oxide moieties. Following this logic, the greater Lewis acidity of softer group 13 M(III) ions toward Ni in NiML complexes may reflect better spatial and/or energetic orbital overlap of the acceptor orbitals of larger group 13 metals with the donor orbitals of Ni, a soft Lewis base, than with those of the harder amide donors.

However, the similarity of the ligand frameworks of the few isostructural series of M→E complexes in the literature present the potential for confounding steric effects of M(III) size and the constraints of the ligand to dictate bonding and Lewis acidity, such that the properties observed in NiML complexes may differ significantly from the intrinsic Lewis acidity of group 13 M(III) ions that would be conferred to Ni within a

different type of ligand framework or in an unsupported Ni→M bond. Indeed, unpublished results by Bianca Ramirez show that removing the capping amine donor, which tethers the three arms of L in NiML complexes and imposes steric constraints along the Ni→M bonding axis, has dramatic effects on the positions of Ni and M and the Ni→M bond distances relative to those in the parent NiML complexes.[97, 169] Importantly, upon relaxing the steric constraints of the ligand by removing the capping amine donor, the Ni(I/0) redox potentials in this new NiML*$_3$ series once again seem to correlate with typical Lewis acidity parameters, like the pK_a of $M(H_2O)_6^{3+}$ complexes.[169] This suggests that the steric implications of M(III) size can have drastic effects on the Lewis acidity conferred to proximal transition metals within multi-dentate chelating ligand frameworks, which can result in deviations in their observed Lewis acidity from that which would be conferred in a M→E bond that is unsupported or one that is ligated by a ligand with less stringent steric constraints. Thus, it seems that it is more accurate to conclude that the discrepancy between the Lewis acidities observed for group 13 M(III) ions in NiML complexes compared with $M(H_2O)_6^{3+}$ complexes is not primarily due to the difference in Lewis base characteristics between transition metals and harder Lewis bases, but instead is largely the result of steric effects imposed by the ligand framework in NiML complexes. Given that utilizing multi-dentate ligands to form supported M→E bonds is a common strategy that has been widely implemented in the literature, consideration of steric effects within such ligand frameworks should not be overlooked as a means of significantly tuning the Lewis acidity of M(III) ions and the properties of proximal transition metals.

Lastly, the perturbations of the supporting metal on the electronic structure of the resulting NiML complexes was interrogated by UV-vis spectroscopy in conjunction with TD-DFT calculations. The aforementioned Ni→M bonding is best described as Ni $3d_z^2$ → M np_z/(n+1)s dative electron donation, which leads to stabilization of the Ni $3d_z^2$ orbital relative to that in $NiLH_3$, in which no such dative interaction is present. Through less direct effects of the supporting metal on Ni, the other four Ni 3d orbitals are destabilized upon the introduction and variation of the supporting metal down group 13. A key indirect effect is that the LUMO, which is best described as the Ni $4p_z$ orbital with contributions from Ni 4s, 4d, M np_z/(n+1)s, and P p orbitals, is stabilized upon introduction and variation of the supporting metal down group 13 in a proportional manner to the strength of the Ni→M interaction. Indeed, complexes with stronger Ni→M dative bonds were seen to have smaller HOMO-LUMO energy gaps, as measured by the lowest energy transition via UV-vis spectroscopy and corroborated by TD-DFT calculations. It is highly unusual for a formally d^{10} transition metal to possess a low-lying, energetically accessible LUMO, and we attribute this anomaly to Lewis acidic stabilization of the primarily Ni-based LUMO.[30, 158]

Overall, supporting Ni with larger M(III) ions was found to increase the electron-deficiency of Ni, the distance which Ni is positioned above the P_3-plane, and the energetic accessibility of the LUMO, all of which will be seen to have significant implications on the propensity of NiML complexes to bind and functionalize small molecule substrates, as detailed in the next three chapters. Gratifyingly, supporting Ni with varying group 13 supporting metals within the L ligand framework has proved to be an effective strategy for significantly modulating the electronic and geometric properties

of Ni. Future chapters will explore the manifestations of these different properties in small molecule binding and catalysis, with the objective of optimizing the electronic and steric environment of Ni through the metal-support interaction to enable NiML complexes to react in desirable ways and mediate catalytic transformations for which Ni complexes are typically poor or incompetent catalysts. This objective fits within the larger goals of the Lu lab, and those of the inorganic chemistry community as a whole, of developing new strategies for utilizing inexpensive and Earth-abundant base metals to catalyze industrially and energetically relevant reactions involving small molecules.

2.4 Experimental Section

2.4.1 Synthetic Considerations

Unless otherwise stated, all manipulations were performed under an Ar or N_2 atmosphere inside a glovebox or using standard Schlenk techniques. Standard solvents were deoxygenated by sparging with N_2 and dried by passing through activated alumina columns of a SG Water solvent purification system. Deuterated solvents were purchased from Cambridge Isotope Laboratories, Inc., degassed via freeze-pump-thaw cycles, and stored over activated 4 Å molecular sieves. All other reagents were purchased from commercial vendors and used without purification unless otherwise noted. The neutral ligand ($N(o\text{-}(NHCH_2P^iPr_2)C_6H_4)_3$ (H_3L), $NiLH_3$ (**4**) and NiAlL (**1**) were synthesized according to literature procedures.[51, 78] Elemental analyses were performed by Robertson Microlit Laboratories (Ledgewood, NJ).

*Synthesis of NiGaL (**2**)*. A solution of H_3L (0.466 g, 0.684 mmol) in Et_2O (c. 10 mL) was frozen in a LN_2 coldwell. The solid was layered with *n*BuLi (0.970 mL, 2.42 mmol),

thawed, and stirred at rt for 2 h. The resulting solution was dried *in vacuo* and reconstituted in THF (c. 8 mL), before it was cooled in a LN_2 coldwell and added to a frozen solution of $GaCl_3$ (0.121 g, 0.687 mmol) in THF (c. 5 mL). The mixture was warmed to rt and stirred for 3 h, yielding a bright orange solution. The reaction was dried *in vacuo*, reconstituted in cold pentane, and filtered through a Celite pad and dried *in vacuo* to give GaL as an orange-brown powder (0.475 g, 90 % yield). The powder was reconstituted in THF (c. 5 mL) and added to a solution of $Ni(COD)_2$ (0.175 g, 6.42 mmol) in THF (c. 8 mL). The resulting mixture quickly turned a deep red color. The reaction was stirred for 2.5 h at rt and dried *in vacuo.* Subsequent washing with cold pentane, extraction into benzene using a Celite pad, and drying *in vacuo* afforded a deep red solid (0.400 g, 80% yield). Single crystals were grown through the slow evaporation of a concentrated pentane solution. $^{1}H\{^{31}P\}$ NMR (ppm, C_6D_6, 300 MHz): 7.60 (dd, *J*=1.3, 7.7 Hz, aryl, 3H), 7.20 (td, *J*=1.3, 7.7 Hz, aryl, 3H), 6.57 (t, *J*=7 Hz, aryl, 6H), 3.30 (d, *J*=13 Hz,C*H*H'P(^{i}Pr)$_2$, 3H), 3.17 (d, *J*=13 Hz, CH*H'*P(^{i}Pr)$_2$, 3H), 2.45 (br, methine, 3H), 1.92 (br, methine, 3H), 1.02 and 0.88 (m, methyl, 36H). ^{13}C NMR (ppm, C_6D_6, 126 MHz): 152.0, 135.1, 127.3, 127.0, 113.7, 109.1, 50.0, 31.2, 26.9, 22.1, 19.7, 18.4, 18.0. ^{31}P NMR (ppm, toluene-d_8, 161.9 MHz): 37.6. UV-vis (THF) λ_{max}, nm (ε, $M^{-1}cm^{-1}$): 464 (3310), 490 sh (2700), 638 br (340). Anal. Calcd for **2** $C_{39}H_{60}N_4P_3GaNi$: 58.10 C, 7.50 H, 6.95 N. Found: 56.24 C, 7.12 H, 6.03 N.

*Synthesis of NiInL (**3**)*. A solution of H_3L (0.204 g, 0.300 mmol) in Et_2O (c. 10 mL) was frozen in a LN_2 coldwell. The solid was layered with *n*BuLi (0.420 mL, 1.05 mmol), thawed, and stirred at rt for 2 h. The resulting solution was dried *in vacuo* and reconstituted in THF (c. 6 mL), before it was cooled in a LN_2 coldwell and added to a

frozen solution of $InCl_3$ (0.067 g, 0.303 mmol) in THF (c. 6 mL). The mixture was warmed to rt and stirred for 3 h, yielding a yellow-orange solution. The reaction mixture was dried *in vacuo*, reconstituted in benzene, and filtered through a Celite pad. The filtrate was dried *in vacuo*, yielding InL as a yellow-orange powder, which was then reconstituted in THF (c. 8 mL) and added to a solution of $Ni(COD)_2$ (0.082 g, 0.298 mmol) in THF (c. 8 mL) under an argon atmosphere. The mixture quickly turned purple-red, and was stirred for 3 h at rt before being dried *in vacuo.* Washing with pentane followed by extraction into benzene using a Celite pad and drying *in vacuo* gave a purple-red product (0.127 g, 50% yield). Single crystals were grown by layering pentane atop a concentrated benzene solution. $^1H\{^{31}P\}$ NMR (ppm, C_6D_6, 300 MHz): 7.73 (d, *J*=7 Hz, aryl, 3H), 7.21 (t, *J*=8 Hz, aryl, 3H), 6.63 (d, *J*=8 Hz, aryl, 3H), 6.55 (t, *J*=7 Hz, aryl, 3H), 3.38 (br, C*H*$_2$P(^{i}Pr)$_2$, 6H), 2.50 (br, methine, 3H), 1.96 (br, methine, 3H), 0.95 (m, methyl, 36H). ^{13}C NMR (ppm, C_6D_6, 126 MHz): 153.1, 135.0, 128.5, 127.0, 113.0, 109.9, 52.6, 29.9, 27.3, 22.2, 19.6, 18.8, 17.8. ^{31}P NMR (ppm, toluene-d_8, 161.9 MHz): 44.4. UV-vis (THF) λ_{max}, nm (ε, $M^{-1}cm^{-1}$): 488 (4000), 530 sh (3400), 699 br (420).

*Synthesis of (N$_2$)NiInL (**3**−N$_2$)*. A solution of H_3L (0.368 g, 0.541 mmol) in Et_2O (c. 10 mL) was frozen in a LN_2 coldwell. The solid was layered with *n*BuLi (0.765 mL, 1.91 mmol), thawed, and stirred at rt for 2 h. The resulting solution was dried *in vacuo* and reconstituted in THF (c. 8 mL), before it was cooled in a LN_2 coldwell and added to a frozen solution of $InCl_3$ (0.120 g, 0.543 mmol) in THF (c. 8 mL). The mixture was warmed to rt and stirred for 3 h, yielding a yellow-orange solution. The reaction mixture was dried *in vacuo*, reconstituted in benzene, and filtered through a Celite pad. The filtrate was dried *in vacuo*, yielding InL as a yellow-orange powder in near quantitative

yield. InL was subsequently reconstituted in THF (c. 8 mL) and added to a solution of $Ni(COD)_2$ (0.149 g, 0.553 mmol) in THF (c. 10 mL) under an N_2 atmosphere. The mixture quickly turned dark red, and was allowed to stir for 2.5 h at rt before being dried *in vacuo.* After washing with cold pentane, the solids were extracted into benzene using a Celite pad, and dried *in vacuo* to give a dark red product (0.340 g, 70% yield). Single crystals were grown through the slow evaporation of a concentrated pentane solution. $^1H\{^{31}P\}$ NMR (ppm, C_6D_6, 300 MHz): 7.74 (d, *J*=6 Hz, aryl, 3H), 7.24 (t, *J*=7.5 Hz, aryl, 3H), 6.66 (d, *J*=6 Hz, aryl, 3H), 6.59 (t, *J*=7.5 Hz, aryl, 3H), 3.16 (br, $CH_2P(^iPr)_2$, 6H), 2.06 (br, methine, 6H), 0.95 (m, methyl, 36H). ^{13}C NMR (ppm, C_6D_6, 126 MHz): 152.7, 135.8, 128.0, 126.9, 113.1, 109.7, 28.4, 19.4, 19.2. ^{31}P NMR (ppm, toluene-d_8, 161.9 MHz): 53.7 (br). UV-vis (THF) λ_{max}, nm (ε, $M^{-1}cm^{-1}$): 462 br (1330). IR: ν(N-N)=2144 cm^{-1} (KBr pellet). Anal. Calcd for **3**$-N_2$, $C_{39}H_{60}N_6P_3InNi$: 53.27 C, 6.88 H, 9.56 N. Found: 53.28 C, 7.15 H, 7.25 N. Nitrogen content was found to be consistently lower than expected due to the lability of N_2 under combustion analysis conditions.

2.4.2 X-ray Crystallographic and Structure Refinement Details

A dark red plate of **2**, a pink plate of **3**, red plate of **3**$-N_2$ were placed onto the tip of a 0.1 mm diameter glass capillary and mounted on a Bruker APEX II CCD diffractometer for data collection at either 123(2) or 173(2) K. The data collection was carried out using either Cu Kα (**3**$-N_2$) or Mo Kα (**2**, **3**) radiation (graphite monochromator). The data intensity was corrected for absorption and decay (SADABS).[172] Final cell constants were obtained from least-squares fits of all measured reflections. The structure was solved using SHELXS-97 and refined using SHELXL-97. A direct-methods solution was calculated which provided most non-hydrogen atoms from

the E-map. Full-matrix least-squares/difference Fourier cycles were performed to locate the remaining non-hydrogen atoms. All non-hydrogen atoms were refined with anisotropic displacement parameters. Hydrogen atoms were placed in ideal positions and refined as riding atoms with relative isotropic displacement parameters.[173] PLATON Squeeze was used to remove a disordered benzene molecule from the unit cells of **2** and **3**, as well as a pentane molecule from the unit cell of **3**−N_2.[174] Images were rendered using POV-ray.[175] Crystallographic data are summarized in Table 2.8. Note that additional crystallographic details are not provided for complexes crystallized by other researchers in our group that were discussed (ie. ML and NiML*$_3$ complexes).

Table 2.8. Crystallographic Details for Complexes **2**, **3**, and **3**−N_2.

	2	**3**	**3**−N_2
chemical formula	$C_{39}H_{60}N_4P_3GaNi$	$C_{39}H_{60}N_4P_3InNi$	$C_{39}H_{60}N_6P_3InNi$
Fw	806.26	851.36	879.37
cryst syst	Triclinic	Hexagonal	Monoclinic
space group	P-1	P-3	$P2_1/c$
a(Å)	11.275(2)	10.879(2)	14.8145(3)
b(Å)	14.152(3)	10.879(2)	14.4294(3)
c(Å)	14.267(3)	21.208(4)	22.8207(4)
α (deg)	70.822(2)	90	90
β (deg)	80.649(2)	90	95.670(1)
γ (deg)	82.759(2)	120	90
V ($Å^3$)	2115.2(7)	2174.0(7)	4854.4(2)
Z	2	6	4
Dcalcd (g cm^{-3})	1.266	1.42	1.343
λ (Å), μ (mm^{-1})	0.71073, 1.226	0.71073, 1.229	1.54178, 5.497
T (K)	173(2)	173(2)	123(2)
θ range (deg)	1.52 to 27.44	0.99 to 26.37	3.63 to 68.21
reflns collected	24408	11828	29361
unique reflns	6957	2089	7761
data/restraint/parameters	9522/0/445	2956/0/149	8834/0/514
R1, wR2 ($I > 2\sigma(I)$)	0.0566, 0.1653	0.0489, 0.1045	0.0547, 0.1465

2.4.3 Physical Methods

^{1}H, ^{13}C, and ^{31}P NMR spectra were recorded on Bruker 400 or 500 MHz and Varian 300, 500, or 600 MHz spectrometers and referenced to internal residual solvent (or H_3PO_4 for ^{31}P). UV-vis spectra were collected on a Cary-14 instrument. IR spectra were obtained in KBr pellets using a Bruker Tensor-37 FTIR with OPUS 6.5 software. Cyclic voltammetry (CV) was conducted using a CH Instruments 600 electrochemical analyzer. The one-cell setup utilized a glassy carbon working electrode, platinum wire counter electrode, and $Ag/AgNO_3$ reference electrode in CH_3CN. Analyte solutions were prepared in either THF or CH_3CN solutions of $[TBA][PF_6]$ (0.1 or 0.4 M) and referenced internally to the $FeCp_2/FeCp_2^+$ redox couple.

2.4.4 Computational Methods

Density Functional Theory (DFT) and Time-Dependent DFT (TD-DFT) Calculations

To find a suitable computational method to study the Ni−M bimetallic systems, we tested four functionals, M06-L,[176] M06-D3,[177] PBE0,[178] and PBE0-D3,[179] with four combinations of basis sets, which are denoted as bs1-bs4 (see Table 2.9). The combination of M06-D3/bs4 were suggested to give accurate results for a Pd−Pd bimetallic system.[180] Geometric structures were optimized in the gas phase at 0 K. Solvation effects were also considered by performing single-point calculations for all stationary points using the SMD[181] solvation model and THF as the solvent. All DFT calculations were performed with the Gaussian 09 program package.[182] TD-DFT calculations (M06-D3[177]/bs4, Gaussian09[182]) with solvent consideration (SMD, THF) were performed to obtain the absorption spectra of the series of NiML complexes (M=Al, Ga, In), along with the mono-nickel complex, $NiLH_3$. The assignments of the electronic transitions in the experimental

UV-vis spectra were made on the basis of TD-DFT calculations. TD-DFT calculations to study the electronic structure of [NiML]$^-$, M=Al ([**1**]$^-$), Ga ([**2**]$^-$), were also performed (M06-D3[177]/bs4), and the SOMO from these calculations is displayed in Figure 2.11b. In addition, preliminary NBO[114] calculations were carried out on DFT-optimized structures, using SDD[183-184] pseudopotentials for both Ni and M, along with 6-31G(d) and 6-311+G(2df,p) basis sets for C, H and N, P atoms, respectively.

Complete Active Space Self-Consistent Field (CASSCF) Calculations

CASSCF[185] calculations were performed on the M06-L[176]/DEF2[186]-optimized structures of [**1**]$^-$ and [**2**]$^-$ with an active space of 11 electrons in 12 orbitals using the MOLCAS-8.1 package[187] with relativistic basis sets of atomic natural orbitals types: ANO-RCC-VDZ[188] for N, P, C, and H atoms and ANO-RCC-VTZP for Ni and Ga atoms.

Table 2.9. Basis sets descriptions

Basis set	M	Ni	N,P	C,H
bs1	def2-TZVPP&SDD	def2-TZVPP	def2-TZVP	def2-SVP
bs2	SDD & SDD	def2-TZVPP	def2-TZVP	def2-SVP
bs3	LANL2DZ	6-31G(d)	6-31G(d)	6-31G(d)
bs4	LANL2DZ	6-311g(d,p)	6-311g(d,p)	6-311g(d,p)

2.4.5 Acknowledgements

Note that DFT, TD-DFT, and CASSCF calculations were carried out by Dr. Jing Xie, with some preliminary work done by Dr. Konstantinos Vogiatzis. Preliminary NBO calculations were carried out by me, with assistance from Dr. Nora Planas and Dr. William Isley III. The synthesis and characterization of NiAlL (**1**) and $NiLH_3$ (**4**) were performed by Dr. P. Alex Rudd and Dr. Laura Clouston, respectively. I would like to thank Dr. Victor Young, Jr., Dr. Laura Clouston, and James Moore for assistance with x-ray

crystallography. I would also like to thank Dr. Reed Eisenhart, Dr. Steve Tereniak, Dr. Laura Clouston, and Dr. P. Alex Rudd for helpful discussions. Lastly, I would like to acknowledge and thank Matt Vollmer, James Moore, and Bianca Ramirez, who allowed me to present some aspects of their work in this chapter in order to tell a more complete story.

Chapter 3

Steric and Electronic Effects of Larger Group 13 Supporting Metals Poise Ni for Small Molecule Binding: Thermodynamic and Kinetic Binding Studies for an Isostructural Series of Ni(η^2-H_2) and Ni(N_2) Adducts

In part from:

Cammarota, R. C.[‡]; Xie, J.[‡]; Vollmer, M. V.; Linehan, J. C.; Burgess, S. A.; Gagliardi, L.; Wang, X. P.; Hoffmann, C.; Young, V. G., Jr.; Lu, C. C.* "Lewis Acidic Group 13 Metalloligands Poise a Proximal Nickel Center for Small Molecule Binding: Thermodynamic and Kinetic Binding Studies and Neutron Diffraction Structure for an Isostructural Series of Ni(η^2-H_2) Adducts." **2018**, *manuscript in preparation*.

Cammarota, R. C.; Lu, C. C.* "Tuning Nickel with Lewis Acidic Group 13 Metalloligands for Catalytic Olefin Hydrogenation." *J. Am. Chem. Soc.* **2015**, *137,* 12486-12489.

Cammarota, R. C.*; Clouston, L. J.; Lu, C. C.* "Leveraging Molecular Metal-Support Interactions for H_2 and N_2 Activation." *Coord. Chem. Rev.* **2017**, *334*, 100-111.

3.1 Overview

With a series of bimetallic complexes in hand with different Ni electronic and geometric properties afforded via dative interactions with group 13 supporting metals, the binding and activation of small molecule substrates was targeted. In light of the increased electron-deficiency of the Ni centers in the NiML complexes relative to a single Ni center (eg. $NiLH_3$), the binding of substrates with favorable σ-donor properties was surveyed. Gratifyingly, the NiML complexes were found to bind many small molecules that $NiLH_3$ was unable to; this was exciting in that binding is the first step in activating small molecules toward further functionalization, and has typically proven to be a particularly difficult step for Ni complexes.[45, 189]

Chapter 3 will describe how the dual electronic and steric effects of larger supporting group 13 metals, which were discussed at length in chapter 2, were found to promote more favorable binding of substrates at Ni. The largest supporting metal ion examined, In(III), was found to promote the binding of a variety of different small molecules to complex **3**, with the relative order of binding found to be CO >> H_2 > N_2 > C_2H_4 > CO_2.[97] Complex **2** was found to bind the strongest σ-donor in that set, CO, as well as H_2.[45, 97, 190] Given the rarity of H_2 binding to Ni complexes and the ubiquity of H_2 binding and activation as a fundamental step in many catalytic processes,[22, 45, 84, 95, 191-192] the products of H_2 binding, (η^2-H_2)NiML, quickly became a primary research focus. In this chapter, the characterization of the (η^2-H_2)NiML complexes is presented, along with thermodynamic and kinetic studies of the H_2 binding equilibria. Notably, these are the first such studies for Ni(η^2-H_2) complexes, as well as the first for an isostructural series of first-row metal H_2 adducts. The isostructural nature of the (η^2-H_2)NiML complexes

provides a unique opportunity to understand H_2 binding and activation at Ni, and to elucidate the influence of the supporting metal on this uncommon reactivity for Ni.

Remarkably, significant modulation of the thermodynamic favorability of H_2 binding to Ni was observed simply by introducing and varying the group 13 supporting metal, with $\Delta G°$ values spanning ~5 kcal/mol and covering the entire range of previously reported values for H_2 binding to all transition metals.[45, 122, 193-194] This wide range of H_2 binding propensities controlled by supporting metal choice may be broadly useful, as inducing H_2 binding and activation at base metals in order to allow subsequent hydrogenation of substrates is often a challenge aspect of replacing precious metal hydrogenation catalysts.[21, 45, 122] The wide range of thermodynamic $\Delta G°$ values manifests in significantly different rates of H_2 self-exchange, binding, and loss, with varying the supporting ion from Al to In found to decrease the H_2 exchange rate by a factor of ~6 at 298 K. Interestingly, the free energy of activation ($\Delta G^{‡}_{bind}$) and the thermodynamic free energy ($\Delta G°$) of H_2 binding was found to correlate linearly across the NiML series, with a 1 kcal/mol decrease in $\Delta G°$ found to correspond to approximately a 1 kcal/mol decrease in $\Delta G^{‡}_{bind}$.

The isostructural nature of the (η^2-H_2)NiML complexes allowed for the identification of supporting metal size as the fundamental property which dictates both H_2 binding propensity and self-exchange kinetics at Ni. The greater Lewis acidity of larger supporting metals toward Ni was found to result in more electron-deficient Ni centers which induce a greater degree of σ-donation from the H−H σ-bond, resulting in slightly greater elongation of the bound H−H bond (In > Ga > Al).[30, 97] Supporting metal size was also found to correlate best with the thermodynamics of N_2 binding to NiML, as N_2 binds

more weakly than H_2 by ~2 kcal/mol (in terms of $\Delta G°$) in all cases. A discussion of the disentanglement of the steric and electronic effects of larger supporting metal ions on the binding of H_2 and N_2 is presented, with steric factors proposed to play a large role in dictating binding favorability. For M=In, the largest supporting metal, strong H_2 binding allowed for unprecedented structural elucidation of (η^2-H_2)NiInL (**3**−H_2) via single-crystal neutron diffraction—the first such study for a Ni(η^2-H_2) complex or any d^{10} M(η^2-H_2) complex.

Lastly, UV-vis studies and time-dependent density functional theory (TD-DFT) calculations were carried out to illustrate the specific electronic structure perturbations of the supporting metal which poise NiML complexes for the binding of small molecule donor substrates, with extended transition state—natural orbitals for chemical valence (ETS-NOCV) calculations indicating that H_2 binding primarily occurs via H−H σ-donation to the empty, Lewis-acid stabilized Ni $4p_z$ orbital. Collectively, this chapter presents a comprehensive understanding of how a group 13 Lewis acidic metal ion poises a proximal transition metal center for small molecule binding and influences both the thermodynamics and kinetics of binding equilibria. Further reactivity of the bound and activated H_2 ligand will be explored in chapters 4 and 5, with NiML complexes found to be competent catalysts for mediating hydrogenation reactions which Ni complexes typically are unable to catalyze.

3.2 Introduction

Utilizing inexpensive and earth-abundant metals as catalysts for energetically-relevant small molecule functionalization reactions while still retaining the excellent catalytic activity and selectivity of precious metal catalysts is highly desirable, and

remains a pervasive goal of inorganic and organometallic chemistry research.[1, 10, 21-22, 84] Aside from the undesirable propensity of first-row metals to undergo unproductive one-electron redox chemistry, base metal catalysts (Mn, Fe, Co, Ni) are often unable to activate substrates effectively to allow catalytic functionalization.[21-22, 45] This is particularly true in the case of developing Ni complexes capable of binding and activating H_2,[30, 45, 195] which is the first step in many important catalytic processes, including hydrogenation, isomerization, hydrogen oxidation, and proton reduction. This chapter will explore the reactivity of the NiML complexes, which were characterized in chapter 2, with small molecules such as H_2 and N_2. Ideally, the interaction with the supporting group 13 metal (M=Al, Ga, In) could promote binding and activation of H_2 and N_2 at Ni, both of which would represent atypical reactivity for Ni complexes.

In general, examples of Ni reacting with H_2 and N_2 are uncommon because Ni tends to be both a poor π-back-donor and a poor σ-acceptor.[30, 45, 196-197] Classical H_2 oxidative addition at a single Ni center has not been reported to our knowledge, attesting to Ni being a poor π-back-donor into the σ* orbital of H_2 compared with its more electronegative first-row metal neighbors on the periodic table, Co and Fe.[30, 44] Likewise, the lower propensity of Ni for engaging in π-back-donation also typically renders N_2 binding unfavorable, since ample π-back-donation into the π* orbitals of N_2 is critical for binding.[81, 189] For this reason, Ni is not the metal of choice for N_2 activation, with only seven reported structurally characterized examples of end-on binding of N_2 to Ni reported to prior to this work.[117, 189, 198-200] Even in those rare cases in which N_2 binds to Ni, the minimal extent of N≡N activation due to the poor π-basicity of Ni render Ni(N_2) complexes less interesting than Ni(H_2) complexes in terms of subsequent reactivity.[97, 117,

[189, 198] For this reason, this chapter will largely focus on the binding and activation of H_2 by the NiML complexes.

In considering H_2 binding to Ni, in addition to Ni being a poor π-back-donor, H_2 σ-donation to Ni is also unfavorable. For zero-valent Ni, all of the *d*-orbitals are filled, and thus unavailable to accept electron density from the H_2 σ-bond. Likewise, typical square-planar Ni(II) complexes have a filled d_z^2 orbital, precluding it from interacting with the H_2 σ-bond as well.[30] Given these limitations, it is perhaps not surprising that thermally stable Ni(η^2-H_2) adducts were not discovered until the past decade, and are still exceedingly rare.[30, 45] Prior to our report of (η^2-H_2)NiGaL and (η^2-H_2)NiInL complexes,[97] which will be detailed in this chapter, only one other H_2 adduct of Ni(0) had been reported,[117] along with three H_2 adducts of cationic Ni(II).[189, 198] As described in chapter 1, utilizing Lewis acidic Z-type metalloligands which engage in direct dative bonds with transition metals has emerged as a promising strategy for stabilizing low-valent, first-row transition metal centers which are reactive toward small molecules like H_2 and N_2.[44, 117-119, 122-127] This strategy has previously been utilized to allow for binding and functionalization of N_2 with Fe−Al and Co−Al pairings within our ligand framework.[78, 83] For NiML complexes, this chapter will detail efforts to investigate the effect of the supporting metal on H_2 and N_2 binding to Ni, which would typically be unfavorable binding equilibria for most Ni complexes.

Despite the ubiquity of H_2 binding, transient or otherwise, as a key fundamental reaction step in catalysis, very limited experimental data has been reported regarding the thermodynamic favorability and kinetic rates of H_2 binding to transition metals.[122, 193-194, 201-206] Experimental insight is particularly limited for H_2 binding to first-row metal

complexes: Co(tris-(*o*-diisopropylphophinophenyl)borane), abbreviated as Co(TPB), and $Cr(CO)_3(PCy_3)_2$ are the only first-row metal complexes for which solution-state thermodynamic measurements of H_2 binding have been reported to our knowledge.[122, 203, 205] A potential rationale for this void in quantitative characterization stems from the notion that without a series of similar M(η^2-H_2) adducts with which to compare, the gains in understanding attained by quantifying H_2 binding to a single metal complex are fairly limited. Excitingly on this front, our double-decker ligand and step-wise metalation procedure have allowed for the characterization of an isostructural series of three bimetallic (η^2-H_2)NiML complexes, which are rare examples of d^{10} M(η^2-H_2) complexes. These isostructural metal-dihydrogen complexes offer a unique opportunity to understand H_2 binding and activation at Ni, as well as the thermodynamics and kinetics of H_2 binding equilibria and the influence of the supporting metal therein. As will be discussed in future chapters, the ability of the supporting metal to modulate H_2 binding and activation at Ni in these complexes can be exploited to mediate the catalytic hydrogenation of both olefins (chapter 4) and carbon dioxide (chapter 5).

3.3 Results and Discussion

3.3.1 A Survey of Small Molecule Reactivity for NiML Complexes

3.3.1.1 A Review of Factors Which Dictate Small Molecule Binding to NiML Complexes

In the previous chapter, a series of bimetallic NiML complexes featuring strong Ni(0)→M(III) dative bonds (M=Al, Ga, In) was characterized in great detail to understand the effects of varying the group 13 supporting metal on the properties of the resulting Ni complexes. Overall, two primary effects of the supporting metal were identified that will greatly inform our understanding of the reactivity of NiML complexes

with small molecule substrates in this chapter. First, the supporting metal was found to exert a dramatic Lewis acidic tuning effect on the electronic environment of the proximal Ni centers in NiML complexes, as evidenced by the modulation of the Ni(I/0) redox potential by ~800 mV in CH_3CN relative to that of complex **4**, a similarly ligated Ni(0) center without a supporting metal. Specifically, larger supporting M(III) ions were found to result in a greater extent of electron withdrawal from Ni (In > Ga > Al > no support). The second primary effect of the supporting metal was a steric effect that was seen to play a key role in dictating the positioning of Ni and M with respect to their binding pockets within the ligand. Specifically, larger M(III) ions were seen to force Ni further above the P_3-plane, and away from its preferred position of approximately coplanar with the phosphines (ie. in **4**), which would allow for optimal Ni−P spatial orbital overlap and bonding. This change in the geometric positioning of Ni to be further above the P_3-plane was hypothesized to be important when considering its reactivity, as less reorganization energy would then be required in order for Ni to adopt the requisite pseudo-tetrahedral geometry for apical substrate binding.[97]

In order to gauge how these two effects dictate reactivity, the propensity of NiML complexes to bind various small molecule substrates was surveyed. It was hypothesized that both of these effects would promote more favorable binding and activation of substrates compared with $NiLH_3$ (**4**). While this chapter will largely focus on the binding and activation of H_2, and to a lesser extent that of N_2, a full scope of small molecule binding reactivity, including CO, CO_2, and C_2H_4, will be discussed at the outset of the chapter.

3.3.1.2 Small Molecule Reactivity as a Function of Supporting Metal and Substrate Donor Strength

Figure 3.1 shows the results of the initial reactivity scope of the NiML complexes with various small molecules. The binding reactions are described as being reversible or irreversible, which refers to the lability of the bound gas molecule to vacuum and serves as a convenient experimental descriptor of the qualitative strength of binding (Figure 3.1).

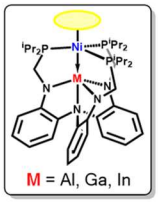

Binding of Small Molecules to NiML

Stronger Donor?

e⁻ poor Ni

Complex	CO_2	C_2H_4	N_2	H_2	CO
$NiLH_3$ (**4**)	–	?	–	–	decomp.
NiAlL (**1**)	–	?	–	weak, low T	decomp.
NiGaL (**2**)	–	–	weak, low T	reversible	irreversible
NiInL (**3**)	reversible	reversible	irreversible	irreversible	irreversible

Figure 3.1. Initial survey of binding reactivity of NiML complexes with small molecules under 1 atm gas pressure. Reversible and irreversible designations used to qualitatively describe the strength of binding based on the lability of the bound gas molecule to vacuum. No reaction is indicated by "–", and "weak, low T" indicates that binding only becomes observable at low T (for 1 atm pressure). A "?" indicates unknown reactivity with that particular substrate, and "decomp." indicates decomposition to multiple products.

In Figure 3.1, the Ni complexes have been ordered based on the degree of electron-deficiency of the Ni center (In > Ga > Al > no support), as judged by CV studies, and the substrates have been arranged to match the observed order of increasing binding strength to the NiML complexes (CO >> H_2 > N_2 > C_2H_4 > CO_2; *vide infra*).[45, 190, 195, 207] It should be noted that C_2H_4 can act as a stronger σ-donor ligand than H_2 and N_2 in some cases, and so this relative ordering is not meant to be portrayed as universal

for binding to all metals. One would expect that more electron-deficient Ni centers would react more readily with substrates that are primarily σ-donors than would more electron-rich Ni centers. Likewise, stronger donor substrates would be expected to react more readily with all complexes than weaker donors. Both of these expectations match the results, as complex **3** is the only complex to react to some extent with all five substrates examined, whereas only H_2 and CO bind to the relatively more electron-rich Ni center in complex **2**. Complex **1**, more electron-rich still, was only observed to bind H_2 weakly at low T, and none of the substrates were observed to bind to complex **4**, which features the most electron-rich Ni center of the series.

It should be noted that the initial reactivity scope summarized in Figure 3.1 was carried out at room temperature (rt) and 1 atm gas pressure, unless otherwise noted by the "low T" designation. As will be seen in the course of this chapter, changing the gas pressure and T can drastically perturb the binding equilibria such that even very weak binding equilibria can be observed and measured. This chapter will largely focus on the binding of H_2 and N_2 to NiML complexes, but to begin with, the binding of CO, CO_2, and C_2H_4 will be briefly discussed. In addition, attempted binding reactions of NiML with N_2O and THF will also be detailed.

3.3.1.3 CO Binding to NiML Complexes: Utilizing IR Spectroscopy of Bound CO as an Indirect Gauge of Electron-Richness of Ni and Supporting Metal Lewis Acidity

The reactivity of CO with NiML complexes was probed, with the goal of generating an isostructural series of (OC)NiML complexes. An attractive feature of such a series would be the fact that the IR stretch of the bound CO molecule, ν(C−O), would serve as a quantitative comparison of the degree of Ni electron-richness and its impact on

substrate activation. A more electron-rich Ni center would be expected to result in a greater degree of CO activation, and thus a lower frequency IR stretch, ν(C−O), via increased π-back-donation from the Ni $3d_{xz}/d_{yz}$ orbital to the CO π* orbitals.[110]

The desired (OC)NiML complexes were targeted via two different synthetic routes: (1) the addition of either 1 atm or 1 equiv CO gas to NiML, and (2) the addition of excess paraformaldehyde to NiML. The latter route had been previously reported to give a carbonyl dihydride species for the Fe(TPB) complex,[124] and had been seen to react similarly by Matt Vollmer in our group to give an unpublished $(OC)Fe(H)_2AlL$ complex. One can envision that such species may be unstable to reductive elimination of H_2 in many cases, resulting in the net addition of CO. Indeed, this is exactly what happens in the reaction of paraformaldehyde with **2** **3** to cleanly generate the (OC)NiML complexes, **2**−CO and **3**−CO (Figure 3.2).

The (OC)NiML complexes can also be generated from the addition of 1 equiv CO to NiML, and in the case of **3**−CO by the less precise addition of 1 atm CO. It should be noted that the addition of 1 atm CO to **2** results in the formation of multiple species. Similar undesired reactivity to give intractable products is observed for the reaction of NiAlL (**1**) and $NiLH_3$ (**4**) with either 1 equiv CO or paraformaldehyde. It is hypothesized that because CO is such a strong ligand, the addition of multiple CO ligands occurs if excess CO is present, which could potentially result in de-ligation of Ni from the phosphine donors of the ligand. It was observed that stronger Ni→M interactions (Al < Ga < In) result in greater stability of (OC)NiML to excess CO, which could be because stronger Ni→M bonds allow for increased stability of binding a single CO molecule

and/or because stronger Ni→M bonds are less prone to cleaving in order to allow Ni to bind additional CO ligands.

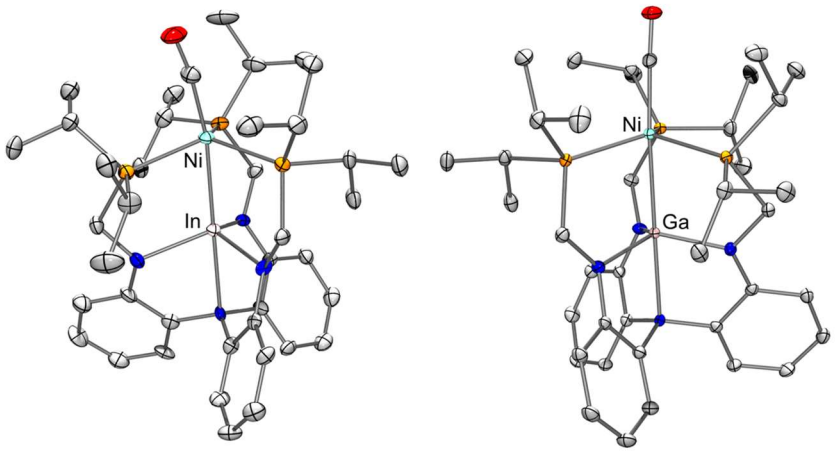

Figure 3.2. Solid-state x-ray structures of (OC)NiInL (**3**−CO, left) and (OC)NiGaL (**2**−CO, right) displayed with 50% thermal ellipsoids. Solvent molecule and H atoms were omitted for clarity. Metal atoms are labeled, and phosphorus (orange), nitrogen (blue), carbon (gray), and oxygen (red) atoms are color coded accordingly. Relevant structural parameters are shown in Table 3.1.

Solid-state structures of **2**−CO and **3**−CO are displayed in Figure 3.2, the former of which was obtained by Matt Vollmer, and selected structural parameters are shown in Table 3.1. In order to bind CO, the Ni center adopts a pseudo-tetrahedral geometry and is positioned further above the P_3-plane by ~0.2 Å in both **2**−CO and **3**−CO relative to their respective NiML complexes. The Ni→M bond weakens but remains intact, with *r* values increasing from 0.97 to 1.03 for **2**−CO and from 0.92 to 0.95 for **3**−CO. This weaker interaction is still consistent with a single dative bond, and results from the drastic re-positioning of Ni upon CO binding which is only partially counteracted by the supporting metal moving ~0.03 Å further above the N_3-plane. Although solid-state C≡O bond distances are not a great indicator of the degree of activation, the minimal elongation of the C≡O bond in **2**−CO and **3**−CO relative to free CO (1.128 Å) is consistent with only marginal activation via Ni→CO π-back-bonding.[110, 208-209]

Table 3.1. Selected structural parameters comparing NiML complexes[97] (**2**, **3**) to their respective CO adducts (**2**−CO, **3**−CO).

Metric	**2**	**2**−CO	**3**	**3**−CO
Ni-M	2.3789(8)	2.5287(3)	2.4573(12)	2.5232(9)
r [a]	0.97	1.03	0.92	0.95
Ni-P_{ave}	2.210(1)	2.2488(3)	2.252(1)	2.303(1)
M-N_{apical}	2.216(3)	2.292(2)	2.309(6)	2.372(4)
M-$N_{eq,\ ave}$	1.954(2)	1.938(1)	2.119(4)	2.113(3)
Ni to P_3-plane	0.13	0.36	0.23	0.42
M to N_3-plane	0.37	0.40	0.48	0.51
Ni-C	−	1.775(2)	−	1.755(6)
C-O	−	1.148(2)	−	1.151(7)

[a]Formal shortness ratio using Alvarez covalent radii[134] for Ni, Ga, and In.

A more informative quantitative gauge of the extent of CO activation and Ni→CO π-back-bonding is provided by comparing the relative values of ν(C−O) for **2**−CO and **3**−CO. As shown in Figure 3.3, ν(C−O) for (OC)NiML shifts to lower frequency by 7 cm^{-1} upon substitution of In (1968 cm^{-1}) for Ga (1961 cm^{-1}; see Figures A.2.6-A.2.7 for IR spectra). Although this 7 cm^{-1} shift is relatively small compared with the range of ~50 cm^{-1} that was compiled by Tolman for $Ni(CO)_3(PR_3)$ complexes with varying phosphine ligands,[210] the lower stretching frequency for **2**−CO compared with **3**−CO is consistent with a slightly more electron-rich Ni center in **2** compared with **3**, which results in more Ni→CO π-back-donation in the former case (Figure 3.3).

The slightly greater electron-richness of the Ni center in **2** compared with **3** is also in line with the Ni(I/0) redox potentials for the two complexes from CV studies, which were discussed in chapter 2. It should be noted that the unknown product of reacting $NiLH_3$ (**4**) with either 1 equiv CO or paraformaldehyde shows two ν(C−O), at ~1926 and ~1981 cm^{-1}. One would expect a lower frequency ν(C−O) for the hypothetical **4**−CO complex due to greater Ni→CO π-back-bonding from the more electron-rich Ni center in

4, but it seems likely that Ni coordinates multiple CO ligand and/or dissociates from the ligand, with the two ν(C−O) potentially attributable to symmetric and asymmetric stretches from a species with multiple CO ligands.

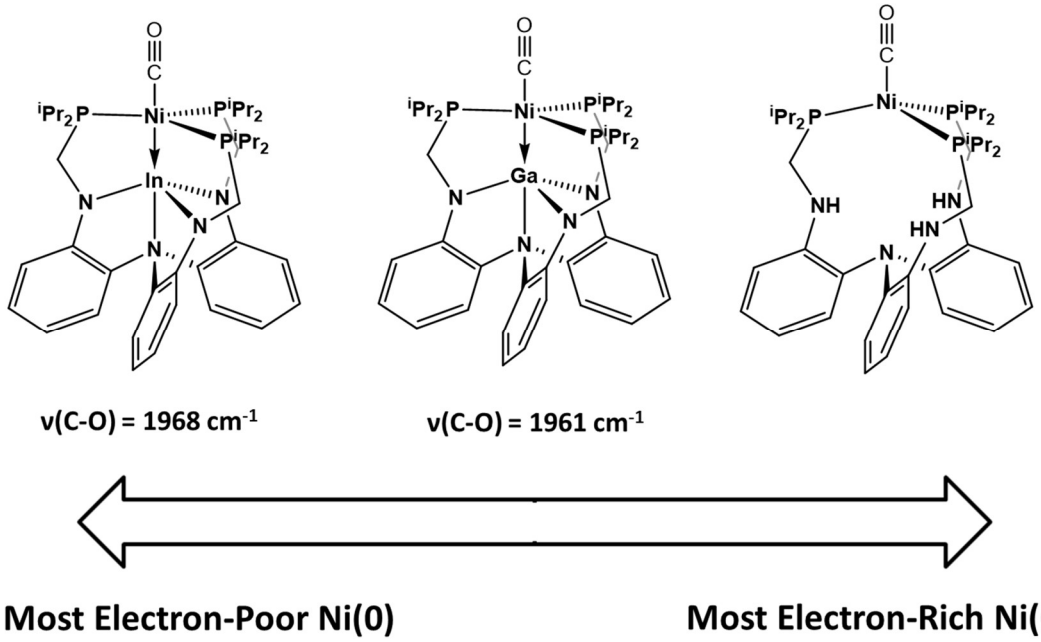

Figure 3.3. Characterization of an isostructural pair of (OC)NiML complexes (M=Ga, In) and evaluation of the relative electron-richness of Ni via IR spectroscopy.

Similar trends were observed in the relative ν(C−N) for an isostructural series of (^{t}BuNC)NiML complexes, which were synthesized by the addition of a slight excess of ^{t}BuCN (1.1 equiv) to NiML in THF. Notably, the NiAlL adduct can be synthesized for ^{t}BuCN but not for CO, likely due to the lesser propensity of multiple ^{t}BuCN ligands to bind and lead to undesired products and decomposition. The terminal ^{t}BuNC adducts of **1**, **2**, and **3** have ν(C−N) of 2091, 2098, and 2099 cm^{-1}, respectively. The relative order of the stretching frequencies (In > Ga > Al) matches what would be expected based on the relative order of Ni electron-deficiency and π-back-bonding propensity, though again it should be noted that the differences in stretching frequency are minor overall. The difference between Ga and In supporting metals is seen to be much smaller for ν(C−N) of

(^{t}BuCN)NiML complexes (1 cm^{-1}) compared with ν(C−O) in (OC)NiML complexes (7 cm^{-1}), while the shift to lower frequency for the ^{t}BuCN adduct of **1** speaks to the slightly greater electron-richness of Ni in **1** relative to **2** and **3**.

Although the CO and ^{t}BuCN adducts of NiML complexes are not useful for further reactivity, they do lend insight into how the different electronic environments of Ni, afforded by the various group 13 supports, may impact reactivity with substrates. These isostructural series of complexes permit indirect quantitative assessment of the electron-richness of Ni and the Lewis acidity of the supporting metal. Furthermore, such a series had long been targeted to assess the electronic influence of the supporting metal on reactivity, and so it is satisfying that it has been realized for both CO and ^{t}BuCN adducts of NiML, and that the relative stretching frequencies, while only slightly different, are well understood in terms of the relative electron-richness of the Ni centers.

3.3.1.4 Binding of Weak Donor Substrates to NiML Complexes: CO_2 and Ethylene

As shown in Figure 3.1, the only evidence under 1 atm pressure for the binding of CO_2 and ethylene (C_2H_4) was observed for complex **3**. That complex **3** would be the only NiML complex to bind CO_2 and ethylene makes intuitive sense, since these are both weaker ligands than CO and complex **3** features the most electron-deficient Ni center, which will prefer an additional donor ligand even if it is a relatively poor one. No structural evidence of CO_2 and ethylene binding was obtained, as both ligands were found to bind to **3** weakly, such that the bound CO_2 and C_2H_4 ligands were labile to vacuum. Figure 3.4 shows ^{31}P NMR spectra for **3** under 1 atm of Ar, N_2, CO_2, and C_2H_4, in comparison those for the irreversibly bound H_2 and CO adducts.

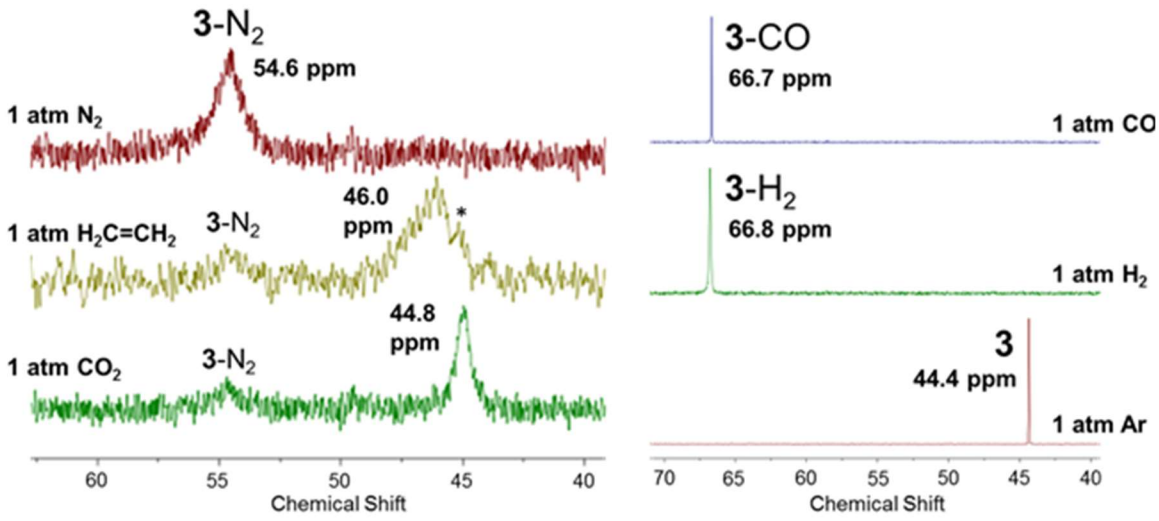

Figure 3.4. Stacked ^{31}P spectra of **3** under 1 atm gas pressure of various small molecules. Addition of ethylene (C_2H_4) and CO_2, to **3**–N_2 after a freeze-pump thaw cycle is shown on the left. Residual **3**–N_2 and **3** (*) are denoted. Addition of H_2 and CO is shown at the right in comparison to **3** under 1 atm Ar. Note that the spectra on the left were obtained in C_6D_6, whereas those on the right were taken in toluene-d_8 (minimal differences in ^{31}P δ were observed between the two solvents).

In general, sharper ^{31}P resonances that are shifted further downfield relative to that of **3** (44.4 ppm under 1 atm Ar) was found to be indicative of stronger binding (*vide infra*), as can be seen by the relatively sharp resonances for **3**–CO and **3**–H_2, which are shifted downfield by ~22 ppm relative to **3**. **3**–H_2 is shown solely for comparison here, and its characterization will be discussed in detail in the remainder of this chapter. Upon exposure of **3**–N_2 to 1 atm CO_2 or C_2H_4, ^{31}P peaks which are considerably broadened, but only slightly shifted downfield of **3**, were observed (Figure 3.4). Note that some **3**–N_2 remains in equilibrium with CO_2 and C_2H_4 despite the much greater pressure of those gases relative to residual N_2 remaining after a freeze-pump-thaw cycle, which is a testament to the very weak binding of CO_2 and C_2H_4 relative to N_2.

As will be explored in much greater and quantitative detail for H_2 and N_2, the broadening and slight downfield shifting observed for ethylene and CO_2 is indicative of

very weak binding via a rapid equilibrium between **3** and the bound adduct species. As will be explained more later in this chapter, because the equilibrium is faster than the ^{31}P NMR timescale (121.4 MHz), the observed ^{31}P peak is equal to the population-weighted average of the chemical shifts of **3** and the fully bound species.[211-213] Thus, the equilibria clearly lie very far toward **3** since the resonances only shift marginally downfield relative to the chemical shift of **3**. Although relatively little **3**–CO_2 and **3**–C_2H_4 species exist in solution relative to **3**, these equilibria can be perturbed and made to favor the bound adduct species to a greater extent by decreasing T and/or increasing the gas pressure, which is shown for CO_2 binding in Figure 3.5.

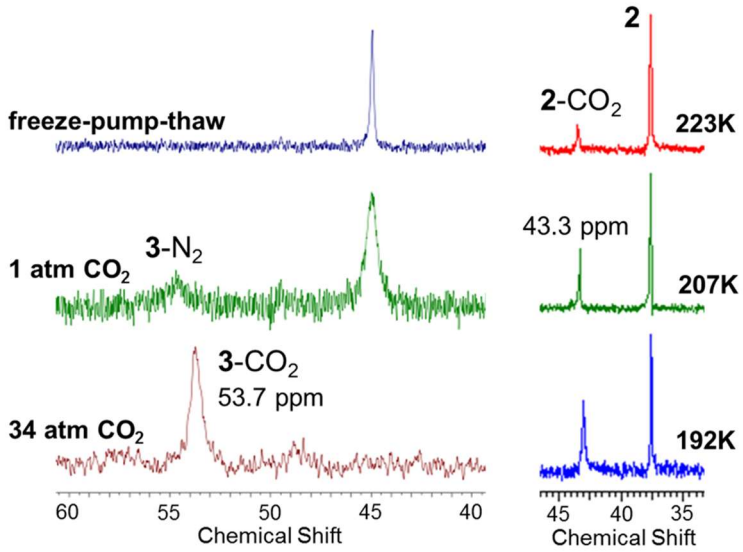

Figure 3.5. Stacked ^{31}P NMR spectra which show perturbations to the CO_2 binding equilibria to favor the bound species by increasing CO_2 pressure (for **3**, left) or decreasing T (for **2** under 34 atm CO_2, right). Note that all spectra were obtained in toluene-d_8, except the top two on the left (C_6D_6), with minimal differences observed between the two solvents for these complexes.

While exposure of **3** to 1 atm CO_2 resulted in only slight broadening and a marginal downfield shift in the ^{31}P NMR spectra (~0.5 ppm), increasing the CO_2 pressure to 34 atm is seen to result in a much more dramatic shift to 53.7 ppm (Figure 3.5). Because CO_2 binding is weak and the equilibrium is fast on the ^{31}P NMR timescale

(202.4 MHz), the true chemical shift of **3**−CO_2 would need to be determined by finding the low T convergence of the ^{31}P shift under high CO_2 pressures. Unlike the fast equilibrium for **3** and **3**−CO_2, a slow interconversion relative to the ^{31}P NMR timescale (202.4 MHz) is observed for **2** and **2**−CO_2, as seen by the distinct ^{31}P peaks observed under 34 atm CO_2 at low T (Figure 3.5).

The new ^{31}P peak assigned to **2**−CO_2 was observed at ~43.3 ppm and was found to grow in concentration relative to **2**, both over time and with decreasing T. It should be noted that extremely forcing conditions were utilized. CO_2 is present as a supercritical liquid in relatively high concentrations compared to solvent at 34 atm CO_2 and low T,[214] and so, for all intents and purposes, **2** does not bind CO_2 under any relevant conditions. Careful binding experiments, akin to those which will be discussed in this chapter for H_2 and N_2 binding, could be performed in principle to quantify the binding equilibria of CO_2 and C_2H_4 to complexes **2** and **3**. Nevertheless, these preliminary qualitative binding studies, in conjunction with the more quantitative binding studies for H_2 and N_2 that will be presented in the remainder of this chapter, have established the relative strength of small molecule binding for complex **3** to be CO >> H_2 > N_2 > C_2H_4 > CO_2.

Based on DFT computational studies conducted by Dr. Jing Xie (Figure A.2.8), this relative order of ligand binding strengths is expected hold true for complex **2**; however, interactions of **2** with C_2H_4 and CO_2 were more difficult to observe experimentally and required forcing conditions. To date, no reaction of **2** with C_2H_4 has been observed, though it is suspected that this is due to the fact that **2** has only been studied under 1 atm C_2H_4, given the observation of **2**−CO_2 under 34 atm CO_2 and the fact that CO_2 seems to bind more weakly than C_2H_4 to **3**. Given the weak binding of CO_2 and

C_2H_4 to **2** and **3**, the binding of CO_2 and C_2H_4 to **1** did not seem to be likely to occur and was not studied in detail. It is interesting that the relative order of small molecule ligand binding for NiML complexes matches that reported by Milstein and co-workers ($H_2 > N_2 > C_2H_4 > CO_2$) for a Rh complex.[215] The weaker binding of CO_2 and C_2H_4 to NiML complexes is consistent with these ligands being relatively poor σ-donors in comparison to CO, which is also an excellent π-acceptor ligand.[45, 190, 195, 207, 216] It seems NiML complexes feature a sufficiently electron-deficient Ni center that prefers to bind reasonably strong and sterically unhindered σ-donors, as will be corroborated later in this chapter via both experimental binding studies and computations.

*3.3.1.5 Solid-State Structural Comparison for Small Molecule Adducts of Complex **3***

A comparison of the structural parameters for the three adducts of **3** which are stable to vacuum, **3**−CO, **3**−H_2, and **3**−N_2, is provided in Table 3.2. The x-ray structure of **3**−H_2 will be discussed further in section 3.3.7, along with the corresponding neutron diffraction structure, while the other structures have already been described in previous sections (3.3.1 and 2.2.5).

Table 3.2. Selected structural parameters for **3** and its adduct complexes (**3**−CO, **3**−H_2, **3**−N_2).

Metric	**3**	**3**−N_2	**3**−H_2[a]	**3**−CO
Ni-M	2.4573(12)	2.5256(7)	2.479(2)	2.5232(9)
r [b]	0.92	0.95	0.93	0.95
Ni-P_{avg}	2.252(1)	2.311(1)	2.2618(2)	2.303(1)
Ni-H/C/N	−	1.848(3)	1.61(2), 1.61(2)	1.755(6)
M-N_{apical}	2.309(6)	2.384(5)	2.366(1)	2.372(4)
M-$N_{eq, avg}$	2.119(4)	2.118(2)	2.1147(6)	2.113(3)
Ni to P_3-plane	0.23	0.38	0.29	0.42
M to N_3-plane	0.48	0.54	0.50	0.51

[a]Data shown for **3**−H_2 is from x-ray structure reported in section 3.3.7 at 100 K, with Ni-H distances given from the neutron structure. [b]Covalent ratio using Alvarez covalent radii for Ni and In.[134]

Notably, Ni is positioned significantly further above the P_3-pane upon binding N_2 and CO than it is upon binding H_2, which results in a greater weakening of the Ni→In bond in **3**−N_2 and **3**−CO than for **3**−H_2, relative to **3**. However, in all cases the Ni→In bond remains intact upon binding, as evidenced by the *r* values remaining less than unity. To accommodate the pseudo-tetrahedral geometry of Ni and maintain the bond, In does move slightly further above the N_3-plane by 0.02 to 0.04 Å. At the present time, no experimental insight into the structures of **3**−C_2H_4 and **3**−CO_2 has been obtained, as the weak binding has precluded crystallization in the solid-state. Side-on binding of ethylene is assumed, as has been well-documented in the literature.[110, 208-209] CO_2 can potentially bind in several different ways, including a linear η^1-CO_2 binding mode via oxygen coordination, or alternatively a "bent" side-on mode via coordination of one of the C=O π-bonds of CO_2.[216-217] Solution-state IR studies under high pressures of CO_2 could potentially differentiate between different binding modes for **2**−CO_2 and **3**−CO_2. Computations favor a linear, η^1-CO_2 binding mode over a "bent", side-on binding mode by ~6 kcal/mol, with both modes predicted to be highly unfavorable (endergonic by ~15 kcal/mol for linear mode; Figures A.2.8-A.2.9).[128-129]

3.3.1.6 Other Binding Experiments: N_2O and THF Do Not Form Adducts with NiML Complexes

Given the propensity of complex **3** to bind nearly any sterically unhindered substrate, the reaction of N_2O with complex **3** was examined. The formation of an N_2O adduct would be extremely rare—only three examples have been reported, with structural characterization remaining elusive until the most recent report by Chang and co-workers.[218-222] Binding and activating N_2O would be an important step forward to

developing catalytic processes which convert N_2O, a greenhouse gas, into more benign and/or useful products.[219] The reaction of **3** with N_2O (1 atm) results in clean conversion to a new diamagnetic product, with a downfield shift from 44.4 to 59 ppm observed by ^{31}P NMR. This result seemed promising initially, as a control experiment in which **2** was exposed to 1 atm N_2O did not result in any reaction or any oxidation of the phosphines. However, crystallization of the product of **3** with N_2O revealed that phosphine oxidation had indeed occurred with concomitant loss of N_2 and Ni (in some form), with the resulting P=O linkages coordinating to In(III) via the oxygen atoms (Figure 3.6). The fact that phosphine oxidation occurs for **3** but not for **2** under 1 atm N_2O may reflect important differences in Ni−P lability that will be examined in greater detail in the chapter 4. While initially disappointing given the desire for N_2O coordination, "InO_3L" turned out to be a useful product to identify, as it was consistently observed to be the primary decomposition product by ^{31}P NMR spectroscopy upon exposure of **3** to oxygen via the leaking of any J. Young experiment.

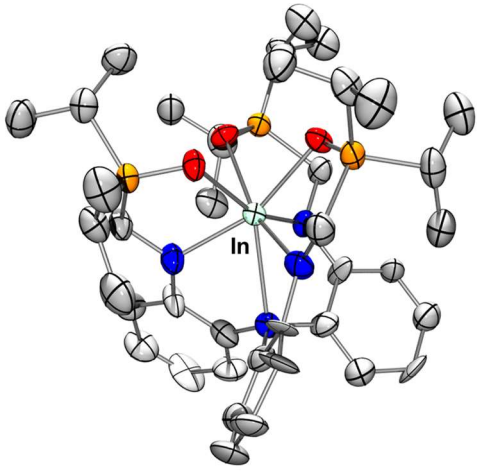

Figure 3.6. Solid-state structure of "InO_3L", obtained from reaction of **3** with N_2O. Ellipsoids are shown at the 50% level and H atoms and solvent molecules are omitted for clarity. Note that this structure is of sufficient quality for atom connectivity only (R1=10%).

Another molecule that was considered as having the potential to bind to complex **3** was THF. Although THF is not a strong σ-donor, it has been reported to bind to a similar phosphine-ligated Ni(DPB) complex.[44] Additionally, the catalytic hydrogenation of CO_2 (chapter 5) and other reactivity with the NiML complexes will be conducted in THF for solubility reasons, and so it is worthwhile to investigate whether THF solvent binding to NiML is occurring to any extent. To test whether THF binding is possible for NiML complexes, complex **3** was tested first, as if no binding was observed to **3**, it stood to reason that no binding would be observed for the other more electron-rich NiML complexes, either. Only a minimal chemical shift change of ~0.1 ppm was observed upon decreasing T from 298 K to ~193 K for complex **3** in a toluene solution which was spiked with ~100 equiv THF relative to **3**. Over all T examined, the ^{31}P chemical shift remained essentially identical to that for NiML in both toluene and pentane, which are not typically regarded as coordinating solvents. If THF binding were occurring, a more significant downfield shift in the ^{31}P resonance would have been expected. Thus, THF binding can be ruled out as playing an appreciable role in the dynamics of NiML complexes in solution. The binding studies for H_2 and N_2 binding which will be presented in this chapter were originally performed in toluene instead of THF to preclude any extent of solvent binding, even though it turns out that THF does not bind appreciably. More strongly coordinating solvents, like CH_3CN, were observed to bind to NiML, as discussed in the previous chapter (section 2.2.6). The remainder of this chapter will focus on the binding of H_2 and N_2 to the NiML complexes, with a large emphasis on understanding H_2 binding to form (η^2-H_2)NiML complexes.

3.3.2 Characterization of (η^2-H_2)NiML Complexes via NMR Spectroscopy

3.3.2.1 Characterization by ^1H and ^{31}P NMR Spectroscopy

The varied electronic and geometric environments of the Ni centers in complexes **1**−**4** manifest in their divergent reactivity with H_2. In the case of **1** and **4**, no reaction with H_2 was readily observable at rt. In contrast, exposing **2** and either **3** or **3**−N_2 to 1 atm H_2 cleanly generated new diamagnetic species, which were formulated as the nonclassical (η^2-H_2)NiML complexes, **2**−H_2 and **3**−H_2. Both **2**−H_2 and **3**−H_2 are characterized by a single ^{31}P resonance in toluene-d_8 at 298 K, at 46.1 ppm and 66.8 ppm, respectively, consistent with the retention of three-fold symmetry upon H_2 binding. The ^{31}P chemical shifts of **2** and **3** under 1 atm H_2 are significantly downfield of those of **2** (37.6 ppm) and **3** (44.4 ppm) under 1 atm argon (Figure 3.7).[30, 97] It should also be noted that the ^{31}P resonance for **2**−H_2 was observed to be very broad at 298 K in comparison to that of **3**−H_2 (Figure 3.7). As will be discussed in more detail later in this chapter, it would later be found that this broadness is attributable to fluxionality from rapid H_2 binding and dissociation, with the true chemical shift of **2**−H_2 converging to a sharp peak at ~56.9 ppm at high H_2 pressure (34 atm) and low T (193 K).

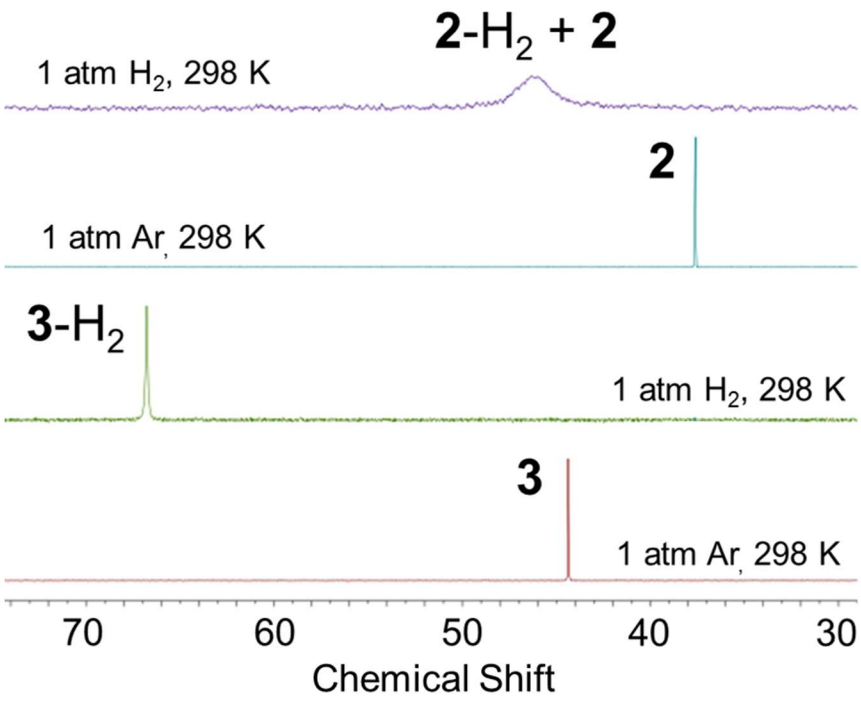

Figure 3.7. Stacked ^{31}P NMR for exposure of **2** and **3** to 1 atm H_2 in toluene-d_8 at 298 K. Note that the ^{31}P resonances under 1 atm H_2 have been increased in intensity for visual clarity relative to those under 1 atm Ar, and so the relative broadness of the NiML to (η^2-H_2)NiML peaks are not shown perfectly to scale.

A broad, unresolved resonance was observed by ^{1}H NMR spectroscopy for the bound H_2 ligand in **2**−H_2 and **3**−H_2 at −2.4 and −2.5 ppm in toluene-d_8, respectively (Figure 3.8).[97] An important subtlety that hinted at differences in the H_2 binding energetics between **2**−H_2 and **3**−H_2 was the fact that cooling a sample of **2** under 1 atm H_2 to T ≤ 253 K was required to observe the bound H_2 resonance of **2**−H_2 by ^{1}H NMR spectroscopy, whereas this resonance was readily observable at rt for **3**−H_2 (Figures A.2.10-A.2.11). The bound H_2 resonance was generally observed to sharpen, in terms of its linewidth, with decreasing T (Figures A.2.10-A.2.11). Additionally, **3**−H_2 was found to be stable to vacuum, whereas **2**−H_2 was observed under 1 atm H_2, but reverted to **2** upon removal of the H_2 atmosphere via evacuation of the headspace.[97] The lability of the H_2 ligand in **2**−H_2 to vacuum, along with the aforementioned broad ^{31}P peak for **2**−H_2

and the requirement of low T to observe the proton resonance for bound H_2, all collectively suggested weaker and more fluxional binding of H_2 to **2** in comparison to **3**.[30] This qualitative conclusion will be explored in much greater detail in the next section on thermodynamic studies of the H_2 binding equilibria.

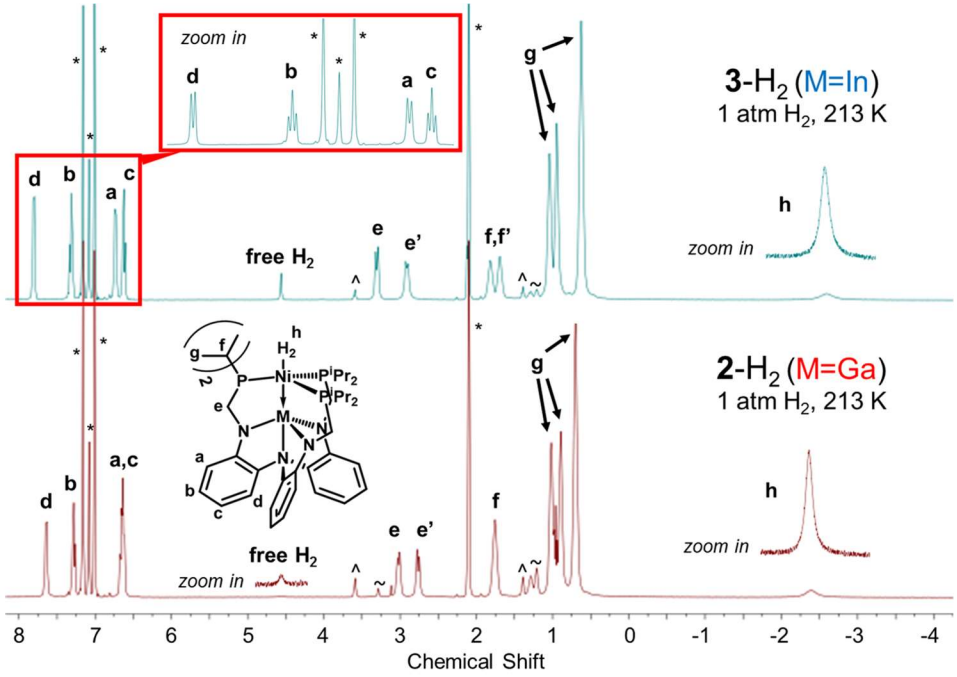

Figure 3.8. Stacked ^{1}H NMR (400 MHz, toluene-d_8, 213 K) of **2**−H_2 and **3**−H_2 generated *in situ* upon exposure of **2** and **3** to 1 atm H_2. Peak assignments are labeled, with close-ups shown for the free and bound H_2 resonances for clarity, as well as for the aryl region of **3**−H_2 to show resolved coupling. Residual solvent peaks for toluene (*), THF (^), diethyl ether and pentane (~) are denoted.

3.3.2.2 Evaluation of Extent of H−H Activation in (η^2-H_2)NiML Complexes via NMR Spectroscopy

In order to confirm the formulation of the (η^2-H_2)NiML complexes as nonclassical dihydrogen adducts with intact H_2 ligands, as opposed to Ni(II) dihydride species in which the H−H bond has been cleaved to give discrete Ni−H moieties, the degree of H−H activation in **2**−H_2 and **3**−H_2 was investigated by evaluating two different parameters via NMR studies: (1) the H−D coupling constant, J_{HD}, in (η^2-HD)NiML

isotopomers, and (2) the minimum spin-lattice relaxation time, T_1(min), of the bound H_2 protons. Free HD gas has a coupling constant (J_{HD}) of 43 Hz, with the NMR resonance appearing as a 1:1:1 triplet due to the I=1 nuclear spin of deuterium.[45, 223] Upon binding to a metal (M) to form M(η^2-HD), the elongation of the H−D bond results in a decrease in the extent of coupling between the H and D atoms as they become further spatially separated. An intact H−D unit bound to a transition metal will typically exhibit a J_{HD} coupling constant of 26 to 37 Hz.[45] Importantly, the observation of H−D coupling to give a 1:1:1 triplet for the bound HD resonance is definitive evidence of an intact HD ligand, and by analogy an intact H_2 unit; classical metal dihydride species, M(H)(D), do not show appreciable J_{HD} coupling because the H−D bond has been fully broken.[45, 224] The (η^2-HD)NiML species, **2**-HD and **3**-HD, were synthesized upon exposure of **2** and **3** to HD gas, and exhibit J_{HD} of 34 Hz and 32 Hz, respectively, upon cooling to 213 K in toluene-d_8 to resolve the coupling (Figure 3.9).[30, 97]

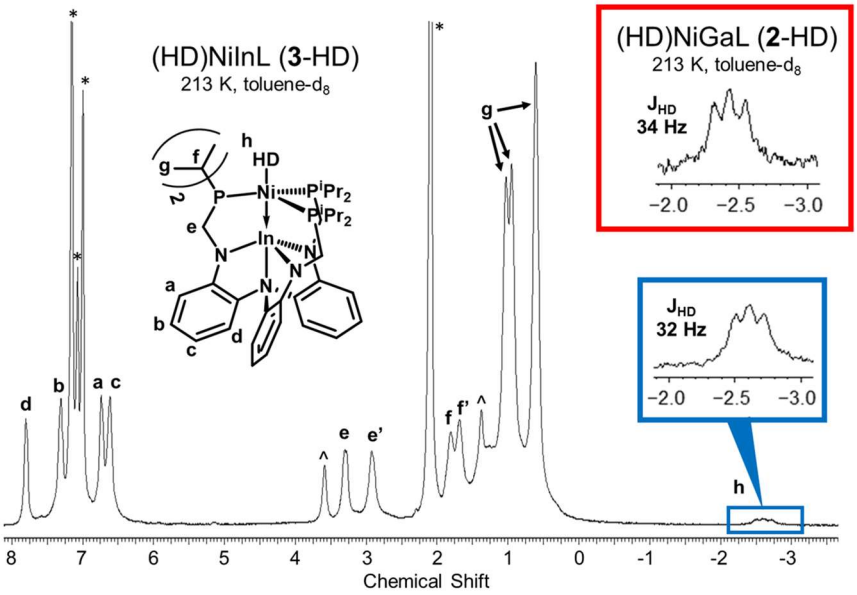

Figure 3.9. ^{1}H NMR (600 MHz, toluene-d_8, 213 K) spectrum of **3**-HD generated *in situ* upon exposure of **3** to HD gas. The inset shows the bound HD resonance observed by ^{1}H NMR (600 MHz, toluene-d_8, 213 K) for the analogous **2**-HD complex. Residual solvent peaks for toluene (*) and THF (^) are denoted.

Both Morris[225] and Heinekey,[223] and their respective co-workers, have independently developed similar empirical relationships which relate the observed J_{HD} coupling constant to the solution-state H−D bond distance, which is assumed to be the same as the H−H distance (d_{HH}; see Equations 3.1 and 3.2).[45]

$$\text{Morris: } d_{HH} \text{ (in Å)} = 1.42 - (0.0167 \cdot J_{HD}) \qquad \text{(Eqn 3.1)}$$

$$\text{Heinekey: } d_{HH} \text{ (in Å)} = 1.44 - (0.0168 \cdot J_{HD}) \qquad \text{(Eqn 3.2)}$$

These empirical relationships rely on dihydrogen complexes in the literature for which more rigorous characterization of d_{HH} by neutron diffraction and/or solid-state NMR studies was reported in addition to the measurement of the J_{HD} coupling constant.[45] The two empirical relationships give similar values for d_{HH}, with that of Morris typically giving values that are ~0.02 Å shorter based on the difference in the y-intercept values. Using Equation 3.2, the coupling constants observed for **2**-HD and **3**-HD correspond to solution-state H−D distances of 0.87 Å and 0.91 Å, respectively.[97] This degree of H_2 activation represents slight H−H elongation compared with free H_2 (0.74 Å), placing **2**−H_2 and **3**−H_2 in the "true H_2 complex" regime of dihydrogen complexes (d_{HH} of 0.8 to 1.0 Å), as classified by Kubas and Crabtree.[45, 224] True H_2 complexes typically exhibit weaker and more reversible H_2 binding than elongated H_2 complexes (d_{HH} = 1.0 to 1.3 Å) and compressed dihydrides (d_{HH} = 1.3 to 1.6 Å), with d_{HH} > 1.6 Å typically taken to indicate H−H bond rupture has occurred to give a metal dihydride species, $M(H)_2$.

T_1 relaxation studies are also informative for distinguishing nonclassical H_2 adducts from metal dihydrides. Typically, T_1 values will decrease as T is decreased, pass through a minimum, which is referred to as T_1(min), and then begin to increase again with further decreases in T. As applied to distinguishing H_2 adducts from metal

dihydrides, the proton resonance of an intact H_2 unit should exhibit a short T_1(min) value due to extremely rapid relaxation from strong dipole-dipole interactions between the two closely positioned protons of H_2. Traditionally, a criterion of <190 ms at 600 MHz has been used for classification as an intact H_2 ligand, though many H_2 adducts have T_1(min) values much shorter than this—often <50 ms.[45, 226] Such fast relaxation times are significantly shorter than those of the protons in most organic molecules, which typically have T_1 values ranging between 1 and 5 s. This "T_1 criterion" is satisfied by **2**−H_2 and **3**−H_2, which have T_1(min) of ≤ 16 ms and 23 ms, respectively, as measured at 600 MHz in toluene-d_8 (Figure 3.10).[97] Thus, T_1 relaxation studies are consistent with intact H_2 ligands in both **2**−H_2 and **3**−H_2, in accordance with the observation of J_{HD} coupling in **2**−HD and **3**−HD.

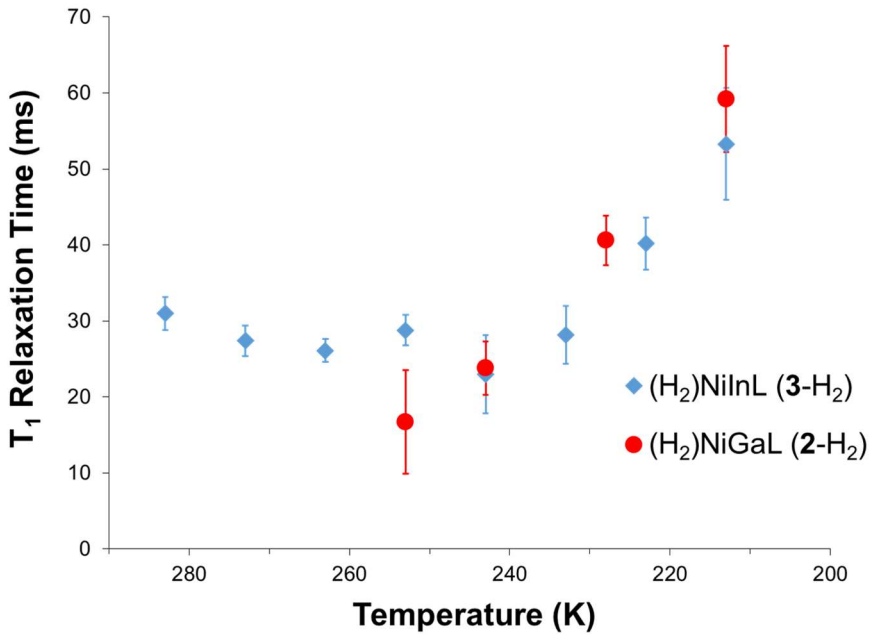

Figure 3.10. Plot of T_1 relaxation time (600 MHz, toluene-d^8) of the bound H_2 resonance of **2**−H_2 (red circles) and **3**−H_2 (blue diamonds) at various T from 283 K to 213 K, with error bars displaying the uncertainty in each T_1 measurement. Note that T_1 values for **2**−H_2 at T > 253 K could not be reliably obtained due to the broadness of the bound H_2 resonance at those T. T_1(min) was observed at ~253 K and ~243 K for **2**−H_2 and **3**−H_2, respectively.

While it is often assumed that the only contribution to the T_1(min) relaxation time of the bound H_2 resonance is from dipolar interactions between the protons of the H_2 ligand, it should be noted that other ligand protons that are in close proximity, as well as metals with spin-active nuclei, can contribute to the T_1 relaxation value for the H_2 ligand to some extent as well. However, for our purposes Ni is not spin-active, and so it does not need to be considered when thinking about the T_1 relaxation of the H_2 ligands. Furthermore, the contributions of ligand protons are typically very small so as to be negligible in comparison to the dipolar-dipolar contribution of the protons of the H_2 ligand itself, as has been studied in remarkable detail by Halpern, Morris, and others.[226-228] This is because the relative contributions to the T_1 relaxation rate through pairwise dipolar interactions is proportional to $1/r^6$, where in this case r would be the distance between a ligand proton and one of the H_2 protons.[226] To this point, accounting for all of the pairwise contributions of the ligand protons to the T_1(min) value for the H_2 resonance of **3**−H_2, in order to rigorously isolate T_1(min) due to dipolar interactions within the H_2 ligand alone, results in a negligible change in the T_1(min) value from 23 ms to 22.2 ms.[226-229] Indeed, pairwise dipolar interactions between all of the ligand protons and H_2 were found to only contribute ~3% of the total dipolar contribution to relaxation, with that between the protons of H_2 contributing ~97%. Such a correction is clearly extremely minor and unnecessary in this case in comparison to the experimental error involved in measuring a T_1(min) value, particularly in the case of a relatively broad dihydrogen resonance like that of **3**−H_2, for which a value of 23 (±5) ms was determined (Figure 3.10).[97]

A considerably more chemically useful exercise in analyzing T_1(min) data for **2**−H_2 and **3**−H_2 involves determining whether the H_2 unit is rotating rapidly about the Ni→M axis. The two limiting cases for H_2 rotation involve invoking either fast or static H_2 rotation relative to molecular tumbling in solution, with each limiting assumption resulting in very different determinations of d_{HH} from the measured T_1(min) values. Equation 3.3 shows the theoretical relationship between d_{HH} and T_1(min) if H_2 rotation is assumed to be fast relative to molecular tumbling, where ν is the spectrometer proton frequency in MHz and T_1 is given in seconds, as reported and applied by Halpern, Morris, and others.[226, 228] Equation 3.4 shows the relationship between d_{HH} in the fast H_2 rotation limit and d_{HH} assuming static rotation, with C = 0.793 as determined and applied by Morris and co-workers.[226-228, 230]

$$d_{HH,fast}\ (\text{in Å}) = 5.81 \cdot \sqrt[6]{T_1/(4\nu)} \qquad \text{(Eqn 3.3)}$$

$$d_{HH,fast}\ (\text{in Å}) = C \cdot d_{HH,static} \qquad \text{(Eqn 3.4)}$$

Assuming the fast H_2 rotation limit relative to molecular tumbling gives d_{HH} = 0.85(3) Å for **3**−H_2, whereas assuming static rotation leads to d_{HH} = 1.07(4) Å. Likewise, the calculated d_{HH} for **2**−H_2 are ≤ 0.80(5) Å and ≤ 1.01(7) Å for assuming either fast or static H_2 rotation relative to molecular tumbling, respectively. Upon comparing these d_{HH} values from T_1(min) to those estimated from the J_{HD} coupling constants (Table 3.3), it is clear that the assumption of fast rotation of H_2 about the Ni→M axis gives better agreement for both **2**−H_2 (~0.86 and ≤0.80 ± 0.05 Å) and **3**−H_2 (~0.91 and 0.85 ± 0.03 Å).[30, 97]

Table 3.3. Estimation of d_{HH} by ^{1}H NMR studies for **2**−H_2 and **3**−H_2.

	J_{HD} Coupling Constant[a]			T_1 Relaxation Time[b]		
Complex	J_{HD} (Hz)	Heinekey[c] d_{HH} (Å)	Morris[d] d_{HH} (Å)	T_1(min) (ms)	$d_{HH, fast}$ (Å)	$d_{HH, static}$ (Å)
2-H_2	34	0.87	0.85	≤ 16(6)[e]	≤ 0.80(5)	≤ 1.01(7)
3-H_2	32	0.91	0.89	23(5)[f]	0.85(3)	1.07(4)

Note that standard error in the last digit of T_1(min) and tabulated d_{HH} values are given in parenthesis. [a]Measured at 213 K in toluene-d_8. [b]measured in toluene-d_8. [c]via Eqn 2.2.[223] [d]via Eqn 2.1.[225] [e]T_1(min) measured at 253 K. Minimum unconfirmed due to broadness of T_1 resonance at T > 253 K. [f]T_1(min) measured at 243 K.

Likewise, prediction of the T_1(min) value for the bound H_2 resonance of **3**−H_2 considering pairwise interactions of all protons with those of H_2 gives expected values of 18 ms and 4.6 ms for the limiting assumptions of fast and static H_2 rotation respectively.[226, 228-229] The assumption of fast H_2 rotation relative to molecular tumbling gives a closer match between the predicted T_1(min) value of 18 ms and the measured value of 23(5) ms, just as it gave a closer match between the estimated d_{HH} values from T_1(min) and those from J_{HD}. Facile and rapid H_2 rotation has been invoked for similar Ni(η^2-H_2) complexes in the literature,[117, 189] and is also consistent with the lack of a preferential orientation of H_2, as π-back-bonding interactions from the Ni d_{xz} and d_{yz} orbitals to the H_2 σ* orbital are likely degenerate and weak, owing to the poor π-basicity of Ni.[30, 81, 110] Indeed, theoretical calculations which will be discussed in section 3.3.8 support the notion of relatively weak π-back-donation from Ni to H_2.

3.3.2.3 A Third Isostructural H_2 Adduct: Re-Examination of NiAlL under High H_2 Pressure

Though no reaction with H_2 was readily observable for NiAlL (**1**) at 298 K and 1 atm H_2,[97] re-examination of this reaction with exposure to higher H_2 pressures and/or lower T resulted in the observation of an H_2 binding equilibrium to form (η^2-H_2)NiAlL

(**1**-H_2). The new *in situ* generated **1**−H_2 species has a diagnostic bound H_2 resonance at −2.0 ppm in toluene-d_8 at 203 K under 34 atm H_2 (Figure 3.11). As the H_2 pressure is increased from 1.0 to 3.8 to 34 atm, the ^{31}P chemical shift for **1** under an H_2 atmosphere shifts continuously downfield relative to the chemical shift of **1** under 1 atm Ar (30.7 ppm), ultimately converging to ~44.3 ppm at high pressure (34 atm H_2) and low T (200 K; Figure 3.11).

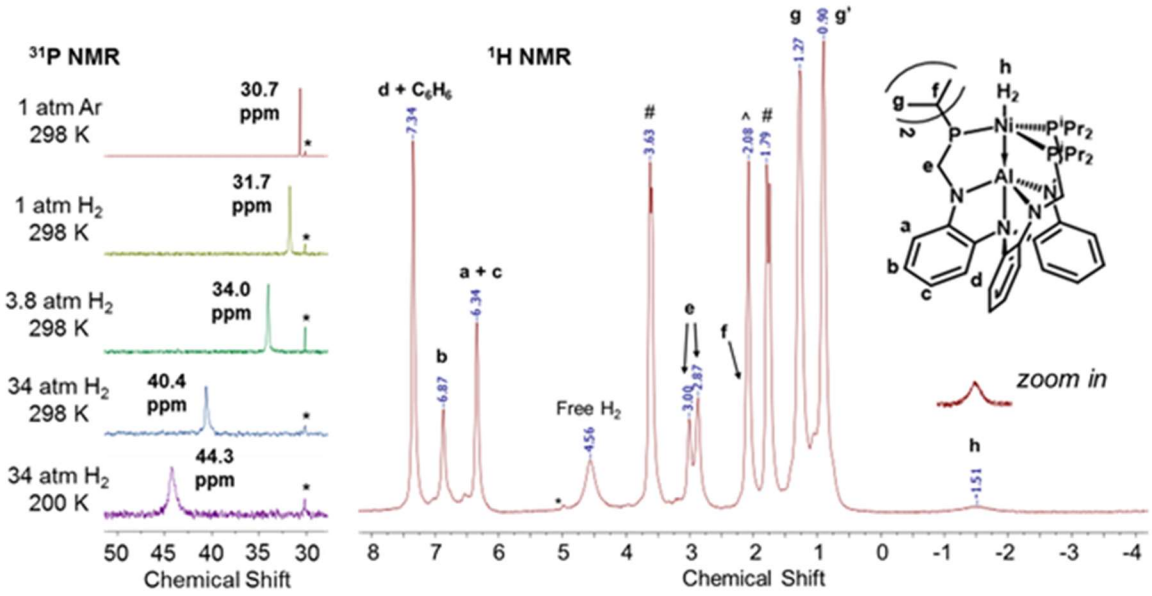

Figure 3.11. Stacked ^{31}P NMR (161.9) spectra for complex **1** under various H_2 pressures (1.0, 3.8, 34 atm) in toluene-d_8 (left). A ^{1}H NMR spectrum (500 MHz, THF-d_8, 232 K) of **1**−H_2 generated *in situ* under 34 atm H_2 is also shown (right). Residual solvent peaks of THF (#), toluene (^), and benzene (C_6H_6) are denoted. A small amount of the ^{31}P chemical shift internal standard, $NiLH_3$ (**4**), is denoted with asterisks (*) in both the ^{1}H (N*H* peak at 5.0 ppm) and ^{31}P (30.1 ppm) spectra.

This behavior is consistent with a weak binding equilibrium between **1** and **1**−H_2 in which the two species are undergoing fast chemical exchange relative to the ^{31}P NMR timescale (202.4 MHz), similar to that observed at lower pressures for the equilibrium between **2** and **2**−H_2.[212-213] These equilibria will be investigated in greater quantitative detail in the next section on the thermodynamic favorability of H_2 binding to NiML. Both

^{1}H and ^{31}P NMR spectra of **1**−H_2 are consistent with the retention of solution-state three-fold symmetry upon binding H_2. Presumably, H_2 binds in a side-on fashion to Ni in the apical binding site *trans* to the supporting metal, as was supported by NMR studies of **2**−H_2 and **3**−H_2.

Analogously to characterization of **2**−H_2 and **3**−H_2, we sought to use NMR to assess the degree of H−H activation in **1**−H_2. However, it was not experimentally feasible to expose **1** to high pressures of HD gas to measure the J_{HD} coupling constant in the resulting **1**−HD complex. To confirm an intact H_2 ligand in **1**−H_2, T_1 relaxation studies were performed for **1**−H_2 generated *in situ* under 34 atm H_2, with T_1(min) found to be 49(±5) ms at 203 K in THF-d_8 (500 MHz; Figure A.2.13). Unfortunately, direct comparison of T_1(min) values for the bound H_2 resonance in **1**−H_2 to those for **2**−H_2 and **3**−H_2 is not currently possible, as the latter two were measured in toluene-d_8 under 1 atm H_2, whereas the former was measured for a highly-concentrated solution in THF-d_8 under 34 atm H_2 due to poor solubility and signal-to-noise of the bound H_2 resonance in toluene-d_8. Ideally, T_1(min) values would be re-measured for all three H_2 adducts under identical conditions to enable direct comparison of estimated d_{HH} values.

The T_1(min) value for **1**−H_2 under 34 atm H_2 in THF gives d_{HH} = 0.99 (±0.02) Å, assuming fast H_2 rotation relative to molecular tumbling.[226] This value is significantly longer than that determined for **2**−H_2 and **3**−H_2 in toluene (Table 3.3). However, given the weak and labile nature of H_2 binding to **1** relative to **2** and **3** (*vide infra*), one would expect that **1**−H_2 would have the shortest T_1(min) value and the shortest H−H distance that is closest to free H_2 (0.74 Å) of the trio of complexes.[45] Furthermore, it should be noted that both **2**−H_2 and **3**−H_2 exhibited longer T_1(min) in THF-d_8 than in toluene-d_8 in

preliminary studies, further reiterating the need for the re-measurement of T_1(min) under identical conditions to allow meaningful comparison and identify if d_{HH} displays solvent-dependence between THF and toluene, or whether the longer T_1(min) than expected for **1**−H_2 in comparison to **2**−H_2 and **3**−H_2 is the result of different H_2 pressures and/or analyte concentrations.

To lend insight into the relative degree of H−H activation in **1**−H_2 relative to **2**−H_2 and **3**−H_2, DFT calculations were performed to optimize the geometry of all three species (M06-L[176]/bs1, see experimental section 3.5 for details). The H−H distance in **1**−H_2 is predicted to be the shortest of the trio of complexes by DFT, at 0.810 Å, compared with 0.827 Å and 0.833 Å for **2**−H_2 and **3**−H_2, respectively (Table A.2.1). DFT calculations have routinely predicted shorter H−H distances than those estimated by solution-state NMR studies in related systems,[44, 117, 167] so the shorter H−H calculated distances (0.81 to 0.83 Å) relative to experimentally estimated distances (0.85 to 0.90 for **2**−H_2 and **3**−H_2) are not particularly surprising or concerning. Importantly, the relative calculated H−H distances are consistent with the experimental trend of slight H−H elongation in (η^2-H_2)NiML upon moving from M=Ga to M=In based on both J_{HD} and T_1(min) NMR studies (*vide supra*). The prediction that **1**−H_2 would have the shortest H−H distance that is closest to free H_2 (0.74 Å) of the three H_2 adducts is in line with the qualitative observations of weak binding and rapid exchange of free and bound H_2 with **1** occurring on the ^{31}P NMR (202.4 MHz) timescale.

*3.3.3 H_2 Binding Equilibria Thermodynamics: H_2 Binding to **2** as a Representative Example*

*3.3.3.1 Overview and VT ^{31}P Studies of **2** Under Various H_2 Pressures*

Initial characterization of (η^2-H_2)NiML complexes revealed the disparate conditions required for H_2 binding in each case, with **3** forming **3**−H_2 under 1 atm H_2 at 298 K compared with the requirement of 34 atm H_2 and 200 K in order to favor near complete H_2 binding to **1**. Excitingly, these divergent qualitative observations served as encouraging preliminary indications that significant differences in the reactivity of Ni toward small molecule substrates could be realized simply by variation of the supporting metal identity. That is, the electronic and geometric differences in the NiML complexes discussed in the previous chapter do indeed result in different propensities for binding and activating small molecules like H_2. Intrigued, we set out to understand how the supporting metal ion influences both the thermodynamics and kinetics of H_2 binding equilibria with NiML.

As described previously, initial characterization of **2**−H_2 led to the observation of a broad resonance by ^{31}P NMR spectroscopy under 1 atm H_2 at rt, which, along with the observed lability of the bound H_2 unit in **2**−H_2 to vacuum, suggested a dynamic and reversible H_2 binding equilibrium. Because of its reversible H_2 binding at ambient conditions, **2** was an ideal candidate for initiating equilibrium studies. In order to properly describe the experiments and data analysis procedures used to extract the thermodynamic binding parameters, $\Delta H°$, $\Delta S°$, and $\Delta G°$, from ^{31}P NMR spectroscopy data, the binding of H_2 to **2** to form **2**−H_2 will be explained thoroughly as an illustrative example. From there, the results for H_2 binding to **2** will be compared to those obtained for H_2 binding to **1** and **3**, which involve similar experiments and data treatments.

To begin with, the behavior of **2** under various H_2 pressures and at various T was studied by NMR spectroscopy, as higher H_2 pressures and/or lower T would be expected to perturb the H_2 binding equilibrium to favor binding to form **2**−H_2. Variable-temperature (VT) ^{31}P NMR spectra of **2** in toluene-d_8 under 6.8 atm H_2 exhibited a single resonance over a wide T range from 370 K to 200 K (Figure 3.12a). The single ^{31}P resonance was observed to shift continuously downfield from 42.7 to 56.9 ppm as T decreased from 368 K to 200 K. As a control experiment, the ^{31}P shift of **2** under 1 atm Ar (37.6 ppm at 298 K) changes minimally over a similar T range ($\Delta\delta \sim 0.5$ ppm, Figure A.2.14). Therefore, temperature-dependent shifts in the ^{31}P NMR spectra were concluded to be reflective of the effect of T on the H_2 binding equilibrium with **2**.

In addition to monitoring **2** under 6.8 atm H_2, VT ^{31}P NMR studies were also carried out for **2** under 1.0, 13.6, and 34.0 atm H_2, with wide T ranges from 193 K to 368 K examined in each case (Figures 3.13, A.2.15). The results of these studies are shown in a combined plot of the observed ^{31}P chemical shift (δ) vs. T (Figure 3.12b). For all H_2 pressures, the same approximate low T convergence of the ^{31}P chemical shift to ~56.9 ppm is observed, which has been assigned as the chemical shift of **2**−H_2. At the other extreme, the observed ^{31}P resonance shifts upfield toward the chemical shift of **2** (37.5 ppm at 368 K under 1 atm Ar) at high T, with the shift of **2** more closely approached at low H_2 pressures (1 atm H_2). This behavior is consistent with a fast H_2 binding equilibrium relative to the ^{31}P NMR timescale (202.4 MHz) between **2** and **2**−H_2, where the latter is favored at low T and both species retain solution-state three-fold symmetry at all T.[211-213] Alternatively, distinct ^{31}P resonances for **2** and **2**−H_2 which change in relative

intensity and integration as T is varied would be expected for an equilibrium in which chemical exchange is slower than the NMR timescale.[212]

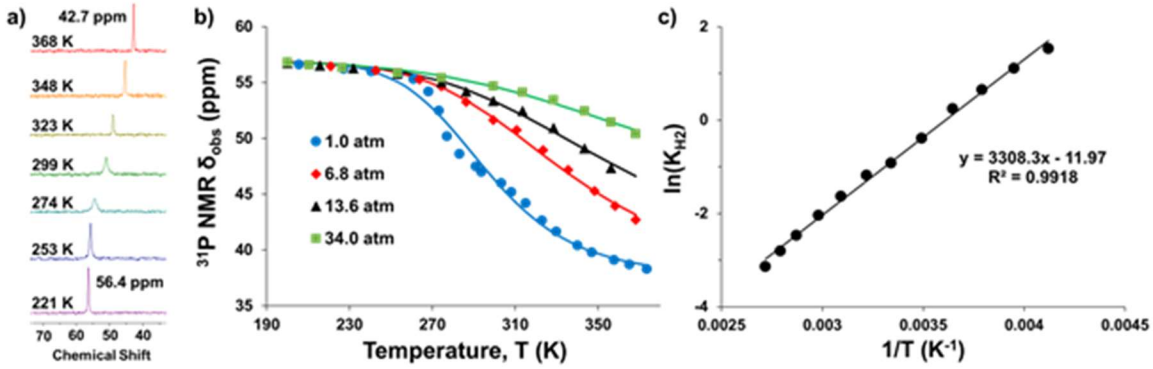

Figure 3.12. (a) VT ^{31}P NMR spectra of **2** under 6.8 atm H_2 in toluene-d_8 (368 to 221 K). (b) Plots of ^{31}P δ vs. T obtained for various H_2 pressures. Data are shown as points, and solid traces represent the best-fit curves obtained by varying $\Delta H°$ and $\Delta S°$ as parameters. (c) Representative van't Hoff plot of $\ln(K_{H_2})$ vs. 1/T at 6.8 atm H_2. The thermodynamic binding parameters shown in Table 3.5 were determined by taking the average of the results from van't Hoff plots for datasets collected at 6.8 and 13.6 atm H_2.

*3.3.3.2 Applying the Principles of Fast Chemical Exchange Equilibria to H_2 Binding to **2***

For two species that are interconverting rapidly relative to the NMR timescale, the observed chemical shift is the population-weighted average of their individual chemical shifts.[211-213, 231] Thus, the observed ^{31}P chemical shift reflects the relative equilibrium populations of **2** and **2**–H_2 at a given T, with ratio of **2**–H_2 to **2** given by Equation 3.5, where δ_{NiML} and $\delta_{(H_2)\mathrm{NiML}}$ are the ^{31}P chemical shifts of the unbound and bound species, and δ_{obs} is the observed ^{31}P chemical shift at a given T.[211]

$$\frac{[(H_2)\mathrm{NiML}]}{[\mathrm{NiML}]} = \frac{\delta_{obs} - \delta_{\mathrm{NiML}}}{\delta_{(H_2)\mathrm{NiML}} - \delta_{obs}} \qquad \text{(Eqn 3.5)}$$

The ^{31}P chemical shifts of **2** and **2**–H_2 are 37.5 ppm and 56.9 ppm, respectively, and so from Equation 3.5 it can be seen that a 50:50 equilibrium mixture of **2** and **2**–H_2 would give rise to an observed ^{31}P peak exactly halfway between their individual chemical shifts, at approximately 47.2 ppm. It follows that the equilibrium constant for

H_2 binding, K_{H_2}, can then be determined via Equation 3.6, where the equilibrium concentration ratio of **2** and **2**−H_2 is determined from the observed ^{31}P chemical shift as described via Equation 3.5, and P_{H_2} is the known H_2 pressure.[211, 213]

$$K_{H_2} = \frac{[(H_2)NiML]}{[NiML] \times P_{H_2}} \qquad \text{(Eqn 3.6)}$$

After determination of K_{H_2} at various T, the thermodynamic parameters for H_2 binding, $\Delta H°$, $\Delta S°$, and $\Delta G°$, can be extracted by way of non-linear fitting of the ^{31}P δ vs. T plot in Figure 3.12b, or alternatively from a van't Hoff plot ($\ln(K_{H_2})$ vs. 1/T) as shown in Figure 3.12c.[231] The van't Hoff plot is the simpler of the two methods for extracting thermodynamic parameters. By rearranging Equation 3.7, one can see that the slope of a van't Hoff plot is $-\Delta H°/R$, with the y-intercept equal to $\Delta S°/R$.[231]

$$-RT \cdot \ln(K_{H_2}) = \Delta G° = \Delta H° - (T \cdot \Delta S°) \qquad \text{(Eqn 3.7)}$$

Non-linear fitting of the ^{31}P δ vs. T plot involves a bit more complex derivation, albeit one involving simple general chemistry equations for the most part. Rearrangement of Equation 3.7 gives Equation 3.8, and the combination of Equations 3.5 and 3.6 allows for the expression of K_{H_2} in terms of δ_{NiML}, $\delta_{(H_2)NiML}$, and P_{H_2}, as shown in Equation 3.9. Lastly, substitution for K_{H_2} in Equation 3.8 using the expression given by Equation 3.9 and solving for the observed ^{31}P chemical shift, δ_{obs}, results in Equation 3.10.

$$K_{H_2} = e^{\frac{-\Delta H°}{RT} + \frac{\Delta S°}{R}} \qquad \text{(Eqn 3.8)}$$

$$K_{H_2} = \frac{\delta_{obs} - \delta_{NiML}}{(\delta_{(H_2)NiML} - \delta_{obs}) \cdot P_{H_2}} \qquad \text{(Eqn 3.9)}$$

$$\delta_{obs} = \frac{\left\{\left[\left(e^{\frac{-\Delta H°}{RT} + \frac{\Delta S°}{R}}\right) \cdot P_{H_2} \cdot (\delta_{(H_2)NiML})\right] + \delta_{NiML}\right\}}{\left\{\left[\left(e^{\frac{-\Delta H°}{RT} + \frac{\Delta S°}{R}}\right) \cdot P_{H_2}\right] + 1\right\}} \qquad \text{(Eqn 3.10)}$$

Using Equation 3.10, $\Delta H°$, $\Delta S°$, and $\delta_{(H_2)NiML}$ were varied as parameters using the SOLVER function in Microsoft Excel to find the best fit of the experimental ^{31}P δ_{obs} data. Specifically, the sum of the squared residuals was minimized between the experimentally observed δ_{obs} and the calculated δ_{obs} using Equation 3.10 for known P_{H_2}, δ_{NiML}, and T values. The solid curves shown in Figure 3.12b are the result of performing this non-linear fitting protocol for the various data sets collected for **2** at different H_2 pressures. This non-linear fitting method is complementary to a van't Hoff plot, as it allows for $\delta_{(H_2)NiML}$ to be fit as a parameter, and subsequently this chemical shift can be used in van't Hoff analysis, along with the more precisely known δ_{NiML} value, to determine K_{H_2} at various T using Equation 3.9. For all equilibrium studies conducted, the thermodynamic binding parameters obtained from non-linear fitting of the ^{31}P δ vs. T plot matched closely with those obtained via van't Hoff analysis, with the two sets of values typically found to be within the experimental error range given from linear regression of the van't Hoff plot (Table A.2.3-A.2.4). For simplicity, thermodynamic values obtained via van't Hoff analysis will be discussed due to the more straightforward nature of evaluating the experimental uncertainty in the extracted values of $\Delta H°$, $\Delta S°$, and $\Delta G°$ via linear regression.

*3.3.3.3 Thermodynamic Binding Parameters for H_2 Binding to **2**: Examination of Chemical Exchange Rate Considerations and Assumptions Which Impact Accuracy and Validity of Results*

Van't Hoff analysis for H_2 binding to **2** gives $\Delta H°$ = −6.0(2) kcal/mol, $\Delta S°$ = −22.2(8) cal/(mol·K), and $\Delta G°$ = +0.6(2) kcal/mol, where we have defined the standard-state conditions as 298 K, 1 atm H_2, and 1 M concentrations of all other species in

toluene. These values were obtained from the average of van't Hoff analyses for data collected at 6.8 atm and 13.6 atm H_2 (Figures 3.12c and A.2.16). Our decision to use only the datasets collected under 6.8 atm and 13.6 atm H_2 for thermodynamic analysis is based on the fact that both of these datasets exhibit fast-exchange kinetics and sufficient variability in ^{31}P chemical shift values, hence allowing for a more accurate and precise determination of the thermodynamic parameters. The datasets collected at 1 atm and 34 atm H_2 were excluded because they failed to meet these general criteria, as will be further explained in the paragraphs that follow.

Data collected under 34 atm H_2 results in the equilibrium mixture containing a larger percentage of **2**−H_2 compared with lower H_2 pressures, in accordance with LeChatelier's principle.[232] As such, the ^{31}P chemical shifts for **2** under 34 atm H_2 vary across a narrower range (56.9 to 50.4 ppm over full T range) than those for lower pressures, such as 6.8 atm and 13.6 atm H_2 (56.9 to 42.7 and 56.9 to 47 ppm, respectively, over full T range; Figure 3.12b). For the 6.8 atm and 13.6 atm H_2 datasests, there is less error associated in determining K_{H_2} because there are fewer data points where the observed ^{31}P chemical shift (δ_{obs}) is close to the $\delta_{(H_2)NiML}$ convergence endpoint, which is fit as a parameter as previously described and subject to small amounts of error itself. For these reasons, the data set collected at 34 atm H_2, while very useful for confirming the convergence of the chemical shift of **2**−H_2, was excluded from van't Hoff analysis. As mentioned, the dataset collected at 1 atm H_2 was also not utilized for thermodynamic analysis, the reasons for which prompt a brief discussion of the effect of the chemical exchange rate on the accuracy of the thermodynamic parameters obtainable from van't Hoff analysis based on ^{31}P δ_{obs} data.

3.3.3.4 Exchange Rate Considerations to Ensure Accurate K_{eq} Determination from ^{31}P δ

The critical assumption made in extracting thermodynamic binding data for an equilibrium governed by fast chemical exchange relative to the NMR timescale is that exchange is truly fast relative to the NMR timescale. Rigorously fast chemical exchange is typically defined as a case where the condition given in Equation 3.11 is satisfied, where $rate_{ex}$ is the exchange rate, δ_A and δ_B are the chemical shifts of the exchanging species, and the values of all variables are in Hz (s^{-1}).[211, 213]

$$rate_{ex}/(\delta_A - \delta_B) > 10 \qquad \text{(Eqn 3.11)}$$

If the condition specified in Equation 3.11 is satisfied, then the assumption of fast chemical exchange is valid, and K_{eq} can be accurately determined because the observed chemical shift is truly equal to the population-weighted average of the chemical shifts of the exchanging species.[211, 213] The validity of the fast exchange assumption can be checked qualitatively by examining the ^{31}P peak shapes. In the fast exchange limit, the observed ^{31}P peak will not broaden significantly as it shifts position between the two end-point chemical shifts of the exchanging species. In contrast, the fast-intermediate and intermediate exchange regimes, where $rate_{ex}$ is between 1 and 10 times the peak separation ($\delta_A - \delta_B$,), are characterized by significant peak broadening as the observed resonance shifts between the two extreme chemical shifts upon perturbation of the equilibrium.[211, 213] In the fast-intermediate and intermediate exchange regimes, complex non-Lorentzian lineshapes and exchange broadening result in the observed chemical shift no longer representing the population-weighted average of the exchanging species (Figure 3.13).[211, 213] Thus, if chemical exchange is not rigorously fast and instead is fast-

intermediate, then the thermodynamic parameters extracted from the observed chemical shifts will be prone to varying degrees of error and may be unreliable.

However, it is not trivial to differentiate fast chemical exchange from fast-intermediate (ie. how much broadening concurrent with peak shifting is problematic?). In practice, borderline cases typically are assumed to be fast exchange to facilitate analysis, with little confirmation that this is indeed the correct assumption.[213] Thus, in order to ensure that the VT ^{31}P NMR spectroscopy studies reported in this thesis gave valid and reliable thermodynamic results, two different complementary approaches were taken. First, it was noticed that conducting H_2 binding studies for **2** under higher H_2 pressures (6.8, 13.6, 34.0 atm) resulted in minimal peak broadening as the ^{31}P peak shifted with varying T, whereas studies performed under 1 atm H_2 resulted in significant peak broadening concurrent with peak shifting, especially at chemical shifts close to the average of the chemical shifts of the exchanging species (Figure 3.13).

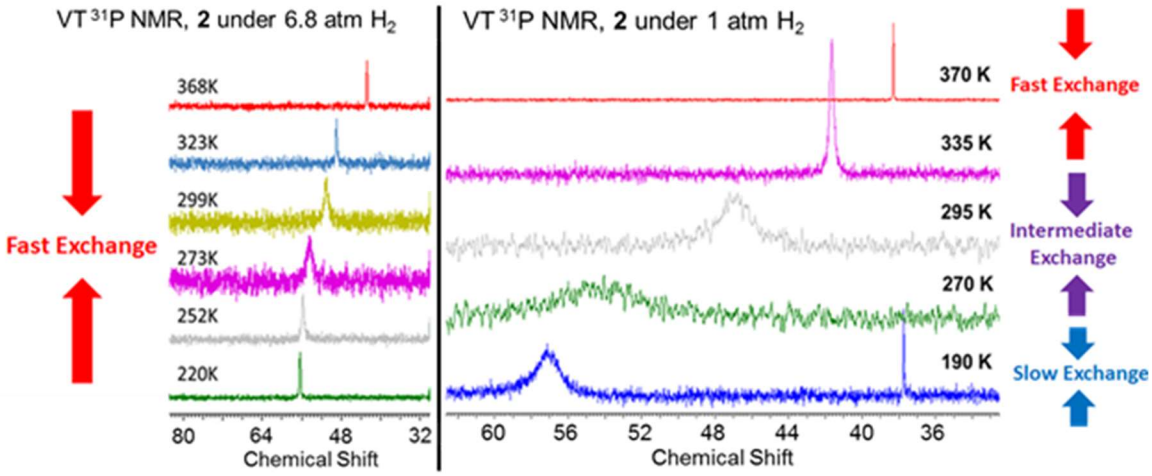

Figure 3.13. Stacked VT ^{31}P NMR spectra for **2** under 6.8 atm (left) and 1.0 atm H_2 (right) shown side-by-side to illustrate the differences in peak shape arising from different chemical exchange rates at the two pressures. Figure A.2.15 shows a similar comparison for higher H_2 pressures, 13.6 and 34 atm, which show sharp ^{31}P peaks at all T, similar to that shown here for 6.8 atm H_2.

Although it should be noted that the horizontal axis (ppm) scales in Figure 3.13 are different for the two sets of spectra, the resonances under 1 atm H_2 are observed to be significantly broader than those under 6.8 atm H_2 even when both are viewed on the same scale. Under 1 atm H_2, interconversion between **2** and **2**−H_2 is observed to be fast relative to the ^{31}P NMR timescale (161.9 MHz) at high T, but transitions to intermediate and slow exchange regimes as T is decreased (Figure 3.13). The lack of peak broadening at higher H_2 pressures qualitatively suggested that faster chemical exchange was occurring at higher H_2 pressures, which was desirable to ensure rigorously fast chemical exchange and the determination of accurate thermodynamic parameters based on the observed ^{31}P chemical shifts. The notion of faster rates of chemical exchange at higher H_2 pressures was confirmed quantitatively based on NMR lineshape simulations, which will be discussed in section 3.3.10 (Figure A.2.17). Thus, in order to ensure that the exchange rate was rigorously fast and that the resulting binding parameters were as reliable as possible, the binding equilibria discussed in this chapter were studied under elevated gas pressures, when possible. For example, H_2 and N_2 binding to **1** were measured at pressures of 34 and 51 atm, respectively, to maximize the rates of chemical exchange. In the case of H_2 binding to **3**, utilizing high pressures of gas to ensure fast chemical exchange was not possible because H_2 binds to **3** too strongly under high pressures to observe an equilibrium; this special case will be briefly re-visited in the next section.

In addition to using elevated gas pressures where possible and visually inspecting the broadness of the ^{31}P peaks, two different quantitative approaches were carried out to ensure rigorously fast exchange was a valid assumption under the conditions which the equilibrium studies were carried out. The first of these approaches involved quantitatively

extracting the exchange rates via NMR lineshape simulations at various T and H_2 pressures, such that one could determine the precise exchange rates and compare them with the peak separation ($\delta_{bound} - \delta_{unbound}$) to evaluate under what conditions the fast exchange condition given by Equation 3.11 holds true (see section 3.3.10 for more details). Table 3.4 shows the results of this analysis for H_2 binding to complexes **1**-**3** under 1 atm H_2, where the minimum T required for Equation 3.11 to hold true was calculated based on the exchange rates measured at various T.[231]

Table 3.4. Comparison of peak separation ($\delta_{bound} - \delta_{unbound}$) to the minimum T needed (under 1 atm H_2) to achieve rigorously fast chemical exchange rates for each NiML complex.

M	^{31}P δ (ppm)[a]		Peak Separation, Δν		Minimum T for Fast Exchange[b]	
	(η^2-H_2)NiML	NiML	161.9	202.4	161.9 MHz	202.4 MHz
Al	44.3	30.7	2200	2750	> 292	> 297
Ga	56.9	37.5	3130	3920	> 308	> 313
In	67.5	44.2	3770	4710	> 341	> 347

[a]Chemical shifts are low T convergence of (η^2-H_2)NiML and high T convergence of NiML (under 1 atm Ar) in toluene-d_8. [b]Minimum T is for 1 atm H_2; the minimum T required for fast exchange decreases with increasing H_2 pressure.

Table 3.4 and Figure 3.13 illustrate the dramatic effect of temperature (T) on exchange rate. It is ideal to study binding equilibria over a wide T range, as this will in principle allow for more data points and a more reliable van't Hoff analysis from which to extract thermodynamic parameters. However, as Figure 3.13 clearly shows for **2** under 1 atm H_2, lower T can result in significantly decreased rates of chemical exchange that lead to the breakdown of the fast exchange assumption, especially at low H_2 pressures. This is reflected in the relatively high minimum T required for fast exchange to be a valid assumption under 1 atm H_2 (Table 3.4). As the H_2 pressure is increased, the exchange rate

increases at all T and fast exchange becomes an increasingly valid assumption at lower T, allowing for a wider T range to be included for van't Hoff analysis.

The second quantitative approach to validating the fast exchange assumption and the results obtained from its application involved close examination of the van't Hoff plots for **2** under both 1 atm and 6.8 atm H_2. In order to clearly illustrate the perils of incorrectly applying the fast exchange assumption and the error that is introduced into the resulting thermodynamic binding parameters, the results from van't Hoff plots for different temperature subsets of the overall datasets for 1 atm and 6.8 atm H_2 were compared (Figures 3.14-3.15).

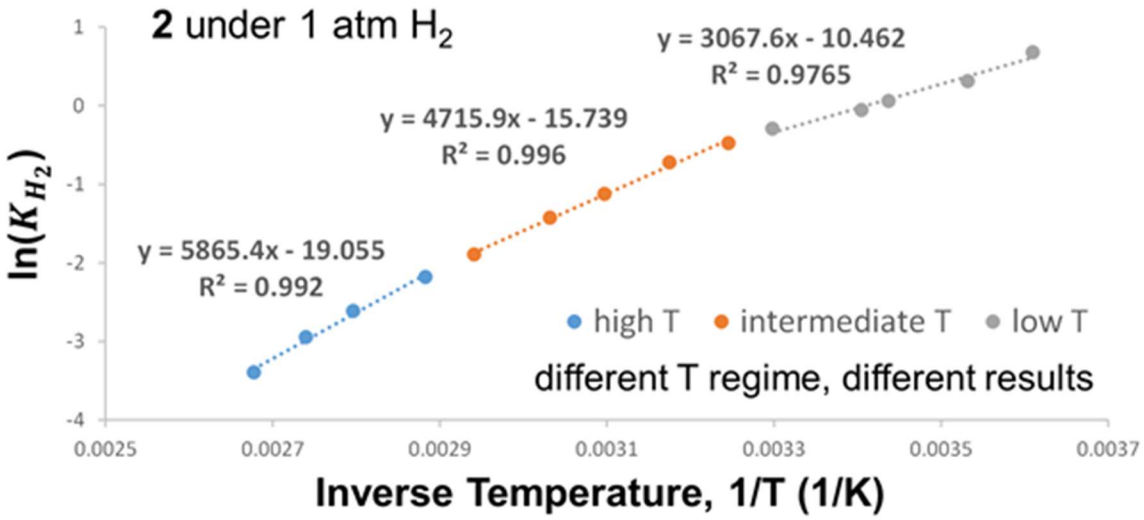

Figure 3.14. Van't Hoff plots of $\ln(K_{H_2})$ vs. 1/T for different T regime subsets for H_2 binding to **2** under 1 atm H_2. The dataset has been divided into three T regimes: intermediate/low T (277 K to 303 K), intermediate/high T (308 K to 340 K), and high T (346 K to 368 K).

Ideally, if the fast exchange assumption holds true for all T included in the van't Hoff analysis, then the binding parameters extracted from the slope and y-intercept of the van't Hoff plot for any given T regime subset should not differ significantly from those obtained from the trendline for the full data set. Thus, trendlines with the same slope in

Figure 3.14 and flat plots in Figure 3.15, which shows the extracted thermodynamic parameters from each T range, are desirable, as that would indicate that the apparent thermodynamic results are the same regardless of which T are considered.

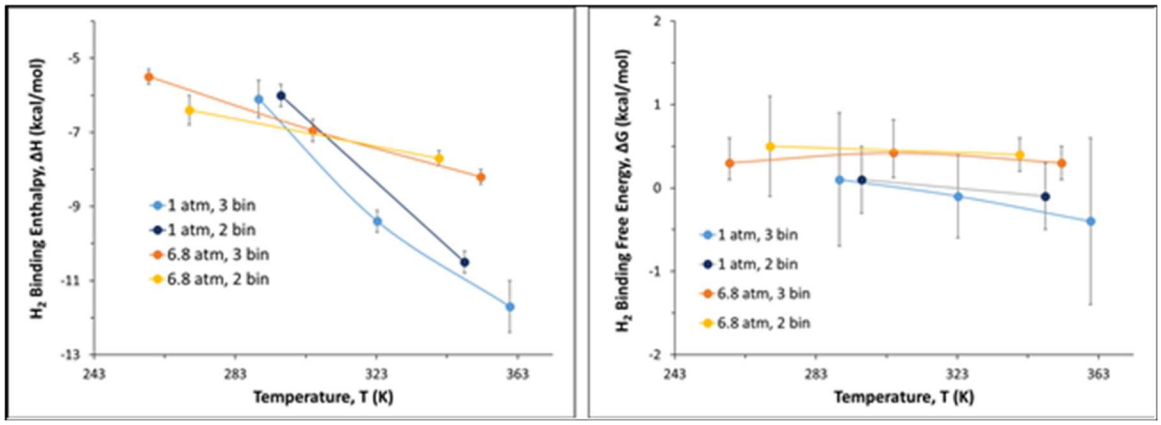

Figure 3.15. Plot of H_2 binding $\Delta H°$ (left) and $\Delta G°$ (right) vs. average T of the T regime subset from which the van't Hoff analysis was conducted, with error bars representing the standard deviation in each value. In addition to breaking the data down into three subsets ("3 bins"), the results for a two-subset breakdown ("2 bins": high T and low T) was also included in the plots. A plot of $\Delta S°$ vs. T subset (Figure A.2.18) looks essentially the same as that as $\Delta H°$.

This is seen to be mostly true for **2** under 6.8 atm H_2, and will only hold true to a greater extent for the higher pressure 13.6 atm H_2 dataset, but clearly is not true for **2** under 1.0 atm H_2 (Figure 3.15). For the 1 atm H_2 data, the apparent $\Delta H°$ was found to be −10.5(3) and −6.0(3) kcal/mol for the data obtained in the high T and low T regimes, respectively. Clearly these values are very different, and their significant temperature-dependence can be attributed to the breakdown of the assumption of fast exchange at 1.0 atm H_2. Despite the clear breakdown of the fast exchange assumption at 1.0 atm H_2 and lower T, it is notable that $\Delta G°$ was found to be relatively insensitive to the T regime, with values of −0.1(4) and +0.1(4) kcal/mol obtained for the high T and low T regimes, respectively. Under 6.8 atm H_2, the thermodynamic parameters extracted are clearly more reliable, as seen visually in the flatter plot of $\Delta H°$ vs. T regime (Figure 3.15). A small

amount of variation is still observed in $\Delta H°$, with values of −7.7(2) and −6.4(4) kcal/mol obtained for the high T and low T regimes, respectively. Similar slight variations are seen for $\Delta S°$ (Figure A.2.18). Once again, $\Delta G°$ was found to be a more robust and reliable parameter, with matching values of +0.4(2) and +0.5(6) kcal/mol extracted from the high T and low T data, respectively. Note that the larger errors in these values as compared to those for the full van't Hoff analysis are due to the fact that there are less data points in the regression analysis for each T regime subset compared with regression of the full dataset.

In summary, the apparent thermodynamic parameters extracted for different T subsets of the data differ drastically for the 1 atm H_2 dataset, but are essentially independent of T for the 6.8 atm H_2 dataset, and will be even more so for the higher pressure 13.6 atm H_2 dataset. This apparent temperature-dependence of the thermodynamic parameters is a consequence of incorrectly applying the assumption of fast exchange to all T in the 1 atm H_2 dataset, which gives $\Delta G°$ values (for the full datasets) that deviate by ~0.5 to 1.0 kcal/mol from those obtained with the proper assumptions at higher H_2 pressures.[213] Even though it looks obvious as displayed in Figure 3.14 that the full dataset for 1 atm H_2 is not perfectly linear over the entire T range, the full data set still has a reasonably high coefficient of determination ($R^2 = 0.983$) and could be easily mistakenly interpreted as a linear plot. Overall, the qualitative and quantitative analyses presented in this section clearly show the dramatic effects of temperature on the exchange rate, and illustrate the danger of applying the assumption of fast exchange to extract thermodynamic parameters for an equilibrium without carefully

considering the validity of such an assumption at all temperature and pressure combinations.

3.3.3.5 Other Assumptions and the Robustness of ΔG° Compared with ΔH° and ΔS°

In examining the considerations regarding the chemical exchange rate, the reliability of experimental $\Delta G°$ values was seen to be relatively greater than $\Delta H°$ and $\Delta S°$ values (ie. less apparent dependence on T). This has been well-documented in the literature, as the co-variance of $\Delta H°$ and $\Delta S°$ can lead to compensation effects which leave $\Delta G°$ unchanged.[231] As a final side note, the robustness of $\Delta G°$ compared with $\Delta H°$ and $\Delta S°$ can also be observed when considering the assumptions made involving the relationship between T and P_{H_2}. In a closed system, such as a J. Young NMR tube, the gas pressure will vary with T in accordance with Guy-Lussac's Law ($P_1/T_1=P_2/T_2$), where P_1 and T_1 are the initial conditions under which the closed system was pressurized.[232] However, the high-pressure studies at 6.8 atm and 13.6 atm H_2, from which thermodynamic parameters for H_2 binding to **2** were extracted, were carried out in PEEK cells pressurized with an ISCO syringe pump which maintains a constant P_{H_2} (see section 3.5 for more details).[214, 233] However, the volume of the PEEK cell in the NMR instrument over which T is varied is small relative to that of the entire high-pressure line, and so the local pressure and H_2 concentration in solution should still be perturbed by local variations in T similarly to the closed system case.[234]

Therefore, it is believed that the best assumption is still to treat P_{H_2} as changing with variations in T using Guy Lussac's Law, but in light of the ambiguity of this "locally heated and cooled" open system, Table A.2.2 shows how assuming constant P_{H_2} would

impact the thermodynamic results for H_2 binding to **2**. Although minor variations are seen in the resulting values for $\Delta H°$ (−4.9 to −6.6 kcal/mol) and $\Delta S°$ (−18.5 to −23.8 cal/[mol·K]) depending on which assumptions are made regarding the dependence of P_{H_2} on T, $\Delta G°$ remains invariant in all cases (0.6 ± 0.2 kcal/mol). Because $\Delta G°$ is not impacted by the ambiguity over whether to assume that pressure varies with T, the assumption that pressure is governed by Guy Lussac's Law will be applied for all other binding equilibria for internal consistency in the relative $\Delta H°$ and $\Delta S°$ values. Collectively, these analyses illustrate that $\Delta G°$ is a more reliable and robust value than $\Delta H°$ and $\Delta S°$ to compare between complexes **1**-**3** and with the binding energetics for other complexes reported in the literature, which is an important subtlety that will be taken into account when interpreting the H_2 binding results in the next section.[231]

3.3.4 Comparison of Thermodynamic Parameters for H_2 Binding to NiML Complexes

The experimental and data analysis protocols used to monitor the H_2 binding equilibrium with complex **2** were subsequently applied to studying the binding equilibria of H_2 with complexes **1** and **3**. For H_2 binding to **1**, VT ^{31}P NMR spectra of **1** under 34 atm H_2 in toluene-d_8 (363 to 210K) show similar a fast-exchange H_2 binding equilibrium to that analyzed for **2**, with a single ^{31}P resonance shifting downfield relative to **1** (30.7 ppm) with decreasing T, and ultimately converging to a chemical shift of ~44.3 ppm for **1**−H_2 (Figure 3.16a-b). The corresponding van't Hoff analysis for H_2 binding to **1** gives $\Delta H°$ = −6.3(2) kcal/mol, $\Delta S°$ = −26.4(4) cal/(mol·K), and $\Delta G°$ = +1.6(2) (Figure 3.16c, Table 3.5). In assessing the validity of the fast exchange assumption, it should be noted that virtually no ^{31}P peak broadening is observed in the VT profile for **1** under 34 atm H_2, which is primarily attributable to the high H_2 pressure employed (Figure 3.16a).

Furthermore, van't Hoff analyses for different T regime subsets yields identical values, within experimental error, for $\Delta H°$, $\Delta S°$, and $\Delta G°$, confirming the reliability of the thermodynamic parameters obtained for **1** (Figures A.2.19-A.2.20).

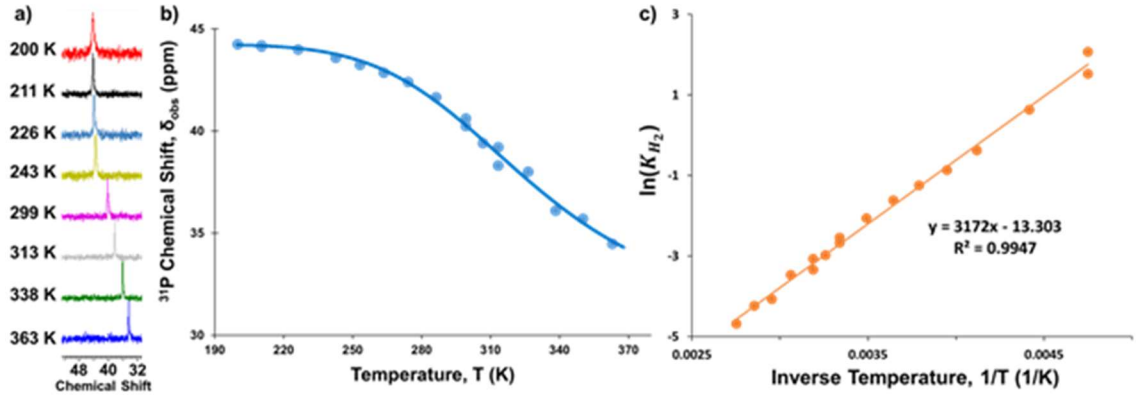

Figure 3.16. (a) VT ^{31}P NMR spectra of **1** under 34 atm H_2 in toluene-d_8 (363 to 200 K). (b) Plot of ^{31}P δ vs. T obtained for **1** under 34 atm H_2. Data are shown as points, with the solid trace representing the best-fit curve obtained by the non-linear fitting of $\Delta H°$ and $\Delta S°$ as parameters. (c) van't Hoff plot of $\ln(K_{H_2})$ vs. 1/T at 34 atm H_2, with the resulting thermodynamic binding parameters displayed in Table 3.5. A comparison of the van't Hoff and non-linear fitting parameters (from the ^{31}P δ vs. T plot in "b") is shown in Table A.2.3.

Because **3** binds H_2 strongly, sub-ambient H_2 pressure was needed to establish an equilibrium between **3** and **3**−H_2. It should be noted that an equilibrium that lies heavily toward **3**−H_2 was observed for **3** under 1 atm H_2, such that extraction of thermodynamic parameters was prone to error due to the proximity of many of the observed ^{31}P chemical shifts to the estimated ^{31}P chemical shift of **3**−H_2 (Figure 3.17b). Thus, sub-ambient pressure of H_2 was utilized to drive the equilibrium further toward **3**. Under 1 atm of a 1:9 gas mixture of H_2 to Ar, where P_{H_2} = 0.1 atm, a single ^{31}P peak was observed from 299 to 357 K, and similar sigmoidal behavior was seen in the corresponding ^{31}P δ vs. T plot (Figure 3.17a-b). From the corresponding van't Hoff plot, the thermodynamic parameters for H_2 binding to **3** are estimated to be $\Delta H°$ = −14.8(6) kcal/mol, $\Delta S°$ = −37(2) cal/mol·K, and $\Delta G°$ = −3.7(7) kcal/mol (Figure 3.17c, Table 3.5). However, these

values for H_2 binding to **3** should be considered estimates, because the broadness of the observed ^{31}P peaks (Figure 3.17a) indicates a problematic fast-intermediate chemical exchange regime relative to the ^{31}P NMR timescale (161.9 MHz) in which complex non-Lorentzian lineshapes and exchange broadening can lead to the extraction of inaccurate thermodynamic values from ^{31}P δ analysis.[213] Because higher H_2 pressures do not result in ample extent of H_2 loss from **3**–H_2 to measure the binding equilibrium, utilizing higher pressure to allow exchange to be rigorously fast is not possible in this instance.

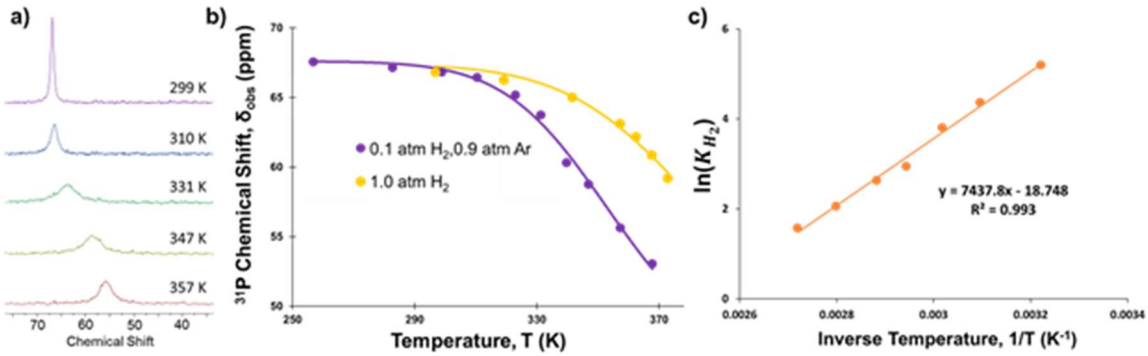

Figure 3.17. (a) VT ^{31}P NMR spectra of **3** under 0.1 atm H_2 in toluene-d_8 (368 to 299 K). (b) Plots of ^{31}P δ vs. T obtained for various H_2 pressures (0.1, 1.0 atm). (c) van't Hoff plot of $\ln(K_{H_2})$ vs. 1/T at 0.1 atm H_2, with the extracted estimates for thermodynamic binding parameters displayed in Table 3.5, and a comparison to the non-linear fitting parameters (from the ^{31}P δ vs. T plot in "b") shown in Table A.2.3.

In order to validate and/or improve the accuracy of the estimated thermodynamic parameters for H_2 binding to **3**, a two-pronged approach was carried out. First, a control experiment showed that the favorability of H_2 binding to **2** was overestimated by 0.7 kcal/mol in terms of $\Delta G°$ when using data obtained in the fast-intermediate exchange regime under identical conditions to those used for monitoring H_2 binding to **3** (0.1 atm H_2, Figure A.2.21). Thus, based on this control, it follows that $\Delta G° = -3.0(7)$ kcal/mol is likely a better estimate for H_2 binding to **3**. Indeed, best-fit lineshape simulations of VT ^{31}P NMR spectra of **3** under 1 atm H_2, which will be discussed further in the H_2 binding

kinetics section (3.3.10), give a value of $\Delta G° = -2.3(2)$ kcal/mol, which is within experimental error of the adjusted estimate of −3.0(7) kcal/mol (Figure A.2.22).[194, 213, 235]

Therefore, it is likely that the binding of H_2 to **3** is representative of a borderline case that is often assumed to be fast chemical exchange to allow facile analysis.[213] By going a bit beyond simply assuming fast exchange, and correcting the estimate based on the aforementioned control experiment and VT ^{31}P NMR lineshape simulations, the value of $\Delta G° = -3.0(7)$ kcal/mol was determined to be the best available estimate for the favorability of H_2 binding to **3**. The thermodynamic binding parameters for H_2 to the trio of NiML complexes are collected in Table 3.5 in section 3.3.6, along with predicted binding free energies from DFT calculations. Before discussing the results for H_2 binding, N_2 binding equilibrium measurements and data analysis will be briefly presented to allow for the trends in both H_2 and N_2 binding to be discussed together.

3.3.5 Thermodynamic Parameters for N_2 Binding to NiML Complexes

After quantifying the H_2 binding equilibria with NiML, it was discovered that the binding equilibria of N_2 could also be investigated via analogous VT ^{31}P NMR spectroscopy experiments. The equilibrium between **2** and **2**−N_2 was monitored under 1 atm N_2 at low T (226 to 193 K), and distinct ^{31}P resonances were observed for both **2** (37.8) and **2**−N_2 (43.5 ppm; Figure 3.18). Recall that the corresponding control experiment for **2** under 1 atm of Ar did not result in the appearance of any new peaks at low T, and so, on this basis, the new resonance observed at 43.5 ppm was confidently assigned as that for **2**−N_2. The observation of distinct resonances for **2** and **2**−N_2 which change in relative integration as a function of T is characteristic of a slow chemical exchange equilibrium relative to the ^{31}P NMR timescale (161.9 MHz; Figure 3.18).[212] A

greater equilibrium concentration of **2**–N_2 relative to **2** was observed at lower T, as would be expected for the intermolecular binding of a gas molecule, which is a considerably unfavorable reaction from an entropic perspective.[205, 232]

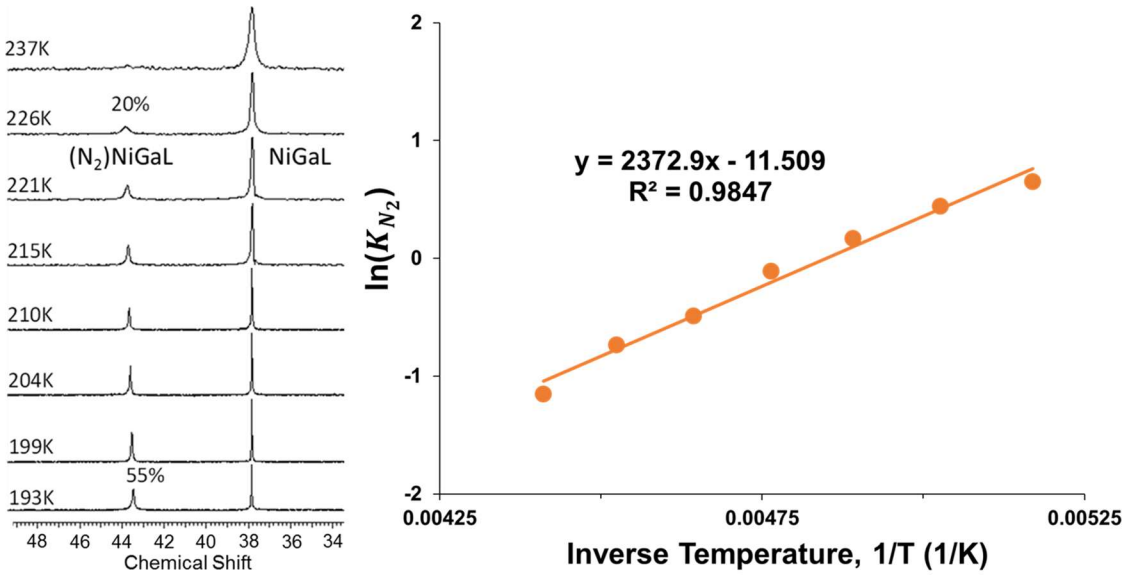

Figure 3.18. Stacked VT ^{31}P NMR spectra (161.9 MHz) of **2** (~15 mM in 0.41 mL toluene-d_8) under 1 atm N_2 (left) and the resulting van't Hoff plot from evaluating K_{N_2} at various T from 226 K to 193 K (right).

Quantitative integration of the ^{31}P peaks for **2** and **2**–N_2 allowed for a straightforward determination of K_{N_2}, according to Equation 3.12, where P_{N_2} is the N_2 pressure:

$$K_{N_2} = \frac{[(N_2)\text{NiML}]}{[\text{NiML}] \times P_{N_2}} \qquad \text{(Eqn 3.12)}$$

By evaluating K_{N_2} at various T, a van't Hoff plot was constructed and thermodynamic binding parameters were extracted for N_2 binding to **2** (Figure 3.18, Table 3.6).[231]

On the other hand, the interconversion of **3** and **3**–N_2 is fast on the ^{31}P NMR timescale (161.9 MHz) at 1 atm N_2 and high T (> 288 K).[212-213, 231] As such, the observed chemical shift of the single ^{31}P NMR resonance represents the population-weighted average of **3** and **3**–N_2, and the data set was modeled and analyzed as described for H_2

binding to **2** (Figure 3.19).[211, 231] The close proximity of the observed ^{31}P chemical shift at 296 K (53.6 ppm) to the low T convergence chemical shift of **3**–N_2 (54.6 ppm) is a testament to the relatively strong binding of N_2 under ambient conditions, and is consistent with the fact that N_2 remains bound in the solid-state based on IR spectroscopy and x-ray crystallography studies (sections 2.2.5 and 3.3.1). Although some line broadening in the ^{31}P peaks for the equilibrium between **3** and **3**–N_2 can be observed in Figure 3.19a, fast exchange was found to be a valid assumption for T > 288 K, as both intermediate (289 K to 325 K) and high T range subsets (333 to 370 K) give nearly identical thermodynamic parameters (Figure A.2.23).

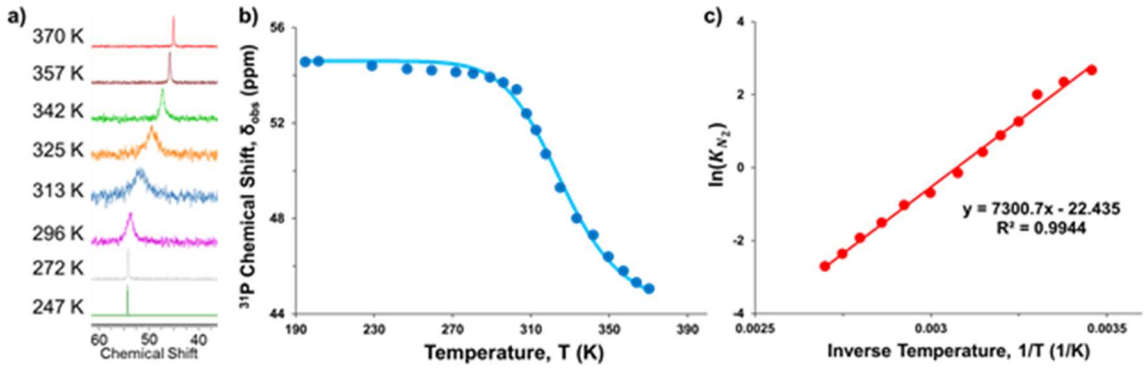

Figure 3.19. (a) VT ^{31}P NMR spectra (161.9 MHz) of **3** under 1 atm N_2 in toluene-d_8 (370 to 247 K). Lower T spectra were also obtained but showed similar ^{31}P δ to that at 247 K, and thus are not shown for clarity. (b) Plot of ^{31}P δ vs. T, with data shown as points, and the solid trace representing the best-fit curve obtained by varying $\Delta H°$ and $\Delta S°$ as parameters. (c) van't Hoff plot of $\ln(K_{N_2})$ vs. 1/T. Thermodynamic binding parameters from van't Hoff analysis are shown in Table 3.6, and a comparison to the non-linear fitting parameters (from the ^{31}P δ vs. T plot in "b") is shown in Table A.2.4.

Lastly, extremely high N_2 pressures were required to observe an equilibrium between **1** and **1**–N_2 due to weak and unfavorable N_2 binding to **1** (*vide infra*). Under 51 atm N_2, the equilibrium between **1** and **1**–N_2 was observed to switch from slow chemical exchange at very low T (≤ 200 K) to fast exchange at higher T (≥ 243 K; Figure 3.20). The ^{31}P peak for **1**–N_2 was observed at ~32.2 ppm, and assigned as such on the basis of

control experiments which showed no such peak for **1** under 1 atm Ar (Figure A.2.14). One potential problem with trying to measure an extremely weak binding equilibrium is that the experimental observable, in this case ^{31}P δ_{obs}, for the fully bound species is unknown, and there is no guarantee that full binding will be attainable under the examined conditions. In this case, the fact that the chemical shift of **1** observed under slow exchange conditions at 190 K and 51 atm N_2 matches that obtained independently under an Ar atmosphere validates the notion that the chemical shift of **1**–N_2 has also reached its "true" chemical shift at 190 K. With the switching of chemical exchange behavior, the ratio of **1**–N_2 to **1** and K_{N_2} were evaluated based on the distinct ^{31}P peak integrations at very low T ($\leq$ 200 K) and based on the observed ^{31}P chemical shift relative to those of **1** and **1**–N_2 at higher T. The resulting van't Hoff plot (Figure 3.20) allowed for the extraction of the thermodynamic binding parameters for N_2 binding to **1** (Table 3.6).

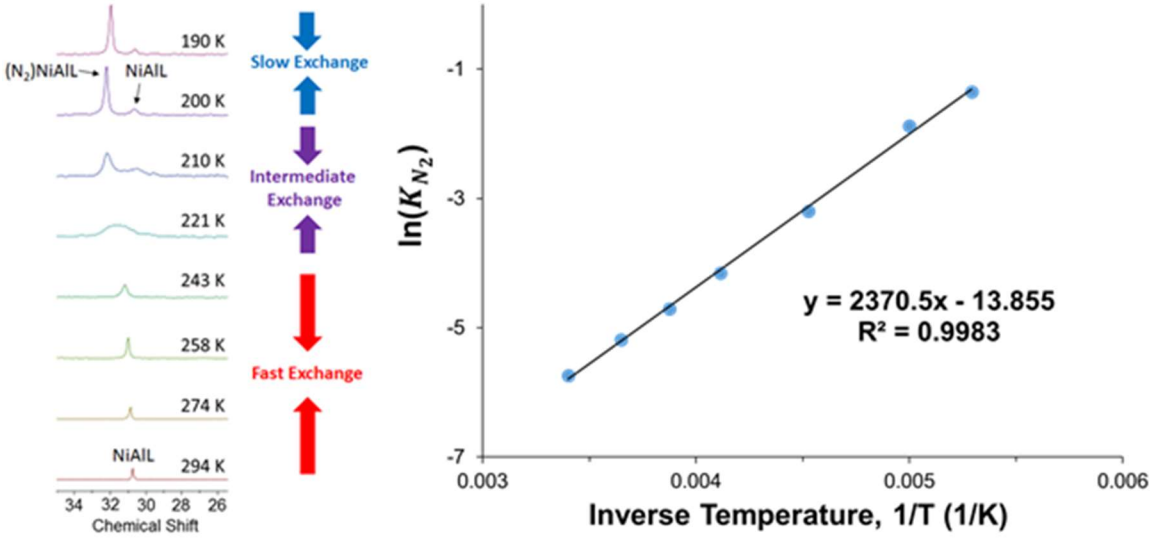

Figure 3.20. Stacked VT ^{31}P NMR spectra (202.4 MHz) of **1** (~16 mM in 0.30 mL toluene-d_8) under 51 atm N_2 (left) and the resulting van't Hoff plot from evaluating K_{N_2} at various T from 294 K to 190 K (right). All spectra shown above were included in the van't Hoff analysis, with the exception of that obtained at 210 K, where the peaks for **1** and **1**–N_2 are overlapping.

3.3.6 Discussion of Thermodynamic Results for H_2 and N_2 Binding to NiML Complexes

3.3.6.1 Summary of Results and Significance

The thermodynamic parameters for the H_2 and N_2 binding equilibria with complexes **1**-**3**, as obtained from the previously described van't Hoff analyses, are compiled in Tables 3.5-3.6. The thermodynamic parameters obtained from non-linear fitting of ^{31}P δ vs. T plots are given in Tables A.2.3-A.2.4, and were found to match closely with those from van't Hoff analyses.

Table 3.5. Measured and calculated H_2 thermodynamic binding parameters for **1**, **2**, and **3**.[a]

	1	**2**[b]	**3**
Δ*H*° (kcal/mol)	−6.3 (0.1)	−6.0 (0.8)	−14.8 (0.6)[d]
Δ*S*° (cal/mol•K)	−26.4 (0.4)	−22 (2)	−37 (2)[d]
Δ*G*° (kcal/mol)	+1.6 (0.2)	+0.6 (0.2)	−3.7 (0.7)[d]
Δ*G*° (DFT)[c]	+2.8	+0.9	−1.9

[a]Entries in parentheses are the standard deviations obtained from van't Hoff linear regression analyses. Standard state is defined as 1 atm H_2 (or N_2 for Table 3.6), 1 M for all other species in toluene, and 298 K. [b]Note that H_2 binding parameters were also obtained for **2** in THF, with Δ*G*° found to be slightly more favorable by ~0.5 kcal/mol (Figures A.2.24-A.2.26). [c]Units of kcal/mol, M06-L[176]/bs1, gas-phase free energies for H_2 (or N_2), solvent-free energies for bound and unbound species (SMD[181], toluene). Calculated by Dr. Jing Xie. [d]Estimated values extracted from fast-intermediate exchange regime data. See text for discussion, but −3.0(7) kcal/mol is reasoned to be a better estimate for Δ*G*°.

Table 3.6. Measured and calculated N_2 thermodynamic binding parameters for **1**, **2**, and **3**[a]

	1	**2**	**3**
Δ*H*° (kcal/mol)	−4.7 (0.2)	−4.7 (0.3)	−14.5 (0.3)
Δ*S*° (cal/mol•K)	−27.5 (0.5)	−23 (1)	−45 (1)
Δ*G*° (kcal/mol)	+3.5 (0.3)	+2.1 (0.5)	−1.2 (0.4)
Δ*G*° (DFT)	+6.3	+3.6	+0.2

[a]See Table 3.5 for footnote details.

Increasing thermodynamic favorability for both H_2 and N_2 binding was observed as the supporting metal was varied down group 13 (In > Ga > Al). By simply varying the supporting metal from Al to Ga to In in the NiML series, the propensity for H_2 or N_2

binding at Ni, as defined by $\Delta G°$ at 1 atm pressure, was tuned by nearly 5 kcal/mol in both cases (Tables 3.5-3.6). Remarkably, this range of H_2 binding favorability for NiML complexes spans nearly the entire range of thermodynamic H_2 binding parameters previously reported for all transition metals ($\Delta G°$= +3 to −2 kcal/mol for 1 atm H_2 standard state; Tables 3.9-3.10).[122, 193-194, 201-202, 205-206] This is especially amazing considering the full range of thermodynamic H_2 binding parameters encompasses binding to Ru,[202] Re,[193] Ir,[194] Cr,[205] Mo,[205] W,[201, 205-206] and Co[122] metal centers in varying ligand environments, whereas binding to the NiML complexes occurs at Ni ligated by the same ligand, with the supporting metal as the only variable atom. It is hypothesized that the *trans* positioning of the group 13 supporting metal relative to the small molecule binding pocket at Ni enables such a dramatic tuning effect.[45, 236] Furthermore, the mononuclear Ni complex, $NiLH_3$ (**4**), did not bind H_2, even at high pressure and low T (34 atm, 193 K), and H_2 binding to **4** is calculated to be unfavorable ($\Delta G°$ = +6.3 kcal/mol, M06-L/bs1).[97, 128] By comparing the two extremes of H_2 binding through DFT calculations, binding to **4** and to **3**, it was found that the supporting metal favorably modulates H_2 binding by ~8 kcal/mol (Table A.2.5). Likewise, N_2 binding to **3** was predicted to be more favorable by ~6 kcal/mol compared with binding to **4** (Table A.2.6).

Tweaking the electronic and steric environment of a transition metal center to achieve desired reactivity is usually performed by varying the steric and electronic properties of the surrounding ligand substituents. For example, variations in the electron-donating properties of phosphine substituents have been seen to exert a dramatic influence on the equilibria between metal dihydrogen and dihydride complexes,[45, 237-240] as well as impact the extent of H−H activation in M(η^2-H_2) complexes.[45, 189, 224, 241] To the

best of my knowledge, utilizing ligand variation to systematically tune the thermodynamic favorability of H_2 binding has not been reported for an isostructural series of metal dihydrogen complexes. Furthermore, our strategy of step-wise metalation has the advantage of eliminating the arduous task of synthesizing several different ligand variants, as libraries of bimetallic complexes with tunable properties and reactivity toward small molecules can be rapidly generated simply by varying the supporting metal within the same ligand framework.[31, 97]

Apart from the dramatic tuning effect of the supporting metal, the determination of both H_2 and N_2 binding energies for first-row metal complexes is also a rarity, with the only other reported examples being Co(TPB) and $Cr(CO)_3(PCy_3)_2$.[122, 205] Across the NiML triad, the binding energies for H_2 are more favorable than those for N_2 by 1.9(4), 1.5(5), and ~1.8(8) kcal/mol for **1**, **2**, and **3**, respectively (Tables 3.5-3.6). The preference of the NiML complexes for binding H_2 over N_2 likely is due to the fact that the Ni centers are relatively electron-deficient due to dative electron withdrawal by the Lewis acidic supporting metal ion, and as such coordination of better σ-donor substrates is favored. A similar trend of more favorable binding of H_2 than N_2 was reported for $Cr(CO)_3(PCy_3)_2$, albeit with a smaller difference in free energy of 1.0(9) kcal/mol (Tables 3.7 and 3.9).[205] On the other hand, the $\Delta G°_{1M}$ (1 M standard state for gases) values for H_2 and N_2 binding to Co(TPB) are the same within experimental error, at −4.4(1.6) and −4.8(9) kcal/mol, respectively (Tables 3.8 and 3.10).[122] That N_2 binding is more competitive with H_2 binding for Co(TPB), a triphosphine-ligated Co center, than it is for NiML complexes, which feature triphosphine-ligated Ni centers, is consistent with the greater π-basicity of low-valent Co relative to low-valent Ni toward stabilizing bound N_2. Indeed, for this

reason the few Ni(N_2) adducts that have been reported display minimal activation of the N≡N bond due to lesser amounts of π-back-bonding from the more electronegative Ni center relative to N_2 adducts of Mn, Fe, and Co.[30, 81, 110]

3.3.6.2 N_2 binding: Comparison of NiML to Literature Complexes

In general, reports of thermodynamic parameters for N_2 binding are relatively sparse, even in comparison to those for H_2 binding. The limited set of reported N_2 binding energies can likely be attributed to the fact that most metal complexes which are studied for N_2 functionalization bind N_2 too strongly and irreversibly to be measured. Tables 3.7-3.8 show a comparison of the thermodynamic N_2 binding parameters for all complexes in the literature, with the standard states defined as 1 atm N_2 (Table 3.7) and 1 M N_2 (Table 3.8).

Table 3.7. Compilation of N_2 thermodynamic binding parameters (for 1 atm N_2 standard state) reported in the literature compared with those for complexes **1**, **2**, and **3**. See Table 3.8 for binding parameters reported for 1 M N_2 standard state.

Complex	$\Delta H°_{1atm}$ (kcal/mol)	$\Delta S°_{1atm}$ (cal/mol•K)	$\Delta G°_{1atm}$ (kcal/mol)	$\Delta G°_{1M}$ (kcal/mol)
1[d]	−4.7 (0.2)	−27.5 (0.5)	+3.5 (0.3)	+0.4 (0.1)
2[d]	−4.7 (0.3)	−23 (1)	+2.1 (0.5)	−1.0 (0.5)
$Cr(CO)_3(PCy_3)_2$[e]	−9.3 (0.2)	−35.4 (2.3)	+1.3 (0.7)	−1.8[b]
$Mo(CO)_3(PCy_3)_2$[e]	−9.0 (0.6)	−32.1 (3.2)	+0.6 (0.1)	−2.5[b]
$[Fe(P_4N_2)]^{+}$[f]	−6.6 (0.1)	−23.4 (0.4)	+0.41 (0.05)	−2.7[b]
$W(CO)_3(PCy_3)_2$[e]	−13.5 (1.0)[a]	–	–	–
3[d]	−14.5 (0.3)	−45 (1)	−1.2 (0.4)	−4.3 (0.4)
$Fe(P_4N_2)$[g]	–	–	−7.0	−10.1[b]

Note that standard deviations are given in parenthesis. Standard state is defined as 1 atm N_2 and 1 M of all other species, at 298 K. [a]Measured via calorimetry.[206] [b]Estimated value based on approximate conversion factor between 1 atm and 1 M standard states for N_2 (for toluene). [d]Measured in toluene via VT ^{31}P NMR spectroscopy. [e]Measured in THF via VT IR spectroscopy.[205] Similar $\Delta H°$ values were measured in both THF and toluene by calorimetry. [f]Measured in fluorobenzene by VT UV-vis spectroscopy.[242] [g]Measured in fluorobenzene by using CV data and the known cation binding parameters to construct a thermochemical cycle.[242]

Table 3.8. Compilation of N_2 thermodynamic binding parameters (for 1 M N_2 standard state) reported in the literature compared with those for complexes **1**, **2**, and **3**. See Table 3.7 for binding parameters reported for 1 atm N_2 standard state.

Complex	$\Delta H°_{1M}$ (kcal/mol)	$\Delta S°_{1M}$ (cal/mol•K)	$\Delta G°_{1M}$ (kcal/mol)	$\Delta G°_{1atm}$ (kcal/mol)
1[d]	−5.4 (0.1)	−19.5 (0.4)	+0.4 (0.1)	+3.5 (0.3)
$[(N_2)Fe_2(\mu\text{-}H)_2(SiP_2O)]$[e]	−9.0 (0.4)	−30 (2)	−0.1 (0.1)	+3.0[a]
2[d]	−5.5 (0.3)	−14.9 (1.3)	−1.0 (0.5)	+2.1 (0.5)
3[d]	−15.2 (0.3)	−36.6 (1.0)	−4.3 (0.4)	−1.2 (0.4)
Co(TPB)[f]	−13.9 (0.7)	−32 (5)	−4.4 (1.6)	−1.3[a]
$[(N_2)Fe_2(\mu\text{-}H)_2(SiP_2O)]^-$	−18[c]	−30[c]	−8.8[b]	−5.7[a]

Note that standard deviations are given in parenthesis. Standard state is defined as 1 M N_2 and 1 M of all other species, at 298 K. [a]Estimated value based on approximate conversion factor between 1 atm and 1 M standard states for N_2 (for toluene). [b]Measured in THF via CV simulation.[243] [c]Estimated based on assumption of similar $\Delta S°$ to that determined for analogous neutral species (see "e"). [d]Measured in toluene via VT ^{31}P NMR spectroscopy. Value for **1** requires the assumption that $[N_2]$ in toluene is proportional to pressure even at high pressures. [e]Measured in hexanes via VT UV-vis spectroscopy.[243] [f]Measured in toluene by VT UV-vis spectroscopy.[122]

It should be noted that in making literature comparisons, it is necessary to convert between standard-state conditions defined as P(gas) = 1 atm and those defined as [gas] = 1 M. The net result is that $\Delta G°_{1M}$ is more favorable by ~3.5 and ~3.1 kcal/mol for H_2 and N_2 binding to NiML complexes, respectively, relative to the values displayed in Tables 3.5-3.6 (where $\Delta G° = \Delta G°_{1atm}$). We believe that defining the standard-state condition as 1 atm gas pressure is more logical, as this better describes typical conditions: at 1 atm pressure in toluene, gas solubility is much lower than 1 M (~0.003 M and ~0.005 M for H_2 and N_2, respectively).[244-245] Furthermore, extrapolating gas solubility to different T can introduce additional sources of error into the determination of equilibrium constants. While conversions between standard states can be rigorously made for NiML complexes (Tables A.2.7-A.2.8), only approximate values can be obtained for converting literature values between standard states, as the exact conversion factors will depend slightly on the gas solubility in the solvent used and the volume and density of the solvent (see Tables 3.7-3.10).

In addition to the previously discussed binding energies for Co(TPB) and $Cr(CO)_3(PCy_3)_2$, N_2 binding studies have also been reported for the group 6 Mo and W congeners of Kubas's complex, $M(CO)_3(PCy_3)_2$.[201, 204-206] Slightly more favorable N_2 binding, albeit within experimental error, was observed for the Mo complex relative to the Cr analogue, with $\Delta G°_{1atm}$ found to be +0.6(1) kcal/mol for the former compared with +1.3(7) kcal/mol for the latter (Table 3.7).[205] Greater enthalpic contributions to binding were generally found upon variation of the metal identity down group 6, with ΔH° values of −9.3(2), −9.8(6), −13.5(1.0) kcal/mol reported for the isostructural Cr, Mo, and W complexes, respectively.[205] These results are loosely consistent with stronger enthalpic contributions to metal-ligand bond formation for second-row and third-row metals relative to first-row metals.[110]

Apart from the equilibrium measurements reported by Hoff and co-workers for Kubas's trio of group 6 complexes, two different sets of Fe complexes are the only other complexes for which thermodynamic N_2 binding parameters have been reported. Mock and co-workers recently reported a tetraphosphine-ligated Fe(I) cationic complex, $[Fe(P_4N_2)]^+$, which binds N_2 with $\Delta G°_{1atm}$= +0.41(5) kcal/mol, with much stronger N_2 binding observed upon one-electron reduction in fluorobenzene to the analogous Fe(0) neutral complex ($\Delta G°_{1atm}$= −7.0 kcal/mol).[242] Likewise, Peters and co-workers have reported a diphosphine-ligated Fe dimer complex, in which two Fe(II) centers are bridged by hydrides, for which N_2 binding data was also reported in two different neighboring charge states.[243] One of the Fe(II) centers in the neutral dimer complex already binds one molecule of N_2 irreversibly, and weak N_2 binding to the other Fe(II) center was observed at low T in hexanes, with $\Delta G°_{1M}$= −0.1(1) kcal/mol.[243] Upon reduction by one electron in

THF, the reduced dimer species binds N_2 much more readily, with $\Delta G°_{1M} \sim -8.8$ kcal/mol.[243]

Compared to this limited set of thermodynamic parameters for N_2 binding ($\Delta H°_{1atm} = -6$ to -18 kcal/mol, $\Delta G°_{1atm} = +3$ to -7 kcal/mol), those obtained for NiML complexes are on the weaker side, with the exception of **3**. N_2 binding to **3** ($\Delta G°_{1M} = -4.3[4]$ kcal/mol) is more favorable than binding to Kubas's Cr and Mo complexes,[205] and on par with the N_2 binding propensity of Co(TPB) ($\Delta G°_{1M} = -4.4[1.6]$ kcal/mol).[122] Complex **1** binds N_2 weaker than all complexes reported, while complex **2** binds N_2 more weakly than all complexes except **1** and the neutral charge state of the Fe(II) dimer reported by Peters and co-workers (Tables 3.7-3.8).[243] Significantly stronger N_2 binding to reduced complexes is illustrated by the Fe complexes of Peters and Mock, which bind N_2 more strongly than their one-electron oxidized analogues by ~7.4 and ~8.7 kcal/mol, respectively.[242-243]

3.3.6.3 H_2 binding: Comparison of NiML to Literature Complexes

A compilation of all thermodynamic H_2 binding parameters for literature complexes is displayed in Tables 3.9-3.10.

Table 3.9. Compilation of H_2 thermodynamic binding parameters (for 1 atm H_2 standard state) reported in the literature compared with those for complexes **1**, **2**, and **3**.

Complex	$\Delta H°_{1atm}$ (kcal/mol)	$\Delta S°_{1atm}$ (cal/mol•K)	$\Delta G°_{1atm}$ (kcal/mol)	$\Delta G°_{1M}$ (kcal/mol)
1[f]	−6.3 (0.1)	−26.4 (0.4)	**+1.6 (0.2)**	−1.9 (0.2)
2[f]	−6.0 (0.8)	−22 (2)	**+0.6 (0.2)**	−2.9 (0.2)
$Mo(CO)_3(PCy_3)_2$[g]	−6.5 (0.2)	−23.8 (2.1)	**+0.6 (0.1)**	−2.9[c]
$Cr(CO)_3(PCy_3)_2$[g]	−7.3 (0.2)	−25.6 (1.7)	**+0.3 (0.1)**	−3.2[c]
$W(CO)_3(PCy_3)_2$[g]	−10 (1)[a]	−29 (3)[d]	**−1.4[c]**	−4.5 (0.1)[b]
3[f]	−14.8 (0.6)[e]	−37 (2)[e]	**−3.7 (0.7)[e]**	−7.1 (0.7)[e]

Note that standard deviations are given in parenthesis. Standard state is defined as 1 atm H_2 and 1 M of all other species, at 298 K. Values were measured in either toluene (complexes **1**-**3**) or THF (all other complexes). [a]Measured via calorimetry.[204, 206] [b]Measured via time-resolved step-scan FTIR and UV-vis spectroscopies.[201] [c]Estimated value based on approximate conversion factor between 1 atm and 1 M standard states for H_2 in toluene. [d]Estimated value based on measured $\Delta H°_{1atm}$ and estimated $\Delta G°_{1atm}$ values. [e]Estimated values extracted from fast-intermediate exchange regime ^{31}P NMR data. See main text for discussion, but −3.0(7) and −6.5(7) kcal/mol are proposed to be better estimates for $\Delta G°_{1atm}$ and $\Delta G°_{1M}$, respectively. [f]Measured via VT ^{31}P NMR spectroscopy. [g]Measured in THF via VT IR spectroscopy. Similar $\Delta H°$ values were measured in both THF and toluene by calorimetry.[205-206]

Table 3.10. Compilation of H_2 thermodynamic binding parameters (for 1 M H_2 standard state) reported in the literature compared with those for complexes **1**, **2**, and **3**.

Complex	$\Delta H°_{1M}$ (kcal/mol)	$\Delta S°_{1M}$ (cal/mol•K)	$\Delta G°_{1M}$ (kcal/mol)	$\Delta G°_{1atm}$ (kcal/mol)
$RuH(Cl)(CO)(P^iPr_3)_2$[d]	−7.7 (0.2)	−23.2 (1.0)	**−0.8 (0.1)**	+2.7[b]
$Ir(H)_2(Cl)(P^tBu_2Ph)_2$[d]	−6.8 (0.2)	−19.2 (0.7)	**−1.1 (0.1)**	+2.4[b]
1[a]	−7.7 (0.1)	−19.5 (0.4)	**−1.9 (0.2)**	+1.6 (0.2)
$Ir(H)_2(Br)(P^tBu_2Ph)_2$[d]	−7.9 (0.9)	−19.7 (3.2)	**−2.0 (0.2)**	+1.5[b]
$Ir(H)_2(I)(P^tBu_2Ph)_2$[d]	−9.3 (0.2)	−22.7 (0.8)	**−2.5 (0.1)**	+1.5[b]
2[a]	−7.4 (0.8)	−15 (2)	**−2.9 (0.2)**	+0.6 (0.2)
Co(TPB)[e]	−12.5 (0.3)	−26 (3)	**−4.8 (0.9)**	−1.3[b]
$[Re(CNR)_3(PCy_3)_2]^{+}$[f]	−18.0 (0.7)	−44(2)	**−4.8 (1.3)**	−1.3[b]
3[a]	−16.2 (0.6)[c]	−30 (2)[c]	**−7.1 (0.7)[c]**	−3.7 (0.7)[c]

Standard state is defined as 1 M for all species at 298 K. All values were determined in toluene unless otherwise noted, with standard deviations shown in parenthesis. [a]Measured by VT ^{31}P NMR spectroscopy. Values for **1**-**2** require the assumption that $[H_2]$ in toluene is proportional to pressure even at high pressures. [c]Estimated value based on approximate conversion factor between 1 atm and 1 M standard states for H_2 in toluene. [c]Estimated values extracted from fast-intermediate exchange regime VT ^{31}P NMR data. See main text for discussion, but −6.5(7) and −3.0(7) kcal/mol are proposed to be better estimates for $\Delta G°_{1M}$ and $\Delta G°_{1atm}$, respectively. [d]Measured by VT NMR spectroscopy.[202] [e]Measured by VT UV-vis spectroscopy.[122] [f]Measured in $CDCl_2$ via VT NMR spectroscopy for R=^{t}Bu.[193]

The thermodynamic parameters obtained for H_2 binding to the NiML complexes generally fall within the ranges typically reported for the limited set of metal complexes

in the literature ($\Delta H°_{1atm}$= −5 to −12 kcal/mol, $\Delta G°_{1atm}$= +3 to −2 kcal/mol; Tables 3.9-3.10).[122, 193-194, 201-202, 205-206] Prior to this work, Co(TPB) and $[Re(CN^tBu)_3(PCy_3)_2]^+$ had the most favorable H_2 binding energies reported, to the best of our knowledge, with $\Delta G°_{1M}$ = −4.8(9) and −4.8(1.3) kcal/mol, respectively (Table 3.10).[122, 193] Notably, **3** binds H_2 even more favorably with $\Delta G°_{1M}$ ~ −6.5(7) kcal/mol, which was obtained by converting the estimated $\Delta G°$ at 1 atm H_2 to $\Delta G°_{1M}$ for $[H_2]$ = 1 M (Table A.2.7). This statement does not imply that H_2 is bound more strongly in **3**−H_2 than in any other M(η^2-H_2) complex, as strong and irreversible binding can often be difficult or impossible to measure experimentally, biasing the strongest reported binding energies away from those that are truly strongest. Furthermore, the vast majority of complexes do not have thermodynamic binding parameters reported, and instead simply qualitatively observe the strength of binding by reporting whether H_2 is labile to vacuum. One likely example of stronger H_2 binding than in **3**−H_2 is that in $[Re(H_2)(H)_4(PhP\{(CH_2)_3PCy_2\}_2)]^+$, in which bound H_2 was inert to substitution by CO;[246] in contrast, H_2 is readily displaced in **3**−H_2 by CO to form **3**−CO, as previously described (Figure 3.2).

While **3** has the most favorable H_2 binding $\Delta G°$ value reported, the $\Delta G°$ value obtained for H_2 binding to **2** places it squarely in the middle of reported literature complexes (Tables 3.9-3.10). With $\Delta G°_{1atm}$ = +0.6(2) kcal/mol, or $\Delta G°_{1M}$ = −2.9(2) kcal/mol, complex **2** binds H_2 more favorably than $RuH(Cl)(CO)(P^iPr_3)_2$ ($\Delta G°_{1M}$ = −0.8(1) kcal/mol) and the series of $Ir(H)_2(X)(P^tBu_2Ph)_2$ complexes reported by Caulton and co-workers ($\Delta G°_{1M}$ = −1.1 to −2.5 kcal/mol for X=Cl, Br, I).[194, 202] Furthermore, complex **2** has similar binding propensity to Kubas's Cr ($\Delta G°_{1atm}$ = +0.3(1) kcal/mol) and Mo ($\Delta G°_{1atm}$ = +0.6(1) kcal/mol) complexes, while the W analogue ($\Delta G°_{1M}$ = −4.5(1)

kcal/mol) and the aforementioned Co(TPB) and $Re(CN^tBu)_3(PCy_3)_2$ complexes have more favorable H_2 binding energies than **2**.[122, 193, 201, 205] Complex **1** ($\Delta G°_{1atm}$ = +1.6(2) kcal/mol, $\Delta G°_{1M}$ = −1.9(2) kcal/mol), binds H_2 more weakly than all complexes except the aforementioned Ru complex and two of the three Ir complexes.[194, 202] As mentioned at the outset, only one example of a Ni(0) dihydrogen complex has been reported, with three additional reports of Ni(II) cationic dihydrogen complexes, and no thermodynamic binding data has been reported for any of these complexes.[117, 189, 198] Thus, the trio of NiML complexes are the first Ni complexes, as well as the first isostructural series of first-row metal complexes, for which thermodynamic H_2 binding parameters have been determined.

3.3.6.4 Entropic and Enthalpic Contributions for H_2 and N_2 Binding to NiML Complexes

In this section, the enthalpic and entropic contributions to binding will be discussed in greater detail for the NiML complexes. Complexes **1** and **2** have nearly identical $\Delta H°$ values for both H_2 (~ −6 kcal/mol) and N_2 (−4.7 kcal/mol) binding. Strikingly, the binding of H_2 and N_2 to **3** are considerably more exothermic compared with binding to **1** and **2** ($\Delta\Delta H° \approx$ −8 and −10 kcal/mol, respectively), which suggests a stronger bonding interaction for **3** with both H_2 and N_2 (Tables 3.5-3.6). The $\Delta S°$ values for both H_2 and N_2 binding to **1**, **2**, and **3** are all negative, which reflects the entropic cost of the intermolecular binding of a gas molecule. In general, a greater entropic cost was observed for N_2 binding than for H_2 binding; this trend has been observed previously and was attributed to the larger absolute entropy of N_2 relative to H_2.[45, 205] In comparing $\Delta S°$ values for complexes **1**-**3**, by far the most negative values are observed for binding to **3**. That complex **3** has the most favorable enthalpic and most unfavorable entropic binding

terms is consistent with tighter and more rigid binding of H_2 and N_2 to Ni for complex **3** compared with binding to complexes **1**-**2**.

In comparing the entropic cost of H_2 and N_2 binding, a slightly greater entropic cost (or more negative $\Delta S°$) was found for binding to complex **1** compared to complex **2**, such that the order of entropic cost is: **2** < **1** << **3** (Tables 3.5-3.6). Because **1** and **2** have identical $\Delta H°$ values for both H_2 and N_2 binding, the overall differences between their respective H_2 and N_2 binding propensities originates from this difference in $\Delta S°$ values. Hence, it is intriguing to consider what factors might be responsible for the $\Delta S°$ differences in binding across the NiML series. For H_2 binding, the two main factors to consider are the reorganization energies of the H_2 and NiML molecular fragments upon binding. A greater extent of H_2 activation in (η^2-H_2)NiML would be expected to result in greater rigidity in the H_2 molecule, resulting in a larger entropic cost. In other words, the less activated and more weakly bound H_2 molecule can rotate more freely and retain a greater degree of the freedom of motion that free H_2 possesses. The second factor is the reorganization of the Ni center, which rises further above the P_3-plane and adopts a pseudo-tetrahedral geometry in order to bind H_2. Consequently, NiML precursors where the Ni center is pre-positioned further above the P_3-plane would be expected to require less reorganization energy to bind H_2. As discussed in the previous chapter, the larger In(III) ion in **3** exerts a greater degree of steric pressure on the Ni center, resulting in Ni being positioned further above the P_3-plane (0.23 Å) than in **1** and **2**, which have nearly identical Ni to P_3-plane distances of 0.13 Å.[97]

Based on this rationale, the entropic cost related to reorganization of the Ni center upon H_2 binding should increase in the order: **3** < **2** ~ **1**. On the other hand, the entropic

cost related to H_2 reorganization increases in the opposite order: **1** < **2** < **3**. Since **3** displays the most negative $\Delta S°$ value for H_2 binding, the latter factor relating to the reorganization of the H_2 fragment appears to be more significant than the former. Based on this analysis, one might expect **2** to have a more negative $\Delta S°$ value than **1** for H_2 binding, but in fact the opposite is observed (Table 3.5-3.6). While this discrepancy is not fully understood, it is possible that reorganization of the supporting metal ion to maintain an intact dative bond with Ni may also be a significant contributing factor to the reorganization of the NiML fragment. Another thing to keep in mind is that the difference in $\Delta S°$ values between **1** and **2** is relatively minor, at ~4.5 cal/(mol·K), compared with the much larger difference of ~10 to 14 cal/(mol·K) between **3** and the other complexes. In light of the greater robustness of $\Delta G°$ compared with $\Delta S°$, perhaps this small entropic difference between **1** and **2** is too minor to be readily explainable.[231] That said, it is more convincing that this small difference is meaningful in light of the fact that a nearly identical difference of ~4.5 cal/(mol·K) between the $\Delta S°$ values for **1** and **2** is observed for both H_2 and N_2 binding. In any case, this subtle difference in entropic binding cost between **1** and **2** has not yet been satisfactorily rationalized.

3.3.6.5 Profiles for H_2 and N_2 Binding to NiML Complexes at Constant T and Variable P

For understanding binding equilibria, it may be more intuitive to compare the relative percentages of bound and unbound species at equilibrium under a similar set of conditions because such an analysis relates directly to experimental observables. For instance, it is a lot easier to understand that a pressure of ~8 atm H_2 is required to reach >75% **2**−H_2 at equilibrium at 298 K, as opposed to simply knowing that $\Delta G° = +0.6(2)$ kcal/mol for H_2 binding to **2**. In this vein, Figure 3.21 displays the binding profiles of the

% of the bound species vs. gas pressure at 298 K. N_2 binding is by far the most favorable for NiInL (**3**), as shown in Figure 3.21, with pressures as small as 1.2 atm N_2 resulting in >90% **3**−N_2 at equilibrium at 298 K. NiAlL (**1**) binds N_2 the weakest, requiring ~41 atm N_2 in order to reach >10% **1**−N_2 at equilibrium at 298 K. NiGaL (**2**) also binds N_2 weakly, albeit stronger than **1**, with ~3.9 atm N_2 required to reach >10% **2**−N_2 and ~35 atm N_2 needed to reach ~50% **2**−N_2 (Figure 3.21).

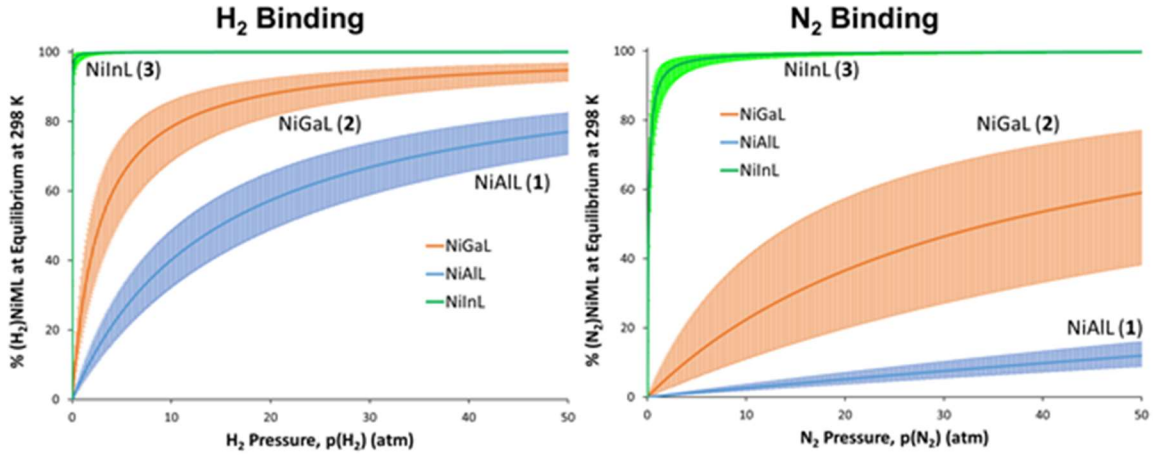

Figure 3.21. H_2 (left) and N_2 (right) binding curves for NiML, which plot the % (L')NiML at equilibrium at 298K vs. L' gas pressure (L'= H_2, N_2). The curves were calculated based on the experimental $\Delta G°$ values (Table 3.5-3.6). The shaded regions on either side of the solid curves represent the range in % bound species that correspond to one standard deviation (based on the experimental error in $\Delta G°$).

Turning our attention to H_2 binding, pressures as small as 0.4 atm H_2 result in >98% **3**−H_2 at equilibrium at 298 K. In contrast, **1** binds H_2 the weakest, requiring ~45 atm H_2 to reach >75% **1**−H_2 at equilibrium at 298 K. Complex **2** binds H_2 moderately relative to the other NiML complexes, only requiring ~8 atm H_2 to reach >75% **2**−H_2 and reaching ~95% **2**−H_2 under ~50 atm H_2 at 298 K. Of note, the shaded error bar regions show that not all errors in $\Delta G°$ values result in the same magnitude of error for the equilibrium mixture composition. For example, **3** has the largest absolute error in the estimate of its H_2 binding $\Delta G°$ value, −3.0(7) kcal/mol, but binding constants of −2.3 or

−3.7 kcal/mol (adding or subtracting the standard deviation) would lead to almost full binding of H_2 to form **3**−H_2 at any substantial pressure anyways, so the error bars are very small for % **3**−H_2. In contrast, **2** has a smaller absolute error in its H_2 binding $\Delta G°$ value, 0.6(2) kcal/mol, but because its $\Delta G°$ value is closer to $\Delta G°$=0 kcal/mol, this smaller error results in more uncertainty in % **2**−H_2 at equilibrium for any given pressure than was the case for **3**−H_2. One last experimentally relevant piece of information concerns the % of bound species present at equilibrium under ambient conditions (1 atm gas pressure and 298 K). These percentages are given for each binding equilibrium in Table 3.11.

Table 3.11. Comparison of Equilibrium Populations of Bound and Unbound Species.

Complex	% of Each Species Present at Equilibrium (1 atm, 298 K)			
	(η^2-H_2)NiML	NiML	(N_2)NiML	NiML
1	7(2)	93	0.3(1)	99.7
2	55(16)	45	3(2)	97
3	99(1)	1	90(10)	10

Note that standard deviation in % bound species is given in parenthesis based on propagation of the standard deviation in the $\Delta G°$ value, and also represents the uncertainty in the associated % NiML value as well. The % bound and unbound species necessarily sum to 100%.

*3.3.7 Characterization of **3**−H_2 in the Solid-State via X-ray and Neutron Diffraction Studies*

The strong binding of H_2 to **3** and the remarkable stability of **3**−H_2 allowed for the isolation of single crystals suitable for both x-ray and neutron diffraction studies (Table 3.12, Figure 3.22). Single crystals were grown by allowing a concentrated solution of **3** in toluene to remain under 1 atm H_2 for several days. While single crystal x-ray diffraction typically allows for structural characterization of all relevant atom positions in a molecule, the positions of hydrogen atoms are not typically refined independently from

the difference map, and instead are placed in idealized positions relative to the heavier atoms to which they are bonded.[173] In a simplified way of thinking about x-ray diffraction, because the electron density distribution in a single crystal is responsible for the diffraction of x-rays in a particular pattern, light atoms with fewer electrons will not contribute as significantly to the diffraction pattern as heavier atoms, and therefore the positions of light atoms will be more difficult to reliably determine. Applying this principle to the case of **3**−H_2, the Ni and H atoms of H_2 are in close proximity, and so because each H atom has one electron and Ni has 28 electrons, it is difficult to reliably determine the position of the H atoms of H_2. This is an unfortunate limitation of x-ray diffraction for studying metal-dihydrogen complexes like **3**−H_2, because the most interesting part of the molecule is arguably the bonding between H_2 and Ni, as defined by the H−H and Ni−H bond lengths and the associated angles.[45]

Fortunately, single crystal neutron diffraction allows for these limitations of x-ray crystallography to be circumvented, and was utilized to determine the positions of the hydrogen atoms of H_2 in **3**−H_2. While x-rays interact with the electron clouds of each atom, neutrons primarily interact with the nucleus of atoms. Unlike x-ray diffraction, neutron diffraction allows for light atoms, like hydrogen, to contribute significantly to the diffracted intensity even when in close spatial proximity to atoms with large atomic numbers.[247-249] Due to the potential hazards of a beam of high energy neutrons which is required for neutron diffraction, neutron sources are limited and only a few facilities in the world are capable of collecting single crystal neutron diffraction data. In collaboration with Dr. Victor Young, Jr. (UMN), Dr. Christina Hoffman, and Dr. Xiaoping Wang, a neutron diffraction study of **3**−H_2 was conducted using the Spallation Neutron Source

(SNS) TOPAZ single crystal diffractometer at Oak Ridge National Laboratory (ORNL).[247, 250] Notably, **3**−H_2 is the first H_2 adduct of Ni or of any d^{10} metal to be structurally characterized by neutron diffraction.[45, 224] A microscope image of crystals of **3**−H_2 (0.35 x 0.30 x 0.30 mm in size) and the structure obtained from neutron diffraction are shown in Figure 3.22, with selected structural parameters given in Table 3.12.

As one would expect, the neutron and x-ray structures are essentially identical (within esd, Table 3.12). An intact H_2 ligand was placed and freely refined anisotropically in the neutron structure, yielding clear crystallographic evidence for H_2 bound side-on to Ni and confirming our original formulation of **3**−H_2 based on T_1(min) and J_{HD} NMR studies.[97] The H−H distance in the solid-state structure was determined to be 0.80(2) Å, which is shorter than the 0.91 Å distance previously estimated from the J_{HD} coupling constant in solution-state NMR studies.[97] However, it is well documented that uncorrected librational motion of H_2 results in slightly shorter apparent solid-state H−H distances relative to those obtained by NMR studies, with the H−H distance found to be shorter by ~0.07 Å on average in complexes which were studied by both techniques.[45, 248, 251] This seems to be a valid rationale for evaluating the discrepancy in the H−H distance between the neutron structure and solution-state NMR studies for **3**−H_2, as the rapid rotation of H_2 about the Ni→In bond vector established by T_1(min) studies likely gives rise to the apparent shortening effect in the solid-state, which is of similar magnitude to that seen for other complexes in the literature.[30, 45, 97]

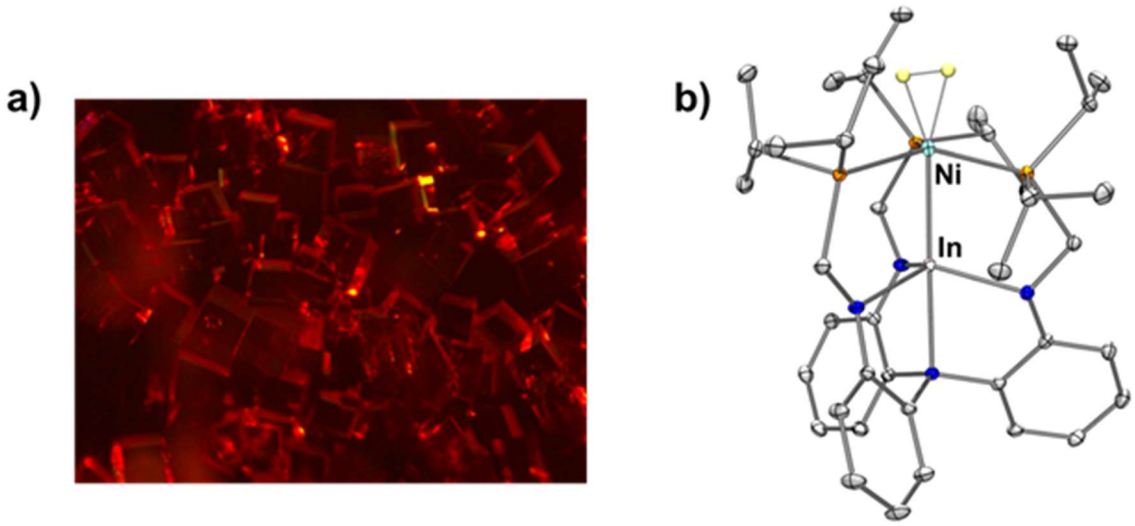

Figure 3.22. (a) Microscope image of gold block single crystals of **3**−H_2. (b) Solid-state structure of **3**−H_2 obtained via neutron diffraction, with 50% ellipsoids shown. H atoms were omitted for clarity, except for those on the apical H_2 ligand (shown in gold). Metal atoms are labeled, and phosphorus (orange), nitrogen (blue), and carbon (gray) atoms are color coded accordingly. Selected structural parameters for both neutron and x-ray structures are shown in Table 3.12.

Unlike the H−H distance (*vide supra*), the Ni−H bond distance is a parameter that neutron diffraction is uniquely able to experimentally evaluate. The Ni−H bond distances were determined to be 1.61(2) and 1.61(2) Å. It makes intuitive geometric sense that the Ni−H distances in a Ni(η^2-H_2) adduct should be longer than those for most terminal Ni hydride species, which typically have distances of 1.32-1.65 Å.[252] Although literature comparisons are more sparse in light of **3**−H_2 being the first Ni(η^2-H_2) adduct to be structurally characterized, its M−H and H−H distances are both similar to those for the only Co(η^2-H_2) adduct to be structurally characterized, (η^2-H_2)Co(TPB), which had distances of 1.66-1.67 Å and 0.83(2) Å, respectively.[121] Interestingly, short contact distances between coordinated H_2 and the hydrogen atoms of the ligand isopropyl groups were observed in both **3**−H_2 and (η^2-H_2)Co(TPB), the closest of which were 2.25-2.27 Å and 2.10-2.17 Å, respectively. These close contacts in (η^2-H_2)Co(TPB) were attributed to

crystal packing forces and deemed to be unlikely to persist in the solution-state.[121, 248] Close contacts between ligand C−H bonds and an activated M(η^2-H_2) or M−H moiety have been previously implicated in facile C−H ortho-metalation processes, though we have not observed evidence of such processes for **3**−H_2.[97, 124]

Table 3.12. Comparison of selected structural parameters for **3**−H_2 from experiment and theory.

Metric	X-ray[a]	Neutron	DFT Calc'd[c]
Ni-In (Å)	2.479(2)	2.49(2)	2.603/2.531
Ni-P_{avg} (Å)	2.2618(2)	2.260(1)	2.287/2.292
Ni to P_3-plane (Å)	0.29	0.31	0.37/0.35
In to N_3-plane (Å)	0.50	0.52	0.43/0.46
In-Neq_{avg} (Å)	2.1147(6)	2.126(1)	2.051/2.079
In-N_{apical} (Å)	2.366(1)	2.39(2)	2.292/2.322
Ni-H (Å)	–[b]	1.61(2), 1.61(2)	1.633,1.639/ 1.628,1.624
H-H (Å)	–[b]	0.80(2)	0.835/0.837

[a]Note that the initially reported x-ray structure[97] was collected at 123 K (Cu source), whereas the structure reported here was re-collected at 100 K (Mo source) so as to more directly compare with the neutron structure (collected at 100 K) and to obtain higher resolution data. [b]Although H−H and M−H distances are generally considered to be unreliable from x-ray data, high resolution data collected to 0.6 Å allowed for distances of 0.92(7) Å, and 1.65(2) and 1.58(2) Å to be determined. [c]values are listed from M06-L/bs1 / M06-D3/bs4. See Table A.2.9 for comparison of structural parameters obtained using different computational methods.

The DFT-computed structure of **3**−H_2 matches reasonably well with that determined experimentally, except for the overestimation of the Ni−In bond distance by all methods examined in both **3** (by 0.01 to 0.06 Å) and **3**−H_2 (by 0.04 to 0.12 Å; see Table 3.12 and Table A.2.9). Similar predictions of slightly longer M→E dative bond distances relative to experiment, albeit with generally smaller discrepancies, has been reported for a similar system in the literature.[101] The calculated Ni−H distances agree well with those determined by neutron diffraction, and H−H distance is predicted to be

slightly longer (0.02 – 0.04 Å) than the experimental value of 0.80 Å from the neutron structure, and slightly shorter by ~0.08 Å than the solution-state distance of 0.91 Å.[97]

3.3.8 Investigating the Interplay of σ-Donation and π-Back-Bonding Interactions in Binding

3.3.8.1 Computational Insight into Binding Interactions

The next few sections will delve deeper into the binding interactions between H_2 and Ni to understand the differences as a function of supporting metal. Although Ni(N_2) complexes are rare, the minimal extent of N−N activation renders the Ni(N_2) complexes less interesting than the Ni(η^2-H_2) complexes in terms of subsequent reactivity, and so the Ni(η^2-H_2) complexes will largely be the focus of much of the remainder of this chapter. In M(η^2-H_2) complexes, two primary interactions are responsible for the strength of the interaction between the metal and H_2: σ-donation (H_2 σ → M) and π-back-bonding (M d_π → H_2 σ*).[45, 197, 224] In order to understand the relative interplay of these two interactions and how they change with different supporting metals, DFT calculations were performed, with extended transition state – natural orbitals for chemical valence (ETS-NOCV) calculations performed on the DFT-optimized structures.[253-255]

Because of the availability of the crystal structure of **3**, the neutron structure of **3**−H_2, and the free energy of H_2 binding to **3**, testing whether various computational methods could accurately reproduce these results seemed like a good starting point for determining which methods were best at describing the interactions between H_2 and Ni for the NiML complexes. To find a suitable computation method, four functionals were tested, M06-L,[176] M06-D3,[177] PBE0,[178] and PBE0-D3,[179] in combination with basis set 1 (denoted as "bs1"; see Table 2.9). Additional basis sets were tested with M06-L (bs0 and

bs2-bs4) and M06-D3 (bs4). Taking into account both the structure and energetics, M06-L/bs1 performs the best for describing H_2 and N_2 binding for the NiML series. As shown in Tables 3.5-3.6, M06-L/bs1 correctly predicts the relative favorability of H_2 and N_2 binding (Al < Ga < In), as well as that H_2 binds stronger than N_2 for each complex, consistent with experimental measurements. Although the absolute $\Delta G°$ values are all predicted to be less favorable than is experimentally observed, the relative binding differences ($\Delta\Delta G°$) between NiML complexes calculated with M06-L/bs1 match the experimental data reasonably well.

With a suitable computational method identified, energy decomposition analysis[254] (EDA, with PBE0-D3/TZ2P method using ADF2017 software[255]) was performed on the optimized structures (M06-L/bs1) for **1**−H_2, **2**−H_2, and **3**−H_2 to better understand the interactions of Ni with H_2. The EDA interaction energy (ΔE_{int}) is calculated by taking the electronic energy difference between (η^2-H_2)NiML and its two fragments, H_2 and NiML. The ΔE_{int} is broken down into many components, including terms pertaining to electrostatic interactions, Pauli repulsion, dispersion, and the orbital interaction energy ($\Delta E_{orbital}$), the latter of which is further decomposed into contributions to chemical bonding by the ETS-NOCV method.[253-255] For the H_2 adducts, the dominating NOCV pairs suggest two types of orbital interactions between H_2 and NiML: 1) forward donation from the σ-bond of H_2 to the empty $4p_z$ orbital of Ni (Figure 3.23, NOCV1 and 3); and 2) π-back-donation from the $3d_{xz}$ and $3d_{yz}$ orbitals of Ni to the σ* antibonding orbital of H_2 (Figure 3.23, NOCV2 and 4). The σ-donation orbital interactions were found to be dominant, with interaction energies contributing ~60% of the total interaction energy for all complexes (Table A.2.10).

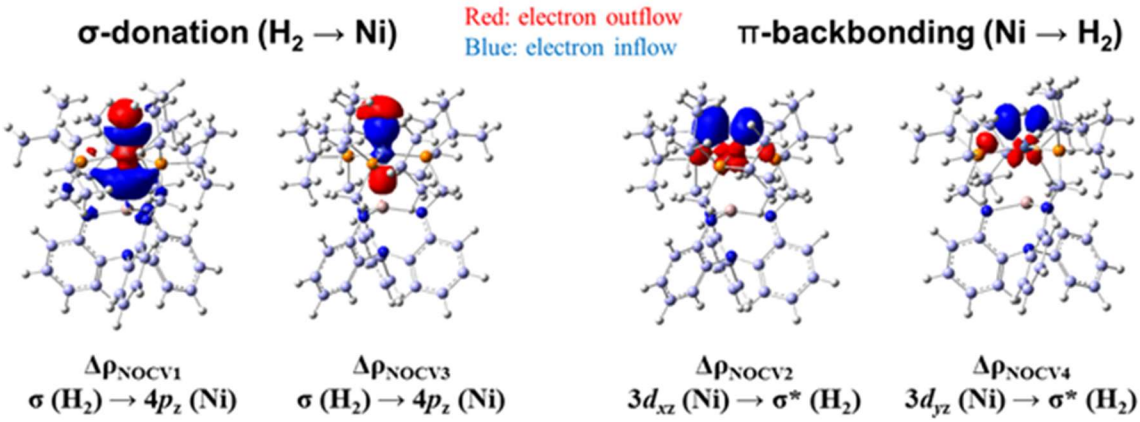

Figure 3.23. Deformation density contributions ($\Delta\rho_{NOCVn}$, isovalue 0.04 a.u.) of NOCV pairs of **3**−H_2. Similar densities were computed for **1**−H_2 and **2**−H_2 complexes. Figure adapted from that provided by Dr. Jing Xie.

Note that similar calculations were carried out for the N_2 adducts of NiML, with the results indicating that σ-donation contributes about ~40-45% of the total interaction energy for all Ni(N_2) complexes, with π-back-donation making up the other 55-60% (Figure A.2.27, Table A.2.11). The fact that σ-donation is less dominant in N_2 binding speaks to the fact that N_2 is generally considered to be a poorer σ-donor than H_2.[45, 190] The fact that the N_2 unit is minimally activated (2144 cm^{-1} IR stretch of **3**−N_2) suggests that σ-donation is more dominant in the N_2 adducts of NiML than is typical for metal-dinitrogen adducts, as was concluded by Peters and co-workers for cationic Ni(II)−N_2 adducts.[189]

3.3.8.2 Rationalizing Trends in H_2 Binding and Activation: Complementary σ-Donation Interactions

The greater contribution of σ-donation to H_2 binding compared with π-back-donation, as predicted by ETS-NOCV calculations, is consistent with the experimentally observed trend that H_2 binding favorability increases (In > Ga > Al >> no support) as Ni becomes more electron-deficient, as judged by the Ni(0/I) oxidation potentials from CV studies.[97] Qualitatively, H_2 binding under mild conditions (1 atm H_2) was observed for

the two most electron-deficient Ni centers in the NiML series, those of **2** and **3**. In contrast, higher H_2 pressures and/or lower T were required to induce H_2 binding to the more electron-rich Ni center in **1**, while **4** did not bind H_2 even under extreme conditions (34 atm, 193 K).[30, 97, 128]

This trend in increased binding propensity due to increased σ-donation from H_2 to more electron-deficient Ni centers also explains the slight elongations in H−H distance upon varying the supporting metal down group 13. Specifically, the elongated H−H bond in **3**−H_2 compared with **2**−H_2 is hypothesized to be the result of two complementary σ-interactions, where the greater electrophilicity of Ni imparted via increased electron withdrawal by In(III) induces increased σ-donation from H_2 to Ni. A similar line of reasoning would explain the longer H−H distance in **2**−H_2 relative to that in **1**−H_2, as predicted by DFT calculations. This scenario of a stronger *trans* σ-acceptor strengthening H_2 binding contrasts the more typical case of a strong *trans* σ-donor weakening H_2 binding.[45] The symbiotic σ-interactions in the unusual bonding motif for (η^2-H_2)NiML, as well as in the isoelectronic [(η^2-H_2)CoML]$^-$ complexes, has been termed the *inverse trans influence*, which differs from the typical case in that the H_2→Ni and Ni→M interactions are complementary and utilize different Ni orbitals, primarily the Ni $4p_z$ and $3d_z^2$, respectively.[30, 97, 167] In the typical case, both the *trans* σ-donor ligand and H_2 are competing to interact with the same metal-based orbital of σ-symmetry, often the d_z^2 orbital (Figure 3.24).[30, 45] The same complementary σ-interactions that induce H_2 binding to the NiML complexes are also thought to be relevant for the binding of N_2, CO, and other ligands to NiML complexes, and will be revisited briefly in examining the electronic structure of these adducts via UV-vis spectroscopy in section 3.3.11.

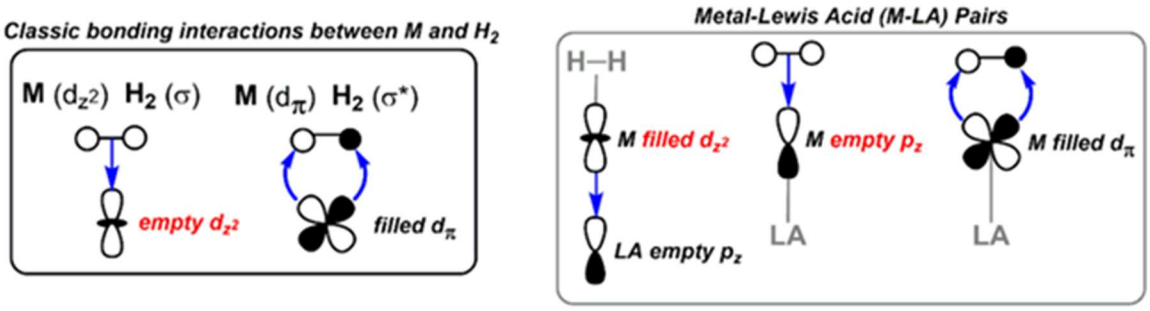

Figure 3.24. Bonding interactions between a transition metal (M) and H_2 in the absence and presence of a Lewis acid support (LA). Ni is the transition metal in the case of NiML complexes, with LA used interchangeably here with "M" to denote the supporting metal in NiML. Figure taken from ref. 30.

Collectively, experimental and computational studies support the notion that a greater extent of σ-donation from H_2 to an increasingly electron-deficient Ni center, as the supporting metal is varied down group 13, is primarily responsible for inducing H_2 binding to the NiML complexes. Strong H_2 binding via σ-donation to electrophilic metal centers is in accordance with Kubas's contention that highly electrophilic and/or cationic metal complexes are excellent at stabilizing H_2 adducts, as increased σ-donation stabilizes bound H_2 and elongates the H−H bond, but will not cause H−H bond rupture without sufficient π-back-donation.[45, 197] In the case of the NiML complexes, electron withdrawal from Ni by the supporting metal only serves to further limit π-back-donation to the H_2 σ* orbital relative to that from a more electron-rich Ni complex, which further stabilizes the H_2 adducts toward oxidative addition. However, as was examined in detail in chapter 2, stronger electron withdrawal from Ni by larger M(III) ions is only part of the story. Indeed, the steric effects of larger M(III) ions were also seen to be significant in dictating the positions of Ni and M relative to their respective binding pockets and to one another. As such, it is important to discuss how these dual effects of larger M(III) ions,

namely increased electron withdrawal and increased steric pressure on Ni, manifest to control the favorability of H_2 and N_2 binding.

3.3.9 What Dictates H_2 and N_2 Binding Free Energies: Consideration of Steric Effects

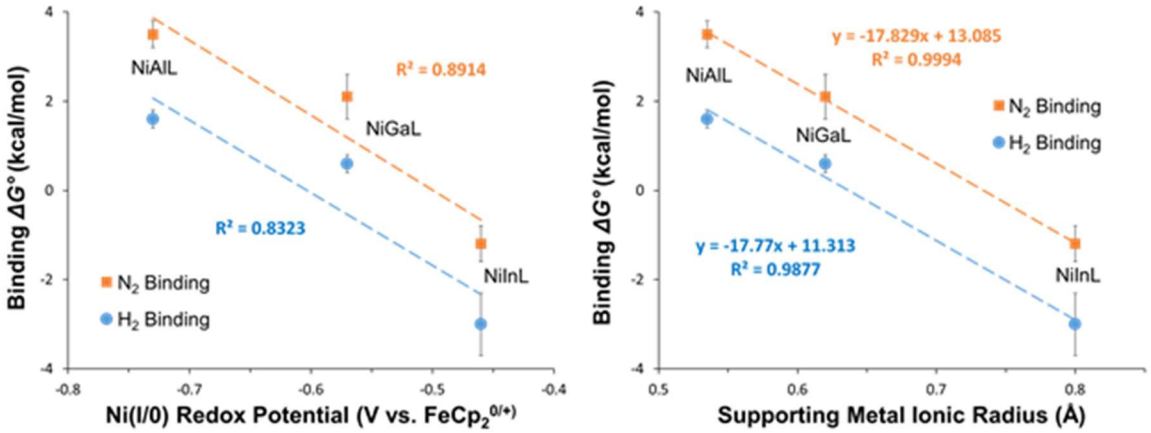

Figure 3.25. Plot of $\Delta G°$ for H_2 (blue circles) and N_2 (orange squares) binding vs. Ni(I/0) redox potential of NiML in CH_3CN (left, with $E°_{1/2}$ found to be identical to that in THF for complexes **1** and **2**) and vs. supporting metal ionic radii, as defined by the Shannon 6-coordinate M(III) values (right).

The plots shown in Figure 3.25 are a good place to begin attempting to disentangle the steric and electronic effects that collectively dictate the propensity of H_2 and N_2 to bind to the NiML complexes. It is worth pointing out that although these correlations are only for three data points, the fact that thermodynamic free energies for both H_2 and N_2 binding have been determined for a single complex is rare, let alone an isostructural series of three complexes. Furthermore, just as examining correlations for the three complexes aided in our understanding of structure and electronic properties in chapter 2, the isostructural nature of these complexes offers a unique opportunity to understand what properties of both the supporting metal and Ni influence binding favorability. Excellent correlations are observed between $\Delta G°$ values for both H_2 (R^2=0.9877) and N_2 (R^2=0.9994) binding to the NiML complexes with the size of the

supporting metal, in terms of the Shannon M(III) ionic radii[133] (Figure 3.25, right). Significantly worse correlations are observed for $\Delta G°$ values for H_2 (R^2=0.8323) and N_2 (R^2=0.8914) binding with the Ni(I/0) redox potentials of the NiML complexes.

Because the Ni(I/0) redox potentials represent the relative electron-richness of the Ni centers, these values represent the effect of the supporting metal on the electronic environment of Ni in NiML complexes. However, this electronic effect is not without confounding factors, as the steric constraints of the ligand framework can impose a stronger Ni→M interaction, as was clearly seen to be the case upon comparing the NiInL and NiInL*$_3$ complexes in chapter 2. Namely, the dual effects of the capping amine forcing larger M(III) ions higher above the N_3-plane and that of Ni preferring to bind as close to coplanar with the P_3-plane as possible work in concert to bring Ni and larger M(III) ions into closer proximity and to promote stronger dative bonding than would otherwise be observed without these constraints of the ligand framework. Furthermore, the fact that a significantly worse correlation with binding favorability ($\Delta G°$) is observed for the Ni(I/0) redox potentials as compared to M(III) size supports the conclusion that electronic effects alone cannot adequately explain the propensity of NiML complexes to bind H_2 and N_2. The principle of two symbiotic σ-interactions where the Lewis acidic group 13 metal induces H_2 and N_2 binding by rendering Ni electron-deficient still holds true qualitatively, as Figure 3.25 (left) shows. But clearly the steric effect of larger M(III) ions is substantial, as the M(III) ionic radius modulates the $\Delta G°$ values for H_2 and N_2 binding in essentially a linear fashion. Furthermore, the similar slopes of the plot of $\Delta G°$ for both H_2 and N_2 binding vs. M(III) ionic radii reflect the similar effect of group 13

supporting metals in promoting both binding equilibria, as well as the importance of σ-donation to promoting the binding of both substrates.

To illustrate the influence of sterics, it is useful to consider the binding of H_2 and N_2 to **3**, since In(III) is the largest of the supporting metals. One way to look at the poor quantitative correlation observed in the plot of $\Delta G°$ values vs. Ni(I/0) redox potentials (Figure 3.25, left), is that binding to NiInL (**3**) is much more favorable (more negative $\Delta G°$ value) than would be expected based on the electron-deficiency of Ni alone. In other words, based on the "trendline" that would be drawn between the data points for complexes **1** and **2**, which can be expected to have similar steric effects based on their identical Ni to P_3-plane distances of 0.13 Å,[78, 97] the $\Delta G°$ values for H_2 and N_2 binding to **3** would be expected to be −0.1 and +1.1 kcal/mol, respectively. Comparing those values to the actual $\Delta G°$ values for H_2 and N_2 binding to **3**, which are ~ −3.0(7) and −1.2(4) kcal/mol, respectively, shows that H_2 and N_2 binding are more favorable by ~2.9 and ~2.3 kcal/mol, respectively, than would be expected based on the Ni(I/0) redox potential of **3** relative to those for **1** and **2**. While this analysis is admittedly somewhat crude, the main question it is exploring is highly relevant. That is, what would the propensity for binding be if all the Ni centers in the series were similarly positioned relative to the P_3-plane and only differed in the degree of electron-deficiency? Importantly, this analysis illustrates that the steric effect of the larger In(III) supporting metal ion is substantial, and that the additional 0.1 Å that Ni is positioned above the P_3-plane in **3** relative to **1** and **2** plays a large role in promoting H_2 and N_2 binding.

Another thing to keep in mind when considering the excellent correlation of M(III) size with $\Delta G°$ values for H_2 and N_2 binding is that, in addition to describing steric

effects, M(III) size also captures the electron-deficiency of Ni to some extent as well. To this point, a qualitative correlation is observed between the M(III) ionic radii and the Ni(I/0) redox potentials (R^2=0.89). In addition to the HSAB effects discussed in the previous chapter which predict that larger M(III) may preferentially interact with Ni(0) rather than the harder amide (N_3) donor set, larger M(III) will also be forced into closer proximity to Ni as a result of the aforementioned constraints of the capping amine and phosphine donors of the ligand.[97, 165] Both of these effects would result in larger M(III) rendering Ni more electron-deficient, and thus would only improve the correlation of M(III) size with the $\Delta G°$ values for H_2 and N_2 binding, relative to whatever correlation would be observed between $\Delta G°$ and a hypothetical parameter describing the steric effect alone. Along these lines, perhaps it is not surprising that M(III) size correlates better with the $\Delta G°$ values for binding than the Ni(I/0) redox potentials; M(III) size is correlated with the electron-deficiency of Ni, but the relative Ni(I/0) potentials contain little information about the positioning of the Ni center relative to the P_3-plane, which clearly significantly impacts binding propensity.

Lastly, it is important to point out that Lewis acidity, as defined by the pK_a of $M(H_2O)_6^{3+}$ complexes, was not found to be a useful parameter in explaining $\Delta G°$ values for H_2 (R^2=0.0214) or N_2 (R^2=0.0533) binding.[136] As proposed in chapter 2, it seems that the steric effects of M(III) size, among other factors, lead to drastic deviations in the Lewis acidities conferred by group 13 M(III) ions toward a water ligand in $M(H_2O)_6^{3+}$ complexes from those conferred toward Ni, which in turn influences the favorability of H_2 binding. Just as comparison of the NiML complexes to the series of NiML*$_3$ complexes proved useful in thinking about the steric effects imposed by the capping

amine donor of "L" in chapter 2, it is also a useful comparison to consider here in regard to the binding of H_2 and N_2. Preliminary reactivity studies conducted by Bianca Ramirez found that all three NiML*$_3$ complexes bind both H_2 and N_2 to some extent under 1 atm pressure at 298 K, in contrast to the much wider differences in conditions required for binding to NiML complexes. Notably, NiGaL*$_3$ results in a slightly greater downfield shift and sharper ^{31}P resonances upon binding both H_2 and N_2 compared with NiInL*$_3$. This suggests that the order of binding strength has been altered for the NiML*$_3$ complexes (Ga > In > Al) relative to that observed for the NiML complexes (In >> Ga > Al). Although thermodynamic binding studies have not been conducted for NiML*$_3$ complexes, it is intriguing that upon removal of the capping amine donor from NiML to give the NiML*$_3$ complexes, the apparent order of binding strength now matches the relative Lewis acidities given by the pK_a values of $M(H_2O)_6^{3+}$ complexes, where Ga (pK_a = 2.6) > In (3.9) > Al (4.95). While these results are only preliminary at this point, it would seem that upon relaxation of the steric constraints imposed by the capping (and tethering) amine donor of L, the Lewis acidities toward Ni match more closely with those exhibited in $M(H_2O)_6^{3+}$ complexes. Thus, it stands to reason that the steric effects of ligating Ni and M within L are likely primarily what leads to NiInL (**3**) displaying the strongest propensity to bind H_2 and N_2.

3.3.10 Beyond Thermodynamics: Kinetics of H_2 Binding and Loss for (η^2-H_2)NiML Complexes

3.3.10.1 VT ^{31}P NMR Lineshape Studies Under 1 atm H_2 and NMR Simulation Protocols

After developing an understanding of the properties of the supporting metal which dictate the thermodynamic favorability of H_2 and N_2 binding to NiML complexes, the

next logical step was to think about how the kinetics of H_2 binding and dissociation at Ni would change as function of the supporting metal. During the course of the previously described VT ^{31}P NMR studies to quantify the thermodynamic binding parameters, it was qualitatively observed that the chemical exchange behavior and the resulting lineshapes of the ^{31}P peaks were very different for complexes **1**, **2**, and **3** under 1 atm H_2, and also varied dramatically with T for each complex. Namely, resonances for both free H_2 and bound H_2 for **3**−H_2 can be observed by ^1H NMR spectroscopy at 298 K under 1 atm H_2, indicating that H_2 exchange is slow on the ^1H NMR timescale (400 MHz). Cooling to 253 K is needed to observe distinct resonances for free and bound H_2 for the equilibrium between **2** and **2**−H_2, indicating that H_2 exchange is faster for **2** relative to **3** for a given T.[97] The most rapid H_2 exchange was observed between **1** and **1**−H_2, with very low T and/or higher pressures needed to resolve free and bound H_2 resonances (Figures A.2.10-A.2.12). This section is about closely examining these differences in ^{31}P NMR lineshapes to extract kinetic rates and free energy barriers ($\Delta G^{\ddagger}$) for H_2 binding and loss. For clarity, the process of H_2 dissociation from (η^2-H_2)NiML to give free H_2 and NiML will be referred to as "H_2 loss," opposed to "H_2 dissociation," which is also sometimes used to describe the cleavage of the H−H bond on a metal surface.

The rates of H_2 self-exchange between (η^2-H_2)NiML and NiML for the trio of complexes were determined via total lineshape analysis of VT ^{31}P NMR spectra collected over a wide T range (213 to 343 K in toluene-d_8). The self-exchange rate has units of s^{-1}, and represents the total number of chemical exchanges that occur per second (ie. the frequency of chemical exchange). A plausible mechanism for self-exchange comprises two elementary steps: (1) the loss of H_2 from (η^2-H_2)NiML to generate NiML and free

H_2, and (2) the binding of free H_2 to NiML to generate (η^2-H_2)NiML. The exchange rates were determined at each T using gNMR version 5.0 and the associated suite of programs to find the best least-squares fit of simulated spectra to the experimental spectra. VT ^{31}P NMR spectra were simulated using a two-site, non-mutual model for H_2 exchange, with the following parameters for both NiML and (η^2-H_2)NiML: chemical shifts (δ), intrinsic linewidths (W) and relative equilibrium concentrations (C). In addition to these known input parameters for the exchanging species, the exchange rate ($rate_{ex}$ in s^{-1}) was fit as a parameter in the simulations.[194, 231, 256]

Factors which could potentially contribute to the broadness of the observed ^{31}P resonances include the intrinsic broadness (ie. linewidths, W) of the exchanging species, NiML and (η^2-H_2)NiML, quadrupolar broadening, broadening from magnetic field inhomogeneity, broadening from coupling to other nuclei, and broadening from chemical exchange.[213, 231, 235, 257] In order to extract accurate exchange rates, it is critical to isolate the broadening arising from chemical exchange from that attributable to these other processes. Thus, obtaining precise values for the input parameters, δ, W, and C, is critical. Otherwise, if these parameters are not accurately known, the same NMR lineshape can be simulated with very different exchange rates, rendering the results of such simulations devoid of the desired chemical meaning.

In the case of our system, no quadrupolar nuclei are present, and no coupling was considered to affect the lineshapes, as the ^{31}P nuclei in NiML and (η^2-H_2)NiML are not coupled to any other nuclei since spectra were collected with proton- and carbon-decoupling. In order to be as precise as possible, the δ and W were measured for NiML at various T (at least seven different T over the range of 214 K to 344 K in toluene-d_8), as

both were found to vary slightly as a function of T (so it would be more appropriate to refer to them as δ(T) and W(T)). After collecting these VT ^{31}P NMR of NiML (~7.5 mM) under 1 atm Ar, the same samples were then pressurized with 1 atm H_2, and VT ^{31}P NMR spectra were again collected at the same set of T as those previously obtained for NiML (Figures A.2.10-A.2.12). By collecting spectra for samples at the exact same concentration and solution volume, in the same J. Young NMR tubes, and with the same NMR instrument, the irregular contributions of magnetic field inhomogeneity and sample shimming to the NMR lineshapes would be accounted for as much as possible, as these factors would be embedded in the measured intrinsic linewidths of NiML at each T.

While the chemical shifts and intrinsic linewidths of NiML in the absence of chemical exchange could be explicitly measured experimentally (*vide supra*), a few assumptions were needed in order to estimate the chemical shifts and intrinsic linewidths of the (η^2-H_2)NiML complexes, since conditions have not been found under which it is possible to observe discrete signals for (η^2-H_2)NiML in the complete absence of chemical exchange. Thus, (OC)NiML complexes were used as model complexes to estimate how the chemical shift and intrinsic linewidth of a complex with an apically bound ligand, (L')NiML, would be affected by T. (OC)NiML was the ideal choice because CO is bound strongly enough that it is isolable and can be studied experimentally under 1 atm of Ar with no additional CO present with which to exchange. The ratio of the linewidth of (OC)NiML to NiML was found to be close to unity (1.0 for Ga, 1.027 for In), and so those factors were used to estimate the intrinsic linewidths for (η^2-H_2)NiML from the explicitly measured linewidth of NiML at a given T. For complex **1**, where no CO adduct

had been isolated, the linewidth ratio of the bound to unbound species was assumed to be 1.0, just as was measured for **2**.

The relative concentrations (C) of NiML and (η^2-H_2)NiML were set to their known values at each T, based on either the relative peak integrations (for slow exchange) or the observed ^{31}P peak position compared with the known chemical shifts of the NiML and (η^2-H_2)NiML species from the thermodynamic H_2 binding equilibrium studies (for fast exchange). From there, iteration of the concentrations was performed to obtain the best fit to the experimental spectrum, with the final C values found to be very close to the initial values in all cases, such that reproduced van't Hoff plots (using the final concentrations after iteration to plot $\ln(K_{H_2})$ vs. 1/T) gave $\Delta G°$ values that were within error of the values obtained from thermodynamic equilibrium studies in all cases. With δ, W, and C determined for both NiML and (η^2-H_2)NiML for a given T, full lineshape iteration was performed by variation of the exchange rate to obtain the best least-squares fit of the simulated spectra to the experimental spectra. The output of the simulation included the exchange rate and associated error that gave the best-fit simulation for each NiML sample (M=Al, Ga, In) at each T.

3.3.10.2 Discussion of H_2 Self-Exchange Rates Extracted from ^{31}P NMR Lineshape Simulations

Figure 3.26 shows a comparison of experimental and simulated ^{31}P NMR spectra for **1** under 1 atm H_2, along with the corresponding exchange rates and uncertainties from simulation. Similarly, H_2 self-exchange rates were also determined via the same NMR simulation protocol for complexes **2** and **3** (Figures A.2.28-A.2.29). In general, satisfactory simulations of the experimental ^{31}P NMR spectra were obtained in all cases,

and the confidence in the input parameters translates into confidence in the absolute and relative exchange rates determined for complexes **1**-**3**, which are displayed in Table 3.13.

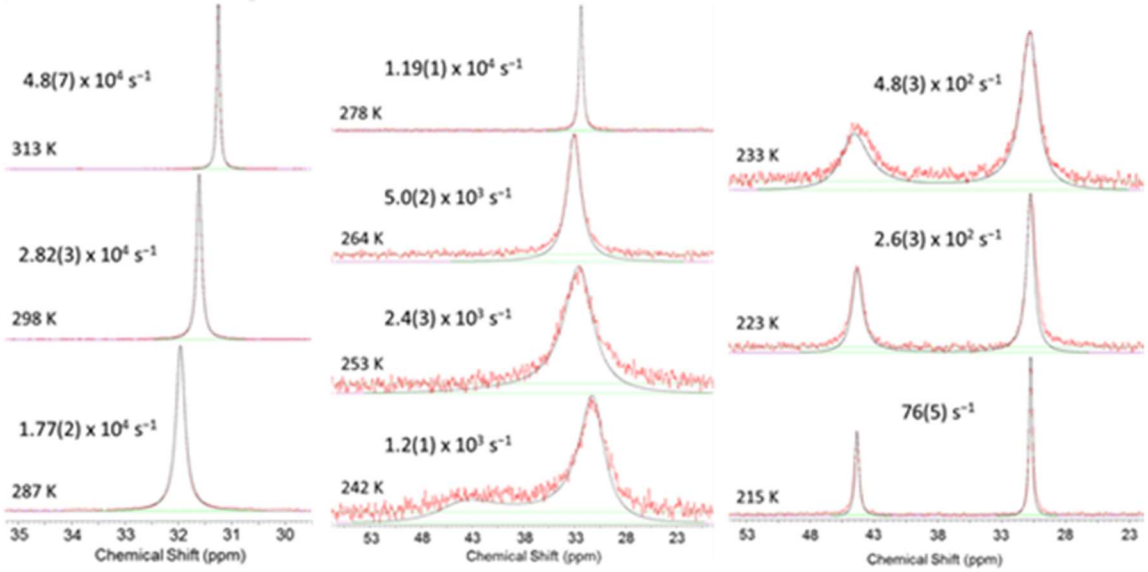

Figure 3.26. Comparison of selected simulations (black lines) and experimental VT ^{31}P NMR spectra (red lines, toluene-d_8, 162 MHz) for **1** (~7.5 mM in 0.70 mL) under 1 atm H_2 from T=215 to 313 K. The exchange rates at each T and the associated uncertainty are also displayed.

Table 3.13. H_2 self-exchange rates and activation parameters for complexes **1**-**3**.

	H_2 self-exchange[a]				
Complex	$Rate_{ex}$ (x10^4)	$Rate_{rel}$	$\Delta H^{\ddagger}_{ex}$	$\Delta S^{\ddagger}_{ex}$	$\Delta G^{\ddagger}_{ex}$
1	2.82(3)	6.4(1)	8.1(2)	−5.4(1)	9.7(2)
2	2.2(2)	4.9(5)	8.1(3)	−5.9(2)	9.8(3)
3	0.437(5)	1.0	8.8(4)	−6.0(2)	10.6(4)

Note: $\Delta H^{\ddagger}$ and $\Delta G^{\ddagger}$ values are in kcal/mol, and $\Delta S^{\ddagger}$ values are in cal/(mol·K). $Rate_{ex}$ is in s^{-1}, and $Rate_{rel}$ is the relative rate compared with that for **3**. Standard deviation in the last digit are shown in parenthesis.
[a]determined for $[Ni]_{total}$ = [NiML] + [(H_2)NiML] = 7.5 mM in toluene-d_8 at 298 K under 1 atm H_2.

Interestingly, an excellent correlation was observed between the rates of H_2 self-exchange at 298 K (Table 3.13) and the H_2 binding free energies ($\Delta G°$) from van't Hoff analyses (R^2=0.996, Figure 3.27), with more thermodynamically favorable H_2 binding equilibria exhibiting slower kinetic rates of self-exchange. A faster self-exchange rate at 298 K also was found to correlate well with a shorter DFT-calculated H−H bond distance

in the (η^2-H_2)NiML complexes (R^2=0.988, Figure 3.27), indicating that less activated H_2 ligands will undergo more facile chemical exchange with free H_2, as might be expected. Notably, simply varying the supporting metal from Al to In also dramatically decreases the relative rate of H_2 self-exchange at Ni by a factor of ~6 at 298 K (Table 3.13), in addition to tuning the favorability ($\Delta G°$) of the H_2 binding equilibria by ~5 kcal/mol (Table 3.5-3.6). Controlling the kinetics of ligand exchange can be highly desirable in catalytic processes, where ligand substitution reactions can often be rate-determining.[110, 258] Indeed, as will be examined in chapter 5, substitution of HCO_2^- by H_2 at the apical binding site of **2** was found to be the rate-determining step in catalytic CO_2 hydrogenation.[128]

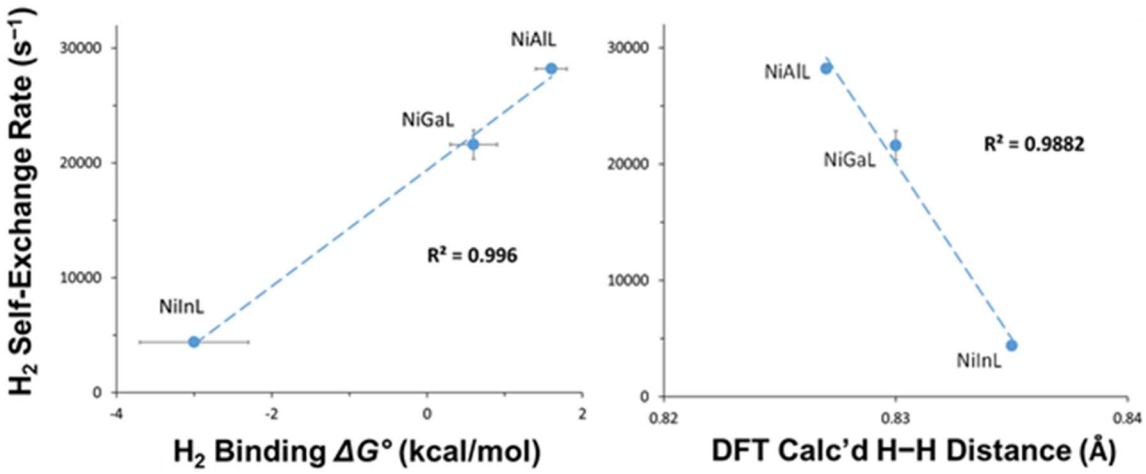

Figure 3.27. Plots of H_2 self-exchange rates at 298 K for NiML (in s^{-1}) vs. thermodynamic H_2 binding $\Delta G°$ (left) and DFT-calculated (M-06L/bs1) H−H distance in (η^2-H_2)NiML (right). Standard deviations in the exchange rates and $\Delta G°$ values are shown with error bars.

3.3.10.3 Discussion of H_2 Self-Exchange Activation Parameters

Eyring plots of ln($rate_{ex}$//T) vs. 1/T were made for complexes **1**-**3** (Figures A.2.30-A.2.32) using the exchange rates ($rate_{ex}$) obtained from best-fit lineshape simulations, and the resulting free energy barriers for H_2 self-exchange ($\Delta G^{‡}_{ex}$) are

displayed in Table 3.13.[231] It can be verified mathematically that the relative H_2 self-exchange rate ($rate_{rel}$) of 6.4 for complex **1** relative to that for complex **3** is consistent with the differences in $\Delta G^{\ddagger}_{ex}$ for the two complexes. The Eyring equation is shown as Equation 3.13, where k is the rate constant at a given T, κ is the transmission coefficient, often taken to be unity, *h* is Planck's constant, k_B is Boltzmann's constant, and R is the ideal gas constant. Taking the ratio of two rate constants, which is equivalent to the ratio of two rates in this case since [H_2] and [Ni] are identical, amounts to taking the ratio of two Eyring equations and simplifying to give Equation 3.14.[231]

$$k = \frac{\kappa k_B T}{h} e^{\frac{-\Delta G^{\ddagger}}{RT}} \qquad \text{(Eqn 3.13)}$$

$$\frac{rate_{ex_1}}{rate_{ex_3}} = \frac{k_1}{k_3} = e^{\frac{\Delta G^{\ddagger}_3 - \Delta G^{\ddagger}_1}{RT}} \qquad \text{(Eqn 3.14)}$$

Using the $\Delta G^{\ddagger}_{ex}$ values for complex **3** and complex **1**, which are 10.6(4) and 9.7(2) kcal/mol, respectively, one calculates using Equation 3.14 that the ratio of exchange rates of **1** to **3** at 298 K should be 4.4 (± 3.3), which matches within experimental error with the value of 6.4 obtained from the simulations at 298 K. This analysis serves to illustrate that a very small difference in $\Delta G^{\ddagger}$ translates into a large difference in observed rates.

The enthalpic and entropic self-exchange activation parameters, $\Delta H^{\ddagger}_{ex}$ and $\Delta S^{\ddagger}_{ex}$, were also determined via the Eyring analyses (Table 3.13). All three complexes were found to have $\Delta H^{\ddagger}_{ex}$ values of 8 to 9 kcal/mol and $\Delta S^{\ddagger}_{ex}$ values of −5 to −6 cal/(mol·K). Although the measured $\Delta S^{\ddagger}_{ex}$ values for H_2 exchange at NiML are slightly negative and most intramolecular self-exchange reactions have $\Delta S^{\ddagger}_{ex} \approx 0$, a bimolecular exchange

transition state for H_2 exchange has been discounted for two reasons. First, the relative contribution of activation entropy to the free energy barrier is minor (ie. $\Delta H^{\ddagger}_{ex} \approx \Delta G^{\ddagger}_{ex}$), whereas a bimolecular exchange reaction would be expected to give a negative $\Delta S^{\ddagger}_{ex}$ value of much larger magnitude than what is observed.[194, 231] Furthermore, such a bimolecular transition state for H_2 exchange would necessitate the close approach of (η^2-H_2)NiML and NiML, both of which possess bulky isopropyl substituents on the ligand phosphines which would likely render such a structure highly unstable for steric reasons.

3.3.10.4 Discussion of Rates and Activation Parameters for H_2 Binding and Loss

The rate constants for H_2 loss from (η^2-H_2)NiML, k_{loss}, were also extracted at each T based on the simulated exchange rates and the known relative concentrations of NiML and (η^2-H_2)NiML. The derivation of an expression for k_{loss} as a function of these variables is shown in the series of equations below. Equation 3.15 defines the exchange rate as the sum of the rates of H_2 binding and H_2 loss, with a standard state of 1 M for all species. The rates for H_2 binding and loss can be expressed in terms of their respective rate constants, k_{bind} and k_{loss}, and the concentrations of H_2, NiML, and (η^2-H_2)NiML (Equation 3.16). Because the reactions are being monitored by ^{31}P NMR spectroscopy at equilibrium, the rates of binding and loss are necessarily equivalent such that the total equilibrium concentrations of NiML and (η^2-H_2)NiML remain constant. Thus, both the rate of H_2 loss and the rate of H_2 binding are equivalent and equal to half the exchange rate, and so k_{loss} can be determined at each T based on the known exchange rate and [(η^2-H_2)NiML] (denoted as [(H_2)NiML]; Equation 3.17).

$$\text{rate}_{ex} = \text{rate}_{bind} + \text{rate}_{loss} \qquad \text{(Eqn 3.15)}$$

$$\text{rate}_{ex} = \{k_{bind} \cdot [H_2][\text{NiML}]\} + \{k_{loss} \cdot [(H_2)\text{NiML}]\} \qquad \text{(Eqn 3.16)}$$

$$k_{loss} = \frac{rate_{ex}}{2 \cdot [(H_2)NiML]} \qquad \text{(Eqn 3.17)}$$

Upon obtaining k_{loss} for complexes **1-3** at various T, another set of Eyring plots allows the free energy barriers for H_2 loss ($\Delta G^{\ddagger}_{loss}$) to be determined. A representative Eyring plot is shown for H_2 loss from **1**−H_2 in Figure 3.28, with the analogous plots for H_2 loss from **2**−H_2 and **3**−H_2 shown in the Appendix (Figures A.2.34-A.2.35). Enthalpic and entropic contributions to the free energy barriers were also determined (Table 3.14).

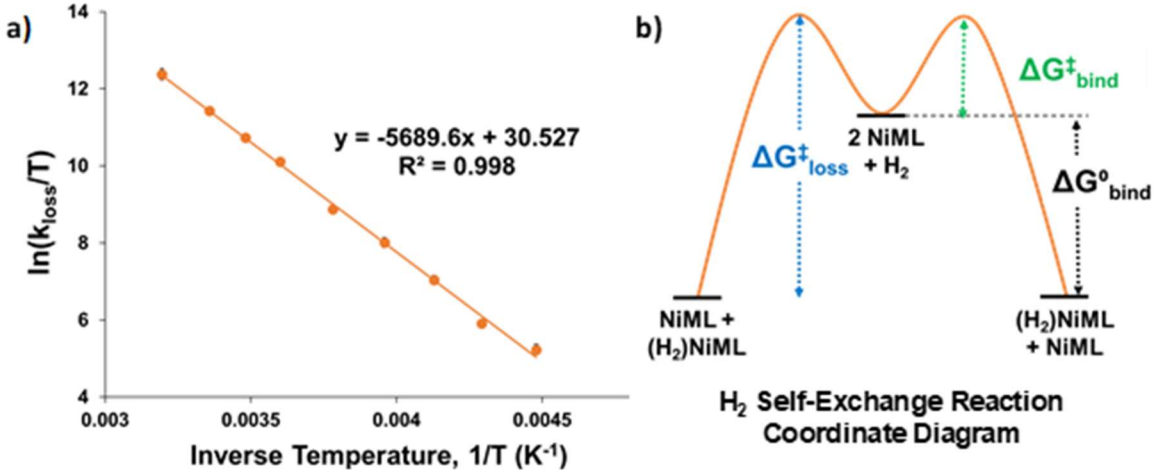

Figure 3.28. (a) Eyring plot of ln(k_{loss}/T) vs. 1/T for **1**−H_2, where k_{loss} is the rate constant for H_2 loss extracted from the exchange rate data. (b) Reaction coordinate diagram for H_2 self-exchange at NiML via unimolecular H_2 loss, which shows relationship between thermodynamic ($\Delta G°$) and kinetic ($\Delta G^{\ddagger}$) parameters for H_2 binding and loss (see Table 3.14 for specific values).

Table 3.14. Rates and activation parameters for H_2 loss from (η^2-H_2)NiML complexes.

	H_2 loss[a]				
Complex	k_{loss} (x10^6)[b]	$k_{loss,rel}$	$\Delta H^{\ddagger}_{loss}$	$\Delta S^{\ddagger}_{loss}$	$\Delta G^{\ddagger}_{loss}$
1	670(30)	2200(130)	11.3(2)	6.7(1)	9.3(2)
2	3.2(2)	10.7(8)	10.1(4)	2.8(1)	9.3(4)
3	0.30(1)	1.0	9.3(4)	−0.9(1)	9.6(4)

Note: $\Delta H^{\ddagger}$ and $\Delta G^{\ddagger}$ values are in kcal/mol, and $\Delta S^{\ddagger}$ values are in cal/(mol·K). k_{loss} values are in s^{-1} and $k_{loss,rel}$ is the relative rate constant compared with that for **3**. Standard deviation in the last digit is shown in parenthesis. [a]Measured under 1 atm H_2 in toluene-d_8. $\Delta G^{\ddagger}_{loss} = \Delta G^{\ddagger}_{ex}$ for an exchange mechanism characterized by unimolecular H_2 loss, and 1 M of all species (see Figure 3.28b). [b]at 298 K.

The activation parameters for H_2 loss from (η^2-H_2)NiML, determined via Eyring analyses, are compiled in Table 3.14.[194, 231, 257] The free energy barriers for H_2 loss ($\Delta G^{\ddagger}_{loss}$) were found to be approximately 9 to 10 kcal/mol, with $\Delta H^{\ddagger}_{loss}$ values of 9 to 11 kcal/mol and $\Delta S^{\ddagger}_{loss}$ values of −1 to +7 cal/(mol·K). The $\Delta H^{\ddagger}_{loss}$ values for H_2 loss from (η^2-H_2)NiML are comparable to those found in the literature for $[Ru(H_2)H_3(PPh_3)_3]^+$ (8.8 ± 0.1), $Cr(H_2)(CO)_3(PCy_3)_2$ (12.1 ± 1.0), and $Ir(H_2)(H)_2X(P^tBu_2Me)_2$ (9.4 to 10.2 for X=Cl, Br, I), and significantly lower than those reported for $W(H_2)(CO)_3(PCy_3)_2$ (16.9 ± 2.2) and $Ru(H_2)(H)_2(PPh_3)_3$ (17.9 ± 0.2), with all values given in kcal/mol.[194, 203-204, 206, 259] Literature entropy of activation ($\Delta S^{\ddagger}$) values vary widely, ranging from −12 to +10 cal/(mol·K).[194, 203-204, 260]

Comparing $\Delta S^{\ddagger}$ for H_2 loss amongst the trio of (η^2-H_2)NiML complexes (Table 3.14), the $\Delta S^{\ddagger}_{loss}$ values become less positive as the supporting metal is varied down group 13 (Al > Ga > In). For **1**−H_2, this is consistent with a "later" transition state for H_2 loss that resembles **1** and free H_2 to a greater extent than for the other complexes, as opposed to an earlier transition state which more closely resembles **1**−H_2. Likewise, the relative $\Delta S^{\ddagger}_{loss}$ values support a relatively "earlier" transition state that more closely resembles **3**−H_2 (than **3** and free H_2) for M=In, with M=Ga falling in between these two extremes. Thus, for more favorable binding equilibria in which (η^2-H_2)NiML is more stable relative to NiML, the transition state geometry is likely closer to that of (η^2-H_2)NiML, as reflected in the less positive $\Delta S^{\ddagger}_{loss}$ value which indicates a lesser degree of freedom of motion for H_2 in the transition state for H_2 loss. To put it in terms of bond-making and bond-breaking, the trend of decreasing $\Delta H^{\ddagger}_{loss}$ and $\Delta S^{\ddagger}_{loss}$ values upon varying the supporting metal down group 13 (Al > Ga > In) is consistent with the greatest

degree of Ni−H_2 bond breaking, upon progressing from (η^2-H_2)NiML to the transition state for H_2 loss, for **1**−H_2, followed by that for **2**−H_2.[110, 231] Overall, the barriers to H_2 loss are similar for the trio of H_2 adducts, with the $\Delta G^{\ddagger}_{loss}$ values all within experimental error of one another (Table 3.14). This may seem odd at first, considering the very different binding favorabilities of the NiML complexes; however, this can be understood by looking at the reaction coordinate diagrams shown in Figures 3.28b and 3.29, as explained in the following paragraphs.

Typically, a self-exchange reaction coordinate diagram is considered to have a transition state connecting the iso-energetic reactants and products, with no discrete intermediates invoked for a self-exchange reaction that proceeds via an unknown reaction mechanism (Figure A.2.33). In this case, self-exchange is proposed to proceed via unimolecular H_2 loss from (η^2-H_2)NiML based on the $\Delta S^{\ddagger}_{ex}$ values and the considerable steric demands of a bimolecular exchange mechanism. As such, a more specific reaction coordinate diagram for self-exchange can be drawn, where H_2 loss from (η^2-H_2)NiML gives two molecules of NiML, followed by subsequent H_2 binding to the other NiML complex to complete the self-exchange reaction (Figure 3.28b). For this two-step reaction coordinate diagram for self-exchange via unimolecular H_2 loss, the free energy barrier to self-exchange would be equivalent to the free energy barrier to H_2 loss from (η^2-H_2)NiML (ie. $\Delta G^{\ddagger}_{ex} = \Delta G^{\ddagger}_{loss}$). Indeed, the $\Delta G^{\ddagger}_{ex}$ and $\Delta G^{\ddagger}_{loss}$ values for each complex are all nearly within experimental error of one another (Tables 3.13-3.14). The slightly lower $\Delta G^{\ddagger}_{loss}$ barriers can be accounted for by the fact that the standard state has been defined as 1 M for all species in the determination of $\Delta G^{\ddagger}_{loss}$, as is typical convention in the literature, as opposed to being defined to be the specific conditions studied in the case of

$\Delta G^{\ddagger}_{ex}$. Therefore, the matching $\Delta G^{\ddagger}_{ex}$ and $\Delta G^{\ddagger}_{loss}$ values are consistent with self-exchange occurring via unimolecular H_2 loss, after accounting for the standard state and considering the experimental standard deviations.

Looking at the H_2 self-exchange diagram in Figure 3.28b, since the reactants and products are both "NiML + (η^2-H_2)NiML" and the intermediate is "2 NiML", the net reaction coordinate from the intermediate to either the reactants or products simplifies to that for the binding of H_2 to NiML to form (η^2-H_2)NiML, which is shown Figure 3.29 in a more typical reaction coordinate diagram.

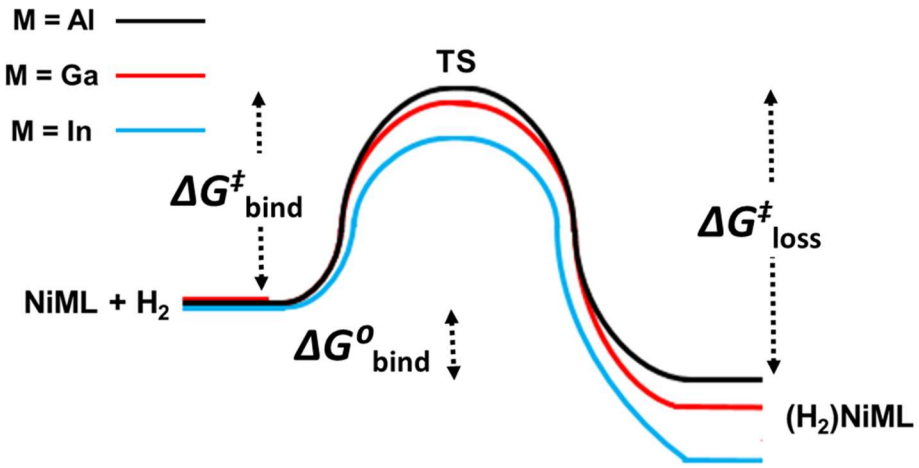

Figure 3.29. Reaction coordinate diagrams for H_2 binding to NiML, with $\Delta G°$ and $\Delta G^{\ddagger}$ values labeled for **1** (M=Al). Note that although the diagram is not rigorously to scale, it correctly shows the relative trends in $\Delta G^{\ddagger}_{bind}$ for H_2 binding (Al > Ga > In) and $\Delta G°$ from the equilibrium studies (Al > Ga > In), while showing similar $\Delta G^{\ddagger}_{loss}$ for H_2 loss for all complexes.

Comparison of $\Delta G^{\ddagger}_{loss}$ values for H_2 loss and $\Delta G°$ values for H_2 binding allows for the tabulation of the free energy barriers ($\Delta G^{\ddagger}_{bind}$) for H_2 binding by subtraction, which gave values of 7.4(2), 6.4(5), and 3.1(8) kcal/mol for **1**, **2**, and **3**, respectively (Figure 3.29, Table 3.15).[194, 203, 231] An excellent correlation between the free energies of activation ($\Delta G^{\ddagger}_{bind}$) and the thermodynamic free energies ($\Delta G°$) for H_2 binding was

observed, with more favorable H_2 binding equilibria (In > Ga > Al) exhibiting lower free energy barriers for H_2 binding (R^2=0.999, Figure 3.30). This relationship of more thermodynamically favorable processes exhibiting faster kinetics through lower free energy barriers is perhaps somewhat intuitive, but need not necessarily be the case, and is not often rigorously measured experimentally. Furthermore, such behavior has been reported to hold true in many different electron-transfer and proton-transfer reactions, among others, and can be taken to follow from Marcus Theory.[261-263] The slope of the plot is approximately unity, at 0.93 (± 0.02), indicating that a more favorable binding equilibrium by 1 kcal/mol is correlated with approximately a 1 kcal/mol decrease in the free energy barrier for H_2 binding (Figure 3.30).

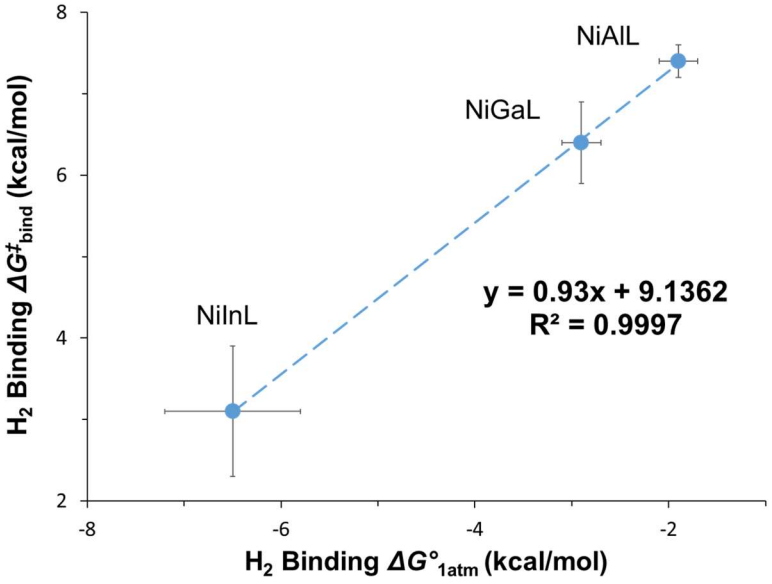

Figure 3.30. Plot of free energy barrier for H_2 binding ($\Delta G^{\ddagger}_{bind}$ in kcal/mol) vs. thermodynamic free energy for H_2 binding (ΔG°_{1M} in kcal/mol), with the standard deviation in all values shown by error bars.

All the tabulated $\Delta G^{\ddagger}$ and ΔG° values for H_2 binding and loss are summarized in Table 3.15, and shown visually in Figures 3.28-3.29. The similar $\Delta G^{\ddagger}_{loss}$ values for H_2 loss between the three (η^2-H_2)NiML complexes can be seen to result from the very

different, and linearly correlated, $\Delta G^{\ddagger}_{bind}$ and $\Delta G°$ values. That is, differences in the favorability of H_2 binding are fully reflected in the different barriers to binding, resulting in $\Delta G^{\ddagger}_{loss}$ values that are necessarily similar (Figure 3.29). One final thing to note is that all the binding free energies, $\Delta G°$, are depicted as downhill in Figure 3.29, meaning that all H_2 binding equilibria are exergonic and favor the bound species, (η^2-H_2)NiML. This is because the standard states for $\Delta G^{\ddagger}_{bind}$, $\Delta G^{\ddagger}_{loss}$, and $\Delta G°$ have all been defined as 1 M of all species, including H_2, to match literature convention for activation parameters, whereas previously 1 atm H_2 had been taken to be the standard state to tabulate the thermodynamic values in Table 3.5. As previously mentioned, defining the standard state as 1 M H_2 rather than 1 atm H_2 has the effect of making $\Delta G°$ more favorable by ~3.5 kcal/mol, resulting in even the weak binding of H_2 to complex **1** becoming exergonic under standard state conditions (Figure 3.29, Table 3.15).

Table 3.15. Summary of thermodynamic and kinetic parameters for H_2 binding and loss.

	Thermodynamics		Kinetics[a]	
Complex	$\Delta G°_{1atm}$	$\Delta G°_{1M}$	$\Delta G^{\ddagger}_{loss}$	$\Delta G^{\ddagger}_{bind}$
1	+1.6(2)	−1.9(2)	9.3(2)	7.4(3)
2	+0.6(2)	−2.9(2)	9.3(4)	6.4(5)
3	−3.0(7)[b]	−6.5(7)[b]	9.6(4)	3.1(8)[b]

Note: $\Delta G°$ and $\Delta G^{\ddagger}$ values are in kcal/mol. See Table A.2.7 for a full table of thermodynamic parameters for the H_2 binding equilibria with a 1 M H_2 standard state. [a]1 M H_2 standard state. $\Delta G^{\ddagger}_{bind}$ was tabulated using the known $\Delta G°_{bind}$ and $\Delta G^{\ddagger}_{loss}$ values and the relationship shown visually in Figure 3.28b. [b]Estimated values, with $\Delta G^{\ddagger}_{bind}$ based on estimated value for $\Delta G°_{bind}$.

3.3.10.5 Comparison of H_2 Binding and Loss Rates to Those for Kubas's W Complex

Kinetic rates of H_2 binding and loss have seldom been reported despite their importance in many catalytic processes; the original Kubas complex, W(η^2-H_2)$(CO)_3(PCy_3)_2$, has been a notable exception in this regard. Hoff and co-workers indirectly measured the second-order rate constant for H_2 addition (k_{bind}) to be 2.2(3) x

$10^6\ M^{-1}s^{-1}$ (at 298 K) via stopped-flow studies of ligand exchange between H_2 and pyridine.[204, 206] Later, Fujita and co-workers revisited this system and directly measured k_{bind} via time-resolved step-scan FTIR and UV-vis spectroscopies, obtaining a value of 2.0(1) x $10^6\ M^{-1}s^{-1}$ which agrees well with Hoff's original value.[201] Our measured rate constants indicate that H_2 binding to NiML occurs much more rapidly than for the $W(CO)_3(PCy_3)_2$, with second-order rate constants of 6.7(3) x $10^8\ M^{-1}s^{-1}$, 8.7(7) x 10^8 $M^{-1}s^{-1}$, and ~5.1(2) x $10^9\ M^{-1}s^{-1}$ obtained for H_2 binding to **1**, **2**, and **3**, respectively, at 298 K. H_2 loss is also more rapid for (η^2-H_2)NiML, with k_{loss} values at 298 K found to be 2.8(2) x $10^7\ s^{-1}$, 3.2(2) x $10^6\ s^{-1}$, and ~3.0(1) x $10^5\ s^{-1}$ for **1**, **2**, and **3**, respectively, compared with 469 s^{-1} for W(η^2-H_2)$(CO)_3(PCy_3)_2$.[45, 205-206] The faster rates of H_2 loss from (η^2-H_2)NiML compared with W(η^2-H_2)$(CO)_3(PCy_3)_2$ are consistent with the significantly greater enthalpic barrier to H_2 loss reported for the latter (16.9 vs. 9 to 11 kcal/mol for (η^2-H_2)NiML).[45, 203-204]

That the relative rates of H_2 addition and loss are significantly greater for NiML than for $W(CO)_3(PCy_3)_2$ can be rationalized by the fact that H_2 is much more activated in the Kubas complex, and thus is less readily able to dissociate as free H_2. The dramatic contrast in the extent of H_2 activation between the two systems is best appreciated by noting that an equilibrium between the H_2 adduct and a dihydride species formed via oxidative addition is readily observable for the Kubas system (with K ~0.25 at 298 K).[45] On the other hand, a dihydride species has not been observed for (η^2-H_2)NiML, as will be discussed further in the next chapter on olefin hydrogenation catalysis.[30, 97] The inferred instability of a Ni(II) dihydride species formed via oxidative H–H cleavage is consistent with the relatively minor extent of Ni → H_2 π-back-donation predicted by ETS-NOCV

calculations (*vide supra*). The lack of accessibility of a dihydride species and the relatively short H−H distances likely contribute to the fast rates of H_2 loss from (η^2-H_2)NiML relative to that for Kubas's W(η^2-H_2)$(CO)_3(PCy_3)_2$ complex, as H_2 loss was measured to be ~13 times slower from the dihydride of the Kubas complex as compared to from the H_2 adduct.[45, 204] It should also be noted that H_2 is displacing an agostic interaction in the Kubas system, which may also slow the rates of H_2 binding and loss relative to those for NiML, which has a vacant coordination site at which H_2 binds.[45, 206]

3.3.11 How Does the Supporting Group 13 Metal Poise Ni for Uncommon Binding of Small Molecules: Examining the Electronic Structure of H_2, N_2, and CO adducts of NiML

In light of the rarity of H_2 and N_2 binding to Ni, especially to formally Ni(0) d^{10} metal centers, we sought to understand the specific electronic perturbations that the supporting group 13 metal ion has on Ni in order to poise NiML for small molecule binding. UV-vis spectroscopy in conjunction with time-dependent density functional theory (TD-DFT) calculations seemed well suited to investigate the electronic structure of (L')NiML complexes (L'= H_2, N_2, CO) to answer these questions. Upon the addition of H_2 to **3**, a dramatic color change is observable from red-purple to yellow-brown; similar color changes are also observed for H_2 binding to **1** (brown to yellow-brown) and **2** (red to orange-yellow), N_2 binding to **3** (red-purple to red), and CO binding to **2** and **3** (red or red-purple to pale yellow). These vibrant color changes manifest in significant changes in the UV/vis spectra of NiML upon binding small molecules, as displayed for NiInL (**3**) and its H_2, N_2, and CO adducts in Figure 3.31.

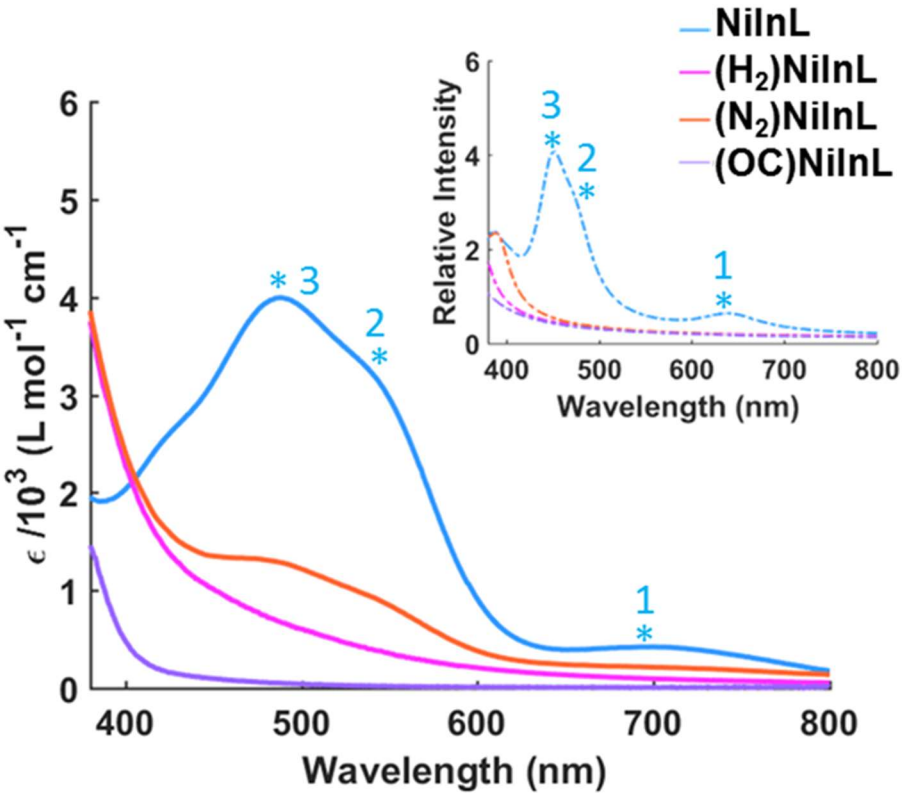

Figure 3.31. UV-vis spectra of **3** (blue), **3**−H_2 (pink), **3**−N_2 (orange), and **3**−CO (purple), with the assignments of the peaks made as follows: (1) d_{xy}/d_x^2-$_y^2$ to LUMO, (2) d_{xz}/d_{yz} to LUMO, and (3) ligand + d_z^2 to LUMO. Spectra for **3**−H_2 and **3**−N_2 were obtained under 1 atm of H_2 and N_2 gas, respectively, whereas **3** and **3**−CO were isolated and their UV-vis spectra were obtained under an inert atmosphere (Ar). The inset shows the corresponding simulated spectra from TD-DFT calculations. Note that this figure is courtesy of Dr. Jing Xie.

The most striking difference between the UV-vis spectrum of **3** and those of **3**−H_2, **3**−N_2, and **3**−CO is that the adduct complexes show no significant transitions in the visible region from 400 – 700 nm, which is also predicted by TD-DFT. It should be noted that small peaks coincident with those of **3** are observed in the UV-vis spectrum of **3**−N_2 (Figure 3.31). This is attributable to the weaker binding of N_2 relative to H_2 and CO, such that some of complex **3** is present in solution at equilibrium and gives rise to these peaks. Similar behavior due to an even weaker binding equilibrium was observed for UV-vis spectra of **2**−H_2, where peaks for **2** are visible and only slightly diminished in intensity.

Ideally, UV-vis spectra could be obtained under elevated pressures of N_2 and H_2 gas for complexes which exhibit weak binding, as this would unambiguously show the lack of transitions in the visible region for these weakly bound adduct complexes. In general, the lack of transitions in the visible region for adducts of complex **3** is predicted to hold true by TD-DFT for all other adducts of H_2, N_2, and CO for complexes **1** and **2** as well, and calculated UV-vis spectra and transition assignments for these species are shown in the Appendix (Figure A.2.34, Tables A.2.12-A.2.14).

In a qualitative sense, this shift to higher energy electronic transitions upon the binding of small molecules can be easily understood: once the low-lying, Lewis-acid stabilized LUMO of NiML interacts with small molecule σ-donors, the unoccupied orbitals of the resulting adduct to which electrons can be excited are of much higher energy relative to the Ni 3*d* manifold. The presence of such a low-lying LUMO in the NiML complexes is not common for a formally d^{10} transition metal center, and this anomaly has been attributed to stabilizing interactions between the supporting metal (M p_z/s) and Ni ($4d_z^2/4p_z/4s$), as discussed in the previous chapter (section 2.2.9).

To understand on a more concrete level how small molecule binding perturbs the electronic structure to give significantly blue-shifted transition energies compared to those for naked NiML complexes, the binding of H_2 to **2** will be considered as a representative example. As established, H_2 σ-donation is key to the stabilization of **2**−H_2, and both the LUMO of **2** (Ni $4d_z^2$, $4p_z/s$ stabilized by Ga $4p_z/5s$) and the filled Ni $3d_z^2$ orbital have the appropriate symmetry to interact with the incoming H_2 σ-bond. The result is a similar LUMO for **2**−H_2 to that for **2**, with additional contributions from mixing with H 1*s* orbitals. This orbital has been termed as the "unoccupied mixing

orbital" since it is not the LUMO for all adducts; for example, it is the LUMO+3 for **1**−H_2. Similar unoccupied mixing orbitals orbitals are observed for **2**−N_2 and **2**−CO, with the additional contributions in those cases from N (*p*) orbitals and C (*s*,*p*) orbitals, respectively.

Notably, the lowest energy transition predicted for all adducts of **2** and **3** is from Ni $3d_{xy/}d_{x^2-y^2}$ + P to the unoccupied mixing orbital, reminiscent of the corresponding Ni $3d_{xy/}d_{x^2-y^2}$ to LUMO transition in the naked NiML complexes. This transition is predicted at 378, 396, and 346 nm for **2**−H_2, **2**−N_2, and **2**−CO, respectively. Likewise, the respective transitions are 375, 391, 337 nm for In, and 353, 372, and 307 nm for Al. All of these transitions are of considerably higher energy than the lowest energy transitions in the corresponding naked NiML species (573 to 650 nm; Table 2.7). This blue shift of the electronic transitions upon binding small molecules is shown visually in the molecular orbital diagram in Figure 3.32 for (η^2-H_2)NiML.

In short, the interaction of the H−H σ orbital with the LUMO of NiML gives rise to the unoccupied mixing orbital of (η^2-H_2)NiML, which ends up at much higher energy relative to the Ni $3d_{xy/}d_{x^2-y^2}$ orbitals than the original LUMO in NiML. Looking at the diagram in Figure 3.32, the H−H σ orbital and the Ni $3d_{z^2}$ orbital also have the appropriate symmetry to mix, although both orbitals are occupied. TD-DFT calculations suggest that this minor interaction slightly destabilizes the Ni $3d_{z^2}$ orbital, which, in conjunction with slight stabilization of the Ni $3d_{xz/}d_{yz}$ orbitals due to π-back-bonding (Ni $d_\pi \rightarrow H_2$ σ*), results in the switching of the relative energies of the Ni $3d_{xz/}d_{yz}$ and $3d_{z^2}$ orbitals relative to their respective energies in the NiML complexes (Figure 3.32). Additionally, it should be noted that the MO diagram in Figure 3.32 depends heavily on

the relative energies of the H−H σ orbital with respect to the LUMO and Ni $3d_z^2$ orbital, with these relative energies qualitatively placed in Figure 3.32 in accordance with TD-DFT calculations and intuition.

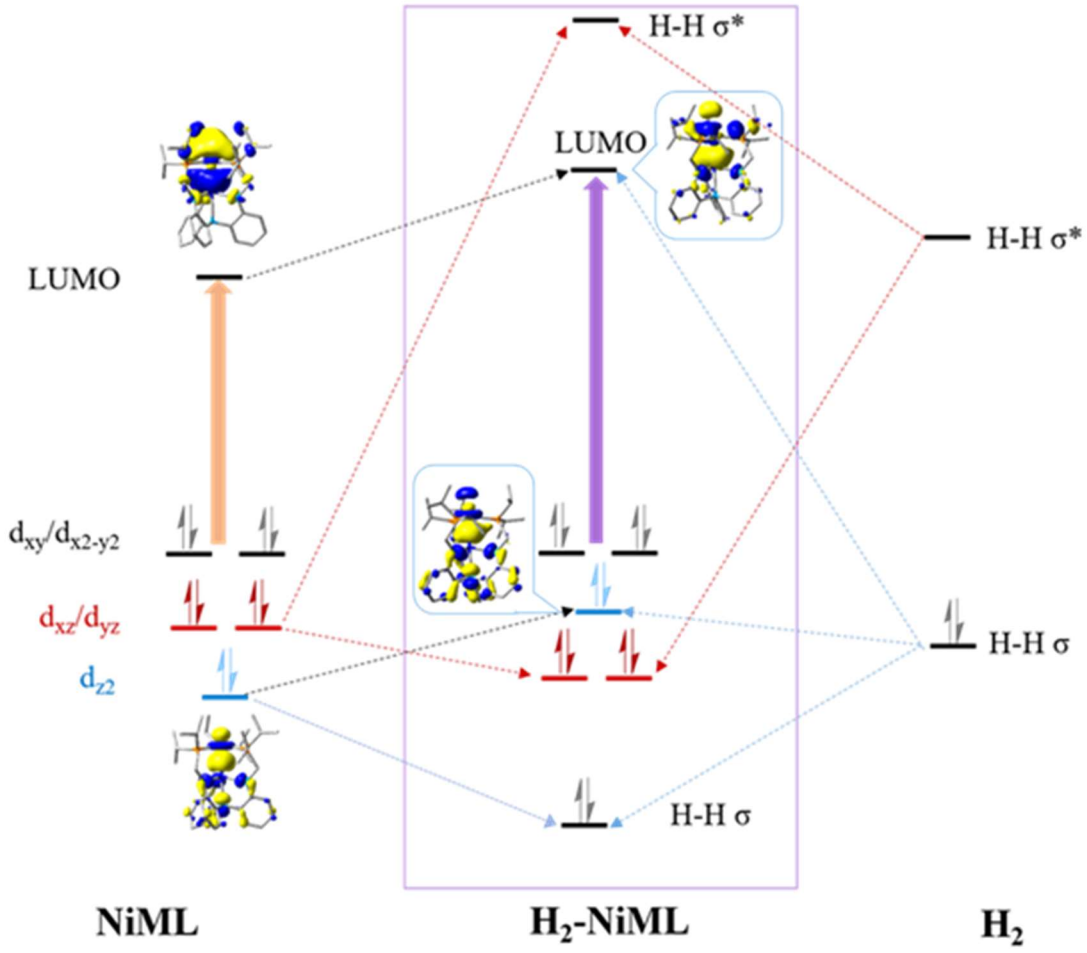

Figure 3.32. A simplified molecular orbital diagram of (η^2-H_2)NiML showing the mixing of the molecular orbitals of H_2 and NiML, with select orbitals from DFT calculations shown. Note that the energy levels are not drawn to scale. This figure is courtesy of Dr. Jing Xie.

One last important trend to note is that reasonably good correlations are observed between the experimental HOMO-LUMO energy gaps for **1**, **2**, and **3** and their respective thermodynamic free energies ($\Delta G°$) for N_2 (R^2=0.981) and H_2 (R^2=0.946) binding (Figure 3.33). In other words, the smaller the energy gap between the HOMO (Ni $3d_{xy}/d_{x^2-y^2}$

orbitals) and LUMO in the naked NiML complex, and presumably the more energetically accessible the LUMO will be, the more thermodynamically favorable it will be to bind H_2 and N_2.

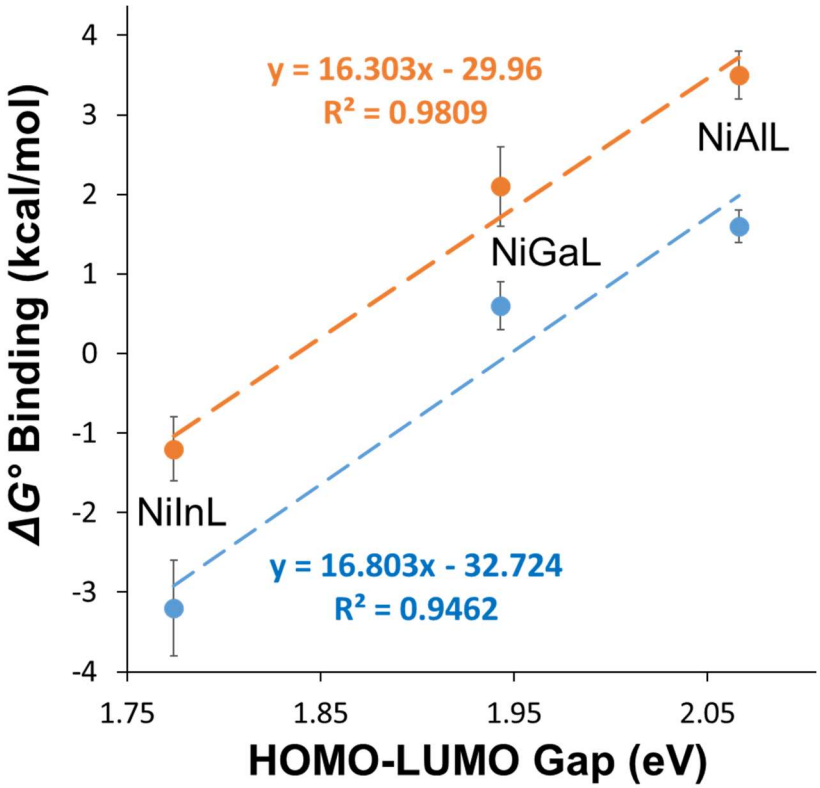

Figure 3.33. Plot of free energy ($\Delta G°$) of H_2 (top, orange) and N_2 binding (bottom, blue) to NiML vs. HOMO-LUMO energy gap for NiML complexes, as measured via experimental UV-vis studies. The slopes are not far off the conversion factor between kcal/mol and eV (23.06 kcal/mol = 1 eV).

Since the HOMO-LUMO gap obviously depends on the energies of both the HOMO and the LUMO, it is, at best, an indirect measure of the relative energetic accessibility of the LUMO. TD-DFT calculations also predict destabilization of the HOMO upon varying the supporting metal down group 13, as discussed in the previous chapter, which likely accounts for a portion of the decreasing HOMO-LUMO gap. However, because the binding energies correlate so well with the HOMO-LUMO gaps, it is hypothesized that the stabilization of the LUMO upon varying the supporting metal

down group 13 is also significant to the decreasing HOMO-LUMO gaps. Alternatively, a large HOMO-LUMO gap for a complex typically reflects greater stability, and so perhaps it should not be assumed that the energy of the LUMO is relevant to small molecule binding. However, in light of TD-DFT and ETS-NOCV calculations, this correlation is interpreted as indirect evidence that the energy of the LUMO is important to small molecule binding propensity, as opposed to the alternative that small molecule binding occurs entirely via interaction with a different orbital or set of orbitals. As discussed in section 2.2.9, the energetic accessibility of the LUMO, a feature that is unique to the electronic structure of NiML complexes compared with $NiLH_3$ and allows for the reactivity of the former with small molecule substrates, is directly tied to the strength of the supporting metal interaction with Ni.

One caveat to note in considering the molecular orbital rationale for small molecule binding is that the LUMO of the NiML complexes have contributions from Ni $4p_z$, $4s$, and $4d$ orbitals, along with significant M p_z/s and P p orbital contributions. Thus, TD-DFT calculations show a more complicated picture of small molecule binding than that predicted using more localized methods like ETS-NOCV methods, which predicts that the Ni $4p_z$ orbital is the primary vacant atomic orbital interacting with the H−H σ orbital in the binding of H_2. Overall, all computational methods and experimental evidence concur that this unusually low-lying, vacant orbital is present for these formally d^{10} metal complexes as a result of Lewis-acidic stabilization provided by the supporting metal, which allows for the uncommon and exciting small molecule reactivity for the Ni complexes that has been presented in this chapter.

3.4 Conclusions

In this chapter, the reactivity of the series of NiML complexes with small molecules, including CO, H_2, N_2, C_2H_4, and CO_2, has been described. In targeting base metal catalysts (Mn, Fe, Co, Ni) for a variety of processes, binding is an important first step for activating small molecules like H_2 to allow for further functionalization of substrates. The binding and activation of H_2 to give reactive metal-dihydrogen and metal-hydride species has proven to be a particularly difficult hurdle for Ni complexes to overcome, and has contributed to the dearth of homogeneous Ni catalysts for processes like hydrogenation, isomerization, proton reduction, and H_2 oxidation. The employment of pendant Lewis basic functionalities has been shown to be an excellent strategy to circumvent the inherent limitations of Ni in H_2 activation, as has the incorporation of direct dative interactions to Lewis acidic borane moieties.[44, 85, 87, 117, 119]

Excitingly, direct dative bonding between heavier supporting group 13 metals and Ni was found to promote the binding of H_2 to NiML to give a rare series of isostructural dihydrogen complexes, (η^2-H_2)NiML, which were characterized by J_{HD} and T_1(min) NMR studies.[97] In contrast, no H_2 binding was observed for $NiLH_3$, a similarly ligated mononuclear Ni center, illustrating the capability of the supporting metal to optimize the properties of Ni for desirable reactivity.[97] In particular, larger group 13 supporting metals were found to induce more favorable thermodynamic binding of both H_2 and N_2 to Ni, with H_2 binding found to be about ~2 kcal/mol more favorable than N_2 in all cases. A drastic tuning effect of the supporting metal on binding favorability at Ni was observed, with $\Delta G°$ values found to span ~5 kcal and essentially cover the entire range of reported values for H_2 binding to any transition metal. Binding favorability is proposed to be

dictated by both the electron-deficiency of Ni and the reorganization energy required to position Ni in the required pseudo-tetrahedral geometry for apical substrate binding. Notably, the size of the supporting M(III) ion correlates best with $\Delta G°$ values for binding, which is the result of larger supporting metals rendering Ni more electron-deficient and forcing Ni to be positioned further above the P_3-plane in the precursor NiML complexes. The better correlation of M(III) size compared with Ni(I/0) redox potential supports the notion that steric effects play a large role in dictating the binding favorability for NiML complexes, although M(III) size does capture the electronic effects to some extent and correlates reasonably well with the N(I/0) redox potentials.

Experimental and theoretical studies support the notion that σ-donation from H_2 to Ni is the predominant interaction which dictates H_2 binding and the extent of H−H activation. ETS-NOCV and TD-DFT calculations indicate that σ-donation occurs via interaction of the H−H σ-bond with a Ni-based LUMO, which has Ni 4p_z character along with contributions from the supporting metal (M p_z/s) and P (p) orbitals. The correlation of the HOMO-LUMO energy gap with the favorability of binding, in conjunction with the computationally predicted binding interactions, suggests that the energy of the LUMO is important for accepting σ-donation from H_2 and N_2. Furthermore, the linear correlation of the HOMO-LUMO gap with the Ni−M r value, discussed in chapter 2, suggests that the LUMO energy is directly tied to the strength of the Ni→M interaction. Thus, complementary σ-interactions are proposed, where electron withdrawal via the σ-interaction between the Ni 3d_z^2 and M np_z/(n+1)s orbitals induces increased σ-donation from the H_2 σ-bond to the Ni-based LUMO.[30, 97] The reinforcement of strong H_2→Ni σ-bonding by the *trans* group 13 σ-acceptor metalloligand (Ni→M) has been termed an

inverse trans influence, and contrasts the typical *trans* influence of strong σ-donors, which weaken the metal-ligand bonds *trans* to them.[45, 167]

In addition to understanding why NiML complexes bind H_2 favorably, the kinetics of H_2 self-exchange, binding, and loss were studied via ^{31}P NMR lineshape studies. The dramatic differences in thermodynamic binding free energies manifests in the self-exchange rates decreasing by a factor of ~6 at 298 K upon the substitution of Al for In. Interestingly, the kinetic free energy barrier to H_2 binding ($\Delta G^{\ddagger}_{bind}$) was found to be linearly correlated to the thermodynamic $\Delta G°$ values, with more favorable H_2 binding equilibria (In > Ga > Al) found to have smaller barriers to binding. Rates for H_2 binding and loss have seldom been measured, and those for NiML complexes were found to be significantly faster than those reported for Kubas's W complex, likely due to both the lesser degree of H−H activation and the lack of a ligand that must be displaced in the case of NiML complexes.[45, 201, 203-204, 206] The slow kinetic loss of H_2 from **3**−H_2 and the strong binding of H_2 to **3** allowed for solid-state characterization of **3**−H_2 via x-ray and neutron diffraction studies, which confirmed the formulation of a side-on bound H_2 ligand, as assigned by NMR spectroscopy.[97] Notably, the neutron structure for **3**−H_2 is the first for a M(η^2-H_2) complex of Ni or any d^{10} metal.[45, 97, 167] The thermodynamic and kinetic binding studies presented are also the first of their kind for Ni(η^2-H_2) and Ni(N_2) complexes, and represent substantial additions to the very limited amount of experimental data on the binding of H_2 and N_2 to first-row metal complexes.

Overall, a thorough understanding of the reactivity of small molecules with NiML complexes has been achieved and presented in this chapter. With an eye toward potential catalytic reactivity, the thermodynamics and kinetics of H_2 binding equilibria with NiML

complexes, as well as the degree of H−H activation in the resulting (η^2-H_2)NiML complexes, have been examined and rigorously quantified. The remainder of this thesis will focus on exploring the propensity of the bound and activated H_2 moiety of the (η^2-H_2)NiML complexes to be transferred to substrate, so as to affect catalytic hydrogenation reactions. The effect of the supporting metal on the binding and activation of H_2 at Ni, as discussed in this chapter, will be seen to have important implications on the activity and selectivity with which NiML complexes mediate the catalytic hydrogenation of both olefins (chapter 4) and CO_2 (chapter 5).

3.5 Experimental Section

3.5.1 Synthetic Considerations

Unless otherwise stated, all manipulations were performed under an Ar or N_2 atmosphere inside a glovebox or using standard Schlenk techniques. Standard solvents were deoxygenated by sparging with N_2 and dried by passing through activated alumina columns of a SG Water solvent purification system. Deuterated solvents and HD gas were purchased from Cambridge Isotope Laboratories, Inc. Deuterated solvents were degassed via freeze-pump-thaw cycles, and either stirred with NaK and distilled, or stored over activated 4 Å molecular sieves. H_2, 10% H_2/90% Ar, N_2, CO, CO_2, and C_2H_4 gases were purchased from Matheson. CO_2 gas was passed through an Agilent Oxygen Moisture Trap (Model #OT-2-SS) drying column to minimize residual oxygen and moisture in the gas stream. Paraformaldehyde was purchased from Aldrich and used as received. All other reagents were purchased from commercial vendors and used without purification unless otherwise noted. The neutral ligand ($N(o\text{-}(NHCH_2P^iPr_2)C_6H_4)_3$ (abbreviated as H_3L), NiAlL (**1**), NiGaL (**2**), NiInL (**3**), (N_2)NiInL (**3**−N_2), and $NiLH_3$ (**4**)

were synthesized according to literature procedure (also described in section 2.2.1 and 2.4).[78, 80, 97] Elemental analyses were performed by Robertson Microlit Laboratories (Ledgewood, NJ).

*Synthesis of (η^2-H_2)NiInL (**3**−H_2).* A solution of **3**−N_2 (0.015 g, 0.017 mmol) in THF (c. 0.7 mL) was added to a J. Young tube. Freeze-pump-thaw cycles were performed and the headspace was evacuated. Subsequent exposure to H_2 (1 atm) resulted in the solution changing colors from dark red to yellow-brown. Single crystals were grown through the slow evaporation of a concentrated toluene solution under an H_2 atmosphere. Although **3**−H_2 is stable to vacuum, it was seen to revert to **3**−N_2 in solution upon prolonged exposure to the N_2 atmosphere of the glovebox. Alternatively, H_2 can be added to **3**, which can be prepared in an Ar glovebox, as detailed in section 2.4. $^1H\{^{31}P\}$ NMR (ppm, THF-d^8, 300 MHz): 7.35 (d, *J*=7.8 Hz, aryl, 3H), 6.83 (t, *J*= 7 Hz, aryl, 3H), 6.36 (t, *J*=7 Hz, aryl, 3H), 6.28 (d, *J*=7.8 Hz, aryl, 3H), 3.17 (s, C*H*$_2$P(^{i}Pr)$_2$, 6H), 2.18 (br, methine, 6H), 1.17 (m, methyl, 36H), −2.3 (br, *H*$_2$-Ni, 2H). ^{13}C NMR (ppm, C_6D_6, 126 MHz): 152.9, 136.1, 128.4, 127.0, 113.0, 109.9, 46.6, 26.9, 19.7, 18.9. ^{31}P NMR (ppm, C_6D_6, 121.4 MHz): 67.5. Anal. Calcd for $C_{39}H_{62}N_4P_3InNi$: 54.89 C, 7.32 H, 6.57 N. Found: 55.07 C, 7.32 H, 6.57 N.

*Syntheses of (OC)NiInL (**3**−CO).* A mixture of **3** (43 mg, 50.5 μmol) and excess paraformaldehyde (11.7 g, 0.4 mmol) was stirred in benzene (4 mL) for 2 h, followed by filtration and reduction *in vacuo*. Crystallization from hexane/toluene at –30˚C yielded near colorless crystals, which were washed with hexane and dried *in vacuo* (22.3 mg, 50% yield). Alternatively, addition of CO (1 atm or 1 equiv) to **3**, followed by an

analogous workup procedure, also yields **3**−CO in excellent yields and purity. Originally, **3**−CO was synthesized by addition of 1 atm CO to **3**−H_2, showing that CO readily displaces bound H_2. $^1H\{^{31}P\}$ NMR (ppm, C_6D_6, 400 MHz): 7.76 (d, 3H, J = 7.4 Hz, ArH) 7.23 (t, 3H, J = 7.4 Hz, ArH), 6.66 (d, 3H, J = 8.0 Hz, ArH) 6.60 (t, 3H, J = 7.4Hz, ArH), 3.07 (br, 6H, C*H*$_2$), 1.96 (mult., 6H, C*H*$(CH_3)_2$), 1.00-0.8 (br, 36H, CH(CH_3)$_2$). ^{31}P NMR (ppm, 162 MHz, C_6D_6): 66.9. IR (KBr pellet, cm^{-1}): ν(C≡O), 1968 cm^{-1}. Elemental anal. calc'd (found) for $C_{40}H_{60}InN_4NiOP_3 \cdot 0.8\ C_6H_{14}$: C 56.74 (57.06), H 7.57 (7.21), N 5.91 (5.88).

*Syntheses of (OC)NiGaL (**2**−CO)*. A mixture of **2** (46 mg, 57 μmol) and excess paraformaldehyde (25 mg, 0.833 mmol) was stirred in benzene (4 mL) for 12 h, before being filtered and reduced *in vacuo*. Crystallization from hexane/benzene at −30˚C yielded near colorless crystals, which were subsequently washed with hexane and dried *in vacuo* (18.5 mg, 39% yield). Alternatively, addition of ~1 equiv CO to **2**, via gas condensation with liquid N_2 using a gas addition bulb of known volume, followed by an analogous workup procedure also yields **2**−CO, albeit with more difficult purification as a result of the formation of small amounts of unidentified products. $^1H\{^{31}P\}$ NMR (ppm, C_6D_6, 400 MHz): 7.62 (d, 3H, J = 7.4 Hz, ArH) 7.20 (t, 3H, J = 7.6 Hz, ArH), 6.63, 6.60 (m, 6H, ArH), 3.13 (br, 3H, C*H*$_2$), 2.73 (br, 3H, C*H*$_2$), 2.08 (mult., 3H, C*H*$(CH_3)_2$), 1.90 (mult. 3H, C*H*$(CH_3)_2$), 1.20-0.6 (br, 36H, CH(CH_3)$_2$). $^{31}P\{^1H\}$ NMR (ppm, 162 MHz, C_6D_6): 55.7. IR (KBr pellet, cm^{-1}): ν(C≡O), 1961 cm^{-1}. Elemental anal. calc'd (found) for $C_{40}H_{60}GaN_4NiOP_3 \cdot 1\ C_6H_{14}$: C 60.02 (60.36), H 8.10 (8.16), N 6.09 (6.10).

*In situ Generation of (η^2-H_2)NiGaL (**2**-H_2)*. A solution of **2** (0.005 g, 0.006 mmol) in either C_6D_6 or toluene-d^8 (c. 0.7 mL) was added to a J. Young tube. Freeze-pump-thaw cycles were performed to evacuate the headspace. Subsequent exposure to H_2 (1 atm) resulted in the solution changing color from dark red to bright orange-red. Lability of H_2 when subjected to vacuum precluded elemental analysis from being obtained. $^1H\{^{31}P\}$ NMR (ppm, toluene-d^8, 300 MHz): 7.59 (d, *J*=7 Hz, aryl, 3H), 7.22 (t, *J*= 7 Hz, aryl, 3H), 6.59 (m, aryl, 6H), 3.04 (d, C*H*$_2$P(^{i}Pr)$_2$, 6H), 1.77 (br, methine, 6H), 1.04, 0.93, 0.72 (m, methyl, 36H), −2.4 (br, *H*$_2$-Ni, 2H). ^{31}P NMR (ppm, toluene-d_8, 121.4 MHz): 56.9 (s, low T convergence at 193 K).

*In situ Generation of (η^2-H_2)NiAlL (**1**-H_2)*. A solution of **1** (15 mg, 19.6 μmol) in THF-d_8 (c. 0.30 mL) was added to a PEEK NMR spectroscopy cell and pressurized to 34 atm H_2 (see general high-pressure procedure in protocol for determining thermodynamic binding parameters). It should be noted that the *in situ* observation of **1**−H_2 was also carried out in toluene for thermodynamic binding studies; however, complex **1** was much more soluble in THF, which allowed for more concentrated solutions with better signal-to-noise in the ^1H NMR for the bound H_2 resonance. This was important in order to reliably measure T_1(min) relaxation values for the bound H_2 resonance (Figure A.2.13) and support its formulation as an intact H_2 ligand, analogous to the previously characterized (η^2-H_2)NiML complexes.[97] Lability of H_2 when subjected to vacuum and upon removal of the high-pressure H_2 atmosphere precluded elemental analysis from being obtained. $^1H\{^{31}P\}$ NMR (ppm, THF-d_8, 232 K, 500 MHz): 7.34 (3H, ArH), 6.87 (3H, ArH), 6.34 (6H, ArH), 3.00 (br, 3H, C*H*$_2$), 2.87 (br, 3H, C*H*$_2$), 2.10 (m, 6H + toluene C*H*$_3$, C*H*(CH$_3$)$_2$), 1.27, 0.90 (br, 36H, CH(*CH*$_3$)$_2$), −1.5 (br, 2H, (*H*$_2$)Ni, T_1(min) ≤ 0.49(5) s at

200K). ^{31}P NMR (ppm, THF-d_8, 200 K, 202.4 MHz): 44.9 (s). ^{31}P NMR (ppm, toluene-d_8, 202.4 MHz): ~44.3 (s, low T convergence under 34 atm H_2, 200 K).

*In situ Observation of (N_2)NiAlL (**1**−N_2) and (N_2)NiGaL (**2**−N_2).* These complexes display the weakest binding for any of the six H_2 and N_2 adducts of NiML which were able to be quantified by VT ^{31}P NMR studies. As such, full conversion to generate **1**−N_2 and **2**−N_2 *in situ* was not possible; for this reason, ^{1}H NMR and elemental analyses are not reported. Fortunately observation of equilibrium mixtures of NiML and (N_2)NiML allowed for quantification of these weak binding equilibria. VT ^{31}P NMR studies (Figures 3.18 and 3.20) allowed for assignment of the ^{31}P NMR resonance for **1**−N_2 and **2**−N_2 based on the observation of slow exchange in toluene-d_8 at low T. For **1**−N_2: ^{31}P NMR (ppm, toluene-d_8, 202.4 MHz): ~32.2 (s, low T convergence at 190 K under 51 atm N_2). For **2**−N_2: ^{31}P NMR (ppm, toluene-d_8, 162 MHz): ~43.5 (s, low T convergence at 193 K under 1 atm N_2).

Experimental Procedure for Determining Thermodynamic Binding Parameters. A concentrated solution of NiML (~15 mM) was prepared in toluene, filtered, and transferred to either a J. Young NMR tube (if pressurizing with 0.1, 1.0, or 3.8 atm gas) or a PEEK NMR tube (if pressurizing with 6.8, 13.6, or 34.0 atm gas), which was designed and implemented at PNNL as described previously.[214, 233] For high-pressure studies, the PEEK cell was sealed and connected to a high-pressure line equipped with a vacuum pump and an ISCO syringe pump. The line was purged with H_2 or N_2 gas three times. Next, the headspace was degassed by opening the PEEK cell to static vacuum (3 × 30 s), and H_2 or N_2 gas was then delivered to the cell from an ISCO syringe pump

running constantly at the desired pressure (i.e. continuous gas feed). The contents of the PEEK cell were mixed using a vortex mixer for approximately 15 minutes prior to NMR data collection to allow for pressure stabilization and equilibration. This procedure general procedure was used for all high-pressure studies.

For both high- and low-pressure studies, VT ^{31}P NMR spectra were acquired at several different T (typically 193 K to 368 K), with adequate scans (64 or 160 scans typically) collected so as to achieve ideal signal-to-noise ratios and clearly identify the observed peak position (for fast exchange) and/or relative integrations (for slow exchange). ^{31}P spectra were typically collected with a delay time of 2 s, and an acquisition time of 1.68 s, with a long delay time of 10 s used in cases where quantitative integration of multiple peaks was required (ie. to determine relative concentrations in slow exchange regime). The choice of gas pressure was made on a case-by-case basis so as to sample as much of the equilibrium as possible, as well as to ensure that the exchange rate was either slow at all T (like N_2 binding to **2**) or as fast as possible so as to validate the assumption of fast exchange and facilitate analysis based on the observed ^{31}P chemical shift (H_2 binding to all three NiML, and N_2 binding to **3**). The effects of pressure on the validity of the assumption of fast chemical exchange was also investigated in detail for H_2 binding to **2**, with pressures of 0.1, 1.0, 6.8, 13.6, and 34 atm H_2 examined. In some cases, extremely low or high pressures were used out of necessity in order to measure extremely weak (N_2 binding to NiAlL at ~51 atm N_2) or extremely strong (H_2 binding to **3** at 0.1 atm H_2/0.9 atm Ar) binding equilibria.

Experimental Procedure for Kinetic Lineshape Studies. A solution of NiML (~7.5 mM in 0.70 mL) was prepared in toluene-d_8, filtered, and transferred to a J. Young NMR tube

(under 1 atm Ar from the glovebox). VT ^{31}P NMR were measured for NiML under 1 atm Ar at various T (at least seven different T over the range of 214 K to 344 K) in order to determine the temperature-dependence of the chemical shifts and intrinsic linewidths. Then, the samples were pressurized with 1 atm H_2 (after freeze-pump thaw cycles), and VT ^{31}P NMR spectra were again obtained at the same set of T as before. ^{31}P spectra were typically collected with a delay time of 2 s, and an acquisition time of 1.68 s, and 160 scans (to obtain good S/N). A long delay time of 10 s was used in cases where quantitative integration of multiple peaks was required (ie. to determine relative concentrations in the slow exchange regime).

3.5.2 X-ray and Neutron Crystallographic and Structure Refinement Details

X-ray Diffraction. A colorless plate of (OC)NiGaL (**2**−CO), a pale gold block of (OC)NiInL (**3**−CO), and a gold block of (η^2-H_2)NiInL (**3**−H_2) were placed onto the tip of a MiTeGen Dual-Thickness MicroLoop™ and mounted on a Bruker Photon II CPAD diffractometer for data collection at either 123(2) K or 100(2) K (see Table 3.16). The data collections were carried out using either Mo or Cu Kα radiation (graphite monochromator), with the assistance of Dr. Laura Clouston, Dr. Victor Young, Jr., and James Moore. The data intensity was corrected for absorption and decay (SADABS).[172] Final cell constants were obtained from least-squares fits of all measured reflections. The structure was solved using SHELXT-16 and refined using SHELXL-16, which were executed from the ShelXle graphical user interface.[264] A direct-methods solution was calculated which provided most non-hydrogen atoms from the E-map. Full-matrix least-squares/difference Fourier cycles were performed to locate the remaining non-hydrogen atoms. All non-hydrogen atoms were refined with anisotropic displacement parameters.

Hydrogen atoms were placed in ideal positions and refined as riding atoms with relative isotropic displacement parameters,[173] with the exception of the apical H_2 ligand in **3**−H_2, for which data were of sufficient quality and resolution (crystals diffracted to 0.6 Å) to place these H atoms from the difference map (albeit not as reliably as desired, hence the neutron structure). Note that the x-ray refinement details for **3**−H_2 shown in Table 3.16 are for a structure obtained at 100 K to match the T at which the neutron structure was obtained. This later structure is displayed here, rather than the originally published structure collected at 123 K,[97] because data was collected to 0.60 Å in the later structure, which permitted more reliable placement of the H atoms of H_2. Note that the structural metrics are all essentially identical within experimental error, and both structures were of excellent quality (R1 < 2% in both cases). PLATON Squeeze was used to remove a disordered solvent molecule from the unit cell of **3**−CO.[174] Images were rendered using POV–ray.[175]

Neutron Diffraction. Neutron diffraction data were collected using the TOPAZ single-crystal time-of-flight (TOF) Laue diffractometer at the Spallation Neutron Source (SNS), at Oak Ridge National Laboratory (Oak Ridge, TN), with the assistance of Dr. Christina Hoffmann, Dr. Xiao-Ping Wang, Dr. Victor Young, Jr., and Junhong He.[247] A block-shaped crystal of **3**−H_2, with dimensions of 0.35 × 0.30 × 0.30 mm, was grown from a concentrated toluene solution allowed to sit for several weeks under an H_2 atmosphere (1 atm) in a cold room (~280 K). The crystal was mounted on the tip of a polyimide capillary using fluorinated grease, and transferred to the TOPAZ goniometer for data collection at 100 K. To ensure good coverage and redundancy, data were collected using crystal orientations optimized with CrystalPlan software[265] for optimal coverage of

symmetry-equivalent reflections of the orthorhombic cell. The integrated raw Bragg intensities were obtained using the 3-D ellipsoidal Q-space integration in accordance with previously reported methods.[266] Data reduction, including neutron TOF spectrum, Lorentz, and detector efficiency corrections, was carried out with the ANVRED3 program.[267] A spherical absorption correction was applied with $\mu = 1.150 + 1.022\ \lambda\ cm^{-1}$. The reduced data were saved as SHELX HKLF2 format in which the wavelength is recorded separately for each reflection. Data were not merged. The neutron crystal structure was refined anisotropically for all atoms using the SHELXL-14/7 program[173, 264] in WinGx.[268]

Table 3.16. Crystallographic details for **2**−CO, **3**−CO, and **3**−H_2 (x-ray and neutron structures).

Complex	(OC)NiGaL (**2-CO**)	(OC)NiInL (**3-CO**)	(H_2)NiInL (**3-H_2**)	(H_2)NiInL (**3-H_2**)
radiation type	x-ray	x-ray	x-ray	neutron
chemical formula	$C_{40}H_{50}ON_4P_3GaNi{\cdot}C_5H_{12}$	$C_{40}H_{50}ON_4P_3InNi$	$C_{39}H_{52}N_4P_3InNi$	$C_{39}H_{52}N_4P_3InNi$
fw	906.4	879.37	853.36	853.36
cryst syst	Monoclinic	Monoclinic	Orthorhombic	Orthorhombic
space group	$P2_1/c$	$P2_1/c$	$P2_12_12_1$	$P2_12_12_1$
a (Å)	11.7707(8)	11.7281(5)	12.2127(4)	12.2010(10)
b (Å)	15.9707(11)	16.1472(7)	14.5402(5)	14.5638(12)
c (Å)	24.2154(17)	11.9776(5)	22.5601(8)	22.547(2)
α (deg)	90	90	90	90
β (deg)	101.136(2)	103.439(1)	90	90
γ (deg)	90	90	90	90
V (Å^3)	4466.5(5)	2206.2(2)	4006.1(2)	4006.4(6)
Z	4	2	4	4
λ (Å), μ (mm^{-1})	0.71073, 1.171	1.54178, 5.986	0.71073, 1.198	1.800, 0.039
T(K)	103(2)	123(2)	100(2)	100(2)
θ	2.46 to 30.53	3.79 to 72.23	2.285 to 36.348	5.794 to 89.921
reflns collected	96446	23188	237431	13289
unique reflns	13664	7625	19473	4077
data/restraint/parameters	13664/0/517	7625/1/464	19473/451/0	4077/991/1068
R1, wR2 ($I > 2\sigma(I)$)	0.0376, 0.0815	0.0455, 0.1265	0.0181, 0.0392	0.0537, 0.1139

3.5.3 Physical Methods

^{1}H and ^{31}P NMR spectra were recorded on Bruker 500 or 400 MHz and Varian 500 MHz or 600 MHz spectrometers and referenced to internal residual solvent (or H_3PO_4 for ^{31}P NMR spectra). VT NMR experiments were carried out using either a methanol (below 298 K) or ethylene glycol (above 298 K) standard to calibrate T, and all samples were allowed to equilibrate at each T for at least 10-15 minutes prior to data collection. High-pressure NMR studies (> 4 atm pressure) were performed at Pacific Northwest National Laboratory (PNNL, Richland, WA), using PEEK high-pressure NMR spectroscopy tubes designed and built at PNNL, as reported previously (see procedure for high-pressure thermodynamic studies for more details).[214, 233] UV-vis spectra were collected on a Cary-14 instrument. IR spectra were obtained in KBr pellets using a Bruker Tensor-37 FTIR with OPUS 6.5 software.

3.5.4 Computational Methods

DFT Calculations

To find a suitable method to study the (η^2-H_2)NiML and (N_2)NiML bimetallic systems, we tested four functionals, M06-L,[176] M06-D3,[177] PBE0,[178] and PBE0-D3,[179] with five combinations of basis sets, which are denoted as bs0 – bs4 (see Table 2.9). The M06-L/bs1 method was used to study the catalytic mechanisms of a similar bimetallic system in a previous study, therefore, it is used in this study as well.[79] The only difference between bs1 and bs0 is that for the H_2 molecule, def2-TZVPP[186] is used in bs1, with an additional diffuse function adding to def2-TZVP (used in bs0). The combination of M06-D3/bs4 were suggested to give accurate energetics for a Pd−Pd bimetallic system.[180] We also considered a smaller basis set combination bs3 for the sake of comparison. Geometric structures were

optimized in the gas phase at 0 K. Vibrational frequency analysis with the harmonic approximation was performed to characterize the nature of the stationary points and transition states. Unless specified otherwise, Gibbs free energies at 298.15 K and 1 atm were computed by adding zero-point vibrational energies and thermal corrections. Solvation effects were also considered by performing single-point calculations for all stationary points using the SMD[181] solvation model and toluene as the solvent. All DFT calculations were performed with the Gaussian 09 program package.[182]

Binding Energy Calculation Method

The binding energies for H_2, N_2, CO, and CO_2 were the free energies of reaction (Equation 3.18).

$$X(gas) + NiML(sol) \rightarrow X\text{-}NiML(sol),\ X = H_2, N_2, CO, CO_2 \qquad \text{(Eqn 3.18)}$$

The gas phase free energies were used for H_2, N_2, CO, and CO_2 due to our desire to compare with experimental results for which 1 atm was defined as the standard state, while solvent free energies were used for the bimetallic species.

Energy Decomposition Analysis

The energy decomposition analysis (EDA),[254] as implemented in the Amsterdam Density Functional (ADF)[255] program package, was applied for the elucidation of the contributions to the H_2–Ni and N_2−Ni interactions in the corresponding adducts of NiML. (η^2-H_2)NiML complexes were fragmented into H_2 and NiML, and (N_2)NiML complexes were similarly fragmented into N_2 and NiML. The EDA interaction energy is calculated by taking the electronic energy difference between the complex and the two fragments. Since the EDA interaction energy includes neither the deformation energy of the fragments nor

any thermal effects, it is termed in the next paragraphs as "$\Delta E_{uncorrected}$". The relationship between binding free energy in solvent, ΔG_{sol}, and $\Delta E_{uncorrected}$ is given in Equation 3.19.

$$\Delta G_{sol} = \Delta E_{uncorrected} + \Delta E_{deformation} + \Delta\Delta G_{solvation} + \Delta\Delta G_{thermal} \quad \text{(Eqn 3.19)}$$

$\Delta E_{deformation}$ results from deforming the fragments from their equilibrium structure to the geometry and electronic state they adopt in the adduct complex. $\Delta\Delta G_{solvation}$ is the solvation energy for the binding reaction upon moving from the gas phase into solution. $\Delta\Delta G_{thermal}$ is the thermal correction to the free energy of the binding reaction.

EDA breaks the total interaction energy into four components:

$$\Delta E_{uncorrected}\,(\text{EDA}) = \Delta E_{electrostatic} + \Delta E_{Pauli} + \Delta E_{orbital} + \Delta E_{dispersion} \quad \text{(Eqn 3.20)}$$

$\Delta E_{electrostatic}$ corresponds to the attractive, quasi-classical electrostatic interaction between the electrons and the nuclei. ΔE_{Pauli} corresponds to repulsive energy between electrons of the same spin due to the anti-symmetrized nature of the wavefunction. $\Delta E_{orbital}$ is obtained from the relaxation (mixing) of the fragment orbitals. Finally, $\Delta E_{dispersion}$ describes the dispersive effects between the two fragments.

The extended transition state—natural orbitals for chemical valence (ETS-NOCV) method,[253] in combination with the energy decomposition scheme, is used to decompose the orbital interaction component ($\Delta E_{orbital}$) into contributions from specific NOCV pairs. The deformation density, $\Delta\rho$, is partitioned into the different components (σ, π, δ) of the chemical bond. Each NOCV pair shows the electron flow, as pictured by red → blue, and thus this can be used to aide in the assignment of the orbital interaction types between the fragments. The ETS-NOCV calculations were performed with the ADF program using PBE0-D3, with the doubly polarized triple-zeta basis set TZ2P for Ni, Al, Ga, In, H_2, and N_2, the polarized triple-zeta basis set TZP for P and N, and the double-zeta for C and H

atoms.[269] Relativistic effects for the heavier In atom were included by applying the zeroth-order regular approximation (ZORA).[270] The ETS-NOCV analysis is not yet available for meta-GGA's or meta-hybrids functionals, such as M06-L and M06, and so PBE0-D3 was used instead despite its slightly inferior match with experimental binding data compared to M06-L.

TD-DFT calculations

TD-DFT calculations (M06-D3/bs4, Gaussian09) with solvent consideration (SMD, THF) were performed to obtain the absorption spectra of the series of NiML, (η^2-H_2)NiML, (N_2)NiML, and (OC)NiML, complexes (M=Al, Ga, In). Structures were optimized with M06-D3/bs4, with the exception of the (OC)NiML complexes, which were optimized with M06-L/bs1.

3.5.5 Acknowledgements

Note that most calculations presented in this chapter were carried out by Dr. Jing Xie, a postdoctoral researcher and collaborator in the research group of Dr. Laura Gagliardi. Dr. Konstantinos Vogiatzis and Dr. Jingyun Ye also contributed to computational studies presented in this chapter. Dr. Samantha Burgess and Dr. John Linehan (Pacific Northwest National Lab) assisted in high-pressure binding studies, and Samantha conducted high-pressure N_2 binding studies for complex **1**. I would also like to thank Dr. Aaron Appel, Dr. Thomas Autrey, Dr. Molly O'Hagan, and Dr. Adrian Houghton (Pacific Northwest National Lab) for helpful discussion and guidance regarding thermodynamic and kinetic binding studies.

Dr. Christina Hoffmann and Dr. Xiao-Ping Wang mounted and collected single-crystal neutron diffraction data for **3**−H_2, with the assistance of Junhong He, at the Spallation Neutron Source at Oak Ridge National Lab (Oakridge, TN). I would also like to thank Dr. Victor Young, Jr., for assistance in writing the proposal to obtain instrument time, as well as Dr. Laura Clouston, and James Moore for assistance in collecting x-ray data for **3**−H_2. I would also like to acknowledge Matt Vollmer for helpful discussions and for obtaining the solid-state structure of **2**−CO, and Bianca Ramirez for her work on the preliminary reactivity of NiML*$_3$ complexes with H_2 and N_2. Lastly, I would like to thank Dr. Letitia Yao for assistance in conducting VT NMR studies.

Chapter 4

Tuning Ni for Catalytic Olefin Hydrogenation: Elucidating the Mechanistic Roles of the Group 13 Supporting Metal in Enabling Catalysis

In part from:

Cammarota, R. C.; Lu, C. C.* "Tuning Nickel with Lewis Acidic Group 13 Metalloligands for Catalytic Olefin Hydrogenation." *J. Am. Chem. Soc.* **2015**, *137,* 12486-12489.

Cammarota, R. C.*; Clouston, L. J.; Lu, C. C.* "Leveraging Molecular Metal-Support Interactions for H_2 and N_2 Activation." *Coord. Chem. Rev.* **2017**, *334*, 100-111.

4.1 Overview and Introduction

Given their earth-abundance and low cost, the development of base metal catalysts (Fe, Co, Ni) for challenging reactions of energetic and industrial relevance would be highly desirable.[21-22] As discussed in chapters 2-3, favorably altering the properties of Ni via interaction with a group 13 supporting metal has proven to be an effective strategy for developing a series of Ni complexes which exhibit divergent small molecule binding reactivity from typical Ni complexes. Moving forward, we were interested in whether the uncommon small molecule binding reactivity by the NiML complexes would allow for catalytic functionalization of substrates that are typically not able to be mediated by mononuclear Ni complexes. Given the propensity of NiML complexes to bind and activate H_2, as described in chapter 3, the hydrogenation of olefins to alkanes was targeted, as it represents an industrially-relevant process for which few homogeneous Ni catalysts have been developed.[271-272]

The primary reason for the scarcity of homogeneous Ni hydrogenation catalysts is the inability of most Ni complexes to bind and activate H_2, which is a critical step in hydrogenation catalysis. As mentioned in chapter 3, the binding of H_2 to Ni is rare, and classical H_2 oxidative addition at a single Ni center has not been reported to our knowledge, attesting to Ni being a poor π-back-donor into the σ* orbital of H_2).[44-45, 81, 110, 272] In general, first-row metals like Ni tend to undergo undesirable one-electron processes rather than productive two-electron redox chemistry that promotes fundamental steps in hydrogenation catalysis, like oxidative addition and reductive elimination.[21-22, 44] To circumvent these limitations of Ni, the employment of bifunctional ligands which allow for the assistance of Lewis basic or acidic moieties has been seen to be a promising

strategy for affecting H−H cleavage and enabling further reactivity and catalysis.[44, 84-85, 92, 120, 170, 273]

Excitingly, group 13 supporting metals remedy the typical limitations of Ni in H_2 activation by promoting more favorable H_2 binding at NiML complexes by up to ~8 kcal/mol relative to a similarly ligated $NiLH_3$ complex (chapter 3). In this chapter, the propensity of (η^2-H_2)NiML complexes to hydrogenate olefins by undergoing oxidative cleavage of the activated H_2 unit will be examined. Catalytic activity was found to be highly dependent on the supporting metal, with NiGaL (**2**) found to catalyze the hydrogenation of relatively unhindered olefins with higher yields and TOF than NiInL (**3**), while NiAlL (**1**) and $NiLH_3$ (**4**) were not catalytically active. Furthermore, divergent catalytic selectivity for hydrogenation versus isomerization was observed for catalysis with **2** and **3**.[30, 97] To understand these trends in catalytic activity and selectivity, a catalytic mechanism for olefin hydrogenation is proposed on the basis of both experimental and computational studies, with the relative order of favorability for each fundamental step in the catalytic cycle considered as a function of the group 13 supporting metal.

4.2 Results and Discussion

4.2.1 Investigating the Catalytic Potential of NiML Complexes for Olefin Hydrogenation

With an isostructural series of NiML complexes in hand that bind and activate H_2 to varying degrees, the next logical step was to investigate whether the activated H_2 moieties could be transferred to unsaturated substrates like olefins in an efficient and selective manner. Styrene was chosen as the initial substrate to test the catalytic hydrogenation activity of the series of NiML complexes in comparison to $NiLH_3$ (**4**).

Table 4.1 shows a comparison of the catalytic results for the series of Ni complexes, as well as a control experiment showing that free ligand, LH_3, is not a competent catalyst.[97]

Table 4.1. Results for catalytic hydrogenation of styrene to ethyl benzene for complexes **1**-**4**.[a]

Entry	Pre-catalyst	% yield[b]	TOF (h^{-1})[c]
1	LH_3	0	0
2	$NiLH_3$ (**4**)	<1[d]	0
3	NiAlL (**1**)	<1	0
4	NiGaL (**2**)	>99	2.4(1)
5	NiInL (**3**)	12(5)[e]	0.10(4)

[a]Catalytic conditions: 5 mol% pre-catalyst, 0.087 M olefin in ca. 700 μL C_6D_6, 1 atm H_2, rt, rotating in J. Young tubes at 16 rpm to promote gas-solvent mixing. [b]Yield at 24 h, triplicate runs, based on ^{1}H NMR spectroscopy and GC-MS analysis. [c]Turnover frequency (TOF) analyzed by ^{1}H NMR spectroscopy at >90% product, or after 24 h if <90% conversion. [d]Duplicate runs. [e]Five trials.

Gratifyingly, complex **2** was catalytically competent in the hydrogenation of styrene under mild reaction conditions (rt and 1 atm H_2), with >90% conversion of styrene to ethyl benzene observed within 8 h, and >99% occurring within 24 h (Figures 4.2 and A.3.1).[97] The catalytic turnover frequency (TOF) for complex **2** was determined to be 2.4 (±0.1) h^{-1} based on the time required to reach >90% ethyl benzene conversion (Table 4.1). Catalysis by **2** was uninhibited in the presence of excess Hg, which supports a homogeneous process rather than one mediated by nanoparticles or other heterogeneous Ni materials.[274-275] Styrene hydrogenation was also catalyzed by complex **3**, albeit significantly more slowly compared with catalysis for **2**, with approximately 2.4 (± 1.0) turnovers observed over 24 h under catalytic conditions with **3** in five replicate trials, giving TOF = 0.1 h^{-1} (Table 4.1).[97] Complexes **1** and **4** were not found to be catalytically active

for styrene hydrogenation, and so no further catalytic experiments were performed for these complexes.

Hydrogenation of 1-octene, another simple and relatively sterically unhindered alkene, was attempted next with complexes **2** and **3** under the previously described catalytic conditions. For complex **2**, hydrogenation of 1-octene was observed to be even faster than that of styrene, with the reaction reaching completion in <1.5 h. Under identical conditions, catalysis with **3** results in the full conversion of 1-octene to generate multiple products, resulting in a mixture of 47(7)% octane and 53(7)% 2-octene, as judged by ^{1}H NMR spectroscopy, with the latter formed in a *trans*:*cis* ratio of 4:1 (Figure 4.1).[97]

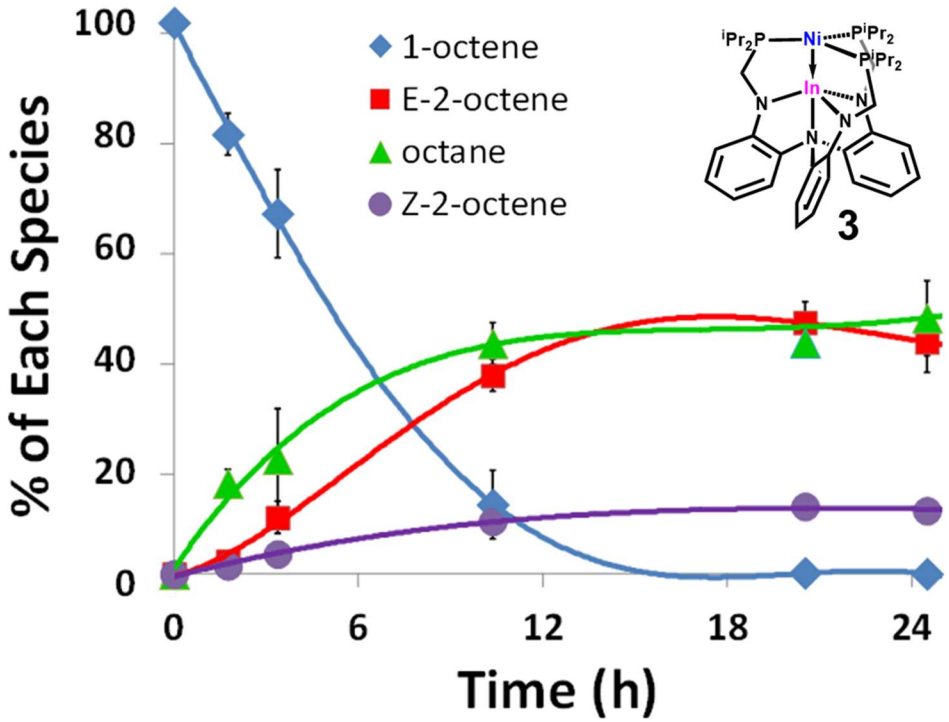

Figure 4.1. Kinetic profile of hydrogenation-isomerization of 1-octene catalyzed by NiInL (**3**), as monitored by ^{1}H NMR spectroscopy. The error bars represent the standard deviation between five replicate trials.

A control experiment established that the isomerization of 1-octene to 2-octene catalyzed by **3** requires H_2, as only trace (<2%) isomerization to 2-octene was observed after 50 h in the absence of H_2, but otherwise identical conditions (Figure A.3.2).[97] These results indicate that hydrogenation, to give octane, and isomerization, to give 2-octenes, are competitive processes under catalytic conditions for **3**, whereas exclusive hydrogenation was catalyzed by **2**. Figure 4.1 shows the kinetic profile of the hydrogenation-isomerization of 1-octene for **3**, while the kinetic profile for the exclusive hydrogenation of 1-octene by **2** is shown in Figure 4.2. It should be noted that while full consumption of 1-octene was observed for both **2** and **3**, the latter required 12 h to reach >90% conversion; thus, significantly faster catalysis was observed for catalysis with **2** compared with **3**, just as was seen for styrene hydrogenation.[97]

The catalytic results for **3** with 1-octene prompted the question of whether the reactivity pattern of competitive hydrogenation and isomerization generally holds true for catalysis with **3**. Isomerization of allylbenzene, another terminal olefin with allylic protons, to β-methylstyrene was observed to be the primary process under catalytic conditions for **3**, with β-methylstyrene (*trans*:*cis*=9:1) formed in a 3.7:1 ratio to propylbenzene, the hydrogenated product. The consumption of allylbenzene is significantly slower than that of 1-octene under catalytic conditions for **3**, as only 47(2)% consumption of allylbenzene was observed after one week (Figure A.3.3), compared with complete 1-octene consumption within 20 h (Figure 4.1).[97] The lower relative yield of the hydrogenated product for allylbenzene (1:3.7 with isomerized product) in comparison to that for 1-octene (~1:1) suggests that allylbenzene is a more difficult substrate for **3** to hydrogenate, with the slower overall rate of consumption suggesting that isomerization of

allylbenzene is also more difficult than that of 1-octene. Hydrogenation of allylbenzene also proved to be difficult to facilitate for complex **2**, with only 7(3)% conversion to propylbenzene observed in 1 week.[97] The results of a wider olefin substrate scope for complex **2** informed our thinking for why allylbenzene hydrogenation is difficult for NiML complexes to mediate, and so this question will be re-visited after discussing the catalytic results for additional substrates.

The final substrate subjected to catalytic conditions for both complexes **2** and **3** was *cis*-cyclooctene, a cyclic olefin rather than a terminal one. Similarly to the results for styrene, complex **2** was found to be a far more active catalyst than complex **3** for hydrogenating *cis*-cyclooctene, with 93(3)% conversion to cyclooctane observed in the former case in 24 h compared with <1% in the latter case.[97] Hydrogenation catalyzed by complex **2** did proceed more slowly for *cis*-cyclooctene in comparison to styrene, with >90% conversion achieved after ~18 h compared with ~8 h, respectively. The slower reaction with *cis*-cyclooctene compared with styrene and lower conversions for both **2** (>99% vs. 93%) and **3** (12% vs. <1%) is hypothesized to be a consequence of the greater steric hindrance associated with di-substituted alkenes relative to terminal, mono-substituted ones.[30, 97]

In light of the sluggish catalytic activity of **3**, as well as its mixed selectivity for hydrogenated and isomerized products, further substrates were not studied; a summary of the catalytic results for complex **3** is shown in Table 4.2.[97] Instead, a wider olefin substrate scope was conducted for complex **2**, as its catalytic activity and selectivity were by far the most promising of the series of Ni complexes (*vide supra*). The intriguing divergence of the catalytic selectivity and activity between complexes **2** and **3** will be

discussed further in section 4.2.4, as it pertains to the catalytic reaction mechanism and the roles of the supporting metal therein.

Table 4.2. Full substrate scope for catalytic hydrogenation-isomerization mediated by **3**.[a]

Entry	pre-catalyst	Substrate	product(s)	% yield[b] (24 h)	time to >90% yield (h)[b]
1	**3**	styrene	ethyl benzene	12(5)[c]	-[d]
2	**3**	*cis*-cyclooctene	cyclooctane	<1	-[e]
3	**3**	1-octene	octane, 2-octene (4:1 E:Z)[f]	>99[c]	12
4	**3**	allylbenzene	propylbenzene, β-methylstyrene (9:1 E:Z)[g]	5(2)	>>168[h]

[a]Catalytic conditions were identical to those given in Table 4.1. Note that catalytic reactions were prepared in J. Young tubes in a glovebox under an N_2 atmosphere, and so the pre-catalyst was technically **3**−N_2. The pre-catalyst was exposed to 1 atm H_2 to generate **3**−H_2, followed by additional evacuation and back-filling with H_2 to rid the headspace of the displaced N_2 (1 equiv). [b]as judged by disappearance of olefin by ^{1}H NMR spectroscopy of triplicate trials unless otherwise indicated. [c]5 replicate trials. [d]19(7)% after 48 h. [e]4(1)% after 120 h. [f]47(7)% octane, 53(7)% 2-octene after 24 h in 5 replicate trials. [g]duplicate trials: 10.0(3)% propylbenzene, 37(3)% β-methylstyrene. [h]47(2)% after 168 h.

*4.2.2 Olefin Hydrogenation Catalyzed by NiGaL (**2**): Results of a Wider Substrate Scope*

Table 4.3 shows the results of the full substrate scope for olefin hydrogenation catalyzed by complex **2**. In addition to the previously discussed results for styrene, 1-octene, allylbenzene, and cis-cyclooctene, the propensity of **2** to catalyze the hydrogenation of 1-hexene, 4-phenyl-1-butene, allyl butyl ether, *trans*-2-octene, *trans*-3-octene, *trans*-4-octene, *cis*-stilbene, 1,1-diphenylethylene, phenyl acetylene, and benzaldehyde was also studied (Table 4.3).[97]

Table 4.3. Olefin substrate scope for hydrogenation catalyzed by **2** (see Table 4.1 for catalytic conditions).[a]

Entry	substrate	% yield[b]	time to >90% yield (h)[b]
1	1-octene	>99	<1.5
2	1-hexene	>99	<2.75
3	styrene	>99	8
4	4-phenyl-1-butene	>99	10
5	*cis*-cyclooctene	93(3)	18
6	allyl butyl ether	68(16)	>116 [c]
7	*trans*-2-octene	10(2)	– [d]
8	allylbenzene	3(2)	– [e]
9	*trans*-3-octene	1(2)	–
10	*trans*-4-octene	1(2)	–
11	*cis*-stilbene[g]	0	–
12	1,1-diphenylethylene	0	–
13	phenyl acetylene	trace[f]	–
14	benzaldehyde[g]	0	–

[a]Note that the hydrogenation of ethylene and norbornene was also observed within 24 h but never rigorously quantified. [b]as judged by ^{1}H NMR spectroscopy of replicate trials after 24 h unless otherwise indicated. Most yields confirmed by GC-MS (Table A.3.1). [c]81(12)% after 116 h. [d]26(2)% after 116 h. [e]9(3)% after 168 h. [f]trace amounts of styrene and ethyl benzene observed by GC-MS. [g]single trial.

While high alkane yields were observed for unhindered hydrocarbon alkenes that are either mono-substituted (e.g. styrene, 1-octene, 1-hexene, and 4-phenyl-1-butene) or cyclic (e.g. *cis*-cyclooctene), little to no hydrogenated products were formed for acyclic, di-substituted olefins such as *cis*-stilbene, 1,1-diphenylethylene, and internal octenes (0 to 10% yields, Table 4.3). Figure 4.2 shows the kinetic profiles for the catalytic hydrogenation of various substrates mediated by **2**, as monitored by ^{1}H NMR spectroscopy. As illustrated by the kinetic profiles, the relative rates of hydrogenation among substrates for which >90% yields were observed within 24 h was observed to be: 1-octene ~ 1-hexene > styrene > *cis*-cyclooctene (Figure 4.2).[30, 97]

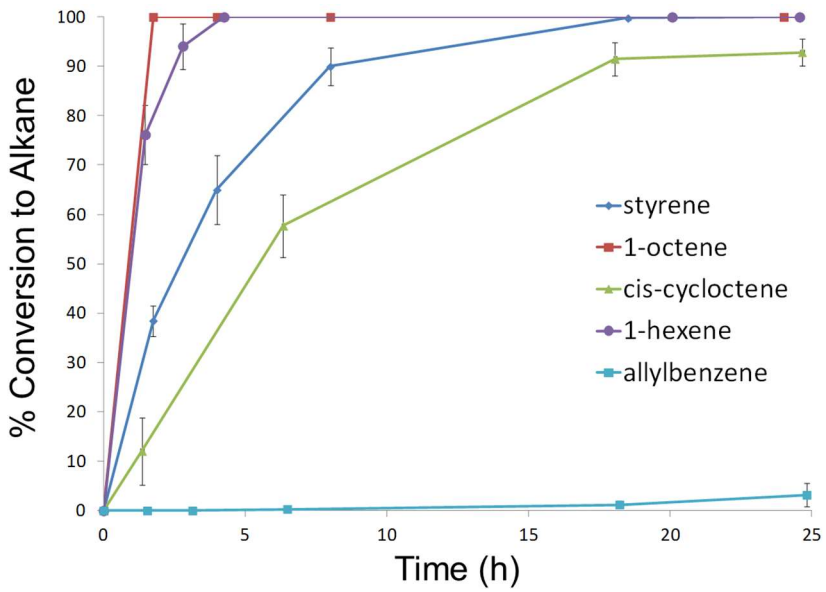

Figure 4.2. Kinetic profiles of hydrogenation catalyzed by NiGaL (**2**), as monitored by the disappearance of olefin by ^{1}H NMR spectroscopy. The error bars represent the standard deviation between triplicate trials.

The poor yields for the hydrogenation of acyclic, di-substituted olefins are hypothesized to be a consequence of unfavorable steric clashes between the bulky olefin substituents and the ligand isopropyl groups, which likely impedes or precludes olefin binding. This greater difficulty in hydrogenating bulkier, more sterically demanding olefins is well-illustrated by the decreasing yields of octane as the position of the double bond to be hydrogenated is moved from terminal, in 1-octene (>99%), to increasingly internal positions, in *trans*-2-octene (10%), *trans*-3-octene (1%), and *trans*-4-octene (1%).[30, 97] The steric considerations associated with olefin binding in conjunction with H_2 activation will be discussed in the catalytic mechanism section (4.2.4).

The inability of **2** to catalyze the hydrogenation of allylbenzene, also a relatively unhindered terminal olefin, was interesting and initially unexpected from a steric perspective. The chart in Figure 4.3 emphasizes the hydrogenation results for three structurally related olefins of the general formula: $H_2C{=}CH{-}(CH_2)_x{-}Ph$, where x=0

(styrene), 1 (allylbenzene), or 2 (4-phenyl-1-butene). In other words, the separation of the phenyl group and the double bond to be hydrogenated is varied from being directly conjugated, in styrene, to being separated by one or two alkyl carbons (Figure 4.3).

substrate	hydrogenated yield (24 h)	TOF (h^{-1})
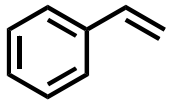	>99%	2.4
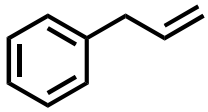	3(2)%	0.03
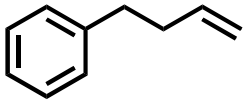	>99%	2.0

Figure 4.3. Comparison chart for hydrogenation of structurally similar terminal olefins by **2**.

One would expect that further separation of the double bond and the phenyl ring would decrease the steric hindrance associated with olefin binding to **2**, as the intervening alkyl chain carbons would likely allow for a greater degree of flexibility to minimize steric clashes between the phenyl ring and the ligand isopropyl groups. The discontinuity in hydrogenation yield observed for allylbenzene, for which little hydrogenation occurs, in comparison to styrene and 4-phenyl-1-butene, which were hydrogenated in quantitative yields with similar TOF, suggests that other factors besides the steric hindrance of the olefins are responsible for the inability of **2** to catalyze allylbenzene hydrogenation. It is hypothesized that the reason for poor hydrogenation of allylbenzene may be the formation of a stable Ni-allyl adduct which impedes catalysis

Lastly, the propensity of **2** to catalyze the hydrogenation of other types of unsaturated functionalities, including alkynes and aldehydes, was also tested. No

appreciable conversion of benzaldehyde to benzyl alcohol or of phenyl acetylene to either styrene or ethyl benzene was observed (Table 4.3).[97] The propensity to preferentially hydrogenate alkenes over alkynes, ketones, and aldehydes would be attractive from a chemoselectivity standpoint, but given that the substrate scope for **2** is already limited to mono-substituted and cyclic olefins, this cannot really be claimed as an advantage in this case. Styrene, phenyl acetylene, and benzaldehyde have similar steric bulk, as they all feature a terminal, mono-substituted unsaturated moiety with a phenyl substituent. Comparing styrene to benzaldehyde, it seems likely that the drastic differences in the yields of hydrogenated product (>99% vs. 0%) likely stem from the general inability of **2** to mediate the hydrogenation of C=O bonds, rather than from steric hindrance preventing the binding of benzaldehyde.

In the case of phenyl acetylene, however, it is possible that its linear structure may impede or prevent coordination for steric reasons, thereby explaining its inability to be hydrogenated. In order to distinguish whether the steric hindrance associated with phenyl acetylene or the inability of **2** to mediate the hydrogenation C≡C bonds is responsible for the observed lack of reactivity, an ideal test substrate would be acetylene. Unfortunately, the hydrogenation of acetylene could not be attempted for logistical and safety reasons pertaining to its limited distribution. It is hypothesized that acetylene would be successfully hydrogenated twice to give ethane if this experiment were conducted, as the facile hydrogenation of ethylene to ethane was catalyzed by **2**, and alkynes typically coordinate to late transition metals and are functionalized more readily than their corresponding alkenes, as exploited by many alkyne semi-hydrogenation catalysts.[110, 276-278] That said, it is acknowledged that simply binding more readily to NiML would not

necessarily lead to hydrogenation for acetylene; to this point, the only complex to which phenyl acetylene was observed to bind is **3**, and no hydrogenation was observed in that case, whereas olefin binding was not observed in any cases for **2**, which was the most active catalyst examined for olefin hydrogenation.

The greater steric difficulty of coordinating phenyl acetylene can be inferred from the fact that the ligand phosphines become inequivalent and give rise to distinct ^{31}P NMR resonances upon the binding phenyl acetylene to **3**. A 2:1 integration ratio of the ^{31}P resonances with a large chemical shift difference is observed, which suggests that significantly greater distortions in the ligand, and potentially the dissociation of one phosphine donor, must occur to accommodate phenyl acetylene binding (Figure A.3.4). This is quite different than what is observed upon the binding of smaller ligands like ethylene or H_2, which both result in the retention of solution-state three-fold symmetry upon binding, as observed by ^{31}P NMR spectroscopy.

*4.2.3 Catalytic Activity Comparison of **2** to Other Ni and First-Row Metal Hydrogenation Catalysts*

Table 4.4 shows how the catalytic performance of NiGaL (**2**) compares to the limited number of homogeneous Ni olefin hydrogenation catalysts in the literature, with the hydrogenation of styrene chosen for comparison since it is a common substrate examined in most catalytic systems. While slightly different catalytic conditions are employed in each case (see Table 4.4 footnotes), the catalysts (pictured in Figure 4.4) are ordered in Table 4.4 based on their reported TOF for ethyl benzene formation.[44, 92, 120, 273, 279-280]

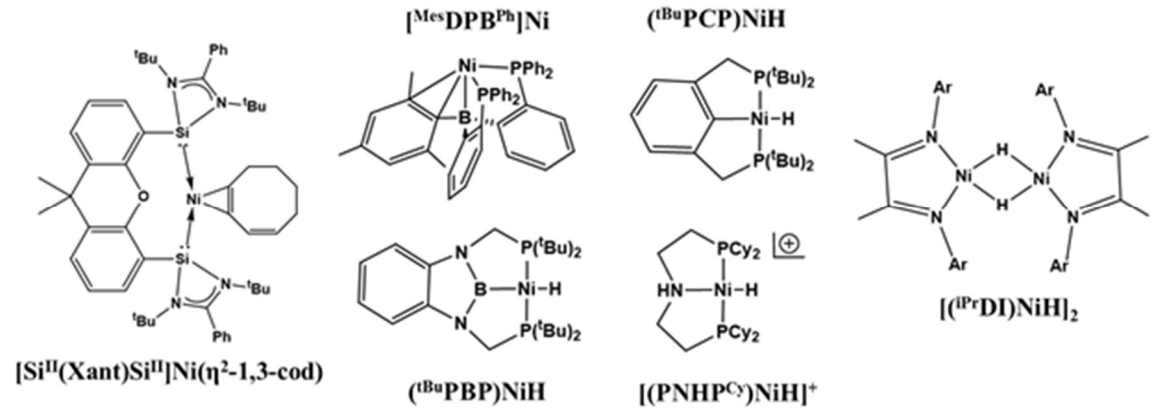

Figure 4.4. Homogeneous Ni catalysts reported in the literature for styrene hydrogenation. Refer to Table 4.4 footnotes for references.

The majority of examples of homogeneous Ni olefin hydrogenation catalysts feature phosphine-based ligands, and often also have some degree of ligand bifunctionality in the form of a coordinated or pendant Lewis acidic or basic group, such as a direct bond to a borane or amine moiety (Figure 4.4).[44, 92, 120, 279] NiGaL (**2**) displays modest catalytic activity in terms of TOF compared with the other Ni catalysts in the literature (Table 4.4).[44, 92, 97, 120, 273, 279-280] That said, slightly different conditions have been employed for the different catalytic systems, which makes meaningful direct comparisons of TOF more difficult. For example, a TOF of 2.4 h^{-1} for NiGaL operating at rt and 1 atm H_2 is arguably superior catalytic performance compared with the *in situ* generated [($^{i\text{Pr}}$DI)NiH]$_2$, which requires 323 K and 4 atm H_2 along with 20 mol% of HBpin as an additive to give TOF = 4 h^{-1} (Table 4.4).[280] In any case, the TOF for **2** is an order of magnitude worse than those of ($^{t\text{Bu}}$PBP)NiH and [$^{\text{Mes}}$DPB$^{\text{Ph}}$]Ni,[44, 120] and two orders of magnitude worse than the best Ni catalyst for styrene hydrogenation reported to date, [Si$^{\text{II}}$(Xant)Si$^{\text{II}}$]Ni(η^2-1,3-cod).[273]

Table 4.4. Comparison of activity of homogeneous Ni catalysts for styrene hydrogenation.[a]

Catalyst	Loading (mol %)	T (K)	P(H_2) (atm)	TOF (h^{-1})
$[Si^{II}(Xant)Si^{II}]Ni(\eta^2\text{-}1,3\text{-cod})$ [b]	0.1	Rt	1	**250**
($^{t\text{Bu}}$PBP)NiH [c]	2	Rt	1	**25**
[$^{\text{Mes}}$DPB$^{\text{Ph}}$]Ni [c]	5	Rt	1	**20**
[($^{i\text{Pr}}$DI)NiH]$_2$ [d]	5	323	4	**4**
NiGaL (**2**) [e]	5	Rt	1	**2.4** [h]
($^{t\text{Bu}}$PCP)NiH [f]	2	Rt	1	**0.7**
[(PNHP$^{\text{Cy}}$)NiH]$^+$ [g]	10	353	4	**0.4**

[a]Overall TON ≈ 100/loading for all catalysts, since all yields were >98%. [b]0.357 M styrene in 3 mL C_6D_6 in Schlenk tube with stirring.[273] [c]In C_6D_6.[44, 120] [d]Catalyst generated *in situ* from 1:1 $Ni(O_2CC_7H_{15})_2$ to $^{i\text{Pr}}$DI ligand, with 20 mol% HBpin additive in C_6D_6.[280] [e]0.087 M styrene in 0.70 mL C_6D_6.[97] [f]Originally reported by Kemp and co-workers.[279] Catalytic activity investigated in C_6D_6 by Peters and co-workers.[120] [g]in THF-d_8 with $[BPh_4]^-$ counteranion.[92] [h]TOF reported as TON/time at 90% conversion time, and J. Young was not re-filled to 1 atm H_2 after initial pressurization.[97]

In addition to its relatively poor TOF, the limited substrate scope for **2** due to steric constraints render it a less versatile catalyst than some of the other catalysts reported. Of note, $[Si^{II}(Xant)Si^{II}]Ni(\eta^2\text{-}1,3\text{-cod})$ allows for the hydrogenation of internal, di-substituted alkenes, including 2-hexene and *trans*-2-stilbene,[273] while [($^{i\text{Pr}}$DI)NiH]$_2$ and the related [($^{\text{Cy}}$ADI)NiH]$_2$ catalysts permit the hydrogenation of tri- and tetra-substituted olefins, albeit with the use of HBpin as an additive and harsher conditions (4 atm H_2, 323 K).[280] It should also be noted that Chirik and Bouwman have also reported other homogeneous Ni olefin hydrogenation catalysts for which styrene hydrogenation was not reported.[171, 281-284] Chirik recently reported *in situ* generated Ni diphosphine catalysts for the asymmetric hydrogenation of tri-substituted alkene moieties in α,β-unsaturated esters.[171] Bouwman and co-workers have reported the high-pressure hydrogenation of 1-octene facilitated by homogeneous Ni catalysts generated from the *in situ* combination of $Ni(OAc)_2$ and various diphosphine ligands, with perhaps the best

result being 1820 turnovers reported in 1 h under 50 bar H_2 in CH_3OH at 298 K using a 1:1 ratio of $Ni(OAc)_2$ to bis(dicyclohexylphosphino)ethane (dcpe).[283-284]

It should also be noted that the activities of most Ni catalysts shown in Table 4.4 pale in comparison to Fe and Co catalysts which represent the state-of-the-art for homogeneous base metal-catalyzed olefin hydrogenation. In particular, Chirik reported a bis(imino)pyridine Fe complex, ($^{i\text{Pr}}$PDI)$Fe(N_2)_2$, which catalyzes styrene hydrogenation with TOF = 1344 h^{-1} and drastically outperforms traditional precious metal catalysts under identical conditions, including 10% Pd/C, Wilkinson's catalyst, and Crabtree's catalyst.[285] In later work, Chirik and co-workers reported efficient hydrogenation of tri-substituted and geminal di-substituted olefins by optimizing catalyst substituent effects for a series of Fe complexes ligated by strong-field N-heterocyclic carbenes and redox-active bis(imino)pyridine ligands.[286-287] Co catalysts have also been recently reported by Chirik and co-workers,[287-288] with enantiopure bis(imino)pyridine Co catalysts reported to mediate the enantioselective hydrogenation of germinal di-substituted olefins,[289] and high-throughput screening of chiral phosphine ligands with simple Co salts reported to facilitate the asymmetric hydrogenation of amino acid and enamide derivatives of relevance to the synthesis of pharmaceutical targets.[290] Lastly, Hanson and co-workers reported a versatile phosphine-ligated Co pincer catalyst capable of mediating the hydrogenation of olefins, ketones, aldehydes, and imines with broad functional group tolerance.[90-91]

Clearly, NiGaL (**2**) does not compare favorably with the state-of-the-art base metal catalysts for olefin hydrogenation when considering either catalytic activity for simple olefins, like styrene, or the propensity to mediate more challenging reactions, such

as the hydrogenation of sterically hindered tri- and tetra-substituted olefins and the asymmetric hydrogenation of germinal di-substituted olefins. Thus, the potentially impactful aspect of **2** as an olefin hydrogenation catalyst does not lie in its catalytic utility, but rather in the fact that the introduction of a supporting metal can modify the properties of Ni to enable catalysis which is not seen for $NiLH_3$ (**4**) and is not typically possible for most Ni complexes. As such, the remainder of this chapter will focus on elucidating the mechanism of olefin hydrogenation catalyzed by **2**, with a particular emphasis on determining the mechanistic role of the supporting metal by comparing the catalytic results for complexes **1**-**4**.

4.2.4 Elucidation the Mechanistic Role of the Supporting Metal in Catalysis

4.2.4.1 Comparison of Catalytic Activity and Selectivity for NiML Complexes

The two supporting metals that induced H_2 binding to NiML complexes at 298 K and 1 atm H_2, M = In (**3**) and Ga (**2**), were the only two complexes found to catalyze any amount of olefin hydrogenation under mild conditions (1 atm H_2, rt). Thus, the catalytic inactivity of $NiLH_3$ (**4**) and NiAlL (**1**) is likely attributable to the fact that initial binding and activation of H_2 is unfavorable for these complexes. Between the two competent catalysts, **2** and **3**, two major differences in catalytic performance were observed. First, catalysis proceeds much more rapidly for **2** than it does for **3**, with about a 25-fold increase in TOF observed for styrene hydrogenation. Secondly, for terminal olefins with allylic protons, **2** catalyzed hydrogenation exclusively, whereas **3** was a nonselective catalyst for both hydrogenation to alkane and isomerization to 2-alkenes. This reactivity is best illustrated by the conversion of 1-octene to octane and 2-octenes in approximately a 1:1 ratio under catalytic conditions for **3**, whereas catalysis with **2** resulted in only

hydrogenation to octane. The divergent reactivity imparted by the various Lewis acid supports motivated in-depth mechanistic studies to understand these differences in rate and product distribution between complexes **2** and **3**.[30, 97]

4.2.4.2 Proposed Olefin Hydrogenation Mechanism

Based on experimental and computational studies, as well as literature precedent, a common mechanistic pathway is proposed for catalysts **2** and **3** (Figure 4.5).[30] The first step in the catalytic cycle is the binding of H_2 to generate the previously discussed (η^2-H_2)NiML adducts (**A**). Olefins were not observed to bind to **2** or **3**, even when present in large excesses in the absence of H_2, which discounted olefin-binding as the first step.[97] Consistent with this, the binding adsorption enthalpy for ethylene was calculated to be more unfavorable than that of H_2 by ~9 kcal/mol, with the greater steric hindrance associated with styrene and other olefins for which catalysis was examined likely making olefin binding even less favorable than that relative to H_2.

The next two steps, olefin binding and H−H cleavage, could occur in either order. Olefin binding requires the dissociation of one of the three phosphine donors because the Ni centers in intermediates **A** and **B** are saturated (Figure 4.5), either electronically (18 electrons) or coordinatively (6-coordinate). In addition to olefin binding with concomitant phosphine dissociation, the initial part of the mechanism must also include H−H cleavage. These three steps could take place in any order to ultimately give intermediate **D** (Figure 4.5).

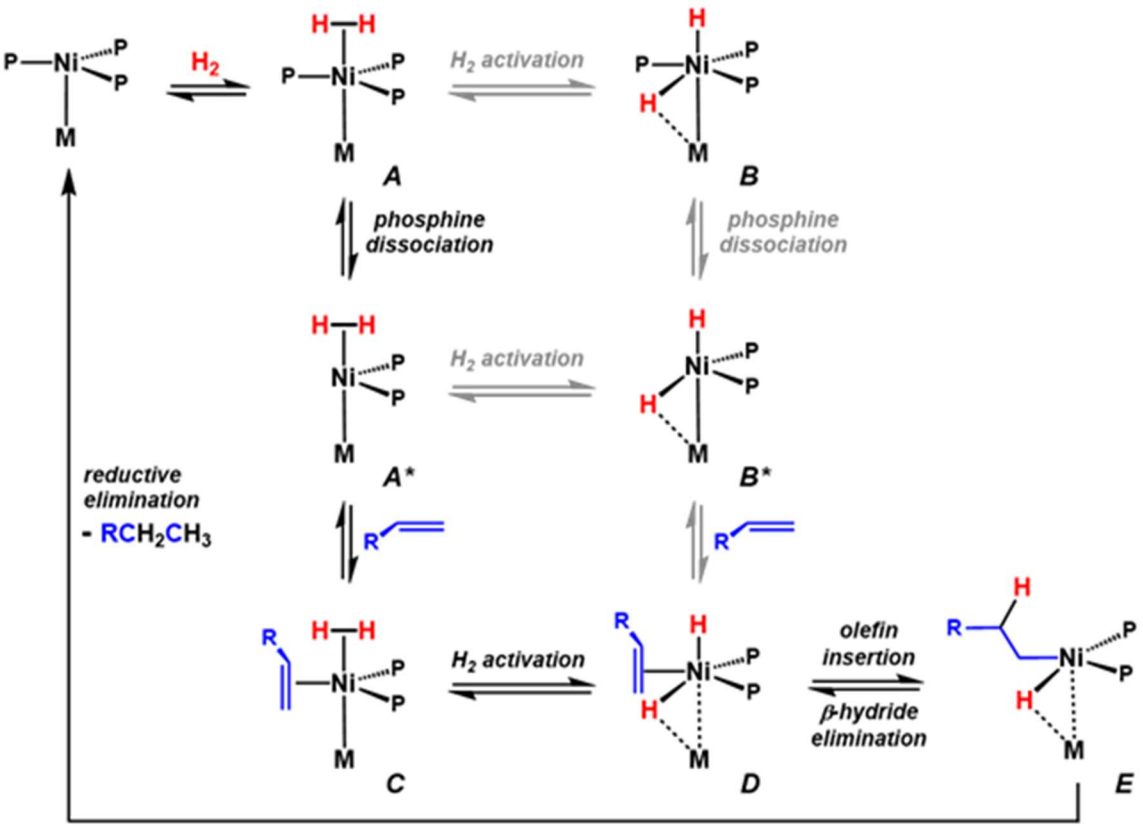

Figure 4.5. Possible mechanistic paths for olefin hydrogenation catalyzed by NiML (M = Ga, In) complexes. A more detailed diagram for the olefin insertion, β-hydride elimination, and reductive elimination steps of the cycle is shown in Figure 4.11. Figure from ref. 30.

Another consideration is the degree to which intermediates formed from H−H cleavage (ie. **B**, **B***, **D**) feature a true bridging hydride, formulated as HNi(μ-H)M in analogy to the HNi(μ-H)B species reported by Peters and co-workers,[44, 117] as alternatively a Ni dihydride species without any interaction of the hydride with the supporting metal could be formed. Experimental and computational studies on the relative viabilities of the possible mechanistic paths for this initial sequence, as well as the proposed formulations of the intermediates, will be presented in the next section. After the initial sequence of H−H cleavage, olefin binding, and phosphine dissociation to form intermediate **D**, olefin insertion into a Ni−H bond gives the Ni alkyl species, **E**,

which can then undergo reductive elimination to liberate alkane and regenerate NiML, completing the catalytic cycle (Figure 4.5).[30]

4.2.4.3 H−H Bond Cleavage and Olefin Binding

Considering the general difficulty of affecting H_2 oxidative addition at a single Ni center, H−H bond cleavage was anticipated to be the rate-determining step (RDS) in the catalysis.[44-45, 272, 291] In support of the involvement of H−H cleavage in the RDS, a primary kinetic isotope effect (KIE) of approximately 1.7(2) was observed for the hydrogenation versus deuteration of styrene catalyzed by **2**.[97] Neglecting the timing of phosphine dissociation for the moment, H−H cleavage could occur directly from the (η^2-H_2)NiML adduct (**A**) to give intermediate **B**, or alternatively it could be preceded by olefin binding (via intermediate **C**). We do not have definitive experimental evidence to rule out either mechanistic pathway, but would like to note four instructive experimental observations that have informed our thinking on this matter:

(1) If rate-determining H−H cleavage were to occur directly from (η^2-H_2)NiML (**A**), one might expect the Ni−In species to have a lower barrier, or at least a comparable one, to that of Ni−Ga, since the H−H distance is slightly more elongated in **3**−H_2 (0.91 Å) relative to that in **2**−H_2 (0.87 Å). However, this is contrary to the observation that catalysis is significantly slower for **3** relative to **2** (*vide supra*).[97] It should be noted that the greater elongation in **3**−H_2 compared to **2**−H_2 is predicted to be predominantly due to increased σ-donation rather than π-back-donation, so perhaps the degree of elongation is not directly tied to the ease of oxidative H−H cleavage.[30, 45] A complicating factor in thinking about the relative ease of H−H cleavage from (η^2-H_2)NiML is that the supporting metal may

also participate to some extent in H−H cleavage to stabilize a bridging hydride moiety in the transition state, products, or both. This nuance will be considered computationally in the next section.

(2) As a corollary, if H−H cleavage proceeded directly from **A** or **A*** prior to olefin binding, then a logical implication is that the H_2 cleavage step could proceed in the absence of olefin. If **B** or **B*** could be formed *in situ* from H_2 and NiML in the absence of olefin, then one might expect that using a H_2/D_2 gas mixture would lead to isotopic scrambling to generate HD. However, no isotopic scrambling was observed for either **2** or **3** upon exposure to H_2/D_2 or HD in the absence of olefin, even with extended heating at 353 K (Figures A.3.5-A.3.6). While this observation does not definitively rule out intermediates **B** and **B*** in the presence of olefin, it does suggest that they are of sufficiently high energy that they are likely not readily accessible.[30, 97]

(3) Catalytic resting state studies are often useful to identify the dominant species that builds up prior to the RDS, though one must be wary of the buildup of off-cycle species as well. The (η^2-H_2)NiML species (**A**) is the observed resting state for catalysis with **3**, as well as with **2** when observed below 233 K. At rt under catalytic conditions for **2**, the ^{31}P NMR spectra are characterized by a single, broad ^{31}P resonance with a chemical shift ranging from 40 to 47 ppm depending on the quantity and identity of the olefin present. A rapid equilibrium between phosphine binding and olefin binding was originally proposed (**A**→**A***→**C**) based on the dependence of the chemical shift on olefin identity and the lack of correspondence of the catalytic resting state peaks to **2**−H_2, **2**, or an olefin

adduct.[30, 97] However, subsequent studies on H_2 binding, which were discussed in chapter 3, showed that the ^{31}P chemical shift varies from 37.6 to 56.9 ppm depending on the H_2 pressure and T. Thus, it is now proposed that **2**−H_2 (**A**) is the catalytic resting state at rt for complex **2** as well, and that the observed dependence of the ^{31}P chemical shift for the resting state on olefin was simply a consequence of different degrees of hydrogenation and depletion of the H_2 atmosphere for different substrates and reaction times. That the H_2 adduct is the catalytic resting state is consistent with the RDS involving H−H cleavage, and while this observation may seem to favor a mechanism in which H−H cleavage precedes olefin binding, it cannot definitively rule out a scenario where H−H cleavage is triggered by olefin binding.

(4) Lastly, the preliminary hydrogenation results for a series of *para*-substituted styrene derivatives (R=H, Cl, F, CF_3) suggests that increasing electron-richness of the olefin generally increases the rate of reaction. The rates of hydrogenation for 4-(trifluoromethyl)styrene and 4-fluoro-styrene were found to be ~3 times and ~1.5 times slower, respectively, than that observed for styrene (Figure A.3.7). Though the relative rates were not observed to correlate with the Hammett substituent parameters to give a linear free energy relationship,[292-293] the general observation of faster catalytic hydrogenation for more electron-rich olefins is consistent with the favorability of olefin binding impacting the reaction rate.

Collectively, these experimental observations do not allow us to definitively rule out either order of the initial sequence of H_2 binding and olefin binding. The primary KIE and the fact that the H_2 adduct is the catalytic resting state prior to the RDS both support

the involvement of H−H cleavage from the H_2 adduct in the RDS. The influence of the electron-richness of olefin, as well as the fact that H_2/D_2 scrambling does not take place in the absence of olefin, both provide support for a mechanism involving olefin binding which triggers H−H cleavage.[30]

Often experimental rate laws can be useful for distinguishing mechanistic possibilities. In this case, two mechanistic possibilities were considered: (1) rate-determining H−H cleavage from **A**, with intermediate **B** as a steady-state intermediate that rapidly binds olefin (or eliminates H_2) upon generation, and (2) a rapid olefin binding pre-equilibrium between **A** and **C**, followed by H−H cleavage from **C** to give **D** (Figure 4.5). The rate laws derived for mechanism 1 and 2 are shown in Equations 4.1 and 4.2, respectively, where K_{H_2} is the H_2 binding equilibrium constant (to form **A**), k_{het} and k_{-het} are the forward and reverse rate constants for H−H cleavage (**A**→**B**), k_{olefin} is the rate constant for olefin binding to **B** to give **D** (presumably via **B***), and $K_{pre,olefin}$ is the equilibrium binding constant for olefin binding to **A** to give **C** (Figure 4.5).[294]

$$\text{Rate} = \frac{K_{H_2} k_{het} k_{olefin}[H_2][NiML][olefin]}{k_{-het} + k_{olefin}[olefin]} \qquad \text{(Eqn 4.1)}$$

$$\text{Rate} = K_{H_2} K_{pre,olefin}[H_2][NiML][olefin] \qquad \text{(Eqn 4.2)}$$

It is likely that $k_{-het} >> k_{het}$ since **B** has not been observed under any conditions and the catalytic resting state is **A**.[30, 97] Therefore, it seems reasonable to conclude that $k_{-het} >> k_{olefin}\cdot[olefin]$, which allows for the simplification of the rate law for mechanism 1 (Equation 4.1) to give Equation 4.3, where K_{het} is the H_2 heterolysis equilibrium constant for **A**→**B** ($K_{het} = \frac{k_{het}}{k_{-het}}$). Alternatively, if one assumes that $k_{-het} <<$

k_{olefin}·[olefin], the rate law for mechanism 1 simplifies to the expression given in Equation 4.4.

$$\text{Rate} = K_{H_2} K_{het} k_{olefin} [H_2][\text{NiML}][\text{olefin}] \qquad \text{(Eqn 4.3)}$$

$$\text{Rate} = K_{H_2} k_{het} [H_2][\text{NiML}] \qquad \text{(Eqn 4.4)}$$

Thus, it can be seen by comparing Equations 4.3 and 4.2, that the rate law shows a first-order dependence on H_2, NiML, and olefin for both mechanistic possibilities, if $k_{-het} << k_{olefin}$·[olefin]. Of relevance, preliminary rate law studies found the rate to be approximately first-order in olefin concentration, consistent with the limiting assumption that $k_{-het} << k_{olefin}$·[olefin] (Equations 4.1 and 4.3). Therefore, the rate law likely cannot be used to distinguish these two different sequences of olefin binding and H−H cleavage. While the dependence of the rate on H_2 pressure and NiML catalyst concentration was not studied, it is hypothesized that first-order dependence on both would be observed for both mechanisms.

*4.2.4.4 Experimental and Theoretical Studies of Ni−P Lability: the Propensity of (η^2-H_2)NiML Complexes to Bind Olefin to Generate Intermediate **C** and Other P_2Ni(L)(L') Complexes*

Given the relevance of the dissociation of one of the three phosphine donors to open a coordination site at Ni to bind olefin, we sought to study how the lability of Ni−P bonds and the propensity to coordinate olefin to (η^2-H_2)NiML complexes (**A**→**C**) depends on the supporting metal. Of relevance, a similar mechanistic pathway in which olefin binding to a M(η^2-H_2) complex occurs with concomitant dissociation of one phosphine donor of a chelating, multi-dentate phosphine ligand was proposed for olefin hydrogenation by an Fe catalyst.[45, 295-296] The addition of olefins to (η^2-H_2)NiML did not

allow for the direct observation of any new species by NMR spectroscopy from 193 K to 298 K, as only the H_2 adduct catalytic resting state and hydrogenated products were observed.[97] Thus, other means of probing the lability of Ni−P bonds and the propensity to coordinate additional ligands were needed.

With this aim in mind, recall that it was originally proposed in section 2.2.4 that the coalescence of the methylene CH_2 protons of the ligand, as observed via ^{1}H NMR spectroscopy, is an indirect gauge of the fluxionality of the ligand arms in bimetallic M'ML complexes. For the methylene protons of NiML complexes to coalesce and resonate as a single peak, they must be rendered chemically equivalent on the ^{1}H NMR timescale by a fluxional process. The thermal energy required for this fluxional process to occur, and thus its free energy barrier, can be quantified by measuring the temperature at which the coalescence of the methylene protons occurs (T_c). Measurement of barriers to the coalescence of diastereotopic ligand protons have been previously reported by Bourissou for similar *C*$_3$-symmetric "propeller"-type M→B complexes, as well as by previous researchers in our laboratory for MM'L complexes.[101, 132, 138] Importantly, this fluxional process which allows for methylene coalescence is thought to involve increased ligand flexibility via M−P bond weakening or cleavage, and so the free energy barriers for methylene coalescence ($\Delta G^{\ddagger}_{MC}$) can serve as an indirect indicator of the ease with which Ni−P bonds in NiML and (η^2-H_2)NiML complexes are able to weaken or dissociate.

The fluxional process which permits methylene coalescence has been previously proposed to occur via one of two possible mechanisms: (1) initial dissociation of one phosphine donor, followed by rotation and re-coordination such that the P−Ni−M−N_{eq}

dihedral angles goes from +x° to −x° with the retention of C_3 symmetry, which prompts the other phosphines to reorient similarly so as to invert the overall helicity of the C_3 propeller-like geometry; or (2) a concerted, "rocking" process by which all three ligand phosphine arms simultaneously flip rapidly between two opposite C_3-propellor geometries, such that on average, solution-state C_{3v} symmetry is observed on the ^{1}H NMR timescale (Figure A.3.8).[101, 132, 138, 297-298] Both of these mechanisms as applied to our system would involve either the complete or partial lability of the Ni−P bonds, and so it is logical that weaker Ni−P bonds would correlate with a lower free energy barrier to methylene coalescence ($\Delta G^{\ddagger}_{MC}$). Because a phosphine donor must dissociate to allow olefin binding to occur, the measurement of the relative $\Delta G^{\ddagger}_{MC}$ values for **2**−H_2 and **3**−H_2 relative to **2** and **3** would provide quantitative information about the lability of their respective Ni−P bonds, which is implicated in one of the two mechanistic pathways being considered (**A**→**A***→**C**).

In order to determine $\Delta G^{\ddagger}_{MC}$ for each complex, the coalescence temperature (T_c) and the maximum peak separation ($\Delta\nu$) were measured by VT ^{1}H NMR spectroscopy. Equation 4.1 shows the calculation of $\Delta G^{\ddagger}_{MC}$ as a function of T_c and $\Delta\nu$, where R is the ideal gas constant, N_A is Avagadro's number, and h is Planck's constant.[231, 298]

$$\Delta G^{\ddagger}_{MC} = RT_c*\ln[1.414*RT_c/(\pi*N_A*h*\Delta\nu)] \qquad \text{(Eqn 4.1)}$$

A representative set of VT ^{1}H NMR spectra is shown for complex **2** in Figure 4.6 to illustrate the measurement of T_c and $\Delta\nu$. As shown in Figure 4.6, one resonance is observed above T_c, which becomes broader as T decreases towards T_c. The two diastereotopic CH_2 protons become inequivalent below T_c, and their mutual coupling to one another gives rise to a set of leaning doublets, as seen in the 296 K spectrum in

Figure 4.6. In this manner, $\Delta G^{\ddagger}_{MC}$ was calculated using the measured T_c and $\Delta\nu$ values for each complex and Equation 4.1. While the mechanistically relevant $\Delta G^{\ddagger}_{MC}$ values are those of **2**−H_2 and **3**−H_2 in comparison to those of **2** and **3**, $\Delta G^{\ddagger}_{MC}$ values were also determined for complexes **1**, **4**, **2**−CO, **3**−CO, and **3**−N_2 to aide in recognizing the factors which dictate $\Delta G^{\ddagger}_{MC}$ (Figure 4.7, Table 4.5).

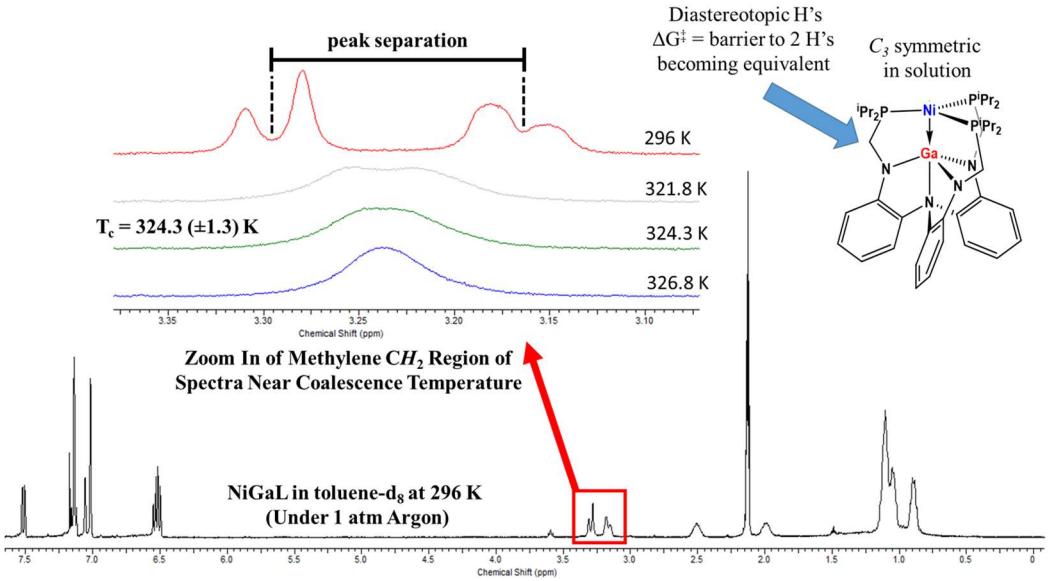

Figure 4.6. VT ^{1}H NMR spectra (toluene-d_8, 400 MHz) for complex **2** shown to illustrate the measurement of the coalescence temperature (T_c) and the maximum peak separation ($\Delta\nu$). ^{1}H NMR spectra were acquired every 2.5 K near T_c; T_c was determined to be 324.3 (±1.3) K for **2** based on these spectra. The diagram shows the peak separation visually; however, it should be noted that the maximum peak separation was not actually observed at 296 K for **2**, but instead at much lower T.

As shown in Figure 4.7 and Table 4.5, the free energy barrier to methylene coalescence, $\Delta G^{\ddagger}_{MC}$, typically decreases by 1-2 kcal/mol upon the apical binding of H_2, N_2, or CO ligands. $\Delta G^{\ddagger}_{MC}$ decreases by 0.6 and 1.2 kcal/mol upon CO and H_2 binding to **2**, respectively, and by 2.0, 2.2, and 2.5 kcal/mol for H_2, N_2, and CO binding to **3**, respectively (Table 4.5). In light of the lower $\Delta G^{\ddagger}_{MC}$ values for **2**−H_2 and **3**−H_2 relative to their respective NiML complexes, it is clear that Ni−P bonds become more labile upon binding H_2. Thus, phosphine dissociation is more likely to occur after H_2 binding, as

expected based on the observation by ^{31}P NMR spectroscopy of the H_2 adducts as the catalytic resting states. Comparing amongst the complexes most relevant to olefin hydrogenation catalysis, **3**−H_2 has a lower $\Delta G^{\ddagger}_{MC}$ value by 1.5 kcal/mol compared to **2**−H_2 (Table 4.5).

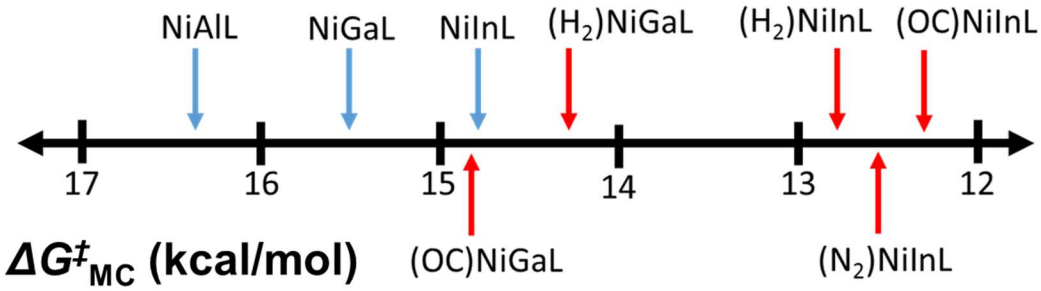

Figure 4.7. Timeline visually displaying $\Delta G^{\ddagger}_{MC}$ (in kcal/mol) for NiML and (L')NiML complexes (M=Al, Ga, In; L'=H_2, N_2, CO).

Table 4.5. Methylene coalescence data for NiML, $NiLH_3$, and (L')NiML complexes (M=Al, Ga, In; L'=H_2, N_2, CO).[a]

Complex	Tc (K)	Δν (Hz)	$\Delta G^{\ddagger}_{MC}$ (kcal/mol)
NiAlL (**1**)	347.3	167 (±10)	16.4 (±0.1)
NiGaL (**2**)	324.3	111 (±10)	15.5 (±0.1)
NiInL (**3**)	292.3	24 (±2)	14.8 (±0.1)
$NiLH_3$ (**4**)	295.9	121 (±10)	14.0 (±0.1)
2−H_2	305.7	162 (±6)	14.3 (±0.1)
3−H_2	280.5	266 (±12)	12.8 (±0.1)
3−N_2	274.0	212 (±10)	12.6 (±0.1)
2−CO	317.1	173 (±5)	14.9 (±0.1)
3−CO	268.7	240 (±5)	12.3 (±0.1)

[a]Note that T_c values all have error bars of ±1.3 K.

The trend of greater $\Delta G^{\ddagger}_{MC}$ values for M=Ga than for M=In that was observed for **2**−H_2 and **3**−H_2 also holds true for NiML complexes, with $\Delta G^{\ddagger}_{MC}$ of 15.5(1) and 14.8(1) for complexes **2** and **3**, respectively (Table 4.5). In general, complexes with stronger Ni→M dative interactions (In > Ga > Al) within each isostructural series (ie. NiML and

(L')NiML) tend to have elongated Ni−P solid-state bond distances and lower $\Delta G^{\ddagger}_{MC}$ values, as shown by the qualitative trend in Figure 4.8. This inverse relationship between Ni→M and Ni−P bond strengths makes intuitive sense given the previously discussed importance of Ni→P π-back-donation: the phosphines compete for electron donation from Ni(0) with M(III), and thus more Ni→M dative electron donation results in less Ni→P π-back-donation, which results in elongated and more labile Ni−P bonds with lower associated $\Delta G^{\ddagger}_{MC}$ values (Figure 4.8).[97] Hence, another important role of the group 13 support in catalysis may be to induce different degrees of phosphine lability and/or olefin affinity through the Ni→M interaction.[30]

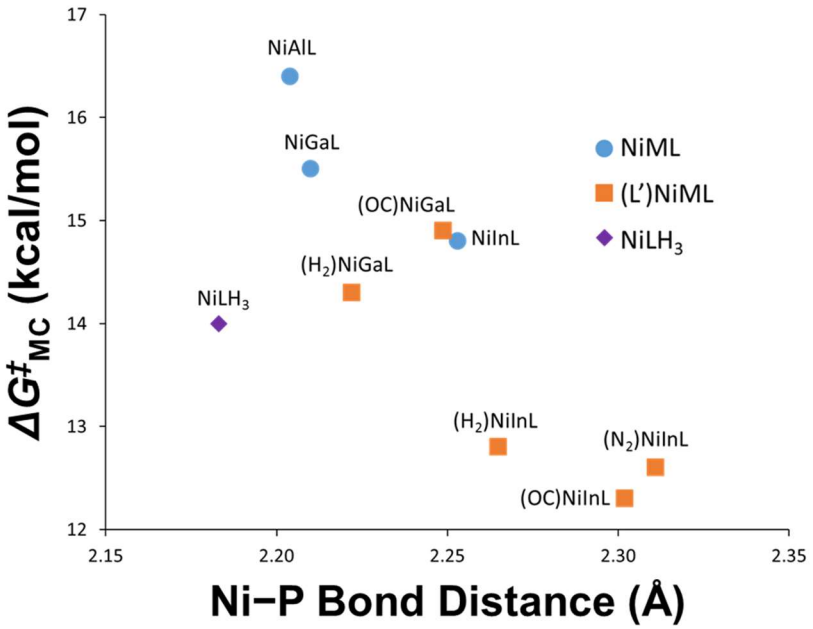

Figure 4.8. Plot of $\Delta G^{\ddagger}_{MC}$ for NiML, and (L')NiML complexes (M=Al, Ga, In; L'=H_2, N_2, CO) vs. average Ni−P solid-state distance (from x-ray structures).

The only real outlier to the qualitative trend between $\Delta G^{\ddagger}_{MC}$ and Ni−P bond distance is $NiLH_3$, which has a lower $\Delta G^{\ddagger}_{MC}$ value than its short Ni−P distance would suggest (Figure 4.8). It is hypothesized that this abnormally low barrier is the result of all other bimetallic complexes being "tethered" at two points on each phosphine arm, via

M−N_{eq} and Ni−P bonds, whereas $NiLH_3$ has no second point of attachment on each ligand arm apart from the Ni−P bonds. Thus, it makes sense in retrospect that $NiLH_3$ would have a greater degree of flexibility than might otherwise be expected. The one-point ($NiLH_3$) versus two-point (NiML) tethering effect presumably has a large impact on the relative $\Delta G^{\ddagger}_{MC}$ values, as otherwise the introduction of the supporting metal would be expected to lower $\Delta G^{\ddagger}_{MC}$ relative to $NiLH_3$ by rendering Ni more electron-poor, thereby reducing Ni→P π-back-donation and increasing the Ni−P lability.

As a side note on methylene coalescence, the determination of $\Delta G^{\ddagger}_{MC}$ for the isostructural series of NiML complexes, along with associated computations regarding the two possible mechanisms for methylene coalescence, allow for some insight into which of the mechanisms may be more feasible. Previous systematic studies by Bourissou and by our lab were complicated by the fact that different metals were bonded to the phosphines; perhaps more can be learned from this series of NiML complexes since this confounding factor has been eliminated.[101, 138] A strong correlation is observed between the experimental $\Delta G^{\ddagger}_{MC}$ values for NiML complexes and the DFT-calculated barrier for a C_{3v} symmetric structure that would be the transition state for the concerted "rocking" mechanism, where the P−Ni−M−N_{eq} angle was constrained to be 0 degrees (R^2=0.996, Figure A.3.9). In comparison, the calculated energies of one of the phosphine arms dissociating from NiML was also evaluated by DFT as a proxy for the favorability of the methylene coalescence mechanism involving phosphine dissociation and re-coordination, and a qualitative correlation with $\Delta G^{\ddagger}_{MC}$ values (Al > Ga > In for both) was observed (R^2=0.819, Figure A.3.10). The better correlation of the calculated values for the concerted "rocking" mechanism with the experimental $\Delta G^{\ddagger}_{MC}$ values leads us to favor

the concerted "rocking" mechanism, though we cannot rule out the phosphine dissociation mechanism. Lastly, one other clue to consider, albeit one which does not intuitively favor one mechanism or the other, is that the methylene and methine protons often coalesce at different T, as previously seen for complex **3** at 298 K in Figure 2.4.

*4.2.4.5 P_2Ni(L')(L'') Complexes as Model Complexes for Intermediate **C**: Evidence for an Inverse Correlation of Ni−P Lability and the Propensity of P_3Ni(L') to Coordinate L''*

The low $\Delta G^{\ddagger}_{MC}$ and T_c for the fluxional process that allows for methylene coalescence for **2**−H_2 (T_c = 305.7 K) and **3**−H_2 (T_c = 280.5 K) show that the Ni−P bonds in these complexes are somewhat labile at or near the ambient conditions under which catalysis is performed. To assess the viability of an olefin hydrogenation mechanism involving phosphine dissociation and olefin binding prior to H−H cleavage (**A**→**A***→**C** in Figure 4.5), the relationship between phosphine lability, as measured indirectly by $\Delta G^{\ddagger}_{MC}$, and the propensity of **2**−H_2 and **3**−H_2 to bind an added ligand was of interest. While it would be ideal to study olefin binding to the (η^2-H_2)NiML complexes, this was not feasible because such experiments resulted in hydrogenation proceeding without the observation of olefin binding by NMR spectroscopy. Likewise, the addition of olefins which were unable to be hydrogenated was similarly unfruitful as far as observing binding, likely because the inability to bind bulky olefins contributes to the lack of hydrogenation in those cases.[30, 97] Therefore, the binding of other exogenous donor ligands to **2**−H_2 and **3**−H_2 by the displacement of one of the three ligand phosphine donors was explored to assess the propensity to form P_2Ni(L')(L'') complexes as models for intermediate **C**, where "P_2" represents the coordination of two of the three phosphine donors of L, L'=H_2, and L'' is an added ligand.

The addition of trimethylphosphine (PMe_3), a monodentate phosphine ligand which is a strong σ-donor, to **2**−H_2 and **3**−H_2 was initially attempted, but because PMe_3 is a much stronger ligand than H_2, PMe_3 simply displaced H_2, and the results were similar to when PMe_3 was added to **2** and **3** without H_2 present (Figure 4.9). Assessing the reactivity of (L')NiML complexes, where L' is PMe_3 rather than H_2, with added L'' ligand, where L'' is also PMe_3, was carried out instead. While it is definitely debatable whether this is a reasonable model of the coordination of olefin to **A*** to form intermediate **C**, this is the best available comparison at this time for the binding of olefin to (η^2-H_2)NiML. Figure 4.9 shows a comparison of the reactivity of (L')NiML complexes with added L'' ligand for M=Ga and M=In, for the case where L'= L''= PMe_3.

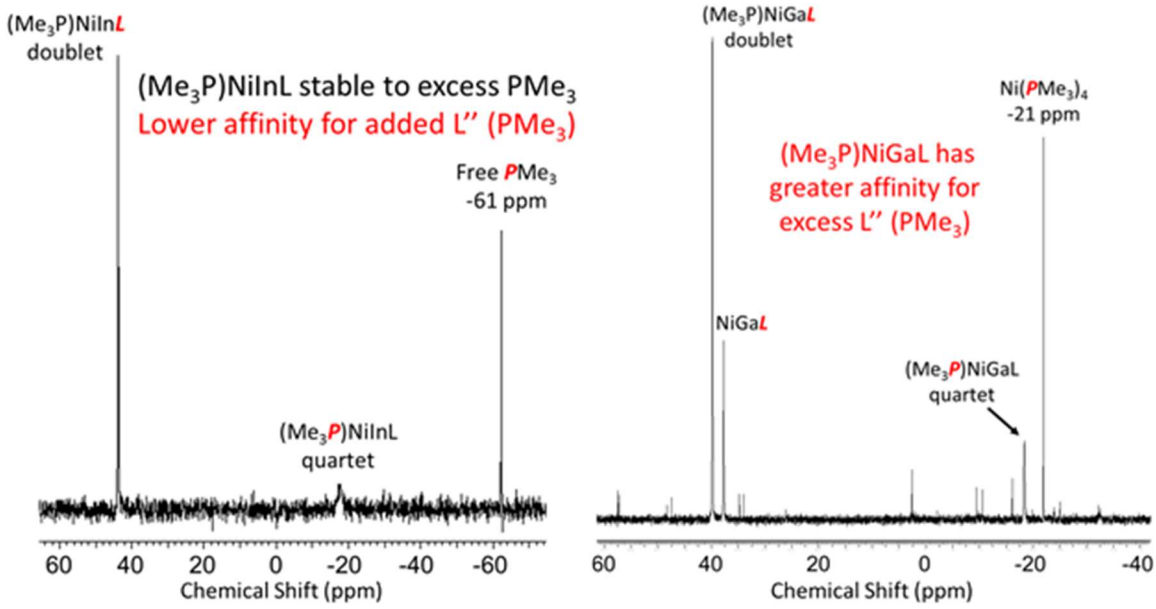

Figure 4.9. ^{31}P NMR spectra acquired after initial addition of excess PMe_3 to NiInL (**3**, left) and NiGaL (**2**, right).

For **3**, clean formation of a terminal PMe_3 adduct, **3**-PMe_3, was observed based on diagnostic ^{31}P NMR resonances at 44 ppm and −16.4 ppm which integrate in approximately a 3:1 ratio (Figure 4.9). Excess PMe_3 (^{31}P δ = −62.6 ppm[299]) is the only

other species observed, which indicates that **3**-PMe_3 is stable to excess PMe_3, at least over this initial timescale. In contrast, the addition of excess PMe_3 to **2** generates **2**-PMe_3, characterized by a doublet at 40 ppm (J_{PP} = 11.5 Hz) and a poorly resolved quartet at −18.6 ppm, but also results in the formation of several other species (Figure 4.9). Among them, a large amount of $Ni(PMe_3)_4$ (^{31}P δ = −21.8 ppm[300]) is formed, indicating that **2**-PMe_3 is unstable to excess PMe_3. Some NiGaL (**2**) is also observed, along with other unidentified species, which could be $P_2Ni(PMe_3)_2$ or $PNi(PMe_3)_3$ species which form prior to the coordination of additional PMe_3 ligands to form $Ni(PMe_3)_4$.

While these experiments are admittedly preliminary, a few important insights from the results that are worth highlighting. The first is that **2**-PMe_3 has a greater affinity for coordinating additional PMe_3 ligands than **3**-PMe_3, although it should be noted that over longer timescales **3**-PMe_3 was also observed to eventually form $Ni(PMe_3)_4$ to some extent also. Given that more labile Ni−P bonds with lower $\Delta G^{\ddagger}_{MC}$ were observed for stronger Ni→M interactions (In > Ga) in isostructural NiML, (η^2-H_2)NiML, and (OC)NiML complexes, one would expect that the trend of lower $\Delta G^{\ddagger}_{MC}$ and more labile phosphines would also hold true for comparing **3**-PMe_3 to **2**-PMe_3. Therefore, although phosphine dissociation must occur to allow olefin to bind, it is proposed that a complex with more labile phosphines will likely have a lower propensity to coordinate added olefin in this NiML system. This proposal is based on the relative stabilities of **3**-PMe_3 and **2**-PMe_3 to excess PMe_3, where decreased reactivity toward added PMe_3 is observed for **3**-PMe_3, which should have more labile Ni−P bonds. In other words, a Ni center which does not coordinate strong ligands like chelating phosphines tightly will also not show a high affinity for added monodentate ligands, like PMe_3 or olefins, either.

In applying this proposal to the catalytic mechanism, these experiments suggest that **2**−H_2 ($\Delta G^{\ddagger}_{MC}$ = 14.3 kcal/mol) would more readily bind olefin to form intermediate **C** than would **3**−H_2 ($\Delta G^{\ddagger}_{MC}$ = 12.8 kcal/mol). Thus, by this logic, the mechanistic pathway from **A**→**A***→**C** should be more favorable under catalytic conditions for **2** than for **3** (Figure 4.5). And while the alternative pathway, which involves phosphine dissociation and olefin binding after H−H cleavage (**B**→**B***→**D** in Figure 4.5), cannot be probed experimentally due to the inability to observe H−H cleavage, it is likely that this path would also be more catalytically viable for **2** compared with **3** based on the validity of the trends in $\Delta G^{\ddagger}_{MC}$ values (In < Ga) for NiML, (η^2-H_2)NiML, and (OC)NiML isostructural series. In summary, the supporting metal indirectly induces different degrees of phosphine lability and affinities for binding added ligands for (L')NiML complexes through the relative strength of its dative electron withdrawal from Ni. Therefore, olefin binding to (η^2-H_2)NiML (**A**) and $(H)_2$NiML (**B**) species, with concomitant dissociation of one phosphine ligand, is proposed to be more facile for M=Ga than for M=In, which could potentially be a contributing factor to the faster catalytic hydrogenation rates observed for **2** compared with the rates for **3**.

4.2.4.6 Computational Insight into Initial Mechanistic Sequence and H−H Cleavage from (η^2-H_2)NiML Complexes

Since experimental studies regarding the order in which H−H cleavage and olefin binding occur in the catalytic mechanism were ambiguous, computational studies were utilized to help clarify the initial sequence of events. DFT calculations (M06-L[176]/bs1; see section 4.4.3 for more details) support H−H cleavage from (η^2-H_2)NiML as the first

step (**A**→**B**), followed by phosphine dissociation (**B**→**B***) and subsequent olefin coordination (**B***→**D**).

Initial olefin binding to **2**−H_2 (**A**→**C**) was calculated to be unfavorable by 23.5 kcal/mol, whereas initial H−H cleavage from **2**−H_2 (**A**→**B**) was predicted to be unfavorable by 17.3 kcal/mol via a transition state with a barrier of 20.8 kcal/mol in benzene (Figure A.3.11). The magnitude of the transition state barrier is consistent with H−H cleavage being a challenging step under ambient conditions, and it is proposed that H_2 binding and loss occurs rapidly many times prior to oxidative addition occurring based on the kinetic studies presented in chapter 3 and literature precedent for such behavior.[45, 201, 204, 206] Computations were also particularly helpful in determining the likely timing of phosphine dissociation relative to H−H cleavage and olefin binding. Phosphine dissociation is predicted to be most favorable after initial H−H cleavage, with **B** and **B*** predicted to be approximately iso-energetic in benzene. In contrast, phosphine dissociation from the H_2 adduct (**A**→**A***) is predicted to be unfavorable by ~19.6 kcal/mol in benzene (Figure A.3.11).

With the initial sequence of mechanistic events predicted to be **A**→**B**→**B***→**D** by DFT calculations, the roles of Ni and the supporting metal in the H−H cleavage step were also examined via computations. Recently, Ke and co-workers discussed the viability of four different H_2 activation mechanisms for the (^{Mes}DPB^{Ph})Ni complex reported by Peters and co-workers, and we sought to compare the mechanism of H−H cleavage for the (η^2-H_2)NiML complexes to their results.[44, 117, 291] The possibilities examined by Ke and co-workers include two different variations each of homolytic and heterolytic H−H cleavage mechanisms. The synergetic heterolytic mechanism, where H_2 is activated via

cooperative activation by the Lewis basic Ni center and the Lewis acidic borane in the transition state, was predicted to be the preferred pathway.[291] Two of the mechanisms examined, the cis homolytic and dissociative heterolytic mechanisms, are not feasible for NiML due to the Ni→M interaction being far less accessible to H_2 than the Ni→B interaction in the (^{Mes}DPB^{Ph})Ni system. Thus, in the terminology of Ke and co-workers, the two possibilities for H_2 activation for NiML complexes were: (1) a *trans* homolytic mechanism, where the H−H bond is oxidatively cleaved at Ni, with no direct interaction of H_2 with the supporting metal in the transition state, and (2) the synergetic heterolytic pathway, where cooperative activation of H_2 occurs across the Ni→M bond.[291] Essentially, the two mechanisms differ in whether the Lewis acidic supporting metal is directly involved in the transition state for H−H cleavage, with both mechanisms allowing for the possibility of stabilization of a bridging hydride by the supporting metal in the product of H−H cleavage (**B**).

The computed energy profile for H_2 binding and H−H cleavage for the NiML (M=Al, Ga, In) complexes is shown in Figure 4.10, along with a diagram showing the general structure of the transition state (**TS**) and intermediate **B**, which correspond to the labels given in Table 4.6 for the optimized structural metrics for these species.

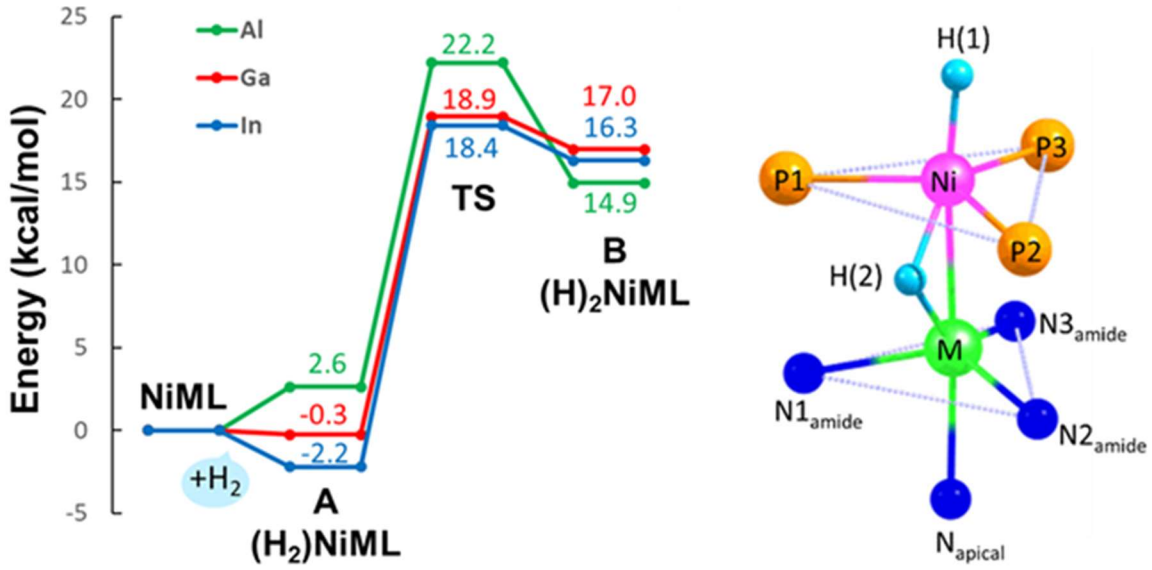

Figure 4.10. Energy profile (left) for H_2 binding and H−H cleavage for NiML (M=Al, Ga, In) complexes, relative to the energy of NiML + H_2 (left). Energies given are free energies at 298 K and 1 atm H_2 in THF (SMD solvation model[181]) computed using M06-L[176]/bs1 method. A similar energy profile in benzene shows similar results for NiGaL (2), and is shown in Figure A.3.11. The general structure of the transition state (**TS**) and $(H)_2$NiML (**B**) complexes, the latter of which could be more precisely formulated as HNi(μ-H)ML, is also shown (right), with the structural metrics for **TS** and **B** which correspond to this general structure given in Table 4.6.

The Ni−H distances in **TS** (1.46 to 1.58 Å) and in intermediate **B** (1.48 to 1.52 Å) are observed to contract relative to those in the H_2 adducts (1.63 to 1.66 Å), consistent with the formation of discrete Ni−H bonds upon H−H cleavage (Table 4.6). The most striking structural metrics that inform whether the supporting metal is involved in the transition state for H−H cleavage are the M−H(2) distances in **TS** and **B**. Specifically, the M−H(2) distances are very long in the **TS** (2.68 to 2.82 Å), suggesting no direct interaction of the hydride with the supporting metal. The M−H(2) distances become much shorter in the species that results from H−H cleavage (**B**), with distances ranging from 1.75 to 1.96 Å (Table 4.6). This dramatic difference suggests that after initial H−H cleavage at Ni, H(2) then becomes stabilized by interacting with the supporting metal, to some extent, as a bridging hydride moiety. Visualization of the imaginary vibrational

frequencies of the transition states reveals that homolytic H−H cleavage at Ni is predicted, followed by the stabilization of the resulting dihydride, $(H)_2$NiML, by the supporting metal to form a bridging hydride species, HNi(μ-H)ML.

Table 4.6. Comparison of DFT-optimized (M06-L[176]/bs1) structures of (η^2-H_2)NiML (**A**), the transition state for H−H cleavage (**TS**) and the resulting $(H)_2$NiML dihydride (**B**) complexes.[a]

	Al			Ga			In		
Metric	**A**	**TS**	**B**	**A**	**TS**	**B**	**A**	**TS**	**B**
Ni−H(1)	1.662	1.575	1.502	1.650	1.468	1.510	1.633	1.561	1.515
Ni−H(2)	1.663	1.465	1.489	1.649	1.562	1.501	1.639	1.476	1.500
M−H(2)	–	2.815	1.749	–	2.665	1.831	–	2.682	1.960
H−H	0.827	2.299	2.885	0.830	2.331	2.835	0.835	2.398	2.857
∠Ni−H(2)−M	–	64.7	110.9	–	66.0	98.6	–	69.3	97.2
Ni−M	2.6	2.558	2.670	2.499	2.464	2.536	2.603	2.565	2.613
Ni to P_3-plane	0.29	0.23	0.18	0.30	0.22	0.16	0.37	0.28	0.23
M to N_3-plane	0.29	0.29	0.20	0.42	0.41	0.33	0.43	0.40	0.35

[a]Note that H(1) and H(2) are the terminal and bridging hydrides, respectively, in **TS** and **B** (see Figure 4.10).

The extent to which H(2) (Figure 4.10) is a true bridging hydride is debatable, and presumably varies as a function of the supporting metal. Figure 4.11 shows two reported examples of a bridging hydride between a late transition metal and group 13 M(III) moiety, which are useful to compare against to assess whether the computed Ni−H(2) and M−H(2) distances are consistent with a true bridging hydride.[301]

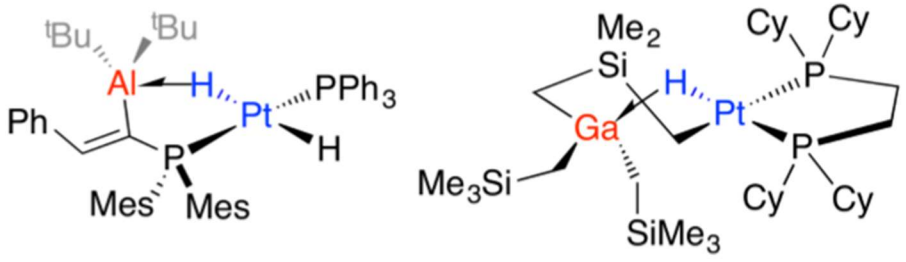

Bourissou 2016 Fischer 2004

Figure 4.11. Examples of hydrides bridging late transition metals and heavier group 13 M (III) moieties (M=Al, Ga). Figure adapted from ref. 301.

Bourissou and co-workers reported the irreversible addition of H_2 across a Pt→Al dative bond in Pt(P(Mes)$_2$C(=CHPh)Al^{t}Bu$_2$) to give a HPt(μ-H)Al species, which DFT calculations predict to have Pt−H and Al−H distances for the bridging hydride of 1.70 Å and 1.80 Å, respectively (Figure 4.11, left).[118] Fischer and co-workers reported a rearrangement reaction of a Pt alkyl complex to give (dcpe)Pt(μ-H)(μ-(CH$_2$Si(CH$_3$)$_2$CH$_2$))Ga(CH$_2$SiMe$_3$)$_2$, where dcpe is bis(dicyclohexylphosphino)ethane, in which the Pt−H and Ga−H distances for the bridging hydride were determined to be 1.75(10) Å and 1.83(10) Å, respectively, based on x-ray diffraction (Figure 4.11, right).[302] In our case, the computed Ga−H(2) distance for the hydride in question in intermediate **B**, the product of H−H cleavage for NiGaL, is 1.83 Å, which is identical to the Ga−H distance in the Pt(μ-H)Ga complex reported by Fischer and similar to the computed Al−H distance of 1.80 Å in the HPt(μ-H)Al species reported by Bourissou. Likewise, similar distances of 1.75 Å and 1.96 Å were predicted for the Al−H(2) and In−H(2) distances for the bridging hydride in intermediate **B**, which are indicative of similarly strong interactions with the bridging hydride once the large size of In is taken into account. It should also be noted that a *bona fide* Ga−H bond would likely have a much shorter distance; for example, the Ga−H bond distance in [K][HGa(CH$_2$SiMe$_3$)$_3$] is 1.494 Å.[302] Furthermore, the two Ni−H distances (~1.50 Å) are both within the range for Ni−H (1.32 to 1.65 Å), although they are predicted to be nearly identical (within 0.02 Å).[252] Moreover, given the relatively short computed M−H(2) distances, it seems reasonable to propose that intermediate **B**, the product of H−H cleavage from (η^2-H$_2$)NiML, is best described as a true HNi(μ-H)M species, akin to the these species

reported by Fischer and Bourissou, as well as to those of Peters and co-workers for M=B upon H_2 addition to ($^{Ar}DPB^{R}$)Ni complexes.[44, 117]

Interestingly, the rearrangement reaction reported by Fischer and co-workers to give the Pt(μ-H)M species (M=Ga) was observed to occur more readily for M=Al, but was not observed to occur for M=In, suggesting that the relative order of stability for a bridging hydride between a transition metal and a group 13 M(III) moiety follows the order Al > Ga > In in this case.[302] Based on this precedent, as well as the known stabilities of Group 13 hydrides and their general propensity to form bridging interactions with transition metal hydrides, the relative order of stabilization provided to Ni−H(2) should decrease in moving down group 13 (Al > Ga > In).[136, 301, 303-304] This ordering is consistent with the calculation that dihydride intermediate **B** is more stable for M=Al relative to both its **TS** structure (+7.3 kcal/mol) and its H_2 adduct (+12.3 kcal/mol) than is the case for M=Ga and M=In (Figure 4.10). The magnitude of the change in the M−H(2) distances along the reaction coordinate also reflects the expected relative propensity of the supporting metal to stabilize a bridging hydride, with contractions of 1.07, 0.83, and 0.72 Å observed in the M−H(2) distances in moving from **TS** to **B** for Al, Ga, and In supporting metals, respectively (Table 4.6). The Ni→M bond also is calculated to be significantly elongated in intermediate **B** relative to that in **TS**, by 0.12, 0.07, and 0.05 Å for Al, Ga, and In supporting metals, respectively. This is consistent with less dative electron donation from Ni to the supporting metal, as would be expected from both an electronic and steric perspective if the supporting metal interacts to stabilize one of the Ni hydrides as a bridging hydride.

Though we have not observed a HNi(μ-H)ML species, the involvement of such a species is supported by the aforementioned DFT calculations, along with the observation of analogous species for diphosphine-ligated Ni→M complexes with more spatially accessible dative interactions by both Peters and co-workers and by other researchers in our group.[44, 117] Thus, another role of the Group 13 support in catalysis is likely to stabilize the H_2 activated intermediate, HNi(μ-H)M, as typically Ni(II) dihydride species are unstable, as evidenced by the incompetence of mononuclear Ni centers in H_2 oxidative addition.[30, 44-45, 272, 291] Furthermore, the greater anticipated thermodynamic stability of a HNi(μ-H)M species for Ga relative to In does translate into a slightly lower calculated transition state barrier for H−H cleavage (**TS** for **A→B**). That said, the calculated TS barriers are very similar for all supporting metals, with calculated values of 19.6, 19.2, and 20.2 kcal/mol for Al, Ga, and In supporting metals, respectively (Figure 4.10). Nevertheless, the lower barrier to H−H cleavage by 1 kcal/mol for **2** compared with **3** would correspond to a faster rate by a factor of ~5.6 under the assumption of rate-determining H−H cleavage (Equation 3.13). This is qualitatively consistent with the faster rates observed for catalysis with **2**, though a factor of ~24 times faster rate for **2** relative to **3**, in terms of TOF, was observed experimentally for styrene hydrogenation.

Additional insight was gained from investigation of the related [(η^2-H_2)CoML]$^-$ complexes (M=Al, Ga, In) and their relative propensities to catalyze olefin hydrogenation, as studied by Matt Vollmer.[167] Unsurprisingly, all three Co complexes outperformed their Ni congeners in preliminary catalytic hydrogenation studies with styrene, which is likely due to more facile H−H cleavage enabled by the greater degree of H−H activation afforded by increased π-back-bonding for Co compared with Ni (M d_π →

H_2 σ*).[45, 81, 167] Interestingly, the relative order of catalytic performance as a function of the group 13 supporting metal was different for the two series: Al > Ga > In for the CoML complexes, as compared with Ga > In > Al for the NiML complexes. These observations have been loosely rationalized by the hypothesis that the transition metal (Co or Ni) must be rendered electron-poor enough, through its interaction with the supporting metal, to bind H_2, but yet still electron-rich enough to oxidatively cleave H_2 to generate a $M(H)_2$ or HM'(μ-H)M species in the presence of olefin. The significantly greater propensity of Al, compared with Ga and In, to stabilize metal dihydrides by forming bridging HM(μ-H)Al species also may be a factor in facilitating facile H−H cleavage once H_2 has bound in the Co system. It should also be noted that too stable of a HM'(μ-H)M species can result in poor catalytic activity as well, but in the case of the NiML complexes this is likely not going to be an issue since these species have not been stable enough to be observed. In any case, a good test would be to perform catalytic olefin hydrogenation under high pressures of H_2, as if the "electron-poor enough to bind, electron-rich enough to oxidatively cleave" hypothesis is correct, then NiAlL (**1**) would be expected to become catalytically competent and exhibit TOF on par with or better than NiGaL (**2**).

4.2.4.7 Olefin Insertion/β-Hydride Elimination and Reductive Elimination

While the initial sequence involving H−H cleavage is likely rate-determining, consistent with the primary KIE observed for styrene hydrogenation with **2**, the fundamental steps which occur downstream in the catalytic cycle, including olefin insertion, β-hydride elimination, and reductive elimination, are important for understanding the differences in selectivity for hydrogenation versus isomerization that

were observed upon substituting In for Ga as the supporting metal. In thinking about the potential roles of the supporting metal in these downstream steps, a similar bridging hydride interaction to that examined in the previous section for intermediate **B** could be invoked in intermediates **D** and **E** as well, thereby potentially influencing the competing rates of the reductive elimination and *β*-hydride elimination. This section will examine these downstream steps and catalytic intermediates via both experimental and computational studies to provide insight into the catalytic selectivity differences observed for 1-octene conversion under catalytic conditions for **2** and **3**.

Figure 4.12 shows the relevant catalytic intermediates that must be considered to think about olefin insertion and *β*-hydride elimination reactions which determine the divergent product selectivity for catalysis with **2** and **3**.[30] Olefin insertion in both 1,2- (**D**→**E**) and 2,1-fashion (**D**→**E'**) and de-insertion via β-hydride elimination (**E** and **E'**→**D**) are reversible and rapid relative to reductive elimination for **2**, as evidenced by the incorporation of deuterium from D_2 into all three olefinic positions of free styrene during catalysis, as observed by ^{2}H NMR spectroscopy (Figure A.3.12).[97] After olefin insertion, reductive elimination from either intermediate **E** or **E'** would result in the loss of alkane and the regeneration of NiML (Figure 4.12). Alternatively, hydrogenolysis could occur via the concerted addition of H_2 across the Ni−C bond in intermediate **E** or **E'**, which would result in the loss of alkane product and the regeneration of intermediate **B**, which could then bind another equivalent of olefin to regenerate intermediate **D** (Figure A.3.13). A control experiment in which sub-stoichiometric H_2 was added under catalytic conditions still resulted in hydrogenation of styrene to ethyl benzene, suggesting that excess H_2, which would be needed for hydrogenolysis to occur, is not a requirement,

and therefore that reductive elimination is likely operable. DFT calculations also favor reductive elimination over hydrogenolysis as the final step in the catalytic cycle.

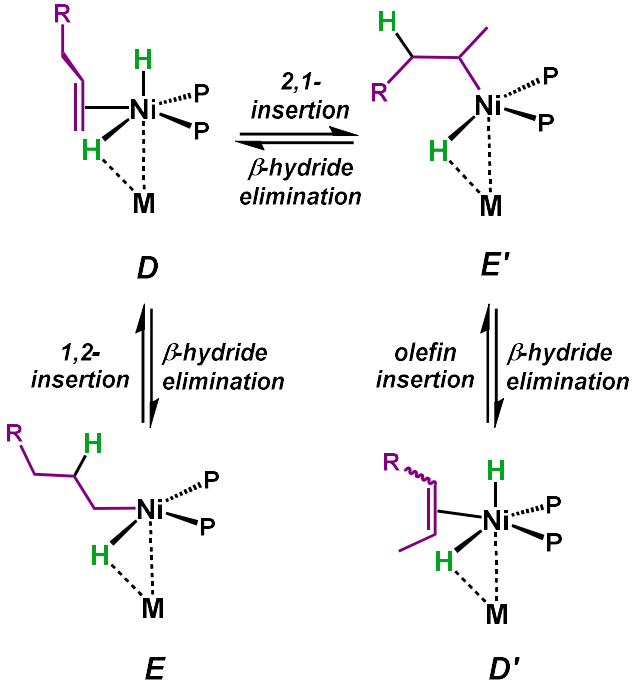

Figure 4.12. Proposed pathway for terminal-to-internal olefin isomerization in the Ni−In system, where the barrier to reductive elimination is large enough for isomerization to compete with hydrogenation.[30]

Alternatively, isomerization of terminal alkenes to give 2-alkenes, which only was observed to occur for catalysis with **3**, is proposed to occur via initial 2,1-insertion (**D→E'**) followed by internal β-H elimination to give a coordinated 2-alkene (**E'→D'**) that is then liberated (Figure 4.12).[30] 2-Alkenes, by virtue of their greater steric bulk, should be more labile, and once liberated would be less susceptible to re-enter the catalytic cycle than 1-alkenes because of the higher barriers associated with the binding and insertion of 2-alkenes.[192] Further "chain-walking" (via insertion from **D'** at the position α to R) to give appreciable amounts of other internal octenes was not observed for **3**. The isomerization of 1-alkenes to 2-alkenes have been reported to be catalyzed by

other Co and Ni complexes in the literature, for which β-hydride elimination mechanisms have been commonly proposed.[92, 120, 273, 277, 280, 284, 305-309] The inferior hydrogenation of 2-alkenes was illustrated by the inferior hydrogenation activity of **2** for *trans*-2-octene (~10% hydrogenation after 24 h) in comparison to 1-octene (>99% hydrogenation in <1.5 h).[97] While it is simple to just conclude that 2-alkenes are not hydrogenated because they do not coordinate to NiML at all, a control experiment shows that **3** catalyzes the isomerization of exclusively *trans*-2-octene to a thermodynamic mixture of *cis* and *trans* isomers, suggesting that coordination is feasible but that reductive elimination of alkane from intermediate **E'** is likely unfavorable. In any case, in the presence of 1-octene, coordination of 2-octene will likely be outcompeted. Moreover, the olefin isomerization process can be mapped directly onto the proposed hydrogenation mechanism based on the requirement of H_2 for isomerization to occur, which makes an alternative isomerization mechanism in which initial C−H activation to give a Ni−allyl intermediate occurs unlikely.[30, 97]

One explanation for why NiGaL (**2**) gives exclusively octane from 1-octene while NiInL (**3**) generates both octane and 2-octenes is that 2,1-insertion (**D→E'**) does not occur for **2**, which then does not allow for β-hydride elimination to occur to give isomerized alkenes (**E'→D'**). However, this explanation can be ruled out based on the aforementioned observation by ^{2}H NMR spectroscopy of deuterium incorporation into all three olefinic positions of free styrene, which can only result if both 1,2- and 2,1-olefin insertions are occurring for **2** (Figure A.3.12).[30, 97] DFT calculations predict that while the barriers for 1,2- and 2,1-insertions from intermediate **D** to give **E** and **E'** are similar for catalysis with **2**, at 10.5 and 12.3 kcal/mol, respectively, the terminal Ni(II) alkyl hydride

intermediate formed from 1,2-insertion (**E**) is more stable than **E'** by 8 kcal/mol (Figure 4.13).

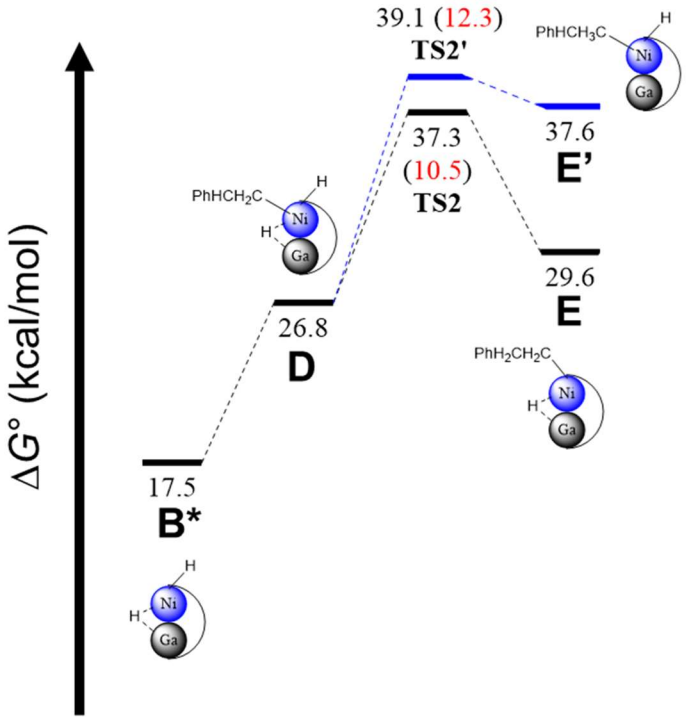

Figure 4.13. DFT-calculated free energy profile of the hydrogenation of styrene mediated by NiGaL (**2**), beginning from intermediate **B***, as calculated using M06-L/bs1 with the SMD solvent model (benzene). Please refer to section 4.4.3 and Table 2.9 for more computational details. In the diagram, two hemispheres connected indicates all three phosphines are coordinated to Ni, whereas one hemisphere disconnected indicates an intermediate in which one phosphine has dissociated. From intermediate **D**, the 1,2-insertion pathway is shown as the black line (lower in energy), with the 2,1-insertion pathway shown as the blue line. Activation energies are shown in red, and energies relative to (η^2-H_2)NiGaL (intermediate **A**) are shown in black. Figure adapted from that provided by Dr. Konstantinos Vogiatzis.

Looking at the geometry of **E** compared with **E'**, it is likely that the instability of **E'** stems from the steric instability of forming a Ni−C(R)(R') linkage with two different R substituents near a crowded Ni center, to which a hydride and two diisopropyl phosphine ligands are also coordinated. That the predicted kinetic barriers are similar for 1,2- and 2,1-insertions is consistent with the notion that both are occurring under catalytic

conditions with **2**, as indicated by results of the deuterium incorporation experiment with styrene (*vide supra*). The DFT-computed pathway outlined above for this portion of the catalytic cycle, beginning from intermediate **B*** and considering subsequent olefin binding, olefin insertion, and β-hydride elimination steps, is shown in Figure 4.13.

Another possible explanation for the divergent reactivity of **2** and **3** would be that isomerization to 2-octenes occurs for both catalysts, but that the isomerized 2-octene products are simply hydrogenated more readily to give alkane in the case of **2**. This explanation can also be discounted on the basis of the poor activity of **2** for the hydrogenation of *trans*-2-octene, where only 10(2)% hydrogenation to octane was observed within 24 h.[97] Thus, it is highly unlikely that isomerized 2-octene products would be hydrogenated fast enough to avoid observation by ^{1}H NMR spectroscopy. That said, experiments with **3** show greater *cis*:*trans* ratios of 2-octene are observed at very early time points in the reaction, which suggest that *cis*-2-octene may be initially generated followed by isomerization to *trans*-2-octene (Figure 4.1). While *cis*-2-octene may be more readily hydrogenated than *trans*-2-octene, it is still unlikely that rapid hydrogenation of all the *cis*-2-octene initially generated explains the lack of observation of isomerized products for catalysis with **2**.

Instead, it is proposed that different relative rates of reductive elimination and β-hydride elimination from intermediates **E** and **E'** are responsible for the selectivity differences. For Ni−In, it is proposed that olefin isomerization is competitive with hydrogenation because of greater barriers to reductive elimination from **E** and **E'**, as compared to the analogous barriers for Ni−Ga. The larger reductive elimination barriers for Ni−In essentially permit olefins to escape the hydrogenation cycle via *β*-hydride

elimination (**D'→E'**) and subsequent release of the isomerized 2-alkenes from the Ni center.[30] The underlying reason as to why Ni−In has a greater barrier to reductive elimination than Ni−Ga is not well understood. A bit of insight into the effect of the supporting metal on the rates of reductive elimination can be gained by considering mononuclear Ni(II) alkyl hydride species without a supporting metal. The fundamental principles of organometallic chemistry would lead to the expectation that, all else being equal, reductive elimination would be faster for the more electron-poor Ni(II) alkyl hydride species, as it would be more readily reduced to Ni(0).[110] Applying this same principle to the LMNi(II) alkyl hydride species generated in catalysis (ie. M=Ga and In for intermediates **E** and **E'** in Figure 4.12), one would expect that if the supporting metal was purely participating in the reductive elimination step as an electronic tuner of Ni, then the more electron-poor LInNi(II) alkyl hydride species would undergo faster reductive elimination than the corresponding Ga species, assuming the relative trend in the electron-richness of the Ni centers in isostructural Ga and In complexes holds true (section 2.3.6).[97] However, this line of reasoning leads to the opposite prediction compared with what has been observed based on the selectivity for 1-octene, as slower reductive elimination for M=In compared with M=Ga was inferred to give rise to competitive isomerization in the former case.[30] Thus, in light of this contradiction, it is proposed that the original assumption of In and Ga participating in reductive elimination as only an electronic tuner of Ni is flawed.

Therefore, it is further proposed that the supporting metal must also play an additional role that makes reductive elimination faster in the case of M=Ga relative to M=In. This additional role could potentially include the stabilization of the bridging

hydride in intermediates **E** and **E'** to different extents, or perhaps the disparate sizes of In and Ga have a more subtle steric effect on the geometry of Ni and the stability of intermediates **E** and **E'**. In considering the former role, DFT calculations predict that the extent to which intermediates **E** and **E'** feature a bridging hydride is significantly less than was predicted for intermediates **B** and **D**; for example, the computed Ga−H distances for the bridging hydride increase from 1.83 Å in **B** to 1.95 Å in **E** (Table A.3.2). Thus, it is hypothesized that the different rates of reductive elimination may be a consequence of the different sizes of In and Ga, which dictate the positioning of Ni and the resulting stability of the **E** and **E'** intermediates, as well as the relative rates of reductive elimination from these intermediates. While merely a speculative hypothesis at this point, it is proposed that the larger size of In relative to Ga results in Ni being positioned further above the P_3-plane in intermediates **E** and **E'** for the M=In case, as was seen for the steric effect of In compared with Ga in isostructural NiML complexes. This could potentially increase the stability of intermediates **E** and **E'** for the M=In case by alleviating steric clashes between the Ni−C(R)(R') groups and the isopropyl substituents on the phosphine ligands. Intermediates **E** and **E'** being relatively more stable for M=In compared with M=Ga would render them less reactive and result in slower relative rates of reductive elimination, thereby allowing for competitive β-hydride elimination to occur to give isomerized 2-alkenes (**E'→D'**) in the case of M=In. This hypothesis is difficult to test experimentally, and would require additional computational studies to support or discount it; at this point, this is the best guess for why reductive elimination might be slower for M=In compared with M=Ga.

4.2.5 Identified Roles of the Group 13 Support in Promoting Catalytic Olefin Hydrogenation

In summary, three specific roles that the supporting group 13 metal plays in catalytic hydrogenation have been proposed:

(1) The Lewis acidic group 13 metal induces H_2 binding and activation at Ni, which is the first step of the catalytic cycle. As discussed in chapter 3, larger group 13 supports render Ni more electron-deficient and geometrically positioned further above the P_3-plane, which enables H_2 to bind (In > Ga > Al).[30, 97]

(2) Through the Ni→M interaction, the Lewis acidic supporting metal influences the amount of electron density at the Ni center, which dictates the extent of Ni→P π-back-bonding and the favorability of the dissociation of a phosphine ligand for an olefin at the Ni center. A stronger Ni→M interaction (In > Ga) seems to increase phosphine lability based on methylene coalescence studies and solid-state Ni−P bond metrics, but is proposed to decrease the affinity for an added olefin ligand. Thus, regardless of whether H−H cleavage precedes or follows olefin binding (either **A**→**A***→**C** or **B**→**B***→**D**), it is proposed that the substitution of one of the phosphine donors for an olefin will be more favorable for Ga compared with In.[30]

(3) The supporting metal is also intimately involved in stabilizing bridging hydride moieties in intermediates **B** and **D,** and to a lesser extent in **E** (Ga > In), potentially affecting the rates of H−H cleavage as well as the competing rates of the reductive elimination and *β*-hydride elimination. The In supporting metal is proposed to have a slower rate of reductive elimination from intermediates **E** and

E' than Ga, which allows isomerization to compete with hydrogenation for catalysis with **3**.[30] The reasons for this are not well understood, but the effect is hypothesized to be a consequence of the steric effect of the larger size of In on the geometry of the Ni center and the stability of intermediates **E** and **E'**.

In addition to these specific roles, the supporting metal also seems to generally accommodate the electronic and steric requirements of the active transition metal (Ni) during catalysis, as evidenced by the DFT-predicted flexibility of the Ni−Ga bond, which is calculated to vary in bond distance from ~2.4 to 2.9 Å in various catalytic intermediates (Table A.3.2).

4.3 Conclusions

Upon finding that group 13 supporting metals induce varying extents of H_2 binding and activation in a series of Ni bimetallic complexes, the propensity of these complexes to act as catalysts in the transfer of the activated H_2 unit to olefins to generate alkanes was examined. Homogeneous Ni olefin hydrogenation catalysts are rare, which can be attributed primarily to the inability of most mononuclear Ni complexes to bind and activate H_2 toward oxidative addition.[44-45, 272, 291] Initial catalytic studies showed that NiAlL (**1**) and $NiLH_3$ (**4**) do not catalyze styrene hydrogenation to ethyl benzene, presumably because H_2 binding to the more electron-rich Ni centers in these complexes is unfavorable (chapter 3). Catalytic hydrogenation activity, however, does not strictly improve with increasing H_2 binding favorability, as NiGaL (**2**) was found to mediate styrene hydrogenation with a TOF that is 24 times faster than that for NiInL (**3**). Similarly, faster catalytic consumption of 1-octene and *cis*-cyclooctene was also observed

for catalysis with **2** compared to **3**, which prompted a substrate scope study for catalysis with **2**.[30, 97]

Complex **2** catalyzes the hydrogenation of mono-substituted, terminal olefins (ie. styrene, 1-hexene, 1-octene, 4-phenyl-1-butene) and cyclic, di-substituted olefins (*cis*-cyclooctene) in good yields with modest TOF. However, acyclic, di-substituted olefins (ie. *cis*-stilbene, 1,1-diphenylethylene) were not amenable to hydrogenation under catalytic conditions for **2**, likely due to the difficulty of binding these more hindered olefins. Benzaldehyde was also not hydrogenated by **2**, showing the preference of the catalyst for the hydrogenation of C=C bonds over C=O bonds.[30, 97] Even though homogeneous Ni catalysts are rare, the catalytic activity of **2** is not particularly impressive when compared to the limited number of Ni catalysts in the literature.[44, 120, 171, 273, 280] Furthermore, the catalytic activity of **2** pales in comparison to the state-of-the-art base metal catalysts based upon Fe and Co,[286, 289-290] and the substrate scope is limited to relatively uninteresting olefins from a synthetic perspective. Thus, the exciting aspect of catalytic olefin hydrogenation with **2** is not its catalytic activity or practical utility, but rather the opportunity to understand how the Ga supporting metal interacts with Ni to enable catalysis that is not possible for $NiLH_3$, as well as how varying the supporting metal to Al and In impacts catalysis.

An intriguing result which prompted in-depth mechanistic studies was the divergent reactivity of **2** and **3** under catalytic conditions with 1-octene. For catalysis with **3**, a ~1:1 ratio of octane to 2-octenes was formed via the competition of hydrogenation and isomerization pathways, whereas exclusive hydrogenation to octane was observed with **2**. A similar tendency of **3** to catalyze the isomerization of terminal olefins with

allylic hydrogen atoms was observed for allylbenzene. The selectivity difference is proposed to result from a slower rate of reductive elimination for the In supporting metal that allows isomerization to become competitive via 2,1-insertion followed by internal β-hydride elimination (**D→E'→D'**). While 2,1-insertion is also observed to be feasible for **2** based on the incorporation of deuterium into all three olefinic positions of free styrene, the rate of reductive elimination from the resulting intermediate, **E'**, must be fast enough to prevent isomerization via β-hydride elimination to **D'**. While it is not entirely clear why M=In would lead to a slower rate of reductive elimination than M=Ga, it is proposed that the supporting metal is not solely functioning to tune the electronics of the Ni(II) alkyl hydride intermediates (**E** and **E'**), as if this were the case a faster relative rate of reductive elimination for a more electron-poor Ni(II) alkyl hydride species for M=In compared with M=Ga would be expected.

Another key difference between catalysis with **2** and **3** are the faster rates and higher yields observed for styrene hydrogenation. It is proposed that the RDS is initial H−H cleavage, which is supported by the observation of a primary KIE of 1.7(2) for styrene hydrogenation with **2**.[97] A slightly lower computed barrier for H−H cleavage is observed for **2** (19.2 kcal/mol) compared with **3** (20.2 kcal/mol), which is qualitatively consistent with the observed rates. However, the lack of H_2/D_2 scrambling in the absence of olefin for both **2** and **3** indicates that H−H cleavage does not readily occur under ambient conditions, and the slower hydrogenation of more electron-poor styrene derivatives suggests that olefin binding may also be important to determining the catalytic rate. To allow olefin binding to occur, the dissociation of one phosphine donor is required, and computations suggest that phosphine dissociation is most favorable after

initial H−H cleavage. Experimental studies established that Ni−P bonds in isostructural complexes will be more labile as the supporting metal is varied down group 13 (In > Ga > Al), and preliminary experiments involving PMe_3 addition to NiML complexes suggest that the affinity for an exogenous ligand may be inversely related to phosphine lability in this NiML system. Thus, regardless of whether H−H cleavage precedes olefin binding, the substitution of an olefin for a phosphine donor is also proposed to be more favorable for M=Ga than M=In.[30, 97]

In summary, several key roles played by the supporting metal have been identified that enable NiML complexes to catalyze olefin hydrogenation, as compared to the catalytically inactive $NiLH_3$ complex. After inducing initial H_2 binding and activation by rendering Ni electron-deficient and optimally positioned for binding (In > Ga > Al), the supporting metal also helps to stabilize the HNi(μ-H)M intermediate (Al > Ga > In) that would typically be unstable for a mononuclear Ni center. The supporting metal also influences the favorability of olefin binding with concomitant phosphine dissociation (Ga > In) by influencing the lability of Ni−P bonds, as well as affecting the rates of reductive elimination of alkane (Ga > In). Importantly, supporting Ni with Ga seems to promote more favorable catalytic steps in all cases examined except for H_2 binding, though H_2 binding still occurs for **2** under ambient conditions. Thus, the better catalyst performance of **2** relative to **3** has been rationalized, and is in accordance with the Sabatier principle, which states that the optimal catalyst is one that binds key intermediates neither too strongly nor too weakly.[310-311] This has been demonstrated quantitatively for H_2 binding to **2** compared with **3** in chapter 3, and it stands to reason that the weaker, more flexible

Ga interaction with Ni will also allow for the fluxional binding of other species in the catalytic cycle for olefin hydrogenation.

While exciting in the sense that the supporting metal was able to promote base metal catalysis that was not possible for a similarly ligated mononuclear Ni center, several limitations must be addressed in future catalytic bimetallic systems to improve catalytic performance. First, the bulky isopropyl substituents on the phosphine ligands likely prohibit the binding of bulkier di-substituted olefins, and so utilizing methyl groups could allow for the hydrogenation of more challenging and synthetically interesting substrates. Two other key steps in catalysis which could be improved upon, relative to the ease with which they occur for **2**, are H−H cleavage and olefin binding. Currently, olefin binding is slowed by the need to dissociate one of the three phosphine donors, and so removing the third phosphine donor could alleviate this limitation. Furthermore, related Ni→B diphosphine systems are more readily able to mediate H−H cleavage by allowing the borane moiety to participate more directly in the cooperative activation of H_2.[44, 117, 120] Therefore, by removing the third phosphine donor, both H−H cleavage and olefin binding could be potentially made more favorable. Alternatively, retaining three phosphine donors but allowing for greater ligand flexibility, as is being probed in the related NiML*$_3$ system, could also promote more facile H−H cleavage to give HNi(μ-H)M species. Current efforts in our lab our focused on these strategies, with the results from this first-generation NiML system potentially being useful in terms of illustrating the roles played by the supporting metal in catalysis and the impact of specific metal-metal combinations on catalytic performance. As for exploring further reactivity of the NiML

system, chapter 5 will examine the generation of discrete Ni hydride species and their ability to catalytically hydrogenate CO_2 to formate.

4.4 Experimental Section

4.4.1 Synthetic Considerations

Unless otherwise stated, all manipulations were performed under a dinitrogen or argon atmosphere inside a glovebox or using standard Schlenk techniques. Standard solvents were deoxygenated by sparging with N_2 and dried by passing through activated alumina columns of a SG Water solvent purification system. Deuterated solvents were purchased from Cambridge Isotope Laboratories, Inc., degassed via freeze-pump-thaw cycles, and stored over activated 4 Å molecular sieves. H_2 gas was purchased from Matheson, and D_2 gas was purchased from Cambridge Isotope Laboratories, Inc. All other reagents were purchased from commercial vendors and used without purification unless otherwise noted. The neutral ligand $(N(o\text{-}(NHCH_2P^iPr_2)C_6H_4)_3$ (abbreviated as H_3L), NiAlL (**1**), NiGaL (**2**), NiInL (**3**), (N_2)NiInL (**3**$-N_2$), and $NiLH_3$ (**4**) were synthesized according to literature procedure (which is also described in sections 2.2.1 and 2.4).[51, 78, 97]

Catalytic Hydrogenation of Olefins Experimental Details. A stock solution of catalyst (**1**, **2**, **3**$-N_2$, or **4**) was prepared in C_6D_6 such that approximately 3 μmol of catalyst was transferred into each sealed J. Young NMR tube, along with 20 equivalents of olefin (0.087 M in 0.70 mL C_6D_6 solution), along with ferrocene (ca. 0.03 M) as an internal NMR integration standard. One freeze-pump-thaw cycle was performed to evacuate the headspace, followed by back-filling with H_2 (1 atm). In the case of **3**, **3**$-N_2$ was used as

the pre-catalyst, and a second freeze-pump-thaw cycle was performed after inverting the J. Young tube in order to rid the atmosphere of displaced N_2 after generating **3**−H_2 *in situ*. Olefin hydrogenation catalysis was monitored by ^{1}H NMR spectroscopy by quantitative integration of the olefin protons against those of the internal ferrocene standard (recycle delay=10 or 20 s). Alkane product peaks were also integrated in cases where they did not overlap with NiML peaks. After the final NMR time point (typically 24 h, unless otherwise noted), a vacuum transfer was performed and GC-MS analysis was conducted to quantify the amount of hydrogenated product formed (Table A.3.1). In order to promote the gas-liquid mixing of H_2 into solution, the J. Young tube was rotated at approximately 16 rpm using a turntable ("D.J. J. Young") when spectra were not being collected. All catalytic hydrogenation experiments were performed in triplicate unless otherwise indicated.

Mercury Inhibition Test for Catalyst Homogeneity. A stock solution of catalyst, NiGaL (**2**), was prepared by dissolving 25.4 mg of **2** in C_6D_6 to make ca. 10 mL of 0.00158 M solution. The stock solution (5 mL aliquot each) and 36 µL of styrene (~20 equiv.) were transferred into two identical 50 mL bomb flasks. Metallic mercury (0.5754 g, 182 equiv.) was added to one of the bomb flasks. A freeze-pump-thaw cycle was performed to evacuate the headspace of the bomb flasks, followed by back-filling with H_2 (1 atm). The bomb flasks were allowed to react for 24 h while being rotated at approximately 16 rpm using a turntable to promote H_2 mixing with solution. Three 500 µL aliquots were taken from each bomb flask and transferred to NMR tubes, with 100 µL of a 0.054 M ferrocene solution added to each tube as an internal standard. ^{1}H NMR spectra were collected, and the conversion of styrene to ethyl benzene was obtained by quantitative

integration relative to ferrocene. Catalysis was uninhibited by the addition of mercury, with 96% conversion in the absence of mercury as compared to 91% conversion in the presence of mercury, consistent with a homogeneous catalytic process.

H_2/D_2 and HD Scrambling Studies. A mixture of 1 atm of ~1:1 H_2/D_2 was added to **2** and **3** in toluene-d_8 in J. Young NMR tubes, which were allowed to rotate for several days on a turntable at ~16 rpm to promote continuous gas-liquid mixing. No evidence of the characteristic 1:1:1 triplet resonances for bound or free HD were observed by ^{1}H NMR spectroscopy at 298 K or 223 K (Figure A.3.5). Likewise, the addition of 1 atm HD to **2** and **3** did not result in any observation of free or bound H_2 by ^{1}H NMR spectroscopy, even after heating to 353 K for 36 h (Figure A.3.6).

Kinetic Isotope Effect (KIE) Studies for Styrene Hydrogenation. Six identical J. Young NMR tubes were prepared as previously described for typical catalytic hydrogenation experiments with **2**. Three of the six trials were pressurized with H_2 (1 atm), while the other three were pressurized with D_2 (1 atm). The appearance of ethyl benzene (or d_2-ethyl benzene) was monitored by ^{1}H NMR spectroscopy after an initial rates period of 45 minutes, during which time the J. Young tubes were rotated at 16 rpm to promote optimal gas-liquid mixing. A normal, primary KIE of 1.7(2) was measured by this method. It is important to note that this method relies on the assumption that deuterium (D) does not wash into free styrene significantly over the initial rates period, as this could then give ethyl benzene with >2 D atoms incorporated, which would then not be accounted for properly by integration of the ^{1}H NMR resonances. This is likely a reasonable assumption based on GC-MS results for the initial rates period, though it should be noted that D

incorporation into free styrene is observed by ^{2}H NMR spectroscopy after overnight mixing under catalytic conditions (Figure A.3.12). Attempts to validate this assumption and verify the KIE using GC-MS gave a value of 2.3 (±1.1) for the KIE for 1-octene hydrogenation with **2** over a 10 minute initial rates period, which is still consistent with a normal, primary KIE, albeit with a larger amount of error.

4.4.2 Physical Methods

^{1}H and ^{31}P NMR spectra were recorded on Bruker 400 MHz and Varian 300 MHz or 500 MHz spectrometers and referenced to internal residual solvent (or H_3PO_4 for ^{31}P NMR spectra). VT NMR experiments were carried out using either a methanol (below 298 K) or ethylene glycol (above 298 K) standard to calibrate T, and all samples were allowed to equilibrate at each T for at least 10-15 minutes prior to data collection. Quantitative integration of ^{1}H NMR spectra was carried out using long recycle delay times of 10-20 s. All GC-MS experiments were conducted on an Agilent Technologies 7890A GC system and 5975C VLMSD. The GC column was a HP-5 ms with dimensions 30 m x 0.25 mm. The standard method used for all runs involved an initial oven temperature of 35°C (held for 12 min), followed by a 30°C min^{-1} ramp to 280°C (held for 10 min).

^{1}H NMR of Peaks for Selected Hydrogenated and Isomerized Products (ppm, C_6D_6)

Ethyl benzene: 2.44 (q, *J*=8 Hz, CH_2, 2H), 1.08 (t, *J*=8 Hz, CH_3, 3H).

Propylbenzene: 2.42 (t, *J*=7.5 Hz, $CH_2CH_2CH_3$, 2H), 1.50 (sextet, *J*=7.5 Hz, $CH_2CH_2CH_3$, 2H), 0.82 (t, *J*=7.5 Hz, CH_3, 3H).

Trans-β-methylstyrene: 6.29 (dd, *J*=16 Hz, 1.4 Hz, PhC*H*CHCH$_3$, 1H), 6.02 (m, *J*=16 Hz, 7 Hz, PhCHC*H*CH$_3$, 1H), 1.64 (dd, *J*=7 Hz, 1.8 Hz, PhCHCHC*H$_3$*, 3H).

Cis-β-methylstyrene: 6.42 (dd, *J*=11.5 Hz, 1.5 Hz, PhC*H*CHCH$_3$, 1H), 5.64 (m, *J*=11.5 Hz, 7 Hz, PhCHC*H*CH$_3$, 1H), 1.70 (dd, *J*=7 Hz, 1.8 Hz, PhCHCHC*H$_3$*, 3H).

4-phenyl-1-butane: 2.46 (t, *J*=7.5 Hz, C*H$_2$*CH$_2$CH$_2$CH$_3$, 2H), 1.47 (quintet, *J*=7.5 Hz, CH$_2$C*H$_2$*CH$_2$CH$_3$, 2H), 1.22 (sextet, *J*=7.5 Hz, CH$_2$CH$_2$C*H$_2$*CH$_3$, 2H), 0.83 (t, *J*=7.5 Hz, CH$_3$, 3H).

Trans-2-octene: 5.43 (m, H$_3$CC*H*C*H*(CH$_2$)$_4$CH$_3$, 2H), 1.61 (d, *J*=5 Hz, *H$_3$*CCHCH(CH$_2$)$_4$CH$_3$, 3H).

Cis-2-octene: 5.47 (m, H$_3$CC*H*C*H*(CH$_2$)$_4$CH$_3$, 2H), 1.55 (d, *J*=5 Hz, *H$_3$*CCHCH(CH$_2$)$_4$CH$_3$, 3H).

4.4.3 Computational Methods

Density Functional Theory (DFT) Calculations of Catalytic Mechanism

DFT calculations using the M06-L local functional[176] have been performed to predict the mechanism for H−H cleavage and for the overall catalytic hydrogenation of styrene, in conjunction with the def2-TZVPP[186] (for Ni, Ga), def2-TZVP (for N, P and reacting species of H$_2$/olefin), and def2-SVP (for C, H) basis sets ("bs 1" from Table 2.9, plus additional considerations for olefin). The choice of the M06-L functional was based on its good performance on mechanistic studies of processes catalyzed by similar bimetallic complexes.[79] The same computational methods were also used to investigate the mechanism of methylene coalescence. All geometry optimizations were performed for the unrestricted singlet state of the NiML, with the optimized intermediate structures found to have only real frequencies. All optimized transition states (TS) were found to have a single

imaginary frequency along the reaction coordinate. Gibbs free energies ($\Delta G°$) at 298.15 K were computed by adding zero-point vibrational energies, and thermal vibrational-rotational entropy in the quasi-harmonic approximation. Solvation effects were also considered by performing single-point calculations for all intermediates and transition states using the SMD solvation model,[181] with either benzene, toluene, or THF as the solvent. All calculations were performed with the Gaussian09 program package.[182]

Binding Adsorption Energy of H_2 and C_2H_4

The H_2 and C_2H_4 binding adsorption energy for NiGaL **(2)** was calculated with the PBE0 functional[178, 312] and the D3 dispersion correction.[179] These calculations were performed as single-point calculations on the M06-L optimized structures, with the PBE0-D3 functional was chosen due to its good performance on weakly interacting complexes.[313] The same basis set combinations were used for these calculations, with the addition of a second set of polarization functions for the bound H_2 and C_2H_4 molecules (def2-TZVPP). Zero-point vibrational energy (ZPVE) and enthalpy corrections were added in the final binding energies. All PBE0-D3 calculations were performed with the Turbomole v6.4 program package,[314] and the counterpoise correction (CP) was applied for the basis set superposition error (BSSE).

4.4.4 Acknowledgements

Note that all calculations regarding the catalytic reaction mechanism, as well as the ethylene and H_2 adsorption energies, were originally performed by Dr. Konstantinos Vogiatzis. Dr. Jing Xie finalized the original work and performed calculations on the portion of the mechanism involving H_2 binding, H−H cleavage, and phosphine dissociation

and lability. Additionally, Nick Smith, a former undergraduate student under my supervision, studied the effect of the electron-richness of styrene derivatives on catalytic rates for **2**, as well as the binding of phenyl acetylene to **3**. Lastly, I would like to thank Dr. Reed Eisenhart for helpful discussions regarding the mechanism of hydrogenation, as well as his genius idea for D.J. J. Young, the best $30 any lab has probably ever spent, as it still spins everyone's J. Young tubes years later.

Chapter 5

Imparting Nobility to First-Row Metal Hydrides: The Role of Unusual Anionic Ni−H Species Stabilized by Group 13 Metalloligands in Catalytic CO_2 Hydrogenation, as Informed by Comprehensive Mechanistic and Thermodynamic Studies

In part from:

Cammarota, R. C.; Vollmer, M. V.; Xie, J.; Ye, J.; Linehan, J. C.; Burgess, S. A.; Appel, A. M.; Gagliardi, L.; Lu, C. C.* "A Bimetallic Nickel-Gallium Complex Catalyzes CO_2 Hydrogenation via the Intermediacy of an Anionic d^{10} Nickel Hydride." *J. Am. Chem. Soc., 139*, 14244-14250.

Ye, J.; **Cammarota, R. C.**; Xie, J.; Vollmer, M. V.; Truhlar, D.; Cramer, C.; Lu, C. C.; Gagliardi, L.* "Rationalizing the Reactivity of Bimetallic Molecular Catalysts for CO_2 Hydrogenation." *ACS Catalysis, Just Accepted.*

5.1 Introduction and Overview

Efficient recycling of CO_2 to commodity chemicals or liquid fuels, such as formic acid or methanol, could generate value-added products from an abundant C_1 feedstock while alleviating the adverse effects associated with rising CO_2 levels. Although a practical CO_2-to-fuel scheme would require efficient CO_2 capture and sustainable H_2 production,[11] our efforts have focused on the singularly formidable challenge of developing base metal catalysts for selective CO_2 hydrogenation under mild conditions.[1, 10, 315-316] CO_2 hydrogenation to methanol remains a daunting task; the few known molecular catalysts rely almost exclusively on precious metals (Ru, Ir),[24-29] with only a single instance of a first-row metal (Co) catalyst.[23] Furthermore, first-row metal catalysts remain uncommon for the hydrogenation of CO_2 to formate.[93, 317-320] In the past decade, impressive catalytic performance has been achieved using phosphine-ligated Fe and Co catalysts, which generate formate with turnover numbers (TONs) from 9000 to 59000 with high turnover frequencies (TOFs).[321-323]

Despite these recent advances of Fe and Co catalysts, the progress of Ni-based systems for CO_2 hydrogenation has been limited.[324-326] The first homogeneous Ni catalyst was reported over 40 years ago: $Ni(dppe)_2$, where dppe = bis(diphenylphosphino)ethane, produced formate from H_2 and CO_2, albeit with poor activity (TON = 7, TOF = 0.35 h^{-1}).[326] Recently, a water-soluble Ni bis(diphosphine) catalyst mediated the H_2/CO_2 to formate reaction in aqueous solution using $NaHCO_3$ as the base, but the activity remained low (TOF of 0.40(5) h^{-1} at 80 ºC and 34 atm of H_2/CO_2).[324] In related work, a Ni PCP-pincer catalyst generated formate from H_2 and $NaHCO_3$ with a comparatively impressive

TON of 3000 at 150 ºC and 54 atm; however, the catalyst was inactive when $NaHCO_3$ was replaced with CO_2.[327]

The dearth of Ni catalysts for CO_2 hydrogenation to formate stems from several inherent limitations. Ni, being more electronegative than Fe and Co, has a lower propensity for binding and activating H_2 to generate Ni−H,[44-45] and once generated, the resulting Ni−H species are typically weak hydride donors.[328] The lack of strong hydride donors is illustrated by the fact that even for $[HNi(dmpe)_2]^+$ (dmpe = bis(dimethylphosphino)ethane), the most hydridic Ni−H reported with a thermodynamic hydricity ($\Delta G°_{H-}$) of 49.9 kcal/mol in CH_3CN,[252] outer-sphere hydride transfer to CO_2 to generate formate (*c.f.* $\Delta G°_{H-}$ = 44 kcal/mol) is thermodynamically unfavorable by ~6 kcal/mol in CH_3CN.[329-331] However, it should be noted that there are several examples of Ni−H complexes which are potent enough hydride donors to react with CO_2 to form η^1-O formate adducts with Ni.[252, 332-336] In these cases, the more salient issue that may prevent catalytic CO_2 hydrogenation is the formation of strong Ni−O bonds, which can impede formate release and preclude catalytic turnover. Catalytic liberation of CO_2 reduction products can still be in these cases by using stoichiometric borane or silane reagents, which permit Ni−O cleavage and drive catalytic turnover via the formation of strong B−O or Si−O bonds. For example, Ni POCOP-pincer complexes can rapidly insert CO_2 into Ni−H bonds and further reduce CO_2 to methoxide derivatives using stoichiometric borane.[333] However, the requirement of B−H or Si−H reductants to drive catalysis, rather than regenerating the catalytically active Ni−H species from H_2, is a drawback in that the overall transformation will lack atom economy.[333, 337]

Circumventing the inherent limitations of Ni in CO_2 hydrogenation could involve stabilizing Ni−H in more reduced charge states and/or lower Ni oxidation states,[330, 338-339] while still allowing the regeneration of Ni−H from H_2 and base.[328, 340] A highly reduced Ni center could potentially allow for both facile hydride transfer from a Ni−H species to CO_2, along with a decreased propensity for prohibitively strong formate binding in the species that is generated upon hydride transfer. Our strategy to stabilize a reduced, low-valent Ni center, as detailed in the previous chapters, involves the incorporation of a Lewis acidic group 13 supporting metal which acts as a σ-acceptor toward Ni in NiML complexes.[78, 97, 119, 127, 341] As described in chapters 2-3, positioning the supporting metal ion directly *trans* to the substrate binding site at Ni allows for H_2 binding to form nonclassical H_2 adducts, (η^2-H_2)NiML.[97] Once bound and activated, H_2 can be transferred catalytically to olefins, as shown in chapter 4; however, H−H cleavage to generate reactive Ni−H species was a challenging step that limited catalytic activity.[30] In this chapter, the propensity of NiML complexes to catalyze the hydrogenation of CO_2 to formate in the presence of base will be examined. Key to this reactivity is the propensity of the group 13 M(III) supporting ion to stabilize d^{10} anionic Ni−H species which are potent hydride donors, with estimated $\Delta G°_{H-}$ values rivaling those of precious metal hydrides.[329] These reactive Ni−H species can be generated from the reaction of NiML, H_2, and base, and they react spontaneously with CO_2 to catalytically generate formate under mild conditions (1 atm H_2/CO_2 gas, rt).[128]

In the first section of this chapter, the catalytic performance of NiGaL (**2**) for CO_2 hydrogenation to formate will be compared to that of $NiLH_3$ (**4**), a similarly ligated mononuclear Ni center, to demonstrate the importance of the supporting metal for

enabling catalysis. Next, a catalytic mechanism will be proposed based on experimental and computational studies which will help rationalize the favorable effect of the Ga(III) supporting metal ion on catalysis. Gratifyingly, two key catalytic intermediates, $[HNiGaL]^-$ ($[\mathbf{2}-H]^-$) and $[(HCO_2)NiGaL]^-$ ($[\mathbf{2}-OCHO]^-$), were independently characterized, which along with the previously described (η^2-H_2)NiML species ($\mathbf{2}-H_2$), represent the three primary intermediates in the proposed catalytic cycle.[128] Computational studies were also utilized to elucidate subtler nuances of the catalytic mechanism.[129] Finally, the catalytic performance of NiAlL (**1**) and NiInL (**3**) were also examined in comparison to NiGaL (**2**) to investigate the influence of varying the supporting metal on catalysis. Excitingly, further experimental mechanistic studies allowed for the determination of the thermodynamic favorability of each of the fundamental reaction steps as a function of the supporting metal. Just as was the case for olefin hydrogenation, supporting Ni with Ga was found to result in optimal catalytic activity for CO_2 hydrogenation to formate, and detailed mechanistic studies have informed our understanding of the relative order of activity (Ga >> In > Al), as well as guided our efforts to develop improved catalysts. Lastly, in order to help understand the reactivity of the catalytically relevant $[HNiML]^-$ and (η^2-H_2)NiML complexes, a comprehensive thermodynamic scheme was compiled which compares the favorability of cleaving the Ni−H and Ni(η^2-H_2) bonds via the transfer of either a hydride, a proton, or a hydrogen atom to substrate.

5.2 Results and Discussion

*5.2.1 CO_2 Hydrogenation Catalysis: Comparison of NiGaL (**2**) to $NiLH_3$ (**4**)*

Although the neutral NiGaL (**2**) precursor does not hydrogenate CO_2, we reasoned that, in the presence of an exogenous base, a more reactive Ni−H species with an anionic charge could be generated that would be more reactive toward CO_2. Indeed, in the presence of Verkade's proazaphosphatrane, 2,8,9-triisopropyl-2,5,8,9-tetraaza-1-phosphabicyclo[3,3,3]undecane (abbrev. as Vkd)[342-343] as a stoichiometric base, complex **2** was found to catalyze CO_2 hydrogenation to formate in 91% yield under ambient conditions (1 atm 1:1 H_2/CO_2, 293 K, 0.36 mol% catalyst loading; Table 5.1, entry 1). Catalyst performance was further optimized by increasing the H_2/CO_2 pressure to 34 atm and decreasing the catalyst loading by ten-fold to 0.03 mol%, which gave near quantitative generation of formate (Table 5.1, entries 2-3). The corresponding kinetic plot in Figure 5.1 shows that catalyst **2** attained 3150 formate turnovers in ~40 min with an initial TOF of 9700 h^{-1}.[128] The high activity of **2** sharply contrasts that of prior Ni homogeneous catalysts (Table A.4.1). Apart from representing by far the highest reported catalytic TOF for a homogeneous Ni catalyst to date,[324-326] this level of catalytic activity is generally impressive for a base metal catalyst operating at ambient temperature without any alkali metal additives.

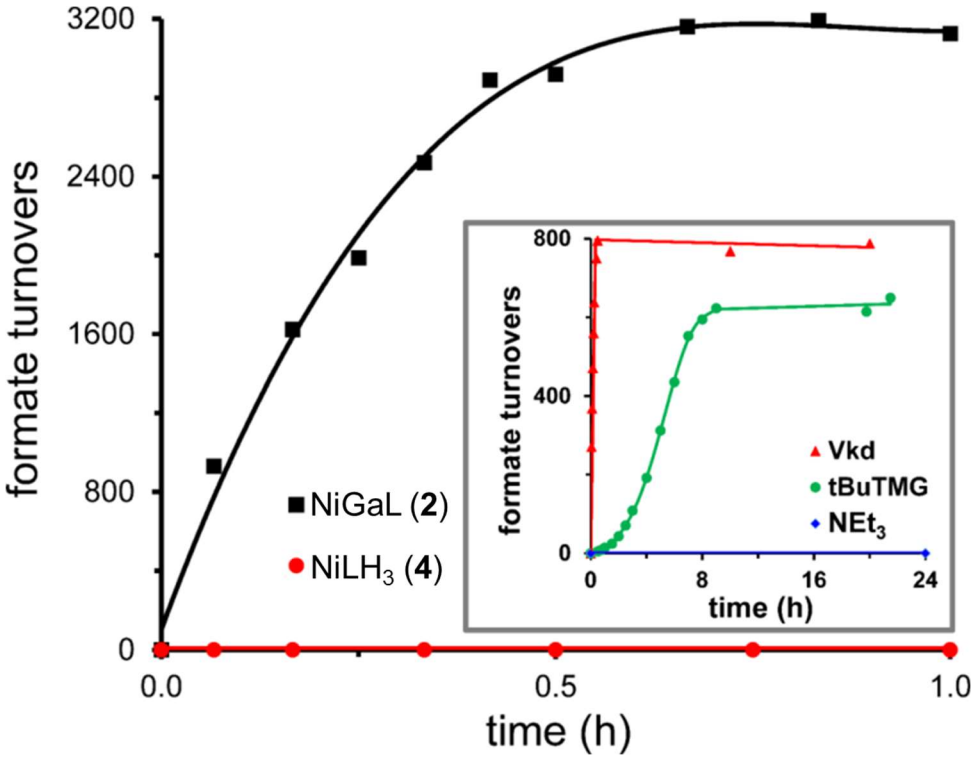

Figure 5.1. Formate turnovers versus time plots for CO_2 hydrogenation reactions catalyzed by **2** and **4** (0.25 mM catalyst, 800 mM Vkd, 34 atm of ~1:1 H_2/CO_2, 293 K, average of two trials for each; see Table 1, entries 3 and 7). Inset shows the kinetic plots for **2** (1 mM or 4 mM) with various bases (Vkd, tBuTMG, and NEt_3; see Table 1, entries 2, 4, and 5). Representative ^{1}H NMR spectra acquired throughout catalysis for **2** and full kinetic profiles of all catalytic trials for **2** and **4** are shown in the Appendix (Figures A.4.7-A.4.12).

A strong base is necessary for catalysis mediated by **2** based on trials with bases of varying strengths (pK_a of conjugate acid in CH_3CN): Vkd (33.6),[342] *t*-butyl tetramethyl guanidine (abbrev. tBuTMG, 26.5),[344] and triethylamine (abbrev. NEt_3, 18.8).[345] Under identical conditions (1 mM **2**, 800 mM base, 34 atm 1:1 H_2/CO_2, 293 K), employing tBuTMG as the base resulted in a lower yield of formate (80%) and a 30-fold decrease in the maximum rate relative to utilizing the stronger Vkd base (Table 5.1, *c.f.* entries 2 and 4). Moreover, an induction period of ~3 h was observed for tBuTMG (Figure 5.1 inset, Figure A.4.12).[128] Of relevance, a similar initial induction period was also reported for CO_2 hydrogenation catalyzed by $HCo(dmpe)_2$ using a base of comparable strength to

tBuTMG.[323, 346] With NEt_3, an even weaker base, no formate was generated (Table 5.1, entry 5). Presumably, NEt_3 is not sufficiently basic to deprotonate the H_2 adduct, (η^2-H_2)NiGaL, to any extent, precluding formation of the catalytically active Ni−H species (*vide infra*).

Table 5.1. Catalytic CO_2 hydrogenation to formate using NiGaL (**2**) or $NiLH_3$ (**4**) with various bases. Reaction conditions: catalyst (0.25 to 4 mM), 800 mM base, ~1:1 H_2/CO_2 (1 or 34 atm), THF-d_8 solution, 293 K.[a]

entry	catalyst	[catalyst] (mM)	base	P(H_2/CO_2) (atm)	formate TON[b]	yield[c] %	TOF (h^{-1}) initial[d]	TOF (h^{-1}) overall[e]
1[f]	**2**	2.9	Vkd	1	250	91	67	41
2	**2**	1	Vkd	34	800	>99	3680	2130
3	**2**	0.25	Vkd	34	3150	99	9700	6900
4	**2**	1	tBuTMG	34	640	80	120[g]	74
5[h]	**2**	4	NEt_3	34	0	0	*N.A.*	*N.A.*
6[f]	**4**	2.9	Vkd	1	0.8	0.3	0.14[i]	0.04
7	**4**	0.25	Vkd	34	0	0	*N.A.*	*N.A.*
8	**4** + $GaCl_3$	0.25	Vkd	34	0	0	*N.A.*	*N.A.*

[a] Conditions apply to all entries unless otherwise noted. TON, % yield, and TOF are reported as averages of two trials. [b]TON based on ^{1}H NMR integration of HCO_2^- relative to an internal capillary standard. [c]% yield based on TON/maximum TON, which closely matched ^{1}H NMR integration of HCO_2^- relative to H(base)$^+$. [d]Initial TOF is the initial linear slope of the formate turnovers vs. time plot (initial ~40 min at 1 atm, or 6-10 min at 34 atm). [e]Overall TOF = turnovers/time for >90% of final yield achieved. [f] 0.40 mL volume for 1 atm runs. [g]Initial TOF is defined from ~3.5 h to 7.5 h over which turnovers/time is linear (after the initial induction period). [h] Single run in 0.75 mL THF in a high-pressure vessel. No HCO_2^- was detected after 150 h at 323 K. [i] Initial TOF determined for the first time point that HCO_2^- was observed (~3.5 h).

The striking effect of the supporting Ga(III) ion is appreciated by comparing **2** with the isostructural Ni-only congener, $NiLH_3$ (**4**).[51] No appreciable yield of formate was generated using **4** as the catalyst (Table 5.1, entries 6-7). Adding $GaCl_3$ as a co-catalyst with **4** also did not yield any formate (Table 5.1, entry 8).[128] Altogether, the catalytic results suggest that the Ni→Ga interaction within our ligand framework provides the requisite tuning effect at Ni to enable catalysis.

5.2.2 How Does the Ga(III) Support Enable Catalysis: Isolating a Reactive Ni−H Intermediate

Because of the remarkable CO_2 hydrogenation activity of **2** relative to known Ni homogeneous catalysts,[324-326] we sought to elucidate the role of the supporting Ga(III) ion in promoting catalysis. Specifically, we sought to identify and study the reactive Ni−H species that is generated when the H_2 adduct, (η^2-H_2)NiGaL (**2**-H_2), is formed in the presence of a strong base. Subjecting **2** to 3-5 equiv of Vkd base and 1 atm of H_2 in THF-d_8 resulted in the *in situ* formation of a new diamagnetic species formulated as the anionic Ni(0) hydride, [VkdH][HNiGaL] ([VkdH][**2**−H]). The ^{31}P NMR spectrum displayed two new resonances at 76 and −12 ppm in a 3:1 ratio for the ion-paired $[HNiGaL]^-$ ($[\mathbf{2}-H]^-$) and $[VkdH]^+$ fragments, respectively (Figure 5.2a). The single ^{31}P signal for $[\mathbf{2}-H]^-$ is consistent with retention of three-fold symmetry, while the hydride resonance in the ^{1}H NMR spectrum appears as a broad peak at −6.4 ppm with no discernible coupling even at low T (Figure 5.2).[128] An excess of Vkd base is required to drive the equilibrium between H_2, Vkd, and NiML toward complete conversion to [VkdH][**2**−H]; it should be noted that the interconversion of **2**−H_2 and [VkdH][**2**−H]

slows relative to the ^{1}H NMR timescale (400 MHz) at low T such that both species become observable (Figure 5.2b).

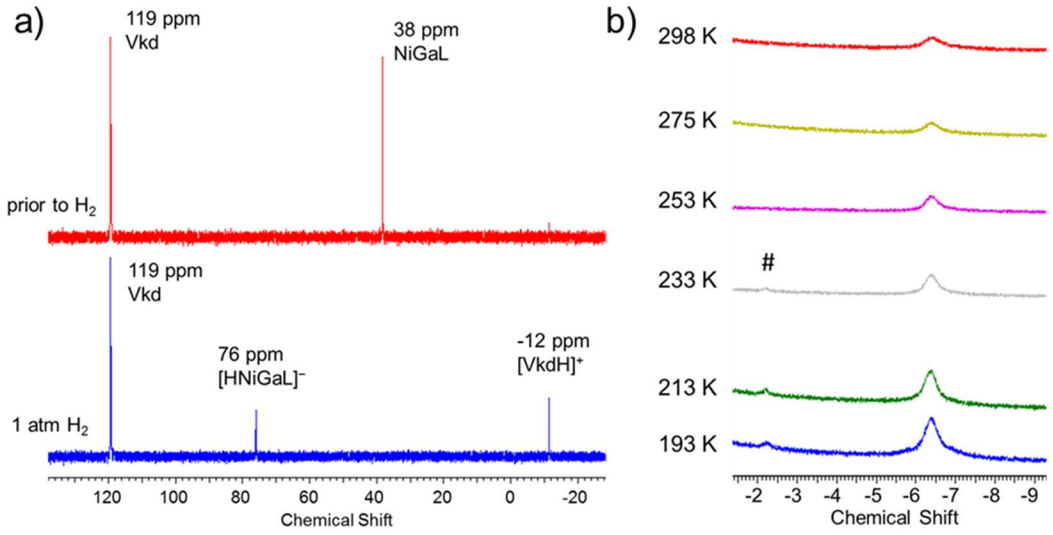

Figure 5.2. (a) ^{31}P NMR spectra (161.9 MHz) and (b) stacked VT ^{1}H NMR spectra (400 MHz) showing the *in situ* generation of [VkdH][HNiGaL] from the addition of H_2 to NiGaL (**2**) in the presence of excess Vkd base in THF-d_8.

Alternatively, independent synthesis of the anionic hydride with different alkali metal cations, [M(THF)$_x$][**2**−H], was carried out via the addition of MBHEt$_3$ (M=Li, Na, K) to **2**. [Li(THF)$_x$][**2**−H] was also synthesized by adding 1.1 equiv *n*BuLi to **1**, presumably via the initial formation of a Ni alkyl species that undergoes subsequent *β*-hydride elimination.[252] Subsequent salt exchange with [bis(triphenylphosphoranylidene)ammonium][tetrakis[3,5-bis(trifluoromethyl)phenyl]borate] ([PPN][BArF]) afforded [PPN][**2**−H] (Figure 5.3).

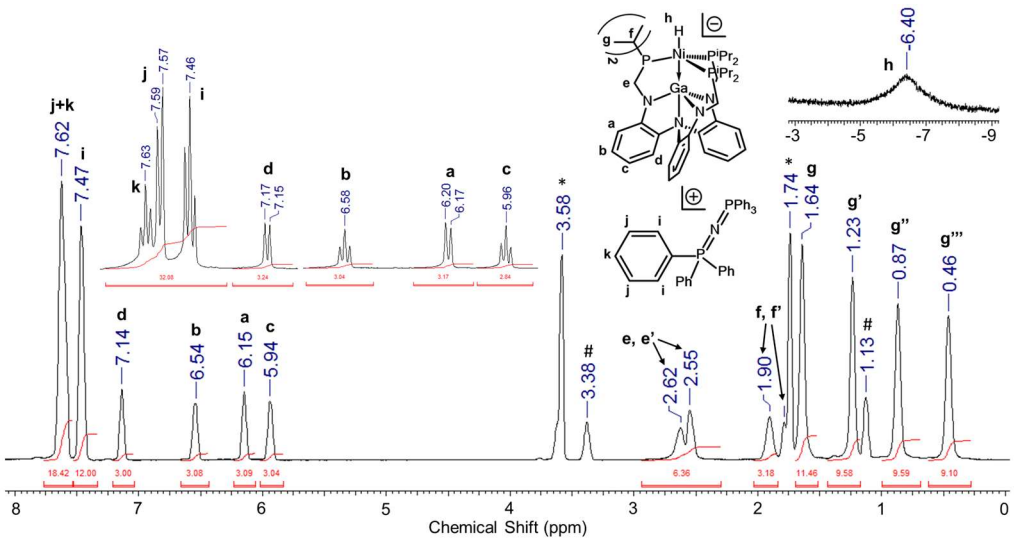

Figure 5.3. ^{1}H NMR spectrum of [PPN][**2**−H] (400 MHz, THF-d_8, 233K). Residual solvent peaks of THF (*) and diethyl ether (#) are denoted. Insets show close-ups of: the hydride region (top right), and resolved coupling in the aryl region at 298 K (top left).

Importantly, the ^{1}H and ^{31}P NMR chemical shifts of the hydride and the phosphines, respectively, in [cation][**2**−H] (cation=Li, Na, K, PPN) are all nearly identical to those of [VkdH][**2**−H], implying that the independently synthesized anionic hydrides are reasonable models of the catalytically relevant [VkdH][**2**−H] species (Figure 5.4a-b).[128]

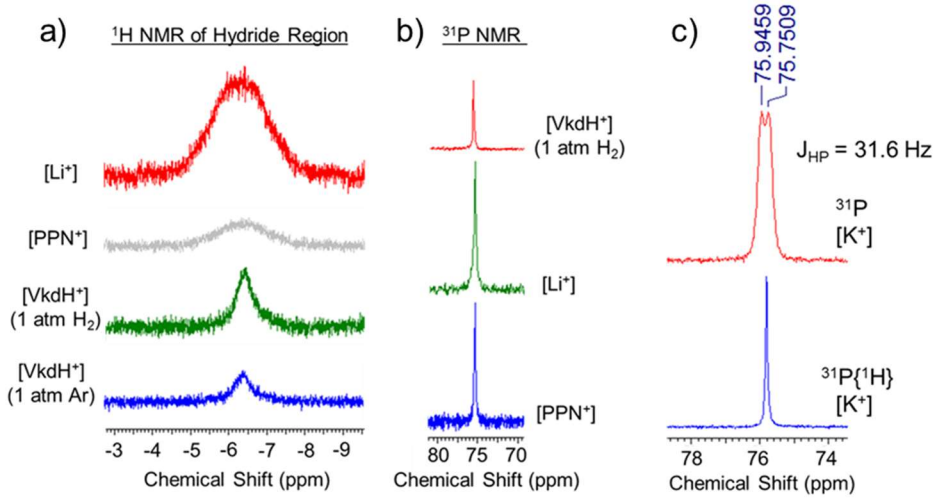

Figure 5.4. (a) Stacked ^{1}H NMR spectra (400 MHz) of the hydride region and ^{31}P NMR spectra (b, 161.9 MHz) for [cation][**2**−H] complexes (cation=VkdH, PPN, Li, K) in THF-d_8. (c) Proton-coupled (top) and proton-decoupled (bottom) ^{31}P NMR spectra of [K(THF)$_x$][**2**−H].

Of note, the proton-coupled ^{31}P NMR spectrum of [K(THF)$_x$][**2**−H] resolves nicely into a doublet with $^{2}J_{PH}$ of 31.6 Hz, as would be expected for the coupling of a terminal hydride to three equivalent phosphorus nuclei (Figure 5.4c).[128] The analogous coupling is difficult to observe by ^{1}H NMR spectroscopy due to the broadness of the hydride resonances in [cation][**2**−H], though it has been resolved into the expected quartet with similar coupling (34.8 Hz) in the case of [Na(THF)$_x$][**2**−H] in ~2:1 THF-d_8/C_6D_6 (Figure A.4.2). As noted, the overall effect of varying the cation in [cation][**2**−H] on the chemical shifts (δ) of the resulting complexes is minimal: ^{31}P δ varies from 75.3 to 75.8 ppm, while ^{1}H δ varies from −6.4 to −6.5 ppm (Figure 5.4a-b). However, it should be noted that the broadness of the hydride resonance does vary for the different cations, with a sharper resonance observed for [VkdH][**2**−H] than for the other [cation][**2**−H] model complexes (Figure 5.4a).

Based on the spectroscopic data, we propose that the hydride ligand is terminally bound to the Ni center and resides in the apical pocket *trans* to the Ga(III) ion. In support of this formulation, a similar $^{2}J_{PH}$ value of 36 Hz was reported for a triphosphine-ligated, terminal Ni−H reported by Peters and co-workers.[189] Additionally, density functional theory (DFT) calculations predicted the terminal Ni−H isomer to be more stable than the bridged Ni(μ−H)Ga isomer by 21.5 kcal/mol (Figure A.4.13, Table A.4.2).[128] To validate the proposed structure of [VkdH][**2**−H], bright-yellow single crystals of [PPN][**2**−H] were obtained from a THF/pentane solution that were suitable for X-ray diffraction (Figure 5.5).

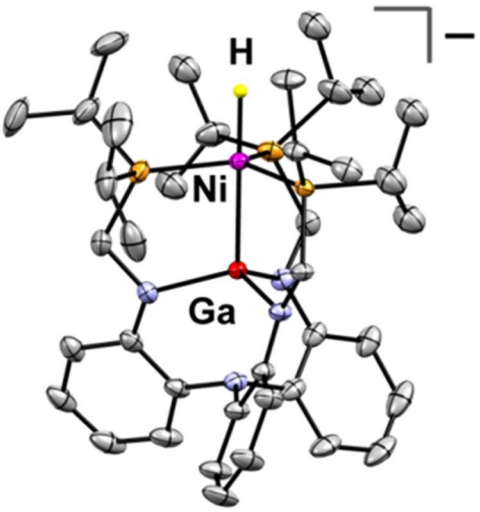

Figure 5.5. Solid-state structure of [PPN][HNiGaL] ([PPN][**2**−H]) displayed with 50% thermal ellipsoids. The apical hydride was placed from the difference map, and the PPN cation and other H atoms were omitted for clarity. Selected structural parameters of [PPN][**2**−H] are shown in Table 5.2. Note that Matt Vollmer synthesized and obtained the crystal structure of [PPN][**2**−H].

The structural characterization of [PPN][**2**−H] is noteworthy because anionic d^{10} hydride complexes are very rare. The only other mononuclear anionic Ni(0) hydride is $[Na(THF)_4][HNi(CO)_3]$, which is unstable at room temperature.[347] Moreover, $[\mathbf{2}{-}H]^-$ has catalytic utility in that it can be generated from H_2 and base, which is in stark contrast to $[Na(THF)_4][HNi(CO)_3]$, which requires stoichiometric $NaHAl(i\text{-}Bu)_3$ to be synthesized.

Table 5.2. Comparison of solid-state structural parameters for **2** and [PPN][**2**−H].[a]

Complex	**2**	[PPN][**2**−H]
Ni−Ga	2.3789(8)	2.3549(4)
r [b]	0.97	0.96
Ni−P [c]	2.210(3)	2.164(7)
Ga−N_{apical}	2.216(3)	2.426(2)
Ga−N_{eq} [c]	1.954(7)	1.977(2)
Ga to N_3-plane	0.369	0.537
Ni to P_3-plane	0.126	0.199

[a]All metrics are in Å except for r (unitless). [a]Covalent ratio (r) = (M−M bond distance)/(sum of Alvarez covalent radii[134] of constituent metals). [b]average value.

In comparison with **2**, [PPN][**2**−H] has subtle structural differences that are instructive to consider. One effect of the hydride donor is that the Ni−Ga bond contracts slightly from 2.3789(8) in **2** to 2.3549(7) Å in [PPN][**2**−H] (Figure 5.5, Table 5.2). Hence, the dative Ni→Ga interaction remains intact upon the introduction of a *trans* hydride. Perhaps the most informative parameters are the positions of the Ni and Ga centers relative to their respective P_3 and N_3 donor planes. In [PPN][**2**−H], both Ni and Ga are displaced further above their respective P_3- and N_3-planes by 0.07 Å and 0.17 Å, respectively, compared to their positions in **2**.[128] Intriguingly, the positioning of Ga changes by more than double that of Ni upon introduction of the hydride ligand, despite the fact that the hydride only interacts directly with Ni! This striking structural feature underscores the cooperativity of the Ni−Ga unit, as both metals reposition together to accommodate the incoming hydride ligand. A complementary interpretation is that a strong Ni→Ga dative interaction assists in stabilizing the electron-rich, anionic Ni−H moiety by attenuating some its electron density.

Another structural change upon the introduction of the apical hydride pertains to the Ni−P bond distances, which contract from 2.210 Å in **2** to 2.164 Å in [PPN][**2**−H].[97, 128] Notably, the Ni−P distance contracts even though its vertical component increases, as the Ni center is repositioned by 0.07 Å further above the P_3-plane to interact with the hydride ligand. The shorter Ni−P bonds in [PPN][**2**−H] are consistent with increased Ni→P π-back-donation to stabilize the electron-rich Ni(0) center of the anionic complex. It should be noted that a dramatic downfield shift is observed for [PPN][**2**−H] (~75.6 ppm) relative to **2** (37.6 ppm) by ^{31}P NMR spectroscopy (Figure 5.2), which could indicate an increase in P→Ni σ-donation accompanying the presumed increase in Ni→P

π-back-donation for [PPN][**2**−H] relative to **2**. The downfield ^{31}P NMR shift of [PPN][**2**−H] relative to **2** could also be attributable to the former complex binding an apical ligand and/or becoming negatively charged (Figure 5.2a).

By IR spectroscopy, a KBr pellet of [PPN][**2**−H] displayed a broad band of medium intensity at 1696 cm^{-1} (Figure 5.6). The assignment of 1696 cm^{-1} as the Ni−H stretching frequency was confirmed by comparison to the IR spectrum for the deuterated analogue, [PPN][**2**−D], which was synthesized via the addition of ~4 atm D_2 to [PPN][**2**−H] with concomitant formation of HD. The isotopic shift upon deuteration is close to the expected shift based on Hooke's law, with ν=1226 cm^{-1} observed for the Ni−D stretch compared with the expectation of 1211 cm^{-1}.[128] While the shift upon deuteration is somewhat difficult to observe in the midst of other features with similar frequency in the IR spectrum, the clear disappearance of the Ni−H stretch at 1696 cm^{-1} upon deuteration is further confirmation of its assignment. It should also be noted that the two features at 2000 to 2400 cm^{-1} that appear in the IR spectrum after exposure of [PPN][**2**−H] to D_2 likely correspond to C(sp^3)−D stretches of the ligand isopropyl groups which have shifted (from 2700 to 3000 cm^{-1}) upon the incorporation of D via a presumed ortho C−H metallation process (Figure 5.6).

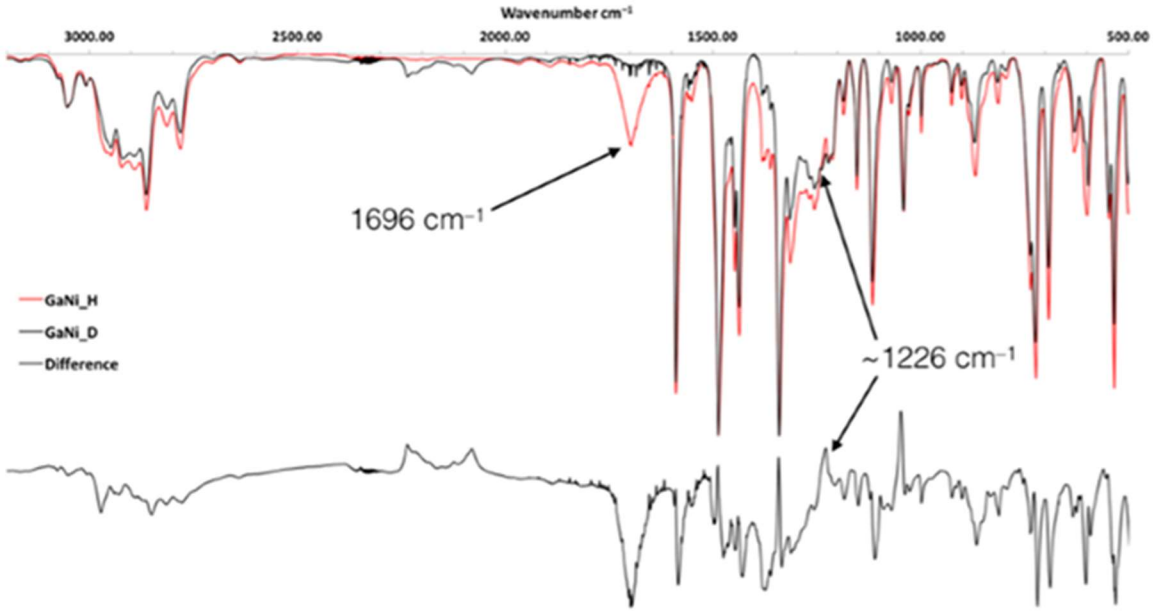

Figure 5.6. IR spectra (KBr pellet) of [PPN][**2**−H] and [PPN][**2**−D], along with the corresponding difference spectra. IR experiments and the figure are courtesy of Matt Vollmer.

The Ni−H stretching frequency was also corroborated by a closely matched value of 1697 cm^{-1} from DFT calculations. Of note, this frequency value is extremely low for terminal hydrides of Ni, and nearly ties with CpNi(IMes)H (1695 cm^{-1}) for the lowest Ni−H stretching frequency.[252, 348] The low stretching frequency would seem to be consistent with a relatively weak Ni−H bond, and it is possible that the polarity of the bond, stemming from the anionic charge of the complex, contributes to this low stretching frequency. The strength of the Ni−H bond in [**2**−H]$^-$, in terms of the bond dissociation free energy (BDFE), will be considered in section 5.2.13.1. Theoretical studies were also conducted to gain additional insight into the nature of the Ni−H bond, which will be presented in the next section.

5.2.3 Understanding the Stability and Reactivity of the Anionic Ni Hydride Intermediate

5.2.3.1 The Nature of Ni−H Bonding: Computational Insight into a Rare d^{10} M−H Species

Perhaps, the most unexpected feature of $[HNiGaL]^-$ ($[\mathbf{2}-H]^-$**)** is its stability as an anionic d^{10} hydride.[349] A simple bonding analysis between a d^{10} metal and a hydride ion ($H:^-$) would require the M−H σ-antibonding orbital to be fully populated. Natural orbitals obtained from complete active space self-consistent field (CASSCF)[185] calculations, however, revealed a distinctly different bonding scheme. While the five Ni 3*d* orbitals are indeed doubly occupied, consistent with Ni(0), they show essentially no bonding to the hydride. Rather, the natural orbital involved in Ni−H σ-bonding has both contributions from both metals [29% Ni, primarily $4p_z$; 10% Ga] and substantial hydridic character [51% H(1*s*)] (Figure 5.7, Table A.4.3).

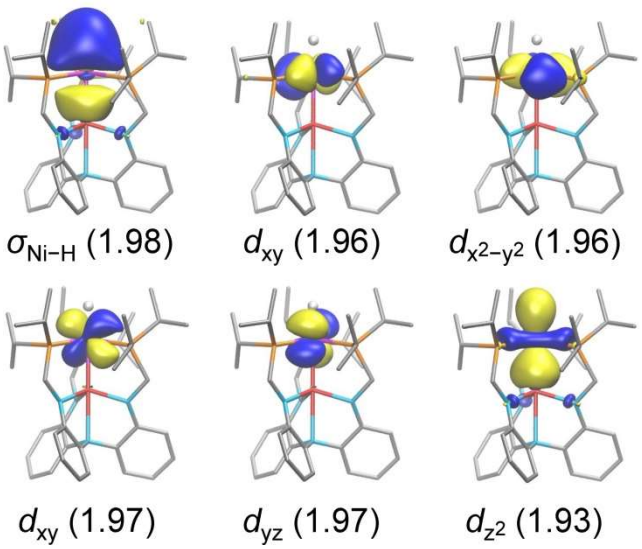

Figure 5.7. Selected natural orbitals for $[\mathbf{2}-H]^-$ obtained from CASSCF calculations. The occupation numbers (shown in parentheses) indicate that these six orbitals are doubly occupied. Thus, $[\mathbf{2}-H]^-$ is best described by a single-determinant wavefunction with five doubly occupied Ni 3*d* orbitals and one doubly occupied Ni−H σ-type orbital, which accounts for 88.9% of the total wavefunction. Note that this figure and the computational results it contains were provided by Dr. Jing Xie. Refer to Figure A.4.14 and Table A.4.3 for additional details.

It is further proposed that the Ni→Ga interaction is critical for stabilizing the Ni(0)−H bond because of the symbiotic nature of two σ-bonding interactions: (1) σ-donation from the hydride to Ni, via H(1*s*)→ Ni(4p_z/4*s*), and (2) σ-donation from Ni to Ga, via Ni(3d_{z2})→Ga(4p_z/4*s*). This stabilization of the Ni−H moiety by Ga(III) can be interpreted as an *inverse trans influence* exerted by the Ga metalloligand, which acts as a σ-acceptor toward Ni and strengthens the Ni−H bond directly *trans* to it.[97, 128, 167] In support, a natural bond orbital (NBO)[114] analysis shows that the Ni→Ga stabilization energy increases by 10 kcal/mol upon the introduction of the hydride, comparing **2** to [**2**−H]$^-$ (Figure A.4.15, Table A.4.4). These two complementary σ-interactions that lead to the stabilization of the anionic Ni−H complex are analogous to those proposed in chapter 3 for H_2 binding, with the only difference being that σ-donation to Ni is from the hydride ligand rather than from the σ-bond of H_2. The importance of Ga(III) for stabilizing the anionic Ni−H moiety is, perhaps, underscored by our inability to synthetically generate the [HNiLH_3]$^-$ ([**4**−H]$^-$) analogue. No H_2 binding to NiLH_3 (**4**) was observed, even at 34 atm H_2 and 193 K, and deprotonation to give [**4**−H]$^-$ was not observed under an H_2 atmosphere in the presence of an excess of strong bases like Vkd base and potassium *tert*-butoxide. Likewise, the addition of MHBEt_3 or *n*BuLi to **4** did not form [**4**−H]$^-$, and instead generated a NiLi_3L species via deprotonation of the NH bonds of the ligand. Subjecting NiLi_3L to additional MHBEt_3, *n*BuLi, or to H_2 and strong base were also not observed to be viable synthetic routes to a [HNiLi_3L]$^-$ species. While the inability to synthesize a mononuclear [HNi]$^-$ species in our hands does not mean it cannot be generated, it does imply that such a species is significantly more unstable than [HNiGaL]$^-$ ([**2**−H]$^-$). DFT calculations suggest that the Ga(III) supporting metal ion

stabilizes [**2**−H]$^-$ from hydride transfer reactivity by ~9 kcal/mol relative to the hypothetical [**4**−H]$^-$ analogue.[128]

5.2.3.2 Thermodynamic Hydricity Measurements of [HNiGaL]$^-$ Reveal a Potent Hydride Donor

Another useful parameter for comparing the reactivity of metal hydride complexes is the thermodynamic hydricity ($\Delta G°_{H-}$), or the free energy needed to cleave a M−H bond to generate a hydride ion.[329-330, 350] The $\Delta G°_{H-}$ of [HNiGaL]$^-$ ([**2**−H]$^-$) was experimentally determined by measuring the H_2 heterolysis equilibrium[330] with NiGaL (**2**) and Vkd base (Equation 5.1), in conjunction with the known pK_a of [VkdH]$^+$ (Equation 5.2)[342] and the H_2 heterolysis constant in CH_3CN (Equation 5.3),[329, 350] as shown below in Equation 5.4.

Equilibrium	$\Delta G°$ (kcal/mol)	
[**2**−H]$^-$ + [VkdH]$^+$ ⇌ **2** + H_2 + Vkd	$\Delta G°_1$ = −1.364·log(K_{eq})	(Eqn 5.1)
Vkd + H^+ ⇌ $VkdH^+$	$\Delta G°_2$ = −1.364(pK_a)	(Eqn 5.2)
H_2 ⇌ H^+ + H^-	$\Delta G°_3$ = +76 kcal/mol	(Eqn 5.3)
[**2**−H]$^-$ ⇌ **2** + H^-	$\Delta G°_{H-} = \Delta G°_1 + \Delta G°_2 + \Delta G°_3$	(Eqn 5.4)

Hydricity values are typically measured in CH_3CN since $\Delta G°_3$ is known (Equation 5.3), and so one caveat to estimating the absolute hydricity of [**2**−H]$^-$ is that K_{eq} of Equation 5.1 was measured in THF due to complications arising from poor solubility of **2** in CH_3CN and competitive binding between H_2 and CH_3CN (see section 5.2.6.2). K_{eq} of Equation 5.1 was measured to be 0.16 (±0.11) in THF based on two independent trials employing different base concentrations which were monitored by ^{31}P

NMR spectroscopy until equilibrium was achieved (Figure A.4.16, Tables A.4.5-A.4.6). If K_{eq} of Equation 5.1 is comparable in THF and CH_3CN solvents, one can estimate $\Delta G°_{H-}$ = 31.3(5) kcal/mol for $[HNiGaL]^-$ in CH_3CN.[128] Although the difference in polarity between THF and CH_3CN may influence K_{eq} of Equation 5.1 via the stability imparted to the $[VkdH]^+$ and $[\mathbf{2}-H]^-$ fragments through ion-pairing interactions, we believe this assumption to be reasonable for estimating $\Delta G°_{H-}$ for $[\mathbf{2}-H]^-$. Indeed, the same assumption was made in the measurement of the hydricity of $HRh(diphosphine)_2$ complexes.[351] Alternatively, one can rigorously measure the difference in $\Delta G°_{H-}$ values between $[\mathbf{2}-H]^-$ and H_2 in THF, or $\Delta G°_{H-}(H_2) - \Delta G°_{H-}([\mathbf{2}-H]^-)$. This difference represents how much more favorable it is to liberate a hydride ion from $[\mathbf{2}-H]^-$ than from H_2, and requires no assumptions about the H_2 heterolysis constant.[329, 350] In THF, this difference, which is equivalent to the difference between Equations 5.4 and 5.3, or $\Delta G°_1 + \Delta G°_2$, is 37.1(6) kcal/mol, which is comparable to the difference of 45 kcal/mol in CH_3CN obtained using the estimated $\Delta G°_{H-}([\mathbf{2}-H]^-)$ of 31 kcal/mol.[128]

To further test the assumption that measuring K_{eq} of Equation 5.1 in THF can lead to meaningful comparisons with $\Delta G°_{H-}$ values measured in CH_3CN, the hydride-transfer equilibrium was probed between **2** and $HCo(dmpe)_2$, for which $\Delta G°_{H-}$ = 36 kcal/mol in CH_3CN.[323, 352] No hydride transfer to **2** was detected in THF over 2.5 weeks, indicating that the $\Delta G°_{H-}$ value of $[\mathbf{2}-H]^-$ is < 33 kcal/mol, under the assumption that a 1:19 ratio of $[\mathbf{2}-H]^-$ to **2** would be detectable by ^{31}P NMR spectroscopy (Figure A.4.17). To verify that the lack of hydride transfer from $HCo(dmpe)_2$ to **2** was not the result of slow hydride transfer kinetics, the reaction was also performed in the reverse direction, where full consumption of $[\mathbf{2}-H]^-$ and $[Co(dmpe)_2]^+$ to give $HCo(dmpe)_2$ and $(CH_3CN)NiGaL$ was

observed within 5 days in ~3:1 CH_3CN/THF (Figure A.4.17). Additionally, DFT studies of hydride transfer between [**2**−H]$^-$ and [Ni(dmpe)$_2$]$^{2+}$ in CH_3CN[329-330] leads to a predicted hydricity of 28-31 kcal/mol for [**2**−H]$^-$, depending on the computational methods employed, which matches well with the experimental estimate (Tables A.4.7-A.4.8).[128]

For comparison, [HNi(diphosphine)$_2$]$^+$ complexes have hydricity values that range from 50 to 68 kcal/mol in CH_3CN.[252, 328-329] With a considerably lower $\Delta G°_{H-}$ value (~31 kcal/mol), [**2**−H]$^-$ is, by a wide margin, the strongest hydride donor of any Ni−H reported to date. The exceptional hydricity of [**2**−H]$^-$ can be attributed to its anionic charge and zero-valent oxidation state of Ni, which is distinct from the cationic Ni(II) hydrides in the literature. Notably, [**2**−H]$^-$ is among the strongest hydride donors of any first-row metal complex (*c.f.* HCo(P_4N_2), $\Delta G°_{H-}$ = 31.8 kcal/mol in CH_3CN),[353] and is even on par with some of the more hydridic precious metal hydrides, (e.g. HRh(diphosphine)$_2$, $\Delta G°_{H-}$ = 26-34 kcal/mol in CH_3CN).[328-329, 351, 354] Of relevance to CO_2 reduction catalysis, the high $\Delta G°_{H-}$ values of [HNi(diphosphine)$_2$]$^+$ complexes do not allow for spontaneous hydride transfer to CO_2, as $\Delta G°_{H-} < 44$ kcal/mol is required for favorable outer-sphere hydride transfer to generate formate in CH_3CN.[331] While stoichiometric reactivity of [HNi(dmpe)$_2$]$^+$ ($\Delta G°_{H-}$ = 49.9 kcal/mol)[329-330] with CO_2 to generate formate derivatives can be accomplished using sacrificial boranes, catalytic CO_2 reduction was not feasible in this system, even in the presence of borane and exogenous base.[355] In contrast to the [HNi(diphosphine)$_2$]$^+$ complexes, the low $\Delta G°_{H-}$ of [**2**−H]$^-$ should allow for spontaneous outer-sphere hydride transfer to CO_2 to occur with an estimated thermodynamic driving force of ~13 kcal/mol. It should be noted, however,

that the thermodynamic driving force for outer-sphere hydride transfer may differ due to Ni–O bond formation after initial hydride transfer (*vide infra*).[128]

5.2.3.3 Characterization of an Anionic Formate Adduct Generated from the Reaction of [HNiGaL]⁻ with CO_2

To test whether hydride transfer from [HNiGaL]⁻ ([**2**–H]⁻) to CO_2 was spontaneous, as determined by comparing the hydricity values of [**2**–H]⁻ and HCO_2^-, the addition of 1 atm CO_2 to [VkdH][**2**–H] was performed. A new diamagnetic species that was formulated as an anionic formate adduct, [VkdH][(η^1-HCO_2)NiGaL] ([VkdH][**2**–O_2CH]), was generated *in situ*. Alternatively, [VkdH][**2**–O_2CH] can be generated via the addition of a slight excess of [VkdH][HCO_2] to **2**. A single resonance was observed at 34.8 ppm by ^{31}P NMR spectroscopy, and a diagnostic ^{1}H NMR resonance at 8.68 ppm was attributed to the coordinated formate proton (*c.f.* 8.79 ppm for free [VkdH][HCO_2]; Figures 5.8 and A.4.3). This intermediate was also isolated as the PPN ion-pair, [PPN][**2**–O_2CH], by exposing [PPN][**2**–H] to 1 atm CO_2 (Figure 5.8).[128]

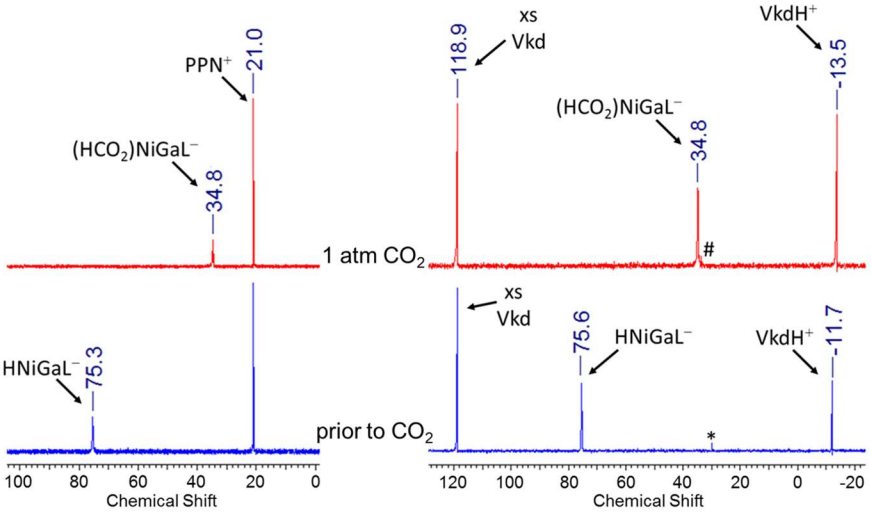

Figure 5.8. Stacked ^{31}P NMR spectra (161.9 MHz, THF-d_8) for the addition of CO_2 (1 atm) to [PPN][**2**–H] (left) and [VkdH][**2**–H] (right) to generate [cation][**2**–O_2CH] complexes. Trace impurities of $NiLH_3$ (*) and [VkdH][ClNiGaL] (#) are denoted in the spectra.

The coordinated formate proton resonance (8.57 ppm) of [PPN][**2**−O_2CH] is located slightly upfield of free [PPN][HCO_2^-] (8.61 ppm), and integrates ~1:3 with each of the four unique aryl protons of the ligand (Figure 5.9).

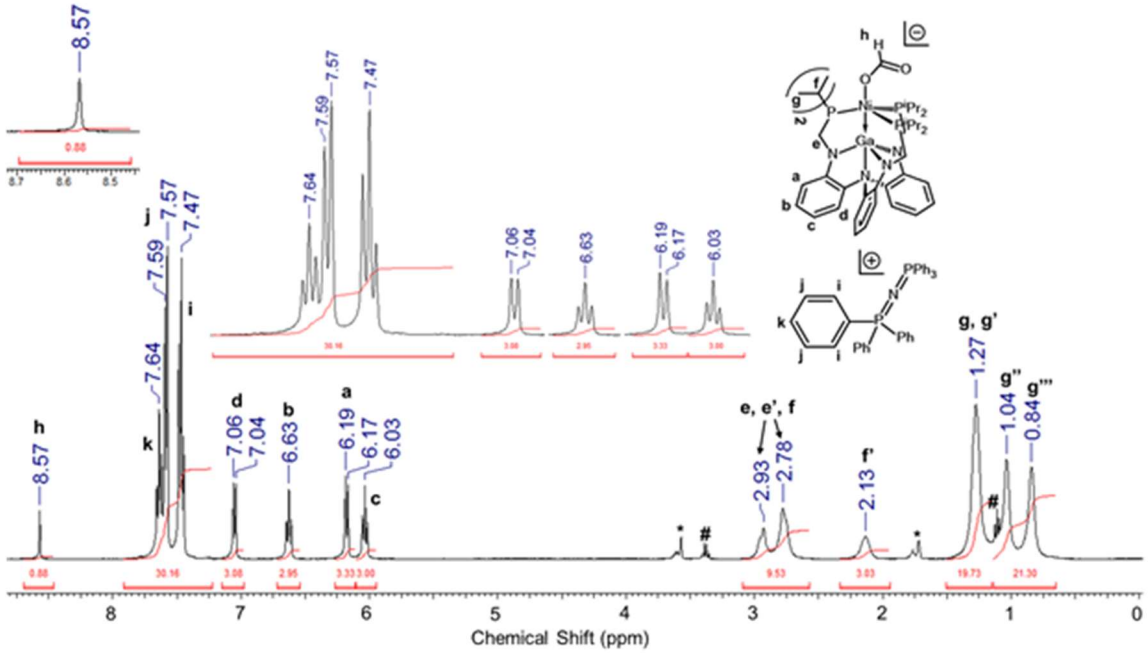

Figure 5.9. ^{1}H NMR spectrum of [PPN][**2**−O_2CH] (400 MHz, THF-d_8). Residual solvent peaks of THF (*) and diethyl ether (#) are denoted. Close-ups of the coordinated formate proton (top left) and of resolved coupling in the aryl region (top, center) are shown for visual clarity.

Additionally, a cross-peak in the ^{1}H-^{13}C HMQC NMR spectrum of [PPN][**2**−O_2CH] allowed for the assignment of a ^{13}C NMR resonance at 167.6 ppm to the carbon of the coordinated formate moiety (Figure A.4.18). The ^{1}H and ^{13}C NMR resonances for coordinated formate are similar to those reported for other η^1-O formate complexes of Ni in the literature, which are typically 8.3-8.9 ppm and 166-169 ppm, respectively.[252, 332-336] The assignment of formate as being coordinated to Ni in the [cation][**2**−O_2CH] complexes is also supported by the fact that NiGaL (**2**) was not observed in the ^{31}P NMR spectra, which would be expected if formate dissociated from [cation][**2**−O_2CH] to give **2** and [cation][HCO_2] (Figure 5.8). In comparing the NMR

spectra of [PPN][**2**−O_2CH] and [VkdH][**2**−O_2CH], the cation was seen to minimally effect the ^{31}P and ^{1}H chemical shifts, with the former found to be nearly identical at 34.8 ppm and the latter only differing by 0.1 ppm, which suggested that [PPN][**2**−O_2CH] could serve as a reasonable model of the catalytically relevant [VkdH][**2**−O_2CH] species.[128]

The solid-state structure of [PPN][**2**−O_2CH] was determined via x-ray crystallography, and shows an η^1-*O* formate ligand and an intact Ni−Ga bond of 2.3789(5) Å, which is essentially identical to that of **2** (Figure 5.10, Table 5.3). In comparing the structure of [PPN][**2**−O_2CH] to that of [PPN][**2**−H], the most striking differences are the repositioning of Ni by ~0.12 Å further above the P_3-plane to interact with formate, which also results in substantial elongation of the Ni−P bonds by ~0.10 Å (Table 5.3). Though the Ni−Ga bond remains intact in [PPN][**2**−O_2CH], the Ga center is not positioned further above the N_3-plane to match the repositioning of Ni, and in fact is positioned slightly closer to the N_3-plane than in [PPN][**2**−H] (Table 5.3).[128]

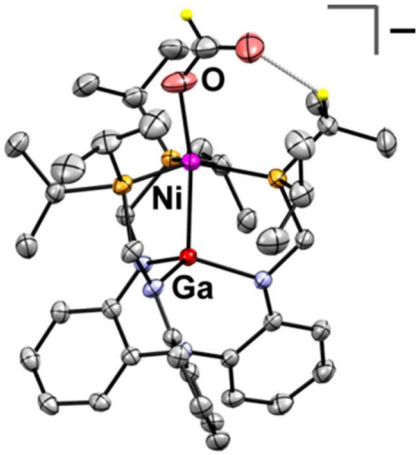

Figure 5.10. Solid-state structure of [PPN][(HCO_2)NiGaL] ([PPN][**2**−O_2CH]) displayed with 50% thermal ellipsoids. The PPN cation and H atoms, except for those on or interacting with the apical ligands, were omitted for clarity. A nonclassical hydrogen-bonding interaction, O(formate)---HC(methine), is shown (light gray line). Note that this crystal structure was obtained by Matt Vollmer. Relevant structural parameters are shown in Table 5.3.

The fact that the Ni−Ga bond only elongates by ~0.02 Å in [PPN][**2**−O_2CH] relative to that in [PPN][**2**−H], even though Ni and Ga are positioned further apart by a total of ~0.15 Å compared with their respective donor planes, illustrates the ability of the ligand to twist and adjust its P−Ni−M−N_{eq} dihedral angle to accommodate the Ni→Ga interaction. The solid-state structure of [PPN][**2**−O_2CH] also shows a close contact of 2.24 Å for an apparent nonclassical hydrogen-bonding interaction between the uncoordinated formate oxygen atom and one of the ligand methine hydrogen atoms. It remains an open question whether this interaction remains intact in solution or is simply the result of crystal packing forces in the solid-state; this distinction will be discussed further in section 5.2.7.2.

Table 5.3. Comparison of structural parameters for **2**, [PPN][**2**−H] and [PPN][**2**−O_2CH].[a]

Complex	**1**	[PPN][**2**−H]	[PPN][**2**−O_2CH]
Ni−Ga	2.3789(8)	2.3549(4)	2.3789(5)
r [a]	0.97	0.96	0.97
Ni−P [c]	2.210(3)	2.164(7)	2.26(1)
Ga−N_{apical}	2.216(3)	2.426(2)	2.372(2)
Ga−N_{eq} [c]	1.954(7)	1.977(2)	1.960(7)
Ga to N_3-plane	0.369	0.537	0.509
Ni to P_3-plane	0.126	0.199	0.321
P−Ni−M−N_{eq} (°) [c]	17.1	11.7	20.6

[a]All metrics are in Å except for *r* (unitless) and P−Ni−M−N_{eq} angle. [b]Covalent ratio (*r*) = (M-M bond distance)/(sum of Alvarez covalent radii[134] of constituent metals). [c]average value.

[PPN][**2**−O_2CH] was also characterized by IR spectroscopy, with two inequivalent stretching frequencies, 1610 and 1339 cm^{-1}, assigned to the coordinated

formate moiety (Figure 5.11).[128] These assignments were confirmed by isotopic labelling, with [PPN][**2**−$O_2{}^{13}$CH] synthesized by the exposure of [PPN][**2**−O_2CH] to $^{13}CO_2$, which also shows that CO_2 insertion into the Ni−H bond of [PPN][**2**−H] is reversible. The shift of the ν(C=O) band at 1610 cm^{-1} to 1565 cm^{-1} upon labeling was close to the expected shift (1575 cm^{-1}) from Hooke's Law. The assignment of ν(C−O) at 1339 cm^{-1} is tentative, and is based on the difference spectrum along with ruling out several potential peaks based on the fact that they are coincident with the IR spectrum of NiGaL (**2**), and are therefore likely attributable to vibrational modes that are unrelated to the coordinated formate ligand (Figure A.4.19).[128] The difference in the two stretching frequencies, Δν(CO), of greater than 200 cm^{-1} indicates that the coordinated formate moiety is best described as a monodentate carboxylate ligand.[356] Furthermore, these assignments are similar to those for other η^1-O formate adducts of Ni in the literature, for which ν(C=O) and ν(C−O) of 1600-1630 and 1310-1320 cm^{-1} were reported.[252, 332-336]

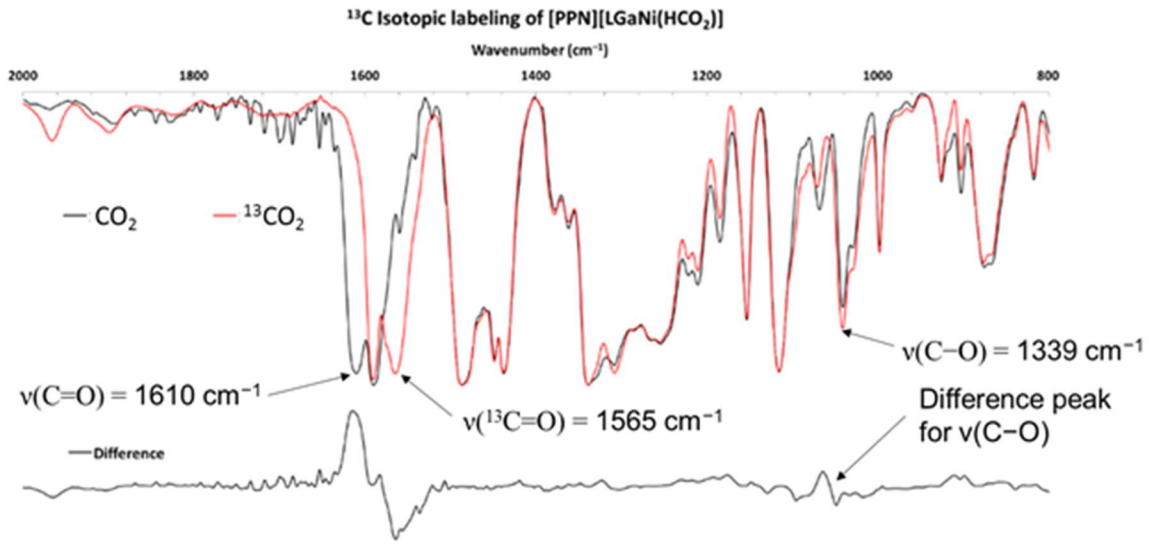

Figure 5.11. IR spectra (KBr pellet) of [PPN][**2**−O_2CH] and [PPN][**2**−$O_2{}^{13}$CH]. Note that these IR experiments and the figure are courtesy of Matt Vollmer.

*5.2.4 Mechanistic Insights into Catalysis Mediated by NiGaL (**2**)*

Based on the isolated intermediates and their stoichiometric reactivity, a simple catalytic cycle is proposed (Figure 5.12): (1) H_2 binding to NiGaL forms (η^2-H_2)NiGaL, (2) deprotonation by base generates [HNiGaL]$^-$, (3) hydride transfer to CO_2 forms [(η^1-HCO_2)NiGaL]$^-$, and (4) liberation of formate regenerates NiGaL. This catalytic mechanism is commonly proposed, albeit typically with $M(H)_2^+$ and a neutral M−H species as the catalytic intermediates instead of M(η^2-H_2) and an anionic M−H species, as proposed here.[10, 323] Excitingly, the four primary species in the proposed catalytic cycle have all been independently characterized (*vide supra*; Figure 5.12).

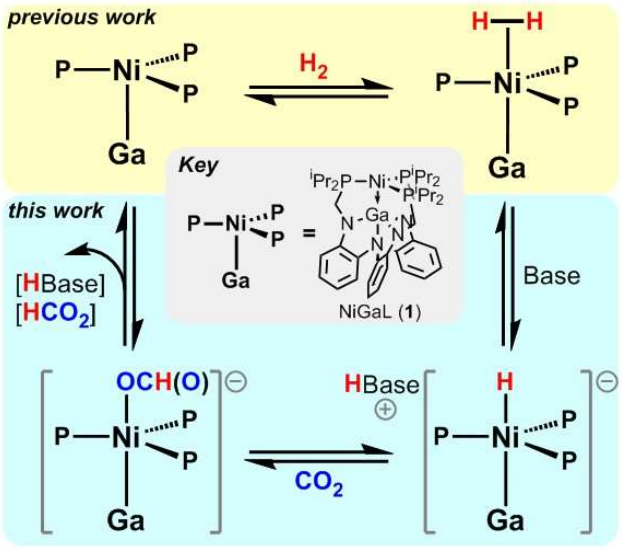

Figure 5.12. General catalytic scheme for H_2/CO_2 to formate mediated by NiGaL (**2**).

The feasibility of the proposed mechanism is further demonstrated by complementary reactivity studies. Initial binding of H_2 is favored as **2** showed no propensity to bind CO_2 at rt, even under 34 atm (chapter 3). Deprotonation of **2**−H_2 to generate [BaseH][**2**−H] occurs readily in the presence of H_2 (1 atm) and excess Vkd (Figures 5.2 and A.4.1). Of interest, the pK_a value of **2**−H_2 was determined to be 27.5(2)

in THF via measurement of the proton-transfer equilibrium between **2**−H_2 and Vkd in the overall H_2 heterolysis reaction (Equation 5.1, Tables A.4.5-A.4.6).[128] Under the assumption that the pK_a difference between $[VkdH]^+$ and **2**−H_2 is the same in both THF and CH_3CN, this would give an estimated pK_a of 33.1(2) in CH_3CN for **2**−H_2 based on the reported pK_a values of $[VkdH]^+$ in THF (~28)[357] and in CH_3CN (33.6).[342] This supports the hypothesis that a strong base is necessary to form the active species, [**2**−H]$^-$. For comparison, the pK_a of H_2 is estimated to be 49 in THF,[358] which means that the acidity of H_2 increases by ~21 pK_a units upon binding to **2**.

After deprotonation, the reaction between [VkdH][**2**−H] and CO_2 (1 atm) was observed to form [VkdH][**2**−O_2CH] (Figure 5.8). Monitoring the Ni speciation during catalysis also provided unique insights. Throughout catalysis with Vkd base, the observed catalyst resting state is the formate adduct, [VkdH][**2**−O_2CH] (Figure A.4.20). From [VkdH][**2**−O_2CH], regeneration of the catalytically active [VkdH][**2**−H] species was observed to occur upon the addition of H_2 (1 atm) in the presence of Vkd (Figure A.4.21). Additionally, isotopic labelling studies confirmed that formate was derived from D_2 and $^{13}CO_2$ (Figure A.4.22). The buildup of the anionic formate adduct during catalysis suggests the rate-determining step (RDS) is the liberation of [VkdH][HCO_2] from [VkdH][**2**−O_2CH] to regenerate **2**, which can then bind H_2 to continue on with catalysis.[128] That formate dissociation would be the RDS is perhaps unsurprising, as Ni formate adducts with strong Ni−O bonds which require sacrificial borane or silane reagents to cleave have been reported in other systems.[332-333] Likewise, formate dissociation is also sluggish for highly active Fe and Co pincer catalytic systems with TONs of ~10^4, and sub-stoichiometric Li^+ additives are needed to promote formate loss

and drive catalytic turnover.[321-322] In the present system, no additives were used. Presumably, formate extrusion is enhanced by the overall anionic charge of the Ni formate intermediate, which likely renders the Ni(0)−OCHO bond comparatively weak and more polarized than is the case in other systems.

5.2.5 Digging Deeper into the Catalytic Cycle: Insights into Important Mechanistic Subtleties from Computations with Support from Experimental Observations

5.2.5.1 Overview of DFT Calculated Reaction Mechanism

Apart from these mechanistic insights, more in-depth studies were also conducted to help understand the catalytic cycle and guide future improvements to catalytic activity. DFT calculations were performed to investigate the viability of the general mechanism proposed in Figure 5.12, as well as identify other mechanistic nuances and important catalytic intermediates that are not isolable. Figure 5.13 shows a more detailed mechanistic pathway for CO_2 hydrogenation that expands on the general proposal given in Figure 5.12.[129]

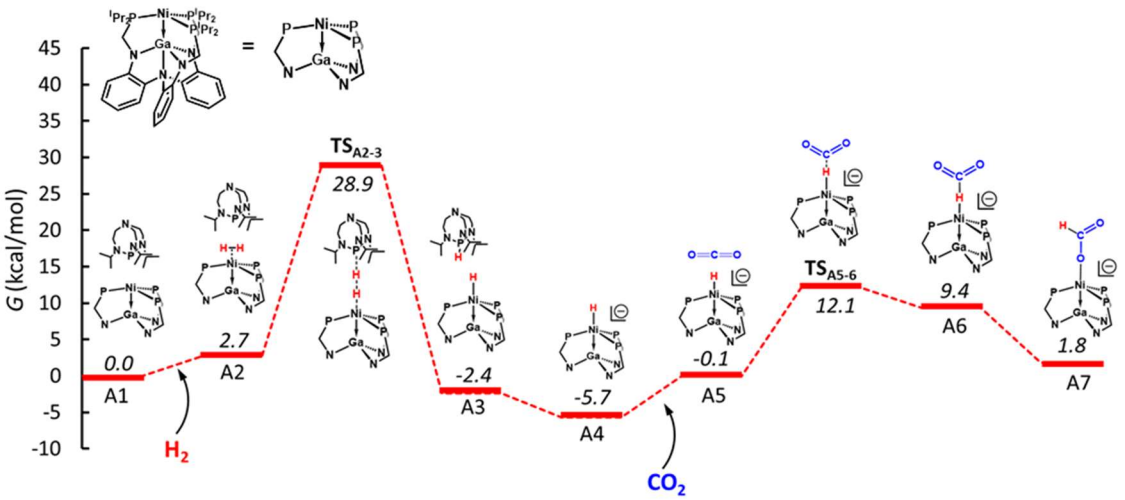

Figure 5.13. DFT-calculated (M06-L/bs1) Gibbs free energy profile for CO_2 hydrogenation catalyzed by NiGaL (**2**). Note that catalytic intermediates have been re-labeled as **A1**, **A2**, and so on, but still represent many of the same species that were previously proposed. This figure and the computational results within it were provided by Dr. Jinyun Ye.

Under standard catalytic conditions, the initial concentration of Verkade's base (800 mM) is significantly higher than the concentration of the NiGaL catalyst (0.25 mM). Hence, the starting point (ie. zero energy in Figure 5.13) was defined as the van der Waals complex [NiGaL][Vkd] (**A1**), rather than NiGaL, along with H_2 (g, 1 atm), and CO_2 (g, 1 atm). The binding of H_2 to **A1** leads to the formation of the H_2 adduct [(η^2-H_2)NiGaL][Vkd] (**A2**), also calculated as a van der Waals complex with Vkd base, which is endergonic by 2.7 kcal/mol. The H_2 adduct (**A2**) can be deprotonated by Verkade's base directly, via transition state $\mathbf{TS_{A2\text{-}3}}$ with a free energy of activation ($\Delta G^{\ddagger}$) of 26.2 kcal/mol, to form the anionic Ni hydride complex, [VkdH][HNiGaL] (**A3**), which is more stable than **A1** by 2.4 kcal/mol.[129] The predicted thermodynamic favorability for H_2 deprotonation is validated by the experimental observation of quantitative conversion to [VkdH][HNiGaL] upon the introduction of H_2 (1 atm) to a THF solution containing NiGaL and ~5 equiv Vkd base.[128]

After diffusion of CO_2 to form the van der Waals complex, **A5**, outer-sphere hydride transfer to CO_2 through transition state $\mathbf{TS_{A5\text{-}6}}$ results in the formation of the η^1-H formate adduct, **A6**. Outer-sphere hydride transfer to CO_2 proceeds with $\Delta G^{\ddagger}$ of 12.2 kcal/mol with respect to the van der Waals complex **A5**, and 17.8 kcal/mol with respect to **A4** and free CO_2. This latter barrier is very similar to the value of 17.2 kcal/mol computed for outer-sphere hydride transfer in THF from the similarly hydridic $HCo(dmpe)_2$ to CO_2, which was predicted to be the RDS for the most active first-row metal catalytic system reported to date for CO_2 hydrogenation to formate.[323, 359] After hydride transfer, the η^1-H formate adduct, **A6**, is predicted to isomerize to generate the η^1-O formate adduct, (**A7**), which is more stable than the H-bound isomer by 7.6

kcal/mol. Alternatively, formate could be released from the η^1-H formate adduct and re-bound η^1-O rather than isomerizing. Initial η^1-H formate adduct formation after hydride transfer to CO_2 followed by rearrangement to the more stable η^1-O formate adduct has been proposed for other systems as well.[359-360] Of note, $\Delta G^{\ddagger}$ for the isomerization of **A6** to **A7** is calculated to be 5.2 kcal/mol, and proceeds through a η^2-O,H transition state in which O and H atoms of formate are partially bound to Ni (Figure 5.18).[129] Finally, the release of formate from **A7** leads to the catalyst regeneration, which is calculated to be slightly exergonic by 1.8 kcal/mol relative to **A1**. With this general mechanistic overview in mind, each major step in catalysis will now be considered in detail by discussing alternative pathways that were considered and the rationale for why they were ruled out.

5.2.5.2 H_2 Deprotonation by Exogenous Base Dictated by Steric Hindrance and Basicity

Three possible mechanisms for the deprotonation of the H_2 adduct (**A2**) by Vkd base were considered, as shown in Figure 5.14.

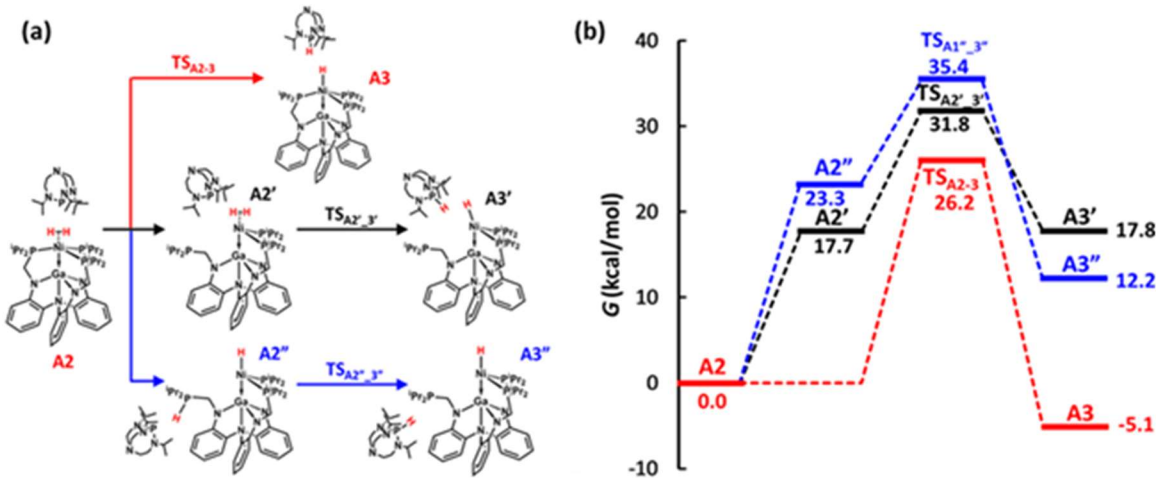

Figure 5.14. (a) Three possible reaction mechanisms for H_2 deprotonation, and (b) the Gibbs free energy profiles for each mechanistic pathway (figure and results provided by Dr. Jingyun Ye).

The first mechanism (top red path) involves Verkade's base approaching and deprotonating the H_2 adduct **A2** directly via $\mathbf{TS_{A2\text{-}3}}$, for which $\Delta G^{\ddagger}$=26.2 kcal/mol (Figure 5.14). The second mechanism (middle black path) involves the dissociation of one phosphine donor, which provides more space for the Vkd base to approach and deprotonate the H_2 adduct. The overall $\Delta G^{\ddagger}$ for H_2 deprotonation is 31.8 kcal/mol for this pathway, which comprises the endergonic dissociation of one phosphorus donor to form **A2'** (17.7 kcal/mol) and, $\Delta G^{\ddagger}$ of 14.1 kcal/mol for the subsequent H_2 deprotonation from **A2'** via the transition state $\mathbf{TS_{A2'\text{-}3'}}$ (Figure 5.14). The third mechanism (bottom blue path) involves one phosphine donor of the ligand serving as an internal base, followed by proton transfer from **A2''** to the external Verkade's base. As shown in Figure 5.14, the third reaction mechanism has the largest free energy of activation (35.4 kcal/mol) of these three possible mechanisms for H_2 deprotonation. As a result, the first reaction mechanism involving the direct deprotonation of H_2 adduct by Verkade's base, without invoking any phosphine dissociation or assistance, is the most favorable mechanism for H_2 deprotonation.[129]

Deprotonation of the H_2 adduct was studied with four bases of varying basicity and steric hindrance to gauge how these two factors influence the favorability of H_2 deprotonation. In addition to tBuTMG and Vkd base (abbrev. as Vkd_iPr in this section) which were examined experimentally for catalysis, the less bulky methyl analogues of Vkd base and tBuTMG, 2,8,9-trimethyl-2,5,8,9-tetraaza-1-phosphabicyclo[3,3,3] undecane (abbrev. as Vkd_Me) and 1,1,3,3-tetramethylguanidine (abbrev. as TMG), respectively, were also examined. Their base strengths are assessed by the reported pK_a values of the conjugate acids in CH_3CN, which are 32.9,[342] 33.6,[342] 23.4,[345] and 26.5[344,

[361] for Vkd_Me, Vkd_iPr, TMG and tBuTMG, respectively. In addition, the formate product, HCO_2^-, can serve as a proton acceptor once it is generated in the catalytic reaction. The pK_a value for HCO_2^- in THF is experimentally unavailable, but the computationally estimated pK_a value for CH_3COOH in THF is 22.1,[362] which should be comparable to the pK_a value of HCOOH. As a result, the potential role of HCO_2^- in the H_2 deprotonation step was also studied.

The Gibbs free energies of activation ($\Delta G^‡$) for deprotonation of the H_2 adduct with tBuTMG (27.8 kcal/mol) and Vkd_iPr (26.2 kcal/mol) are predicted to be larger compared to those of their less bulky TMG (12.0 kcal/mol) and Vkd_Me (24.7 kcal/mol) analogs. This analysis shows that $\Delta G^‡$ for the deprotonation reaction at the relatively crowded Ni site is largely dictated by steric effects, such that a weaker base with less steric bulk (e.g. TMG) can have a lower $\Delta G^‡$ for H_2 deprotonation than stronger bases with greater associated steric hindrance (e.g. Vkd_Me, Vkd_iPr, tBuTMG). Although basicity does not seem to be as important as steric effects in determining the barrier to H_2 deprotonation, the use of a strong base is still crucial for catalysis because the proton transfer from (η^2-H_2)NiGaL (p$K_a \approx 33.1$ in CH_3CN) to exogenous base is only an exergonic process when the base is Vkd_iPr (p$K_a = 33.6$), and is endergonic for Vkd_Me, tBuTMG, and TMG.[128-129] The significant influence that steric effects are predicted to have on $\Delta G^‡$ for H_2 deprotonation is likely a consequence of the bulky isopropyl groups on the phosphines of the ligand, which likely impede the close approach of bulky exogenous bases required to facilitate direct deprotonation of the H_2 adduct.

Keeping with the trend of lower $\Delta G^‡$ for H_2 deprotonation for less bulky bases, calculations indicate that $\Delta G^‡$ for deprotonation is significantly lowered by formate

assistance, as formate can approach (η^2-H_2)NiGaL more easily than can a stronger but bulkier base like Vkd_iPr. Remarkably, $\Delta G^{\ddagger}$ for H_2 deprotonation by formate is only 2.7 kcal/mol, which is significantly lower than the barrier for direct deprotonation by Vkd_iPr (26.2 kcal/mol). This low predicted barrier for H_2 deprotonation by formate is in line with Urakawa and co-workers' calculation of a low barrier of 5 kcal/mol for deprotonation of a Ru(η^2-H_2) complex by an outer-sphere formate molecule.[360] When Vkd_iPr base is present in solution, formate can readily transfer the proton it accepted from (η^2-H_2)NiGaL to Vkd_iPr, which is exergonic by 4.1 kcal/mol. Thus, formate is regenerated and can further participate as a base in subsequent H_2 deprotonation events, as shown in Figure 5.15. This prediction is consistent with experimental observations that the catalysis stops when Vkd_iPr has been consumed, as a sufficiently strong base is needed to drive the overall catalytic reaction starting from H_2 and CO_2.[128-129]

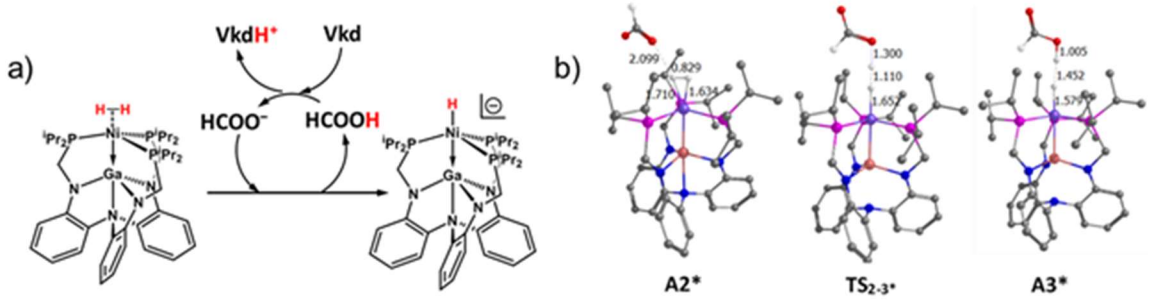

Figure 5.15. H_2 deprotonation by Vkd assisted by formate, along with the relevant structures and bond distances in (Å) for **A2***, **TS$_{1\text{-}2}$*** and **A3***. Figure and results courtesy of Dr. Jingyun Ye.

Therefore, it is proposed that Vkd_iPr directly deprotonates (η^2-H_2)NiGaL, as shown in Figure 5.13, until enough formate is generated in solution to serve as a proton shuttle between the H_2 adduct and Vkd_iPr. This would mean that as formate builds up with time, the reaction rate should increase until the solution is saturated with formate, at which point the rate would be constant (ie. linear HCO_2^- vs. time kinetics plot) until it is

slowed by the depletion of base. While catalysis with Vkd is too fast for this behavior to be observed, catalysis with tBuTMG does show an induction period during which the reaction rate accelerates slowly over the first ~3 h until about ~100 equiv HCO_2^- are generated relative to catalyst, followed by a period from ~3.5 to 7.5 hours where the rate remains constant at 120 h^{-1}.[128-129] Thus, the two kinetic periods observed for tBuTMG lend support to the computationally proposed mechanism for H_2 deprotonation with formate assistance. A key experiment that would unambiguously support the assistance of formate in deprotonation would be to add [cation][formate] at the beginning of a catalytic trial with tBuTMG and directly compare the initial reaction rate with an identical trial in which no formate was added; if our hypothesis of formate assistance is correct, the induction period would be minimized or eliminated by the initial addition of formate.

The proposal that formate can act as an intermediary base is also consistent with the observation of very low concentrations of formic acid (in a ~1:5 ratio with formate) during catalysis only when nearly all the Vkd_iPr base has been consumed (Figure A.4.7). This has been interpreted as proton transfer between formate and Vkd_iPr becoming slow relative to the ^{1}H NMR timescale (500 MHz), and thus observable, when Vkd_iPr is depleted and not present in high enough concentration to readily accept the proton. The alternative explanation, that the observed formic acid resulted from an acid-base equilibrium with [(Vkd_iPr)H][HCO_2], was discounted on the basis of the exceedingly large difference of ~6 pK_a units between [(Vkd_iPr)H]$^+$ and formic acid (*vide supra*). Overall, the remarkably low $\Delta G^{\ddagger}$ for H_2 deprotonation by formate relative to Vkd_iPr means that the RDS will switch from H_2 deprotonation to outer-sphere hydride transfer to CO_2 once formate builds up to a sufficient concentration during catalysis.[129]

5.2.5.3 Hydride Transfer to CO_2: How does it Occur?

Three different mechanisms for hydride transfer to CO_2 were considered (Figure 5.16): (1) hydride transfer from (η^2-H_2)NiGaL prior to deprotonation to give a Ni(II) complex with both hydride and formate ligands (**C2**) which can then be deprotonated by exogenous base (blue path). (2) direct, outer-sphere, hydride transfer from $[HNiGaL]^-$ (**A4**) to CO_2 (red path, also shown in Figure 5.13); and (3) an inner-sphere hydride transfer mechanism in which phosphine dissociation allows for the close approach and pre-coordination of CO_2 to Ni prior to migratory insertion of CO_2 into the Ni−H bond of **A4** (black path).

The first mechanism involves hydride transfer occurring directly from (η^2-H_2)NiGaL to CO_2, rather than deprotonation occurring initially to form the anionic hydride species. After the H_2 adduct (**A2**) forms, the diffusion of CO_2 results in a van der Waals complex [(η^2-H_2)NiGaL][CO_2], **C1**, which is 1.4 kcal/mol lower in energy than **A1**. The Gibbs free energy of activation ($\Delta G^{\ddagger}$) for direct hydride transfer from the H_2 adduct to CO_2 was found to be 33.9 kcal/mol (**C1** to **C2** via $\mathbf{TS}_{C1\text{-}2}$), which was deemed to be prohibitively high.[129] From **C2**, the catalytic cycle would be completed by formate release and deprotonation of the Ni−H by Vkd_iPr, which could occur in either order or in a concerted fashion. This path was not investigated further because $\Delta G^{\ddagger}$ for hydride transfer from the H_2 adduct to CO_2 is much larger than the highest barriers predicted for the other hydride transfer pathways (Figure 5.16). Consistent with the computational conclusion that direct hydride transfer from the H_2 adduct to CO_2 is not energetically feasible, no products other than the H_2 adduct were observed experimentally when NiGaL was exposed to H_2/CO_2 (1 atm) in the absence of base. This experiment indicates

that neither the H_2 adduct, nor a Ni(II) dihydride species which could hypothetically be formed but has never been observed,[97] was hydridic enough to react with CO_2 to transfer a hydride and form intermediate **C2**.

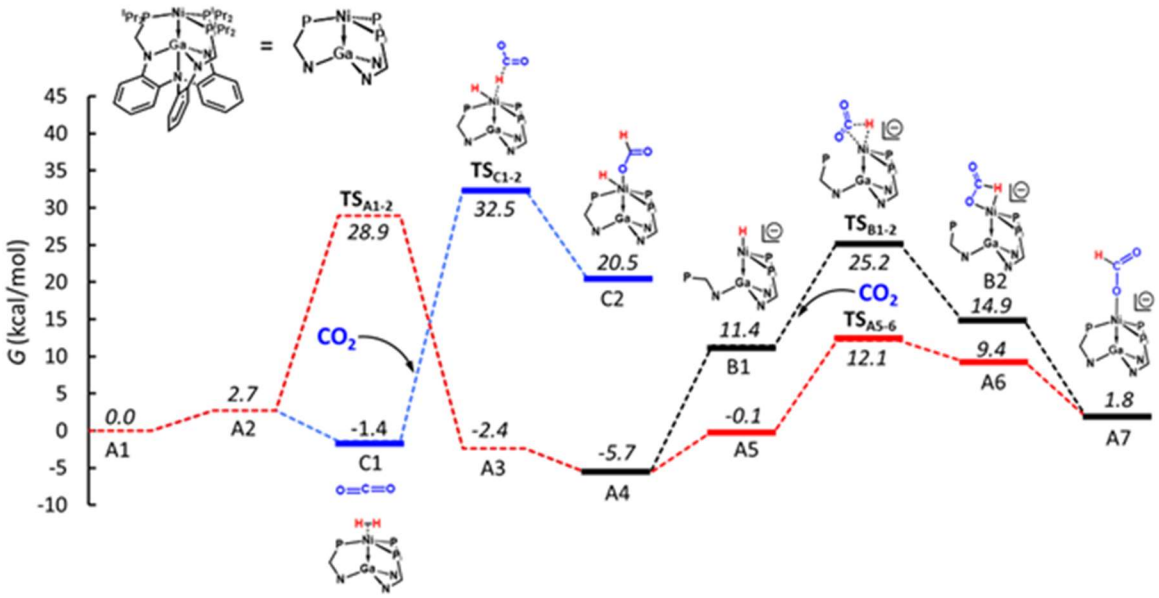

Figure 5.16. Gibbs free energy profile for CO_2 hydrogenation via three different hydride transfer pathways. In addition to the direct, outer-sphere hydride transfer path shown in red (and in Figure 5.13), an inner-sphere pathway involving phosphine dissociation (Path 2 from **A4**, black line), and hydride transfer from (η^2-H_2)NiGaL (Path 3 from **C1**, blue line) were also considered. Note that this figure and the computational results within it were provided by Dr. Jingyun Ye.

The other two possible hydride transfer pathways under consideration differ in whether CO_2 has coordinated to Ni prior to hydride transfer. Hydride transfer to a coordinated CO_2 ligand is referred to as inner-sphere hydride transfer or migratory insertion (black path, Figure 5.16), whereas hydride transfer without initial CO_2 coordination is referred to as direct, outer-sphere hydride transfer (red path, Figures 5.13 and 5.16). The feasibility of inner-sphere hydride transfer as compared to an outer-sphere mechanism is a relevant distinction because metal hydrides are well-known to undergo migratory insertion of the hydride ligand into bound, unsaturated substrates like CO_2.[363]

That said, the hydricity of [**2**−H]$^-$ compared with HCO_2^- would also suggest that a direct outer-sphere mechanism should be thermodynamically favorable by ~13 kcal/mol (*vide supra*).

For the inner-sphere mechanism, the first step involves phosphine dissociation from [HNiGaL]$^-$ (**A4**) to form **B1**, which has an open coordination site at Ni to which CO_2 can bind. That CO_2 binding requires the dissociation of one of the phosphine donors is reminiscent to the requirements for olefin binding to (η^2-H_2)NiML or $(H)_2$NiML (chapter 4). CO_2 binding to **B1** to form [(H)(CO_2)NiGaL]$^-$ with one unbound phosphine is predicted to be energetically unfavorable; instead, calculations favor CO_2 closely approaching **B1** and reacting to form an η^2-O,H formate adduct (**B2**) without discrete prior coordination of CO_2 to form an intermediate [(H)(CO_2)NiGaL]$^-$ species. The transition state, $\mathbf{TS_{B1\text{-}2}}$, involves the close approach of CO_2 to Ni, hydride transfer, and the phosphine donor re-coordinating to Ni in a concerted fashion (Figure 5.16). The η^2-O,H formate adduct (**B2**) ultimately converts to the more stable η^1-O formate adduct (**A7**), and subsequent formate release, H_2 binding, and deprotonation continue the catalytic cycle to regenerate [HNiGaL]$^-$ (**A4**).

In comparing the energetic feasibility of the inner-sphere and outer-sphere hydride transfer pathways, $\Delta G^‡$ in the inner-sphere mechanism for CO_2 reacting with **B1** to form η^2-O,H formate adduct **B2** is 13.8 kcal/mol (via $\mathbf{TS_{B1\text{-}2}}$). Since the dissociation of the phosphorus donor from **A4** to fom **B1** requires 17.1 kcal/mol of free energy, the overall barrier for the inner-sphere pathway is 30.9 kcal/mol. In comparison, outer-sphere hydride transfer has a much lower $\Delta G^‡$ of 17.8 kcal/mol relative to [HNiGaL]$^-$ (**A4**) and free CO_2.[129] Thus, outer-sphere hydride transfer is ~13 kcal/mol more favorable than the

inner-sphere hydride transfer pathway, with the difference mostly attributable to the unfavorable dissociation of a phosphorus donor needed to accommodate the close approach of the incoming CO_2 ligand. Interestingly, a linear relationship between $\Delta G^{\ddagger}$ for hydride transfer to CO_2 and $\Delta G°_{H-}$ of the metal hydride was predicted to generally hold true for many different M'ML complexes studied (Figure A.4.23), indicating that more thermodynamically favorable hydride transfer to CO_2 (ie. from M−H with lower ΔG_{H-} values) require less activation energy (ie. proceed with a lower barrier in terms of $\Delta G^{\ddagger}$).[129] Notably, for a series of Co diphosphine catalysts in which hydride transfer to CO_2 is the RDS, a linear relationship between log(TOF) and $\Delta G°_{H-}$ was observed,[364] which implies that the thermodynamics and kinetics of hydride transfer are linked, just as is predicted computationally for our bimetallic system.

5.2.5.4 Catalytic Turnover: Formate Dissociation and H_2 Binding to Complete Cycle

In addition to the consideration of H_2 deprotonation and hydride transfer to CO_2, the relative favorability of binding H_2, HCO_2^-, or CO to the catalyst can also play an important role in CO_2 hydrogenation. Highly active catalysts for CO_2 hydrogenation should have relative binding energies that allow the release of formate (HCO_2^-) and subsequent binding of H_2, as catalytic turnover will be impeded or stopped if formate binds too strongly, and may require high H_2 pressure, high T, and/or $[Li]^+$ additives to facilitate. The dissociation of formate is proposed to be the RDS for catalysis with NiGaL based on the experimental observation by ^{31}P NMR spectroscopy that the anionic η^1-O formate adduct, $[(HCO_2)NiGaL]^-$, is the catalytic resting state throughout the course of catalysis.[128] A similar rate-determining ligand substitution of H_2 for bound formate was also predicted for

Ru, Fe,and Co catalysts, the latter of which required $[Li]^+$ additives to assist in formate liberation.[321-322, 360, 365] In addition, CO binding was considered because CO has been reported as a byproduct of CO_2 hydrogenation catalysis via either the reverse water-gas shift reaction or formate dihydroxylation, and irreversible binding of CO can ultimately poison the catalyst.[346] These CO generation pathways will be discussed in more detail in section 5.2.17 on the catalyst deactivation mechanism.

With these binding criteria in mind, H_2, HCO_2^-, and CO binding to NiGaL were calculated to have $\Delta G°$ values of −0.4, −0.3, and −18.6 kcal/mol, respectively. Clearly, CO will outcompete H_2 and formate and bind strongly to NiGaL if it is generated, and thereby inhibit catalytic activity. However, it is important to note that the calculated relative binding energies of H_2 and formate are greatly influenced by whether their respective van der Waals complexes are considered. Considering van der Waals interactions with protonated Vkd base greatly stabilizes the binding of formate at NiGaL ($\Delta G° = -2.3$ kcal/mol), which could result from the electrostatic interaction between the protonated base and formate ions and from van der Waals interactions between the H atoms of Vkd and the O atom of formate. Overall, formate and H_2 binding to NiGaL are predicted to be similarly favorable with $\Delta G°$ of −0.4 and −0.3 kcal/mol, respectively, but once the electrostatic and van der Waals interactions with Vkd and $[VkdH]^+$ are considered, formate binding is predicted to be ~5 kcal/mol more favorable than H_2 binding.[129]

Of note, the calculated $\Delta G^‡$ for formate release from [VkdH][(HCO_2)NiGaL] (2.3 kcal/mol) is smaller than that for hydride transfer to CO_2 from $[HNiGaL]^-[CO_2]$ (12.2 kcal/mol), which is calculated to be the RDS after the sufficient buildup of formate lowers the H_2 deprotonation barrier. The significantly larger activation barrier predicted for

hydride transfer relative to formate release would be expected to result in the anionic Ni hydride species being the catalytic resting state. Instead, the formate adduct, [VkdH][(HCO_2)NiGaL], is observed as the catalytic resting state by ^{31}P NMR spectroscopy. Of relevance, an intriguing experimental observation may help to reconcile this discrepancy between experiment and theory in regard to the RDS and the expected resting state of the catalyst. Upon the replacement of H_2/CO_2 with $D_2/^{13}CO_2$, both [DNiGaL]$^-$ and [($D^{13}CO_2$)NiGaL]$^-$ were observed during catalysis by *in situ* ^{31}P NMR spectroscopy, in contrast to only [(HCO_2)NiGaL]$^-$ being observed as the catalytic resting state with H_2/CO_2 (Figure A.4.24). While the underlying basis for these isotopic effects are not fully understood, the detection of both [DNiGaL]$^-$ and [($D^{13}CO_2$)NiGaL]$^-$ bridges the apparent discrepancy between experiment and theory by suggesting that hydride transfer and formate dissociation likely have somewhat similar free energies of activation, such that using heavier isotopomers puts the two barriers on par with one another by slowing hydride transfer and allowing the build-up of both [DNiGaL]$^-$ and [($D^{13}CO_2$)NiGaL]$^-$ during catalysis. The discrepancy between theory and experiment regarding formate dissociation highlights the fact that solvation energies for small, charged ions like formate can be challenging to calculate accurately, and hence, a greater degree of uncertainty exists for the computed formate dissociation energies and barriers than would otherwise be expected.[129]

5.2.6 Experimental Investigation of the Favorability of Formate Binding Relative to H_2 Binding

5.2.6.1 H_2/Formate Binding Study Leads to Observation of Hydride Transfer Reversibility

In light of the discrepancy between theory and experiment on the thermodynamic and kinetic favorability of formate dissociation, further experimental studies of the $[(HCO_2)NiGaL]^-$ species ($[\mathbf{2}{-}O_2CH]^-$) were conducted. In particular, direct comparison of the thermodynamic favorability of formate binding to the previously measured H_2 binding energies would be desirable, since the substitution of formate by H_2 seems to be the RDS based on *in situ* ^{31}P NMR spectroscopy. Given the ease of quantifying H_2 and N_2 binding via VT ^{31}P NMR studies (chapter 3), similar studies were attempted for formate binding in THF. Specifically, ^{31}P NMR spectra of the model complex, [PPN][**2**−O_2CH], were acquired at high T to determine if formate dissociates from [PPN][**2**−O_2CH] to give a measurable equilibrium with **2** and [PPN][HCO_2]. Figure 5.17a shows that only a very small amount of **2** is formed at 337 K, which is as high as spectra could be acquired in THF. Unfortunately, [PPN][**2**−O_2CH] is insoluble in toluene, and so the boiling point of THF represented the upper T bound for commonly available NMR solvents. Heating [PPN][**2**−O_2CH] for an extended period of 18 h at 333 K was seen to result in a greater amount of formate dissociation to give **2** (Figure 5.17b).

Another possible complication to heating [PPN][**2**−O_2CH] is that in addition to formate liberation, it is also possible for CO_2 to be liberated via de-insertion (decarboxylation) to reform [PPN][**2**−H]. However, only trace amounts of [PPN][**2**−H] were observed in the VT ^{31}P spectrum at 337 K, and none was observed after extended heating for 18 h at 333 K (Figure 5.17). This would seem to suggest that de-insertion is

unfavorable; however, the addition of $^{13}CO_2$ (1 atm) to [PPN][**2**−O_2CH] at rt gave full conversion to [PPN][**2**−$O_2{}^{13}$CH], which indicates that de-insertion can indeed occur under ambient conditions. Reversible CO_2 insertion/de-insertion was also observed based on $^{13}CO_2$ incorporation for several other reported examples of Ni η^1-O formate adducts.[333, 335]

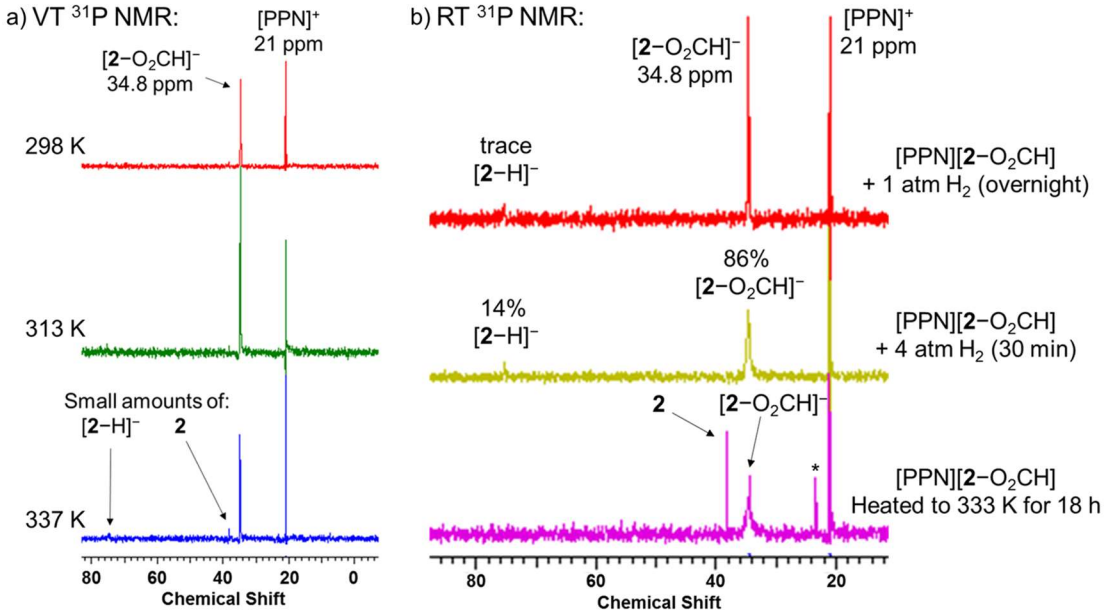

Figure 5.17. (a) VT ^{31}P NMR spectra of [PPN][**2**−O_2CH] in THF, and (b) RT ^{31}P NMR spectra of [PPN][**2**−O_2CH] after exposure to H_2 (1 or ~4 atm) or extended heating.

Since the formate binding equilibrium was not amenable to quantification by simple VT experiments, the next attempt to quantify it was made by exposure of [PPN][**2**−O_2CH] to H_2. Since the H_2 binding energy in THF is known (section 3.3.6, Equation 5.5), the measurement of the equilibrium between H_2 binding and formate binding (K_{eq}, Equation 5.9) would then allow for the determination of the formate binding energy (Equation 5.6) based on the estimated dissociation constants (K_d) for 1:1 ion-pairing in THF for $\{[PPN][HCO_2]\}_{ip}$ and $\{[PPN][\mathbf{2}{-}O_2CH]\}_{ip}$ (Equations 5.7-5.8). In Equations 5.7-5.8, $\{[X][Y]\}_{ip}$ represents a 1:1 ion-pair, as typically predominates in

dilute THF solutions,[358] and K_d represents the equilibrium constant for the separation of the ion-pair into its constituent $[X]^+$ and $[Y]^-$ ions.

Equilibrium	$\Delta G°$ (kcal/mol)	
2−H_2 ⇌ **2** + H_2	$+1.364 \cdot \log(K_{H_2})$	(Eqn 5.5)
$[HCO_2]^-$ + **2** ⇌ [**2**−$O_2CH]^-$	$-1.364 \cdot \log(K_{\text{formate}})$	(Eqn 5.6)
$\{[PPN][HCO_2]\}_{ip}$ ⇌ $[HCO_2]^-$ + $[PPN]^+$	$-1.364 \cdot \log(K_{d_{[PPN][HCO_2]}})$	(Eqn 5.7)
$[PPN]^+$ + [**2**−$O_2CH]^-$ ⇌ $\{[PPN][\mathbf{2}-O_2CH]\}_{ip}$	$+1.364 \cdot \log(K_{d_{[PPN][2-O_2CH]}})$	(Eqn 5.8)
2−H_2 + $\{[PPN][HCO_2]\}_{ip}$ ⇌ $\{[PPN][\mathbf{2}-O_2CH]\}_{ip}$ + H_2	$-1.364 \cdot \log(K_{eq})$	(Eqn 5.9)

Surprisingly, the exposure of [PPN][**2**−O_2CH] to ~4 atm H_2 did not result in the observation of an equilibrium between **2**−H_2 and [PPN][**2**−O_2CH] (Equation 5.9), but instead formed a small amount of [PPN][**2**−H] (~14% conversion from [PPN][**2**−O_2CH]) via an unknown mechanism. It is possible that the addition of H_2 results, for some unknown reason, in an increased amount of decarboxylation from [PPN][**2**−O_2CH] to give [PPN][**2**−H]. A few different possible mechanisms have been proposed (Figure 5.18). The possibilities include: (1) initial formation of **2**−H_2 followed by deprotonation by formate to give [PPN][**2**−H] and formic acid; (2) initial formation of **2**−H_2, which leads to an equilibrium with **2** when H_2 dissociates, and subsequent reaction of **2** and [PPN][**2**−O_2CH] facilitates CO_2 loss via a bimolecular formate complex; and (3) unimolecular CO_2 loss via an η^2-O,H formate adduct transition state[129] (Figure 5.18).

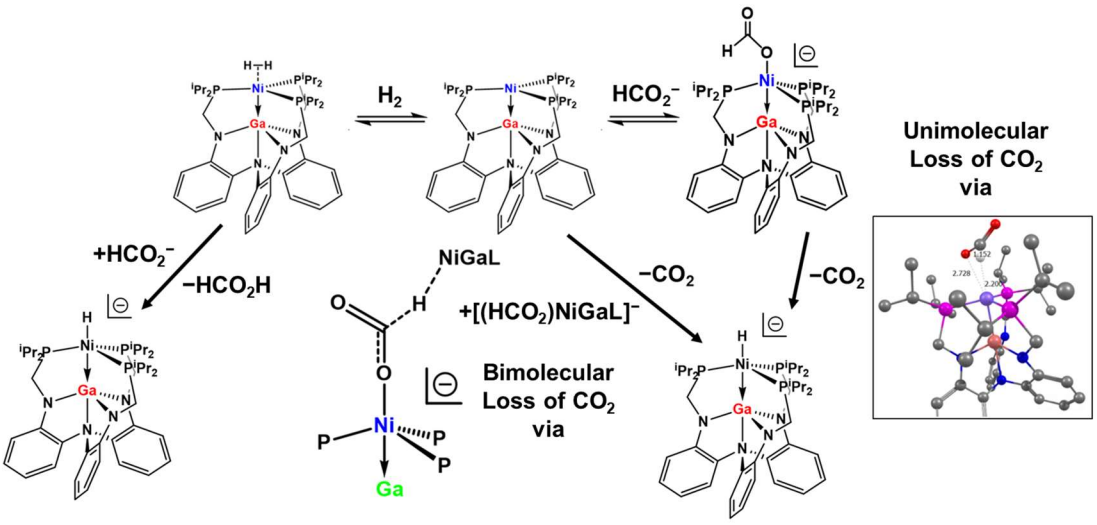

Figure 5.18. Possible mechanisms for reversion of [PPN][**2**−O_2CH] to [PPN][**2**−H] under an H_2 atmosphere. The unimolecular CO_2 loss TS was calculated by Dr. Jingyun Ye (section 5.2.5.1).

The deprotonation of **2**−H_2 with formate to give [PPN][**2**−H] and formic acid seems to be the simplest explanation; however, in this instance there is not a strong base like Vkd to which formic acid can ultimately transfer the proton. Therefore, it seems that the pK_a difference of ~6 units between formate and **2**−H_2 would make proton transfer to give [PPN][**2**−H] and formic acid unfavorable (*vide supra*). Furthermore, no formic acid was observed by ^{1}H NMR in a preliminary experiment. Therefore, H_2 exposure inducing CO_2 loss is favored. To test whether a bimolecular mechanism was operative, **2** and [PPN][**2**−O_2CH] were mixed in a 1:1 ratio in THF, which resulted in the observation of a new broad resonance at ~36 ppm by ^{31}PNMR spectroscopy, but no formation of [PPN][**2**−H]. Additionally, the bimolecular mechanism would yield **2** and [PPN][**2**−H] in a 1:1 ratio, in contrast to the lack of formation of **2**. Thus, a unimolecular decarboxylation mechanism is favored, which is somehow promoted by the addition of H_2; such a mechanism was previously calculated to have a low $\Delta G^{\ddagger}$ of 5.2 kcal/mol relative to [**2**−O_2CH]$^-$.[129]

These experiments collectively suggest that de-insertion of CO_2 to regenerate [**2**−H]$^-$ is relatively facile under the ambient conditions under which catalysis is run. The reversibility of hydride transfer, along with the previously studied reversibility of both the H_2 binding and deprotonation steps, prompted the examination of whether catalysis could be run in the reverse direction for **2**. That is, could [VkdH][HCO_2] be catalytically converted to H_2, CO_2, and Vkd base? The ability to catalyze this reaction in both directions depending on the reaction conditions is critical for utilizing formic acid and formate derivatives as reversible H_2 storage media. Preliminary studies showed that the addition of 1 equiv [VkdH][HCO_2] to **2**, followed by evacuation of the headspace and allowing the mixture to react overnight, resulted in the detection of small amounts of both H_2 and CO_2 by headspace GC-MS analysis, whereas a control GC-MS sample did not show the presence of these gases. More rigorous quantification would be needed to gauge whether the reverse reaction was catalytic and proceeding at an adequate rate, but the fact that the reaction proceeds in the reverse direction to any extent is further evidence that the individual equilibria in the catalytic cycle are well-matched in energy (ie. no step is too favorable or unfavorable).

5.2.6.2 Indirect Measurement of the Binding Energy of Formate

Although it is interesting that [PPN][**2**−O_2CH], the catalytic resting state, reverts to [PPN][**2**−H] to some extent under an H_2 atmosphere, the initial experiment of exposing [PPN][**2**−O_2CH] to H_2 was ultimately unsuccessful in that it did not allow for the measurement of a binding equilibrium between H_2 and formate, as originally desired. Thus, an alternative means of measuring the binding energy of formate was needed. An observation by Matt Vollmer that dissolving [PPN][**2**−O_2CH] in CH_3CN resulted in

multiple species prompted a series of experiments to indirectly measure the formate binding energy. Namely, it was hoped that CH_3CN could serve as an intervening ligand that binds more strongly than H_2 but more weakly than formate, such that the binding equilibria between CH_3CN and H_2 along with that between CH_3CN and formate could both be independently measured. If that were the case, because the H_2 binding energy is known, the absolute binding energies of CH_3CN and formate could then be determined relative to H_2.

A preliminary VT ^{31}P NMR study of **2** in the presence of ~1.2 equiv of CH_3CN in THF showed that CH_3CN binds to **2**, giving rise to a sharp ^{31}P resonance at 40.55 ppm, with little change (<0.2 ppm) in the chemical shift is observed upon increasing T up to the boiling point of THF. Thus, just as was the case for formate binding, CH_3CN binds to **2** more strongly than H_2, and too strongly to directly measure by VT experiments. However, if CH_3CN also binds more weakly than formate, then it could satisfy the criteria for being an intervening ligand. Equations 5.10-5.17 show how utilizing CH_3CN as an intervening ligand allows for the determination of the binding energy for formate to **2**. If K_{eq_1}, the equilibrium constant between H_2 and CH_3CN binding can be measured (Equation 5.12), then $\Delta G°$ for CH_3CN binding can be determined (Equation 5.10), since $\Delta G°$ for H_2 binding is known (Equation 5.11).

Equilibrium	$\Delta G°$ (kcal/mol)	
2 + CH_3CN ⇌ **2**–$NCCH_3$	$-1.364 \cdot \log(K_{CH_3CN})$	(Eqn 5.10)
2–H_2 ⇌ **2** + H_2	$+1.364 \cdot \log(K_{H_2})$	(Eqn 5.11)
2–H_2 + CH_3CN ⇌ **2**–$NCCH_3$ + H_2	$-1.364 \cdot \log(K_{eq_1})$	(Eqn 5.12)

From there, the binding energy of formate (Equation 5.17) can be determined based on the following: (1) the measurement of K_{eq_2}, the equilibrium constant between CH_3CN and formate binding (Equation 5.13); (2) the now known $\Delta G°$ for CH_3CN binding, as determined using Equations 5.10-5.13 (Equation 5.14); and (3) the estimated dissociation constants (K_d) for 1:1 ion-pairs in THF of $\{[PPN][HCO_2]\}_{ip}$ and $\{[PPN][\mathbf{2}{-}O_2CH]\}_{ip}$ (Equations 5.15-5.16).

Equilibrium	$\Delta G°$ (kcal/mol)	
$\mathbf{2}{-}NCCH_3 + \{[PPN][HCO_2]\}_{ip} \rightleftharpoons \{[PPN][\mathbf{2}{-}O_2CH]\}_{ip} + CH_3CN$	$-1.364 \cdot \log(K_{eq_2})$	(Eqn 5.13)
$\mathbf{2} + CH_3CN \rightleftharpoons \mathbf{2}{-}NCCH_3$	$-1.364 \cdot \log(K_{CH_3CN})$	(Eqn 5.14)
$[HCO_2]^- + [PPN]^+ \rightleftharpoons \{[PPN][HCO_2]\}_{ip}$	$+1.364 \cdot \log(K_{d_{[PPN][HCO_2]}})$	(Eqn 5.15)
$\{[PPN][\mathbf{2}{-}O_2CH]\}_{ip} \rightleftharpoons [PPN]^+ + [\mathbf{2}{-}O_2CH]^-$	$-1.364 \cdot \log(K_{d_{[PPN][2-O_2CH]}})$	(Eqn 5.16)
$\mathbf{2} + [HCO_2]^- \rightleftharpoons [\mathbf{2}{-}O_2CH]^-$	$-1.364 \cdot \log(K_{formate})$	(Eqn 5.17)

To test the relative binding favorability of CH_3CN and formate, 1.2 equiv CH_3CN were added to $[PPN][\mathbf{2}{-}O_2CH]$ in THF, and the J. Young NMR tube was allowed to mix using a turntable (at ~16 rpm) until the reaction reached equilibrium, as judged by the relative integrals of the resonances observed by ^{31}P NMR spectroscopy. Likewise, the relative binding favorability of CH_3CN and H_2 were tested by exposure of a mixture of **2** and 1.2 equiv CH_3CN to 1 atm and ~3.8 atm H_2. The resulting ^{31}P NMR spectra for both of these equilibria are shown in Figure 5.19.

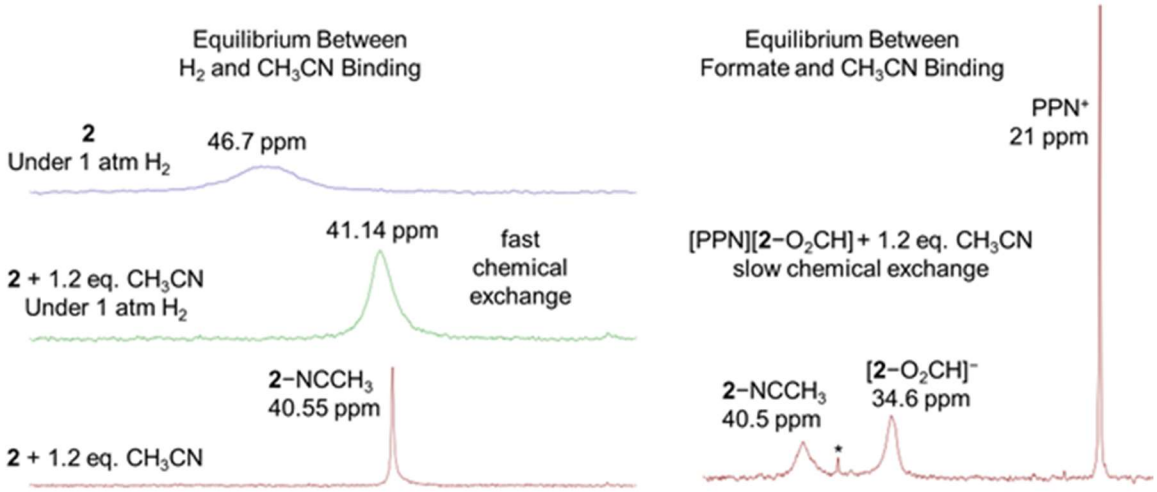

Figure 5.19. ^{31}P NMR spectra (161.9 MHz, THF) showing the binding equilibrium between CH_3CN and H_2 (left) and that between CH_3CN and formate (right) for binding to NiGaL (**2**).

Gratifyingly, both H_2 and formate binding were found to be in equilibrium with CH_3CN binding. Fast interconversion between **2**−$NCCH_3$ and **2**−H_2 was observed relative to the ^{31}P NMR timescale (161.9 MHz) at 298K, which allowed for the evaluation of K_{eq_2} based on the observed chemical shift, as described in chapter 3, along with the known H_2 pressure and CH_3CN concentration (Figure 5.19, Equation 5.12). K_{eq_1} was determined to be 4(3) x 10^3 atm/M based on the average for trials under 1 and ~3.8 atm H_2, which equates to $\Delta G°$ = −4.8(5) kcal/mol for Equation 5.12. Since $\Delta G°$= 0.1(1) kcal/mol for H_2 binding to **2** in THF (Equation 5.11), $\Delta G°$ for CH_3CN binding to **2** was then found to be −4.7(6) kcal/mol (Equation 5.10).

In contrast, the interconversion of (CH_3CN)NiGaL (**2**−$NCCH_3$) and [PPN][**2**−O_2CH] was slow relative to the ^{31}P NMR timescale (161.9 MHz) at 298 K, allowing for the K_{eq_2} to be evaluated based on the relative integrals of the ^{31}P resonances and the known concentrations of CH_3CN and [PPN][HCO_2] (Figure 5.19, Equation 5.13). K_{eq_2} was determined to be 2.4(3), which equates to $\Delta G°$ = −0.50(5) kcal/mol for

Equation 5.13. From the H_2/CH_3CN binding equilibrium, $\Delta G°$ for Equation 5.14 was found to be −4.7(6) kcal/mol. $\Delta G°$ for Equations 5.15-5.16 are dependent on the K_d values for the dissociation of the 1:1 ion pairs, which Morris and others have shown can be estimated using the Fuoss equation to within one order of magnitude of the conductometrically measured values.[358] Equation 5.18 shows the Fuoss equation for estimating K_d, where $b = (-e'^2)/(a\epsilon kT)$, $e' = 4.80 \times 10^{-10}$ esu, N_A is Avagadro's number, $k = 1.38 \times 10^{-16}$ erg/K, ϵ is the dielectric constant (7.58 for THF), T is the temperature in Kelvin, and a = the inter-ion distance, which is equal to the sum of the Fuoss ion-pair radii, r^+ and r^-, for the monocation and monoanion (in cm).[366]

$$K_d = (3000e^b)/(4\pi N_A a^3) \qquad \text{(Eqn 5.18)}$$

Morris and co-workers utilized the crystal structures to determine the Fuoss ion-pair radii, r^+ and r^-, for the monocation and monoanion.[229, 358] Using the approximation that the crystallographic volume of a non-hydrogen atom is 18 Å^3, the volume of $[PPN]^+$, $[HCO_2]^-$, and $[\mathbf{2}-O_2CH]^-$ were determined. The Fuoss ion-pair radii were then estimated by assuming each ion to be spherical, such that $V=(4/3)\pi r^3$. Using this method, the Fuoss ion-pair radii for $[PPN]^+$, $[HCO_2]^-$, and $[\mathbf{2}-O_2CH]^-$ were determined to be 5.51, 2.34, and 7.39 Å, respectively. The inter-ion distances for $\{[PPN][HCO_2]\}_{ip}$ and $\{[PPN][\mathbf{2}-O_2CH]\}_{ip}$ were then determined to be 7.86 and 12.80 Å by adding the Fuoss ion-pair radii for the constituent ions. $K_{d_{[PPN][HCO_2]}}$ and $K_{d_{[PPN][2-O_2CH]}}$ were then determined to be 5.7×10^{-5} M and 5.3×10^{-4} M (Equation 5.18), which results in $\Delta G°$ values of −5.8 kcal/mol and +4.5 kcal/mol for Equations 5.15 and 5.16, respectively. These K_d values are within the typical range of 10^{-4} to 10^{-8} M for ion-pair concentrations of 10 mM or less in THF.[358, 367-369] While these K_d values are only estimates to within one

order of magnitude based on the work of Morris and co-workers, it stands to reason that the error will be minimized because both opposing K_d estimates being considered here will be incorrect for the same reasons, and likely in the same direction, relative to their true values. The relative K_d values estimated from the Fuoss equation make intuitive sense: $K_{d_{[PPN][HCO_2]}} < K_{d_{[PPN][2-O_2CH]}}$ because stronger ion-pairing is expected between ions with smaller Fuoss radii, and $[HCO_2]^-$ is considerably smaller than $[\mathbf{2}{-}O_2CH]^-$ (*vide supra*). This can be seen mathematically by closely examining the Fuoss equation, and can also explain why $[Li]^+$ salts typically form the stronger ion-pairs than $[Na]^+$ or $[K]^+$ salts.

Summing up the $\Delta G°$ values for Equations 5.13-5.16 gives $\Delta G° = -6.5(8)$ kcal/mol for the binding energy of formate (Equation 5.17), with the difference in $\Delta G°$ between the two ion-pair dissociations, 1.3 kcal/mol, considered to have an error of ~0.5 kcal/mol (Equations 5.15-5.16). Thus, formate binding to **2** is ~6.6 kcal/mol more favorable than H_2 binding in THF. This large difference means that nearly all of **2** will be present as $[\mathbf{2}{-}O_2CH]^-$ rather than $\mathbf{2}{-}H_2$ during catalysis, which is in line with [VkdH][$\mathbf{2}{-}O_2CH$] being observed as the catalytic resting state by *in situ* ^{31}P NMR spectroscopy. Based on $\Delta\Delta G°$ of 6.6(8) kcal/mol between formate and H_2 binding, Figure 5.20 shows the % of the catalyst that is not in the catalytic resting state, [VkdH][$\mathbf{2}{-}O_2CH$], over the time course of catalysis, where the concentration of formate generated over time was determined for catalytic trials collected under 1 and 34 atm H_2/CO_2 (Table 5.1, entries 1 and 3).[128] For the purposes of this plot, the % of active catalyst not in the catalytic resting state is assumed to be equivalent to the % $\mathbf{2}{-}H_2$, as any

2−H_2 formed in the binding equilibrium with [VkdH][**2**−O_2CH] is assumed to enter the catalytic cycle and react productively to generate formate (Figure 5.20).

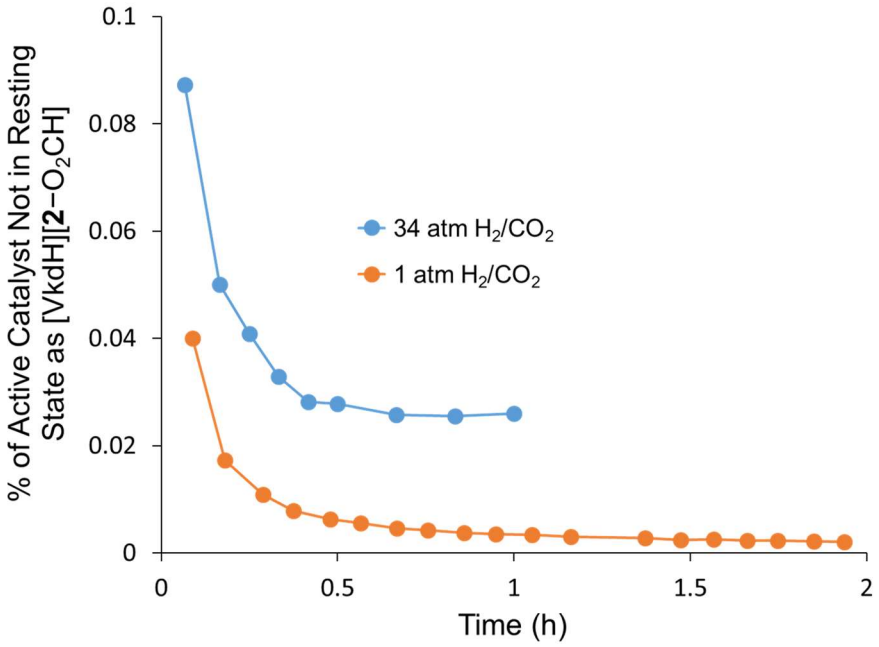

Figure 5.20. Plot of % of active catalyst not in the catalytic resting state, [VkdH][**2**−O_2CH], over the time course of catalysis under 1 or 34 atm H_2/CO_2.

The higher pressure of H_2 results in a slightly greater portion of the catalyst binding H_2 and continuing on in the catalytic cycle from the catalytic resting state, [VkdH][**2**−O_2CH] (Figure 5.20). Likewise, the formate concentration increases as time goes on during catalysis, resulting in a greater amount of the catalyst in which formate is bound at later time points (Figure 5.20). The extremely low relative concentration of the catalyst that is not in the catalytic resting state at any given time prompts the question of whether formate must actually dissociate for H_2 to bind and the catalytic cycle to continue. Alternatively, one could imagine a concerted mechanism in which H_2 reacts directly with [VkdH][**2**−O_2CH] across the Ni−O bond to directly regenerate [VkdH][**2**−H], rather than formate dissociating and subsequently assisting in the

deprotonation of the bound H_2 unit. However, a transition state that was energetically reasonable was not found computationally for the concerted mechanism. Interestingly, the DFT-predicted mechanism which calls for formate dissociation from [VkdH][**2**−O_2CH], followed by H_2 binding and deprotonation assisted by an outer-sphere formate, is nearly the same as that proposed by Urakawa and co-workers for a Rh catalyst.[360]

*5.2.7 Ion-Pairing and Potential Hydrogen-Bonding in [cation][**2**−H] and [cation][**2**−O_2CH]*

5.2.7.1 Effect of Ion-Pairing on Formate Dissociation

Given that formate dissociation is endergonic by ~6.5 kcal/mol, the effect of ion-pairing could be utilized as one means to promote formate liberation. Figure 5.21 shows that the addition of 1 atm CO_2 to [Li(THF)$_x$][**2**−H] results in the formation of **2**, with the liberation of [Li][HCO_2], rather than the formation of an anionic formate adduct, [Li(THF)$_x$][**2**−O_2CH]. This is in contrast to the reactivity of [cation][**2**−H] (cation = PPN, VkdH) with CO_2, where the anionic formate adduct was formed without any initial observation of **2** forming from formate dissociation (Figure 5.8). Thus, it seems that the liberation of [Li][HCO_2] is promoted by the stronger ion-pairing in the resulting [Li][HCO_2] complex compared with [PPN][HCO_2] or [VkdH][HCO_2], which would form via the liberation of formate from the other [cation][**2**−O_2CH] complexes.

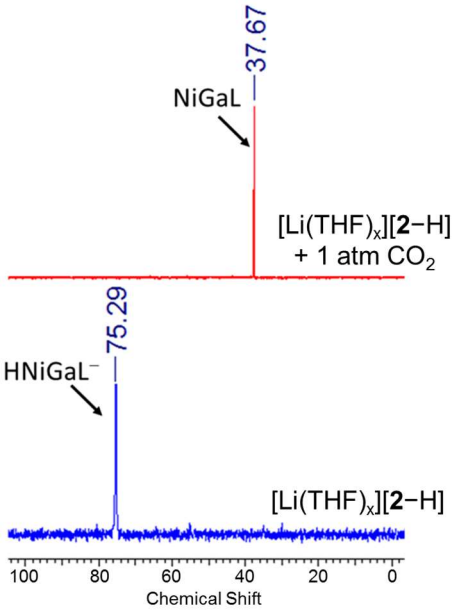

Figure 5.21. ^{31}P NMR spectra (161.9 MHZ, THF-d_8) showing the addition of 1 atm CO_2 to [Li(THF)$_x$][**2**−H], as performed by Matt Vollmer. Comparison spectra for the analogous reaction with $[PPN]^+$ and $[VkdH]^+$ cations were previously shown in Figure 5.8.

This prediction is validated by the estimates obtained for K_d for the 1:1 ion-pairs in THF for the various formate salts, $\{[cation][HCO_2]\}_{ip}$, as the $[Li]^+$, $[VkdH]^+$, and $[PPN]^+$ salts are estimated using Equation 5.18 to have K_d values of 8.0 x 10^{-8} M, 1.9 x 10^{-5} M, and 5.7 x 10^{-5} M, respectively.[358, 366] These K_d values indicate that the ion-pairing in $[Li][HCO_2]$ is stronger than that for $[VkdH]^+$ and $[PPN]^+$ by 3.2 and 3.9 kcal/mol, respectively, in terms of the difference in $\Delta G°$ values for ion-pair dissociation. Furthermore, the ion-pairing in $[Li][HCO_2]$ is also estimated to be substantially stronger than that in the hypothetical [Li][**2**−O_2CH] complex, by 4.4 kcal/mol. In contrast, the ion-pairing in $[cation][HCO_2]$ is only stronger than that in [cation][**2**−O_2CH] by 1.3 and 1.8 kcal/mol for $[PPN]^+$ and $[VkdH]^+$, respectively, which is apparently not enough to overcome the favorable binding energy of formate to **2**. However, it should also be noted that THF molecules likely coordinate to $[Li]^+$ to some extent to form $[Li(THF)_x]^+$ cations,

which will increase the Fuoss ion-pair radii and weaken the ion-pairing for $[Li]^+$ relative to the other cations. The weakening of the ion-pairing would be fairly dramatic if three THF molecules coordinate to give $[Li(THF)_3]^+$ cations, with the ion-pairing estimated to be weakened by ~3 kcal/mol and ~0.6 kcal/mol relative to $[Li][HCO_2]$ and $[Li][\mathbf{2}{-}O_2CH]$, respectively, based on the predicted larger radius of $[Li(THF)_3]^+$. Alternatively, $[Li][HCO_2]$ is likely only sparingly soluble in THF, and so its precipitation from solution as a salt could also be important to the dissociation of formate occurring.

Given the stronger ion-pairing of formate with the $[Li]^+$ cation, one strategy that could be utilized to help promote formate dissociation and increase the catalytic rate of formate generation is to add $[Li]^+$ salts as catalytic additives. This strategy has been routinely employed by Hazari, Bernskoetter, and co-workers to achieve dramatic improvements in the TON and TOF for CO_2 hydrogenation to formate with Fe and Co pincer catalysts relative to their catalytic performance in the absence of $[Li]^+$ additives. For example, the $[Co(PN(Me)P)(CO)_2][Cl]$ catalyst was reported to generate 10,000 turnovers of formate in 16 h at 68 atm of 1:1 H_2/CO_2 and 353 K with 80,000 equiv DBU base (1,8-diazabicyclo[5.4.0]undec-7-ene) and 10,600 equiv [Li][OTf] additive; however, in the absence of [Li][OTf] additive only 460 turnovers were reported under otherwise identical conditions.[321] Similarly, for an Fe pincer catalyst also reported by Hazari and Bernskoetter, a formate TON of 58,990 is reported over 24 h under the previously described conditions with 16,000 equiv [Li][OTf], as compared to a TON of 2790 without [Li][OTf] as an additive.[322] Given the dramatic improvements observed for these catalysts, along with the observation of formate liberation after the addition of CO_2 to $[Li(THF)_x][\mathbf{2}{-}H]$, perhaps more facile formate dissociation and improved catalytic TON

and TOF could also be achieved in our system simply by adding [Li][OTf] as an additive. This has not been explored to date, but could be a promising avenue for improving catalytic performance within the framework of the current system.

*5.2.7.2 Does the Nonclassical Hydrogen Bonding Interaction Observed in the Solid-State Structure of [**2**−O_2CH]$^-$ Persist in Solution?*

As shown in the solid-state structure of [PPN][**2**−O_2CH] in Figure 5.10, a short contact of 2.24 Å was observed between the oxygen atom of formate which is not coordinated to Ni and one of the ligand methine hydrogen atoms. While this could simply be an artifact of crystal packing in the solid-state, similar C−H---O nonclassical hydrogen bonds have been proposed in the literature. In nonclassical C−H---O hydrogen bonded dimers, gas phase H---O distances between 2.1 and 2.5 Å have been predicted.[370] Thus, the 2.24 Å H---O solid-state distance observed in [PPN][**2**−O_2CH] is short enough to be in this range, and is also well within the sum of the van der Waals radii for O and H (2.7 Å).[371] Furthermore, classical hydrogen bonding between the non-coordinated oxygen atom of formate and more protic NH moieties has previously been reported by Hazari, among others.[372]

VT ^{1}H NMR studies of [PPN][**2**−O_2CH] in THF-d_8 were conducted to assess whether the close contact, which could potentially be a nonclassical hydrogen bond, persists in solution. The ^{1}H NMR spectrum of [PPN][**2**−O_2CH] at 298 K was shown in Figure 5.9. One interesting spectral feature is that one of the two methine ***H***$C(CH_3)_2$ proton resonances on each ligand arm has a similar chemical shift (~2.8 ppm) to the methylene CH_2 protons. This is highly unusual, as typically the methine protons resonate upfield by 0.6 to 1.1 ppm relative to the methylene protons, and the two sets of

resonances have not been observed to overlap like this in any other bimetallic complex studied to date, to my knowledge, over a wide range of T.

Two possible explanations could explain the abnormally downfield shift of one of the methine proton resonances [PPN][**2**−O_2CH]. One explanation would be that the formate ligand is bulkier than most apical ligands previously examined, which requires the ligand to twist and distort more than is typical. To this point, the twist can be quantified by examining the average P−Ni−M−N_{eq} dihedral angle, which is larger in [PPN][**2**−O_2CH] (20.6°) compared with [PPN][**2**−H] (11.7°), which has a much less sterically demanding terminal hydride ligand. This greater distortion of the ligand in [PPN][**2**−O_2CH] could render the chemical environments of the inequivalent methine and methylene protons are more disparate than is typical, which would result in a greater separation in the chemical shifts for the two methine protons, with one much more downfield than the other. An alternative explanation would be that the nonclassical hydrogen bonding C−H---O interaction persists in solution, but is fluxional such that one ligand methine proton on each ligand arm is interacting with the formate oxygen at any given time. One of the two methine hydrogen atoms on each arm is typically oriented toward Ni such that this would be feasible, and the interaction between the relatively electronegative oxygen atom and the methine hydrogen nuclei would result in a greater de-shielding of the latter, resulting in one of the two sets of methine protons resonating further downfield than usual in the ^{1}H NMR spectrum.

A good experiment which could lend insight into which of the two explanations holds more merit would be a VT ^{1}H NMR study of the [PPN][(^{t}BuO)NiGaL] complex, which was synthesized by Matt Vollmer via the addition of KO^{t}Bu to **2** followed by

subsequent salt exchange with [PPN][BArF]. *Tert*-butoxide is an apical ligand of similar steric bulk to formate which would likely require a similarly large ligand distortion to accommodate it, but the ^{t}Bu group would not be able to engage in a hydrogen bond with a methine hydrogen atom. Therefore, if the methine protons in [PPN][(^{t}BuO)NiGaL] have a large separation in chemical shift, with one of the two equivalent sets giving rise to a resonance that is shifted downfield and approaching or overlapping with the chemical shift of the methylene protons, as was the case for [PPN][**2**−O_2CH], then the steric bulk of the apical formate ligand leading to disparate chemical environments for the inequivalent methine protons is likely the best explanation for this spectral anomaly. On the other hand, if the methine protons in [PPN][(^{t}BuO)NiGaL] both resonate in their typical positions upfield of the methylene protons, the persistence of the nonclassical hydrogen bonding interaction would be a more likely explanation.

Another potential technique that can lend insight into a potential hydrogen bonding interaction with formate is IR spectroscopy. The two inequivalent IR stretches in the solid-state of coordinated formate are slightly more similar in [PPN][**2**−O_2CH] ($\Delta\nu$ = 281 cm^{-1}) than in two other η^1-O formate adducts of Ni ($\Delta\nu$ = 309 and 311 cm^{-1}) reported by Darensbourg, Hazari, and their respective co-workers.[335-336] A C−H---O=C hydrogen bonding interaction with the carbonyl oxygen atom would be expected to slightly weaken the C=O bond, leading to a lower stretching frequency that is slightly closer relative to that for the other C−O bond of formate. That said, this shift is minor and the assignment of the lower frequency ν(C−O) as 1339 cm^{-1} is tentative, so this is a fairly inconclusive line of reasoning. While these IR spectra were collected as KBr pellets in the solid-state,

perhaps solution-state IR studies could also be useful in determining the persistence, or lack thereof, of a nonclassical hydrogen bonding interaction in solution.

*5.2.7.3 Effect of Ion-Pairing and Potential Dihydrogen Bonding in [cation][**2**−H] Complexes*

Although the ^{1}H and ^{31}P chemical shifts do not change significantly in [cation][**2**−H] complexes (cation=Li, PPN, VkdH), the broadness of the hydride resonance is clearly impacted by the cation, as shown in Figure 5.4a. Specifically, the hydride resonance in [VkdH][**2**−H] is much sharper than those in for the $[Li]^{+}$ and $[PPN]^{+}$ analogues. Since the hydride resonance was relatively more resolved in [VkdH][**2**−H], and H_2 loss from [VkdH][**2**−H] is calculated to be relatively facile via a transition state with a short H−H distance, the presence of a hydrogen bonding interaction between the protic hydrogen of $[VkdH]^{+}$ and the hydridic hydrogen of $[\mathbf{2}{-}H]^{-}$ was considered as a possible reason for the relative decrease in linewidth for the hydride resonance in [VkdH][**2**−H].

A similar hydrogen bonding interaction between an acidic W−H complex and a hydridic Ni−H complex was characterized by Peruzzini and co-workers. This type of hydrogen bonding interaction between protic and hydridic hydrogen atoms which are in close proximity and may react to release H_2 is relatively rare, and has been termed *dihydrogen bonding*. Peruzzini and co-workers characterized the dihydrogen bond between the two metal hydrides via T_1(min) relaxation studies, with the close proximity of the two hydrogens resulting in a significantly lower T_1(min) value for the hydride resonance of the Ni−H, by ~400 ms relative to its T_1 values in the absence of the other metal hydride.[373] This shorter T_1(min) was proposed to be due to the additional dipolar

contributions to relaxation stemming from the close spatial proximity of the two hydrogens in the dihydrogen bond.

A similar T_1(min) study was conducted to probe the presence of a dihydrogen bonding interaction in [VkdH][**2**−H], which also has been found to undergo rapid exchange of free H_2, bound H_2, and the hydride ligand relative to the ^{1}H NMR timescale (400 MHz) at 298 K that can be slowed to allow all three species to be observable at low T in THF-d_8. Figure 5.22 shows the T_1 profile for the hydride resonance of [VkdH][**2**−H] in comparison to that of [PPN][**2**−H].

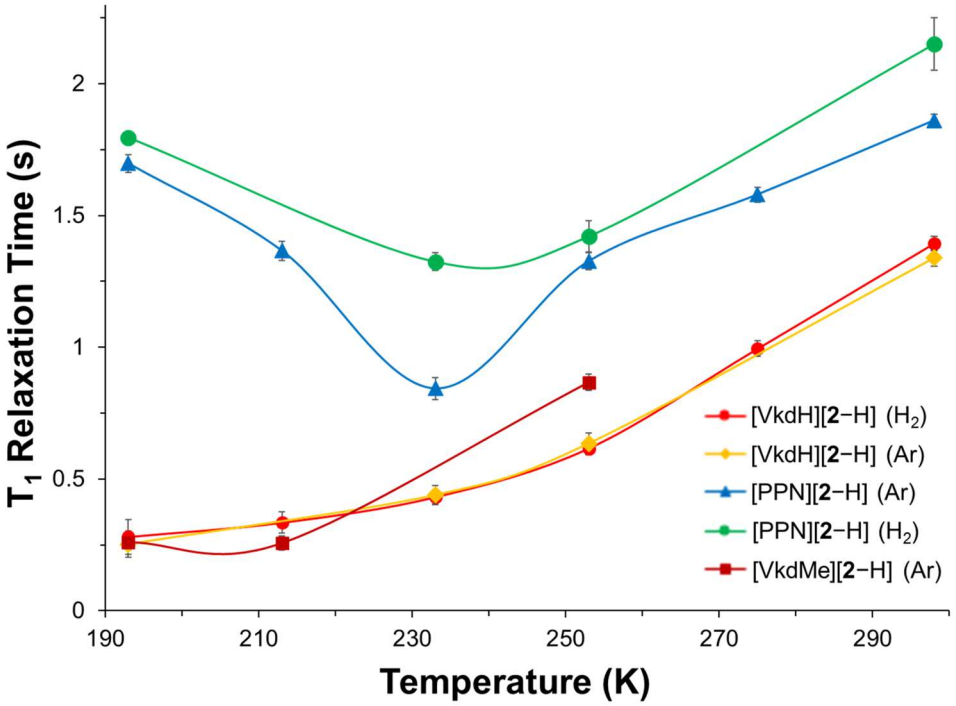

Figure 5.22. T_1 relaxation time of hydride resonance (in s, measured at 400 MHz) vs. T for [cation][**2**−H] complexes (~10 mM in THF-d_8) under 1 atm of both Ar and H_2.

The T_1 values were examined for both [cation][**2**−H] complexes under both Ar and H_2 (1 atm in each case) to verify that the exchange of the hydride ligand with free H_2 did not impact the T_1 values for [VkdH][**2**−H], which was generated *in situ* from **2** and a slight excess of Vkd under 1 atm H_2. The T_1 values for [VkdH][**2**−H] were found to be

essentially identical under Ar and H_2. Likewise, the presence of an Ar or H_2 atmosphere also did not lead to drastic changes in the T_1 profile for [PPN][**2**−H], with slightly lower T_1 values observed under Ar (Figure 5.22). Different T_1 behavior was observed for [VkdH][**2**−H] and [PPN][**2**−H], with the latter passing through a minimum at ~233 K with T_1(min) = 0.49(5) s, while the T_1 values for the former continuously decreased with T. Furthermore, the T_1 values are significantly lower, by ~600 ms on average, for the hydride resonance of [VkdH][**2**−H] compared with that of [PPN][**2**−H], which was taken to be a potential indicator of dihydrogen bonding in the study performed by Peruzzini and co-workers.[373] That the T_1 relaxation behavior for the hydride would be so different for the same anionic hydride with different cations was intriguing, and would seem to suggest that the differences stem from different ion-pairing interactions with the cation.

If a dihydrogen bond is formed in [VkdH][**2**−H], then it would make intuitive sense that this weak interaction would become more prevalent in solution at lower T, potentially explaining the continual decrease of T_1 with decreasing T observed for the hydride resonance of [VkdH][**2**−H]. To test the hypothesis that a *bona fide* dihydrogen bond was the cause of the lower T_1 values and lack of a T_1(min) value (over the range of 193 K to 298 K) for the hydride of [VkdH][**2**−H], a T_1 profile of [VkdMe][**2**−H], a close analogue which only differs in the substitution of a $[P{-}Me]^+$ for the $[P{-}H]^+$ unit on the Vkd cation, was also obtained. The T_1 profile for [VkdMe][**2**−H] was found to be very similar to that of [VkdH][**2**−H], with T_1 decreasing and somewhat levelling off at low T (Figure 5.22). The similarity of the T_1 values for [VkdMe][**2**−H] and [VkdH][**2**−H] suggests that a dihydrogen bond likely is not formed, but rather that the differences in T_1 behavior between [VkdX][**2**−H] (X=Me, H) and [PPN][**2**−H] likely stem from more

general differences in ion-pairing. In retrospect, [VkdMe][**2**−H] was not the perfect control, as a methyl group is still small and is expected to carry a partial positive charge which could interact with the hydridic Ni−H similarly to $[VkdH]^+$; [VkdR][**2**−H] with a bulkier alkyl group (R) would be a better control, as this would perturb the ion-pairing to a large extent and might result in T_1 behavior approaching that seen for [PPN][**2**−H]. Consistent with the conclusion that no dihydrogen bond is formed, a distance of 2.76 Å is predicted for the two hydrogen atoms in question in [VkdH][**2**−H], which is much longer than the calculated distances of 2.41 Å for the Ni−H----H−W dihydrogen bonding interaction reported by Peruzzini and co-workers.[373]

One other interesting observation regarding the ion-pairing of $[K(THF)_x]$[**2**−H], that likely also applies to the other alkali metal ion-pairs of $[\mathbf{2}-H]^-$ as well, is that $[K]^+$ appears to interact with the aryl rings of the ligand if it is not chelated by either THF or 2,2,2-cryptand. In support of this, the aryl protons shift dramatically upfield by ~0.1 ppm by ^{1}H NMR spectroscopy upon the chelation of [K][**2**−H] by 2,2,2-cryptand, compared to < 0.05 ppm shifts for the aryl protons typically observed in entirely different bimetallic complexes. Additionally, ^{31}P NMR studies revealed that the phosphorus nuclei in [K][**2**−H] are inequivalent in a ~2:1 ratio in C_6D_6, with three-fold symmetry restored and the typical sharp ^{31}P peak observed upon the addition of 2,2,2-cryptand or re-dissolving the same sample in THF (Figure A.4.25). These experiments and spectroscopic data are consistent with $[K]^+$ coordinating to one or two of the aryl rings unless it is chelated by 2,2,2-cryptand or THF. The interaction of $[K]^+$ with the aryl rings of the ligand had previously been observed in the solid-state in an anionic bimetallic Cr complex,[138] and is

apparently preferred for [K][**2**−H] in benzene solution rather than direct interaction of $[K]^+$ with the metal hydride itself.

5.2.8 Exploring the Effect of the Supporting Metal: Synthesis and Characterization of a Series of Anionic [HNiML]⁻ Complexes by ^{1}H NMR Spectroscopy and X-ray Crystallography

In light of the excellent catalytic activity of **2** for CO_2 hydrogenation, which has been shown to proceed via the anionic Ni(0) hydride, [**2**−H]⁻, the propensity of the other group 13 supporting metals to stabilize analogous $[HNiML]^-$ species (M=Al, In) was investigated. The same synthetic routes were utilized as previously described for [PPN][**2**−H], as originally carried out by Matt Vollmer.[128] Namely, the addition of 1.1 equiv *n*BuLi to NiML (M=Al, In) generated $[Li(THF)_x][HNiML]$ *in situ*, and subsequent salt-exchange as previously described with [PPN][BArF] yielded [PPN][HNiAlL] ([PPN][**1**−H]) and [PPN][HNiInL] ([PPN][**3**−H]) in adequate yields of ~25% and ~75%, respectively. This synthetic protocol is highly convenient in that it bypasses the difficult process of removing triethylborane that originally plagued the purification of $[M(THF)_x][HNiML]$ synthesized using $MHBEt_3$. The initial 1-butene by-product formed via β-hydride elimination is volatile, and subsequent purification utilizes the differences in solubility of [PPN][HNiML] and [Li][BArF], with the former precipitating out of a concentrated THF solution (~1-2 mL) layered with a copious amount of diethyl ether (~15 mL).

The relatively lower yield of [PPN][**1**−H] hinted at its instability, as did the original observation that the addition of $NaHBEt_3$ to **1** only resulted in ~25% conversion to $[Na(THF)_x][$**1**−H] with the majority of the starting material, **1**, remaining. To this

point, even storing [PPN][**1**−H] as a solid at −35°C in the freezer resulted ~15% decomposition to **1** over the course of one month, which could fortunately be removed via additional washing with benzene and extraction into THF. Figure 5.23 shows the ^{1}H spectrum of [PPN][**3**−H], and Figure 5.24 shows a comparison of the ^{31}P NMR spectra (left) and the ^{1}H NMR spectra of the hydride region (right) for the trio of [PPN][HNiML] complexes (M=Al, Ga, In).

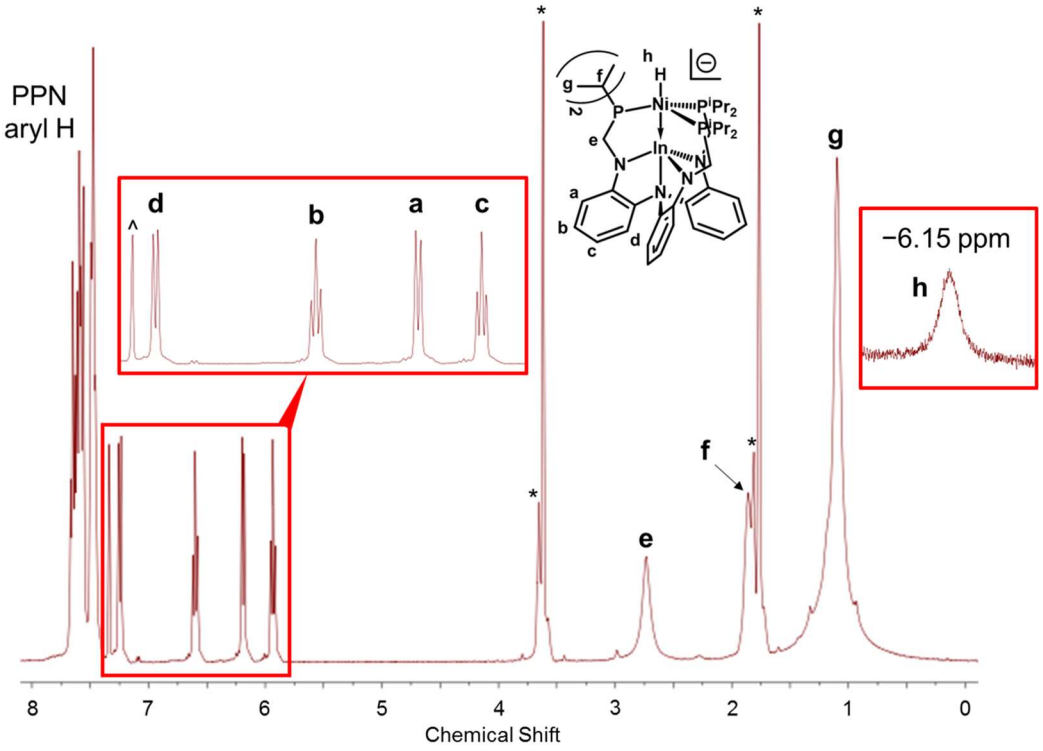

Figure 5.23. ^{1}H NMR spectrum of [PPN][**3**−H] (400 MHz, THF-d_8). Solvent peaks for THF (*) and residual benzene (^) are denoted. Close-ups of aryl region with resolved coupling (left) and of the hydride resonance (right) are shown for visual clarity.

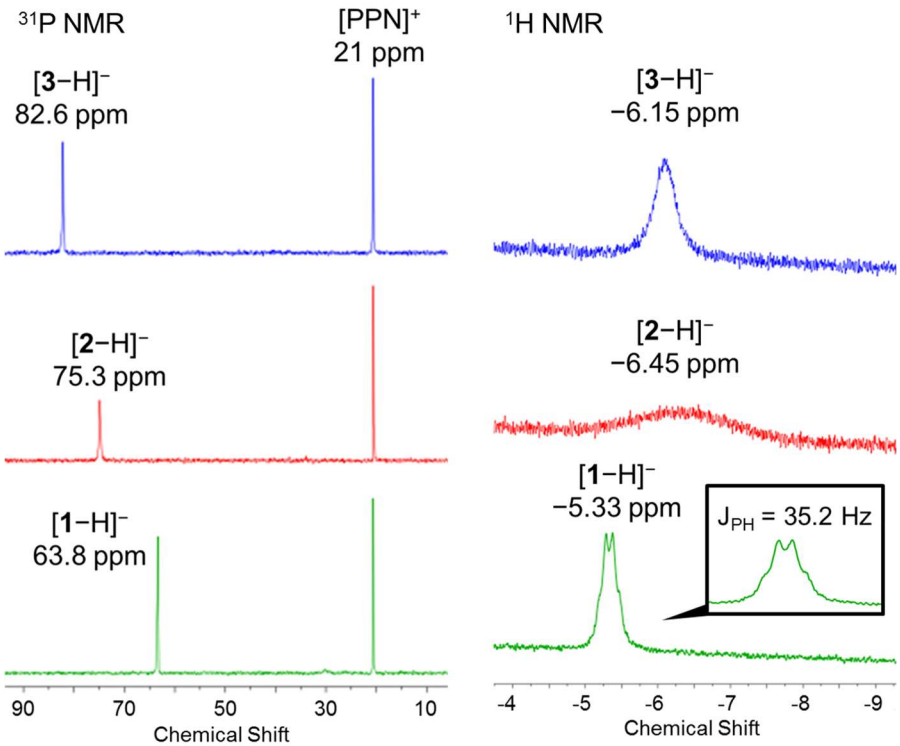

Figure 5.24. Stacked ^{31}P NMR spectra (left, 161.9 MHz) and ^{1}H NMR spectra of the hydride region (right, 400 MHz) for [PPN][HNiML] complexes (M=Al, Ga, In) in THF-d_8 at 298 K. A close-up of the hydride resonance for [PPN][**1**−H] is shown with resolved $^{2}J_{PH}$ coupling.

[PPN][**3**−H] exhibits C_{3v} symmetry in solution, as each of the three ligand arms are equivalent at 298 K in THF-d_8, giving rise to four aryl, one methylene, one methine, and one methyl resonance (Figure 5.23). [PPN][**1**−H] and [PPN][**2**−H] are similarly C_{3v}-symmetric at 298 K (Figure A.4.4), with C_3 symmetry observed at lower T for each of the three complexes, as the methylene, methine, and methyl protons become inequivalent (see Figures A.4.26-A.4.28 for VT ^{1}H NMR spectra). The coalescence of the methylene protons was also measured, just as described previously and in section 4.2.4.4,[101, 231, 298] and $\Delta G^{\ddagger}_{MC}$ in THF-d_8 was determined to be 13.4(1), 14.2(1), and 12.7(1) for [PPN][**1**−H], [PPN][**2**−H], and [PPN][**3**−H], respectively (Figure 5.25).

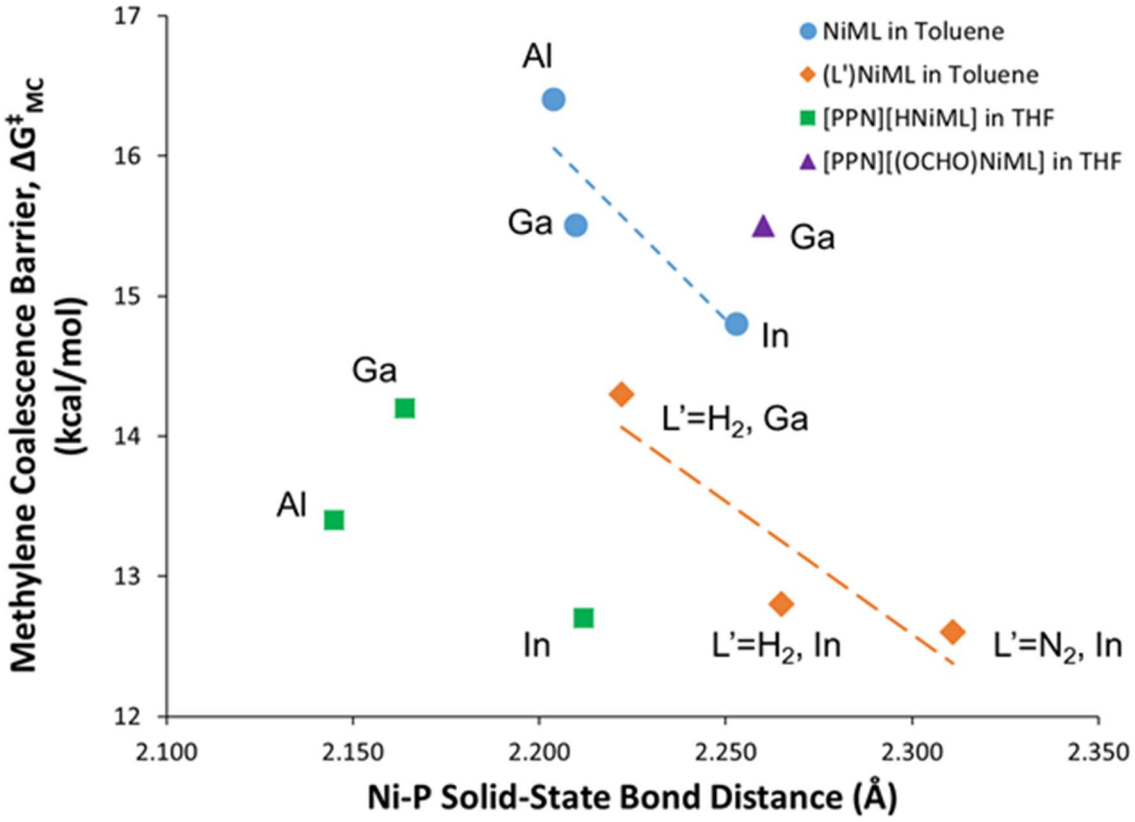

Figure 5.25. Summary plot of methylene coalescence barriers (in kcal/mol) for NiML, (L')NiML, [PPN][HNiML], and [PPN][(OCHO)NiML] complexes vs. Ni−P solid-state bond distance (in Å). Note that all charged complexes were measured in THF-d_8, all neutral complexes were measured in toluene-d_8, and all $\Delta G^{\ddagger}_{MC}$ values have a standard deviation of ±0.1 kcal/mol.

A lower $\Delta G^{\ddagger}_{MC}$ is observed for [PPN][HNiML] with In as the supporting metal compared to Ga, just as was found for isostructural NiML, (η^2-H_2)NiML, and (OC)NiML complexes (section 4.2.4.4). However, this is the first case where M=Al does not have a higher $\Delta G^{\ddagger}_{MC}$ than M=Ga and M=In for a series of isostructural complexes. Interestingly, all [PPN][HNiML] complexes have lower $\Delta G^{\ddagger}_{MC}$ values than [PPN][**2**−O_2CH], which has a barrier of 15.5(1) kcal/mol. This is likely due to the decreased flexibility of the ligand in [PPN][**2**−O_2CH] as a result of the increased distortion required to accommodate the bulkier formate ligand compared with the terminal hydride in [PPN][HNiML]. Similar to the finding that the binding of apical L-type ligands to NiML complexes

increases the phosphine lability and decreases $\Delta G^{\ddagger}_{MC}$, the introduction of a hydride ligand has a very similar effect, with $\Delta G^{\ddagger}_{MC}$ for [PPN][HNiML] complexes in THF-d_8 found to be nearly identical to those for (η^2-H_2)NiML complexes in toluene-d_8 (Figure 5.25). The low barriers for [PPN][HNiML] complexes despite short Ni−P bonds, as well as the high barrier for [PPN][**2**−O_2CH] despite elongated Ni−P bonds, both serve to illustrate that an elongated Ni−P distance is only part of what allows for a low methylene coalescence barrier. Other factors include whether an additional ligand is bound, as well as the steric bulk of the added ligand and the required distortion of the phosphinoamide ligand to accommodate its binding.

One other interesting observation from the ^{1}H NMR spectra of [PPN][HNiML] is that the hydride resonance varies dramatically in broadness depending on the supporting metal in the [PPN][HNiML] complexes (Figure 5.24). The difference between the hydride resonance for [PPN][**2**−H] and [PPN][**1**−H] is particularly extreme, with a very broad resonance spanning ~3 ppm observed for the former compared with a sharp resonance with resolved $^2J_{PH}$ coupling for the latter. These differences in broadness are not well understood at the present time. Of note, the $^2J_{PH}$ coupling constant of 35.2 Hz observed for [PPN][**1**−H] is similar to that observed for [Na(THF)$_x$][**2**−H] (34.8 Hz in ~2:1 THF-d_8/C_6D_6) and that for a similar triphosphine-ligated, terminal Ni−H reported by Peters and co-workers (36 Hz).[189]

Three-fold symmetry was observed by ^{31}P NMR spectroscopy for all [PPN][HNiML] complexes at all T, and the ^{31}P resonances for the $[PPN]^+$ and $[HNiML]^-$ fragments integrate in the expected ~2:3 ratio. The ^{31}P resonance for $[HNiML]^-$ shifts downfield as the supporting metal is varied down group 13, just as was observed for the

isostructural series of NiML and (η^2-H_2)NiML complexes. For the NiML complexes, this downfield shift in the ^{31}P resonances was accompanied by elongation of the solid-state Ni−P distances, which collectively was attributed to a decrease in Ni→P π-back-donation upon varying the supporting metal down group 13.[97] A similar trend is observed for [PPN][HNiML] complexes, with the average Ni−P solid-state distances elongating from 2.145(1) to 2.164(7) to 2.212(2) Å for the Al, Ga, and In analogues, respectively, as the ^{31}P nuclei become more de-shielded and the resonance shifts downfield (Figure 5.24, Table A.4.9). Therefore, the Ni→P π-back-donation is proposed to decrease upon varying the supporting metal down group 13 for the trio of [PPN][HNiML] complexes as well. It should be noted that the Ni−P solid-state distances in the [PPN][HNiML] complexes are all shorter relative to those in the corresponding NiML complexes by 0.04 to 0.06 Å, despite the fact that the vertical component of the Ni−P bond elongates by 0.05 to 0.07 Å due to Ni being positioned further above the P_3-plane to interact with the hydride ligand. The solid-state structures of [PPN][**1**−H] and [PPN][**3**−H], which were obtained by Matt Vollmer, are displayed in Figure 5.26, along with selected structural parameters given in Table A.4.9.

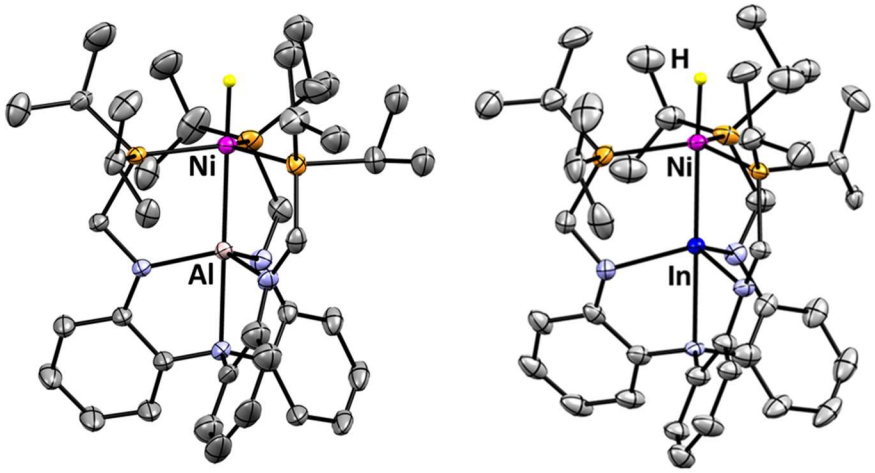

Figure 5.26. Solid-state structures of [PPN][HNiAlL] ([PPN][**1**−H], left) and [PPN][HNiInL] ([PPN][**3**−H], right) obtained by Matt Vollmer. Thermal ellipsoids are shown at 50% probability, and solvent atoms, PPN cations, and H atoms were omitted for clarity, with the exception of the apical hydride ligands which were placed from the difference map.

The Ni−M distances in the [PPN][HNiML] complexes were observed to contract slightly relative to those in the corresponding NiML complexes, with *r* values decreasing from 1 to 0.99, from 0.97 to 0.96, and from 0.92 to 0.91 upon introduction of the hydride ligand for M=Al, Ga, and In, respectively (Table A.4.9). Just as was seen for [PPN][**2**−H], the supporting Al and In metals reposition by more than twice as much as Ni upon the introduction of the hydride ligand at Ni.[97, 128] Specifically, Al and In are positioned further above their respective N_3-planes by 0.17 and 0.11 Å in [PPN][HNiML] relative to NiML, while Ni is positioned further above the P_3-plane by 0.07 and 0.05 Å in [PPN][**1**−H] and [PPN][**3**−H], respectively, relative to the corresponding NiML complexes (Table A.4.9). As discussed previously for [PPN][**2**−H], the dramatically greater change in the position of the supporting metal compared to that of Ni, even though Ni is the metal directly interacting with the hydride ligand, shows that the bimetallic Ni−M unit acts cooperatively to stabilize the anionic hydride species. The supporting metal likely helps to attenuate the electron-richness of the anionic Ni(0)−H

moiety, as evidenced by the slightly shorter Ni−M distances and the supporting metal moving much further above the N_3-plane toward Ni.

5.2.9 Electrochemical Studies of the [HNiML]⁻ Complexes

Cyclic voltammetry (CV) studies were conducted to assess whether the trends in electron-richness of the Ni centers observed for NiML complexes (Al > Ga > In) also holds true for the [HNiML]⁻ complexes. Figure 5.27a shows CVs of the trio of [HNiML]⁻ complexes, which all showed an irreversible Ni(0/I) redox event. It should be noted that CV studies were conducted using the PPN salts, [PPN][HNiML], for M=Ga and In, whereas [P$_4$^{t}BuH][**1**−H] was used due to its higher yielding synthesis relative to [PPN][**1**−H]. Additionally, note that all redox potentials discussed in this section are relative to that of the $FeCp_2^{0/+}$ redox couple, even if it is not explicitly mentioned for every potential given.

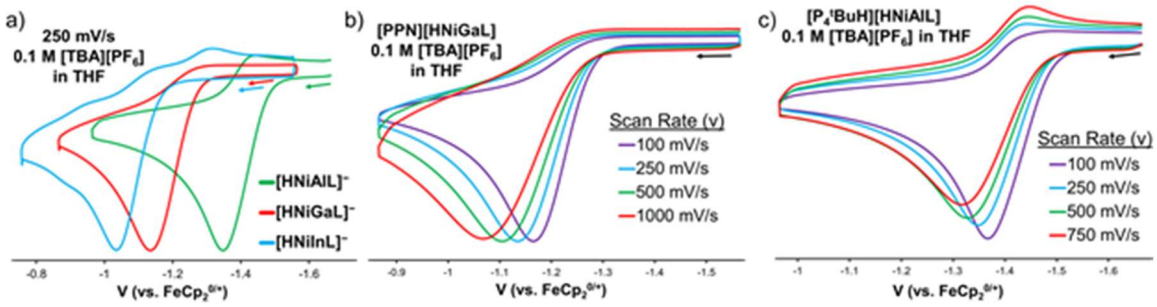

Figure 5.27. (a) CV of [HNiML]⁻ complexes (~1 mM in THF, 0.1 M [TBA][PF_6]), with the isolation of the mostly irreversible Ni(0/I) oxidation events displayed. Scan rate studies, with current (*i*) corrected for scan rate (ν) based on the proportionality of *i* to ($\nu^{0.5}$), are shown for: (b) [PPN][**2**−H] and (c) [P$_4$^{t}BuH][**1**−H].

At a scan rate of 250 mV/s, the Ni(0/I) oxidations were found to have E_{pa} values of −1.35 V, −1.13 V, and −1.03 V (all vs. $FeCp_2^{0/+}$ redox couple) for M=Al, Ga, and In, respectively (Figure 5.27a). The redox events were irreversible, as little to no current for the return reduction event was observed at slow scan rates in all cases. Nevertheless, the

relative ease of oxidation as a function of the supporting metal appears to be analogous to that observed for the neutral NiML complexes, with the electron-richness of the Ni center decreasing upon variation of the supporting metal down group 13 (Al > Ga > In). A scan rate study for [PPN][**2**−H] showed that the Ni(0/I) oxidation event was completely irreversible at all scan rates up to 1 V/s (Figure 5.27b). In contrast, quasi-reversibility was observed for [$P_4{}^t$BuH][**1**−H] at faster scan rates. This can be seen in Figure 5.27c, as the current for the return reduction grows relative to that for the oxidation at faster scan rates, with the i_{pa}/i_{pc} ratio decreasing from 5.0 to 3.3 as the scan rate was increased from 250 to 750 mV/s. At 750 mV/s, $E_{pc} = -1.45$ V, which gives $E°_{1/2} = -1.38$ V for the Ni(I/0) redox couple for [$P_4{}^t$BuH][**1**−H]. A similar scan rate study was also performed for [PPN][**3**−H], and the Ni(0/I) oxidation event was observed to be completely irreversible at all scan rates up to 1 V/s (Figure A.4.29). Although a small return reduction peak can be seen in the CV of [PPN][**3**−H] (Figure 5.27a), it is not believed to be related to the Ni(0/I) oxidation peak because shifts in E_{pa} with varying scan rate did not result in concomitant shifts in the potential of the small reduction peak, which remained constant at $E_{pc} = -1.32$ V at all scan rates examined (Figure A.4.29).

Irreversible electrochemical events are often the result of decomposition or other side-reactions that rapidly consume the electrochemically generated species, preventing re-generation of the original complex on the return scan.[142] In regard to why the Ni(0/I) oxidation events for the $[HNiML]^-$ complexes are all irreversible at slow scan rates, it is proposed that bimolecular loss of H_2 occurs upon electrochemical oxidation of $[HNiML]^-$ to generate HNiML, which results in the formation of the neutral NiML complexes in

addition to 0.5 equiv H_2 (Figure 5.28d). Full CVs of [P_4^{t}BuH][**1**−H] will be considered in detail in order to help support this mechanistic proposal (Figure 5.28a-c).

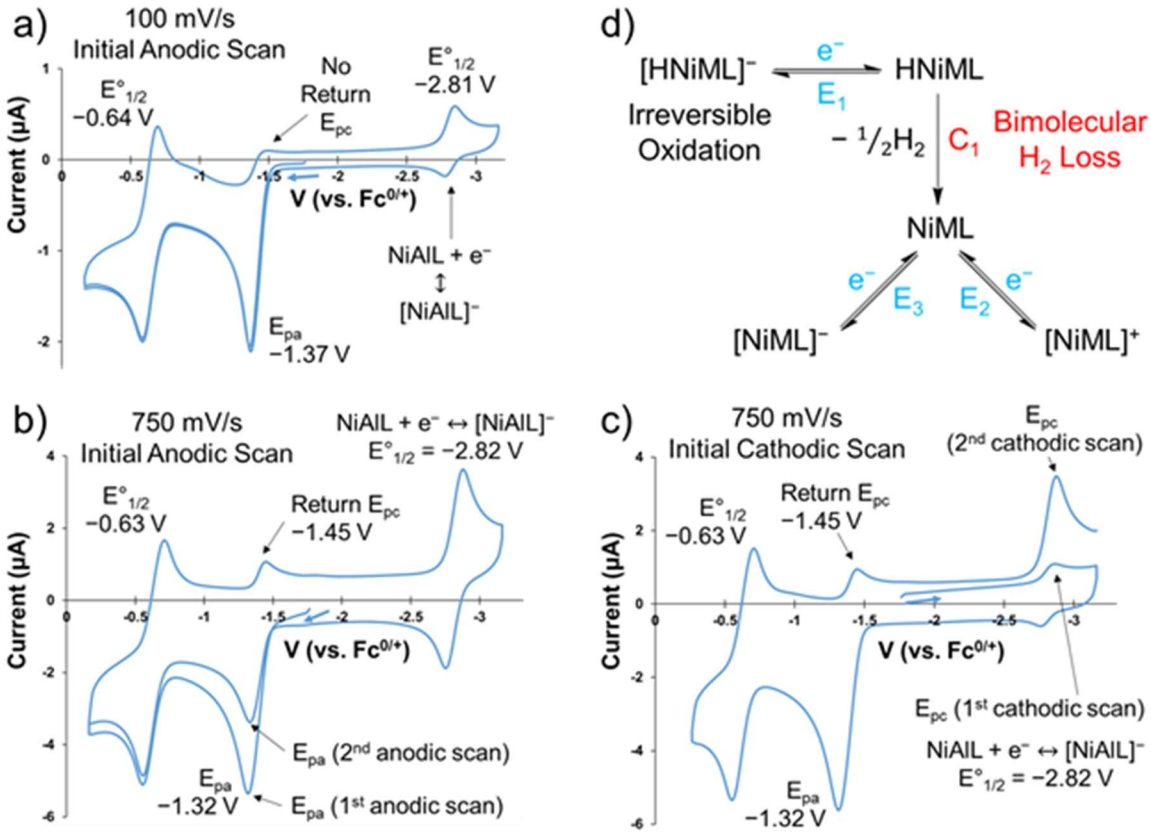

Figure 5.28. Full CVs of [P_4^{t}BuH][**1**−H] (~1 mM) obtained in 0.1 M [TBA][PF_6] in THF under 1 atm Ar, with the following variations: (a) scan rate (ν) of 100 mV/s, with an initial anodic scan, (b) ν = 750 mV/s, with an initial anodic scan, and (c) ν = 750 mV/s, with an initial cathodic scan (after stirring to minimize the amount of NiAlL (**1**) at the electrode surface from previous CV scans). (d) Mechanistic proposal for the decomposition of HNiML, formed initially upon electrochemical oxidation of the [HNiML]$^-$ complexes, via bimolecular H_2 loss.

First, a quasi-reversible reduction event at $E°_{1/2}$ = −2.82 V (vs. $FeCp_2^{0/+}$ redox couple) was observed after the initial oxidation of [**1**−H]$^-$ (Figure 5.28a-b). This feature matches up exactly with the quasi-reversible reduction of NiAlL (**1**) to [NiAlL]$^-$ (section 2.2.6.4).[158] Furthermore, the concentration of **1** at the electrode surface was observed to be relatively low for an initial cathodic scan at 750 mV/s, but after the oxidation of [**1**−H]$^-$, the second cathodic scan has a much greater i_{pc} for the reduction of **1** indicating

that the concentration of **1** has increased since the initial cathodic scan. Thus, **1** is being generated as a result of the intervening anodic scan. Because the oxidative feature at $E°_{1/2}$ = −0.63 V is reversible, the reaction of the neutral HNiAlL (**1**−H) after the initial oxidation of [**1**−H]$^-$ likely forms **1** and gives rise to the irreversibility of the Ni(I/0) redox wave for [**1**−H]$^-$.

The nature of the reversible oxidative feature at $E°_{1/2}$ = −0.63 V is a bit more ambiguous. One would think that this feature would be simply be attributable to the Ni(I/0) redox couple of NiAlL (**1**). However, it is shifted to slightly less negative potential relative to the Ni(I/0) redox couple of **1** ($E°_{1/2}$ = −0.74 V).[78] One possibility is that the Ni(I/0) redox potential shifts in the presence of [P$_4$^{t}BuH][X] in solution. The current passed for the oxidative feature at $E°_{1/2}$ = −0.63 V is similar to that for the reduction wave of **1** at 750 mV/s, and its i_{pa} is always nearly identical to that of the preceding Ni(0/I) oxidation of [**1**−H]$^-$ (Figure 5.28a-c). While the identical i_{pa} of the successive oxidation events could be explained by the feature at $E°_{1/2}$ = −0.63 V being attributable to a second oxidation of [**1**−H]$^-$, this has been discounted for several reasons. In addition to this representing a relatively close potential separation for two successive redox events (~0.7 V from the initial oxidation), $E°_{1/2}$ = −0.63 V would also be too mild for the Ni(II/I) redox couple of neutral HNiAlL (**1**−H), especially considering the Ni(I/0) redox couple for **1** occurs at $E°_{1/2}$ = −0.74 V. Instead, it is proposed that the identical i_{pa} for the two oxidation events simply indicates a clean decomposition of **1**−H to one species, which is proposed to be **1** based on the matching reduction potential, despite the unexplained shift in the oxidation potential.

To help understand this oxidation feature and lend further insight into the decomposition of the neutral HNiML complexes initially formed upon electrochemical oxidation, the full CV of [**2**−H]$^-$ and [**3**−H]$^-$ were also considered (Figure 5.29). In the case of [**2**−H]$^-$, this oxidation feature occurs at $E°_{1/2}$ = −0.59 V, which is with the experimental error of ~20 mV of the Ni(I/0) redox couple for NiGaL (**2**).[97] Additionally, another complication to consider is that the neutral NiML complexes could bind the H_2 that is generated, which would potentially slightly shift the Ni(I/0) redox potentials for the NiML complexes from their typical values. In the case of **2**, it is likely that any binding of H_2 to generate **2**−H_2 would make the Ni center slightly more electron-rich and more easily reduced relative to **2**, which could be consistent with the slight shift to milder potential from −0.57 to −0.59 V. In the case of [**3**−H]$^-$, the additional oxidative feature was observed at $E°_{1/2}$ = −0.49 V, which is at slightly milder potential than the irreversible Ni(0/I) oxidation of **3** (E_{pa} ~ −0.40 V).[97] Previous CVs of **3** have been observed to result in decomposition to give an unidentified species, which is hypothesized to be a Ni−F species, with $E°_{1/2}$ ~ −0.46 V, and so this oxidation has tentatively been assigned to this species. Alternatively, it is possible that this oxidative feature could be assigned to **3**−H_2, although control CV experiments of **3** under an H_2 atmosphere showed a more irreversible oxidation event than what is observed in the CV of [**3**−H]$^-$.

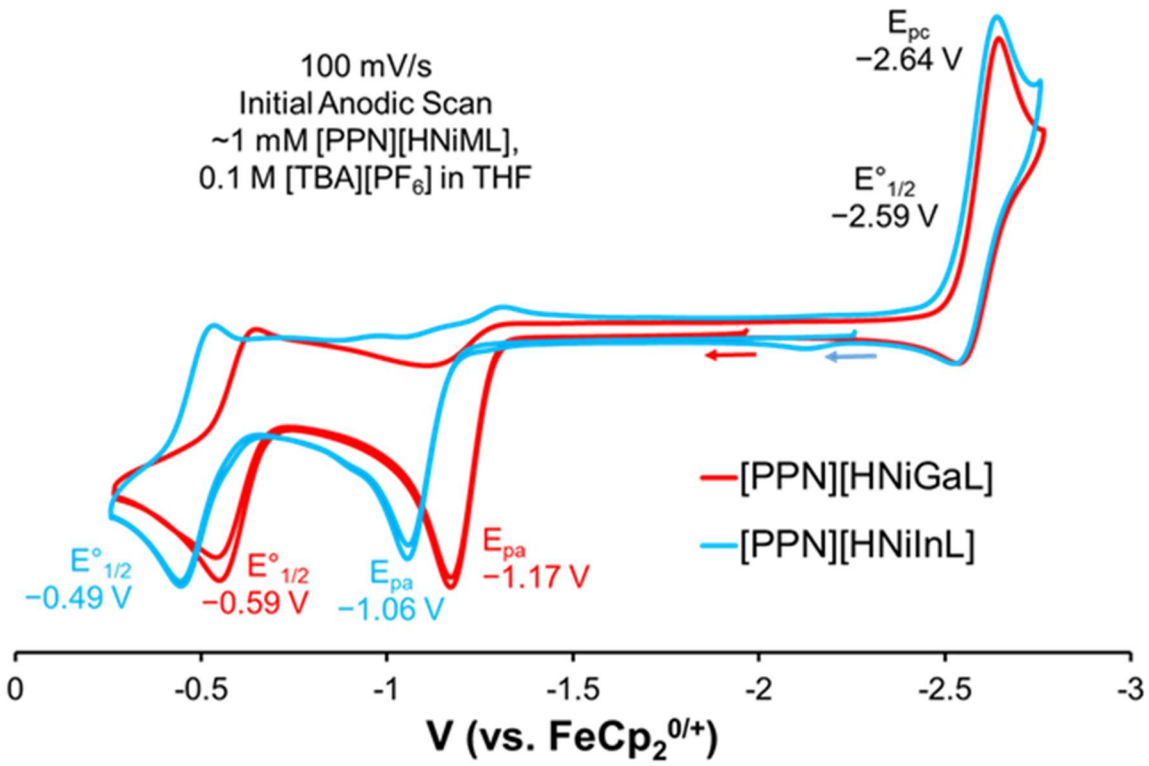

Figure 5.29. Full CV of [PPN][**2**−H] and [PPN][**3**−H] (~1 mM) with 0.1 M [TBA][PF_6] in THF under 1 atm Ar, with a scan rate of 100 mV/s and initial anodic scans. All redox potentials are relative to the $FeCp_2^{0/+}$ redox couple. Note that scans to more negative potentials at the edge of the solvent window (< −2.8 V) were not performed.

Unlike the full CV of [**1**−H]$^-$, which showed the diagnostic reduction event for **1**, no supporting metal-dependent reduction was observed in the CVs of [**2**−H]$^-$ and [**3**−H]$^-$. An identical quasi-reversible reduction event was observed at $E°_{1/2}$ = −2.59 V in the CVs of both [**2**−H]$^-$ and [**3**−H]$^-$, which has been tentatively assigned as a [PPN]$^+$-based reduction event. Consistent with this assignment, no such reduction was observed when the [$P_4{}^t$BuH]$^+$ counter-ion[374] was substituted for [PPN]$^+$ with [**1**−H]$^-$. The lack of other reduction events was initially confusing, as this would seem to be contradictory to the proposal that the neutral NiML complexes have formed since **2** and **3** have reduction events with $E°_{1/2}$ of −2.48 V and −2.34 V, respectively. However, if **3** does decompose to the aforementioned unidentified species that may be a Ni−F species, no reduction events

were observed for this species in previous CV experiments. Alternatively, if **3** remains in solution to any extent, it likely binds the H_2 that was formed to some extent, and control CV experiments of **3** under 1 atm H_2 do not show any reduction event at accessible potentials. This makes intuitive sense, as the reduction of **3**−H_2 would result in a 19-electron species which would presumably be unfavorable to form. In general support of the proposal of bimolecular H_2 loss from the neutral HNiInL species (**3**−H), the chemical oxidation of [**3**−H]$^-$ with [$FeCp_2$][PF_6] resulted in formation of $FeCp_2$ and **3**−N_2. This indicates that the small amount of H_2 generated is eventually outcompeted by N_2 in the glovebox atmosphere for binding to **3**, which is presumably generated via the decomposition of **3**−H after it is initially formed upon one-electron oxidation of [**3**−H]$^-$. To confirm the generation of H_2, chemical oxidation in a J. Young NMR tube could be performed, which would be expected to result in the binding of H_2 to generate **3**−H_2 to some extent. While the eventual loss of H_2 for N_2 in the chemical oxidation experiment might be taken to suggest that H_2 binding will also not occur in the CV experiments performed in an Ar glovebox, it is not known on what timescale H_2 is lost, and **3** has been measured to bind H_2 very strongly (section 3.3.6).

In the case of **2**, its quasi-reversible reduction event was observed to shift from $E°_{1/2}$ = −2.48 V to −2.58 V upon the exposure of **2** to 1 atm H_2. Thus, if **2**−H_2 exists in solution, its reduction feature has been previously measured to be exactly coincident with the redox wave tentatively assigned as a [PPN]$^+$-based reduction, and so it is difficult to tell if any current for this reduction is attributable to the reduction of **2**−H_2. The binding of H_2 to **2** is also much less favorable than that to **3** (chapter 3), and so the presence of a reduction feature in the former case likely reflects the binding equilibrium occurring

rapidly on the CV timescale. Importantly, because NiAlL (**1**) binds H_2 very weakly, such that 93% of the equilibrium mixture at 1 atm H_2 exists as complex **1** (section 3.3.6.5), it makes sense that the reduction of **1** is the only one of the three NiML complexes that is readily observable. Furthermore, the other NiML complexes (M=Ga, In) bind H_2 more favorably and would not be as readily reduced after binding H_2, since this would result in the formation of 19-electron species that are likely unstable. Furthermore, much less H_2 is being generated in this case than is present upon exposure to 1 atm H_2, and so it stands to reason that very little H_2 binding would occur in the case of complex **1**, allowing for the reduction of **1** to be observed at its characteristic potential.

Both the full CVs and scan rate studies can also lend insight into the rate of decomposition of the electrochemically generated neutral HNiML species. First, the fact that the Ni(0/I) oxidation for [**1**−H]$^-$ is completely irreversible at 100 mV/s but becomes quasi-reversible at 750 mV/s is consistent with the full decomposition of **1**−H occurring prior to the return cathodic scan only at slower scan rates (Figure 5.28a-b). Additionally, i_{pa} for the Ni(0/I) oxidation of [**1**−H]$^-$ for both the initial anodic scan and the subsequent anodic scan are identical at 100 mV/s, as seen by the fact that the two CV traces overlay nearly perfectly in Figure 5.28a. However, at a scan rate of 750 mV/s, i_{pa} decreases dramatically for the second anodic scan, to ~60% of that observed for the initial anodic scan (Figure 5.28b). This decrease in i_{pa} for the second anodic scan, along with the fact that i_{pa} remains constant in both anodic scans for the subsequent oxidation feature at $E°_{1/2}$ = −0.64 V, indicates that the concentration of [**1**−H]$^-$ available to be oxidized at the electrode surface has been depleted after the initial anodic scan, at least at faster scan rates (Figure 5.28b). These results are interpreted as follows: at slow scan rates, full

decomposition of **1**−H occurs upon electrochemical oxidation of [**1**−H]$^-$ before the return cathodic scan, but slow scan rates allow for the full replenishment of the concentration of [**1**−H]$^-$ at the electrode surface to occur by diffusion prior to the second anodic scan. On the other hand, at faster scan rates, the return cathodic scan occurs before **1**−H fully decomposes, resulting in the observed quasi-reversibility of the Ni(I/0) redox couple, but the second anodic scan also happens sufficiently quickly that the concentration of [**1**−H]$^-$ at the electrode surface has not had enough time to be completely restored by the diffusion of additional [**1**−H]$^-$ from the bulk solution (Figure 5.28).

Another interesting observation is that the magnitude of the current passed for the reduction of **1** is significantly smaller than that for both the Ni(0/I) oxidation of [**1**−H]$^-$ and the oxidation event at $E°_{1/2}$ = −0.63 V at 100 mV/s, but all three redox events have similar current magnitudes when the scan rate was increased to 750 mV/s (Figure 5.28a-b). This is interpreted to be due to the fact that faster scan rates do not allow **1**, which is formed during the anodic scan after the oxidation of [**1**−H]$^-$, to diffuse away from the electrode surface prior to the cathodic scan reaching its harsh reduction potential of $E°_{1/2}$ = −2.82 V. Lastly, it is not well understood why the bimolecular loss of H_2 from the neutral HNiML complexes would occur the most slowly for M=Al, such that quasi-reversibility was observed at fast scan rates in this case but not for M=Ga and In. The irreversibility of the Ni(0/I) oxidation event for the [HNiML]$^-$ complexes will be revisited in section 5.2.13, as it pertains to the determination of thermodynamic bond dissociation free energies (BDFEs). Specifically, it will be shown that the BDFE of the Ni−H bonds in the unstable HNiML species are much less than 52 kcal/mol, validating

the notion that Ni−H bond cleavage to form H_2, with a stronger H−H bond of ~103.6 kcal/mol,[329] would be thermodynamically favorable.

5.2.10 Generation of Anionic [HNiML]⁻ Complexes (M=Al, In) by H_2 Heterolysis with Base

5.2.10.1 Effect of the Supporting Metal on Acidity of (η^2-H_2)NiML Complexes

After observing that [cation][HNiML] complexes for M=Al and M=In could be synthesized using *n*BuLi and $MHBEt_3$, the next logical step was to attempt to generate the analogous [BaseH][HNiML] complexes from H_2 heterolysis with NiML and an exogenous base,[330] as this is the reaction that is relevant for catalysis. In addition to simply finding a base strong enough to generate [BaseH][HNiML] *in situ* under catalytic conditions for CO_2 hydrogenation, it was also hoped that the pK_a values could be determined via the use of a suitable base that allows for the measurement of K_{eq} for Equation 5.19.[329]

Equilibrium	$\Delta G°$ (kcal/mol)	
3−H_2 + base ⇌ [baseH][**3**−H]	$-1.364 \cdot \log(K_{eq})$	(Eqn 5.19)
$[baseH]^+$ ⇌ base + $[H]^+$	$+1.364 \cdot pK_a$	(Eqn 5.20)
3−H_2 ⇌ [**3**−H] + $[H]^+$	$+1.364 \cdot pK_a$	(Eqn 5.21)

The addition of either a 1:2 or 3:4 ratio of Vkd to NiInL (**3**, 10 mM) under 1 atm H_2 in THF resulted in essentially complete conversion of **3**−H_2 and Vkd to [VkdH][**3**−H] over a period of ~2 days, as judged by ^{31}P NMR spectroscopy. Assuming that a 1:19 ratio of **3**−H_2 to $[\mathbf{3}-H]^-$ and of base to $[baseH]^+$ would be detectable by ^{31}P NMR spectroscopy, the observation of essentially complete conversion means that $K_{eq} > 360$

(Equation 5.19). Based on the known pK_a of Vkd and this lower bound for K_{eq}, an upper bound that the pK_a of **3**−H_2 < 25.5 in THF was determined. Assuming Vkd base also would fully deprotonate **3**−H_2 in CH_3CN, which seems likely given that the products in Equation 5.19 are charged species and CH_3CN is a more polar solvent than THF, this result indicates that the pK_a of **3**−H_2 < 31.1 in CH_3CN.

Since Vkd completely deprotonated **3**−H_2, the weaker phosphazene base *tert*-butylimino-tri(pyrrolidino)phosphorene ($P_1{}^tBu$, pK_a^{MeCN} = 28.4)[345] was tested next. Over the course of 3 weeks, no appreciable deprotonation of **3**−H_2 to give [$P_1{}^tBuH$][**3**−H] was observed under 1 atm H_2 for 1:1, 3:2, and 5:2 ratios of $P_1{}^tBu$ (10 mM) to **3** in THF. Under the assumption that a 1:19 ratio of [**3**−H]$^-$ to **3**−H_2 and of [baseH]$^+$ to base would be detectable by ^{31}P NMR spectroscopy, this experiment establishes that K_{eq} < 2.8 x 10^{-3} for Equation 5.19. Using the relationships defined in Equations 5.19-5.21, it follows that pK_a^{THF} for **3**−H_2 > 25.3. This means that pK_a^{MeCN} > 30.9 for **3**−H_2, assuming that the aforementioned bound for K_{eq} holds in CH_3CN, and that ΔpK_a for Vkd and $P_1{}^tBu$ is similar in THF and CH_3CN.[351] Since the pK_a of **3**−H_2 is >30.9 and <31.1 in CH_3CN based on these two bracketing H_2 heterolysis experiments, ~31.0 seems to be a good estimate for the pK_a of **3**−H_2, or ~25.4 in THF. A standard deviation of 0.5 pK_a units seems reasonable for this estimate from bracketing studies, and so the pK_a of **3**−H_2 was concluded to be 31.0(5) in CH_3CN, or 25.4(5) in THF.

H_2 heterolysis studies with exogenous base were also carried out for complex **1** by Matt Vollmer. Because H_2 binds weakly to **1**, the H_2 binding equilibrium must also be taken into account in determining the pK_a, as shown in Equations 5.22-5.25.[329-330]

Equilibrium	$\Delta G°$ (kcal/mol)	
1 + H_2 + base ⇌ [baseH][**1**−H]	$-1.364 \cdot \log(K_{eq})$	(Eqn 5.22)
1−H_2 ⇌ **1** + H_2	$+1.364 \cdot \log(K_{H_2})$	(Eqn 5.23)
$[baseH]^+$ ⇌ base + $[H]^+$	$+1.364 \cdot pK_a$	(Eqn 5.24)
1−H_2 ⇌ [**1**−H] + $[H]^+$	$+1.364 \cdot pK_a$	(Eqn 5.25)

No formation of $[\mathbf{1}-H]^-$ was observed upon the addition of 40 equiv Vkd base to **1** in THF under ~3.8 atm H_2, indicating that the pK_a of **1**−H_2 is higher than those of **2**−H_2 and **3**−H_2. Under the assumption that a 1:19 ratio of $[\mathbf{1}-H]^-$ to **1** and of $[VkdH]^+$ to Vkd would be observable by ^{31}P NMR spectroscopy, it can be concluded that $K_{eq} < 7.3 \times 10^{-4}$ atm^{-1}, which means that $\Delta G°$ for Equation 5.22 is > 4.3 kcal/mol. The $\Delta G°$ value for H_2 binding to **1** in toluene was found to be +1.6(2) kcal/mol, which can be adjusted to +1.4(2) kcal/mol based on the prediction of slightly more favorable H_2 binding in THF and CH_3CN relative to toluene from DFT calculations (Table A.2.5). Because the H_2 binding equation is written in reverse, $\Delta G°$ takes the value of −1.4(2) kcal/mol. With $\Delta G°$ for Equations 5.22 and 5.23 evaluated, and the pK_a of Vkd known in both THF (~28)[357] and CH_3CN (33.6),[342] the pK_a of **1**−H_2 can be calculated to be > 30.1 in THF, or > 35.7 in CH_3CN.

The propensity of stronger bases to deprotonate **1**−H_2 was also studied (by Matt Vollmer). Extremely strong bases like potassium *tert*-butoxide (KO^{t}Bu) and the phosphazene base P$_4$^{t}Bu (pK_a^{MeCN} = 42.7)[375] gave complete conversion to [baseH][**1**−H] in the presence of **1** under an H_2 atmosphere. Slightly weaker bases including potassium bis(trimethylsilyl)amide (pK_a^{THF} ~ 29.5) and nBu-N=P$_1$(tmg)$_3$ (pK_a^{MeCN} ~ 38.7, tmg =

tetramethylguanidine)[375] also resulted in full conversion to [baseH][**1**−H]. Based on the reaction with ^{n}Bu-N=P$_1$(tmg)$_3$, the pK_a of **1**−H$_2$ can be calculated to be < 35.1 in CH$_3$CN. This result is slightly contradictory to the range of > 35.7 estimated from the lack of reaction with Vkd, so at this point the pK_a of **1**−H$_2$ has been approximated to be 35.4(5) in CH$_3$CN, or ~29.5 in THF.

5.2.10.2 Comparison of Group 13 σ-Acceptor Metalloligands to the Effect of Other Common Ligands on the Acidity of M(η^2-H$_2$) Complexes

Based on the results of H$_2$ heterolysis studies with exogenous base, it is evident that variation of the supporting group 13 metal has a significant influence on the pK_a of (η^2-H$_2$)NiML complexes, with pK_a^{MeCN} values ranging from 31.0(5) to 35.6(5) for **1**−H$_2$ and **3**−H$_2$, respectively, with **2**−H$_2$ found to have an intermediate pK_a^{MeCN} value of 33.1(2). Recently, Morris and co-workers developed an empirical method for estimating the pK_a of M(η^2-H$_2$) and M−H complexes, which utilizes ligand acidity constants extrapolated from literature data to quantitatively describe the influence of different commonly employed ligands on the pK_a values. The general expression reported by Morris is shown in Equation 5.26, where A$_L$ are the ligand acidity constants for all ligands bound to the metal, C$_{charge}$ is equal to the charge (x) of the conjugate base [ML$_n$]^x, C$_{nd}$ is zero for first-row metals, and C$_{d6}$ is a correction factor that is only applied to account for the additional stability of conjugate acids with a d^6 octahedral configuration.[236]

$$p K_a^{THF} = \sum A_L + C_{charge} + C_{nd} + C_{d6} \qquad \text{(Eqn 5.26)}$$

Since group 13 σ-acceptor ligands are not common ligands for a transition metal, ligand acidity constants have not been tabulated for these ligands. Thus, it seemed to be a worthwhile exercise to determine the ligand acidity constants for the Al, Ga, and In metalloligands to gauge how their impact on the acidity of (η^2-H_2)NiML complexes compares to that of other common ligands on the pK_a of M(η^2-H_2) and M−H complexes. To accomplish this, the pK_a of the hypothetical (η^2-H_2)NiLH_3 complex was considered. The A_L constant for each alkyl phosphine ligand is 4.9, C_{nd} and C_{d6} are zero, and C_{charge} = 30 because the $[HNiML]^-$ conjugate base is anionic, which gives an estimated pK_a^{THF} of 44.7 for (η^2-H_2)NiLH_3.[236] By comparing the measured pK_a^{THF} values of (η^2-H_2)NiML complexes with the estimated pK_a^{THF} for (η^2-H_2)NiLH_3, ligand acidity constants (A_L) for the group 13 metalloligands were estimated. Based on pK_a^{THF} values of ~29.5(5), 27.5(2), and 25.4(5) determined for **1**−H_2, **2**−H_2, and **3**−H_2, respectively, A_L values for Al(III), Ga(III), and In(III) metalloligands were estimated to be −15.2, −17.2, and −19.3, respectively. As shown in Figure 5.30, the magnitude of the A_L values for the group 13 σ-acceptor ligands are relatively large in comparison to those for other common ligands.

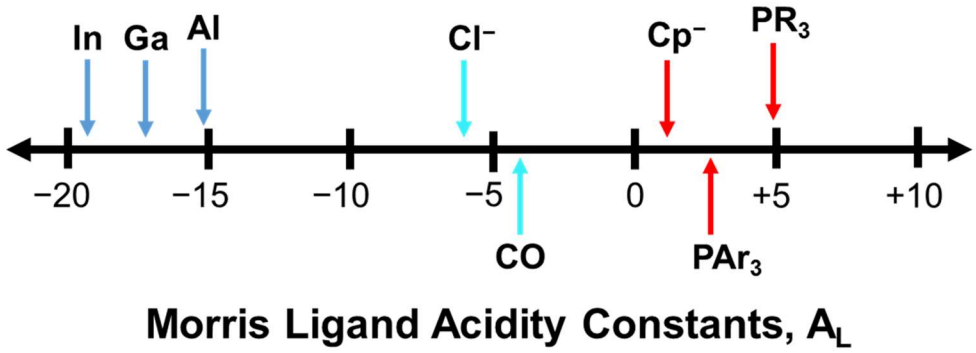

Figure 5.30. Scale showing how select ligand acidity constants (A_L) determined by Morris compare to those estimated for the Al, Ga, and In metalloligands based on the pK_a^{THF} values of the (η^2-H_2)NiML complexes and the estimated pK_a^{THF} of (η^2-H_2)NiLH_3.

Strong σ-donor ligands that increase the electron-richness of the metal center, like alkyl phosphines (PR_3, $A_L = 4.9$), increase the pK_a of M(η^2-H_2) and M−H complexes, whereas ligands which can aide in stabilizing an increase in negative charge have the effect of decreasing the pK_a, such as a good π-acceptor ligand like CO ($A_L = -4.1$).[236] Remarkably, the group 13 σ-acceptor ligands ($A_L = -15$ to -20) have the effect of lowering the pK_a of (η^2-H_2)NiML complexes to a much greater extent than CO (Figure 5.30). Caution should be applied when considering the AL values estimated for the group 13 σ-acceptor ligands from the pK_a of (η^2-H_2)NiML complexes, as the estimated A_L values are based on only one set of three complexes in comparison to the estimated pK_a of (η^2-H_2)NiML, whereas typically 7 to 90 different complexes were considered by Morris in the tabulation of the other A_L constants. The large magnitude of A_L for group 13 M(III) ions relative to other A_L constants may also be partially attributable to the fact that the group 13 metalloligands are positioned *trans* to the acidic site in the (η^2-H_2)NiML complexes. The ligand in the *trans* position has been well-documented to have an outsized influence on metal-bound H_2 ligands,[45] so perhaps the smaller magnitude for A_L for other ligand types could be partially due to the fact that the ligand in question was not positioned *trans* to the acidic site in all the literature complexes considered by Morris for determining A_L. Nevertheless, it is clear that group 13, Z-type σ-acceptor ligands exert a large influence on the pK_a of the (η^2-H_2)NiML complexes in comparison to the effects that other common ligands have on the pK_a of other M(η^2-H_2) and M−H complexes reported in the literature.[236]

5.2.11 Effect of Varying the Supporting Metal on the Thermodynamic Hydricity of [HNiML]$^-$ (M=Al, In) Complexes

The effect of the supporting metal on the thermodynamic favorability of hydride donation from [HNiML]$^-$ was studied next by quantifying the hydricity ($\Delta G°_{H-}$) of [**1**−H]$^-$ and [**3**−H]$^-$ in comparison to the previously discussed value of 31.3(5) for [**2**−H]$^-$. Because a measurable H_2 heterolysis equilibrium (Equations 5.19 and 5.22) was not achieved for either **1** or **3**, isodesmic hydride transfer reactions of **1** and **3** with M−H complexes for which $\Delta G°_{H-}$ is known were performed to determine $\Delta G°_{H-}$ of [**1**−H]$^-$ and [**3**−H]$^-$. HRh(dmpe)$_2$ ($\Delta G°_{H-}$ = 26.4 kcal/mol)[351] and HCo(dmpe)$_2$ ($\Delta G°_{H-}$ = 36 kcal/mol)[323, 352] were chosen, and synthesized according to literature procedures, because they were expected to have similar $\Delta G°_{H-}$ values to [**1**−H]$^-$ and [**3**−H]$^-$, respectively. Equations 5.27-5.29 show that if the equilibrium constant for hydride transfer between the two complexes can be measured, then the $\Delta G°_{H-}$ of [HNiML]$^-$ can be determined since $\Delta G°_{H-}$ is known for the HM(dmpe)$_2$ complexes.[329]

Equilibrium	$\Delta G°$ (kcal/mol)	
NiML + H:$^-$ ⇌ [HNiML]$^-$	$-\Delta G°_{H-}$[HNiML$^-$]	(Eqn 5.27)
HM(dmpe)$_2$ ⇌ [M(dmpe)$_2$]$^+$ + H:$^-$	$+\Delta G°_{H-}$[HM(dmpe)$_2$]	(Eqn 5.28)
HM(dmpe)$_2$ + NiML ⇌ [M(dmpe)$_2$][HNiML]	$-1.364 \cdot \log(K_{eq})$	(Eqn 5.29)

An equimolar mixture of HRh(dmpe)$_2$ and NiAlL (**1**) in THF (~10 mM) was found to reach equilibrium after approximately one week, and was monitored over the course of one month to be sure that equilibrium had been achieved. K_{eq} was found to be 0.2(1) over replicate trials, which gives a $\Delta G°_{H-}$ value of 25.4(3) kcal/mol for [HNiAlL]$^-$

([**1**−H]$^-$). The equilibrium was also examined in the reverse direction by combining [P$_4$^{t}BuH][**1**−H] with [Rh(dmpe)$_2$][OTf] in a 1:1 ratio in THF to generate HRh(dmpe)$_2$, **1**, and 1 equiv [P$_4$^{t}BuH][OTf], which also reached equilibrium similarly to validate the results obtained in the opposite direction. To assess the hydricity of [**3**−H]$^-$, an equimolar amount of **3**−N$_2$ and HCo(dmpe)$_2$ were mixed in THF. After 2.5 h, the formation of a small amount of [Co(dmpe)$_2$]$^+$ and [**3**−H]$^-$ was observed, along with a few unidentified side products. While this result did not allow for rigorous quantification of $\Delta G°_{H-}$ of [**3**−H]$^-$, the fact that a small amount of detectable hydride transfer occurred suggests that $\Delta\Delta G°_{H-}$ between [**3**−H]$^-$ and HCo(dmpe)$_2$ is < 3.4 kcal/mol. Coupled with the fact that N$_2$ must dissociate from **3**−N$_2$ (ΔG° = +1.2(4) kcal/mol) in order for hydride transfer to occur, the observation of a small amount of hydride transfer allows for the bracketing of the $\Delta G°_{H-}$ value of [**3**−H]$^-$ between 34 and 40 kcal/mol.

One complication to determining $\Delta G°_{H-}$ values in this way is that $\Delta G°_{H-}$ is known in CH$_3$CN for HM(dmpe)$_2$, but the hydride transfer equilibria were measured in THF due to the poor solubility of NiML and [HNiML]$^-$ in CH$_3$CN and the competitive binding of CH$_3$CN to NiML. In doing so, the assumption is made that the difference in hydricity values ($\Delta\Delta G°_{H-}$) between [HNiML]$^-$ and HM(dmpe)$_2$ is approximately the same in both THF and CH$_3$CN.[351] However, it should be noted that the equilibrium in Equation 5.29 results in the formation of two charged ions from the initial reaction of two neutral complexes. Thus, the greater polarity of CH$_3$CN (ϵ = 37.5) relative to THF (ϵ = 7.58) would be expected to stabilize the charged species in the equilibrium to a greater extent, thereby potentially perturbing the equilibrium such that K_{eq} would likely be larger in CH$_3$CN than in THF. It is not clear how much K_{eq} would change between THF and

CH_3CN, and so it is also unclear whether the $\Delta G°_{H-}$ values determined are precise. While the fact that an equilibrium could be achieved in the reverse direction was an encouraging sign, the reverse equilibrium still results in a net difference in the number of ionic species between the reactants and products. This is not an issue that is typically dealt with in measuring hydride transfer reactions, as usually the two M−H species involved have the same charge, whereas $HM(dmpe)_2$ and $[HNiML]^-$ do not.[329, 351-352]

In order to validate the $\Delta G°_{H-}$ values and ranges obtained via hydride transfer studies, it was recognized that $\Delta G°_{H-}$ values could also be determined based on the known pK_a values of (η^2-H_2)NiML, the known $\Delta G°$ values for H_2 binding to NiML, and the known H_2 heterolysis constant in CH_3CN, as shown in Equations 5.30-5.33.[329]

Equilibrium	$\Delta G°$ (kcal/mol)	
$[H]^+ + [HNiML]^- \rightleftharpoons (\eta^2\text{-}H_2)NiML$	$-1.364 \cdot pK_a[(H_2)NiML]$	(Eqn 5.30)
$H_2 \rightleftharpoons [H]^+ + [H:]^-$	+76.0 kcal/mol	(Eqn 5.31)
$(\eta^2\text{-}H_2)NiML \rightleftharpoons H_2 + NiML$	$-\Delta G°_{H_2}$	(Eqn 5.32)
$[HNiML]^- \rightleftharpoons NiML + [H]^-$	$\Delta G°_{H-}[HNiML^-]$	(Eqn 5.33)

Because the H_2 heterolysis constant is known in CH_3CN but has not been defined for THF (Equation 5.31), estimating $\Delta G°_{H-}$ for $[HNiML]^-$ on the CH_3CN scale was necessary, and would also allow for more facile comparison with the $\Delta G°_{H-}$ values of other M−H in the literature.[329] The only caveat in doing that is that, while the pK_a values for (η^2-H_2)NiML in CH_3CN have been estimated using the assumption that the relative pK_a differences between exogenous bases and (η^2-H_2)NiML complexes are similar in THF and CH_3CN, the $\Delta G°_{H_2}$ values for H_2 binding have been measured in toluene.

Fortunately, $\Delta G°_{H_2}$ has been measured in both toluene and THF for complex **2**, and DFT calculations have been performed to predict the differences in the thermodynamic favorability for H_2 binding to NiML complexes in toluene, THF, and CH_3CN solvents (Table A.2.5).

For H_2 binding to **3**, the binding energy in toluene, −3.0(7) kcal/mol, was adjusted to account for the prediction of a slightly more favorable binding equilibrium in CH_3CN. H_2 binding to **3** was calculated by DFT (M06-L/bs1) to be more favorable by ~0.4 kcal/mol in CH_3CN relative to binding in toluene, and the binding energy was predicted to be identical in THF and CH_3CN. This is consistent with the experimental finding that the binding of H_2 to **2** was more favorable by ~0.5 kcal/mol in THF relative to toluene. Therefore, $\Delta G°_{H_2}$ in CH_3CN for **3** was taken to be −3.4(7) kcal/mol. Likewise, a slight increase in the favorability of H_2 binding to **1** was also predicted by DFT, and so $\Delta G°_{H_2}$ was estimated to be +1.4(2) kcal/mol in CH_3CN compared with the value of +1.6(2) kcal/mol obtained in toluene. A slightly larger difference in $\Delta G°_{H_2}$ for H_2 binding to **2** of ~1.3 kcal/mol between toluene and CH_3CN was predicted by DFT, which would give $\Delta G°_{H_2}$ = −0.7(2) kcal/mol in CH_3CN. However, DFT predicts that H_2 binding to **2** in THF is only 0.1 kcal/mol less favorable than in CH_3CN, and so based on the experimentally measured $\Delta G°_{H_2}$ value of 0.1(1) kcal/mol in THF, $\Delta G°_{H_2}$ = 0 kcal/mol might be a better estimate in CH_3CN. The average of the two estimates, $\Delta G°_{H_2}$ = −0.4(4) kcal/mol, was taken to be the binding energy of H_2 to **2** in CH_3CN.

Based on the pK_a[**3**−H_2] = 31.0(5) and $\Delta G°_{H_2}$ = −3.4(7) kcal/mol, $\Delta G°_{H^-}$ was determined to be 37(1) kcal/mol for [**3**−H]$^-$. This value fits within the range of 34-40

kcal/mol estimated from the hydride transfer equilibrium with $HCo(dmpe)_2$. Likewise, $\Delta G°_{H-}$ was determined to be 26.3(7) kcal/mol for [**1**−H]$^-$ based on pK_a[**1**−H_2] = 35.4(5) and $\Delta G°_{H_2}$ = +1.4(2) kcal/mol. This value matches well, within the experimental error ranges, with the value of 25.4(3) kcal/mol determined from hydride transfer between **1** and $HRh(dmpe)_2$, validating the both values as reasonable estimates. Averaging the two values, which gives $\Delta G°_{H-}$ = 25.9(4) kcal/mol, was taken to be the best estimate for $\Delta G°_{H-}$ of [**1**−H]$^-$. Using Equations 5.30-5.33 also gives an identical value of $\Delta G°_{H-}$ = 31.3(5) kcal/mol for [**2**−H]$^-$, as the H_2 binding equilibrium and pK_a[**2**−H_2] is embedded in the measurement of the base heterolysis equilibrium of **2** with H_2 and Vkd base (Equation 5.1).[128]

A summary of the experimentally determined $\Delta G°_{H-}$ values for [HNiML]$^-$ (M=Al, Ga, In) complexes is displayed in Figure 5.31, which shows that the hydricity ($\Delta G°_{H-}$) of [HNiML]$^-$ complexes can be tuned by ~11 kcal/mol by varying the supporting metal down group 13 (Table 5.4). This is a large amount for the variation of a single atom, and reflects the large influence of the group 13 trans σ-acceptor ligand. However, it should be noted that libraries of different diphosphine ligands have been shown to influence $\Delta G°_{H-}$ for $[HNi(diphosphine)_2]^+$ complexes by ~18 kcal/mol, albeit in a much less reactive range from 50 to 68 kcal/mol.[252, 328-329] Notably, $\Delta G°_{H-}$ for [**1**−H]$^-$ of 25.9(4) kcal/mol would be the lowest value reported for any soluble transition metal hydride in CH_3CN,[329] narrowly surpassing $HRh(dmpe)_2$ (26.4 kcal/mol),[351] as well as the previous most hydridic first-row metal hydrides, $HCo(P_4N_2)$ (31.8 kcal/mol)[353] and [**2**−H]$^-$ (31.3 kcal/mol).[128] Remarkably, the hydricity of [**1**−H]$^-$ is on par with that of strong borohydride reagents like $[BEt_3H]^-$ ($\Delta G°_{H-}$ = 26 kcal/mol),[351] which explains why

synthesis of [**1**−H]$^-$ in adequate yields was not feasible via hydride transfer from $KBEt_3H$ (*vide supra*).

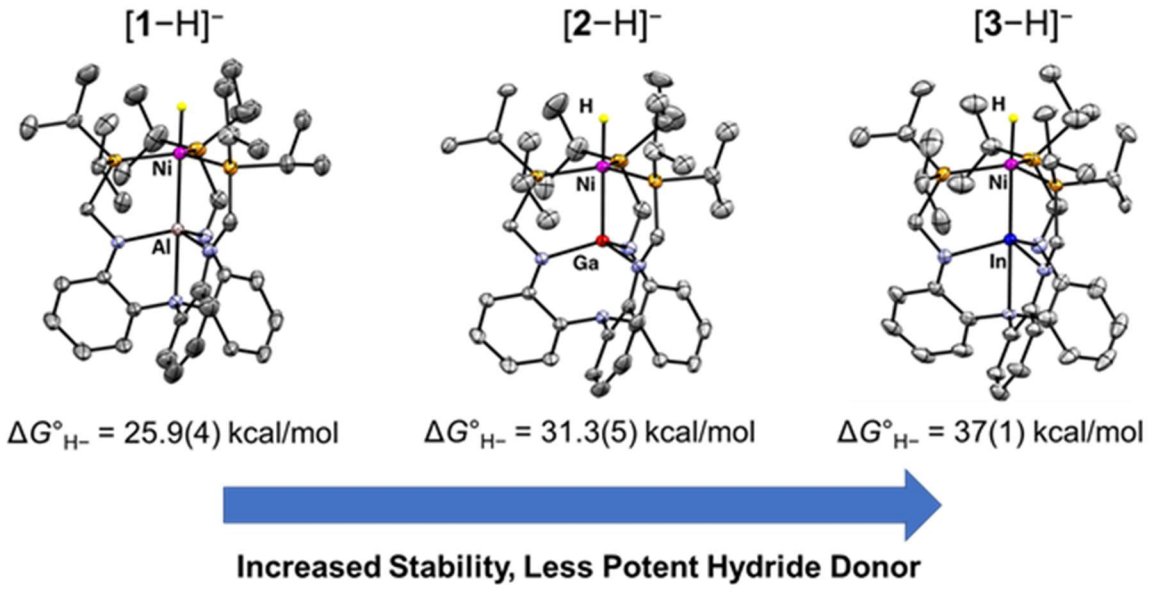

Figure 5.31. Comparison of the effect of the supporting metal on $\Delta G°_{H-}$ values for [HNiML]$^-$ complexes on the CH_3CN scale.

In order to further validate the relative hydride donor strengths of the [HNiML]$^-$ complexes, intra-series hydride transfer experiments were also performed, as shown in Equations 5.34-5.36.

Equilibrium	$\Delta G°$ (kcal/mol)	
NiML + H:$^-$ ⇌ [HNiML]$^-$	$-\Delta G°_{H-}$[HNiML$^-$]	(Eqn 5.34)
[HNiM'L]$^-$ ⇌ NiML + H:$^-$	$+\Delta G°_{H-}$[HNiM'L$^-$]	(Eqn 5.35)
[PPN][HNiM'L] + NiML ⇌ NiM'L + [PPN][HNiML]	$-1.364 \cdot \log(K_{eq})$	(Eqn 5.36)

All six possible combinations of [PPN][HNiM'L] and NiML were combined in a 1:1 ratio in THF (~9.6 mM in 0.80 mL) in J. Young NMR tubes and allowed to mix using a turntable (at ~16 rpm), with periodic ^{31}P NMR spectra acquired to monitor the concentrations of all species. Because [**1**−H]$^-$ is the most reactive hydride donor, it would

be expected that hydride transfer from [PPN][**1**−H] to both **2** and **3** would occur to give [PPN][**2**−H] and [PPN][**3**−H], respectively, along with **1** in both cases. Likewise, since [**2**−H]$^-$ is a more reactive hydride donor than [**3**−H]$^-$, hydride transfer from [PPN][**2**−H] to **3** to generate **2** and [PPN][**3**−H] would be expected. On the other hand, no hydride transfer would be expected from [PPN][**3**−H] to either **1** or **2**, or from [PPN][**2**−H] to **1**. Based on the relatively large $\Delta\Delta G°_{H-}$ values of 5.4, 5.7, and 11.1 kcal/mol for the different pairings of [HNiML]$^-$ complexes, it can be calculated using Equations 5.34-5.36 that hydride transfer should proceed to >99% completion in the three cases where it is thermodynamically favorable, and to <1% completion in the three cases where it is unfavorable. Figure 5.32 shows ^{31}P NMR spectra over time and the corresponding kinetic plot for hydride transfer from [PPN][**1**−H] to **3**, which was observed to react to completion to form [PPN][**3**−H] and **1**, as expected.

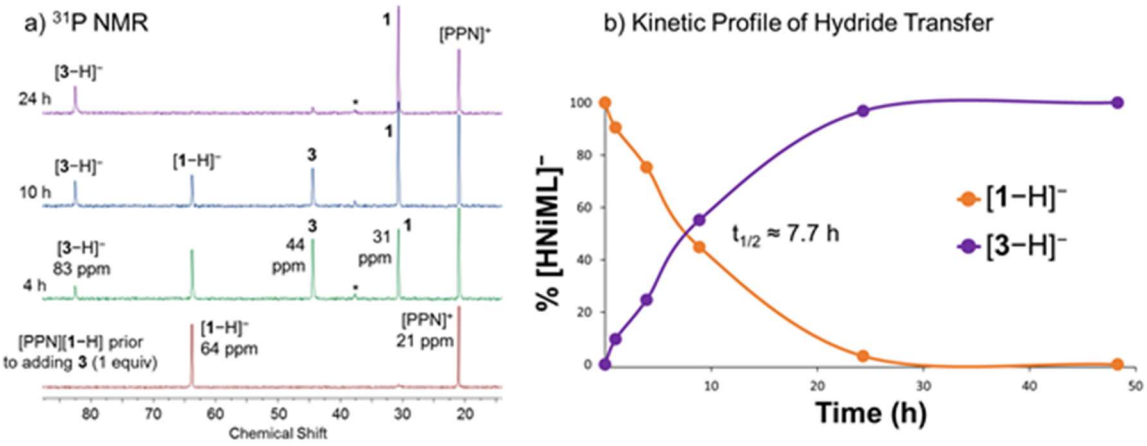

Figure 5.32. (a) Stacked ^{31}P NMR spectra (161.9 MHz) of hydride transfer from [PPN][**1**−H] to **3** in THF. (b) Kinetic profile of the reaction based on quantitative integration of ^{31}P resonances.

As expected, complete hydride transfer was also observed within 24 h from [PPN][**1**−H] to **2** and from [PPN][**2**−H] to **3** (Figures A.4.30-A.4.33). No appreciable hydride transfer was observed over the course of 2 weeks from [PPN][**3**−H] to either **1** or

2, or from [PPN][**2**−H] to **1**. These results are all consistent with the relative hydricity values determined for the trio of $[HNiML]^-$ complexes (Figure 5.31).

5.2.12 Comparison of pK_a and Hydricity of $[HNiML]^-$ to $[HNi(diphosphine)_2]^+$ Complexes

A summary of the experimentally determined pK_a and $\Delta G°_{H-}$ values for $[HNiML]^-$ (M=Al, Ga, In) complexes is displayed in Table 5.4.

Table 5.4. Comparison of pK_a and $\Delta G°_{H-}$ values for $[HNiML]^-$ complexes on CH_3CN scale.[a]

Supporting Metal	pK_a $[HNiML]^-$	$\Delta G°_{H-}$ $[HNiML]^-$
Al	35.4(5)	25.9(4)
Ga	33.1(2)	31.3(5)
In	31.0(5)	37(1)

[a]Note that $\Delta G°_{H-}$ values are in kcal/mol.

DuBois and co-workers reported a series of $[HNi(diphosphine)_2]^+$ complexes with various diphosphine ligands, and the pK_a values for the complexes were found to correlate well with the Ni(I/0) redox potential of the corresponding $Ni(diphosphine)_2$ complexes (Figure 5.33).[330, 350] Plotting the pK_a values for deprotonating the (η^2-H_2)NiML complexes versus the Ni(I/0) redox potentials of the NiML complexes also gives a linear correlation (Figure 5.33). The pK_a values are very different between the two series of complexes, which can be at least partially attributed to the fact that the (η^2-H_2)NiML and $[HNi(diphosphine)_2]^+$ complexes are in different charge states. Based on Morris's expression for estimating pK_a of M(η^2-H_2) and M−H complexes (Equation 5.26), one would expect a difference of approximately 15 pK_a units for a difference in charge of one unit,[236] with the deprotonation of (η^2-H_2)NiML to generate the anionic

hydride species expected to have a greater pK_a than the deprotonation of $[HNi(diphosphine)_2]^+$ to generate a neutral complex. Empirically, it seems that subtracting 25 pK_a units from the pK_a values of the (η^2-H_2)NiML complexes, rather than the 15 units estimated by Morris for the typical case, places our system approximately onto the same trendline as the $[HNi(diphosphine)_2]^+$ complexes. While this discrepancy is not fully understood, one other factor to consider is that in our system an intact H_2 ligand is being deprotonated, whereas a discrete Ni–H is being deprotonated in the $[HNi(diphosphine)_2]^+$ complexes.

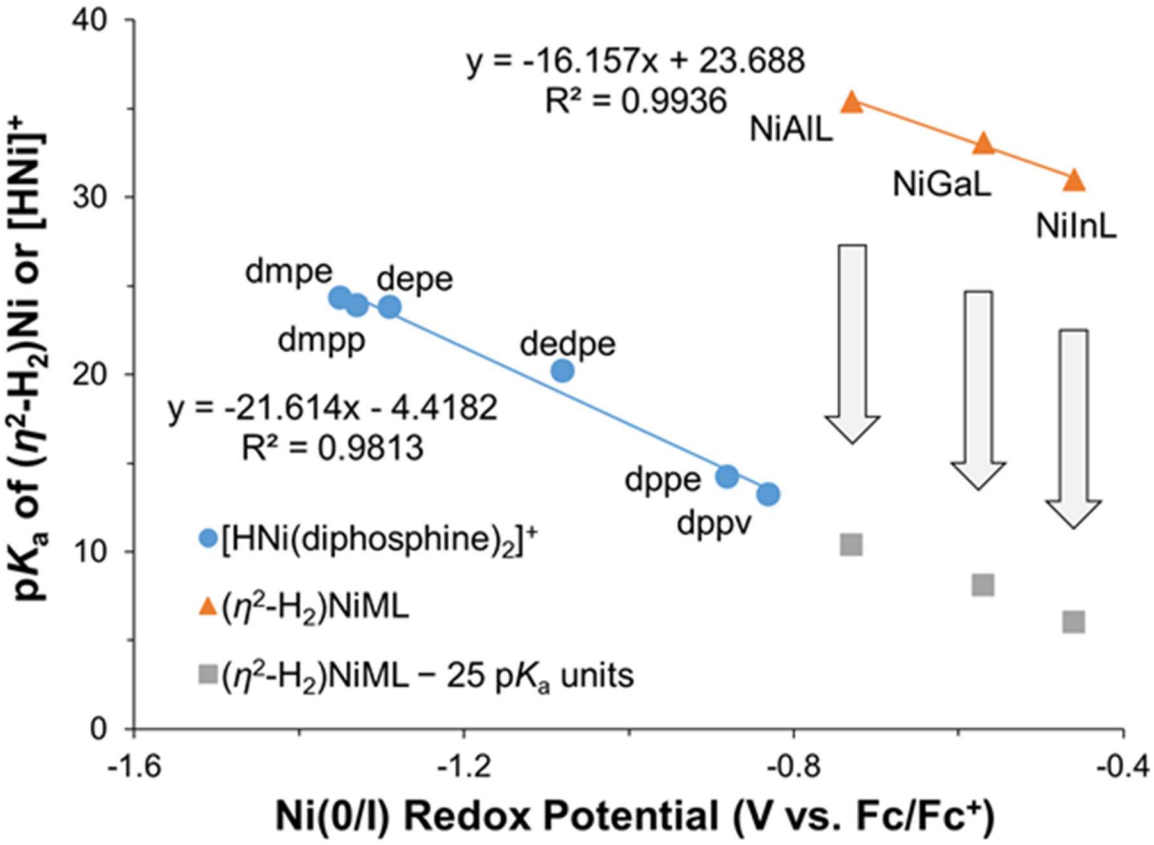

Figure 5.33. Plot of pK_a^{MeCN} of the (η^2-H_2)NiML and [HNi(diphosphine)$_2$]+ complexes vs. the Ni(I/0) redox potentials (vs. $FeCp_2^{0/+}$) of the parent NiML and Ni(diphosphine)$_2$ complexes. The data points are labeled, and the various diphosphine ligands are shown in Figure A.4.34.

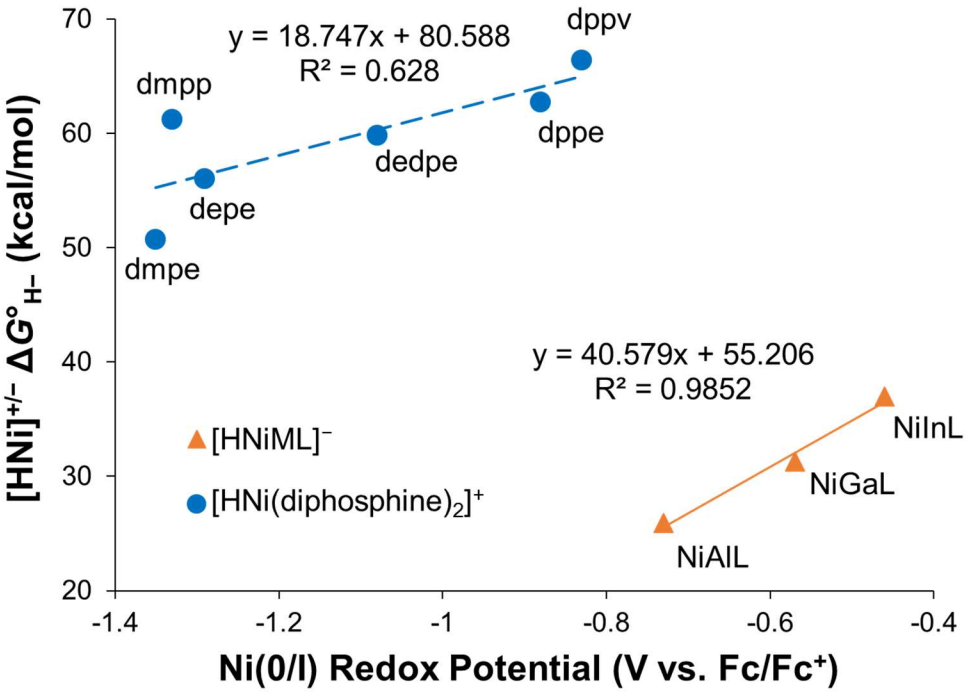

Figure 5.34. Plot of $\Delta G°_{H-}$ values for $[HNiML]^-$ and $[HNi(diphosphine)_2]^+$ complexes vs. the Ni(I/0) redox potentials (vs. $FeCp_2^{0/+}$) of the parent NiML and Ni(diphosphine)$_2$ complexes. The data points are labeled, and the various diphosphine ligands are shown in Figure A.4.34.

Plotting the $\Delta G°_{H-}$ values for the $[HNiML]^-$ complexes against the Ni(I/0) redox potentials of the NiML complexes also results in a near linear correlation (R^2 = 0.9852, Figure 5.34). The relative order of hydricity ($\Delta G°_{H-}$: Al < Ga < In) is in line with what would be expected based on the electronic influence of the supporting metal on Ni, as a more electron-poor Ni center should better stabilize a hydride ligand and result in less reactive hydride donors (ie. greater $\Delta G°_{H-}$ values). In contrast, a poor correlation is observed between $\Delta G°_{H-}$ values and Ni(I/0) redox potentials for the series of $[HNi(diphosphine)_2]^+$ complexes (R^2 = 0.628, Figure 5.34).[328, 330, 350] This can be best appreciated by comparing the dmpp, depe, and dmpe analogues in Figure 5.34, which have significantly different $\Delta G°_{H-}$ values (50 to 62 kcal/mol) despite having nearly identical Ni(I/0) redox potentials (within 60 mV). This indicates that the electron-richness

of the Ni center alone does not dictate the hydricity of the $[HNi(diphosphine)_2]^+$ complexes. Indeed, DuBois and co-workers, among others, have proposed that the bite angles of the diphosphine ligands also have a large impact on the hydricity of $[HM(diphosphine)_2]^{0/+}$ complexes.[329-330] Namely, a smaller bite angle diphosphine ligand will lead to a lower $\Delta G°_{H-}$ value by allowing for closer to optimal formation of the square-planar geometry preferred by the d^8, 16-electron complexes that result after hydride transfer, as well as for more facile reorganization upon hydride transfer.

The fact that Ni(I/0) redox potentials correlate nearly linearly with $\Delta G°_{H-}$ values for the $[HNiML]^-$ complexes, but not for the $[HNi(diphosphine)_2]^+$ complexes, shows that the electron-richness of the Ni center dictates hydricity in our system and that steric factors are relatively less important. Perhaps this is unsurprising, as the steric differences are more minimal between the NiML complexes since only the supporting metal atom is varied, compared to the $[HNi(diphosphine)_2]^+$ complexes which have entirely different diphosphine ligands. The $[HNi(diphosphine)_2]^+$ complexes also must reorganize more dramatically after hydride transfer from a distorted tetrahedral geometry to a square-planar one, whereas Ni and M simply reposition closer to their respective P_3- and N_3-planes in NiML after hydride transfer from the $[HNiML]^-$ complexes. In addition to the required geometric reorganization being less pronounced for our system, comparing the structures of the $[HNiML]^-$ complexes to those of the NiML complexes formed after hydride transfer shows that the amount of structural reorganization required is very similar for all three different supporting metals. Specifically, the sum of the Ni to P_3-plane, M to N_3-plane, and Ni–P distances for $[\mathbf{1}–H]^-$, $[\mathbf{2}–H]^-$, and $[\mathbf{3}–H]^-$ are 0.30, 0.29, and 0.21 Å, respectively.[97, 128] The similar amount of reorganization required for hydride

transfer from the three $[HNiML]^-$ complexes likely allows for electronic factors alone to dictate hydricity (*vide supra*).

5.2.13 A Comprehensive Thermodynamic Scheme for Understanding NiML Reactivity

5.2.13.1 Thermodynamic Bond Dissociation Free Energies (BDFEs) of Ni−H bonds in $[HNiML]^-$ Complexes: Relative Favorability of Hydride Transfer vs. Hydrogen Atom Transfer

The measured hydricity values determined for the trio of $[HNiML]^-$ complexes, along with the known reduction potentials for the NiML complexes, allow for the determination of the thermodynamic bond dissociation free energies (BDFEs) for the Ni−H bonds (Equations 5.37-5.40).[329, 376]

Equilibrium	$\Delta G°$ (kcal/mol)	
$NiML + e^- \rightleftharpoons [NiML]^-$	$-23.06 \cdot E°_{1/2}$	(Eqn 5.37)
$[HNiML]^- \rightleftharpoons NiML + H:^-$	$+\Delta G°_{H-}$	(Eqn 5.38)
$H:^- \rightleftharpoons H\bullet + e^-$	−26.0	(Eqn 5.39)
$[HNiML]^- \rightleftharpoons [NiML]^- + H\bullet$	BDFE	(Eqn 5.40)

The free energy for Equation 5.39 is a constant for the loss of an electron from a solvated hydride ion ($H:^-$) to form a solvated hydrogen atom (H•) in CH_3CN. It should be noted that the value of this constant, along with the previously utilized H_2 heterolysis constant (Equation 5.3), are difficult to determine precisely because the free energy of solvation of a hydride ion cannot be readily measured experimentally and is challenging to predict computationally. As such, the true values of constants like these have historically been a source of debate, but the values utilized in this thesis are those that have been generally agreed upon in the literature for CH_3CN.[329] Importantly, as long as

these constants are universally adopted, the absolute error between these constants and their true values will cancel when comparing the thermodynamic properties (hydricity, BDFE, etc.) determined via thermochemical cycles for two different complexes, allowing the relative differences between the two complexes to be known precisely.

Along with the use of the constant in Equation 5.39 which is known in CH_3CN, Equation 5.38 represents the hydricity ($\Delta G°_{H-}$), which was also estimated on the CH_3CN scale. Therefore, the reduction potentials of NiML in CH_3CN ($E°_{1/2}$ in V vs. $FeCp_2^{0/+}$ redox couple, Equation 5.37) should also be used in order to determine the BDFEs in CH_3CN (Equation 5.40). The reduction potential for NiAlL (**1**) in CH_3CN was found to be −2.86 V (vs. $FeCp_2^{0/+}$ redox couple). However, one complication is that the reductions of NiGaL (**2**) and NiInL (**3**) were found to be irreversible in CH_3CN, presumably due to the dissociation of bound CH_3CN upon reduction and/or decomposition of $[NiML]^-$ in CH_3CN (section 2.2.6.4). Fortunately, the reduction events for **2** and **3** were reversible or quasi-reversible in THF, and the redox potentials determined in both CH_3CN and THF are nearly identical for all complexes once referenced to the $FeCp_2^{0/+}$ redox couple.[78, 97, 158] Indeed, the Ni(I/0) redox couples have essentially identical potentials (within 10 mV) between THF and CH_3CN, and the reduction of **1** occurs at similar potential in both solvents as well, with $E°_{1/2}$ = −2.86 V in CH_3CN compared to −2.82 V in THF). Thus, it seems to be a fair assumption that the reduction potentials of **2** and **3** in THF are reasonable estimates for their values in CH_3CN. Based on the difference in the redox potentials for **1** in THF and CH_3CN, the $E°_{1/2}$ values in THF for **2** and **3** were similarly adjusted by 40 mV to give estimated potentials in CH_3CN of −2.52 V and −2.38 V vs. the $FeCp_2^{0/+}$ redox couple, respectively.

Based on these reduction potentials with an assumed 40 mV uncertainty, along with $\Delta G°_{H-}$ values of 25.9(4), 31.3(5), and 37(1) kcal/mol for [**1**-H]$^-$, [**2**-H]$^-$, and [**3**-H]$^-$, respectively, the BDFE in CH_3CN for the Ni−H bonds of [HNiML]$^-$ complexes were found to be 66(1), 63(1), and 66(1) kcal/mol, respectively. Clearly, the opposing effects of the redox potential ($|E°_{1/2}|$: Al > Ga > In) and the hydricity (In > Ga > Al) must both be considered to rationalize the relative order of Ni−H BDFE values for the trio of [HNiML]$^-$ complexes. It is interesting that the order of Ni−H bond strengths does not follow a continuous trend upon varying the supporting metal down group 13: Al ~ In > Ga. That said, the BDFE values are still very similar between M=Ga and the other anionic hydrides, especially when considering the experimental error in each case.

These BDFE values of 63-66 kcal/mol for the [HNiML]$^-$ complexes are slightly stronger than the median values of the reported range for M−H bonds, which are typically between 52 and 70 kcal/mol. The Ni−H BDFE values indicate stronger M−H bonds for the [HNiML]$^-$ complexes compared with those for other first-row metal hydrides in the literature, which are typically in the range of 52 to 62 kcal/mol. While typically first-row metal hydrides serve as reactive hydrogen atom donors, cleavage of the Ni−H bonds of the [HNiML]$^-$ complexes is actually much more favorable via hydride ion transfer ($\Delta G°_{H-}$ = 25 to 37 kcal/mol) than via hydrogen atom transfer (BDFE = $\Delta G°_{H\bullet}$ = 63 to 66 kcal/mol). This is likely attributable to the electron-richness of the Ni centers and the anionic charge state of these complexes. Furthermore, it is intuitive that formation of the neutral, 16-electron NiML complexes (via hydride transfer) would be more favorable than the generation of the highly-reduced 17-electron [NiML]$^-$ radical anions that would be formed after hydrogen atom transfer (HAT). A similar finding was recently reported

by Norton and co-workers for an anionic $[Cp(CO)_3VH]^-$ species, which has the strongest M−H bond to my knowledge for a first-row metal (BDFE > 69 kcal/mol).[377] Hydride transfer from $[Cp(CO)_3VH]^-$ ($\Delta G°_{H-}$ < 50 kcal/mol) was found to be significantly more favorable than HAT by >19 kcal/mol, just as was found to be the case for the $[HNiML]^-$ complexes, where hydride transfer was more favorable than HAT by 29 to 40 kcal/mol (*vide supra*).

5.2.13.2 Thermodynamic Bond Dissociation Free Energies (BDFEs) of the Bound H−H Bonds in (η^2-H_2)HNiML Complexes

In addition to determining the BDFEs for the Ni−H bonds in the $[HNiML]^-$ complexes, the BDFE of the bound H−H bonds in (η^2-H_2)NiML complexes can also be determined via the utilization of a thermochemical cycle (Equations 5.41-5.44).[329, 378]

Equilibrium	$\Delta G°$ (kcal/mol)	
(η^2-H_2)NiML ⇌ $[HNiML]^-$ + $[H]^+$	+1.364·pK_a	(Eqn 5.41)
$[HNiML]^-$ ⇌ HNiML + e^-	+23.06·$E°_{1/2}$	(Eqn 5.42)
$H^+ + e^-$ ⇌ H•	53.6	(Eqn 5.43)
(η^2-H_2)NiML ⇌ HNiML + H•	BDFE	(Eqn 5.44)

The pK_a values for deprotonating the (η^2-H_2)NiML complexes are known in CH_3CN (Equation 5.41), as is the constant for the formation of a solvated hydrogen atom from a proton and an electron (Equation 5.43). However, recall that the one-electron oxidations of the $[HNiML]^-$ complexes were completely irreversible at all scan rates up to 1 V/s for M=Ga and In. Fortunately, $E°_{1/2}$ values for the one-electron oxidations of the $[HNiML]^-$ complexes (Equation 5.42) can be estimated accurately using the method

reported by Baik and co-workers for estimating the standard redox potentials of irreversible redox events.[379] This method requires conducting a study of how the irreversible redox wave is affected by varying the scan rate, which was performed for each of the $[HNiML]^-$ complexes at four different scan rates between 100 mV/s and 1 V/s (Figures 5.28b-c and A.4.29). Equations 5.45-5.48 define the relationships of the relevant variables needed to estimate $E°_{1/2}$ values. Equation 5.45 shows the Marcus relationship between the electron transfer coefficient, α, the applied potential (E_{app}), the standard redox potential ($E°_{1/2}$), the reorganization energy (λ), and Faraday's constant (F).

$$\alpha = 0.5 + \frac{F}{2\lambda}(E_{app} - E°_{1/2}) \quad \text{(Eqn 5.45)}$$

The electron transfer coefficient can be determined experimentally using Equation 5.46, where δE_{pa} is the voltammetric peak width in mV, which is defined in Equation 5.47, where $E_{pa/2}$ is the potential at the half-height of the peak. Additionally, E_{app} is defined as the average of E_{pa} and $E_{pa/2}$ (Equation 5.48).[379]

$$\alpha = \frac{47.4}{\delta E_{pa}} \quad \text{(Eqn 5.46)}$$

$$\delta E_{pa} = \left| E_{pa} - E_{pa/2} \right| \quad \text{(Eqn 5.47)}$$

$$E_{app} = \frac{E_{pa} + E_{pa/2}}{2} \quad \text{(Eqn 5.48)}$$

These variables defined in Equations 5.45-5.48 are illustrated and labeled in Figure 5.35a for the irreversible Ni(0/I) oxidation of [PPN][HNiGaL].

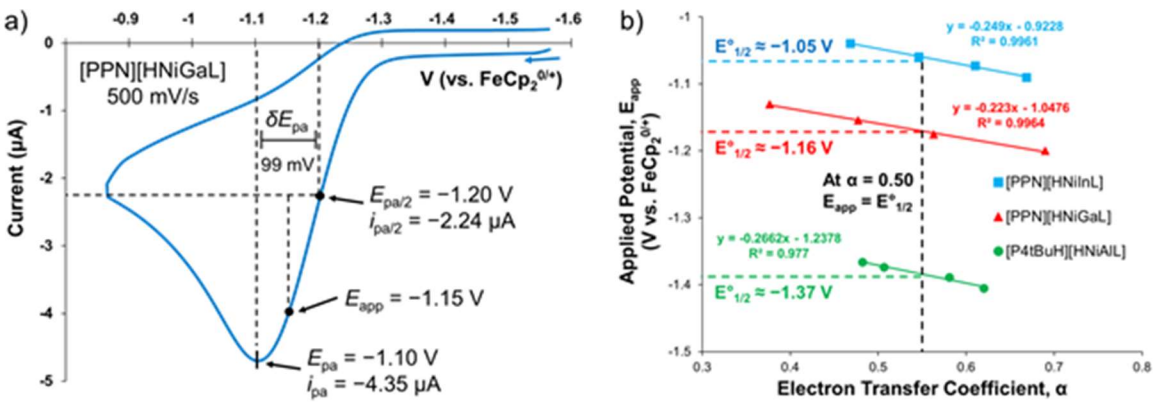

Figure 5.35. (a) Diagram visually illustrating E_{pa}, $E_{pa/2}$, δE_{pa}, and E_{app} for the CV of [PPN][HNiGaL] obtained at 500 mV/s in 0.1 M [TBA][PF_6] in THF. These variables are utilized, along with Equations 5.45-5.48, to estimate the standard redox potentials, $E°_{1/2}$ for the irreversible Ni(0/I) oxidation waves of the $[HNiML]^-$ complexes. (b) Plot of applied potential, E_{app}, vs. the electron transfer coefficient, α, which allows for the determination of $E°_{1/2}$ based on the fact that $E_{app} = E°_{1/2}$ when α = 0.50.

As previously shown in the overlay of the CVs at different scan rates for [PPN][HNiGaL] (Figure 5.27b), E_{pa} shifts to less negative potentials and the voltammetric peak broadens (δE_{pa} increases) at faster scan rates. Shifts in E_{pa} are also reflected in shifts for $E_{pa/2}$ and E_{app}, and so α is linearly dependent on the scan rate.[379] Thus, a plot of α vs. E_{app} allows for the determination of $E°_{1/2}$, since $E_{app} = E°_{1/2}$ when α = 0.5 (Equation 5.45). As seen in Figure 5.35b, the α values are relatively close to 0.5 in most cases, indicating an electron transfer event, the oxidation of $[HNiML]^-$, followed by a subsequent chemical reaction, as opposed to a concerted process which would have a larger reorganization energy and an α value << 0.5. α values > 0.5 indicate a rapid chemical step relative to the initial electron transfer, which is observed to be the case for the slower scan rates (ν = 100 mV/s and 200 mV/s) but not for ν ≥ 500 mV/s (Figure 5.35b).[379] A rapid chemical step relative to electron-transfer is also indicated by slopes of 50-100 mV per decade for E_{pa} vs. log(ν) plots for the $[HNiML]^-$ complexes (Figure

A.4.35). Additionally, linear plots of current (i_{pa}) vs. $(\nu)^{0.5}$ indicate that electron transfer from $[HNiML]^-$ is diffusion- controlled (Figure A.4.36).[354]

As shown in Figure 5.35b, the scan rate studies and Equations 5.45-5.48 allow for the estimation of $E°_{1/2}$ for the Ni(I/0) redox couple of the $[HNiML]^-$ complexes to be −1.37(4) V, −1.16(7) V, and −1.05(6) V (vs. $FeCp_2^{0/+}$ redox couple) for [**1**−H]$^-$, [**2**−H]$^-$, and [**3**−H]$^-$, respectively. The error in the redox potentials was determined based on linear regression of the α vs. E_{app} plots, with the exception of [**1**−H]$^-$, where the error was taken to be the range in $E°_{1/2}$ values obtained for the quasi-reversible wave at various scan rates. As an initial validation of the application of the method of Baik and co-workers to this redox process, the $E°_{1/2}$ value of −1.37 V predicted for [**1**−H]$^-$ from the α vs. E_{app} plot matches closely with the value of −1.38 V that would be obtained from using the E_{pa} and E_{pc} values once the peak becomes quasi-reversible at a scan rate of 750 mV/s (Figure 5.27c).

Utilizing these estimated redox potentials, along with the pK_a^{MeCN} values of 35.4(5), 33.1(2), and 31.0(5) for **1**−H_2, **2**−H_2, and **3**−H_2, respectively, the BDFEs for the bound H−H bond in the (η^2-H_2)NiML complexes were found to be 70(1) (M=Al), 72(2) (M=Ga), and 72(2) kcal/mol (M=In). It should be noted that the redox potentials estimated in THF for the $[HNiML]^-$ complexes were assumed to be within ~40 mV of their true values in CH_3CN for the BDFE determination, which was seen to be a reasonable assumption for the NiML complexes. Clearly, the BDFE values do not vary as a function of the supporting metal, as all three values are within the experimental error of each other. In any case, the H−H bond is substantially weakened by ~32 kcal/mol, relative to the H−H bond strength of 103.6 kcal/mol for free H_2,[329] upon binding to the

NiML complexes. Based on the relative H_2 binding energies determined in chapter 3 for the NiML complexes, it would be expected that the H−H bond is weakened more as the supporting metal is varied down group 13. However, the experimental errors of 1-2 kcal/mol do not allow for much differentiation between the different supporting metals, if there is any such differentiation in their true values. These are the first BDFE values determined for the H−H bond of a first-row metal dihydrogen complex, to the best of my knowledge.

Moreover, the BDFE of the bound H−H bond is more complex than a typical BDFE in that it depends on the strength of both the Ni−H_2 bond and the H−H bond of the bound H_2 unit, along with that of the Ni−H formed upon hydrogen atom loss, whereas a typical BDFE only depends on the strength of the M−H bond and the stability of the resulting metal fragment.[378] The BDFE values of 70-72 kcal/mol for the (η^2-H_2)NiML complexes lie slightly below the range of 76 to 87 kcal/mol reported for cationic and dicationic M(η^2-H_2) adducts of Ru and Os, upon properly adjusting the BDE values for solvation in CH_3CN,[378] indicating a greater degree of weakening of the H_2 bond in the case of the (η^2-H_2)NiML complexes. This was initially surprising, because typically second-row and third-row metals are known to weaken the H−H bond to a greater extent for a given ligand set than do first-row metals. Rest assured that the relative ordering of metal-ligand bond strengths for first-, second-, and third-row metals is not being overturned here;[110, 376, 378] in this case, the second-row and third-row metals that we are comparing to are cationic and dicationic, which likely means there is very minimal M→H_2 π-back-bonding and consequently less weakening of the H−H bond than might be expected for H_2 bound to a second-row or third-row metal.[45] Furthermore, more electron

rich second-row and third-row metals invariably oxidatively add H_2 in more reduced charge states, and so measurement of the greater weakening of the H−H bond in those cases is not possible, since it has been weakened so much that the bond was broken in favor of two M−H bonds.

5.2.13.3 Thermodynamic Bond Dissociation Free Energies (BDFEs) of the Ni−H Bonds in the Putative Neutral HNiML Complexes

Lastly, the BDFEs of the Ni−H bonds in the neutral HNiML complexes, which are proposed to form initially upon electrochemical oxidation of the $[HNiML]^-$ complexes, were quantified in two different ways. The fact that the neutral HNiML complexes rapidly lose H_2 in a bimolecular fashion suggests that the BDFEs of the Ni−H bonds in the HNiML complexes are < 52 kcal/mol, since H_2 has a BDFE of ~103.6 kcal/mol (*vide supra*). The first of the two possible thermochemical cycles for quantifying the BDFE values for the Ni−H bonds in the neutral HNiML complexes is shown in Equations 5.49-5.52, and utilizes the previously determined $E°_{1/2}$ and $\Delta G°_{H-}$ values.[329]

Equilibrium	$\Delta G°$ (kcal/mol)	
$HNiML + e^- \rightleftharpoons [HNiML]^-$	$-23.06 \cdot E°_{1/2}$	(Eqn 5.49)
$[HNiML]^- \rightleftharpoons NiML + [H:]^-$	$+\Delta G°_{H-}$	(Eqn 5.50)
$[H:]^- \rightleftharpoons H\bullet + e^-$	−26.0	(Eqn 5.51)
$HNiML \rightleftharpoons NiML + H\bullet$	BDFE	(Eqn 5.52)

This method gives values of 31(1), 32(2), and 35(2) kcal/mol for M=Al, Ga, and In, respectively. Alternatively, this BDFE can also be determined from the known BDFE

for H_2 in CH_3CN, the previously determined BDFE for the H−H bond in the (η^2-H_2)NiML complexes, and the previously determined binding energy of H_2 to the NiML complexes (Equations 5.53-5.56).[329]

Equilibrium	$\Delta G°$ (kcal/mol)	
$H_2 \rightleftharpoons 2\ H•$	+103.6	(Eqn 5.53)
$HNiML + H• \rightleftharpoons (\eta^2\text{-}H_2)NiML$	−BDFE	(Eqn 5.54)
$(\eta^2\text{-}H_2)NiML \rightleftharpoons NiML + H_2$	$-\Delta G°_{H2}$	(Eqn 5.55)
$HNiML \rightleftharpoons NiML + H•$	BDFE	(Eqn 5.56)

The BDFE values determined from this second thermochemical cycle are 32(1), 31(2), and 35(2) kcal/mol for M=Al, Ga, and In, respectively. The BDFE values determined by way of these two different thermochemical cycles match almost exactly, providing validation for the individual values and demonstrating the self-consistency of the many measurements discussed in this thesis. Averaging the two sets of values gives BDFEs of 32(1), 32(2), and 35(2) kcal/mol for the Ni−H bonds in the neutral HNiML complexes for M=Al, Ga, and In, respectively. These are clearly very weak M−H bonds, and the fact that the BDFE values are << 52 kcal/mol is consistent with the mechanistic proposal that the HNiML complexes undergo biomolecular H_2 loss, giving rise to the irreversible Ni(0/I) oxidation waves observed for the $[HNiML]^-$ complexes (section 5.2.9).

5.2.13.4 Completion of a Comprehensive Thermodynamic Scheme for NiML Complexes

Nearly all the thermodynamic values determined in the course of studying the reactivity of NiML complexes (except the H_2 binding energies) are displayed in the comprehensive scheme shown in Figure 5.36.

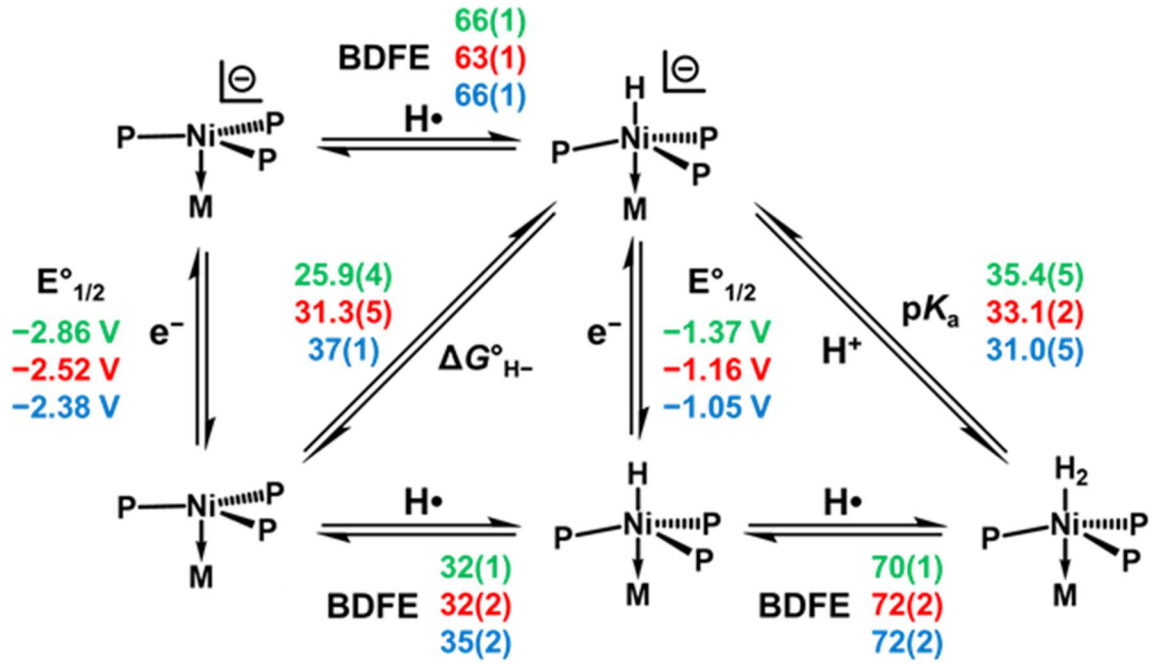

Figure 5.36. A comprehensive thermodynamic scheme for understanding the reactivity of the NiML complexes. Values are color coded and ordered according to the supporting metal identity: Al (green, top), Ga (red, middle), and In (blue, bottom). Note that BDFE and $\Delta G°_{H-}$ values are given in kcal/mol, all redox potentials are given in V relative to the $FeCp_2^{0/+}$ couple, and all pK_a values are given in pK units. All values were determined on the CH_3CN solvent scale.

Please note that BDFE values are typically depicted as the diagonal equilibria in most thermodynamic square schemes, but here they are shown as the horizontal equilibria for spatial purposes within Figure 5.36. Although the BDFE values do not vary much as a function of the supporting metal, the $E°_{1/2}$, $\Delta G°_{H-}$, and pK_a values all vary significantly based on the supporting metal. Thus, the similar BDFE values are the result of compensation effects between the disparate component values of the step-wise processes that combine to represent the net hydrogen atom transfer. Overall, the BDFE values

indicate that the (η^2-H_2)NiML and $[HNiML]^-$ complexes are poor hydrogen atom transfer reagents: the latter is a significantly better hydride donor ($\Delta G°_{H-}$ = 25 to 37 kcal/mol) than hydrogen atom donor ($\Delta G°_{H\bullet}$ = 63 to 66 kcal/mol), whereas the former is a better proton donor ($\Delta G°_{H+}$ = 42 to 49 kcal/mol) than a hydrogen atom donor ($\Delta G°_{H\bullet}$ = 70 to 72 kcal/mol). Additionally, the neutral HNiML complexes form such weak Ni−H bonds (32 to 35 kcal/mol) that they rapidly decompose via bimolecular H_2 loss upon generation via the electrochemical oxidation of the $[HNiML]^-$ complexes. Similar comprehensive thermodynamic schemes have been elucidated by DuBois and co-workers for diphosphine-ligated Co and Ni complexes.[350, 380]

Additionally, Figure 5.36 illustrates that the pK_a values for the protonation of the $[NiML]^-$ complexes can be determined in two different ways (Equations 5.57-5.64).[329]

Method 1	$\Delta G°$ (kcal/mol)	
$HNiML + e^- \rightleftharpoons [HNiML]^-$	$-23.06 \cdot E°_{1/2}$	(Eqn 5.57)
$[HNiML]^- \rightleftharpoons [NiML]^- + H\bullet$	BDFE	(Eqn 5.58)
$H\bullet \rightleftharpoons [H]^+ + e^-$	−53.6	(Eqn 5.59)
$HNiML \rightleftharpoons [NiML]^- + [H]^+$	$+1.364 \cdot pK_a$	(Eqn 5.60)

Method 2	$\Delta G°$ (kcal/mol)	
$NiML + e^- \rightleftharpoons [NiML]^-$	$-23.06 \cdot E°_{1/2}$	(Eqn 5.61)
$HNiML \rightleftharpoons NiML + H\bullet$	BDFE	(Eqn 5.62)
$H\bullet \rightleftharpoons [H]^+ + e^-$	−53.6	(Eqn 5.63)
$HNiML \rightleftharpoons [NiML]^- + [H]^+$	$+1.364 \cdot pK_a$	(Eqn 5.64)

The results from these two different methods agree very well, with the difference between analogous pK_a values from the two methods never exceeding ~0.3 pK_a units. Averaging the values from both methods gives pK_a^{MeCN} values for neutral HNiML complexes of 32.2(7), 26.6(9), and 26.8(9) for M=Al, Ga, and In, respectively. These values indicate that the radical anions are less basic than their corresponding anionic hydride complexes, $[HNiML]^-$, which have pK_a^{MeCN} values of 35.4(5), 33.1(2), and 31.0(5) for M=Al, Ga, and In, respectively. This makes intuitive sense in retrospect, as protonation of $[NiML]^-$ results in the formation of a very weak Ni−H bond in HNiML, whereas protonation of $[HNiML]^-$ results in the formation of the more stable (η^2-H_2)NiML complexes. Furthermore, $[NiAlL]^-$ is the most basic of the three radical anion complexes, as would be expected based on the trends observed in the electron-richness of Ni as the supporting metal is varied down group 13. However, it is not clear based on these pK_a values why the reductions of NiGaL (**2**) and NiInL (**3**) are irreversible in CH_3CN, but the reduction of NiAlL (**1**) is quasi-reversible, since the decomposition of the anions via deprotonation of CH_3CN was thought to be one possible factor contributing to the irreversibility. Clearly, binding of CH_3CN and/or other decomposition reactions of the radical anions in CH_3CN must also contribute to the irreversibility of the reduction waves for **2** and **3** in CH_3CN (section 2.2.6.4).

As far as other complexes and thermodynamic values which could be added to this thermodynamic scheme, the complex omitted from the top right corner would be the anionic H_2 adducts of NiML, which are likely not stable on account of being 19-electron anionic complexes. Nevertheless, in principle, the redox potentials under an H_2 atmosphere can be determined, which would allow for the tabulation of the BDFEs of the

bound H−H ligand in the [(η^2-H_2)NiML]$^-$ complexes. Although tempting to fill in the redox potentials determined under 1 atm H_2, CVs under high pressures of H_2 are needed in order to ensure that the redox potential reflects the true redox potentials of the (η^2-H_2)NiML complexes, as opposed to that for an equilibrium mixture of the bound and unbound species. The redox potentials for NiML under an H_2 atmosphere would be expected to be irreversible, since [(η^2-H_2)NiML]$^-$ complexes would likely lose H_2 rapidly upon generation, but the $E°_{1/2}$ values could be estimated in a similar fashion to those for the irreversible oxidation of the [HNiML]$^-$ complexes.[379]

Future studies could also focus on the cationic charge states of these complexes, which seem to be accessible based on CV studies but have been relatively unexplored to this point. Notably, even though it has not been labeled on the thermodynamic diagram, the Ni(I/0) redox potentials of the NiML complexes have been measured in CH_3CN (section 2.2.6.2). These redox potentials, along with the previously determined BDFE of the Ni−H bonds in the neutral HNiML complexes, allow for the hydricity ($\Delta G°_{H-}$) of these unstable HNiML complexes to be calculated. Hydricity values for the neutral HNiML complexes of 40.9(9), 44(1), and 51(1) kcal/mol were determined for M=Al, Ga, and In, respectively. Comparison of these hydricity values to the previously determined BDFEs for HNiML show that it is more favorable to cleave the Ni−H bond in the neutral HNiML complexes via hydrogen atom transfer than via hydride ion transfer by 9 to 16 kcal/mol (*vide supra*). Additionally, even though the HNiML species are unstable and so these $\Delta G°_{H-}$ values are not useful for informing reactivity, they are interesting to compare with the low $\Delta G°_{H-}$ values of the [HNiML]$^-$ complexes in thinking about the influence of charge and oxidation state on hydricity. The additional electron at the Ni center, which

lowers the oxidation state from Ni(I) to Ni(0) and makes the complex anionic, results in hydride transfer becoming more favorable by ~13 to 15 kcal/mol in all cases. For comparison, a difference in hydricity of ~10 kcal/mol was reported between similar diphosphine-ligated Co(I) and Co(II) hydrides in the same charge state.[380]

Lastly, it is suspected that the cationic $[HNiML]^+$ and $[(\eta^2\text{-}H_2)NiML)]^+$ complexes would also be stable, and could display interesting reactivity and/or simply add to the thermodynamic scheme. The former would likely be a diamagnetic Ni(II) species, which could potentially be formed via the reaction of weak acids with the neutral NiML complexes. The $[(\eta^2\text{-}H_2)NiML)]^+$ complexes would be more difficult to characterize on account of being paramagnetic, but it is suspected that cationic Ni(I) centers would be susceptible to induce the binding of H_2 via σ-donation from H_2. Indeed, the isoelectronic paramagnetic CoML complexes bind H_2, and the cationic charge of the Ni(I) complex likely would further increase H_2 σ-donation and limit $M \rightarrow H_2$ π-back-bonding. Lastly, an interesting idea proposed by Matt Vollmer was to attempt hydride transfer from the $(\eta^2\text{-}H_2)NiML$ complexes to boranes of known hydride affinity, which could result in the formation of the $[HNiML]^+$ species upon hydride transfer and allow for the estimation of the hydricity of the $(\eta^2\text{-}H_2)NiML)$ complexes. Direct hydride transfer from the H_2 adducts, either via a transient dihydride species or directly from the H_2 adduct, was considered computationally in the study of the mechanism of CO_2 hydrogenation catalysis (section 5.2.5.3). It is currently known from preliminary experiments that the hydricity of the $(\eta^2\text{-}H_2)NiGaL$ complex (**2**$-H_2$) is > 44 kcal/mol because no reaction was observed upon the addition of H_2 and CO_2 to **2** in the absence of a strong base.[331]

5.2.14 Effect of Varying the Supporting Metal on Catalytic CO_2 Hydrogenation Activity

Since [**1**−H]$^-$ and [**2**−H]$^-$ both were found to be strong enough hydride donors to react with CO_2 to generate formate (ie. $\Delta G°_{H-} < 44$ kcal/mol in CH_3CN),[323, 331] their catalytic activity for CO_2 hydrogenation to formate was also investigated. The results for employing complexes **1** and **3** as pre-catalysts in comparison to complex **2** are shown in Table 5.5 and Figure 5.37.

Table 5.5. Effect of the supporting metal on H_2/CO_2 to formate catalytic activity.[a]

Catalyst	Initial TOF[b] (h^{-1})	TON after 14 h	Final TON[c]	% Yield Formate[c]
NiGaL (**2**)	25(1)	80(12)	90(4)	90(4)
NiInL (**3**)	7.9(3)	51(5)	87(1)	87(1)
NiAlL (**1**)	4.9(6)	43(5)	–[d]	–[d]

[a]catalytic conditions: 8 mM NiML, 800 mM Vkd in 0.40 mL THF-d_8, 1 atm 1:1 H_2/CO_2 at 293K. All experiments were run in duplicate, with parenthesis indicating the standard deviation in replicate trials. [b]Over initial 40-minute period (first 6 data points collected). [c]After ~24 h, based on integration of HCO_2^- resonance in ^{1}H NMR spectra relative to an internal capillary standard. [d]Final formate % yield and TON not determined.

The catalytic activity, in terms of the initial TOF, follows the order Ga > In > Al, with $NiLH_3$ not found to catalyze the reaction to any appreciable extent (Figure 5.37). It should be noted that although catalysis is more sluggish for the In and Al supporting metals, a comparable final yield of formate was generated in the case of In compared with Ga (Table 5.5). Likewise, a similar formate TON after 14 h for M=Al and M=In was reached, and so it is likely that comparable final yields of formate after 24 h would be generated for M=Al as well despite its slower reaction rate. Even though NiInL (**3**) and NiAlL (**1**) are inferior catalysts compared to NiGaL (**2**), it is noteworthy that no other Ni catalysts, and only a few examples of other first-row metal catalysts, have been reported

to catalyze CO_2 hydrogenation to formate under ambient conditions (1 atm gas pressure, 293 K).[323]

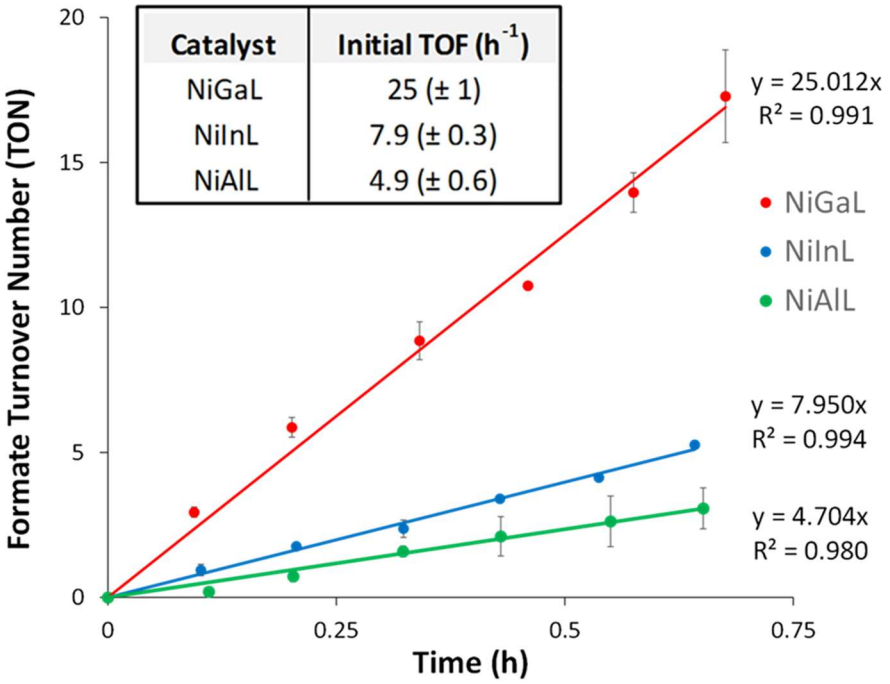

Figure 5.37. Kinetic plot of formate turnover number (TON) vs. time (h) over the initial period of catalytic CO_2 hydrogenation mediated by NiML complexes with Vkd base (8 mM NiML, 800 mM Vkd base, 1 atm of ~1:1 H_2/CO_2, 293 K), with the slopes representing the initial TOF (h^{-1}).

Preliminary catalysis studies under 34 atm of ~1:1 H_2/CO_2 found that **2** is a far better catalyst than **1** and **3**, with TON = 3150 (99% yield) for **2** in ~40 minutes compared with TON = 45 (1.4% yield) and TON = 54 (1.7% yield) for **1** and **3**, respectively, over a period of 3 h. It is hypothesized that complexes **1** and **3** are more prone to decomposition than complex **2** in the high-pressure trials which utilize low catalyst loadings (0.25 mM), leading to significantly worse catalytic performance for **1** and **3** in the high-pressure trials than would be expected based on the moderate activity displayed under ambient pressure with higher catalyst loadings. The specific decomposition pathways occurring will be discussed in more detail in section 5.2.17.

5.2.15 Understanding Trends in Catalytic CO_2 Hydrogenation Activity for NiML Complexes

The amenability of our catalytic system to the determination of the thermodynamic favorability for many of the fundamental steps in catalysis should aide in rationalizing the relative order of catalytic activity (Ga > In > Al). Figure 5.38 summarizes the thermodynamic data for the first three proposed steps in the catalytic cycle: (1) H_2 binding to NiML, (2) deprotonation of (η^2-H_2)NiML, and (3) hydride transfer to CO_2 from [HNiML]$^-$.

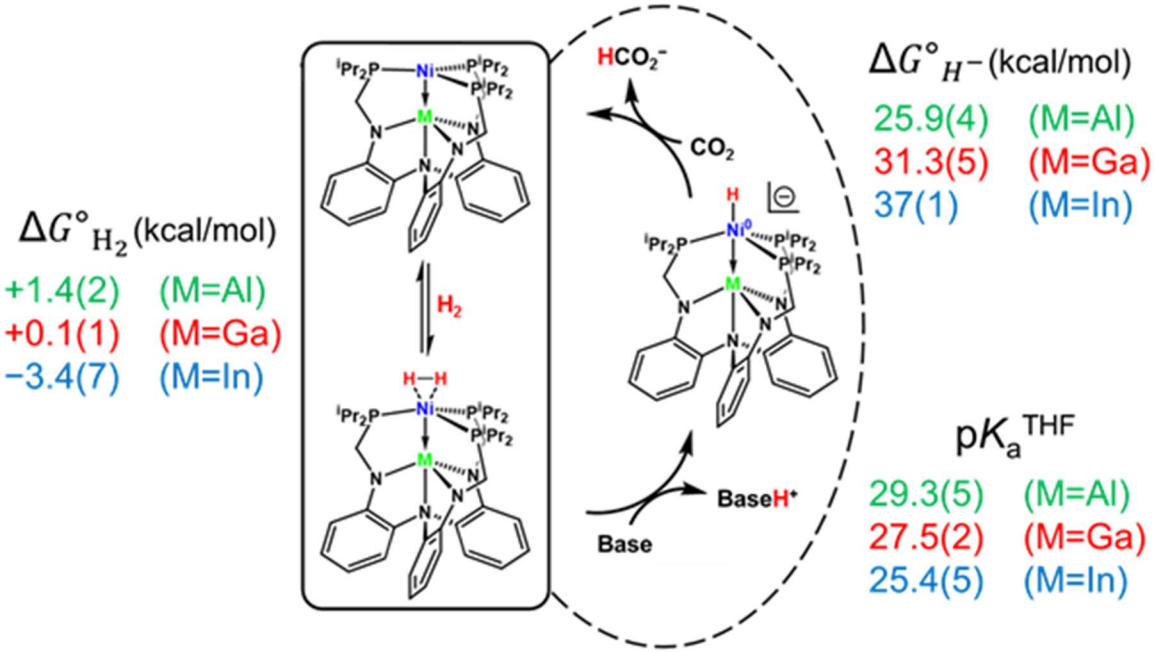

Figure 5.38. Simplified catalytic mechanism for CO_2 hydrogenation to formate, with the favorability of each of the three fundamental steps in THF shown as a function of the supporting metal: Al (top, green), Ga (middle, red), In (bottom, blue).

As labeled in Figure 5.38, the thermodynamic favorability for each of the three fundamental reaction steps in the catalytic cycle is intermediate for NiGaL (**2**) relative to those of NiAlL (**1**) and NiInL (**3**). Deprotonation of the H_2 adduct is the most difficult in the case of **1**−H_2, with the reaction of the extremely hydridic [**1**−H]$^-$ complex with CO_2 being the most favorable hydride transfer reaction of the trio. On the other hand,

deprotonation of **3**−H_2 to form [**3**−H]$^-$ is the most facile of the series, with [**3**−H]$^-$ still readily able to react with CO_2, albeit with the lowest thermodynamic driving force for hydride transfer (~7 kcal/mol) of the three complexes.

The relative favorabilities of deprotonation and hydride transfer for **1** and **3** illustrate that pK_a and hydricity are inversely related, as a more reactive metal hydride species will be more difficult to generate (Equations 5.30-5.33, Figure 5.39).[329]

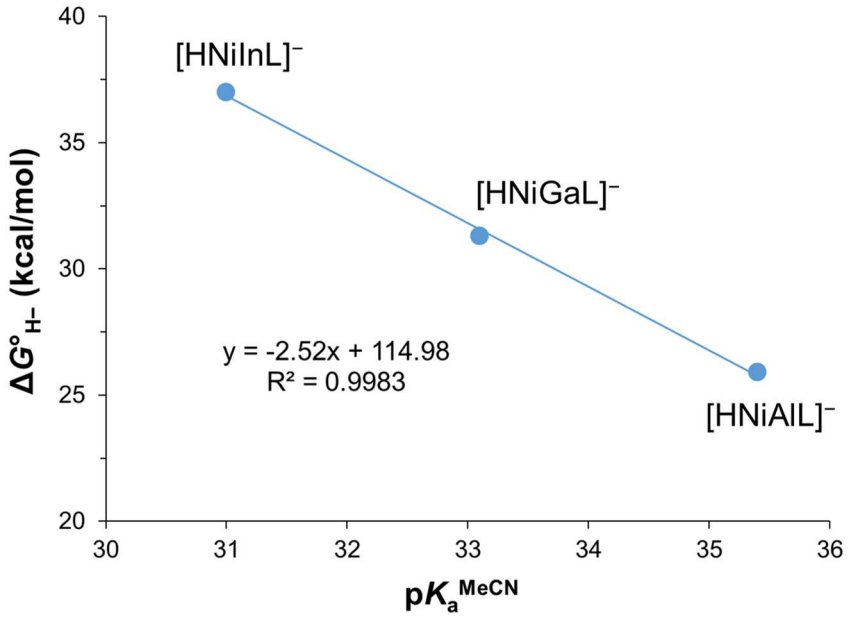

Figure 5.39. Plot of $\Delta G°_{H-}$ (in kcal/mol) vs. pK_a^{MeCN} for the trio of [HNiML]$^-$ complexes.

In addition to the intermediate pK_a and $\Delta G°_{H-}$ values for M=Ga relative to the other supporting metals, H_2 binding is also the closest to thermodynamically neutral for **2**, and so one explanation for its superior catalytic activity is that various steps in catalysis are well-matched in energy, such that no step is too difficult. Examining the favorability of each step makes it reasonably clear why **1** is the worst of the three catalysts, as H_2 binding and deprotonation are both the most unfavorable for **1** of the three complexes. Thus, generating the reactive hydride species, [**1**−H]$^-$, is prohibitively

difficult and likely impedes catalysis. Of note, the catalytic resting state for complex **1** at later time points in catalysis appears to be the anionic formate adduct, [VkdH][(HCO_2)NiAlL] ([VkdH][**1**−O_2CH]), as judged by *in situ* ^{31}P NMR spectroscopy. At early time points, the chemical shift of the catalytic resting state is ~30 ppm, which is close to that of **1**, with the ^{31}P resonance shifting further upfield to ~28-29 ppm observed over the course of catalysis. A slight upfield shift to ~29 ppm relative to the chemical shift of **1** (30.7 ppm) was observed for the independently synthesized anionic formate adduct, [PPN][(HCO_2)NiAlL] ([PPN][**1**−O_2CH]), which was generated by exposing [PPN][**1**−H] to 1 atm CO_2 (Figure A.4.5). Therefore, it is proposed that catalysis mediated by **1** will be inhibited by formate binding at later time points, in addition to being impeded relative to catalysis with **2** and **3** by both the H_2 binding and deprotonation steps.

In the case of **3**, it is not immediately clear why it performs worse as a catalyst than **2**. H_2 binding and deprotonation of the H_2 adduct are significantly more favorable for **3** than **2**, indicating that the $[HNiML]^-$ species should be more readily generated in the case of **3**. Even though hydride transfer is less favorable for M=In relative to M=Ga, $[\mathbf{3}{-}H]^-$ is still expected to be sufficiently reactive toward CO_2 that outer-sphere hydride transfer is thermodynamically favorable by ~7 kcal/mol.[331] In fact, the hydricity of $[\mathbf{3}{-}H]^-$ ($\Delta G°_{H^-}$ = 37 kcal/mol) is actually very similar to that of HCo(dmpe)$_2$ ($\Delta G°_{H^-}$ = 36 kcal/mol), which is the most active first-row metal catalyst for CO_2 hydrogenation under mild conditions (1 atm H_2/CO_2, rt, no additives), though hydride transfer was rate-limiting in that system.[323, 359] This prompts the question of why is **3** an inferior CO_2 hydrogenation catalyst in comparison to **2**.

Additional insight was provided by *in situ* ^{31}P NMR spectroscopy, which identified that the catalytic resting state throughout catalysis under catalytic conditions for **3** was the anionic formate adduct, [VkdH][(HCO_2)NiInL] ([VkdH][**3**−O_2CH]), just as was the case for catalysis with **2**.[128] The catalytic resting state was identified as [VkdH][**3**−O_2CH] based on its diagnostic ^{31}P chemical shift of 37.6, which closely matches that upon the addition of excess [VkdH][HCO_2] to **3**, as well as that of the independently synthesized [PPN][**3**−O_2CH] complex (Figure A.4.6). This result suggests that formate dissociation to allow H_2 to bind is the RDS for catalysis mediated by both **2** and **3**, and so one possible explanation for the slower catalytic rates for **3** would be slower ligand substitution of H_2 for formate. The next section will compare the thermodynamics and kinetics of formate dissociation for complexes **2** and **3** to determine whether the relative rates of catalysis (TOF) can be explained by the rates of ligand substitution.

While the analysis so far has focused on the thermodynamics of each step, the catalytic rate is dictated by the kinetics of each step, which is often correlated with the thermodynamic favorability. Although kinetic studies have not been pursued as thoroughly and have not been as fruitful in a quantitative sense as the thermodynamic studies, a few qualitative observations are worth noting. The kinetics of H_2 binding were previously quantitatively examined in chapter 3, and the rapid rates of H_2 binding and dissociation are not expected to limit the rate of catalysis. The rate of H_2 adduct deprotonation appears to be qualitatively slower than that of H_2 binding, based on the fact that incomplete deprotonation of **3**−H_2 was observed in the presence of a slight excess Vkd base after ~15 minutes. That said, under catalytic conditions there is a significant

excess of base, and of formate to assist the base as catalysis goes on, and so the rate of deprotonation is not expected to be an impediment to catalysis. An additional consideration is that catalysis may be mass-transport limited by the rate of liquid-gas mixing under certain conditions (Figures A.4.37-A.4.38).

The kinetics of hydride transfer were also investigated experimentally. Hydride transfer from [PPN][**3**−H] to CO_2 to generate [PPN][**3**−O_2CH] was found to be prohibitively fast to measure by conventional NMR techniques. Namely, a frozen solution of [PPN][**3**−H] in THF-d_8 in a J. Young NMR tube was exposed to 1 atm CO_2, thawed for 30 seconds in a dry ice/acetone bath (195 K), inverted once, and inserted directly into the NMR instrument, which was already cooled to 195 K. An initial ^{31}P NMR spectrum acquired ~1 minute after the sample was thawed already showed complete consumption of [PPN][**3**−H] and the formation of [PPN][**3**−O_2CH]. That hydride transfer from [HNiML]$^-$ to CO_2 is rapid is consistent with the large thermodynamic driving forces of 7 kcal/mol (In) to 18 kcal/mol (Al) expected for hydride transfer based on the measured hydricities of the [HNiML]$^-$ complexes. Moreover, it seems that alternative techniques would need to be utilized in order to measure the rapid rates of hydride transfer to CO_2.

Since hydride transfer to CO_2 proved too fast to measure by conventional NMR methods, the relative rates of hydride transfer between two metal hydrides in the isodesmic hydride transfer experiments were also considered as a function of the supporting metal. Hydride transfer from HRh(dmpe)$_2$ to **1** to generate [**1**−H]$^-$ reached equilibrium after ~1 week, whereas complete hydride transfer from HRh(dmpe)$_2$ to **2** and **3** was observed by Matt Vollmer, as expected based on the larger $\Delta\Delta G°_{H-}$ values. Much

faster hydride transfer was observed from $HRh(dmpe)_2$ to **3**, with complete conversion to $[Rh(dmpe)_2][\mathbf{3}-H]$ observed within one hour, than to **2**, which took several days to fully convert to $[Rh(dmpe)_2][\mathbf{2}-H]$. It appears that faster hydride transfer kinetics were observed for more thermodynamically favorable hydride transfer reactions involving $HRh(dmpe)_2$ and NiML, at least qualitatively. However, hydride transfer between $[HNiML]^-$ and NiM'L were not observed to adhere to this principle in all cases (Figures A.4.30-A.4.33), as hydride transfer from $[\mathbf{1}-H]^-$ to **2** ($\Delta\Delta G°_{H-}$ = 5.4 kcal/mol, $t_{1/2} \approx 4.6$ h) proceeded more rapidly than hydride transfer from $[\mathbf{1}-H]^-$ to **3** ($\Delta\Delta G°_{H-}$ = 11.1 kcal/mol, $t_{1/2} \approx 7.7$ h). Clearly there are other factors, including the steric crowding of the metal centers involved in hydride transfer, that could lead to deviations from the correlation of the kinetic rate and thermodynamic favorability of hydride transfer. That said, DFT calculations do predict a linear relationship between the free energy of activation for hydride transfer from $[HNiML]^-$ to CO_2 ($\Delta G^‡$) and the thermodynamic hydricity ($\Delta G°_{H-}$), and so hydride transfer rates would be expected to follow the relative order Al > Ga > In for $[HNiML]^-$ complexes based on this prediction.[129] Other experimental efforts to examine the relative rates of hydride transfer from $[HNiML]^-$ complexes to CO_2 as a function of the supporting metal could focus on utilizing other C=X substrates which react more slowly as a model for hydride transfer to CO_2, as this would allow for the rates of hydride transfer to be more readily measurable by conventional techniques.

5.2.16 Effect of the Supporting Metal on the Thermodynamics and Kinetics of Ligand Substitution of H_2 for Formate

With the kinetics and thermodynamics of the first three fundamental steps in catalysis examined, the primary considerations remaining are the kinetics and thermodynamics of ligand substitution of H_2 for formate, which will be considered in this section as a function of the supporting metal. Namely, the thermodynamics and kinetics of formate binding to **2** and **3** will be compared, since this is one step that could explain the inferior catalytic performance of the latter. Just as was discussed with complex **2**, even though the strong binding of formate precludes direct measurement of its thermodynamic binding energy to **3**, CH_3CN can be used as an intervening ligand to quantify the relative thermodynamic favorability of formate binding relative to that of H_2 binding (Equations 5.10-5.17). Figure 5.40 shows ^{31}P NMR spectra of the equilibria of CH_3CN binding with H_2 binding (left) and with formate binding (right).

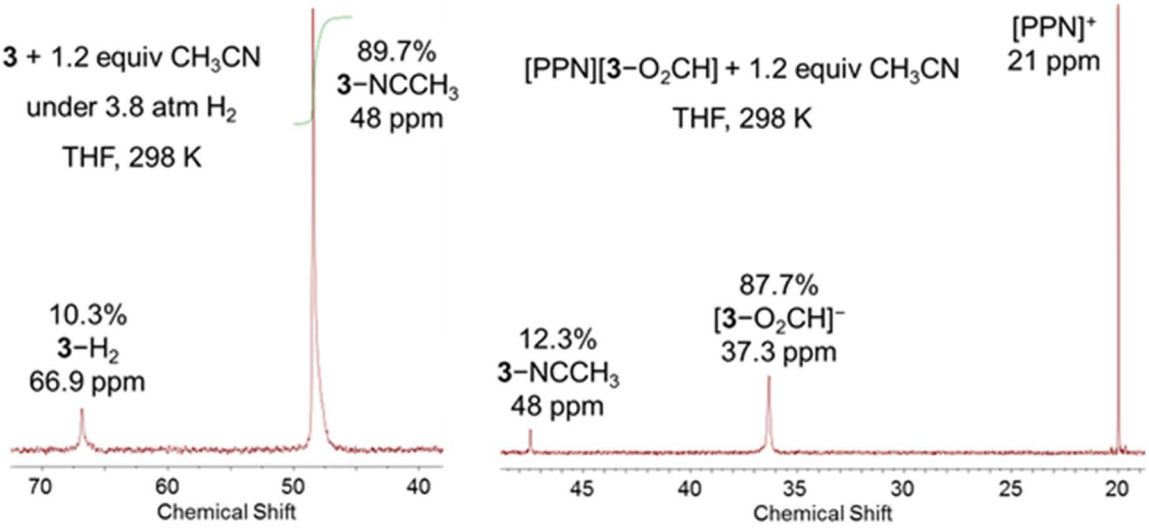

Figure 5.40. ^{31}P NMR spectra (161.9 MHz, THF) showing the binding equilibrium between CH_3CN and H_2 (left) and that between CH_3CN and formate (right) for binding to NiInL (**3**).

Equilibrium	$\Delta G°$ (kcal/mol)	
3−H_2 + CH_3CN ⇌ **3**−$NCCH_3$ + H_2	$-1.364 \cdot \log(K_{eq_1})$	(Eqn 5.65)
3−$NCCH_3$ + {[PPN][HCO_2]}$_{ip}$ ⇌ {[PPN][**3**−O_2CH]}$_{ip}$ + CH_3CN	$-1.364 \cdot \log(K_{eq_2})$	(Eqn 5.66)

Exposure of a mixture of **3** and 1.2 equiv CH_3CN in THF to both 1 atm and ~3.8 atm H_2 allowed for the measurement of K_{eq_1} to be 2.4(2) x 10^3 atm/M, as judged by the relative integrals of the resonances observed by ^{31}P NMR spectroscopy, which translates into $\Delta G°$ = −4.6(1) kcal/mol for Equation 5.65 (Figure 5.40). Since $\Delta G°$ = −3.4(7) kcal/mol was estimated for H_2 binding to **3** in THF, this means that $\Delta G°$ = −8.0(7) kcal/mol for CH_3CN binding to **3**. K_{eq_2} was found to be 61 when [PPN][**3**−O_2CH] and 1.2 equiv CH_3CN were allowed to reach equilibrium in THF over ~3 days (Figure 5.40). This equates to $\Delta G°$ = −2.4 kcal/mol for Equation 5.66, which gives $\Delta G°$ = −12(1) kcal/mol for formate binding once ion-pairing interactions in THF are considered,[358, 366] just as was described for formate binding to **2** (Equations 5.13-5.18).

Table 5.6 compares the binding energies of H_2, CH_3CN, and formate (HCO_2^-) to complexes **2** and **3**.

Table 5.6. Comparison of $\Delta G°$ values for H_2, CH_3CN, and formate (HCO_2^-) binding to complexes **2** and **3** in THF.[a]

Complex	H_2	CH_3CN	HCO_2^-
NiGaL (**2**)	+0.1(1)b	−4.7(6)	−6.5(8)[d]
NiInL (**3**)	−3.4(7)c	−8.0(7)	−12(1)[d]

[a]Note that all values are $\Delta G°$ in kcal/mol. [b]Experimental value from which absolute binding energies of CH_3CN and HCO_2^- were determined. [c]Estimated binding value from experimental value of −3.0(7) kcal/mol in toluene, based on adjusting by DFT-predicted $\Delta\Delta G°$ between toluene and THF. Absolute binding energies of CH_3CN and HCO_2^- to **3** were then determined relative to this estimated H_2 binding energy. [d]Single equilibration trial.

The fact that formate binds considerably more strongly to **3** than to **2** indicates that formate dissociation will be less favorable under catalytic conditions with **3**. Furthermore, ligand substitution involving H_2 binding and formate dissociation will be more unfavorable for complex **3**, at $\Delta G°$ = +8.6(1.2) kcal/mol, than for complex **2**, at $\Delta G°$ = +6.6(8) kcal/mol. This indicates that a larger fraction of the catalyst will be in the catalytic resting state, the anionic formate adduct, in the case of catalysis with **3**. The kinetic exchange rates of CH_3CN, a neutral ligand, and formate can also be compared for complexes **2** and **3**, as they should show the same trend and serve as an adequate model of the relative exchange rates of H_2 for formate that are of relevance to the catalytic rates.

Figure 5.41 shows the ^{31}P NMR lineshape simulations for the equilibria between CH_3CN and formate binding for complexes **2** and **3**. While chemical exchange of CH_3CN for formate is slow relative to the ^{31}P NMR timescale (161.9 MHz) for both species, exchange is much slower for complex **3** than for complex **2**, as sharp resonances are observed for the former compared with broader resonances for the latter. The exchange rates of CH_3CN and formate were estimated to be ~2.0(3) x 10^2 s^{-1} and ~2(1) s^{-1} for complexes **2** and **3**, respectively. This same relative trend can be seen more dramatically in the chemical exchange rates of CH_3CN for H_2, where slow interconversion relative to the ^{31}P NMR timescale (161.9 MHz) can be observed for complex **3**, but fast interconversion is observed in the case of complex **2** (Figures 5.19 and 5.40). Likewise, this matches the relative trend in the rates of H_2 self-exchange determined by ^{31}P NMR lineshape simulations in chapter 3, where complex **2** was found to have a faster H_2 self-exchange rate by a factor of ~5 relative to complex **3**.

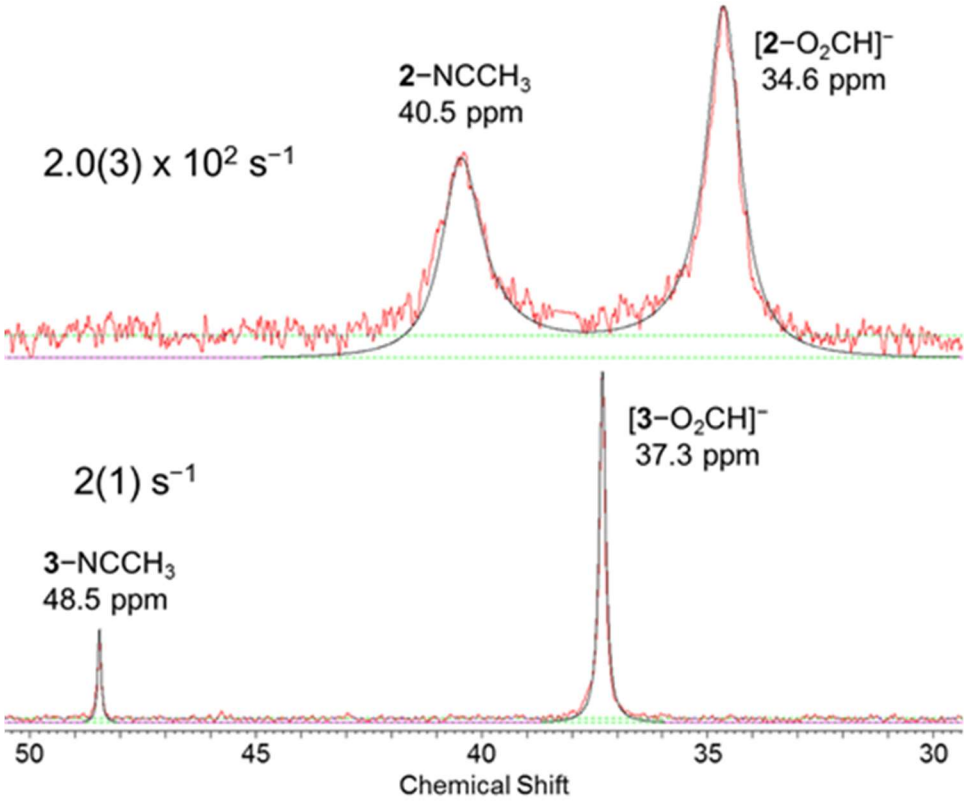

Figure 5.41. Comparison of simulated (black lines) and experimental ^{31}P NMR spectra (red lines, THF-d_8, 161.9 MHz) for the binding equilibria between formate and CH_3CN for complexes **2** and **3** at 298 K. The estimated exchange rates and uncertainties are also displayed.

Therefore, all evidence points to the fact that ligand exchange of H_2 for formate should occur at a faster rate for complex **2** compared with complex **3**. Given that the initial TOF in catalytic trials performed at ambient pressure differed by a factor of ~3 (Table 5.5), it is proposed that this difference in rates may be attributable to the faster ligand exchange rate of H_2 for formate in complex **2** compared with complex **3**. Although the exchange rate of CH_3CN for formate, which was used as a model for the exchange of H_2 for formate, was found to be faster by a factor of ~100 for **2** relative to **3**, the experimental conditions were such that only ~1 equiv of formate and CH_3CN were present in solution. Under catalytic conditions, H_2 is present in large excess relative to formate over the initial period of catalysis, and so the exchange rates would likely be

faster for both complexes due to the presence of excess H_2, and the relative exchange rates would likely be much less disparate than the factor of ~100 observed. Thus, the kinetics of ligand substitution of formate for H_2 seems to be a reasonable explanation for the relative differences in initial TOF for catalysis at ambient pressure with complexes **2** and **3**. However, this does not explain the catalytic results at high pressure (~34 atm), where the performance of **2** (3150 TON, 99% yield) was drastically better compared with **3** (54 TON, 1.7% yield). To explain this, it is proposed that catalyst **3** is more prone to decomposition in high- pressure trials where low catalyst loadings (0.25 mM) were employed, compared with the ambient pressure trials where higher catalyst loadings were used (8 mM). The next section will briefly present what is currently known about the mechanism of catalyst decomposition, and why it might be more prevalent in the case of catalysis with complex **3** than with complex **2**.

5.2.17 Catalyst Decomposition Pathways and Their Dependence on the Supporting Metal

5.2.17.1 Decomposition to Catalytically Inactive CO Adducts

Studying catalytic decomposition pathways is important because understanding catalyst deactivation can potentially aide in improving catalyst lifetime and overall performance. Monitoring catalyst speciation throughout the course of catalysis via *in situ* ^{31}P NMR spectroscopy was particularly useful in elucidating the primary catalytic species, both active and inactive, which build up in solution during catalysis. As described previously, the anionic formate adducts, [VkdH][(HCO_2)NiML], were identified as the primary catalyst resting state for M=Ga and M=In based on *in situ* ^{31}P NMR spectroscopy, which indicated that formate dissociation was likely the RDS for catalysis with both **2** and **3**. The notion that the formate adduct remains catalytically

active, as opposed to being an inactive form of the catalyst, was validated by stoichiometric experiments which showed that the reactive anionic hydride species, [VkdH][HNiML], could be regenerated upon the addition of H_2 to the formate adduct in the presence of Vkd base (Figure A.4.21).[128] Additionally, catalytic generation of formate was observed to resume upon the replenishment of H_2/CO_2 gas to [VkdH][**2**−O_2CH] under catalytic conditions in the presence of Vkd base. Apart from the formate adducts, the primary species generated under catalytic conditions for both **2** and **3** with low H_2/CO_2 pressures and/or low catalyst loadings were the CO adducts, (OC)NiML.

Figure 5.42 shows *in situ* ^{31}P NMR spectra collected throughout catalysis with **2** and **3** under 1 atm of ~1:1 H_2/CO_2.

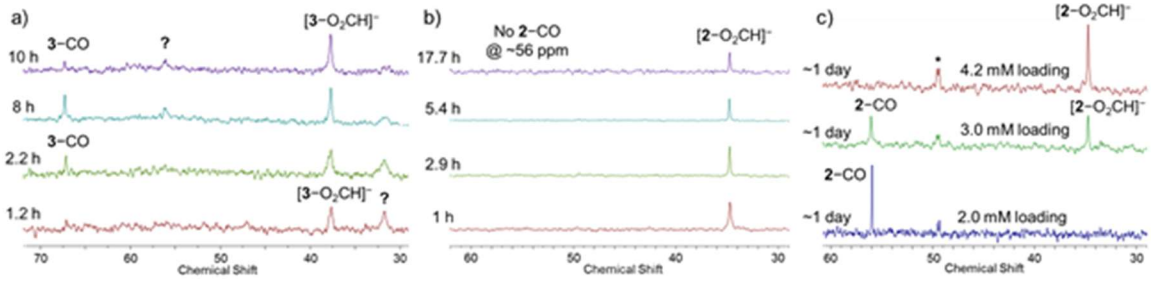

Figure 5.42. *In situ* ^{31}P NMR spectra collected during catalysis under mild conditions (~1:1 H_2/CO_2 in 0.40 mL THF-d_8 at 293 K) for: (a) 8 mM NiInL (**3**) and 800 mM Vkd base, (b) 8 mM NiGaL (**2**) and 800 mM Vkd base, and (c) varying [**2**] with 500 mM Vkd base. ^{31}P resonances of the formate and CO adducts of **2** and **3** have been identified and labeled, with a few unidentified peaks also denoted (?, *). ^{31}P spectra are zoomed in to more clearly show the different catalyst species, so it should be noted that peaks for Vkd, $[VkdH]^+$ and impurities in the base are present in the spectra but not shown.

For a catalyst loading of 8 mM NiGaL (**2**) with 800 mM Vkd base, the only species observed throughout catalysis is the formate adduct, [VkdH][**2**−O_2CH] (Figure 5.42b). In contrast, under identical catalytic conditions with NiInL (**3**), early time points show the formate adduct, [VkdH][**3**−O_2CH], as the primary catalyst resting state, along with an unidentified peak at 31.7 ppm (Figure 5.42a). Over time, the unidentified peak

disappears and (OC)NiInL (**3**−CO) is formed in greater concentration. The final time point shows that the relative concentration of **3**−CO has decreased and that of [VkdH][**3**−O_2CH] has increased, along with the appearance of a small unidentified peak at ~56 ppm (Figure 5.42a).

Clearly, the catalyst speciation is more complicated in the case of catalysis with **3** than with **2**, as the only species observed under catalytic conditions with **2** is the catalytically active formate adduct. However, upon lowering the catalyst loading of **2** from 8 mM to either 2 mM or 3 mM, the formation of substantial amounts of (OC)NiGaL (**2**−CO) was observed. The effect of lower catalyst loading is illustrated in Figure 5.42c, where **2**−CO is the primary species observed, after ~24 h, with a 2 mM catalyst loading of **2**, forms in a ~1:1 ratio with [VkdH][**2**−O_2CH] with a 3 mM loading, and is not observed at all with a 4.2 mM loading. Small amounts of CO gas were also consistently detected by GC-MS analysis of the headspace of the J. Young NMR tubes after catalysis (Figure A.4.39), consistent with the formation of small amounts of CO under catalytic conditions.

To address whether the (OC)NiML complexes (M=Ga, In) were inactive forms of the catalyst, **2**−CO and **3**−CO were independently prepared (as described in section 3.5.1) and subjected to catalytic conditions. Figure 5.43 shows the catalytic results for the (OC)NiML complexes in comparison to their respective NiML complexes. Almost no formate is formed under catalytic conditions for both **2**−CO and **3**−CO, with TON of 1.6 and 0.6 observed after ~2 h, respectively, and initial TOF = 0.4 h^{-1} in each case over the initial 50-minute period (Figure 5.43). In contrast, catalysis with **2** and **3** generated 105

and 21 turnovers of formate in ~2 h, respectively, with the initial TOF for **2** (67 h^{-1}) found to be ~6 times greater than that for **3** (11 h^{-1}) under these conditions (Figure 5.43).

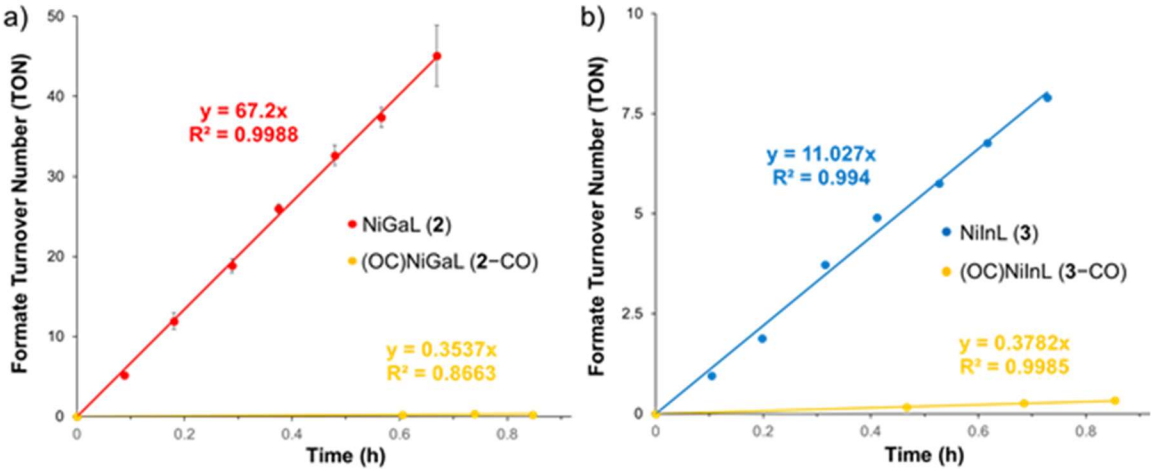

Figure 5.43. Comparison of formate turnover number (TON) vs. time plots for: (a) **2** compared with **2**−CO, and (b) **3** compared with **3**−CO. Catalytic conditions for **2** and **3** were: 2.9 mM NiML and 800 mM Vkd base in ~0.40 mL THF-d_8, at 1 atm of ~1:1 H_2/CO_2 and 293 K. Catalytic conditions were nearly identical but slightly different for (OC)NiML, with a 3 mM catalyst loading and 750 mM Vkd base utilized. Data points for NiML complexes are the average of duplicate trials, whereas only a single trial was performed for each (OC)NiML complex. The slope gives the approximate turnover frequency (TOF) over the initial time period (in h^{-1}).

Clearly, **2**−CO and **3**−CO are inactive forms of their respective catalysts, for all intents and purposes, as they exhibit little appreciable catalytic activity relative to that of **2** and **3**. That **2**−CO and **3**−CO would not be catalytically active makes intuitive sense, as CO binding would be expected to be strong enough to effectively prevent the binding of H_2. Thus, catalysis would not occur because the generation of the reactive anionic hydride species, [VkdH][HNiML], would not be possible due to CO outcompeting H_2 for binding to NiML and effectively poisoning the catalyst. This proposal is supported by the DFT-calculated binding energies of CO and H_2 to NiML (M06-L/bs1), which predict CO binding to be more significantly favorable than H_2 binding by 18.6 and 21.0 kcal/mol (in terms of $\Delta\Delta G°$) for complexes **2** and **3**, respectively.[129] The CO adducts were also the

only species observable during the catalytic trials with both **2**−CO and **3**−CO, which also supports the notion that displacement of CO to allow for H_2 binding is the limiting step that is effectively preventing catalysis from occurring.

One interesting observation that potentially contradicts this simplified picture of catalyst decomposition comes from comparing *in situ* ^{31}P NMR spectra collected at 8 h and 10 h time points for catalysis with **3** (Figure 5.42a). The decrease in the relative concentration of **3**−CO between these two time points suggests that the CO adduct need not simply sit in solution once it is formed, and that it can react in some way under catalytic conditions. The large excess of H_2 relative to CO could, in principle, result in a very small fraction of the catalyst binding H_2, which could lead to productive catalysis and account for the minimal amounts of formate generated under catalytic conditions for **3**−CO and **2**−CO. Of relevance, the complete disappearance of **3**−CO and the generation of the catalytically active [**3**−H]$^-$ species was observed by *in situ* ^{31}P NMR spectroscopy between two different time points in catalysis upon the complete consumption of CO_2 in the J. Young NMR tube (Figure A.4.40). However, this result could be due to the decomposition of **3**−CO to other unidentified species, possibly those which grow in between ~56 and 61 ppm, and the conversion of some [**3**−O_2CH]$^-$ to [**3**−H]$^-$ once CO_2 is depleted, rather than from the conversion of **3**−CO directly back to the catalytically active [**3**−H]$^-$ species. In any case, the extremely large energy difference between H_2 and CO binding to **3** (~21 kcal/mol based on DFT calculations) and the negligible catalytic activity of **3**−CO make it unlikely that the decrease in the relative concentration of **3**−CO between successive time points is due to productive catalysis. It is more likely that further

decomposition of **3**−CO occurs, possibly to form the unidentified species between ~56 and 61 ppm, which are also presumably catalytically inactive.

Collectively, the *in situ* ^{31}P NMR studies and catalytic trials with **2**−CO and **3**−CO indicate that the CO adducts are the primary species formed from catalyst decomposition, and that once formed they are essentially catalytically inactive. Additionally, catalyst decomposition occurs more readily for **3** to **3**−CO than for **2** to **2**−CO under identical catalytic conditions with 8 mM catalyst loadings. Only upon lowering the catalyst loading to 3 mM is the analogous extent of catalyst decomposition to the CO adduct observed for complex **2**. This is an important observation in that it can help rationalize the dramatically better performance at low catalyst loading (0.25 mM) and high pressure (34 atm of ~1:1 H_2/CO_2) of catalyst **2** (3150 TON, 99% yield) compared with catalyst **3** (54 TON, 1.7% yield). Namely, it is proposed that catalyst **3** is more prone to decomposition than catalyst **2** in these high-pressure trials where low catalyst loadings were employed. Although the catalyst concentrations are too low to directly observe by ^{31}P NMR spectroscopy whether decomposition to **2**−CO and **3**−CO also occurs under catalytic conditions in these high-pressure trials, it seems reasonable that **3** will decompose more readily than **2** in these trials based on the fact that this was seen to be the case for identical catalyst concentrations at ambient pressure (Figure 5.42a-b). The greater predicted favorability of CO binding to **3** relative to **2** indicates that there is likely a greater thermodynamic driving force for the formation of **3**−CO compared with **2**−CO.

5.2.17.2 Possible Mechanisms of Catalyst Decomposition

There are several possible mechanisms by which the catalytically inactive (OC)NiML complexes could be formed under catalytic conditions. Four different possibilities that were considered are shown in Equations 5.67-5.70, with all the reactions presumed to be metal-mediated processes, with the possible exception of Equation 5.70.

Reverse water-gas shift	$H_2 + CO_2 \rightleftharpoons CO + H_2O$	(Eqn 5.67)
Formate dehydroxylation	$HCO_2^- \rightleftharpoons CO + OH^-$	(Eqn 5.68)
CO_2 disproportionation	$2\ CO_2 + 2\ e^- \rightleftharpoons CO + CO_3^{2-}$	(Eqn 5.69)
Phosphine oxidation	$CO_2 + PR_3 \rightarrow CO + O{=}PR_3$	(Eqn 5.70)

The reverse water-gas shift reaction and formate dehydroxylation were the two primary decomposition pathways considered in detail for the decomposition of a diphosphine-ligated Co catalyst, $[Co(dmpe)_2]^+$, to its catalytically inactive CO adduct, $[(CO)Co(dmpe)_2]^+$.[346] Reductive disproportionation of CO_2 to give CO and carbonates and/or bicarbonates has also been reported to be catalyzed by a number of different transition metal complexes, among them the closely related diphosphine-ligated Fe complex, $H_2Fe(dmpe)_2$.[381] Additionally, net disproportionation of CO_2 to CO and CO_3^{2-} was also reported by Holland and co-workers to proceed through the formation of a cobalt-carbonyl adduct and a dimeric cobalt oxo species, which reacts with additional CO_2 to generate a dimeric cobalt carbonate species.[382] Lastly, the similar decomposition of CO_2 to CO via the generation of a phosphine oxide was also considered, either via oxidation of the ligand phosphines or of the Vkd proazaphosphatrane base. While no

definitive conclusions can be made as to the exact pathway(s) of decomposition, several important observations have been made which are worthwhile to consider.

In regard to the reverse water-gas shift reaction (Equation 5.67), Linehan and co-workers concluded it to be the more likely pathway for CO formation in the $HCo(dmpe)_2$ system, rather than formate dehydroxylation, on the basis of the fact that CO formation only occurred at higher CO_2:H_2 ratios, whereas formate dehydroxylation would not be expected to be affected as drastically by the gas ratio.[346] Although different gas ratios were not tested in our system, catalyst decomposition to the (OC)NiML complexes occurred at low gas pressures (1 atm), whereas higher gas pressures would be expected to promote the endothermic reverse water-gas shift reaction to a greater extent.[383] Additionally, the amount of CO gas in the headspace was relatively low based on GC-MS analysis, at 0.5 to 1.5 % for various catalytic trials, whereas a much more significant amount of CO gas, ~17% of the headspace gas analyzed, was generated in the case of the $HCo(dmpe)_2$ system. The lower CO gas content suggests that the NiML complexes are not catalyzing the reverse water-gas shift reaction as readily as $HCo(dmpe)_2$, but it cannot rule out the reverse water-gas shift reaction completely as a potential source of CO in our system.

To test the feasibility of CO_2 disproportionation (Equation 5.69), NiML complexes were subjected to high pressures of CO_2 in the absence of H_2 and base. No decomposition to **2**−CO was observed for **2** over the course of 12 h under 34 atm CO_2, albeit in toluene-d_8, whereas a significant amount of decomposition of **3** to **3**−CO was observed, but only upon heating to 368 K. The lack of decomposition to give (OC)NiML complexes at 293 K under high pressures of CO_2 does not rule out all possible

disproportionation mechanisms, as no Vkd base was present in these control experiments. A control experiment with Vkd base and CO_2 showed a slow reaction over the course of days that generated the product of phosphine oxidation, Vkd(P=O). It is presumed that CO could be one of the other byproducts of this phosphine oxidation reaction, although the possibility that trace moisture plays a role in this process cannot be discounted. In any case, the lack of decomposition to give the (OC)NiML complexes at 293 K under high pressures of CO_2 would seem to suggest that oxidation of the ligand phosphines, either to form InO_3L (section 3.3.1.6) or a $(OC)(P)_2Ni(\mu\text{-}O)P$ species, likely does not occur readily under ambient conditions (1 atm gas pressure, 293 K). That said, a small amount of InO_3L (section 3.3.1.6) was observed in some cases under catalytic conditions for complex **3** (Figure A.4.40), which prevents the disproportionation of CO_2 via phosphine oxidation from being ruled out completely.

In regard to formate dehydroxylation (Equation 5.68) being a viable pathway for catalyst decomposition, several control reactions were performed that provided useful insights. [VkdH][**2**−O_2CH] was independently synthesized *in situ*, by first generating[VkdH][**2**−H] via the addition of H_2 (1 atm) to **2** in the presence of excess Vkd base, followed by subsequent exposure to CO_2 to form [VkdH][**2**−O_2CH] after a freeze-pump-thaw cycle. Over the course of 1 week, substantial decomposition (~50%) of [VkdH][**2**−O_2CH] to form **2**−CO and two unidentified species was observed by ^{31}P NMR spectroscopy (Figure 5.44a). **2**−CO, species **B**, and an unidentified species at 33.1 ppm are formed in an estimated 2:3:2 ratio (Figure 5.44a).

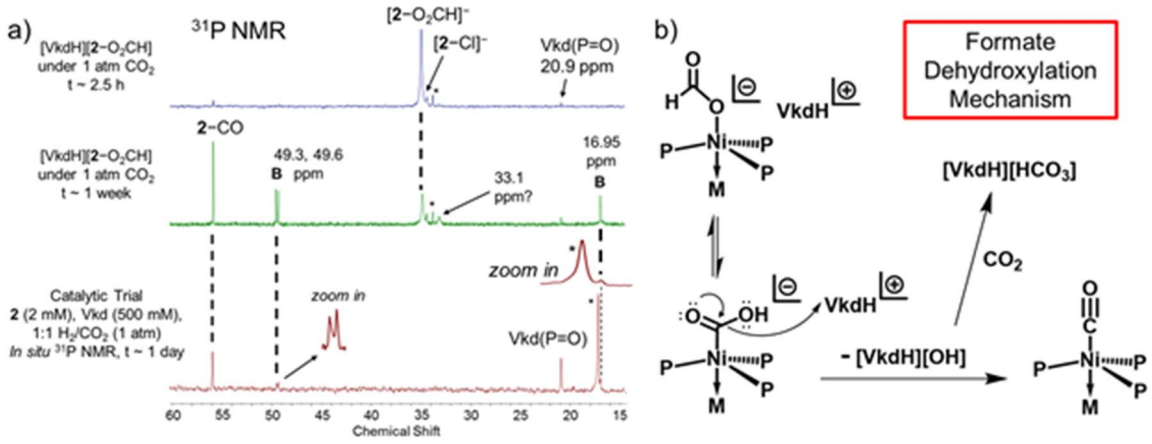

Figure 5.44. (a) Stacked ^{31}P NMR spectra (162 MHz, THF-d_8) showing decomposition of [VkdH][**2**−O_2CH] to **2**−CO (55.8 ppm), species **B** (49.6, 49.3, 16.95 ppm), and an unidentified species (33.1 ppm) over the course of 1 week under 1 atm CO_2. Note that large peaks for Vkd base (119 ppm) and $[VkdH]^+$ (−13.6 ppm) are present in all spectra, but are not shown for visual clarity. Also not shown in the catalytic trial spectrum are Vkd-derived peaks at 1.9 and 9.7 ppm. An unknown Vkd-derived peak is denoted at 17.2 ppm (*), as are small impurities of [X][**2**−Cl], Vkd(P=O), and a small unidentified peak at 33.8 ppm (*). (b) A mechanistic proposal for formate dehydroxylation of [VkdH][**2**−O_2CH] to generate **2**−CO and [VkdH][HCO_3] under a CO_2 atmosphere.

Both **2**−CO (55.8 ppm) and species **B** (49.6/49.3 and 16.95 ppm in a 2:1 ratio) are the two primary decomposition products typically observed under catalytic conditions with complex **2**, as shown by comparing the ^{31}P NMR spectrum of the formate adduct decomposition experiment to that obtained during catalysis (Figure 5.44a). While the structure of species **B** is not known precisely, the large disparity in ^{31}P chemical shifts indicates that the phosphine donors have been significantly differentiated in some manner; it is likely that either one phosphine has dissociated from Ni, or that one or two of the phosphines have become oxidized. Additionally, a new resonance at ~8.0 ppm was observed by ^{1}H NMR spectroscopy, which is upfield relative to that of corrdinated formate in [VkdH][**2**−O_2CH] at ~8.7 ppm. Thus, it is hypothesized that the unidentified species at 33.1 ppm, or possibly species **B**, contains a coordinated formate moiety. Other possible coordination modes of formate could include η^2-O,O formate binding (with

either phosphine dissociation or coordination of one oxygen atom to the supporting metal), a bridging dimeric binding mode (Ni−OCHO−Ni), or η^1-C formate binding, potentially similar to the isomerization of formate depicted in the mechanism in Figure 5.44b.

Because the primary decomposition products observed during catalysis, **2**−CO and species **B**, are also observed in the formate adduct decomposition experiment, it is proposed that formate dehydroxylation is favored as the primary pathway for catalyst decomposition. Similar decomposition of [VkdH][**3**−O_2CH] under CO_2 to generate **3**−CO, along with other species including InO_3L, was also observed by ^{31}P NMR spectroscopy over the course of ~1 week. Figure 5.44b illustrates the proposed mechanism of catalyst decomposition via formate dehydroxylation through initial isomerization of the coordinated formate unit. Other important control experiments shed light on the potential roles of excess Vkd base and/or CO_2 in promoting formate dehydroxylation. Decomposition of [PPN][**2**−O_2CH] to **2**−CO was not observed to any extent over the course of ~5 days under 1 atm Ar, even upon extended heating to 333 K for 18 h. Likewise, [PPN][**2**−O_2CH] did not decompose to **2**−CO under an H_2 atmosphere. Therefore, it is proposed that CO_2 gas and/or excess Vkd base are required for decomposition of [**2**−O_2CH]$^-$ to **2**−CO to occur.

While the roles played by Vkd base and/or CO_2 in the decomposition reaction of [**2**−O_2CH]− to **2**−CO are unclear, it is possible that the reaction of CO_2 with [VkdH][OH] to form [VkdH][HCO_3], which is reported to be poorly soluble in THF, could help drive the reaction. However, it should be noted that bicarbonate was not definitively identified by ^{1}H NMR spectroscopy in the initial experiment, which could indicate that it does not

form to an appreciable extent, or alternatively that either [VkdH][OH] or [VkdH][HCO_3] precipitates out of solution. Additionally, excess Vkd base may play a role in promoting the reaction as well, as evidenced by the lack of decomposition of [PPN][**2**−O_2CH], albeit under an Ar atmosphere. It should be noted that Vkd base was also required for the similar reaction of NiInL (**3**) with ethyl formate to generate **3**−CO and [VkdH][OEt], although H_2 was required as well in that case. As previously mentioned, it is possible that Vkd base somehow slowly becomes oxidized in order to generate CO from CO_2. Control experiments to monitor the extent of decomposition of [PPN][**2**−O_2CH] to **2**−CO in the presence of excess Vkd base under Ar, compared with that under a CO_2 atmosphere in the absence of Vkd base, would differentiate whether excess Vkd base, CO_2, or both are required for decomposition to occur.

An additional clue to the pathway for catalyst decomposition came in the form of the detection of small peaks at ~9.35 and ~9.6 ppm by *in situ* ^{1}H NMR spectroscopy during catalytic trials, which are believed to be the attributable to [VkdH][HCO_3] and/or other bicarbonate salts. In support of this assignment, ^{13}C NMR spectra showed minor peaks at 158-159 ppm, which match reasonably well with the reported chemical shift of 157.7 ppm of [VkdH][HCO_3].[346] Although the reverse water-gas shift reaction and formate dehydroxylation, as written in Equations 5.67-5.68, do not explicitly result in the formation of bicarbonate salts, both reactions would be expected to lead to bicarbonate formation under catalytic conditions. Namely, [VkdH][OH] would be formed in both cases, from the reaction of the water formed with Vkd base in the case of the reverse water-gas shift reaction, and the subsequent reaction of hydroxide with additional CO_2 would generate [VkdH][HCO_3]. Therefore, all decomposition pathways being considered

could be expected to generate bicarbonate, with the exception of direct phosphine oxidation to give CO and $O{=}PR_3$. However, small amounts of bicarbonate were also detected in catalytic trials in which no catalyst decomposition to (OC)NiML was observed; therefore, it is more likely that the detection of small amounts of [VkdH][HCO_3] is the result of the reaction of trace amounts of water with CO_2 in the presence of Vkd base, as opposed to being related to the catalyst decomposition mechanism. Notably, the generation of bicarbonate as a byproduct under catalytic conditions was also reported by Linehan and co-workers in the $HCo(dmpe)_2$ system from residual water, likely generated primarily as a byproduct of the reverse water-gas shift reaction (Equation 5.67).[346]

In summary, formate dehydroxylation is proposed to be the predominant catalyst decomposition pathway based on the similarity of the decomposition products observed under catalytic conditions to those observed after allowing the formate adduct to sit in solution over time. One or both of Vkd base and CO_2 are required for decomposition to occur, but H_2 is not required, which indicates that the reverse water-gas shift reaction is likely not the primary contributor to the formation of CO or catalyst decomposition. Similarly, the tentative lack of correlation between the formation of carbonate or bicarbonate salts and catalyst decomposition does not support, or rule out, CO_2 disproportionation as viable catalyst decomposition pathway. Specifically, CO_2 disproportionation to CO via the oxidation of one or more of the ligand phosphines, or Vkd base, may cause catalyst decomposition to some extent, as evidenced by the formation of small amounts of Vkd(P=O) and InO_3L, along with the possibility that species **B** features oxidized phosphine donor(s). The correlation between lower catalyst

loadings and greater extent of catalyst decomposition is not well understood, but it is worth noting that the amount of CO detected by headspace GC-MS was also lower at greater catalyst loadings (Figures A.4.39 and A.4.41). Greater catalyst decomposition at lower catalyst loadings could be due to either greater sensitivity to trace impurities of H_2O and O_2, or alternatively to slower catalytic rates allowing the formate adduct catalytic resting state to be more susceptible to interception to participate in undesirable reactions which lead to catalyst decomposition. The latter explanation is supported by the dramatic dependence of catalytic performance, for a given catalyst concentration, on H_2/CO_2 gas pressure (Table 5.7).

While nearly quantitative formate yields were observed with 0.25 mM catalyst loading and 800 mM Vkd base under 34 atm of ~1:1 H_2/CO_2, reducing the pressure five-fold to 6.8 atm resulted in low yields of formate which were highly variable, at 13 (±11) turnovers (entries 1-2, Table 5.7). Likewise, a single trial at 1 atm of ~1:1 H_2/CO_2, albeit with lower base concentration, also gave poor yields of formate (entry 3, Table 5.7).

Table 5.7. Effect of H_2/CO_2 gas pressure on catalytic activity for NiGaL (**2**).[a]

Entry	[Catalyst] (mM)	[Vkd] (mM)	P(H_2/CO_2) (atm)	Formate TON[e]	% Yield Formate[f]
1[b]	0.25	800	34.0	3150 (±40)	99 (1)
2[b,c]	0.25	800	6.8	410 (±360)	13 (±11)
3[d]	0.25	500	1.0	190	10

[a]catalytic conditions: ~1:1 H_2/CO_2 mixture, 293 K, 0.30 mL THF-d_8 unless otherwise noted. All experiments were run in duplicate, unless otherwise noted, with parenthesis indicating the standard deviation in replicate trials. [b]Constant gas pressure maintained in PEEK cell by ISCO pump. [c]four trials. [d]single trial in 0.40 mL THF-d_8, re-pressurized to 1.0 atm gas pressure manually between NMR data collection (every ~6 minutes). [e]After ~24 h, based on integration of HCO_2^- resonance in ^{1}H NMR spectra relative to an internal capillary standard. [f]100% yield indicates all Vkd base consumed generates formate.

That gas pressure would lead to such a dramatic difference in catalyst performance supports the notion that elevated H_2 gas pressures promote catalytic

turnover by maximizing the ability of H_2 binding to **2** to compete with formate binding. Furthermore, the fact that catalysis at lower gas pressures is not just slower in terms of TOF, but also leads to very low final yields of formate, suggests that the catalyst likely decomposes more readily at lower gas pressures. Speculatively, this would be consistent with the idea that formate dehydroxylation occurs more readily if the formate adduct is present in solution for a greater duration before H_2 binding re-starts the catalytic cycle. Additionally, it should be noted that the residual water content in the H_2/CO_2 gas stream was measured to be significantly less using the drying apparatus for 1.0 atm gas pressure trials (~2 ppm) than for high-pressure trials (~50 ppm for 34 atm and 6.8 atm trials). This may contribute to the comparable formate yields observed at 1.0 atm and 6.8 atm gas pressures, as the higher pressure should allow for a faster rate of formate production, but the greater water content likely leads to more rapid catalyst decomposition as well compared with the 1.0 atm trial.

Unfortunately, these preliminary insights into the catalyst decomposition mechanism remain somewhat speculative and do not provide any special way by which catalyst decomposition could be minimized, since the formation of the formate adduct is a consequence of the catalytic generation of large amounts of formate product. Thus, the way to prevent catalyst decomposition would seem to be analogous to the means of improving catalytic TOF: by promoting more facile and rapid formate dissociation. In addition to minimizing the favorability of formate binding relative to H_2 binding, it seems that limiting the stability of the CO adducts also results in the catalyst being less prone to decomposition, as was observed in comparing M=Ga to M=In.

5.2.18 Adapting the Catalytic System for Electrocatalytic CO_2 Reduction

Developing molecular electrocatalysts for CO_2 reduction based on inexpensive metals has garnered increased research efforts in recent years, as it would allow electrical energy to be used along with CO_2, a renewable feedstock, to store energy until it is needed.[10] Specifically, it would entail replacing H_2 with a proton source, with the electrons provided via the application of an electrical potential. An initial observation that hinted that electrocatalytic CO_2 reduction may be feasible with the NiML complexes was the chemical reduction of NiML to $[NiML]^-$ using excess potassium graphite (KC_8) in THF. In the case of M=Ga and In, it was observed that a significant amount of the $[HNiML]^-$ complexes were generated in this reaction, which represents the net addition of a hydrogen atom to the intended product, the $[NiML]^-$ species. The propensity under reducing conditions to generate the $[HNiML]^-$ complexes, which have been shown to react with CO_2 to generate formate, suggested that NiML could potentially be competent electrocatalysts for CO_2 reduction to formate. The reduction potentials for the reduction of NiML to $[NiML]^-$ are −1.85 and −1.98 V (vs. SCE) for M=In and Ga,[97, 158] respectively, which, while not exceedingly mild, are much more favorable than that of CO_2 to $CO_2^{\bullet-}$ (−2.2 V vs. SCE).[10] These relatively harsh redox potentials will necessitate the use of weak acids in order to allow the reduction of CO_2 to outcompete the undesired reduction of protons to H_2. Alternatively, the use of hydrogen atom donors could be used to allow the generation of the reactive $[HNiML]^-$ species from $[NiML]^-$, which should be readily formed under reducing conditions.

The envisioned electrocatalytic process is shown in Figure 5.45. Initial electrochemical reduction of NiML would generate $[NiML]^-$, which would then react to

generate $[HNiML]^-$, and subsequent hydride transfer to CO_2 would generate formate and regenerate the NiML complex. The generation of the reactive $[HNiML]^-$ species from $[NiML]^-$ could take place in one of two ways: (1) reaction of $[NiML]^-$ with hydrogen atom donor reagents, or (2) initial proton transfer from a weak acid to generate HNiML, followed by subsequent electron transfer. In principle, electron transfer could precede proton transfer, but this is not feasible here because it would require generating a dianionic $[NiML]^{2-}$ species which then becomes protonated to give the $[HNiML]^-$ complex.

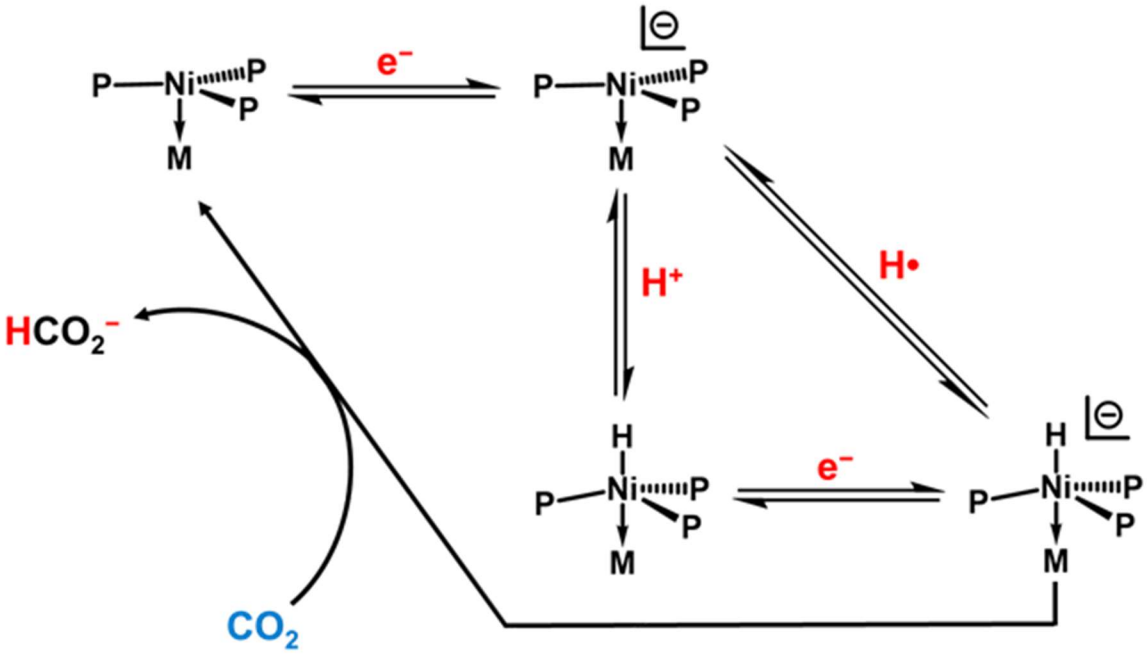

Figure 5.45. Envisioned pathway for electrocatalytic CO_2 reduction to formate mediated by NiML complexes.

In order to test the feasibility of this catalytic cycle, stoichiometric experiments were carried out to test the propensity of the $[NiML]^-$ complexes to react to generate the $[HNiML]^-$ complexes. In these reactivity studies, $[K(THF)_x][NiML]$ complexes were first generated *in situ* via the filtration of a solution of NiML in THF through a plug of excess KC_8. This method was determined to be a suitable means of synthesizing $[NiML]^-$

in yields of 60-85% for M=Al and Ga in the presence of 2,2,2-cryptand as an encapsulating agent for $[K]^+$, though it was later shown by Matt Vollmer that the radical anion complexes are isolable and stable if stored at −35°C. While the reduction potential to reduced **3** species is the mildest of the trio of NiML complexes, the resulting $[NiInL]^-$ ($[\mathbf{3}]^-$) complex has not proven amenable to characterization by EPR spectroscopy.[158] That said, the quasi-reversibility of the electrochemical reduction event for **3** at fairly mild potential (−2.34 V vs. $FeCp_2^{0/+}$) indicates that the formation of $[\mathbf{3}]^-$ should be feasible under reducing conditions, as well as that $[\mathbf{3}]^-$ is sufficiently stable, at least on the timescale of successive CV scans that is relevant to electrocatalysis.

Upon generation of $[NiML]^-$, reactions with both weak acids and hydrogen atom transfer reagents were explored to assess the propensity of $[HNiML]^-$ to form. In light of the increased stability of the anionic hydrides of M=Ga and In relative to that of M=Al (ie. larger $\Delta G°_{H-}$ values), reactivity studies were only studied for the former two supporting metals. The initial observation of the formation of $[HNiML]^-$ complexes (M=Ga, In) upon the addition of excess KC_8 to NiML in THF was determined to proceed via initial proton transfer to $[NiML]^-$, from an unknown proton source that may presumably be trace amounts of water, to generate HNiML, followed by electron transfer in the presence of excess KC_8 to form low yields of $[HNiML]^-$ complexes (10-25% yields by ^{31}P NMR spectroscopy). An alternative explanation for the formation of the $[HNiML]^-$ complexes would be hydrogen atom transfer from THF to $[NiML]^-$; however, this was ruled out because no formation of $[DNiML]^-$ was detected in THF-d_8, as well as the fact that similar yields and rates of formation of $[HNiML]^-$ were observed in both proteo-THF and THF-d_8. In retrospect, the C−H bonds in THF are on the order of ~92

kcal/mol,[384] which are much stronger than the Ni−H bonds that were forming (63-66 kcal/mol), so HAT from THF to $[NiML]^-$ would be highly unfavorable and can be ruled out as the mechanism for $[HNiML]^-$ formation in these experiments.

In light of the low yields of $[HNiML]^-$ via the apparent initial reaction with residual protons, it was hoped that the intentional addition of a weak acid could lead to improved yields of the $[HNiML]^-$ complexes, which would ideally allow for electrocatalysis to occur in the presence of weak acids. Reaction of the *in situ* generated $[\mathbf{3}]^-$ species with 1.25 equiv of the trifluoromethanesulfonate (OTf) salt of the conjugate acid of 1,8-diazabicyclo(5.4.0)undec-7-ene (DBU), [DBUH][OTf], only resulted in trace amounts of $[\mathbf{3}{-}H]^-$ forming, and instead $NiLH_3$ (**4**) was observed as the primary product by ^{31}P NMR spectroscopy. This result illustrates the challenge of adding even weak acids to the NiML complexes, as the $M{-}N_{amide}$ bonds can easily be cleaved via protonation of the amide and the loss of MX_3 species. As a result, an even weaker acid, the tetrakis(pentafluorophenyl)borate salt of the conjugate acid of Vkd base, $[VkdH][B(C_6F_5)_4]$, was utilized in electrocatalytic experiments.

The reaction of $[NiML]^-$ complexes with hydrogen atom donor reagents was also explored to assess whether this would be a feasible means of generating $[HNiML]^-$ from NiML under reducing conditions. The addition of 40 equiv tributyltin hydride to *in situ* generated $[\mathbf{2}]^-$ resulted in only ~20 % conversion of $[\mathbf{2}]^-$ to $[\mathbf{2}{-}H]^-$ after 22 h, as quantified by ^{31}P NMR spectroscopy, with other unidentified products also formed. Likewise, poor yields of the desired anionic hydride species were also observed upon the addition of excess 9,10-dihydroanthracene to *in situ* generated $[\mathbf{3}]^-$. Relative to a control experiment where no 9,10-dihydroanthracene was added, the yield of $[\mathbf{3}{-}H]^-$ only

increased from 20% to 34% upon the addition of 20 equiv 9,10-dihydroanthracene, with only ~0.2 equiv anthracene detected by ^{1}H NMR spectroscopy. Therefore, it does not seem that the formation of $[HNiML]^-$ in adequate yields via hydrogen atom transfer to the $[NiML]^-$ complexes is feasible. In retrospect, this makes sense given the fact that the Ni−H bonds in the $[HNiML]^-$ complexes have BDFE values of 63-66 kcal/mol, whereas the C−H and Sn−H bonds in 9,10-dihydroanthracene and tributyltin hydride which would need to be broken to affect the net transfer of a hydrogen atom are stronger than this, with BDFE values of 78 and 74 kcal/mol, respectively.[385-386]

In light of the inability to generate the $[HNiML]^-$ complexes via hydrogen atom transfer, electrocatalytic experiments were attempted for NiInL (**3**), with $[VkdH][B(C_6F_5)_4]$ ($pK_a^{MECN} = 33.6$)[342] employed as the proton source. Complex **3** was chosen for initial testing because $[\mathbf{3}-H]^-$ is the most stable of the anionic hydrides, and therefore would likely be the most readily formed under reducing conditions (*vide supra*). Despite its additional stability, $[\mathbf{3}-H]^-$ has been still been shown to react rapidly with CO_2 to generate formate. Additionally, the reduction potential to generate $[\mathbf{3}]^-$ is the mildest of the trio of NiML complexes,[158] which should help mitigate the competitive reduction of protons to H_2. Lastly, the pK_a of $[\mathbf{3}-H]^-$ is the lowest of the trio of anionic hydrides, which should prevent undesirable protonation of $[\mathbf{3}-H]^-$ to give $\mathbf{3}-H_2$, which is unreactive toward CO_2. All of these factors collectively were considered, with the rationale being that if electrocatalytic CO_2 reduction was not feasible with **3**, then it would likely also not be possible for the other NiML complexes.

Figure 5.46 shows the CVs obtained for various combinations of NiInL (**3**), CO_2, and $[VkdH][B(C_6F_5)_4]$ (abbrev. as $[VkdH]^+$ in Figure 5.46). The CV of **3** under an N_2

atmosphere (blue) shows the characteristic irreversible Ni(0/I) oxidation wave and quasi-reversible reduction wave which becomes more reversible at faster scan rates (which were also examined). The Ni(0/I) redox couple for $NiLH_3$ (**4**) can also be observed, indicating the presence of this species as an impurity which may be present initially in small concentration, and grows in further during the course of the CV experiments.[51] Upon the addition of ~4 equiv [VkdH][$B(C_6F_5)_4$] (orange), little change is observed, although i_{pc} for the reduction wave of **3** decreases slightly, perhaps indicating the decomposition of a small amount of **3** in the presence of [VkdH][$B(C_6F_5)_4$] (Figure 5.46).

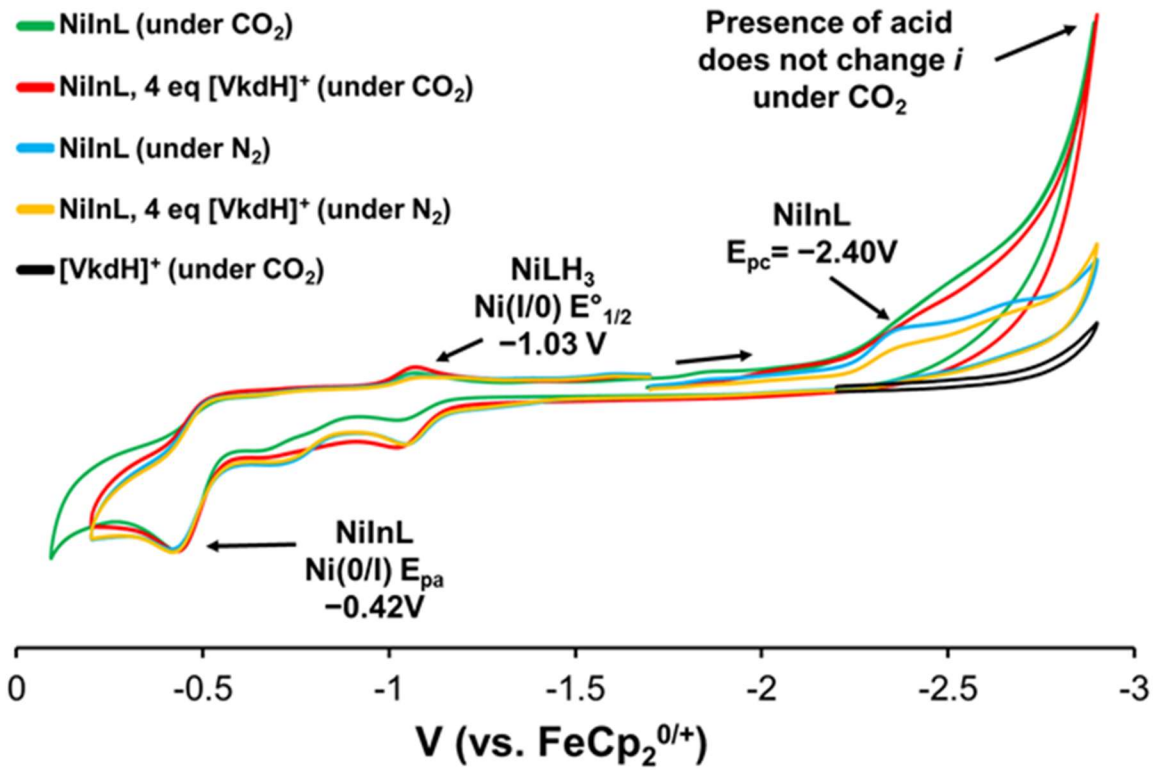

Figure 5.46. CVs obtained for various combinations of NiInL (**3**), CO_2, and [VkdH][$B(C_6F_5)_4$] in 0.1 M [TBA][PF_6] in THF at 100 mV/s.

A control experiment of just CO_2 and [VkdH][$B(C_6F_5)_4$] also showed no redox events apart from a small amount of current upon a cathodic scan to harsh potentials, which resembles the CV under CO_2 alone, but also could be attributable to onset potential

for the reduction of protons to H_2. A significant increase in current was observed upon the cathodic scan for **3** in the presence of both CO_2 and ~4 equiv [VkdH][$B(C_6F_5)_4$] (red); however, this same current profile was also observed in the absence of acid (green, Figure 5.46). The similarity of the CVs for **3** under CO_2 in both the presence and absence of acid suggests that the [**3**]$^-$ species which is generated upon electrochemical reduction reacts directly with CO_2, rather than reacting with the acid and an additional electron to form [**3**−H]$^-$. Consistent with the lack of formation of [**3**−H]$^-$, the irreversible oxidation peak for [**3**−H]$^-$ (E_{pa} = −0.98 to −1.05 V depending on the scan rate) was not observed at any scan rate examined. Thus, electrocatalytic CO_2 reduction to formate via the generation of [**3**−H]$^-$ from NiML under reducing conditions was not achieved using [VkdH][$B(C_6F_5)_4$].

In summary, even though electrocatalytic CO_2 reduction was not achieved in this system, it is worthwhile to mention a few key insights that the previously discussed thermodynamic studies have revealed about why this system is not able to mediate electrocatalysis. Figure 5.47 shows the updated electrocatalysis mechanism envisioned, with the thermodynamic values labeled to inform a brief discussion of the many problems that prevent electrocatalytic CO_2 reduction in this system. There are many issues which collectively prevent electrocatalysis from occurring. First, it turns out that the [HNiML]$^-$ complexes are more basic than the [NiML]$^-$ complexes, which was not initially expected to be the case (Figure 5.47). This is a significant issue, as this means that any weak acid which protonates [NiML]$^-$ to generate HNiML would also more readily protonate any [HNiML]$^-$ that is formed to generate the corresponding (η^2-H_2)NiML complex, which is unreactive toward CO_2.

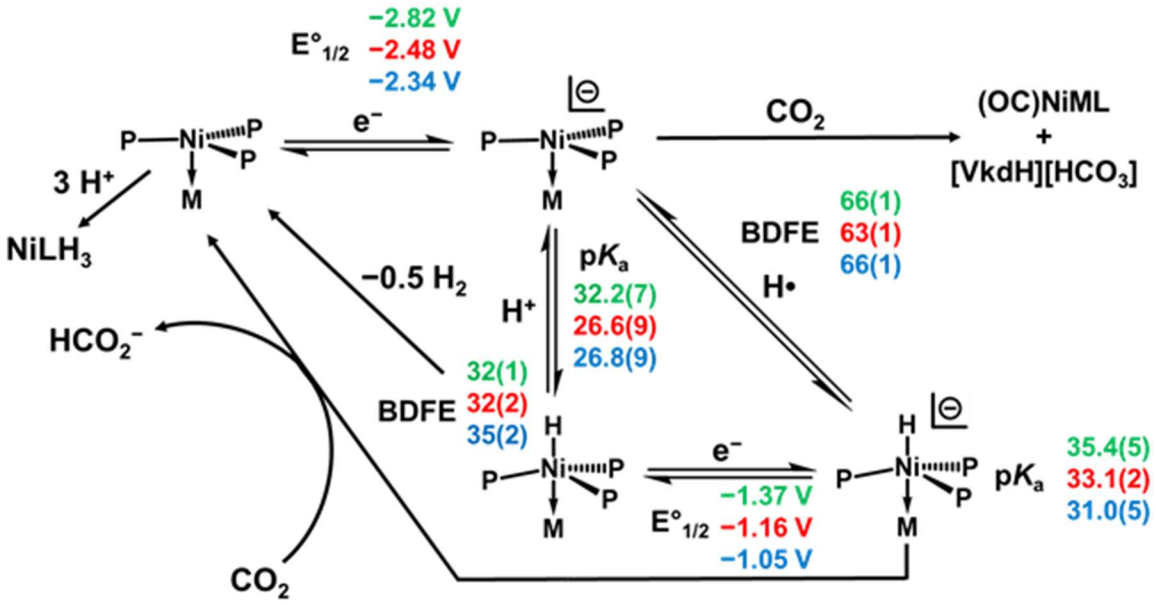

Figure 5.47. Envisioned pathway for electrocatalytic CO_2 reduction to formate mediated by NiML complexes, labeled with thermodynamic values for each step, as well as problematic side-reactions which are hypothesized to occur. The thermodynamic values are given for each supporting metal: Al (green, top), Ga (red, middle), and In (blue, bottom).

Additionally, the rapid bimolecular loss of H_2 observed upon electrochemical generation of the neutral HNiML species due to the weak Ni−H bonds does not bode well for electrocatalysis either, as H_2 loss from HNiML could potentially outcompete electron transfer to generate the $[HNiML]^-$ species. Furthermore, $[VkdH][B(C_6F_5)_4]$ (pK_a^{MECN} = 33.6) is actually too weak of an acid to readily protonate $[\mathbf{3}]^-$ (pK_a^{MECN} = 26.8), and so it is not surprising in retrospect that $[\mathbf{3}]^-$ appeared by CV to react directly with CO_2 rather than with $[VkdH][B(C_6F_5)_4]$. While further experiments with an acid of pK_a closer to that of $[\mathbf{3}]^-$ could solve this particular issue, there is nothing that suggests that the reaction of $[\mathbf{3}]^-$ with weak acid would outcompete its direct reaction with CO_2. Moreover, the dual issues of H_2 loss from **3**−H competing with electron transfer, and that of protonation of $[\mathbf{3}\text{−H}]^-$ to the unreactive **3**−H_2 complex competing with hydride transfer to CO_2, would still remain problematic. Additionally, as mentioned previously, the BDFE values of 63-

66 kcal/mol for the Ni−H bonds in the $[HNiML]^-$ complexes are not strong enough to allow for hydrogen atom transfer reagents to be utilized to enable the generation of $[HNiML]^-$ from NiML under reducing conditions. The only favorable thermodynamic consideration is that the redox potentials are such that rapid reduction of the neutral HNiML species should occur upon its initial generation, as any potential at which $[NiML]^-$ is readily formed (< −2.3 V)[97, 158] will be more than sufficient to reduce HNiML to $[HNiML]^-$ (Figure 5.47).

Lastly, two other problematic side reactions occur which consume the NiML species, thereby preventing any hope of electrocatalysis. As mentioned previously, protonation of the $M-N_{amide}$ bonds can occur in the presence of weak acid to decompose NiML to $NiLH_3$ (**4**), which has no accessible reduction event and is unreactive toward CO_2.[51, 128] Additionally, it was observed from the CV experiments that $[\mathbf{3}]^-$ appears to react with CO_2. It was discovered by Matt Vollmer that the reaction of [K(2,2,2-cryptand)][**1**] with CO_2 generates (OC)NiAlL (**1**−CO) and K_2CO_3. Thus, it is proposed that the analogous reaction likely occurred in the attempted electrocatalysis CV studies for $[\mathbf{3}]^-$, with carbonate likely reacting to form $[VkdH][HCO_3]$ in the presence of acid. While it is interesting that the $[NiML]^-$ complexes facilitate the disproportionation of CO_2 to CO and carbonate, this reaction does not have the potential to be catalytic, as CO binds strongly and irreversibly to the NiML complexes upon being generated. Clearly, there are many issues which do not allow the NiML complexes to mediate electrocatalytic CO_2 reduction, and these issues can be easily appreciated based on the thorough thermodynamic studies which have been conducted for this system. While it is not clear how these problems could all be remedied, it is hoped that some of the common

pitfalls encountered in this system could potentially inform future efforts in the group toward developing bimetallic electrocatalysts.

5.3 Conclusions

In summary, the strategy of supporting Ni with a Ga(III) metalloligand was seen to enable catalytic CO_2 hydrogenation to formate in the presence of Vkd base with TON (3150) and TOF (9700 h^{-1}) which are respectable in comparison to those of the state-of-the-art homogeneous first-row metal catalysts for this process (ie. Fe, Co). Furthermore, the catalytic performance of NiGaL (**2**) is unprecedented for Ni, and its propensity to catalyze CO_2 hydrogenation under mild conditions (1 atm gas pressure, 293 K) and without additives places it in rare company among first-row metal catalysts. The importance of the Ga(III) supporting metal to enabling catalysis was illustrated by the inability of $NiLH_3$ (**4**) to catalyze the reaction, with the addition of $GaCl_3$ to **4** also not observed to result in any appreciable yield of formate. Specifically, the Ga(III) supporting metal acts to circumvent the inherent limitations of Ni for CO_2 hydrogenation, by both inducing H_2 binding and by stabilizing an anionic Ni hydride species which is a potent hydride donor capable of reacting spontaneously with CO_2 to generate formate.[128]

The role of the supporting metal in promoting this unprecedented CO_2 hydrogenation catalytic activity for a homogeneous Ni complex was investigated further via the isolation and characterization of the reactive anionic Ni(0) hydride species, $[HNiGaL]^-$ ($[\mathbf{2}{-}H]^-$). The Ga(III) support plays a pivotal role in stabilizing $[\mathbf{2}{-}H]^-$, which is by far the strongest Ni–H donor reported to date ($\Delta G°_{H^-} \approx 31$ kcal/mol) and on par with the most hydridic first-row metal hydrides and many precious metal hydrides. The Ga(III) support likely stabilizes $[\mathbf{2}{-}H]^-$ by attenuating the electron density of the

highly reduced, anionic Ni(0)−H moiety, as evidenced by the cooperative structural rearrangement of the Ni−Ga unit where Ga is repositioned dramatically and forms a stronger interaction with Ni upon the introduction of the hydride ligand at Ni. Two complementary σ-donation interactions, that from the hydride to Ni and that from Ni to Ga, are proposed to reinforce each other and be critical to the stability of the anionic hydride, just as was proposed for the (η^2-H_2)NiML complexes in chapter 3. The stability of [**2**−H]$^-$ as a d^{10} anionic hydride was initially surprising, and CASSCF calculations show five occupied Ni 3*d* orbitals and indicate that Ni(0)−H bonding occurs through the interaction of the hydride ligand with an orbital that has primarily Ni 4p_z and Ga p_z/*s* character and resembles the LUMO of NiML.[128]

Stoichiometric reactivity studies showed that: (1) [**2**−H]$^-$ can be formed from **2** and H_2 in the presence of Vkd, (2) [**2**−H]$^-$ reacts readily with CO_2 to generate the anionic formate adduct, [(η^1-HCO_2)NiGaL]$^-$ ([**2**−O_2CH]$^-$), and (3) that exposure of [**2**−O_2CH]$^-$ to H_2 in the presence of Vkd regenerates [**2**−H]$^-$. From these observations, a simple catalytic mechanism was proposed with four steps: (1) H_2 binding to **2** forms **2**−H_2, (2) deprotonation by base generates [**2**−H]$^-$, (3) hydride transfer to CO_2 forms [**2**−O_2CH]$^-$, and (4) liberation of formate regenerates **2**. Computational studies proved useful for understanding a few key catalytic nuances. Formate assistance in the deprotonation of **2**−H_2 substantially lowers the barrier (by ~23.5 kcal/mol) relative to direct deprotonation by Vkd, and so once formate is formed it is proposed to act as a proton shuttle between **2**−H_2 and Vkd. After deprotonation to form [**2**−H]$^-$, outer-sphere hydride transfer to CO_2 is predicted to be the favored pathway, with an η^1-H formate adduct formed initially that rearranges to give the more stable η^1-O formate adduct. The experimental observation by

in situ 3^1P NMR spectroscopy that the formate adduct is the catalytic resting state throughout catalysis suggests that formate dissocation, which is required to allow H_2 to bind and catalysis to continue, is the RDS.[128-129]

Formate binding was experimentally determined to be 6.6(8) kcal/mol more favorable than H_2 binding by indirect measurements in which CH_3CN was utilized as an intervening ligand which has measurable binding equilibria with both H_2 and formate. This large difference in binding energy is consistent with ligand substitution of H_2 for formate limiting the rate of catalysis. Furthermore, one strategy which could be employed for promoting formate liberation is the addition of $[Li]^+$ additives, which are known to facilitate formate dissociation by engaging in strong ion-pairing interactions with formate and have been shown to dramatically improve catalytic performance by Hazari and Bernskoetter for highly-active Fe and Co pincer catalysts.[321-322] A stoichiometric experiment illustrated the potential of applying this strategy to our system, as the addition of CO_2 to $[Li(THF)_x][\mathbf{2}{-}H]$ resulted in the formation of **2** and $[Li][HCO_2]$, whereas the analogous reaction with $[VkdH]^+$ and $[PPN]^+$ cations resulted in formate remaining coordinated to Ni in the $[cation][\mathbf{2}{-}O_2CH]$ complexes. The effects of ion-pairing and the potential presence of hydrogen bonding interactions were explored for two key intermediates in the catalytic cycle $[VkdH][\mathbf{2}{-}H]$ and $[\mathbf{2}{-}O_2CH]^-$ complexes, with ambiguous results.

The effect of varying the supporting metal on the propensity to stabilize anionic Ni(0) hydride species was also explored, with $[HNiAlL]^-$ ($[\mathbf{1}{-}H]^-$) and $[HNiInL]^-$ ($[\mathbf{3}{-}H]^-$) synthesized in the same manner as $[\mathbf{2}{-}H]^-$. X-ray crystallography showed a similar cooperative structural rearrangement for these species upon the introduction of

the hydride to NiML as was seen for [**2**−H]$^-$, with Al and In both repositioned by twice the change in the position of Ni and slight contractions in the Ni→M bond observed in both cases. Electrochemistry studies of the [HNiML]$^-$ complexes show an irreversible oxidation event which shifts to harsher potentials as the supporting metal is varied down group 13, with the irreversibility proposed to be the result of bimolecular H_2 loss from the neutral HNiML species which are initially formed upon oxidation. [**1**−H]$^-$ and [**3**−H]$^-$ were able to be generated from H_2 and base, and probing the H_2 heterolysis reaction with various bases allowed for estimation of the pK_a and $\Delta G°_{H-}$ values. A wide range of ~4.5 pK_a units and ~11 kcal/mol was observed for the pK_a and $\Delta G°_{H-}$ values for the [HNiML]$^-$ complexes, respectively, upon variation of the supporting metal down group 13 from Al to In, illustrating the dramatic effect of the supporting metal on reactivity occurring at the Ni center. The relative values of pK_a (Al > Ga > In) and $\Delta G°_{H-}$ (In > Ga > Al) for the [HNiML]$^-$ complexes correlate well with the electron-richness of the Ni center, as judged by the Ni(I/0) redox couple of the NiML complexes. Notably, [**1**−H]$^-$ is the most potent hydride donor reported of any metal hydride complex, and is on par with the hydricity of [BEt_3H]$^-$ ($\Delta G°_{H-}$ ~ 26 kcal/mol).

A comprehensive thermodynamic scheme was constructed for each supporting metal, which allowed for the elucidation of several important considerations regarding the reactivity of the NiML complexes. First, both the [HNiML]$^-$ and (η^2-H_2)NiML complexes are poor hydrogen atom transfer reagents, with $\Delta G°_{H\bullet}$ values ranging from 63-66 kcal/mol and 70-72 kcal/mol, respectively, depending on the supporting metal. Instead, the [HNiML]$^-$ complexes prefer to donate a hydride ion ($\Delta G°_{H-}$ = 26-37 kcal/mol) and the (η^2-H_2)NiML complexes prefer to donate a proton ($\Delta G°_{H+}$ = 42-49

kcal/mol) to form the $[HNiML]^-$ complexes. Additionally, the neutral HNiML complexes form such weak Ni−H bonds (32-35 kcal/mol) that they rapidly decompose via bimolecular H_2 loss upon electrochemical oxidation of the $[HNiML]^-$ complexes. Other interesting findings include that the H−H bond of H_2 is weakened by ~32 kcal/mol upon binding to the NiML complexes, the $[NiML]^-$ complexes are less basic than the $[HNiML]^-$ complexes by 3-6 pK_a units, and that reducing the HNiML species by one electron to the $[HNiML]^-$ complexes lowers the hydricity by 13-15 kcal/mol. Overall, the BDFE values do not vary by much as a function of the supporting metal (< 3 kcal/mol in all cases). This lack of variation in the BDFE values, despite the fact that large variations in pK_a, $\Delta G°_{H-}$, and $E°_{1/2}$ values are observed for different supporting metals, illustrates the compensation effects of the various components of a net hydrogen atom transfer (ie. H^+ and e^-, $H:^-$ and loss of e^-, etc.). The thorough thermodynamic understanding of the reactivity in this system also allows the failure of the system to be adapted for electrocatalytic CO_2 reduction to be easily understood.

With a range of different hydride donor strengths afforded by variation of the supporting metal, the catalytic activity of **1**, **2**, and **3** for CO_2 hydrogenation was compared. Catalytic trials under 1 atm of ~1:1 H_2/CO_2 at 293 K established the relative order of catalytic activity to be: Ga > In > Al >> no supporting metal. This ordering can be understood by considering the relative thermodynamic favorability of each step in catalysis. $NiLH_3$ (**4**) is unable to bind H_2 or stabilize an anionic hydride species, which results it being catalytically inactive. For NiAlL (**1**), H_2 binding and deprotonation are the least favorable of the NiML complexes, meaning that it is difficult to generate the reactive anionic hydride species, $[\mathbf{1}{-}H]^-$. The thermodynamic favorability of H_2 binding,

deprotonation, and hydride transfer from $[HNiML]^-$ to CO_2 for M=Ga are all intermediate relative to those for M=In and M=Al. Thus, each step is well-matched in energy and no step is too difficult for catalysis with NiGaL (**2**), which may be a contributing factor to its superior catalytic performance relative to the other NiML complexes.

Nevertheless, it is not immediately clear why **2** is a better catalyst than **3**. H_2 binding and deprotonation to form the anionic hydride species are both more favorable for **3** than **2**, and $[\mathbf{3}{-}H]^-$ is still a potent enough hydride donor to react rapidly with CO_2. The key differences lie in the thermodynamics and kinetics of formate dissociation: the rate-limiting substitution of H_2 for formate is predicted to be more unfavorable for **3** (8.6 ± 1.2 kcal/mol) than for **2** (6.6 ± 0.8 kcal/mol), and the ligand exchange rate for the similar substitution of CH_3CN for formate was estimated to proceed ~100 times faster for **2** than for **3**. Additionally, catalyst decomposition to the inactive (OC)NiML complexes, which likely occurs primarily via a formate dehydroxylation mechanism, was found to occur more readily under analogous conditions for **3** than for **2**, consistent with the more favorable binding energy of CO to **3**. This increased catalyst robustness for **2** compared with **3** was observed to result in dramatically better performance by **2** at the low catalyst loadings utilized at high pressures.

Overall, the detailed mechanistic and thermodynamic studies of CO_2 hydrogenation catalyzed by the NiML complexes have highlighted the importance of the supporting metal for enabling catalysis not otherwise possible for a similarly ligated Ni center. The specific roles of the supporting metal in stabilizing key catalytic intermediates have been elucidated, and the relative catalytic activities of various metal-

metal combinations are now well understood based on the thermodynamic favorability and kinetic rates of the fundamental steps in the catalytic mechanistic. One of the more hopeful goals of investigating the homogeneous catalytic performance and the mechanism for various metal-metal combinations is that understanding the role of both metals and the metal-metal interaction in the reactivity could inform future *a priori* choices of metal-metal pairings in rationally designing catalysts, both homogeneous and heterogeneous, for specific applications. With this aim in mind, it should be noted that Ni−Ga pairings have been shown to be excellent heterogeneous catalysts for CO_2 reduction to methanol,[387-392] as well as alkyne semi-hydrogenation,[393] as well as that Ga as a supporting metal has proven critical for the selectivity of multimetallic heterogeneous catalysts for unpublished alkyne semihydrogenation in our laboratory.

Furthermore, the high level of detail with which this NiML system was able to be studied has allowed for the identification of a few ways by which catalytic performance could be improved in future homogeneous systems: (1) minimizing the binding energy of both formate and CO relative to H_2 and/or utilizing $[Li]^+$ additives to promote more facile formate dissociation; (2) lowering the pK_a of the H_2 adduct to allow for the use of weaker and less expensive bases, which could be accomplished with more electron-poor phosphine substitutents or by installing electron-withdrawing groups on the aryl rings of the ligand base; (3) utilizing less bulky phosphine substituents to allow for more facile access to the metal center for exogenous base and CO_2. Collectively, the results presented in this chapter demonstrate that group 13 metalloligands exert a dramatic tuning effect on the reactivity of proximal Ni(η^2-H_2) and Ni−H species, which can be rationally applied to enable unprecedented CO_2 hydrogenation activity for a homogeneous Ni catalyst.

5.4 Experimental Section

5.4.1 Synthetic Considerations

Unless otherwise stated, all manipulations were performed under a dinitrogen or argon atmosphere inside a glovebox or using standard Schlenk techniques. Standard solvents were deoxygenated by sparging with N_2 and dried by passing through activated alumina columns of a SG Water solvent purification system. Deuterated solvents and D_2 gas were purchased from Cambridge Isotope Laboratories, Inc., degassed via freeze-pump-thaw cycles, and either stirred with NaK and distilled, or stored over activated 4 Å molecular sieves. H_2, CO_2 and a ~1:1 H_2/CO_2 gas mixture were purchased from Matheson. CO_2 and H_2/CO_2 gas was passed through an Agilent Oxygen Moisture Trap (Model #OT-2-SS) drying column to minimize residual oxygen and moisture in the gas stream. GC-MS analysis showed the mixture used for catalysis to be 48% H_2 and 52% CO_2 (~1:1 H_2/CO_2) after passing through the drying column. The neutral ligand (N(*o*-$(NHCH_2P^iPr_2)C_6H_4)_3$ (abbreviated as H_3L), NiAlL (1), NiGaL (**2**), NiInL (**3**), and $NiLH_3$ (**4**) were synthesized according to literature procedure. *t*-Butyl tetramethylguanidine (abbreviated as tBuTMG), 2,8,9-triisopropyl-2,5,8,9-tetraaza-1-phosphabicyclo[3,3,3]undecane (Verkade's base, abbreviated as Vkd), and bis(triphenylphosphoranylidene)ammonium chloride (abbreviated as PPN·Cl) were purchased from Aldrich and used as received. $HM(dmpe)_2$, and $[M(dmpe)_2]^+$ complexes (M=Co, Rh) were synthesized according to literature procedures.[351-352] [VkdH][$B(C_6F_5)_4$] was synthesized via salt metathesis with [VkdH][HCO_2], which was synthesized according to literature procedure.[346] Other organic bases were either synthesized by Matt Vollmer or purchased. All other reagents were purchased from commercial vendors and

used without purification unless otherwise noted. Elemental analyses were performed by Robertson Microlit Laboratories (Ledgewood, NJ).

Synthesis of New Complexes

*Synthesis of [N(P(C$_6$H$_5$)$_3$)$_2$][HNiGaL] ([PPN][**2**−H])*. A stirring solution of NiGaL (**2**, 114 mg, 138 μmol) in 8 mL THF was cooled to –78˚C under argon over 15 min. To this solution, 62.4 μL (156 μmol) of *n*BuLi solution (2.5 M in hexanes) was added, and the color rapidly changed from deep red to red–yellow. This solution was allowed to warm to rt over the course of 12 h. Subsequent salt exchange was performed by adding solid [bis(triphenylphosphoranylidene)ammonium][tetrakis{3,5-bis(trifluoromethyl)phenyl}borate] ([PPN][BArF], 415 mg, 283 μmol), and the solution was concentrated *in vacuo*, resulting in precipitation of solids. Diethyl ether was added until the total volume was ~20 mL and the mixture was stirred vigorously for 3 h, affording a bright yellow precipitate. This precipitate was collected by filtration and washed with diethyl ether (2 x10 mL) to give [PPN][**2**−H] as a bright yellow powder (101 mg, 731 μmol, 40% yield). Single crystals of [PPN][**2**−H] suitable for X-ray diffraction were grown by layering a THF solution with pentane. Additionally, the analogous deuteride complex, [PPN][**2**−D], was synthesized *in situ* by overnight exposure of [PPN][**2**−H] (10 mg, 7.4 μmol) to D_2 (4 atm) in THF-d$_8$ (298 K) in a J. Young NMR tube. ^{1}H{^{31}P} NMR (ppm, THF-d$_8$, 400 MHz): 7.62 (t, *J*=7.4 Hz, [PPN]$^+$, 6H), 7.56 (d, *J*=7.7 Hz, [PPN]$^+$, 12H), 7.44 (t, *J*=7.5 Hz, [PPN]$^+$, 12H), 7.12 (d, *J*=7.4 Hz, aryl, 3H), 6.56 (t, *J*=7.5 Hz, aryl, 3H), 6.14 (d, *J*=7.9 Hz, aryl, 3H), 5.94 (t, *J*=7.3 Hz, aryl, 3H), 2.60 (br, C*H*$_2$P(^{i}Pr)$_2$, 6H), 1.77 (br, C*H*(CH$_3$)$_2$, 3H), 1.56 (br, C′*H*(CH$_3$)$_2$, 3H), 1.05−0.60 (br, CH(*CH$_3$*)$_2$, 36H), −6.45 (br, Ni*H*, 1H, T_1(min)≤0.84(4) s at 233K).

$^{31}P\{^{1}H\}$ NMR (ppm, THF-d_8, 162 MHz): 75.3 (s, 3P, $[HNiGaL]^-$), 21.0 (s, 2P, $[PPN]^+$). IR (KBr pellet, cm^{-1}): ν(Ni−H) = 1696 (1226 for [PPN][**2**−D]). Anal. calcd for [PPN][**2**−H], $[C_{36}H_{30}NP_2][C_{39}H_{61}N_4P_3NiGa]$ (%): C, 66.93; H, 6.82; N, 5.20. Anal. calcd for [PPN][**2**−H]·O_2 (%): C, 65.38; H, 6.66; N, 5.08. Found: C, 65.24; H, 6.90; N, 4.86. Elemental analysis consistently showed a low carbon percentage that could be consistent with oxidation by one equiv of O_2.

*Syntheses of [cation][HNiGaL] ([cation][**2**−H], where cation = Li, Na, K, and VkdH)*. Various [cation][**2**−H] compounds can be prepared via two routes: (1) addition of 1 equiv $MBHEt_3$ to NiGaL (**2**) in THF yielded $[M(THF)_x]$[**2**−H] (M = Li, Na, and K); or (2) addition of H_2 (1 atm) and Verkade's base (>3 equiv) to **2** in THF generated [VkdH][**2**−H] *in situ*. In the case of $[M(THF)_x]$[**2**−H], the product was isolated by washing with hexanes to separate BEt_3, followed by extraction into THF and drying *in vacuo*. ^{1}H and ^{31}P NMR chemical shifts of [cation][**2**−H] show minimal perturbation upon substitution of the cation (Figure 5.4). For *in situ* generation of [VkdH][**2**−H]: $^{1}H\{^{31}P\}$ NMR (ppm, THF-d_8, 400 MHz, 253K): 7.25 (d, *J*=7.4 Hz, aryl, 3H), 6.70 (t, *J*=7.5 Hz, aryl, 3H), 6.21 (d, *J*=7.7 Hz, aryl, 3H), 6.09 (t, *J*=7.4 Hz, aryl, 3H), 4.81 (s, $[VkdH]^+$, ~1H), 3.52 (br, $CH(CH_3)_2$ of $[VkdH]^+$, overlapped with THF), 2.57-2.46 ($CH_2P(^iPr)_2$ & CH_2 peaks of $[VkdH]^+$, overlapped with excess Vkd), 1.96 (br, $CH(CH_3)_2$, 3H), 1.77 (br, $C'H(CH_3)_2$, 3H), 1.65 (br, CH_3 of $[VkdH]^+$, 9H), 1.25 (br, CH_3, 9H), 1.09 (br, $C'H_3$ of $[VkdH]^+$, overlapped with Vkd), 0.99 (br, $C'H_3$, 9H), 0.90 (br, $C''H_3$, 9H), 0.54 (br, $C'''H_3$, 9H), −6.45 (br, Ni*H*, 1H, T_1(min) ≤ 0.28(7) *s* at 193K). (Note: peaks for excess free Vkd base and H_2 are also observed). $^{31}P\{^{1}H\}$ NMR (ppm, THF-d_8, 162

MHz): 75.6 (s, 3P, [**2**−H]$^-$), −11.8 (s, 1P, [VkdH]$^+$). (Note: excess free Vkd base observed as singlet at 119.0 ppm).

*Synthesis of [N(P(C$_6$H$_5$)$_3$)$_2$][(η^1-HCO$_2$)NiGaL] ([PPN][**2**−O$_2$CH])*. A sealable Schlenk tube containing a solution of [PPN][**2**−H] (43 mg, 32 μmol) in ca. 10 mL THF was subjected to a single freeze–pump–thaw cycle. The tube was refilled with CO_2 (1 atm) that had been dried through a CO_2 drying column (Alltech Associates), which had been pre-sparged with ultra-high purity argon. Upon exposure to CO_2, the solution color rapidly turned from yellow to orange. Upon allowing it to stir for 15 minutes and drying *in vacuo*, the title compound was generated (32 mg, 72% yield). Single crystals of [PPN][**2**−O$_2$CH] suitable for X-ray diffraction were grown by layering a THF solution with pentane. Additionally, the analogous ^{13}C-labeled complex, [PPN][**2**−O$_2{}^{13}$CH], was synthesized *in situ* in an identical manner by exposure of [PPN][**2**−H] to $^{13}CO_2$ (1 atm) in THF-d$_8$ (298 K) in a J. Young NMR tube. ^{1}H{^{31}P} NMR (ppm, THF-d$_8$, 400 MHz): 8.57 (s, (*H*CO$_2$)NiGaL, 1H), 7.64 (t, *J*=7.3 Hz, [PPN]$^+$, 6H), 7.58 (d, *J*=7.6 Hz, [PPN]$^+$, 12H), 7.47 (t, *J*=7.6 Hz, [PPN]$^+$, 12H), 7.06 (d, *J*=7.4 Hz, aryl, 3H), 6.64 (t, *J*=7.4 Hz, aryl, 3H), 6.19 (d, *J*=7.8 Hz, aryl, 3H), 6.05 (t, *J*=7.2 Hz, aryl, 3H), 2.95 (br, C*H*H′P(^{i}Pr)$_2$, 3H), 2.81–2.79 (br, overlapping C*H*(CH$_3$)$_2$ and CH*H*′P(^{i}Pr)$_2$, 6H), 2.15 (br, C′*H*(CH$_3$)$_2$, 3H), 1.28 (br, CH(*CH$_3$*)$_2$, 18H), 1.04 (br, C′*H*$_3$, 9H), 0.87 (br, C″*H*$_3$, 9H). ^{31}P{^{1}H} NMR (ppm, THF-d$_8$, 162 MHz): 34.8 (s, 3P, [(HCO$_2$)NiGaL]$^-$), 21.0 (s, 2P, [PPN]$^+$). ^{13}C{^{1}H} NMR (ppm, THF-d$_8$, 125.7 MHz): 167.6 (s, (H*C*O$_2$)NiGaL). IR (KBr pellet, cm^{-1}): ν(C=O) = 1610 (1565 for [PPN][**2**−O$_2{}^{13}$CH]). Anal. calcd for [PPN][**2**−O$_2$CH], [C$_{36}$H$_{30}$NP$_2$][C$_{40}$H$_{61}$O$_2$N$_4$P$_3$NiGa] (%): C, 65.68; H, 6.60; N, 5.04. Found: C, 65.54; H, 6.56; N, 5.02.

*In situ syntheses of [$C_{15}H_{33}N_4PH$][(η^1-HCO_2)NiGaL] ([VkdH][**2**−O_2CH])*. NiGaL (**2**, 5 mg, 6.2 μmol) and an excess (~5 equiv) of Vkd base (9.4 mg, 31 μmol) were dissolved in THF-d_8, transferred to a J. Young NMR tube, and exposed to H_2 (1 atm) to generate [VkdH][**2**−H] (red-orange solution) *in situ*. A freeze-pump-thaw cycle was performed, followed by exposure to CO_2 (1 atm) that had been dried through a CO_2 drying column (Alltech Associates) to generate [VkdH][**2**−O_2CH] (orange solution) *in situ*. Alternatively, [VkdH][**2**−O_2CH] was synthesized via addition of an excess (~4 equiv) of [VkdH][HCO_2] (7.7 mg, 22 μmol) to **2** (4.5 mg, 5.6 μmol) in 0.5 mL THF-d_8 solution, and the resultant NMR spectrum was consistent with [VkdH][**2**−O_2CH]. Of note, the addition of a single equiv of [VkdH][HCO_2] to **2** resulted in considerable formation of [VkdH][**2**−H] (as observed by ^{31}P NMR spectroscopy), which presumably formed from [VkdH][**2**−O_2CH] via CO_2 loss (as detected by GC-MS analysis of headspace). ^{1}H{^{31}P} NMR (ppm, THF-d_8, 500 MHz): 8.68 (s, coordinated *H*CO_2, 1H), 7.12 (d, *J*=7.9 Hz, aryl, 3H), 6.71 (t, *J*=7 Hz, aryl, 3H), 6.22 (d, *J*=6.7 Hz, aryl, 3H), 6.14 (t, *J*=6.7 Hz, aryl, 3H), 5.52 (d, J_{HP}=495 Hz, [Vkd*H*]$^+$, 1H), ~3.6 (br, C*H*$(CH_3)_2$ of [VkdH]$^+$, overlapped with THF), 3.52 (br, C*H*H' of [VkdH]$^+$, 6H), 3.05 (br, CH*H'* of [VkdH]$^+$, 6H), ~3.05 (br, C*HH'*P(^{i}Pr)$_2$, 3H, overlapping with [VkdH]$^+$ CH_2 peak), 2.87 (br, C*HH'*P(^{i}Pr)$_2$, 3H), 2.70−2.50 (br, CH_2 of Vkd, [VkdH]$^+$ & C*H*$(CH_3)_2$, 15H), 2.31, 2.20 (br, C'*H*$(CH_3)_2$, 6H), 1.30−0.92 (CH_3's of L, [VkdH]$^+$, overlapped with CH_3's excess of either Vkd or [VkdH][HCO_2] depending on synthetic method).

Note: Proton resonances for excess Vkd base were observed at 3.3, 2.7, and 1.1 ppm in the case of the *in situ* synthesis of [VkdH][**2**−O_2CH] from [VkdH][**2**−H]. In the alternative synthesis, peaks for [VkdH][HCO_2] overlapped with those of

[VkdH][**2**−O_2CH] in the aliphatic region. The spectra observed for [VkdH][**2**−O_2CH] matched closely by way of both synthetic routes. The peak for coordinated *H*CO_2 was shifted slightly upfield (8.68 ppm) compared to an NMR sample of pure [VkdH][HCO_2] (*c.f.* 8.79 ppm for *H*CO_2).[346] In the alternative synthesis with excess [VkdH][HCO_2] + **2**, the coordinated formate resonance appears at 8.70 ppm and is much more broad than in the synthesis from [VkdH][**2**−H] + CO_2. This broadening may arise due to an exchange equilibrium under these conditions between free and coordinated formate (i.e. between [VkdH][HCO_2] and [VkdH][**2**−O_2CH]). $^{31}P\{^1H\}$ NMR (ppm, THF-d_8, 162 MHz): 34.7 (s, 3P, [**2**−O_2CH]$^-$), −13.5 (s, P, [VkdH]$^+$).

*Synthesis of [N(P(C$_6$H$_5$)$_3$)$_2$][HNiAlL]$^-$ ([PPN][**1**−H])*. A stirring solution of NiAlL (**1**, 65.5 mg, 85.8 μmol) in ~8 mL THF was cooled to –78˚C under argon over 15 min. To this solution, 38 μL (95 μmol) of *n*BuLi solution (2.5 M in hexanes) was added, and the color rapidly changed from brown to yellow. This solution was allowed to warm to rt over the course of 12 h. Subsequent salt exchange was performed by adding 1.5 equiv solid [bis(triphenylphosphoranylidene)ammonium][tetrakis{3,5-bis(trifluoromethyl)phenyl}borate] ([PPN][BArF]), and the solution was concentrated *in vacuo*, resulting in precipitation of solids. Diethyl ether was added until the total volume was ~15 mL and the mixture was stirred vigorously for ~2 h, affording a bright yellow precipitate. This precipitate was collected by filtration and washed with diethyl ether (2 x10 mL) to give [PPN][**1**−H] as a bright yellow powder (27.2 mg, 20.9 μmol, 24% yield). Single crystals of [PPN][**1**−H] suitable for X-ray diffraction were grown by layering a THF solution with pentane. In light of the low yield of [PPN][**1**−H], an alternative synthesis of [P$_4$*t*BuH][**1**−H] was developed that involves the exposure of **1** and P$_4$*t*Bu

base in THF to an H_2 atmosphere. $^1H\{^{31}P\}$ NMR (ppm, THF-d_8, 400 MHz): 7.62 ($[PPN]^+$, 6H), 7.56 ($[PPN]^+$, 12H), 7.44 ($[PPN]^+$, 12H), 7.15 (d, *J*=7.3 Hz, aryl, 3H), 6.62 (t, *J*=7.4 Hz, aryl, 3H), 6.17 (d, *J*=7.8 Hz, aryl, 3H), 5.99 (t, *J*=7.3 Hz, aryl, 3H), 2.66 (br, C*H*$_2$P(^{i}Pr)$_2$, 6H), 1.75 (br and overlapping with THF, C*H*(CH_3)$_2$, 6H), 1.05 (br, CH(*CH*$_3$)$_2$, 36H), −5.35 (q, J_{HP}=37.5 Hz at ~213 K, Ni*H*, 1H). $^{31}P\{^1H\}$ NMR (ppm, THF-d_8, 162 MHz): 64.8 (s, 3P, $[HNiAlL]^-$), 21.0 (s, 2P, $[PPN]^+$).

*Synthesis of [N(P(C$_6$H$_5$)$_3$)$_2$][HNiInL] ([PPN][**3**−H])*. A stirring solution of NiInL (**3**, 160.9 mg, 189 μmol) in ~12 mL THF was cooled to –78˚C under argon over 15 min. To this solution, 85 μL (213 μmol) of *n*BuLi solution (2.5 M in hexanes) was added, and the color rapidly changed from deep red to yellow-orange. This solution was allowed to warm to rt over the course of 12 h. Subsequent salt exchange was performed by adding 1.5 equiv solid [bis(triphenylphosphoranylidene)ammonium][tetrakis{3,5-bis(trifluoromethyl)phenyl}borate] ([PPN][BArF]), and the solution was concentrated *in vacuo*, resulting in precipitation of solids. Diethyl ether was added until the total volume was ~20 mL and the mixture was stirred vigorously for ~3 h, affording a bright yellow precipitate. This precipitate was collected by filtration and washed with diethyl ether (2 x10 mL) to give [PPN][**3**−H] as a bright yellow powder (197.8 mg, 142 μmol, 75% yield). Single crystals of [PPN][**3**−H] suitable for X-ray diffraction were grown by layering a THF solution with pentane. $^1H\{^{31}P\}$ NMR (ppm, THF-d_8, 400 MHz): 7.62 ($[PPN]^+$, 6H), 7.56 ($[PPN]^+$, 12H), 7.44 ($[PPN]^+$, 12H), 7.22 (d, *J*=7.5 Hz, aryl, 3H), 6.57 (t, *J*=7.5 Hz, aryl, 3H), 6.16 (d, *J*=7.9 Hz, aryl, 3H), 5.91 (t, *J*=7.3 Hz, aryl, 3H), 2.71 (br, C*H*$_2$P(^{i}Pr)$_2$, 6H), 1.83 (br, C*H*(CH_3)$_2$, 6H), 1.07 (br, CH(*CH*$_3$)$_2$, 36H), −6.17 (br, Ni*H*,

1H). $^{31}P\{^{1}H\}$ NMR (ppm, THF-d_8, 162 MHz): 82.5 (s, 3P, $[HNiInL]^-$), 21.0 (s, 2P, $[PPN]^+$).

*Synthesis of [N(P(C$_6$H$_5$)$_3$)$_2$][(η^1-HCO$_2$)NiAlL] ([PPN][**1**−O$_2$CH])*. A J. Young tube containing a solution of [PPN][**1**−H] (4.6 mg, 3.5 μmol) in ca. 0.45 mL THF was subjected to a single freeze–pump–thaw cycle. The tube was re-filled with CO_2 (1 atm) that had been dried through a CO_2 drying column (Alltech Associates), which had been pre-sparged with ultra-high purity argon. Upon exposure to CO_2, the solution color rapidly turned from yellow to mahogany-brown, and the title compound was generated in quantitative yield based on NMR spectroscopy. $^{1}H\{^{31}P\}$ NMR (ppm, THF-d_8, 400 MHz): 8.72 (s, (*H*CO$_2$)NiAlL, 1H), 7.68 ($[PPN]^+$, 6H), 7.64 ($[PPN]^+$, 12H), 7.51 ($[PPN]^+$, 12H), 7.21 (d, *J*=7.4 Hz, aryl, 3H), 6.79 (t, *J*=7.4 Hz, aryl, 3H), 6.24 (d, *J*=7.9 Hz, aryl, 3H), 6.22 (t, aryl, 3H), 3.14 (br, C*H*H′P(^{i}Pr)$_2$, 3H), 2.99 (br, C*H*H′P(^{i}Pr)$_2$, 3H), 2.66 (br, C′*H*(CH$_3$)$_2$, 3H), 2.21 (br, C′*H*(CH$_3$)$_2$, 3H), 1.31 (br, CH(*CH$_3$*)$_2$, 18H), 1.11 (br, C′*H*$_3$, 9H), 0.93 (br, C″*H*$_3$, 9H). $^{31}P\{^{1}H\}$ NMR (ppm, THF-d_8, 162 MHz): 29.4 (s, 3P, $[(HCO_2)NiAlL]^-$), 21.0 (s, 2P, $[PPN]^+$).

*Synthesis of [N(P(C$_6$H$_5$)$_3$)$_2$][(η^1-HCO$_2$)NiInL] ([PPN][**3**−O$_2$CH])*. A J. Young tube containing a solution of [PPN][**3**−H] (6.5 mg, 4.7 μmol) in ca. 0.45 mL THF was subjected to a single freeze–pump–thaw cycle. The tube was re-filled with CO_2 (1 atm) that had been dried through a CO_2 drying column (Alltech Associates), which had been pre-sparged with ultra-high purity argon. Upon exposure to CO_2, the solution color rapidly turned from yellow to orange, and the title compound was generated in quantitative yield based on NMR spectroscopy. Alternatively, [VkdH][**3**−O$_2$CH] was

generated *in situ* by the addition of ~4 equiv [VkdH][HCO_2] to **3** in THF. $^1H\{^{31}P\}$- NMR (ppm, THF-d_8, 400 MHz): 8.72 (s, (HCO_2)NiInL, 1H), 7.65 (t, *J*=7.4 Hz, $[PPN]^+$, 6H), 7.59 (m, $[PPN]^+$, 12H), 7.48 (td, *J*=7.7 Hz and 3.2 Hz, $[PPN]^+$, 12H), 7.05 (d, *J*=7.6 Hz, aryl, 3H), 6.63 (t, *J*=7.7 Hz, aryl, 3H), 6.20 (d, *J*=7.6 Hz, aryl, 3H), 5.98 (t, *J*=7.2 Hz, aryl, 3H), 3.00 (br, $CH_2'P(^iPr)_2$, 6H), 2.28 (br, $CH(CH_3)_2$, 6H), 1.15, 1.11 (br, $CH(CH_3)_2$, 36H). $^{31}P\{^1H\}$ NMR (ppm, THF-d_8, 162 MHz): 37.3 (s, 3P, $[(HCO_2)NiInL]^-$), 21.0 (s, 2P, $[PPN]^+$).

Catalytic CO_2 Hydrogenation Studies

High-Pressure Reactions in PEEK NMR Tubes. CO_2 hydrogenation reactions at 34 atm of ~1:1 H_2/CO_2 were performed in PEEK high-pressure NMR spectroscopy tubes designed and built at Pacific Northwest National Laboratory, as reported previously.[214, 233] CAUTION: operators of high- pressure equipment should take proper precautions to minimize the risk of personal injury. In a typical catalytic experiment (0.25 mM NiGaL catalyst, 800 mM Vkd base), a stock solution of NiGaL (11.8 mg, 14.6 μmol) in 1 mL THF-d_8 was prepared. A 0.875 M solution of Vkd (168 mg, 560 μmol) in 640 μL THF-d_8 was also prepared. Dilution of the NiGaL stock solution (100 μL) with 400 μL THF-d_8, and subsequent addition of 60 μL of the resulting solution to the Vkd solution gave the desired concentrations for the catalytic reactions (700 μL of 800 mM Vkd, 0.25 mM NiGaL). Note that preparations were adjusted accordingly to afford other concentrations of NiGaL (or of NiAlL, NiInL, or $NiLH_3$) and/or other bases, including tBuTMG and NEt_3. Lastly, 300 μL of the reaction solution was added to two different PEEK cells, which each contained a capillary of $CoCl_2$ in D_2O as an internal NMR reference.

The PEEK cell was sealed and connected to a high-pressure line equipped with a vacuum pump and an ISCO syringe pump. The line was purged with gas three times. The headspace was degassed by opening the PEEK cell to static vacuum (3 × 30 s). Gas was delivered to the cell from an ISCO syringe pump running constantly at 34 atm (i.e. continuous gas feed). The contents of the PEEK NMR spectroscopy cell were mixed using a vortex mixer for approximately 3 minutes until the pressure stabilized. After stabilization, the cell was inserted into the NMR spectrometer to acquire data for the first time point. The time for the catalysis experiments started upon initial exposure of the PEEK cell to the H_2/CO_2 gas mixture, and later time points corresponded to the start of each NMR acquisition. ^{1}H NMR spectra were collected approximately every 5 minutes using the following parameters: 4 scans each, delay time of 5 s, acquisition time of 2.19 s, pulse width of 2 μs (20 degree pulse), and gain of 2 (total time of 30 s per spectrum). The concentration of the formate was determined by integration of the formate resonance relative to that of residual ***H***DO (5.6 ppm) in the internal capillary standard of $CoCl_2$ in D_2O. ^{31}P spectra were collected every 10 minutes, with 4 scans per spectrum, a delay time of 10 s, and an acquisition time of 5 s (total time of 45 s per spectrum). The contents of the PEEK NMR spectroscopy cell were mixed using a vortex mixer when NMR data was not being collected to promote optimal dissolution of gas into the reaction solution throughout catalysis.

Ambient Pressure Reactions in J. Young NMR Tubes. Hydrogenation reactions at 1 atm of ~1:1 H_2/CO_2 were run in J. Young NMR tubes. In a typical experiment (2.9 mM NiGaL catalyst, 800 mM Vkd base), a stock solution of NiGaL (12.5 mg, 15.5 μmol) in 1 mL THF-d_8 was prepared, of which 75 μL was added to each J. Young tube (total of two

tubes for replicate trials). Vkd base (192 mg, 640 μmol) was dissolved to make a 650 μL solution in THF-d_8, of which 325 μL was added to each tube. The resulting solution (400 μL of 2.9 mM NiGaL catalyst, 800 mM Vkd base) was inverted several times to mix. Note that preparations were adjusted accordingly to afford other concentrations of NiGaL (or of NiAlL, NiInL, or $NiLH_3$). Each tube also contained a capillary of $CoCl_2$ in D_2O as an internal NMR standard. The headspace was degassed by opening the tube to static vacuum. Subsequently, 1 atm of ~1:1 H_2/CO_2 gas was delivered to the tube. The H_2/CO_2 gas mixture was passed through a stainless steel joint submerged in a propylene glycol/water (60/40%) bath cooled with excess dry ice in order to remove residual moisture from the gas stream. The contents of the tube were mixed using a vortex mixer for approximately 20 s, followed by re-filling with 1 atm H_2/CO_2. After vortex mixing for another 20 s, the NMR spectrum for the first time point was collected. For the remaining time points, after the collection of each NMR spectrum, the sample was vortex mixed for 20 s, followed by re-filling with 1 atm H_2/CO_2, and vortex mixed again for 20 seconds, followed by the next NMR time point. This protocol resulted in re-filling the tube with 1 atm H_2/CO_2 every 6 to 7 minutes. Acquisition of ^1H and ^{31}P NMR spectra was carried out with the same procedure and parameters as described above for the high-pressure reactions.

Thermodynamic Studies for Measuring Hydricity ($\Delta G°_{H-}$) and pK_a of $[HNiML]^-$ Complexes

General experimental procedure for H_2 heterolysis equilibria. Two or three different ratios of NiML to base in THF were added to separate J. Young NMR tubes in THF. The solutions were degassed and the headspace of each was evacuated by freeze-pump-thaw

cycles, followed by exposure to 1 atm or ~3.8 atm H_2. The reactions were monitored periodically by ^{31}P NMR spectroscopy until successive time points gave identical results, indicating that equilibrium had been achieved. The J. Young NMR tubes were inverted continuously using a turntable (D.J. J. Young at ~16 rpm) to promote gas-liquid mixing when NMR spectra were not being collected. Reactions typically reached equilibrium within 1-2 days, but in some cases were monitored for 3-4 weeks to confirm no reaction was occurring or to allow equilibrium to be reached. ^{31}P spectra were collected with 50-100 scans for each spectrum, a delay time of 10 s, and an acquisition time of 1.68 s. Each time point was taken to be the approximate midpoint time in the NMR data collection (about 15-20 minutes per collection).

General experimental procedure for hydride transfer equilibria. A metal hydride and a metal complex capable of accepting a hydride ion were added in a ~1:1 ratio to a J. Young NMR tube in THF. Apart from not adding H_2 gas, the rest of the procedure was analogous to that described for the H_2 heterolysis equilibria. The reactions were monitored periodically by ^{31}P NMR spectroscopy until successive time points gave identical results, indicating that equilibrium had been achieved. The J. Young NMR tubes were inverted continuously using a turntable (D.J. J. Young at ~16 rpm) to promote mixing of the solution when NMR spectra were not being collected. ^{31}P spectra were collected with 50-100 scans for each spectrum, a delay time of 10 s, and an acquisition time of 1.68 s, with each time point was taken to be the approximate midpoint time in the NMR data collection (about 15-20 minutes per collection).

5.4.2 X-ray Crystallographic and Structure Refinement Details

A yellow plate of [PPN][HNiGaL] ([PPN][**2**−H]) and an orange plate of [PPN][(η^1–HCO_2)NiGaL] ([PPN][**2**−O_2CH]) were placed onto the tip of a MiTeGen Dual-Thickness MicroLoop™ and mounted on a Bruker Photon II CPAD diffractometer for data collection at 123(2) K. The data collections were carried out using Mo Kα radiation (graphite monochromator). The data intensity was corrected for absorption and decay (SADABS).[172] Final cell constants were obtained from least-squares fits of all measured reflections. The structure was solved using SHELXT-16 and refined using SHELXL-16, which were executed from the ShelXle graphical user interface.[264] A direct-methods solution was calculated which provided most non-hydrogen atoms from the E-map. Full-matrix least-squares/difference Fourier cycles were performed to locate the remaining non-hydrogen atoms. All non-hydrogen atoms were refined with anisotropic displacement parameters. Hydrogen atoms were placed in ideal positions and refined as riding atoms with relative isotropic displacement parameters.[173] The hydride ligand in [PPN][**2**−H] was placed directly from the difference Fourier map. PLATON SQUEEZE was used to remove two disordered THF molecules in [PPN][**2**−H].[174] Images were rendered using POV–ray.[175] The structures of both [PPN][**2**−H] (#1553935) and [PPN][**2**−O_2CH] (#1553936) were deposited in the Cambridge Structural Database (CSD).

Note that the crystallographic details for [PPN][**1**−H] and [PPN][**3**−H], which were also obtained by Matt Vollmer, were not included, as these structures were only briefly discussed to validate the structural trends observed upon the introduction of a hydride ligand to **2**.

Table 5.8. Crystallographic details for [PPN][**2**−H] and [PPN][**2**−O_2CH].

Complex	[PPN][HNiGaL] ([PPN][**2**−H])	[PPN][(η^1–CO_2H)NiGaL] ([PPN][**2**−O_2CH])
chemical formula	$[C_{36}H_{30}N_2P]$ $[C_{39}H_{61}GaN_4NiP_3]$	$[C_{36}H_{30}N_2P]$ $[C_{40}H_{61}GaN_4NiO_2P_3]$
fw	1345.79	1389.81
cryst syst	monoclinic	Triclinic
space group	$P2_1/C$	P–1
a(Å)	22.6991(12)	11.2791(6)
b(Å)	13.8494(7)	15.7374(10)
c(Å)	25.4751(12)	20.7033(13)
α (deg)	90	100.669(2)
β (deg)	103.819(2)	105.203(2)
γ (deg)	90	92.850(2)
V (Å^3)	7776.8(7)	3466.2(4)
Z	4	2
λ (Å), μ (mm^{-1})	0.71073, 0.732	0.71073, 0.826
T(K)	123(2)	123(2)
θ	2.208 to 33.182	2.29 to 30.533
reflns collected	175554	76891
unique reflns	29695	21129
data/restraint/parameters	29695/24/716	21129/0/773
R1, wR2 (I > 2σ(I))	0.0599, 0.1638	0.0576, 0.1540

5.4.3 Physical Methods

^{1}H, ^{13}C, and ^{31}P NMR spectra were recorded on Bruker 500, or 400 MHz and Varian 300 MHz, 500 MHz, or 600 MHz spectrometers and referenced to internal residual solvent (or H_3PO_4 for ^{31}P NMR spectra). Variable-temperature (VT) NMR experiments were carried out using either a methanol (below 298 K) or ethylene glycol (above 298 K) standard to calibrate the temperature, and all samples were allowed to equilibrate at each temperature for at least 10-15 minutes prior to data collection. IR spectra were obtained for solid samples in KBr pellets using a Bruker Tensor-37 FTIR with OPUS 6.5 software. Cyclic voltammetry was conducted using a CH Instruments 600 electrochemical analyzer. The one-cell setup utilized a glassy carbon working electrode,

platinum wire counter electrode, and $Ag/AgNO_3$ reference electrode in CH_3CN. Analyte solutions were prepared in THF with 0.1 M $[N(^nBu)_4][PF_6]$ ([TBA][PF_6]) and referenced internally to the $FeCp_2^{0/+}$ redox couple.

5.4.4 Computational Methods

Density Functional Theory (DFT) Calculations Regarding NiML and Anionic Hydride and Formate Complexes

Gas-phase geometry optimizations of were performed with DFT using the M06-L local functional,[176] as implemented in the Gaussian 09 program package.[182] The def2-SVP basis set was used for the C and H atoms of the ligand (L); def2-TZVP for N and P atoms, and def2-TZVPP for Ni, Ga, and any atom(s) comprising the hydride and formate substrates bound to Ni.[186] This method is denoted as M06-L/DEF2. The choice of the M06-L functional was based on its overall good performance on bimetallic systems and on the catalytic mechanism studies by similar bimetallic complexes.[78-79, 82, 394] Geometric structures were optimized in the gas phase at 0 K, and all stationary points were confirmed as energy minima by vibrational analyses. Gibbs free energies at 298.15 K were computed by adding zero-point vibrational energies and thermal corrections. Solvation effects were also considered by performing single-point calculations for all stationary points using the SMD[181] solvation model with THF as the solvent. For the hydride and proton transfer reactions, the B3P86/LANL2DZ+p[395-396] level of theory and the C-PCM[397] solvent model (CH_3CN) were employed. In the NiGa bimetallic complexes, the Ni→Ga interaction, which can be classified as a donor-acceptor-type bond, was also scrutinized using natural bond orbitals (NBO) analysis, wherein the

stabilization energy of the donor-acceptor interaction was estimated using second-order perturbation theory.[114]

Complete Active Space Self-Consistent Field (CASSCF) Calculations

CASSCF calculations of were performed using the DFT-optimized structure (no symmetry constraints) with the MOLCAS-8.1 package.[187] Relativistic basis sets of atomic natural orbital types of double-ζ quality (ANO-RCC-VDZ)[188] were used for N, P, C, H atoms, and ANO-RCC-VTZ were used for Ni and Ga atoms. Scalar relativistic effects were included using the Douglas-Kroll-Hess Hamiltonian.[398-400] The computational cost arising from the two-electron integrals was reduced by employing the Cholesky decomposition techniques.[401] For the anionic hydride complex ([**2**−H]$^-$), the complete active space consisted of 12 electrons in 12 orbitals.

Thermodynamic Hydricity Calculations in CH_3CN

The thermodynamic hydricity of transition-metal hydride complexes is defined as the standard Gibbs free energy change (ΔG^o_{H-}) of the reaction shown in Equation 5.71, where L = ligand(s) and M = transition metal.

$$LMH^{n+} \rightarrow LM^{(n+1)+} + H:^- \qquad \text{(Eqn 5.71)}$$

Our method is similar to that described in an *ab initio* benchmark study of thermodynamic hydricities for various Co and Ni hydride complexes.[328] As described previously, the hydricity (ΔG^o_{H-}) of LMH^{n+} can be determined by considering the isodesmic hydride transfer reaction with a reference complex, for which we have selected $[HNi(dmpe)_2]^+$, the most hydridic Ni−H species in the literature prior to the report of [**2**−H]$^-$:

$$LMH^{n+} + [Ni(dmpe)_2]^{2+} \rightarrow LM^{(n+1)+} + [HNi(dmpe)_2]^{+} \quad \text{(Eqn 5.72)}$$

With the free energy of the hydride transfer reaction in acetonitrile ($\Delta G_{exchange/H-}$), we can calculate the ΔG_{H-} of the metal hydride of interest, LMH^{n+}, according to Equation 5.73, where ΔG^{o}_{H-} of $[HNi(dmpe)_2]^{+}$ is set to 50.7 kcal/mol based on experiment.[330-331]

$$\Delta G^{o}_{H-}(LMH^{n+}) = \Delta G^{\circ}_{H-}([HNi(dmpe)_2]^{+}) + \Delta G_{exchange/H-} \quad \text{(Eqn 5.73)}$$

Previously, the B3P86/LANL2DZ+p and B3P86/BS2 levels of theory were reported to provide the most accurate hydricity values.[328] In addition, we examined several other methods (Table A.4.7-A.4.8), including the M06-L/DEF2, which was used in geometry optimization of the NiGa bimetallic complexes. All the structures were optimized in gas phase followed with frequency calculation at 298 K and 1 atm to confirm their stationary point nature. Single-point calculations in acetonitrile were then performed with either C-PCM[397, 402] or the SMD solvent model. Basis set LANL2DZ+p stands for that an effective core potential LANL2DZ[395-396] are used for all elements, and in the case of the P atom and transition-metal atoms a *d*-polarization shell or an *f*-polarization shell was added.[403-404] BS2, the basis set for transition metals is LANL2DZ+p, the basis set for N, P is 6-311+G**, and the basis set for the other elements is 6-31+G*.

DFT Calculations Regarding the Mechanism of Catalytic CO_2 Hydrogenation

Gaussian 09 calculations[182] were performed with the M06-L density functional[176] using a def2-SVP basis set for C and H atoms that remain invariant during the reaction, a

def2-TZVP basis set for N and P, and a def2-TZVPP basis set for Ni, Ga, Al, In, and the atoms involved in the reaction (C, O, H atoms in CO_2, CO, HCO_2^-, H^-, H_2).[186] The SDD effective core potential was used for In.[183] The structures of all species were optimized in the gas phase. Harmonic vibrational frequencies were computed to confirm the nature of all intermediates (no imaginary frequencies) and transition state structures (one imaginary frequency). The gas-phase Gibbs free energies, *G*, were calculated at $T = 298.15$ K and 1 atm pressure by using the harmonic approximation for the optimized structures. The solvation effect of THF was included by performing single-point energy calculations at the gas-phase geometries using the SMD[181] solvation model. The relative solution-phase Gibbs free energies were calculated by adding solvation energies to the gas-phase relative Gibbs free energies. The energy values reported in the main text are Gibbs free energies (298.15 K, standard state of 1 atm for gases and 1 M for solutes) including the solvent effect of THF.

5.4.5 Acknowledgements

I would like to several people that were instrumental in the work carried out in this chapter. First, I would like to thank my advisor Connie Lu for pushing me to apply for the DOE-SCGSR fellowship that allowed me to work on this project for five months at Pacific Northwest National Laboratory (PNNL). Without the expertise and assistance of Dr. Samantha Burgess, Dr. Aaron Appel, and Dr. John Linehan, as well as the use of their specialized high-pressure apparatus for monitoring catalyst speciation and kinetics, much of this work would not have been possible.

Matt Vollmer also contributed greatly to this project, and his development of an improved synthesis of the anionic hydride and formate species, which allowed him to

obtain crystal structures of both species, was critical for advancing our understanding of these reactive catalytic intermediates. Matt and I also have worked together to investigate the hydricity and pK_a values of the $[HNiML]^-$ complexes and their dependence on the supporting metal, with Matt's expertise in the synthesis of organic superbases, in particular, proving very helpful to this endeavor. His observation of the formation of two species upon dissolving the anionic formate adducts in CH_3CN proved to be very useful, and prompted my indirect equilibrium studies to better understand the RDS of CO_2 hydrogenation catalysis. Matt was also very generous in allowing me to use his materials at times, and in general kept reminding me of why I was excited about this project in the first place. I thank Matt for the useful discussions we have had, as well as for giving me permission to discuss many aspects of his work on this project in this thesis in order to tell a more coherent story.

I am also grateful for the wonderful computational collaborators that I have had over the past few years on this project. Dr. Jingyun Ye, a postdoctoral researcher in the groups of Dr. Laura Gagliardi and Dr. Chris Cramer, performed the computations regarding the mechanism of CO_2 hydrogenation that were discussed in detail in this chapter. I thank her for her enthusiasm and hard work on this project, as her calculations have allowed us to understand many important subtleties about this catalytic process. Dr. Jing Xie, a postdoctoral researcher in the group of Dr. Laura Gagliardi, also was instrumental to our understanding of bonding and hydricity of the reactive anionic hydride species. Jing's calculations on the effect of varying the solvent on the H_2 binding energies for the NiML complexes were also very important to estimating BDFEs on the CH_3CN scale in this chapter.

Finally, Molly O'Hagan also provided helpful tips for NMR lineshape simulations, and discussion with Dr. Steve Tereniak prompted the initial reactions which led to the synthesis of the anionic hydride complexes. I would also like to thank Dr. Kit Zall, who worked in both our lab and as a postdoctoral researcher at PNNL, for his useful insights into studying the thermodynamics of my system, as well as for his tips for working productively at PNNL. Lastly, I would like to thank Dr. Reed Eisenhart for presenting an interesting paper at lit club several years ago which I used as a model for early studies into the CO_2 hydrogenation mechanism.

References

1. Appel, A. M.; Bercaw, J. E.; Bocarsly, A. B.; Dobbek, H.; DuBois, D. L.; Dupuis, M.; Ferry, J. G.; Fujita, E.; Hille, R.; Kenis, P. J. A.; Kerfeld, C. A.; Morris, R. H.; Peden, C. H. F.; Portis, A. R.; Ragsdale, S. W.; Rauchfuss, T. B.; Reek, J. N. H.; Seefeldt, L. C.; Thauer, R. K.; Waldrop, G. L., Frontiers, Opportunities, and Challenges in Biochemical and Chemical Catalysis of CO2 Fixation. *Chem Rev* **2013,** *113* (8), 6621-6658.
2. Le Quere, C.; Moriarty, R.; Andrew, R. M.; Canadell, J. G.; Sitch, S.; Korsbakken, J. I.; Friedlingstein, P.; Peters, G. P.; Andres, R. J.; Boden, T. A.; Houghton, R. A.; House, J. I.; Keeling, R. F.; Tans, P.; Arneth, A.; Bakker, D. C. E.; Barbero, L.; Bopp, L.; Chang, J.; Chevallier, F.; Chini, L. P.; Ciais, P.; Fader, M.; Feely, R. A.; Gkritzalis, T.; Harris, I.; Hauck, J.; Ilyina, T.; Jain, A. K.; Kato, E.; Kitidis, V.; Goldewijk, K. K.; Koven, C.; Landschutzer, P.; Lauvset, S. K.; Lefevre, N.; Lenton, A.; Lima, I. D.; Metzl, N.; Millero, F.; Munro, D. R.; Murata, A.; Nabel, J. E. M. S.; Nakaoka, S.; Nojiri, Y.; O'Brien, K.; Olsen, A.; Ono, T.; Perez, F. F.; Pfeil, B.; Pierrot, D.; Poulter, B.; Rehder, G.; Rodenbeck, C.; Saito, S.; Schuster, U.; Schwinger, J.; Seferian, R.; Steinhoff, T.; Stocker, B. D.; Sutton, A. J.; Takahashi, T.; Tilbrook, B.; van der Laan-Luijkx, I. T.; van der Werf, G. R.; van Heuven, S.; Vandemark, D.; Viovy, N.; Wiltshire, A.; Zaehle, S.; Zeng, N., Global Carbon Budget 2015. *Earth Syst Sci Data* **2015,** *7* (2), 349-396.
3. Aresta, M.; Dibenedetto, A.; Angelini, A., Catalysis for the Valorization of Exhaust Carbon: from CO2 to Chemicals, Materials, and Fuels. Technological Use of CO2. *Chem Rev* **2014,** *114* (3), 1709-1742.
4. Boden, T. A.; Andres, R. J.; Marland, G. *Global, Regional, and National Fossil-Fuel CO2 Emissions*; Carbon Dioxide Information Analysis Center: Oak Ridge National Laboratory, U.S. Department of Energy, Oak Ridge, TN, 2017.
5. Dlugokencky, E.; Tans, P. NOAA/ESRL. www.esrl.noaa.gov/gmd/ccgg/trends/.
6. Jacobson, M. Z., Climate response of fossil fuel and biofuel soot, accounting for soot's feedback to snow and sea ice albedo and emissivity. *J Geophys Res-Atmos* **2004,** *109* (D21).
7. Jacobson, M. Z., Control of fossil-fuel particulate black carbon and organic matter, possibly the most effective method of slowing global warming. *J Geophys Res-Atmos* **2002,** *107* (D19).
8. Bullock, R. M.; Helm, M. L., Molecular Electrocatalysts for Oxidation of Hydrogen Using Earth-Abundant Metals: Shoving Protons Around with Proton Relays. *Accounts Chem Res* **2015,** *48* (7), 2017-2026.
9. Lennox, J. C.; Kurtz, D. A.; Huang, T.; Dempsey, J. L., Excited-State Proton-Coupled Electron Transfer: Different Avenues for Promoting Proton/Electron Movement with Solar Photons. *Acs Energy Lett* **2017,** *2* (5), 1246-1256.
10. Wang, W. H.; Himeda, Y.; Muckerman, J. T.; Manbeck, G. F.; Fujita, E., CO2 Hydrogenation to Formate and Methanol as an Alternative to Photo- and Electrochemical CO2 Reduction. *Chem Rev* **2015,** *115* (23), 12936-12973.
11. Olah, G. A.; Prakash, G. K. S.; Goeppert, A., Anthropogenic Chemical Carbon Cycle for a Sustainable Future. *J Am Chem Soc* **2011,** *133* (33), 12881-12898.
12. Walter, M. G.; Warren, E. L.; McKone, J. R.; Boettcher, S. W.; Mi, Q. X.; Santori, E. A.; Lewis, N. S., Solar Water Splitting Cells. *Chem Rev* **2010,** *110* (11), 6446-6473.
13. Holladay, J. D.; Hu, J.; King, D. L.; Wang, Y., An overview of hydrogen production technologies. *Catal Today* **2009,** *139* (4), 244-260.
14. *Hydrogen Production: Natural Gas Reforming*; U.S. Department of Energy, Office of Energy Efficiency & Renewable Energy: Washington, DC.
15. Thomas, J. M.; Thomas, W. J., Fischer-Tropsch Catalysis. In *Principles and Practice of Heterogeneous Catalysis*, VCH: 1996.

16. Smil, V., *Enriching the Earth: Fritz Haber, Carl Bosch, and the Transformation of World Food Production*. MIT Press: Cambridge, Massachusetts, 2001.
17. Knobloch, D. J.; Lobkovsky, E.; Chirik, P. J., Dinitrogen cleavage and functionalization by carbon monoxide promoted by a hafnium complex. *Nat Chem* **2010,** *2* (1), 30-35.
18. Olah, G. A., Beyond oil and gas: The methanol economy. *Angew Chem Int Edit* **2005,** *44* (18), 2636-2639.
19. Mellmann, D.; Sponholz, P.; Junge, H.; Beller, M., Formic acid as a hydrogen storage material - development of homogeneous catalysts for selective hydrogen release. *Chem Soc Rev* **2016,** *45* (14), 3954-3988.
20. Shilov, A. E., Catalytic reduction of molecular nitrogen in solutions. *Russ Chem B+* **2003,** *52* (12), 2555-2562.
21. Chink, P.; Morris, R., Getting Down to Earth: The Renaissance of Catalysis with Abundant Metals. *Accounts Chem Res* **2015,** *48* (9), 2495-2495.
22. Chirik, P. J., Catalysis Without Precious Metals. Bullock, R. M., Ed. Wiley-VCH: Weinheim, Germany, 2010; p 83.
23. Schneidewind, J.; Adam, R.; Baumann, W.; Jackstell, R.; Beller, M., Low-Temperature Hydrogenation of Carbon Dioxide to Methanol with a Homogeneous Cobalt Catalyst. *Angew Chem Int Edit* **2017,** *56* (7), 1890-1893.
24. Sordakis, K.; Tsurusaki, A.; Iguchi, M.; Kawanami, H.; Himeda, Y.; Laurenczy, G., Carbon Dioxide to Methanol: The Aqueous Catalytic Way at Room Temperature. *Chem-Eur J* **2016,** *22* (44), 15605-15608.
25. Kothandaraman, J.; Goeppert, A.; Czaun, M.; Olah, G. A.; Prakash, G. K. S., Conversion of CO2 from Air into Methanol Using a Polyamine and a Homogeneous Ruthenium Catalyst. *J Am Chem Soc* **2016,** *138* (3), 778-781.
26. Wesselbaum, S.; Moha, V.; Meuresch, M.; Brosinski, S.; Thenert, K. M.; Kothe, J.; Stein, T. V.; Englert, U.; Holscher, M.; Klankermayer, J.; Leitner, W., Hydrogenation of carbon dioxide to methanol using a homogeneous ruthenium-Triphos catalyst: from mechanistic investigations to multiphase catalysis. *Chem Sci* **2015,** *6* (1), 693-704.
27. Rezayee, N. M.; Huff, C. A.; Sanford, M. S., Tandem Amine and Ruthenium-Catalyzed Hydrogenation of CO2 to Methanol. *J Am Chem Soc* **2015,** *137* (3), 1028-1031.
28. Wesselbaum, S.; vom Stein, T.; Klankermayer, J.; Leitner, W., Hydrogenation of Carbon Dioxide to Methanol by Using a Homogeneous Ruthenium-Phosphine Catalyst. *Angew Chem Int Edit* **2012,** *51* (30), 7499-7502.
29. Huff, C. A.; Sanford, M. S., Cascade Catalysis for the Homogeneous Hydrogenation of CO2 to Methanol. *J Am Chem Soc* **2011,** *133* (45), 18122-18125.
30. Cammarota, R. C.; Clouston, L. J.; Lu, C. C., Leveraging molecular metal-support interactions for H-2 and N-2 activation. *Coordin Chem Rev* **2017,** *334*, 100-111.
31. Eisenhart, R. J.; Clouston, L. J.; Lu, C. C., Configuring Bonds between First-Row Transition Metals. *Accounts Chem Res* **2015,** *48* (11), 2885-2894.
32. Hoffman, B. M.; Lukoyanov, D.; Yang, Z. Y.; Dean, D. R.; Seefeldt, L. C., Mechanism of Nitrogen Fixation by Nitrogenase: The Next Stage. *Chem Rev* **2014,** *114* (8), 4041-4062.
33. Spatzal, T.; Aksoyoglu, M.; Zhang, L. M.; Andrade, S. L. A.; Schleicher, E.; Weber, S.; Rees, D. C.; Einsle, O., Evidence for Interstitial Carbon in Nitrogenase FeMo Cofactor. *Science* **2011,** *334* (6058), 940-940.
34. Lancaster, K. M.; Roemelt, M.; Ettenhuber, P.; Hu, Y. L.; Ribbe, M. W.; Neese, F.; Bergmann, U.; DeBeer, S., X-ray Emission Spectroscopy Evidences a Central Carbon in the Nitrogenase Iron-Molybdenum Cofactor. *Science* **2011,** *334* (6058), 974-977.
35. Einsle, O.; Tezcan, F. A.; Andrade, S. L. A.; Schmid, B.; Yoshida, M.; Howard, J. B.; Rees, D. C., Nitrogenase MoFe-protein at 1.16 angstrom resolution: A central ligand in the FeMo-cofactor. *Science* **2002,** *297* (5587), 1696-1700.

36. Hoffman, B. M.; Lukoyanov, D.; Dean, D. R.; Seefeldt, L. C., Nitrogenase: A Draft Mechanism. *Accounts Chem Res* **2013,** *46* (2), 587-595.
37. Zhang, C. X.; Chen, C. H.; Dong, H. X.; Shen, J. R.; Dau, H.; Zhao, J. Q., A synthetic Mn4Ca-cluster mimicking the oxygen-evolving center of photosynthesis. *Science* **2015,** *348* (6235), 690-693.
38. Cox, N.; Pantazis, D. A.; Neese, F.; Lubitz, W., Biological Water Oxidation. *Accounts Chem Res* **2013,** *46* (7), 1588-1596.
39. Umena, Y.; Kawakami, K.; Shen, J. R.; Kamiya, N., Crystal structure of oxygen-evolving photosystem II at a resolution of 1.9 angstrom. *Nature* **2011,** *473* (7345), 55-U65.
40. Pushkar, Y. L.; Yano, J.; Sauer, K.; Boussac, A.; Yachandra, V. K., Structural changes in the Mn4Ca cluster and the mechanism of photosynthetic water splitting. *P Natl Acad Sci USA* **2008,** *105* (6), 1879-1884.
41. Yano, J.; Kern, J.; Sauer, K.; Latimer, M. J.; Pushkar, Y.; Biesiadka, J.; Loll, B.; Saenger, W.; Messinger, J.; Zouni, A.; Yachandra, V. K., Where water is oxidized to dioxygen: Structure of the photosynthetic Mn4Ca cluster. *Science* **2006,** *314* (5800), 821-825.
42. Tsui, E. Y.; Tran, R.; Yano, J.; Agapie, T., Redox-inactive metals modulate the reduction potential in heterometallic manganese-oxido clusters. *Nat Chem* **2013,** *5* (4), 293-299.
43. Siegbahn, P. E. M., Structures and Energetics for O-2 Formation in Photosystem II. *Accounts Chem Res* **2009,** *42* (12), 1871-1880.
44. Harman, W. H.; Peters, J. C., Reversible H-2 Addition across a Nickel-Borane Unit as a Promising Strategy for Catalysis. *J Am Chem Soc* **2012,** *134* (11), 5080-5082.
45. Kubas, G. J., Fundamentals of H-2 binding and reactivity on transition metals underlying hydrogenase function and H-2 production and storage. *Chem Rev* **2007,** *107* (10), 4152-4205.
46. Lubitz, W.; Ogata, H.; Rudiger, O.; Reijerse, E., Hydrogenases. *Chem Rev* **2014,** *114* (8), 4081-4148.
47. Kampa, M.; Pandelia, M. E.; Lubitz, W.; van Gastel, M.; Neese, F., A Metal-Metal Bond in the Light-Induced State of [NiFe] Hydrogenases with Relevance to Hydrogen Evolution. *J Am Chem Soc* **2013,** *135* (10), 3915-3925.
48. Volbeda, A.; Amara, P.; Darnault, C.; Mouesca, J. M.; Parkin, A.; Roessler, M. M.; Armstrong, F. A.; Fontecilla-Camps, J. C., X-ray crystallographic and computational studies of the O-2-tolerant [NiFe]-hydrogenase 1 from Escherichia coli. *P Natl Acad Sci USA* **2012,** *109* (14), 5305-5310.
49. Shomura, Y.; Yoon, K. S.; Nishihara, H.; Higuchi, Y., Structural basis for a [4Fe-3S] cluster in the oxygen-tolerant membrane-bound [NiFe]-hydrogenase. *Nature* **2011,** *479* (7372), 253-U143.
50. Fritsch, J.; Scheerer, P.; Frielingsdorf, S.; Kroschinsky, S.; Friedrich, B.; Lenz, O.; Spahn, C. M. T., The crystal structure of an oxygen-tolerant hydrogenase uncovers a novel iron-sulphur centre. *Nature* **2011,** *479* (7372), 249-U134.
51. Clouston, L. J.; Siedschlag, R. B.; Rudd, P. A.; Planas, N.; Hu, S. X.; Miller, A. D.; Gagliardi, L.; Lu, C. C., Systematic Variation of Metal-Metal Bond Order in Metal-Chromium Complexes. *J Am Chem Soc* **2013,** *135* (35), 13142-13148.
52. Tsui, E. Y.; Agapie, T., Reduction potentials of heterometallic manganese-oxido cubane complexes modulated by redox-inactive metals. *P Natl Acad Sci USA* **2013,** *110* (25), 10084-10088.
53. Perrin, D. D., *Ionisation Constants of Inorganic Acids and Bases in Aqueous Solution*. Pergamon: 1982.
54. Powers, T. M.; Betley, T. A., Testing the Polynuclear Hypothesis: Multielectron Reduction of Small Molecules by Triiron Reaction Sites. *J Am Chem Soc* **2013,** *135* (33), 12289-12296.

55. Powers, T. M.; Fout, A. R.; Zheng, S. L.; Betley, T. A., Oxidative Group Transfer to a Triiron Complex to Form a Nucleophilic mu(3)-Nitride, [Fe-3(mu(3)-N)](-). *J Am Chem Soc* **2011,** *133* (10), 3336-3338.
56. Krogman, J. P.; Foxman, B. M.; Thomas, C. M., Activation of CO2 by a Heterobimetallic Zr/Co Complex. *J Am Chem Soc* **2011,** *133* (37), 14582-14585.
57. Krogman, J. P.; Bezpalko, M. W.; Foxman, B. M.; Thomas, C. M., Synthesis, Structure, and Reactivity of an Anionic Zr-Oxo Relevant to CO2 Reduction by a Zr/Co Heterobimetallic Complex. *Inorg Chem* **2013,** *52* (6), 3022-3031.
58. Krogman, J. P.; Bezpalko, M. W.; Foxman, B. M.; Thomas, C. M., Multi-electron redox processes at a Zr(IV) center facilitated by an appended redox-active cobalt-containing metalloligand. *Dalton T* **2016,** *45* (27), 11182-11190.
59. Wu, B.; Bezpalko, M. W.; Foxman, B. M.; Thomas, C. M., A heterobimetallic complex featuring a Ti-Co multiple bond and its application to the reductive coupling of ketones to alkenes. *Chem Sci* **2015,** *6* (3), 2044-2049.
60. Napoline, J. W.; Krogman, J. P.; Shi, R.; Kuppuswamy, S.; Bezpalko, M. W.; Foxman, B. M.; Thomas, C. M., Activation of E-H and E-E (E = S, O) Bonds by Heterobimetallic Zr/Co Complexes: Evidence for Both One- and Two-Electron Processes. *Eur J Inorg Chem* **2013,** *2013* (22-23), 3874-3882.
61. Napoline, J. W.; Bezpalko, M. W.; Foxman, B. M.; Thomas, C. M., N-H activation of hydrazines by a heterobimetallic Zr-Co complex: promotion of one-electron chemistry at Zr. *Chem Commun* **2013,** *49* (39), 4388-4390.
62. Marquard, S. L.; Bezpalko, M. W.; Foxman, B. M.; Thomas, C. M., Stoichiometric C=O Bond Oxidative Addition of Benzophenone by a Discrete Radical Intermediate To Form a Cobalt(I) Carbene. *J Am Chem Soc* **2013,** *135* (16), 6018-6021.
63. Thomas, C. M.; Napoline, J. W.; Rowe, G. T.; Foxman, B. M., Oxidative addition across Zr/Co multiple bonds in early/late heterobimetallic complexes. *Chem Commun* **2010,** *46* (31), 5790-5792.
64. Wu, B.; Gramigna, K. M.; Bezpalko, M. W.; Foxman, B. M.; Thomas, C. M., Heterobimetallic Ti/Co Complexes That Promote Catalytic N-N Bond Cleavage. *Inorg Chem* **2015,** *54* (22), 10909-10917.
65. Zhou, W.; Marquard, S. L.; Bezpalko, M. W.; Foxman, B. M.; Thomas, C. M., Catalytic Hydrosilylation of Ketones Using a Co/Zr Heterobimetallic Complex: Evidence for an Unusual Mechanism Involving Ketyl Radicals. *Organometallics* **2013,** *32* (6), 1766-1772.
66. Zhou, W.; Napoline, J. W.; Thomas, C. M., A Catalytic Application of Co/Zr Heterobimetallic Complexes: Kumada Coupling of Unactivated Alkyl Halides with Alkyl Grignard Reagents. *Eur J Inorg Chem* **2011,** (13), 2029-2033.
67. Cooper, B. G.; Napoline, J. W.; Thomas, C. M., Catalytic Applications of Early/Late Heterobimetallic Complexes. *Catal Rev* **2012,** *54* (1), 1-40.
68. Thomas, C. M., Metal-Metal Multiple Bonds in Early/Late Heterobimetallic Complexes: Applications toward Small Molecule Activation and Catalysis. *Comment Inorg Chem* **2011,** *32* (1), 14-38.
69. Okamura, M.; Kondo, M.; Kuga, R.; Kurashige, Y.; Yanai, T.; Hayami, S.; Praneeth, V. K. K.; Yoshida, M.; Yoneda, K.; Kawata, S.; Masaoka, S., A pentanuclear iron catalyst designed for water oxidation. *Nature* **2016,** *530* (7591), 465-468.
70. Zhou, Y. Y.; Hartline, D. R.; Steiman, T. J.; Fanwick, P. E.; Uyeda, C., Dinuclear Nickel Complexes in Five States of Oxidation Using a Redox-Active Ligand. *Inorg Chem* **2014,** *53* (21), 11770-11777.
71. Powers, I. G.; Andjaba, J. M.; Luo, X. Y.; Mei, J. G.; Uyeda, C., Catalytic Azoarene Synthesis from Aryl Azides Enabled by a Dinuclear Ni Complex. *J Am Chem Soc* **2018,** *140* (11), 4110-4118.

72. Pal, S.; Zhou, Y. Y.; Uyeda, C., Catalytic Reductive Vinylidene Transfer Reactions. *J Am Chem Soc* **2017,** *139* (34), 11686-11689.
73. Hartline, D. R.; Zeller, M.; Uyeda, C., Catalytic Carbonylative Rearrangement of Norbornadiene via Dinuclear Carbon-Carbon Oxidative Addition. *J Am Chem Soc* **2017,** *139* (39), 13672-13675.
74. Steiman, T. J.; Uyeda, C., Reversible Substrate Activation and Catalysis at an Intact Metal-Metal Bond Using a Redox-Active Supporting Ligand. *J Am Chem Soc* **2015,** *137* (18), 6104-6110.
75. Pal, S.; Uyeda, C., Evaluating the Effect of Catalyst Nuclearity in Ni-Catalyzed Alkyne Cyclotrimerizations. *J Am Chem Soc* **2015,** *137* (25), 8042-8045.
76. Mazzacano, T. J.; Mankad, N. P., Base Metal Catalysts for Photochemical C-H Borylation That Utilize Metal-Metal Cooperativity. *J Am Chem Soc* **2013,** *135* (46), 17258-17261.
77. Walker, W. K.; Kay, B. M.; Michaelis, S. A.; Anderson, D. L.; Smith, S. J.; Ess, D. H.; Michaelis, D. J., Origin of Fast Catalysis in Allylic Amination Reactions Catalyzed by Pd-Ti Heterobimetallic Complexes. *J Am Chem Soc* **2015,** *137* (23), 7371-7378.
78. Rudd, P. A.; Liu, S. S.; Gagliardi, L.; Young, V. G.; Lu, C. C., Metal-Alane Adducts with Zero-Valent Nickel, Cobalt, and Iron. *J Am Chem Soc* **2011,** *133* (51), 20724-20727.
79. Siedschlag, R. B.; Bernales, V.; Vogiatzis, K. D.; Planas, N.; Clouston, L. J.; Bill, E.; Gagliardi, L.; Lu, C. C., Catalytic Silylation of Dinitrogen with a Dicobalt Complex. *J Am Chem Soc* **2015,** *137* (14), 4638-4641.
80. Rudd, P. A.; Liu, S. S.; Planas, N.; Bill, E.; Gagliardi, L.; Lu, C. C., Multiple Metal-Metal Bonds in Iron-Chromium Complexes. *Angew Chem Int Edit* **2013,** *52* (16), 4449-4452.
81. Holland, P. L., Metal-dioxygen and metal-dinitrogen complexes: where are the electrons? *Dalton T* **2010,** *39* (23), 5415-5425.
82. Clouston, L. J.; Bernales, V.; Carlson, R. K.; Gagliardi, L.; Lu, C. C., Bimetallic Cobalt-Dinitrogen Complexes: Impact of the Supporting Metal on N-2 Activation. *Inorg Chem* **2015,** *54* (19), 9263-9270.
83. Rudd, P. A.; Planas, N.; Bill, E.; Gagliardi, L.; Lu, C. C., Dinitrogen Activation at Iron and Cobalt Metallalumatranes. *Eur J Inorg Chem* **2013,** *2013* (22-23), 3898-3906.
84. DuBois, D. L., Development of Molecular Electrocatalysts for Energy Storage. *Inorg Chem* **2014,** *53* (8), 3935-3960.
85. Helm, M. L.; Stewart, M. P.; Bullock, R. M.; DuBois, M. R.; DuBois, D. L., A Synthetic Nickel Electrocatalyst with a Turnover Frequency Above 100,000 s(-1) for H-2 Production. *Science* **2011,** *333* (6044), 863-866.
86. Galan, B. R.; Schoffel, J.; Linehan, J. C.; Seu, C.; Appel, A. M.; Roberts, J. A. S.; Helm, M. L.; Kilgore, U. J.; Yang, J. Y.; DuBois, D. L.; Kubiak, C. P., Electrocatalytic Oxidation of Formate by [Ni((P2N2R ')-N-R)(2)(CH3CN)](2+) Complexes. *J Am Chem Soc* **2011,** *133* (32), 12767-12779.
87. Dubois, M. R.; Dubois, D. L., Development of Molecular Electrocatalysts for CO2 Reduction and H-2 Production/Oxidation. *Accounts Chem Res* **2009,** *42* (12), 1974-1982.
88. Frey, M., Hydrogenases: Hydrogen-activating enzymes. *Chembiochem* **2002,** *3* (2-3), 153-160.
89. He, T.; Tsvetkov, N. P.; Andino, J. G.; Gao, X. F.; Fullmer, B. C.; Caulton, K. G., Mechanism of Heterolysis of H-2 by an Unsaturated d(8) Nickel Center: via Tetravalent Nickel? *J Am Chem Soc* **2010,** *132* (3), 910-+.
90. Zhang, G. Q.; Vasudevan, K. V.; Scott, B. L.; Hanson, S. K., Understanding the Mechanisms of Cobalt-Catalyzed Hydrogenation and Dehydrogenation Reactions. *J Am Chem Soc* **2013,** *135* (23), 8668-8681.

91. Zhang, G. Q.; Scott, B. L.; Hanson, S. K., Mild and Homogeneous Cobalt-Catalyzed Hydrogenation of C=C, C=O, and C=N Bonds. *Angew Chem Int Edit* **2012,** *51* (48), 12102-12106.
92. Vasudevan, K. V.; Scott, B. L.; Hanson, S. K., Alkene Hydrogenation Catalyzed by Nickel Hydride Complexes of an Aliphatic PNP Pincer Ligand. *Eur J Inorg Chem* **2012,** (30), 4898-4906.
93. Zell, T.; Milstein, D., Hydrogenation and Dehydrogenation Iron Pincer Catalysts Capable of Metal Ligand Cooperation by Aromatization/Dearomatization. *Accounts Chem Res* **2015,** *48* (7), 1979-1994.
94. Morris, R. H., Exploiting Metal-Ligand Bifunctional Reactions in the Design of Iron Asymmetric Hydrogenation Catalysts. *Accounts Chem Res* **2015,** *48* (5), 1494-1502.
95. Noyori, R.; Sandoval, C. A.; Muniz, K.; Ohkuma, T., Metal-ligand bifunctional catalysis for asymmetric hydrogenation. *Philos T Roy Soc A* **2005,** *363* (1829), 901-912.
96. MacMillan, S. N.; Harman, W. H.; Peters, J. C., Facile Si-H bond activation and hydrosilylation catalysis mediated by a nickel-borane complex. *Chem Sci* **2014,** *5* (2), 590-597.
97. Cammarota, R. C.; Lu, C. C., Tuning Nickel with Lewis Acidic Group 13 Metalloligands for Catalytic Olefin Hydrogenation. *J Am Chem Soc* **2015,** *137* (39), 12486-12489.
98. Derrah, E. J.; Sircoglou, M.; Mercy, M.; Ladeira, S.; Bouhadir, G.; Miqueu, K.; Maron, L.; Bourissou, D., Original Transition Metal -> Indium Interactions upon Coordination of a Triphosphine-Indane. *Organometallics* **2011,** *30* (4), 657-660.
99. Amgoune, A.; Bourissou, D., sigma-Acceptor, Z-type ligands for transition metals. *Chem Commun* **2011,** *47* (3), 859-871.
100. Sircoglou, M.; Mercy, M.; Saffon, N.; Coppel, Y.; Bouhadir, G.; Maron, L.; Bourissou, D., Gold(I) Complexes of Phosphanyl Gallanes: From Interconverting to Separable Coordination Isomers. *Angew Chem Int Edit* **2009,** *48* (19), 3454-3457.
101. Sircoglou, M.; Bontemps, S.; Bouhadir, G.; Saffon, N.; Miqueu, K.; Gu, W. X.; Mercy, M.; Chen, C. H.; Foxman, B. M.; Maron, L.; Ozerov, O. V.; Bourissou, D., Group 10 and 11 Metal Boratranes (Ni, Pd, Pt, CuCl, AgCl, AuCl, and Au+) Derived from a Triphosphine-Borane. *J Am Chem Soc* **2008,** *130* (49), 16729-16738.
102. Johnson, M. P.; Shriver, D. F., Lewis Basicity of Metals .2. Interaction of Group 6 and 7 Transition Metal Cyclopentadienyl Derivatives with Bf3 Bcl3 and B2h6. *J Am Chem Soc* **1966,** *88* (2), 301-+.
103. Shriver, D. F., Lewis Basicity of a Transition Metal - a Boron Trifluoride Adduct of Biscyclopentadienyltungsten Dihydride. *J Am Chem Soc* **1963,** *85* (21), 3509-&.
104. Burlitch, J. M.; Leonowicz, M. E.; Petersen, R. B.; Hughes, R. E., Coordination of Metal-Carbonyl Anions to Triphenylaluminum, Triphenyl-Gallium, and Triphenyl-Indium and the Crystal-Structure of Tetraethylammonium Triphenyl((Eta-5-Cyclopentadienyl)Dicarbonyliron)Aluminate(Fe-Al). *Inorg Chem* **1979,** *18* (4), 1097-1105.
105. Braunschweig, H.; Gruss, K.; Radacki, K., Interaction between d- and p-block metals: Synthesis and structure of platinum-alane adducts. *Angew Chem Int Edit* **2007,** *46* (41), 7782-7784.
106. Hill, A. F.; Owen, G. R.; White, A. J. P.; Williams, D. J., The sting of the scorpion: A metallaboratrane. *Angew Chem Int Edit* **1999,** *38* (18), 2759-2761.
107. Golden, J. T.; Peterson, T. H.; Holland, P. L.; Bergman, R. G.; Andersen, R. A., Adduct formation and single and double deprotonation of Cp*(PMe3)Ir(H)(2) with main group metal alkyls and aryls: Synthesis and structure of three novel Ir-Al and Ir-Mg heterobimetallics. *J Am Chem Soc* **1998,** *120* (1), 223-224.
108. Bauer, J.; Braunschweig, H.; Dewhurst, R. D., Metal-Only Lewis Pairs with Transition Metal Lewis Bases. *Chem Rev* **2012,** *112* (8), 4329-4346.

109. Green, M. L. H., A New Approach to the Formal Classification of Covalent Compounds of the Elements. *J Organomet Chem* **1995,** *500* (1-2), 127-148.
110. Hartwig, J. F., *Organotransition Metal Chemistry: From Bonding to Catalysis*. 1st ed.; University Science Books: Sausalito, CA, 2010.
111. Hill, A. F., An unambiguous electron-counting notation for metallaboratranes. *Organometallics* **2006,** *25* (20), 4741-4743.
112. Parkin, G., A simple description of the bonding in transition-metal borane complexes. *Organometallics* **2006,** *25* (20), 4744-4747.
113. Pang, K. L.; Quan, S. M.; Parkin, G., Palladium complexes with Pd -> B dative bonds: Analysis of the bonding in the palladaboratrane compound [kappa(4)-B(mim(But))(3)]Pd(PMe3). *Chem Commun* **2006,** (48), 5015-5017.
114. Weinhold, F. L., C. R., Natural Bond Orbitals and Extensions of Localized Bonding Concepts. *Chem. Educ. Res. Pract.* **2001,** (2), 91-104.
115. Enemark, J. H.; Feltham, R. D., Principles of Structure, Bonding, and Reactivity for Metal Nitrosyl Complexes. *Coordin Chem Rev* **1974,** *13* (4), 339-406.
116. Enemark, J. H.; Feltham, R. D., Stereochemical Control of Valence .3. [Cono]8 Group in Ligand Fields of C4upsilon, C2upsilon, and Cs Symmetry. *J Am Chem Soc* **1974,** *96* (15), 5004-5005.
117. Harman, W. H.; Lin, T. P.; Peters, J. C., A d(10) Ni-(H-2) Adduct as an Intermediate in H-H Oxidative Addition across a Ni-B Bond. *Angew Chem Int Edit* **2014,** *53* (4), 1081-1086.
118. Devillard, M.; Declercq, R.; Nicolas, E.; Ehlers, A. W.; Backs, J.; Saffon-Merceron, N.; Bouhadir, G.; Slootweg, J. C.; Uhl, W.; Bourissou, D., A Significant but Constrained Geometry Pt -> Al Interaction: Fixation of CO2 and CS2, Activation of H-2 and PhCONH2. *J Am Chem Soc* **2016,** *138* (14), 4917-4926.
119. Bouhadir, G.; Bourissou, D., Complexes of ambiphilic ligands: reactivity and catalytic applications. *Chem Soc Rev* **2016,** *45* (4), 1065-1079.
120. Lin, T. P.; Peters, J. C., Boryl-Metal Bonds Facilitate Cobalt/Nickel-Catalyzed Olefin Hydrogenation. *J Am Chem Soc* **2014,** *136* (39), 13672-13683.
121. Gunderson, W. A.; Suess, D. L. M.; Fong, H.; Wang, X. P.; Hoffmann, C. M.; Cutsail, G. E.; Peters, J. C.; Hoffman, B. M., Free H-2 Rotation vs Jahn Teller Constraints in the Nonclassical Trigonal (TPB)Co-H-2 Complex. *J Am Chem Soc* **2014,** *136* (42), 14998-15009.
122. Suess, D. L. M.; Tsay, C.; Peters, J. C., Dihydrogen Binding to Isostructural S=1/2 and S=0 Cobalt Complexes. *J Am Chem Soc* **2012,** *134* (34), 14158-14164.
123. Tsoureas, N.; Kuo, Y. Y.; Haddow, M. F.; Owen, G. R., Double addition of H-2 to transition metal-borane complexes: a 'hydride shuttle' process between boron and transition metal centres. *Chem Commun* **2011,** *47* (1), 484-486.
124. Moret, M. E.; Peters, J. C., N-2 Functionalization at Iron Metallaboratranes. *J Am Chem Soc* **2011,** *133* (45), 18118-18121.
125. Del Castillo, T. J.; Thompson, N. B.; Peters, J. C., A Synthetic Single-Site Fe Nitrogenase: High Turnover, Freeze-Quench Fe-57 Mossbauer Data, and a Hydride Resting State. *J Am Chem Soc* **2016,** *138* (16), 5341-5350.
126. Anderson, J. S.; Rittle, J.; Peters, J. C., Catalytic conversion of nitrogen to ammonia by an iron model complex. *Nature* **2013,** *501* (7465), 84-+.
127. Takaya, J.; Iwasawa, N., Synthesis, Structure, and Catalysis of Palladium Complexes Bearing a Group 13 Metalloligand: Remarkable Effect of an Aluminum-Metalloligand in Hydrosilylation of CO2. *J Am Chem Soc* **2017,** *139* (17), 6074-6077.
128. Cammarota, R. C.; Vollmer, M. V.; Xie, J.; Ye, J. Y.; Linehan, J. C.; Burgess, S. K.; Appel, A. M.; Gagliardi, L.; Lu, C. C., A Bimetallic Nickel-Gallium Complex Catalyzes CO2 Hydrogenation via the Intermediacy of an Anionic d(10) Nickel Hydride. *J Am Chem Soc* **2017,** *139* (40), 14244-14250.

129. Ye, J. C., R. C.; Xie, J.; Vollmer, M. V.; Truhlar, D. G.; Cramer, C. J.; Lu, C. C.; Gagliardi, L., Rationalizing the Reactivity of Bimetallic Molecular Catalysts for CO2 Hydrogenation. *Acs Catal* **2018,** (submitted).
130. Clouston, L. J.; Bernales, V.; Cammarota, R. C.; Carlson, R. K.; Bill, E.; Gagliardi, L.; Lu, C. C., Heterobimetallic Complexes That Bond Vanadium to Iron, Cobalt, and Nickel. *Inorg Chem* **2015,** *54* (24), 11669-11679.
131. Pauling, L., Atomic Radii and Interatomic Distances in Metals. *J Am Chem Soc* **1947,** *69* (3), 542-553.
132. Moore, J. T.; Smith, N. E.; Lu, C. C., Structure and dynamic NMR behavior of rhodium complexes supported by Lewis acidic group 13 metallatranes. *Dalton T* **2017,** *46* (17), 5689-5701.
133. Shannon, R. D., Revised Effective Ionic-Radii and Systematic Studies of Interatomic Distances in Halides and Chalcogenides. *Acta Crystallogr A* **1976,** *32* (Sep1), 751-767.
134. Cordero, B.; Gomez, V.; Platero-Prats, A. E.; Reves, M.; Echeverria, J.; Cremades, E.; Barragan, F.; Alvarez, S., Covalent radii revisited. *Dalton T* **2008,** (21), 2832-2838.
135. Cotton, F. A. M., C. A.; Walton, R. A., *Multiple Bonds Between Metal Atoms*. 3rd ed.; Springer: New York.
136. Downs, A. J., *Chemistry of Aluminum, Gallium, Indium, and Thallium*. Chapman & Hall: London, 1993.
137. Miller, D. L.; Siedschlag, R. B.; Clouston, L. J.; Young, V. G.; Chen, Y. S.; Bill, E.; Gagliardi, L.; Lu, C. C., Redox Pairs of Diiron and Iron-Cobalt Complexes with High-Spin Ground States. *Inorg Chem* **2016,** *55* (19), 9725-9735.
138. Eisenhart, R. J.; Rudd, P. A.; Planas, N.; Boyce, D. W.; Carlson, R. K.; Tolman, W. B.; Bill, E.; Gagliardi, L.; Lu, C. C., Pushing the Limits of Delta Bonding in Metal-Chromium Complexes with Redox Changes and Metal Swapping. *Inorg Chem* **2015,** *54* (15), 7579-7592.
139. Tereniak, S. J.; Carlson, R. K.; Clouston, L. J.; Young, V. G.; Bill, E.; Maurice, R.; Chen, Y. S.; Kim, H. J.; Gagliardi, L.; Lu, C. C., Role of the Metal in the Bonding and Properties of Bimetallic Complexes Involving Manganese, Iron, and Cobalt. *J Am Chem Soc* **2014,** *136* (5), 1842-1855.
140. Zall, C. M.; Clouston, L. J.; Young, V. G.; Ding, K. Y.; Kim, H. J.; Zherebetskyy, D.; Chen, Y. S.; Bill, E.; Gagliardi, L.; Lu, C. C., Mixed-Valent Dicobalt and Iron-Cobalt Complexes with High-Spin Configurations and Short Metal-Metal Bonds. *Inorg Chem* **2013,** *52* (16), 9216-9228.
141. Zall, C. M.; Zherebetskyy, D.; Dzubak, A. L.; Bill, E.; Gagliardi, L.; Lu, C. C., A Combined Spectroscopic and Computational Study of a High-Spin S=7/2 Diiron Complex with a Short Iron-Iron Bond. *Inorg Chem* **2012,** *51* (1), 728-736.
142. Zanello, P., *Inorganic Electrochemistry: Theory, Practice, and Application*. Royal Society of Chemistry: Cambridge, UK, 2003.
143. Herbert, D. E.; Lionetti, D.; Rittle, J.; Agapie, T., Heterometallic Triiron-Oxo/Hydroxo Clusters: Effect of Redox-Inactive Metals. *J Am Chem Soc* **2013,** *135* (51), 19075-19078.
144. Christe, K. O.; Dixon, D. A.; McLemore, D.; Wilson, W. W.; Sheehy, J. A.; Boatz, J. A., On a quantitative scale for Lewis acidity and recent progress in polynitrogen chemistry. *J Fluorine Chem* **2000,** *101* (2), 151-153.
145. Reath, A. H.; Ziller, J. W.; Tsay, C.; Ryan, A. J.; Yang, J. Y., Redox Potential and Electronic Structure Effects of Proximal Nonredox Active Cations in Cobalt Schiff Base Complexes. *Inorg Chem* **2017,** *56* (6), 3713-3718.
146. Lin, P. H.; Takase, M. K.; Agapie, T., Investigations of the Effect of the Non-Manganese Metal in Heterometallic-Oxido Cluster Models of the Oxygen Evolving Complex of Photosystem II: Lanthanides as Substitutes for Calcium. *Inorg Chem* **2015,** *54* (1), 59-64.

147. Evangelisti, F.; More, R.; Hodel, F.; Luber, S.; Patzke, G. R., 3d-4f {Co(3)(II)Ln(OR)(4)} Cubanes as Bio-lnspired Water Oxidation Catalysts. *J Am Chem Soc* **2015,** *137* (34), 11076-11084.
148. Breeze, P. A.; Burdett, J. K.; Turner, J. J., Charged Carbonyls in Matrices - an Infrared Structural Characterization of Ni(Co)3-, Cr(Co)5-, and Fe(Co)4-. *Inorg Chem* **1981,** *20* (10), 3369-3378.
149. Jonas, K.; Kruger, C., Alkali Metal-Transition Metal Pi-Complexes. *Angewandte Chemie-International Edition in English* **1980,** *19* (7), 520-537.
150. Jonas, K., Dilithium-Nickel-Olefin Complexes - Novel Bimetal Complexes Containing a Transition-Metal and a Main Group Metal. *Angewandte Chemie-International Edition in English* **1975,** *14* (11), 752-753.
151. Burdett, J. K., Production of Carbonyl Anions by Vacuum Ultraviolet Photolysis of Matrix-Isolated Metal-Carbonyls. *J Chem Soc Chem Comm* **1973,** (19), 763-764.
152. Sloane, R. H.; Press, R., The formation of negative ions by positive-ion impact on surfaces. *Proc R Soc Lon Ser-A* **1938,** *168* (A933), 284-301.
153. Jonas, K., *Adv. Organomet. Chem.* **1981,** (19), 97-112.
154. Protchenko, A. V.; Dange, D.; Harmer, J. R.; Tang, C. Y.; Schwarz, A. D.; Kelly, M. J.; Phillips, N.; Tirfoin, R.; Birjkumar, K. H.; Jones, C.; Kaltsoyannis, N.; Mountford, P.; Aldridge, S., Stable GaX2, InX2 and TlX2 radicals. *Nat Chem* **2014,** *6* (4), 315-319.
155. Nakamoto, M.; Yamasaki, T.; Sekiguchi, A., Stable mononuclear radical anions of heavier group 13 elements: [((Bu2MeSi)-Bu-t)(3)E.-]center dot[K+(2.2.2-cryptand)] (E = Al, Ga). *J Am Chem Soc* **2005,** *127* (19), 6954-6955.
156. Brand, J. C.; Roberts, B. P., An Electron-Spin-Resonance Study of the Gallane Radical-Anion. *J Chem Soc Chem Comm* **1984,** (2), 109-110.
157. Giles, J. R. M.; Roberts, B. P., Electron-Spin-Resonance Spectra and Reactivity of Alane Radical-Anions in Solution. *J Chem Soc Chem Comm* **1981,** (22), 1167-1168.
158. Vollmer, M. V. X., J.; Cammarota, R. C.; Young, V. G.; Bill, E.; Gagliardi, L.; Lu, C. C., Formal nickelate (-I) complexes supported by group 13 ions: where are the valence electrons? *Angew. Chemie. Int. Ed.* **2018**, submitted.
159. Berry, J. F., Two-Center/Three-Electron Sigma Half-Bonds in Main Group and Transition Metal Chemistry. *Accounts Chem Res* **2016,** *49* (1), 27-34.
160. Yao, S. A.; Martin-Diaconescu, V.; Infante, I.; Lancaster, K. M.; Gotz, A. W.; DeBeer, S.; Berry, J. F., Electronic Structure of Ni2E2 Complexes (E = S, Se, Te) and a Global Analysis of M2E2 Compounds: A Case for Quantized E-2(n-) Oxidation Levels with n=2, 3, or 4. *J Am Chem Soc* **2015,** *137* (15), 4993-5011.
161. Berry, J. F., A Definitive Answer to a Bonding Quandary? The Role of One-Electron Resonance Structures in the Bonding of a {Cu3S2}(3+) Core. *Chem-Eur J* **2010,** *16* (9), 2719-2724.
162. Berry, J. F.; Bill, E.; Bothe, E.; Cotton, F. A.; Dalal, N. S.; Ibragimov, S. A.; Kaur, N.; Liu, C. Y.; Murillo, C. A.; Nellutla, S.; North, J. M.; Villagran, D., A fractional bond order of 1/2 in Pd-2(5+) - Formamidinate species; The value of very high-field EPR spectra. *J Am Chem Soc* **2007,** *129* (5), 1393-1401.
163. Pearson, R. G., Hard and Soft Acids and Bases. *J Am Chem Soc* **1963,** *85* (22), 3533-&.
164. Sivaev, I. B.; Bregadze, V. I., Lewis acidity of boron compounds. *Coordin Chem Rev* **2014,** *270*, 75-88.
165. Pearson, R. G., Hard and Soft Acids and Bases - the Evolution of a Chemical Concept. *Coordin Chem Rev* **1990,** *100*, 403-425.
166. Pauling, L., The Resonating-Valence-Bond Theory of Metals. *Acta Crystallogr* **1960,** *13* (12), 983-984.

167. Vollmer, M. V.; Xie, J.; Lu, C. C., Stable Dihydrogen Complexes of Cobalt(-I) Suggest an Inverse trans-Influence of Lewis Acidic Group 13 Metalloligands. *J Am Chem Soc* **2017,** *139* (19), 6570-6573.
168. Braunschweig, H.; Gruss, K.; Radacki, K., Reactivity of Pt-0 complexes toward gallium(III) halides: Synthesis of a platinum gallane complex and oxidative addition of gallium halides to Pt-0. *Inorg Chem* **2008,** *47* (19), 8595-8597.
169. Ramirez, B., Unpublished results. **2018**.
170. Karunananda, M. K.; Mankad, N. P., Cooperative Strategies for Catalytic Hydrogenation of Unsaturated Hydrocarbons. *Acs Catal* **2017,** *7* (9), 6110-6119.
171. Shevlin, M.; Friedfeld, M. R.; Sheng, H. M.; Pierson, N. A.; Hoyt, J. M.; Campeau, L. C.; Chirik, P. J., Nickel-Catalyzed Asymmetric Alkene Hydrogenation of alpha,beta-Unsaturated Esters: High-Throughput Experimentation-Enabled Reaction Discovery, Optimization, and Mechanistic Elucidation. *J Am Chem Soc* **2016,** *138* (10), 3562-3569.
172. Krause, L.; Herbst-Irmer, R.; Sheldrick, G. M.; Stalke, D., Comparison of silver and molybdenum microfocus X-ray sources for single-crystal structure determination. *J Appl Crystallogr* **2015,** *48*, 3-10.
173. Sheldrick, G. M., Crystal structure refinement with SHELXL. *Acta Crystallogr C* **2015,** *71*, 3-8.
174. Spek, A. L., Single-crystal structure validation with the program PLATON. *J Appl Crystallogr* **2003,** *36*, 7-13.
175. *Persistence of Vision (TM) Raytracer*. Persistence of Vision Pty. Ltd.: Williamstown, Victoria, Australia, 2004.
176. Zhao, Y.; Truhlar, D. G., A new local density functional for main-group thermochemistry, transition metal bonding, thermochemical kinetics, and noncovalent interactions. *J Chem Phys* **2006,** *125* (19).
177. Zhao, Y.; Truhlar, D. G., The M06 suite of density functionals for main group thermochemistry, thermochemical kinetics, noncovalent interactions, excited states, and transition elements: two new functionals and systematic testing of four M06-class functionals and 12 other functionals. *Theor Chem Acc* **2008,** *120* (1-3), 215-241.
178. Adamo, C.; Barone, V., Toward reliable density functional methods without adjustable parameters: The PBE0 model. *J Chem Phys* **1999,** *110* (13), 6158-6170.
179. Grimme, S.; Antony, J.; Ehrlich, S.; Krieg, H., A consistent and accurate ab initio parametrization of density functional dispersion correction (DFT-D) for the 94 elements H-Pu. *J Chem Phys* **2010,** *132* (15).
180. He, G.; Lu, G.; Guo, Z. W.; Liu, P.; Chen, G., Benzazetidine synthesis via palladium-catalysed intramolecular C-H amination. *Nat Chem* **2016,** *8* (12), 1131-1136.
181. Marenich, A. V.; Cramer, C. J.; Truhlar, D. G., Universal Solvation Model Based on Solute Electron Density and on a Continuum Model of the Solvent Defined by the Bulk Dielectric Constant and Atomic Surface Tensions. *J Phys Chem B* **2009,** *113* (18), 6378-6396.
182. Frisch, M. T., G.; Schlegel, H. B.; Scuseria, G.; Robb, M.; Cheeseman, J.; Scalmani, G.; Barone, V.; Mennucci, B.; Petersson, G., *Gaussian 09, revision D. 01*. Gaussian, Inc: Wallingford, CT, 2009.
183. Andrae, D.; Haussermann, U.; Dolg, M.; Stoll, H.; Preuss, H., Energy-Adjusted Abinitio Pseudopotentials for the 2nd and 3rd Row Transition-Elements. *Theor Chim Acta* **1990,** *77* (2), 123-141.
184. Dolg, M.; Wedig, U.; Stoll, H.; Preuss, H., Energy-Adjusted Abinitio Pseudopotentials for the 1st-Row Transition-Elements. *J Chem Phys* **1987,** *86* (2), 866-872.
185. Roos, B. O.; Taylor, P. R.; Siegbahn, P. E. M., A Complete Active Space Scf Method (Casscf) Using a Density-Matrix Formulated Super-Ci Approach. *Chem Phys* **1980,** *48* (2), 157-173.

186. Weigend, F.; Ahlrichs, R., Balanced basis sets of split valence, triple zeta valence and quadruple zeta valence quality for H to Rn: Design and assessment of accuracy. *Phys Chem Chem Phys* **2005,** *7* (18), 3297-3305.
187. Aquilante, F.; Autschbach, J.; Carlson, R. K.; Chibotaru, L. F.; Delcey, M. G.; De Vico, L.; Galvan, I. F.; Ferre, N.; Frutos, L. M.; Gagliardi, L.; Garavelli, M.; Giussani, A.; Hoyer, C. E.; Li Manni, G.; Lischka, H.; Ma, D. X.; Malmqvist, P. A.; Muller, T.; Nenov, A.; Olivucci, M.; Pedersen, T. B.; Peng, D. L.; Plasser, F.; Pritchard, B.; Reiher, M.; Rivalta, I.; Schapiro, I.; Segarra-Marti, J.; Stenrup, M.; Truhlar, D. G.; Ungur, L.; Valentini, A.; Vancoillie, S.; Veryazov, V.; Vysotskiy, V. P.; Weingart, O.; Zapata, F.; Lindh, R., Molcas 8: New capabilities for multiconfigurational quantum chemical calculations across the periodic table. *J Comput Chem* **2016,** *37* (5), 506-541.
188. Roos, B. O.; Lindh, R.; Malmqvist, P. A.; Veryazov, V.; Widmark, P. O., Main group atoms and dimers studied with a new relativistic ANO basis set. *J Phys Chem A* **2004,** *108* (15), 2851-2858.
189. Tsay, C.; Peters, J. C., Thermally stable N-2 and H-2 adducts of cationic nickel(II). *Chem Sci* **2012,** *3* (4), 1313-1318.
190. Dapprich, S.; Frenking, G., Ligand effects in transition metal dihydrogen complexes: A theoretical study. *Organometallics* **1996,** *15* (21), 4547-4551.
191. Hounjet, L. J.; Stephan, D. W., Hydrogenation by Frustrated Lewis Pairs: Main Group Alternatives to Transition Metal Catalysts? *Org Process Res Dev* **2014,** *18* (3), 385-391.
192. Holland, P. L., Distinctive Reaction Pathways at Base Metals in High-Spin Organometallic Catalysts. *Accounts Chem Res* **2015,** *48* (6), 1696-1702.
193. Heinekey, D. M.; Voges, M. H.; Barnhart, D. M., Rhenium Dihydrogen Complexes with Isonitrile Coligands: Novel Displacement of Chloride by Hydrogen. *J Am Chem Soc* **1996,** *118* (44), 10792-10802.
194. Hauger, B. E.; Gusev, D.; Caulton, K. G., Hydrogen binding to and fluxional behavior of Ir(H)2X(P-tert-Bu2R)2 (X = Cl, Br, I; R = Me, Ph). *J Am Chem Soc* **1994,** *116* (1), 208-214.
195. Kubas, G. J., Dihydrogen complexes as prototypes for the coordination chemistry of saturated molecules. *P Natl Acad Sci USA* **2007,** *104* (17), 6901-6907.
196. Kubas, G. J., Activation of dihydrogen and coordination of molecular H-2 on transition metals. *J Organomet Chem* **2014,** *751*, 33-49.
197. Kubas, G. J., Chemistry - Breaking the H-2 marriage and reuniting the couple. *Science* **2006,** *314* (5802), 1096-1097.
198. Connelly, S. J.; Zimmerman, A. C.; Kaminsky, W.; Heinekey, D. M., Synthesis, Structure, and Reactivity of a Nickel Dihydrogen Complex. *Chem-Eur J* **2012,** *18* (50), 15932-15934.
199. Zhu, D.; Thapa, I.; Korobkov, I.; Gambarotta, S.; Budzelaar, P. H. M., Redox-Active Ligands and Organic Radical Chemistry. *Inorg Chem* **2011,** *50* (20), 9879-9887.
200. Waterman, R.; Hillhouse, G. L., Synthesis and structure of a terminal dinitrogen complex of nickel. *Can J Chem* **2005,** *83* (4), 328-331.
201. Grills, D. C.; van Eldik, R.; Muckerman, J. T.; Fujita, E., Direct measurements of rate constants and activation volumes for the binding of H-2, D-2, N-2, C2H4, and CH3CN to W(CO)(3)(PCy3)(2): Theoretical and experimental studies with time-resolved step-scan FTIR and UV-Vis spectroscopy. *J Am Chem Soc* **2006,** *128* (49), 15728-15741.
202. Gusev, D. G.; Vymenits, A. B.; Bakhmutov, V. I., Reactions of carbonylchlorohydridobis(triisopropylphosphine)ruthenium with molecular hydrogen in solution. New molecular hydrogen complexes of ruthenium: RuH(H2)Cl(CO)[P(iso-Pr)3]2 and Ru(H)2(H2)(CO)[P(iso-Pr)3]2. *Inorg Chem* **1992,** *31* (1), 1-2.
203. Millar, J. M.; Kastrup, R. V.; Melchior, M. T.; Horvath, I. T.; Hoff, C. D.; Crabtree, R. H., Kinetics by high-pressure nuclear magnetic resonance: reversible hydrogen binding in

chromium carbonyl dihydrogen triphenylphosphine complex (.eta.2-H2)Cr(CO)3[P(C6H11)3]2. *J Am Chem Soc* **1990,** *112* (26), 9643-9645.
204. Zhang, K.; Gonzalez, A. A.; Hoff, C. D., Stopped-flow kinetic study of the reaction of tungsten complexes [P(C6H11)3]2W(CO)3(L) (L = hydrogen, deuterium or nitrogen) with pyridine. Kinetic resolution of reaction of dihydride versus molecular hydrogen complexes. *J Am Chem Soc* **1989,** *111* (10), 3627-3632.
205. Gonzalez, A. A.; Hoff, C. D., Entropy of binding molecular hydrogen and nitrogen in the complexes tricarbonylbis(tricyclohexylphosphine)transition metal (transition metal chromium, molybdenum, tungsten). *Inorg Chem* **1989,** *28* (23), 4295-4297.
206. Gonzalez, A. A.; Zhang, K.; Nolan, S. P.; Lopez de la Vega, R.; Mukerjee, S. L.; Hoff, C. D.; Kubas, G. J., Thermodynamic and kinetic studies of the complexes W(CO)3(PCy3)2L (L = H2, N2, NCCH3, pyridine, P(OMe)3, CO). *Organometallics* **1988,** *7* (12), 2429-2435.
207. Frenking, G.; Pidun, U., Ab initio studies of transition-metal compounds: The nature of the chemical bond to a transition metal. *J Chem Soc Dalton* **1997,** (10), 1653-&.
208. Tomaru, Y., *Modern Organonickel Chemistry*. Wiley-VCH: Weinheim, Germany, 2006.
209. Wilke, P. W. J. a. G., *The Organic Chemistry of Nickel*. Academic Press, Inc: New York, 1974; Vol. I.
210. Tolman, C. A., Steric Effects of Phosphorus Ligands in Organometallic Chemistry and Homogeneous Catalysis. *Chem Rev* **1977,** *77* (3), 313-348.
211. Williamson, M. P., Using chemical shift perturbation to characterise ligand binding. *Prog Nucl Mag Res Sp* **2013,** *73*, 1-16.
212. Bryant, R. G., The Nmr Time Scale. *J Chem Educ* **1983,** *60* (11), 933-935.
213. Feeney, J.; Batchelor, J. G.; Albrand, J. P.; Roberts, G. C. K., The effects of intermediate exchange processes on the estimation of equilibrium constants by NMR. *Journal of Magnetic Resonance (1969)* **1979,** *33* (3), 519-529.
214. Yonker, C. R.; Linehan, J. C., The use of supercritical fluids as solvents for NMR spectroscopy. *Prog Nucl Mag Res Sp* **2005,** *47* (1-2), 95-109.
215. Vigalok, A.; Ben-David, Y.; Milstein, D., Complexation of N2, H2, CO2, and Ethylene to a T-Shaped Rhodium(I) Core. *Organometallics* **1996,** *15* (7), 1839-1844.
216. Paparo, A.; Okuda, J., Carbon dioxide complexes: Bonding modes and synthetic methods. *Coordin Chem Rev* **2017,** *334*, 136-149.
217. Aresta, M., My journey in the CO2-chemistry wonderland. *Coordin Chem Rev* **2017,** *334*, 150-183.
218. Piro, N. A.; Lichterman, M. F.; Harman, W. H.; Chang, C. J., A Structurally Characterized Nitrous Oxide Complex of Vanadium. *J Am Chem Soc* **2011,** *133* (7), 2108-2111.
219. Tolman, W. B., Binding and Activation of N2O at Transition-Metal Centers: Recent Mechanistic Insights. *Angew Chem Int Edit* **2010,** *49* (6), 1018-1024.
220. Paulat, F.; Kuschel, T.; Nather, C.; Praneeth, V. K. K.; Sander, O.; Lehnert, N., Spectroscopic properties and electronic structure of pentammineruthenium(II) dinitrogen oxide and corresponding nitrosyl complexes: Binding mode of N2O and reactivity. *Inorg Chem* **2004,** *43* (22), 6979-6994.
221. Pamplin, C. B.; Ma, E. S. F.; Safari, N.; Rettig, S. J.; James, B. R., The nitrous oxide complex, RuCl2(eta(1)-N2O)(P-N)(PPh3) (P-N = [o-(N,N-dimethylamino)phenyl]diphenylphosphine); Low temperature conversion of N2O to N-2 and O-2. *J Am Chem Soc* **2001,** *123* (35), 8596-8597.
222. Bottomley, F.; Brooks, W. V. F., Mode of Bonding of Dinitrogen Oxide (Nitrous-Oxide) in (Dinitrogen Oxide)Pentaammineruthenium. *Inorg Chem* **1977,** *16* (2), 501-502.
223. Luther, T. A.; Heinekey, D. M., Synthesis, characterization, and reactivity of dicationic dihydrogen complexes of osmium and ruthenium. *Inorg Chem* **1998,** *37* (1), 127-132.
224. Crabtree, R. H., Dihydrogen Complexation. *Chem Rev* **2016,** *116* (15), 8750-8769.

225. Maltby, P. A.; Schlaf, M.; Steinbeck, M.; Lough, A. J.; Morris, R. H.; Klooster, W. T.; Koetzle, T. F.; Srivastava, R. C., Dihydrogen with frequency of motion near the H-1 Larmor frequency. Solid-state structures and solution NMR spectroscopy of osmium complexes trans-[Os(H center dot center dot H)X(PPh(2)CH(2)CH(2)PPh(2))(2)](+) (X=Cl, Br). *J Am Chem Soc* **1996,** *118* (23), 5396-5407.
226. Desrosiers, P. J.; Cai, L. H.; Lin, Z. R.; Richards, R.; Halpern, J., Assessment of the T1 Criterion for Distinguishing between Classical and Nonclassical Transition-Metal Hydrides - Hydride Relaxation Rates in Tris(Triarylphosphine)Osmium Tetrahydrides and Related Polyhydrides. *J Am Chem Soc* **1991,** *113* (11), 4173-4184.
227. Morris, R. H.; Wittebort, R. J., Effect of a libration or hopping motion of the eta(2)-dihydrogen ligand on longitudinal nuclear magnetic resonance relaxation. *Magn Reson Chem* **1997,** *35* (4), 243-250.
228. Bautista, M. T.; Earl, K. A.; Maltby, P. A.; Morris, R. H.; Schweitzer, C. T.; Sella, A., Estimation of the H-H Distances of Eta-2-Dihydrogen Ligands in the Complexes Trans-[M(Eta-2-H-2)(H)(Pr2ch2ch2pr2)2]+ [M = Fe, Ru, R = Ph - M = Os, R = Et] by Solution Nmr Methods. *J Am Chem Soc* **1988,** *110* (21), 7031-7036.
229. Morris, R. H.
230. Gross, C. L.; Young, D. M.; Schultz, A. J.; Girolami, G. S., Neutron diffraction study of the 'elongated' molecular dihydrogen complex [(C5Me5)Os(H-2)H-2(PPh3)](+). *J Chem Soc Dalton* **1997,** (18), 3081-3082.
231. Sandstrom, J. R., *Dynamic Nuclear Resonance Spectroscopy*. 1st ed.; Academic Press, Inc: San Diego, CA, 1983.
232. Silberberg, M. S., *Principles of General Chemistry*. 3rd ed.; McGraw-Hill: New York, 2012.
233. Yonker, C. R.; Linehan, J. C., Investigation of the hydroformylation of ethylene in liquid carbon dioxide. *J Organomet Chem* **2002,** *650* (1-2), 249-257.
234. Linehan, J. C., personal communication.
235. Jaeschke, A.; Muensch, H.; Schmid, H. G.; Friebolin, H.; Mannschreck, A., Conformers of a Nitrosamine and a Carboxamide - Comparison of Nmr Line Shape and Equilibration Methods. *J Mol Spectrosc* **1969,** *31* (1), 14-+.
236. Morris, R. H., Estimating the Acidity of Transition Metal Hydride and Dihydrogen Complexes by Adding Ligand Acidity Constants. *J Am Chem Soc* **2014,** *136* (5), 1948-1959.
237. Jessop, P. G.; Morris, R. H., Reactions of transition metal dihydrogen complexes. *Coordin Chem Rev* **1992,** *121*, 155-284.
238. Kubas, G. J.; Ryan, R. R.; Unkefer, C. J., Molecular hydrogen complexes. 5. Electronic control of .eta.2-H2 vs. dihydride coordination. Dihydride structure of MoH2(CO)(R2PC2H4PR2)2 for R = Et, iso-Bu versus .eta.2-H2 for R = Ph. *J Am Chem Soc* **1987,** *109* (26), 8113-8115.
239. Kubas, G. J.; Unkefer, C. J.; Swanson, B. I.; Fukushima, E., Molecular hydrogen complexes of the transition metals. 4. Preparation and characterization of M(CO)3(PR3)2(.eta.2-H2) (M = molybdenum, tungsten) and evidence for equilibrium dissociation of the H-H bond to give MH2(CO)3(PR3)2. *J Am Chem Soc* **1986,** *108* (22), 7000-7009.
240. Kubas, G. J.; Ryan, R. R.; Wrobleski, D. A., Molecular hydrogen complexes of the transition metals. 3. Evidence for a new complex, Mo(CO)(dppe)2(H2), and for solution equilibrium between dihydrogen and dihydride forms, M-.eta.2-H2 .dblarw. H-M-H, in M(CO)3(PR3)2(H2). *J Am Chem Soc* **1986,** *108* (6), 1339-1341.
241. Heinekey, D. M.; Law, J. K.; Schultz, S. M., Kubas Complexes Revisited: Novel Dihydride Complexes of Tungsten. *J Am Chem Soc* **2001,** *123* (50), 12728-12729.

242. Prokopchuk, D. E.; Wiedner, E. S.; Walter, E. D.; Popescu, C. V.; Piro, N. A.; Kassel, W. S.; Bullock, R. M.; Mock, M. T., Catalytic N2 Reduction to Silylamines and Thermodynamics of N2 Binding at Square Planar Fe. *J Am Chem Soc* **2017,** *139* (27), 9291-9301.
243. Rittle, J.; McCrory, C. C. L.; Peters, J. C., A 106-Fold Enhancement in N2-Binding Affinity of an Fe2(μ-H)2 Core upon Reduction to a Mixed-Valence FeIIFeI State. *J Am Chem Soc* **2014,** *136* (39), 13853-13862.
244. Jabloniec, A.; Horstmann, S.; Gmehling, J., Experimental determination and calculation of gas solubility data for nitrogen in different solvents. *Ind Eng Chem Res* **2007,** *46* (13), 4654-4659.
245. Brunner, E., Solubility of Hydrogen in 10 Organic-Solvents at 298.15-K, 323.15-K, and 373.15-K. *J Chem Eng Data* **1985,** *30* (3), 269-273.
246. Kim, Y.; Deng, H.; Meek, D. W.; Wojcicki, A., Unusual molecular hydrogen complex of rhenium: a long hydrogen-hydrogen bond and inertness to substitution. *J Am Chem Soc* **1990,** *112* (7), 2798-2800.
247. Frost, M.; Hoffmann, C.; Thomison, J.; Overbay, M.; Austin, M.; Carman, P.; Viola, R.; Miller, E.; Mosier, L., Initial testing of a Compact Crystal Positioning System for the TOPAZ Single-Crystal Diffractometer at the Spallation Neutron Source. *J Phys Conf Ser* **2010,** *251*.
248. Kubas, G. J.; Burns, C. J.; Eckert, J.; Johnson, S. W.; Larson, A. C.; Vergamini, P. J.; Unkefer, C. J.; Khalsa, G. R. K.; Jackson, S. A.; Eisenstein, O., Neutron structure and inelastic-neutron-scattering and theoretical studies of molybdenum complex Mo(CO)(H2)[(C6D5)2PC2H4P(C6D5)2]2.cntdot.4.5C6D6, a complex with an extremely low barrier to hydrogen rotation. Implications on the reaction coordinate for H-H cleavage to dihydride. *J Am Chem Soc* **1993,** *115* (2), 569-581.
249. Kubas, G. J., Molecular-Hydrogen Complexes - Coordination of a Sigma-Bond to Transition-Metals. *Accounts Chem Res* **1988,** *21* (3), 120-128.
250. Jogl, G.; Wang, X. P.; Mason, S. A.; Kovalevsky, A.; Mustyakimov, M.; Fisher, Z.; Hoffman, C.; Kratky, C.; Langan, P., High-resolution neutron crystallographic studies of the hydration of the coenzyme cob(II)alamin. *Acta Crystallogr D* **2011,** *67*, 584-591.
251. Albinati, A.; Klooster, W. T.; Koetzle, T. F.; Fortin, J. B.; Ricci, J. S.; Eckert, J.; Fong, T. P.; Lough, A. J.; Morris, R. H.; Golombek, A. P., Single-crystal X-ray and neutron diffraction structure determination and inelastic neutron scattering study of the dihydrogen complex trans-[Ru(H-2)(H)(dppe)(2)] [BPh4]. *Inorg Chim Acta* **1997,** *259* (1-2), 351-357.
252. Eberhardt, N. A.; Guan, H. R., Nickel Hydride Complexes. *Chem Rev* **2016,** *116* (15), 8373-8426.
253. Mitoraj, M. P.; Michalak, A.; Ziegler, T., On the Nature of the Agostic Bond between Metal Centers and beta-Hydrogen Atoms in Alkyl Complexes. An Analysis Based on the Extended Transition State Method and the Natural Orbitals for Chemical Valence Scheme (ETS-NOCV). *Organometallics* **2009,** *28* (13), 3727-3733.
254. Mitoraj, M. P.; Michalak, A.; Ziegler, T., A Combined Charge and Energy Decomposition Scheme for Bond Analysis. *J Chem Theory Comput* **2009,** *5* (4), 962-975.
255. te Velde, G.; Bickelhaupt, F. M.; Baerends, E. J.; Guerra, C. F.; Van Gisbergen, S. J. A.; Snijders, J. G.; Ziegler, T., Chemistry with ADF. *J Comput Chem* **2001,** *22* (9), 931-967.
256. Hulley, E. B.; Helm, M. L.; Bullock, R. M., Heterolytic cleavage of H-2 by bifunctional manganese(I) complexes: impact of ligand dynamics, electrophilicity, and base positioning. *Chem Sci* **2014,** *5* (12), 4729-4741.
257. Sudmeier, J. L.; Evelhoch, J. L.; Jonsson, N. B. H., Dependence of Nmr Lineshape Analysis Upon Chemical Rates and Mechanisms - Implications for Enzyme Histidine Titrations. *J Magn Reson* **1980,** *40* (2), 377-390.
258. *Molecular Electrochemistry of Inorganic, Bioinorganic, and Organometallic Compounds*. 1st ed.; Springer Science and Business Media: 1993.

259. Halpern, J.; Cai, L.; Desrosiers, P. J.; Lin, Z., Kinetics of dissociation of H2 from transition-metal polyhydride complexes. *Journal of the Chemical Society, Dalton Transactions* **1991,** (S), 717-723.
260. Bell, R. P., In *The Tunnel Effect in Inorganic Chemistry*, Chapman and Hall: London and New York, 1980.
261. Mayer, J. M., Understanding Hydrogen Atom Transfer: From Bond Strengths to Marcus Theory. *Accounts Chem Res* **2011,** *44* (1), 36-46.
262. Mayer, J. M.; Rhile, I. J., Thermodynamics and kinetics of proton-coupled electron transfer: stepwise vs. concerted pathways. *Bba-Bioenergetics* **2004,** *1655* (1-3), 51-58.
263. Suhnel, J., The Marcus Cross Relation for Hydrogen-Transfer Reactions. *J Phys Org Chem* **1993,** *6* (5), 281-286.
264. Sheldrick, G. M., A short history of SHELX. *Acta Crystallogr A* **2008,** *64*, 112-122.
265. Zikovsky, J.; Peterson, P. F.; Wang, X. P. P.; Frost, M.; Hoffmann, C., CrystalPlan: an experiment-planning tool for crystallography. *J Appl Crystallogr* **2011,** *44*, 418-423.
266. Schultz, A. J.; Jorgensen, M. R. V.; Wang, X. P.; Mikkelson, R. L.; Mikkelson, D. J.; Lynch, V. E.; Peterson, P. F.; Green, M. L.; Hoffmann, C. M., Integration of neutron time-of-flight single-crystal Bragg peaks in reciprocal space. *J Appl Crystallogr* **2014,** *47*, 915-921.
267. Schultz, A. J.; Srinivasan, K.; Teller, R. G.; Williams, J. M.; Lukehart, C. M., Single-Crystal Time-of-Flight Neutron-Diffraction Structure of Hydrogen Cis-Diacetyltetracarbonylrhenate, [Cis-(Oc)4re(Ch3co)2]H - a Metallaacetylacetone Molecule. *J Am Chem Soc* **1984,** *106* (4), 999-1003.
268. Farrugia, L. J., ORTEP-3 for Windows - a version of ORTEP-III with a Graphical User Interface (GUI. *J Appl Crystallogr* **1997,** (30), 565.
269. Van Lenthe, E.; Baerends, E. J., Optimized slater-type basis sets for the elements 1-118. *J Comput Chem* **2003,** *24* (9), 1142-1156.
270. vanLenthe, E.; Snijders, J. G.; Baerends, E. J., The zero-order regular approximation for relativistic effects: The effect of spin-orbit coupling in closed shell molecules. *J Chem Phys* **1996,** *105* (15), 6505-6516.
271. Keim, W., Nickel - an Element with Wide Application in Industrial Homogeneous Catalysis. *Angewandte Chemie-International Edition in English* **1990,** *29* (3), 235-244.
272. Robinson, S. J. C.; Heinekey, D. M., Hydride & dihydrogen complexes of earth abundant metals: structure, reactivity, and applications to catalysis. *Chem Commun* **2017,** *53* (4), 669-676.
273. Wang, Y. W.; Kostenko, A.; Yao, S. L.; Driess, M., Divalent Silicon-Assisted Activation of Dihydrogen in a Bis(N-heterocyclic silylene)xanthene Nickel(0) Complex for Efficient Catalytic Hydrogenation of Olefins. *J Am Chem Soc* **2017,** *139* (38), 13499-13506.
274. Crabtree, R. H., Resolving Heterogeneity Problems and Impurity Artifacts in Operationally Homogeneous Transition Metal Catalysts. *Chem Rev* **2012,** *112* (3), 1536-1554.
275. Widegren, J. A.; Finke, R. G., A review of the problem of distinguishing true homogeneous catalysis from soluble or other metal-particle heterogeneous catalysis under reducing conditions. *J Mol Catal a-Chem* **2003,** *198* (1-2), 317-341.
276. Yu, Y.; Smith, J. M.; Flaschenriem, C. J.; Holland, P. L., Binding affinity of alkynes and alkenes to low-coordinate iron. *Inorg Chem* **2006,** *45* (15), 5742-5751.
277. Tokmic, K.; Fout, A. R., Alkyne Semihydrogenation with a Well-Defined Nonclassical Co-H-2 Catalyst: A H-2 Spin on Isomerization and E-Selectivity. *J Am Chem Soc* **2016,** *138* (41), 13700-13705.
278. Karunananda, M. K.; Mankad, N. P., Heterobimetallic H-2 Addition and Alkene/Alkane Elimination Reactions Related to the Mechanism of E-Selective Alkyne Semihydrogenation. *Organometallics* **2017,** *36* (1), 220-227.

279. Boro, B. J.; Duesler, E. N.; Goldberg, K. I.; Kemp, R. A., Synthesis, Characterization, and Reactivity of Nickel Hydride Complexes Containing 2,6-C6H3(CH2PR2)(2) (R = tBu, cHex, and iPr) Pincer Ligands. *Inorg Chem* **2009,** *48* (12), 5081-5087.
280. Leonard, N. G.; Chirik, P. J., Air-Stable alpha-Diimine Nickel Precatalysts for the Hydrogenation of Hindered, Unactivated Alkenes. *Acs Catal* **2018,** *8* (1), 342-348.
281. Angulo, I. M.; Kluwer, A. M.; Bouwman, E., Fast and selective homogeneous hydrogenation with nickel(II) phosphane catalysts. *Chem Commun* **1998,** (24), 2689-2690.
282. Angulo, I. M.; Bouwman, E., Kinetics of the hydrogenation of 1-octene catalyzed by [Ni(o-MeO-dppp)(OAc)(2)]. *J Mol Catal a-Chem* **2001,** *175* (1-2), 65-72.
283. Angulo, I. M.; Bouwman, E.; van Gorkum, R.; Lok, S. M.; Lutz, M.; Spek, A. L., New nickel-containing homogeneous hydrogenation catalysts - Structures of [Ni(o-MeO-dpppol)Cl-2] and [Ni(dcpe)Cl-2]. *J Mol Catal a-Chem* **2003,** *202* (1-2), 97-106.
284. Mooibroekt, T. J.; Wenker, E. C. M.; Smit, W.; Mutikainen, I.; Lutz, M.; Bouwman, E., Homogeneous Hydrogenation and Isomerization of 1-Octene Catalyzed by Nickel(II) Complexes with Bidentate Diarylphosphane Ligands. *Inorg Chem* **2013,** *52* (14), 8190-8201.
285. Bart, S. C.; Lobkovsky, E.; Chirik, P. J., Preparation and molecular and electronic structures of iron(0) dinitrogen and silane complexes and their application to catalytic hydrogenation and hydrosilation. *J Am Chem Soc* **2004,** *126* (42), 13794-13807.
286. Yu, R. P.; Darmon, J. M.; Hoyt, J. M.; Margulieux, G. W.; Turner, Z. R.; Chirik, P. J., High-Activity Iron Catalysts for the Hydrogenation of Hindered, Unfunctionalized Alkenes. *Acs Catal* **2012,** *2* (8), 1760-1764.
287. Chirik, P. J., Iron- and Cobalt-Catalyzed Alkene Hydrogenation: Catalysis with Both Redox-Active and Strong Field Ligands. *Accounts Chem Res* **2015,** *48* (6), 1687-1695.
288. Yu, R. P.; Darmon, J. M.; Milsmann, C.; Margulieux, G. W.; Stieber, S. C. E.; DeBeer, S.; Chirik, P. J., Catalytic Hydrogenation Activity and Electronic Structure Determination of Bis(arylimidazol-2-ylidene)pyridine Cobalt Alkyl and Hydride Complexes. *J Am Chem Soc* **2013,** *135* (35), 13168-13184.
289. Monfette, S.; Turner, Z. R.; Semproni, S. P.; Chirik, P. J., Enantiopure C-1-Symmetric Bis(imino)pyridine Cobalt Complexes for Asymmetric Alkene Hydrogenation. *J Am Chem Soc* **2012,** *134* (10), 4561-4564.
290. Friedfeld, M. R.; Shevlin, M.; Hoyt, J. M.; Krska, S. W.; Tudge, M. T.; Chirik, P. J., Cobalt Precursors for High-Throughput Discovery of Base Metal Asymmetric Alkene Hydrogenation Catalysts. *Science* **2013,** *342* (6162), 1076-1080.
291. Li, Y. W.; Hou, C.; Jiang, J. X.; Zhang, Z. H.; Zhao, C. Y.; Page, A. J.; Ke, Z. F., General H-2 Activation Modes for Lewis Acid-Transition Metal Bifunctional Catalysts. *Acs Catal* **2016,** *6* (3), 1655-1662.
292. Hammett, L. P., The effect of structure upon the reactions of organic compounds benzene derivatives. *J Am Chem Soc* **1937,** *59*, 96-103.
293. Hansch, C.; Leo, A.; Taft, R. W., A Survey of Hammett Substituent Constants and Resonance and Field Parameters. *Chem Rev* **1991,** *91* (2), 165-195.
294. Espenson, J. H., *Chemical Kinetics and Reaction Mechanisms*. McGraw-Hill: New York, 1981.
295. Bianchini, C.; Meli, A.; Peruzzini, M.; Frediani, P.; Bohanna, C.; Esteruelas, M. A.; Oro, L. A., Selective Hydrogenation of 1-Alkynes to Alkenes Catalyzed by an Iron(Ii) Cis-Hydride Eta-2-Dihydrogen Complex - a Case of Intramolecular Reaction between Eta-2-H-2 and Sigma-Vinyl Ligands. *Organometallics* **1992,** *11* (1), 138-145.
296. Bianchini, C.; Meli, A.; Peruzzini, M.; Vizza, F.; Zanobini, F.; Frediani, P., A Homogeneous Iron(Ii) System Capable of Selectively Catalyzing the Reduction of Terminal Alkynes to Alkenes and Buta-1,3-Dienes. *Organometallics* **1989,** *8* (8), 2080-2082.

297. Bailey, P. J.; Dawson, A.; McCormack, C.; Moggach, S. A.; Oswald, L. D. H.; Parsons, S.; Rankin, D. W. H.; Turner, A., Barriers to racemization in C-3-symmetric complexes containing the hydrotris(2-mercapto-1-ethylimidazolyl)borate (Tm-Et) Ligand. *Inorg Chem* **2005,** *44* (24), 8884-8898.
298. Foreman, M. R. S.; Hill, A. F.; White, A. J. P.; Williams, D. J., Poly(azolyl) chelate chemistry. Part 10 - Hydrotris(methimazolyl)borato alkylidyne complexes of tungsten. *Organometallics* **2003,** *22* (19), 3831-3840.
299. Jaska, C. A.; Clark, T. J.; Clendenning, S. B.; Grozea, D.; Turak, A.; Lu, Z. H.; Manners, I., Poisoning of heterogeneous, late transition metal dehydrocoupling catalysts by boranes and other group 13 hydrides. *J Am Chem Soc* **2005,** *127* (14), 5116-5124.
300. Karsch, H. H.; Appelt, A., Functional Trimethylphosphinoderivatives .25. A Tri-Spirocyclic Organoaluminumphosphine-Nickel(0) Complex. *J Organomet Chem* **1986,** *314* (1-2), C5-C8.
301. Butler, M. J.; Crimmin, M. R., Magnesium, zinc, aluminium and gallium hydride complexes of the transition metals. *Chem Commun* **2017,** *53* (8), 1348-1365.
302. Fischer, R. A.; Weiss, D.; Winter, M.; Muller, I.; Kaesz, H. D.; Frohlich, N.; Frenking, G., The reaction of the group-13 alkyls ER3 (E = Al, Ga, In; R=CH(2)t-Bu, CH2SiMe3) with the platinum-complex [(dcpe)Pt(H)(CH(2)t-Bu)]. *J Organomet Chem* **2004,** *689* (24), 4611-4623.
303. Maity, A.; Teets, T. S., Main Group Lewis Acid-Mediated Transformations of Transition-Metal Hydride Complexes. *Chem Rev* **2016,** *116* (15), 8873-8911.
304. Aldridge, S.; Downs, A. J., Hydrides of the main-group metals: New variations on an old theme. *Chem Rev* **2001,** *101* (11), 3305-3365.
305. Suh, H. W.; Guard, L. M.; Hazari, N., Synthesis and reactivity of a masked PSiP pincer supported nickel hydride. *Polyhedron* **2014,** *84*, 37-43.
306. Breitenfeld, J.; Vechorkin, O.; Corminboeuf, C.; Scopelliti, R.; Hu, X. L., Why Are (NN2)Ni Pincer Complexes Active for Alkyl-Alkyl Coupling: beta-H Elimination Is Kinetically Accessible but Thermodynamically Uphill. *Organometallics* **2010,** *29* (17), 3686-3689.
307. Wang, X. T.; Woo, L. K., Isomerization of olefin carboxylic esters catalyzed by nickel and palladium compounds. *J Mol Catal a-Chem* **1998,** *130* (1-2), 171-176.
308. Tolman, C. A., Chemistry of Tetrakis(Triethyl Phosphite)Nickel Hydride,Hni[P(Oet)3]4+ .4. Mechanism of Olefin Isomerization. *J Am Chem Soc* **1972,** *94* (9), 2994-&.
309. Cramer, R.; Lindsey, R. V., Mechanism of Isomerization of Olefins with Transition Metal Catalysts. *J Am Chem Soc* **1966,** *88* (15), 3534-&.
310. Wuttig, A.; Yaguchi, M.; Motobayashi, K.; Osawa, M.; Surendranath, Y., Inhibited proton transfer enhances Au-catalyzed CO2-to-fuels selectivity. *P Natl Acad Sci USA* **2016,** *113* (32), E4585-E4593.
311. Sabatier, P., Announcement. Hydrogenation and dehydrogenation for catalysis. *Ber Dtsch Chem Ges* **1911,** *44*, 1984-2001.
312. Perdew, J. P.; Emzerhof, M.; Burke, K., Rationale for mixing exact exchange with density functional approximations. *J Chem Phys* **1996,** *105* (22), 9982-9985.
313. Mavrandonakis, A.; Vogiatzis, K. D.; Boese, A. D.; Fink, K.; Heine, T.; Klopper, W., Ab lnitio Study of the Adsorption of Small Molecules on Metal-Organic Frameworks with Oxo-centered Trimetallic Building Units: The Role of the Undercoordinated Metal Ion. *Inorg Chem* **2015,** *54* (17), 8251-8263.
314. TURBOMOLE V6.4 2012, a development of University of Karlsruhe and Forschungszentrum Karlsruhe GmbH, 1989-2007, TURBOMOLE GmbH, since 2007.
315. Klankermayer, J.; Wesselbaum, S.; Beydoun, K.; Leitner, W., Selective Catalytic Synthesis Using the Combination of Carbon Dioxide and Hydrogen: Catalytic Chess at the Interface of Energy and Chemistry. *Angew Chem Int Edit* **2016,** *55* (26), 7296-7343.

316. Aresta, M.; Dibenedetto, A., Utilisation of CO2 as a chemical feedstock: opportunities and challenges. *Dalton T* **2007,** (28), 2975-2992.
317. Ziebart, C.; Federsel, C.; Anbarasan, P.; Jackstell, R.; Baumann, W.; Spannenberg, A.; Beller, M., Well-Defined Iron Catalyst for Improved Hydrogenation of Carbon Dioxide and Bicarbonate. *J Am Chem Soc* **2012,** *134* (51), 20701-20704.
318. Federsel, C.; Ziebart, C.; Jackstell, R.; Baumann, W.; Beller, M., Catalytic Hydrogenation of Carbon Dioxide and Bicarbonates with a Well-Defined Cobalt Dihydrogen Complex. *Chem-Eur J* **2012,** *18* (1), 72-75.
319. Langer, R.; Diskin-Posner, Y.; Leitus, G.; Shimon, L. J. W.; Ben-David, Y.; Milstein, D., Low-Pressure Hydrogenation of Carbon Dioxide Catalyzed by an Iron Pincer Complex Exhibiting Noble Metal Activity. *Angew Chem Int Edit* **2011,** *50* (42), 9948-9952.
320. Federsel, C.; Boddien, A.; Jackstell, R.; Jennerjahn, R.; Dyson, P. J.; Scopelliti, R.; Laurenczy, G.; Beller, M., A Well-Defined Iron Catalyst for the Reduction of Bicarbonates and Carbon Dioxide to Formates, Alkyl Formates, and Formamides. *Angew Chem Int Edit* **2010,** *49* (50), 9777-9780.
321. Spentzos, A. Z.; Barnes, C. L.; Bernskoetter, W. H., Effective Pincer Cobalt Precatalysts for Lewis Acid Assisted CO2 Hydrogenation. *Inorg Chem* **2016,** *55* (16), 8225-8233.
322. Zhang, Y. Y.; MacIntosh, A. D.; Wong, J. L.; Bielinski, E. A.; Williard, P. G.; Mercado, B. Q.; Hazari, N.; Bernskoetter, W. H., Iron catalyzed CO2 hydrogenation to formate enhanced by Lewis acid co-catalysts. *Chem Sci* **2015,** *6* (7), 4291-4299.
323. Jeletic, M. S.; Mock, M. T.; Appel, A. M.; Linehan, J. C., A Cobalt-Based Catalyst for the Hydrogenation of CO2 under Ambient Conditions. *J Am Chem Soc* **2013,** *135* (31), 11533-11536.
324. Burgess, S. A.; Kendall, A. J.; Tyler, D. R.; Linehan, J. C.; Appel, A. M., Hydrogenation of CO2 in Water Using a Bis(diphosphine) Ni-H Complex. *Acs Catal* **2017,** *7* (4), 3089-3096.
325. Tai, C. C.; Chang, T.; Roller, B.; Jessop, P. G., High-pressure combinatorial screening of homogeneous catalysts: Hydrogenation of carbon dioxide. *Inorg Chem* **2003,** *42* (23), 7340-7341.
326. Inoue, Y.; Izumida, H.; Sasaki, Y.; Hashimoto, H., Catalytic Fixation of Carbon-Dioxide to Formic-Acid by Transition-Metal Complexes under Mild Conditions. *Chem Lett* **1976,** (8), 863-864.
327. Enthaler, S.; Bruck, A.; Kammer, A.; Junge, H.; Irran, E.; Gulak, S., Exploring the Reactivity of Nickel Pincer Complexes in the Decomposition of Formic Acid to CO2/H-2 and the Hydrogenation of NaHCO3 to HCOONa. *Chemcatchem* **2015,** *7* (1), 65-69.
328. Qi, X. J.; Fu, Y.; Liu, L.; Guo, Q. X., Ab initio calculations of thermodynamic hydricities of transition-metal hydrides in acetonitrile. *Organometallics* **2007,** *26* (17), 4197-4203.
329. Wiedner, E. S.; Chambers, M. B.; Pitman, C. L.; Bullock, R. M.; Miller, A. J. M.; Appel, A. M., Thermodynamic Hydricity of Transition Metal Hydrides. *Chem Rev* **2016,** *116* (15), 8655-8692.
330. Curtis, C. J.; Miedaner, A.; Ellis, W. W.; DuBois, D. L., Measurement of the hydride donor abilities of [HM(diphosphine)(2)](+) complexes (M = Ni, Pt) by heterolytic activation of hydrogen. *J Am Chem Soc* **2002,** *124* (9), 1918-1925.
331. DuBois, D. L.; Berning, D. E., Hydricity of transition-metal hydrides and its role in CO2 reduction. *Appl Organomet Chem* **2000,** *14* (12), 860-862.
332. Chakraborty, S.; Patel, Y. J.; Krause, J. A.; Guan, H. R., Catalytic properties of nickel bis(phosphinite) pincer complexes in the reduction of CO2 to methanol derivatives. *Polyhedron* **2012,** *32* (1), 30-34.
333. Chakraborty, S.; Zhang, J.; Krause, J. A.; Guan, H. R., An Efficient Nickel Catalyst for the Reduction of Carbon Dioxide with a Borane. *J Am Chem Soc* **2010,** *132* (26), 8872-+.
334. Darensbourg, M. Y.; Ludwig, M.; Riordan, C. G., Spectroscopic and Chemical Studies of Nickel(Ii) Hydrides. *Inorg Chem* **1989,** *28* (9), 1630-1634.

335. Darensbourg, D. J.; Darensbourg, M. Y.; Goh, L. Y.; Ludvig, M.; Wiegreffe, P., The Reaction of (Cy3p)2ni(H)(Ch3) with Carbon-Dioxide - Formation of a Hydridonickel Formate Complex, Hni(O2ch)(Cy3p)2. *J Am Chem Soc* **1987,** *109* (24), 7539-7540.
336. Schmeier, T. J.; Hazari, N.; Incarvito, C. D.; Raskatov, J. A., Exploring the reactions of CO2 with PCP supported nickel complexes. *Chem Commun* **2011,** *47* (6), 1824-1826.
337. Lu, Z. Y.; Williams, T. J., Di(carbene)-Supported Nickel Systems for CO2 Reduction Under Ambient Conditions. *Acs Catal* **2016,** *6* (10), 6670-6673.
338. Zimmermann, P.; Limberg, C., Activation of Small Molecules at Nickel(I) Moieties. *J Am Chem Soc* **2017,** *139* (12), 4233-4242.
339. Yoo, C.; Lee, Y., AT-Shaped Nickel(I) Metalloradical Species. *Angew Chem Int Edit* **2017,** *56* (32), 9502-9506.
340. Mondal, B.; Neese, F.; Ye, S. F., Toward Rational Design of 3d Transition Metal Catalysts for CO2 Hydrogenation Based on Insights into Hydricity-Controlled Rate-Determining Steps. *Inorg Chem* **2016,** *55* (11), 5438-5444.
341. You, D.; Gabbai, F. P., Unmasking the Catalytic Activity of a Platinum Complex with a Lewis Acidic, Non-innocent Antimony Ligand. *J Am Chem Soc* **2017,** *139* (20), 6843-6846.
342. Kisanga, P. B.; Verkade, J. G.; Schwesinger, R., pK(a) measurements of P(RNCH2CH3)(3)N. *J Org Chem* **2000,** *65* (17), 5431-5432.
343. Wroblewski, A. E.; Pinkas, J.; Verkade, J. G., Strongly basic proazaphosphatranes: P(EtNCH2CH2)(3)N and P(iso-PrNCH2CH2)(3)N. *Main Group Chem* **1995,** *1* (1), 69-79.
344. Zall, C. M.; Linehan, J. C.; Appel, A. M., A Molecular Copper Catalyst for Hydrogenation of CO2 to Formate. *Acs Catal* **2015,** *5* (9), 5301-5305.
345. Kaljurand, I.; Kutt, A.; Soovali, L.; Rodima, T.; Maemets, V.; Leito, I.; Koppel, I. A., Extension of the self-consistent spectrophotometric basicity scale in acetonitrile to a full span of 28 pK(a) units: Unification of different basicity scales. *J Org Chem* **2005,** *70* (3), 1019-1028.
346. Jeletic, M. S.; Helm, M. L.; Hulley, E. B.; Mock, M. T.; Appel, A. M.; Linehan, J. C., A Cobalt Hydride Catalyst for the Hydrogenation of CO2: Pathways for Catalysis and Deactivation. *Acs Catal* **2014,** *4* (10), 3755-3762.
347. Kleimann, W.; Porschke, K. R.; Wilke, G., On the Lewis Acidity of Nickel(0) .4. On the Reaction of Tris(Ethene)Nickel(0) with Alkali-Metal Hydridotrialkylaluminates, Hydridogallates, and Hydridoborates at -78-Degrees-C. *Chem Ber-Recl* **1985,** *118* (1), 323-331.
348. Abernethy, C. D.; Baker, R. J.; Cole, M. L.; Davies, A. J.; Jones, C., Reactions of a carbene stabilised indium trihydride complex, [InH3{CN(Mes)-C2H2N(Mes)}] Mes=55 mesityl, with transition metal complexes. *Transit Metal Chem* **2003,** *28* (3), 296-299.
349. Darensbourg, M. Y.; Ash, C. E., In *Advances in Organometallic Chemistry*, Stone, F. G. A.; West, R., Eds. Academic Press, Inc.: San Diego, CA, 1987.
350. Berning, D. E.; Noll, B. C.; DuBois, D. L., Relative hydride, proton, and hydrogen atom transfer abilities of [HM(diphosphine)(2)]PF6 complexes (M = Pt, Ni). *J Am Chem Soc* **1999,** *121* (49), 11432-11447.
351. Mock, M. T.; Potter, R. G.; Camaioni, D. M.; Li, J.; Dougherty, W. G.; Kassel, W. S.; Twamley, B.; DuBois, D. L., Thermodynamic Studies and Hydride Transfer Reactions from a Rhodium Complex to BX3 Compounds. *J Am Chem Soc* **2009,** *131* (40), 14454-14465.
352. Mock, M. T.; Potter, R. G.; O'Hagan, M. J.; Camaioni, D. M.; Dougherty, W. G.; Kassel, W. S.; DuBois, D. L., Synthesis and Hydride Transfer Reactions of Cobalt and Nickel Hydride Complexes to BX3 Compounds. *Inorg Chem* **2011,** *50* (23), 11914-11928.
353. Wiedner, E. S.; Appel, A. M.; DuBois, D. L.; Bullock, R. M., Thermochemical and Mechanistic Studies of Electrocatalytic Hydrogen Production by Cobalt Complexes Containing Pendant Amines. *Inorg Chem* **2013,** *52* (24), 14391-14403.
354. Lilio, A. M.; Reineke, M. H.; Moore, C. E.; Rheingold, A. L.; Takase, M. K.; Kubiak, C. P., Incorporation of Pendant Bases into Rh(diphosphine)(2) Complexes: Synthesis,

Thermodynamic Studies, And Catalytic CO2 Hydrogenation Activity of [Rh(P2N2)(2)](+) Complexes. *J Am Chem Soc* **2015,** *137* (25), 8251-8260.
355. Miller, A. J. M.; Labinger, J. A.; Bercaw, J. E., Trialkylborane-Assisted CO2 Reduction by Late Transition Metal Hydrides. *Organometallics* **2011,** *30* (16), 4308-4314.
356. Deacon, G. B.; Phillips, R. J., Relationships between the Carbon-Oxygen Stretching Frequencies of Carboxylato Complexes and the Type of Carboxylate Coordination. *Coordin Chem Rev* **1980,** *33* (3), 227-250.
357. Morris, R. H., Bronsted-Lowry Acid Strength of Metal Hydride and Dihydrogen Complexes. *Chem Rev* **2016,** *116* (15), 8588-8654.
358. Abdur-Rashid, K.; Fong, T. P.; Greaves, B.; Gusev, D. G.; Hinman, J. G.; Landau, S. E.; Lough, A. J.; Morris, R. H., An acidity scale for phosphorus-containing compounds including metal hydrides and dihydrogen complexes in THF: Toward the unification of acidity scales. *J Am Chem Soc* **2000,** *122* (38), 9155-9171.
359. Kumar, N.; Camaioni, D. M.; Dupuis, M.; Raugei, S.; Appel, A. M., Mechanistic insights into hydride transfer for catalytic hydrogenation of CO2 with cobalt cornplexes. *Dalton T* **2014,** *43* (31), 11803-11806.
360. Urakawa, A.; Jutz, F.; Laurenczy, G.; Baiker, A., Carbon dioxide hydrogenation catalyzed by a ruthenium dihydride: A DFT and high-pressure spectroscopic investigation. *Chem-Eur J* **2007,** *13* (14), 3886-3899.
361. Zall, C. M.; Linehan, J. C.; Appel, A. M., Triphosphine-Ligated Copper Hydrides for CO2 Hydrogenation: Structure, Reactivity, and Thermodynamic Studies. *J Am Chem Soc* **2016,** *138* (31), 9968-9977.
362. Ding, F. Z.; Smith, J. M.; Wang, H. B., First-Principles Calculation of pK(a) Values for Organic Acids in Nonaqueous Solution. *J Org Chem* **2009,** *74* (7), 2679-2691.
363. Ni, S. F.; Dang, L., Insight into the electronic effect of phosphine ligand on Rh catalyzed CO2 hydrogenation by investigating the reaction mechanism. *Phys Chem Chem Phys* **2016,** *18* (6), 4860-4870.
364. Jeletic, M. S.; Hulley, E. B.; Helm, M. L.; Mock, M. T.; Appel, A. M.; Wiedner, E. S.; Linehan, J. C., Understanding the Relationship Between Kinetics and Thermodynamics in CO2 Hydrogenation Catalysis. *Acs Catal* **2017,** *7* (9), 6008-6017.
365. Urakawa, A.; Iannuzzi, M.; Hutter, J.; Baiker, A., Towards a rational design of ruthenium CO2 hydrogenation catalysts by ab initio metadynamics. *Chem-Eur J* **2007,** *13* (24), 6828-6840.
366. Fuoss, R. M., Ionic Association .3. The Equilibrium between Ion Pairs and Free Ions. *J Am Chem Soc* **1958,** *80* (19), 5059-5061.
367. Antipin, I. S.; Gareyev, R. F.; Vedernikov, A. N.; Konovalov, A. I., Cryptate Acidity Scales - Solvent Polarity Effect on Ion-Pair and Free-Ion Acidity of Organic-Compounds. *J Phys Org Chem* **1994,** *7* (4), 181-191.
368. Kaufman, M. J.; Gronert, S.; Streitwieser, A., Carbon Acidity .73. Conductimetric Study of Lithium and Cesium Salts of Hydrocarbon Acids - a Scale of Free Ion Acidities in Tetrahydrofuran - Revision of the Ion-Pair Scales. *J Am Chem Soc* **1988,** *110* (9), 2829-2835.
369. Salomon, M., Ion Association in 2-(Chloromethyl)Tetrahydrofuran. *Electrochim Acta* **1985,** *30* (8), 1021-1026.
370. Johnston, R. C.; Cheong, P. H. Y., C-H center dot center dot center dot O non-classical hydrogen bonding in the stereomechanics of organic transformations: theory and recognition. *Org Biomol Chem* **2013,** *11* (31), 5057-5064.
371. Batsanov, S. S., Van der Waals radii of elements. *Inorg Mater+* **2001,** *37* (9), 871-885.
372. Schmeier, T. J.; Dobereiner, G. E.; Crabtree, R. H.; Hazari, N., Secondary Coordination Sphere Interactions Facilitate the Insertion Step in an Iridium(III) CO2 Reduction Catalyst. *J Am Chem Soc* **2011,** *133* (24), 9274-9277.

373. Levina, V. A.; Rossin, A.; Belkova, N. V.; Chierotti, M. R.; Epstein, L. M.; Filippov, O. A.; Gobetto, R.; Gonsalvi, L.; Lledos, A.; Shubina, E. S.; Zanobini, F.; Peruzzini, M., Acid-Base Interaction between Transition-Metal Hydrides: Dihydrogen Bonding and Dihydrogen Evolution. *Angew Chem Int Edit* **2011,** *50* (6), 1367-1370.
374. Schwesinger, R.; Schlemper, H.; Hasenfratz, C.; Willaredt, J.; Dambacher, T.; Breuer, T.; Ottaway, C.; Fletschinger, M.; Boele, J.; Fritz, H.; Putzas, D.; Rotter, H. W.; Bordwell, F. G.; Satish, A. V.; Ji, G. Z.; Peters, E. M.; Peters, K.; vonSchnering, H. G.; Walz, L., Extremely strong, uncharged auxiliary bases; Monomeric and polymer-supported polyaminophosphazenes (P-2-P-5). *Liebigs Ann-Recl* **1996,** (7), 1055-1081.
375. Saame, J.; Rodima, T.; Tshepelevitsh, S.; Kutt, A.; Kaljurand, I.; Haljasorg, T.; Koppel, I. A.; Leito, I., Experimental Basicities of Superbasic Phosphonium Ylides and Phosphazenes. *J Org Chem* **2016,** *81* (17), 7349-7361.
376. Tilset, M.; Parker, V. D., Solution Homolytic Bond-Dissociation Energies of Organotransition-Metal Hydrides. *J Am Chem Soc* **1989,** *111* (17), 6711-6717.
377. Kuo, J. L. Using First Row Transition Metal Hydrides as Hydrogen Atom Donors. Columbia University, 2017.
378. Tilset, M., The Thermodynamics of Organometallic Systems Involving Electron-Transfer Paths. In *Electron Transfer in Chemistry*, Balzani, V., Ed. WILEY-VCH Verlag GmbH: 2001.
379. McCormick, M. C.; Keijzer, K.; Polavarapu, A.; Schultz, F. A.; Baik, M. H., Understanding Intrinsically Irreversible, Non-Nernstian, Two-Electron Redox Processes: A Combined Experimental and Computational Study of the Electrochemical Activation of Platinum(IV) Antitumor Prodrugs. *J Am Chem Soc* **2014,** *136* (25), 8992-9000.
380. Ciancanelli, R.; Noll, B. C.; DuBois, D. L.; DuBois, M. R., Comprehensive thermodynamic characterization of the metal-hydrogen bond in a series of cobalt-hydride complexes. *J Am Chem Soc* **2002,** *124* (12), 2984-2992.
381. Allen, O. R.; Dalgarno, S. J.; Field, L. D., Reductive disproportionation of carbon dioxide at an iron(II) center. *Organometallics* **2008,** *27* (14), 3328-3330.
382. Al-Afyouni, M. H.; Suturina, E.; Pathak, S.; Atanasov, M.; Bill, E.; DeRosha, D. E.; Brennessel, W. W.; Neese, F.; Holland, P. L., Spin Isomers and Ligand Isomerization in a Three-Coordinate Cobalt(I) Carbonyl Complex. *J Am Chem Soc* **2015,** *137* (33), 10689-10699.
383. Wang, W.; Wang, S. P.; Ma, X. B.; Gong, J. L., Recent advances in catalytic hydrogenation of carbon dioxide. *Chem Soc Rev* **2011,** *40* (7), 3703-3727.
384. Laarhoven, L. J. J.; Mulder, P., alpha-C-H bond strengths in tetralin and THF: Application of competition experiments in photoacoustic calorimetry. *J Phys Chem B* **1997,** *101* (1), 73-77.
385. Bordwell, F. G.; Cheng, J. P.; Satish, A. V.; Twyman, C. L., Acidities and Homolytic Bond-Dissociation Energies (Bdes) of Benzyl-Type C-H Bonds in Sterically Congested Substrates. *J Org Chem* **1992,** *57* (24), 6542-6546.
386. Chatgilialoglu, C.; Ingold, K. U.; Lusztyk, J.; Nazran, A. S.; Scaiano, J. C., Formation, Decay, and Spectral Characterization of Some Alkyl-Substituted Carbon-Centered, Silicon-Centered, Germanium-Centered, and Tin-Centered Radicals. *Organometallics* **1983,** *2* (10), 1332-1335.
387. Nguyen, H. K. D. D., T. H.; Nguyen, N. L. T.; Nguyen, H. T.; Dinh, N. T., Novel Ni-Ga alloy based catalyst for converting CO2 to methanol. *The Canadian Journal of Chemical Engineering* **2018,** *96* (4), 832-837.
388. Tang, Q. L.; Shen, Z. M.; Huang, L.; He, T.; Adidharma, H.; Russell, A. G.; Fan, M. H., Synthesis of methanol from CO2 hydrogenation promoted by dissociative adsorption of hydrogen on a Ga3Ni5(221) surface. *Phys Chem Chem Phys* **2017,** *19* (28), 18539-18555.
389. Chiang, C. L.; Lin, K. S.; Lin, Y. G., Preparation and Characterization of Ni5Ga3 for Methanol Formation via CO2 Hydrogenation. *Top Catal* **2017,** *60* (9-11), 685-696.

390. Torelli, D. A.; Francis, S. A.; Crompton, J. C.; Javier, A.; Thompson, J. R.; Brunschwig, B. S.; Soriaga, M. P.; Lewis, N. S., Nickel-Gallium-Catalyzed Electrochemical Reduction of CO2 to Highly Reduced Products at Low Overpotentials. *Acs Catal* **2016,** *6* (3), 2100-2104.
391. Studt, F.; Sharafutdinov, I.; Abild-Pedersen, F.; Elkjaer, C. F.; Hummelshoj, J. S.; Dahl, S.; Chorkendorff, I.; Norskov, J. K., Discovery of a Ni-Ga catalyst for carbon dioxide reduction to methanol. *Nat Chem* **2014,** *6* (4), 320-324.
392. Sharafutdinov, I.; Elkjaer, C. F.; de Carvalho, H. W. P.; Gardini, D.; Chiarello, G. L.; Damsgaard, C. D.; Wagner, J. B.; Grunwaldt, J. D.; Dahl, S.; Chorkendorff, I., Intermetallic compounds of Ni and Ga as catalysts for the synthesis of methanol. *J Catal* **2014,** *320*, 77-88.
393. Li, C. M.; Chen, Y. D.; Zhang, S. T.; Zhou, J. Y.; Wang, F.; He, S.; Wei, M.; Evans, D. G.; Duan, X., Nickel-Gallium Intermetallic Nanocrystal Catalysts in the Semihydrogenation of Phenylacetylene. *Chemcatchem* **2014,** *6* (3), 824-831.
394. Bao, J. L.; Zhang, X.; Xu, X. F.; Truhlar, D. G., Predicting bond dissociation energy and bond length for bimetallic diatomic molecules: a challenge for electronic structure theory. *Phys Chem Chem Phys* **2017,** *19* (8), 5839-5854.
395. Wadt, W. R.; Hay, P. J., Abinitio Effective Core Potentials for Molecular Calculations - Potentials for Main Group Elements Na to Bi. *J Chem Phys* **1985,** *82* (1), 284-298.
396. Hay, P. J.; Wadt, W. R., Abinitio Effective Core Potentials for Molecular Calculations - Potentials for K to Au Including the Outermost Core Orbitals. *J Chem Phys* **1985,** *82* (1), 299-310.
397. Cossi, M.; Rega, N.; Scalmani, G.; Barone, V., Energies, structures, and electronic properties of molecules in solution with the C-PCM solvation model. *J Comput Chem* **2003,** *24* (6), 669-681.
398. Hess, B. A., Relativistic Electronic-Structure Calculations Employing a 2-Component No-Pair Formalism with External-Field Projection Operators. *Phys Rev A* **1986,** *33* (6), 3742-3748.
399. Hess, B. A., Applicability of the No-Pair Equation with Free-Particle Projection Operators to Atomic and Molecular-Structure Calculations. *Phys Rev A* **1985,** *32* (2), 756-763.
400. Douglas, M.; Kroll, N. M., Quantum Electrodynamical Corrections to Fine-Structure of Helium. *Ann Phys-New York* **1974,** *82* (1), 89-155.
401. Aquilante, F.; Lindh, R.; Pedersen, T. B., Unbiased auxiliary basis sets for accurate two-electron integral approximations. *J Chem Phys* **2007,** *127* (11).
402. Barone, V.; Cossi, M., Quantum calculation of molecular energies and energy gradients in solution by a conductor solvent model. *J Phys Chem A* **1998,** *102* (11), 1995-2001.
403. Hollwarth, A.; Bohme, M.; Dapprich, S.; Ehlers, A. W.; Gobbi, A.; Jonas, V.; Kohler, K. F.; Stegmann, R.; Veldkamp, A.; Frenking, G., A Set of D-Polarization Functions for Pseudo-Potential Basis-Sets of the Main-Group Elements Al-Bi and F-Type Polarization Functions for Zn, Cd, Hg. *Chem Phys Lett* **1993,** *208* (3-4), 237-240.
404. Ehlers, A. W.; Bohme, M.; Dapprich, S.; Gobbi, A.; Hollwarth, A.; Jonas, V.; Kohler, K. F.; Stegmann, R.; Veldkamp, A.; Frenking, G., A Set of F-Polarization Functions for Pseudo-Potential Basis-Sets of the Transition-Metals Sc-Cu, Y-Ag and La-Au. *Chem Phys Lett* **1993,** *208* (1-2), 111-114.

Appendix 1: Supplemental Figures for Chapter 2

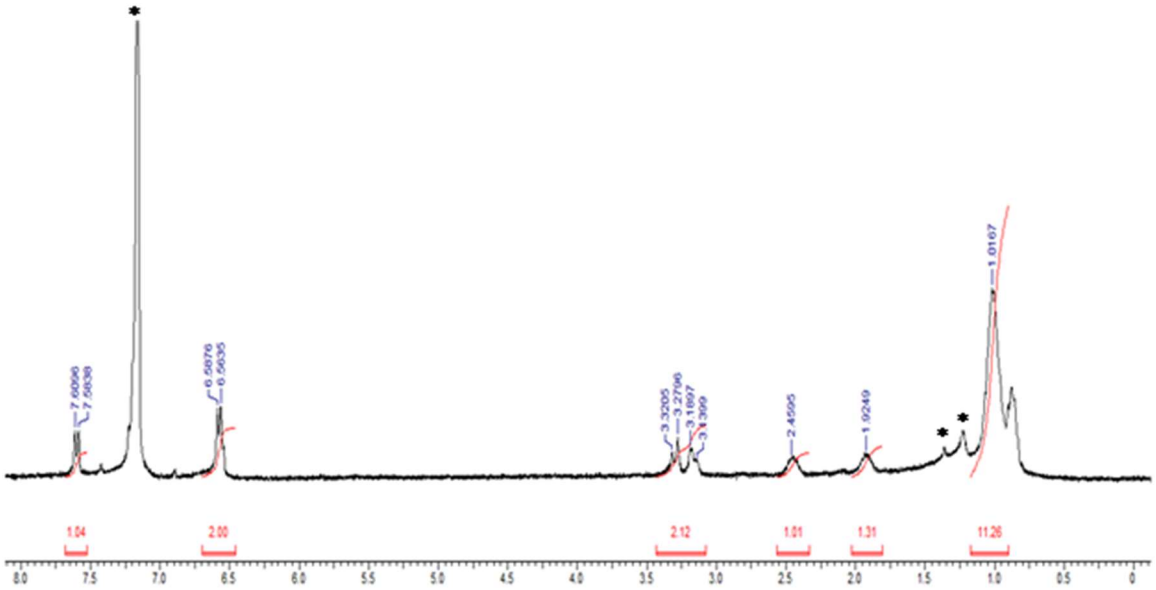

Figure A.1.1. ^{1}H NMR spectrum (300 MHz, C_6D_6) of NiGaL (**2**). Residual solvent peaks of benzene, THF, and pentane are denoted by asterisks (*).

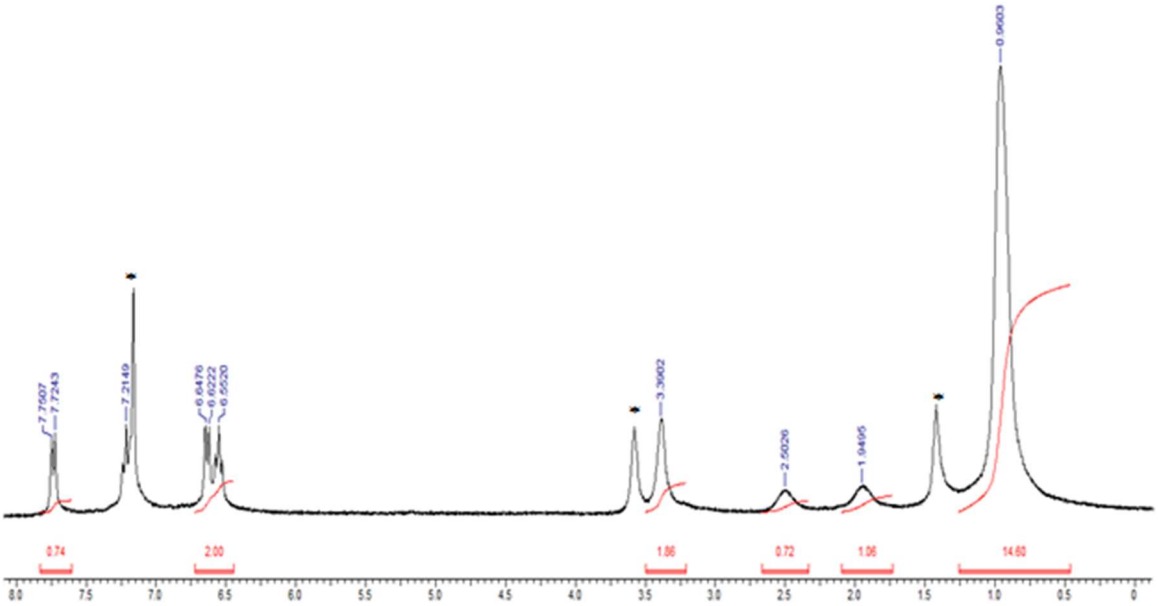

Figure A.1.2. ^{1}H NMR spectrum (300 MHz, C_6D_6) of NiInL (**3**). Residual solvent peaks of benzene and THF are denoted by asterisks (*).

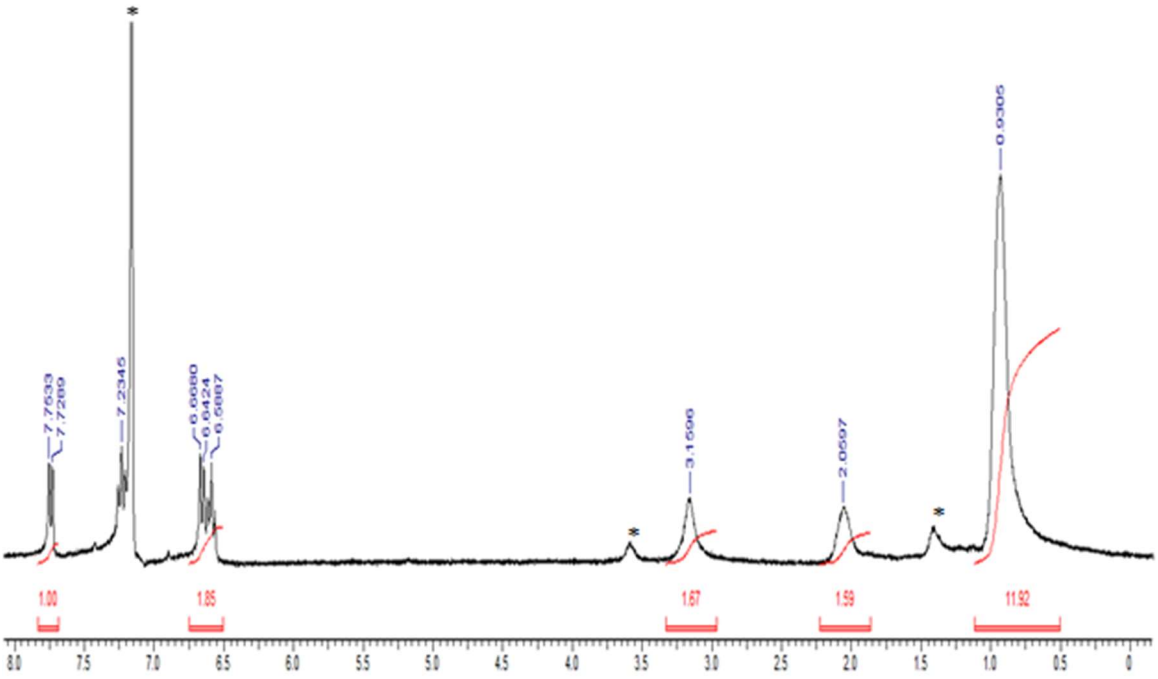

Figure A.1.3. ^{1}H NMR spectrum (300 MHz, C_6D_6) of (N_2)NiInL (**3**−N_2). Residual solvent peaks for benzene and THF are denoted by asterisks (*).

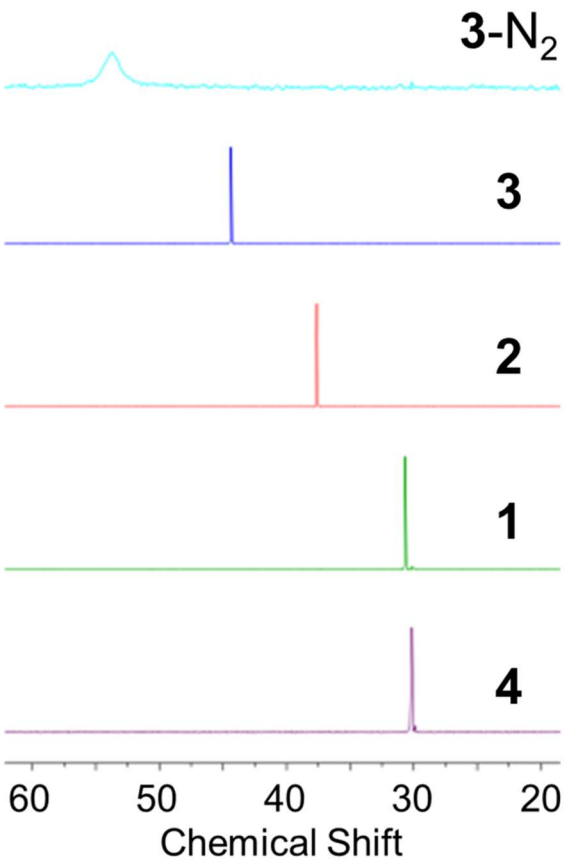

Figure A.1.4. Stacked ^{31}P NMR (161.9 MHz, toluene-d_8) spectra of complexes **1**-**4** and **3**−N_2, which have peaks at 30.7, 37.6, 44.4, 30.1 and 53.7 ppm at 298 K, respectively. Note that the peak for **3**−N_2 at 298 K represents a fast equilibrium on the NMR timescale between the **3**−N_2 and **3**, which lies heavily toward **3**−N_2 (more details on this in chapter 3). This equilibrium and the fluxionality of N_2 in solution accounts for the broadness of the peak for **3**−N_2 relative to those for the other complexes. Low T NMR (195 K) shows that the true chemical shift for **3**−N_2 is ~54.6 ppm.

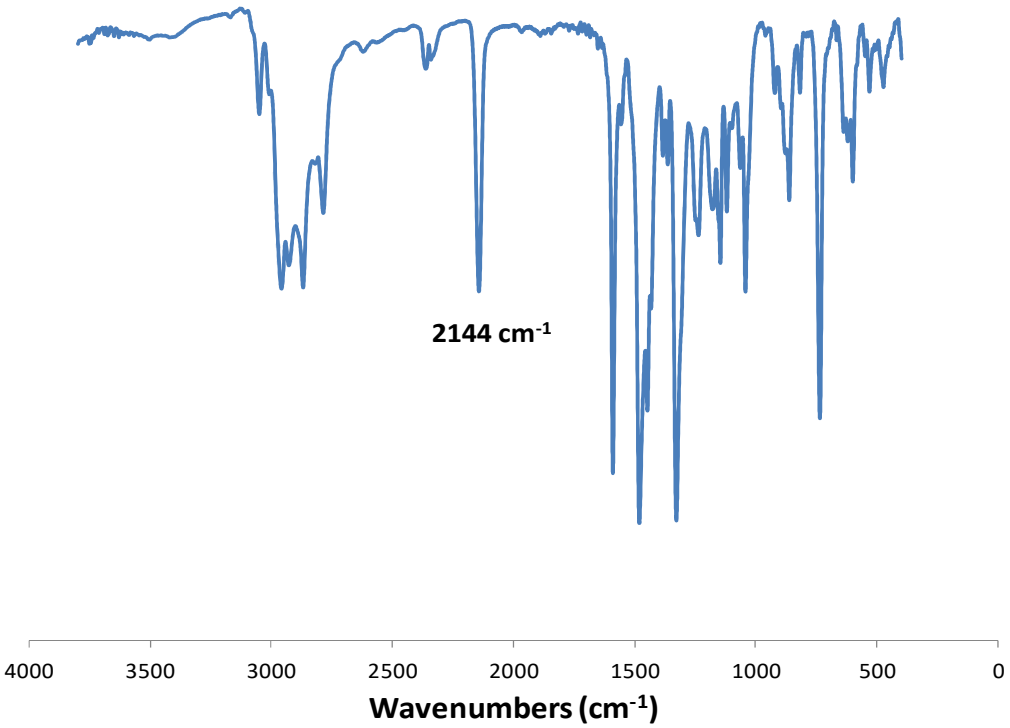

Figure A.1.5. IR spectrum (KBr pellet) of (N_2)NiInL (**3**–N_2).

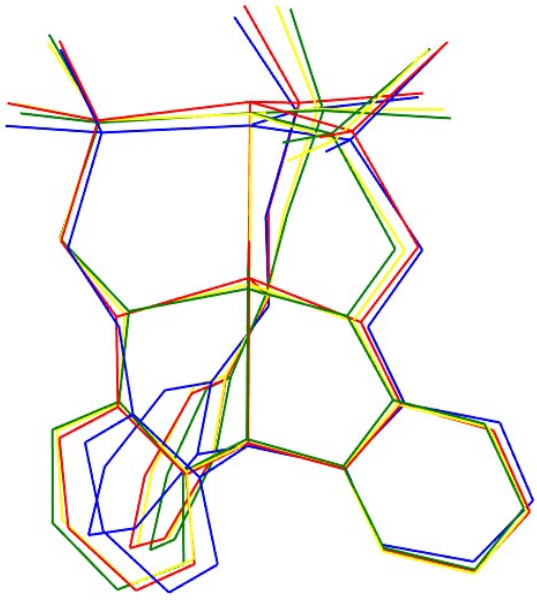

Figure A.1.6. Solid-state structural overlay of complexes **1**-**4**, with labelling as follows: NiAlL (**1**, green), NiGaL (**2**, yellow), NiInL (**3**, red), and $NiLH_3$ (**4**, blue). M(III) is positioned further above the N_3-plane in moving down group 13, which in turn "forces" Ni higher above the P_3-plane relative to its position in **4**.

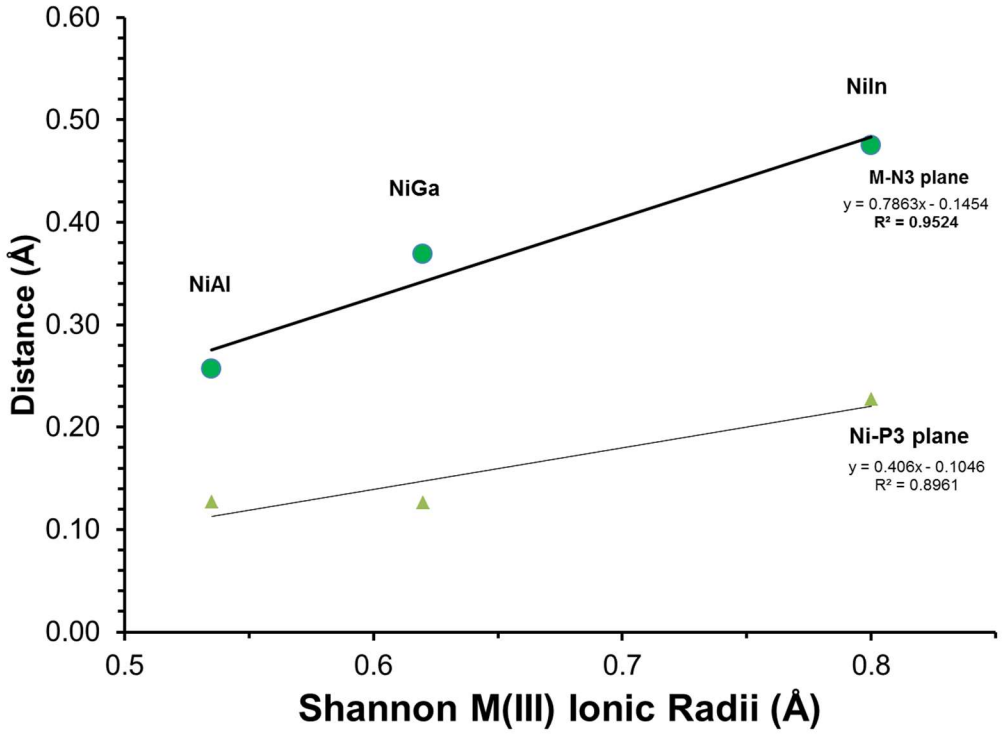

Figure A.1.7. Plot of M to N_3-plane and Ni to P_3-plane distances vs. M(III) ionic radii.

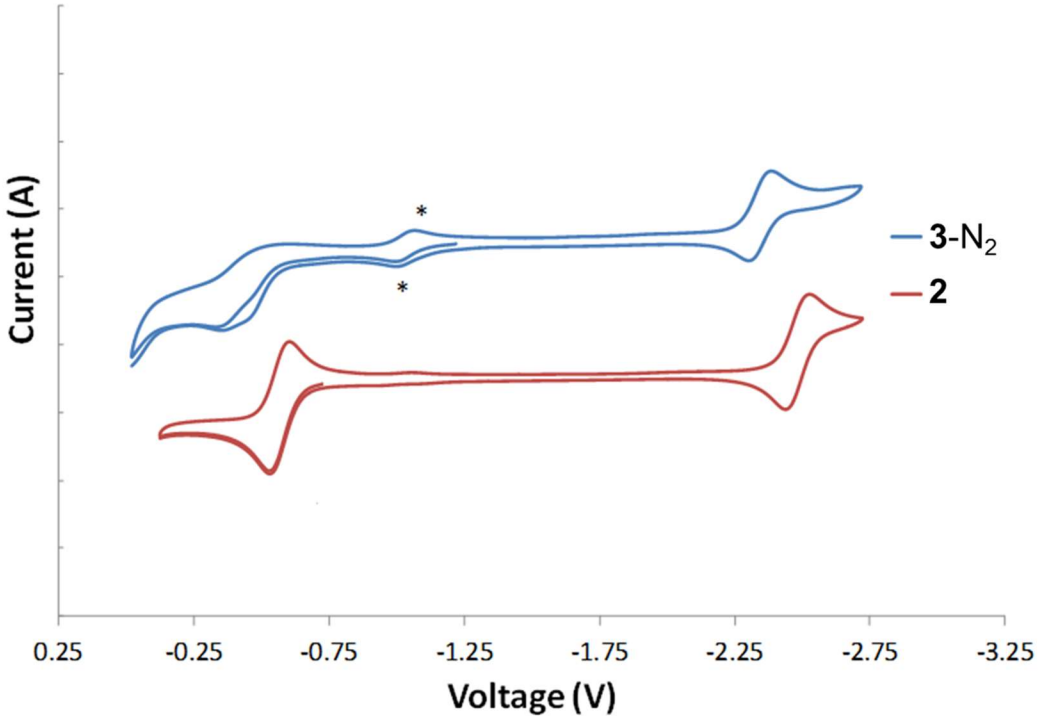

Figure A.1.8. Full cyclic voltammograms of **2**, and **3**−N_2 obtained in 0.1 M [TBA][PF_6] in THF at 25 mV/s. An asterisk (*) indicates an impurity of **4** that grows in over time.

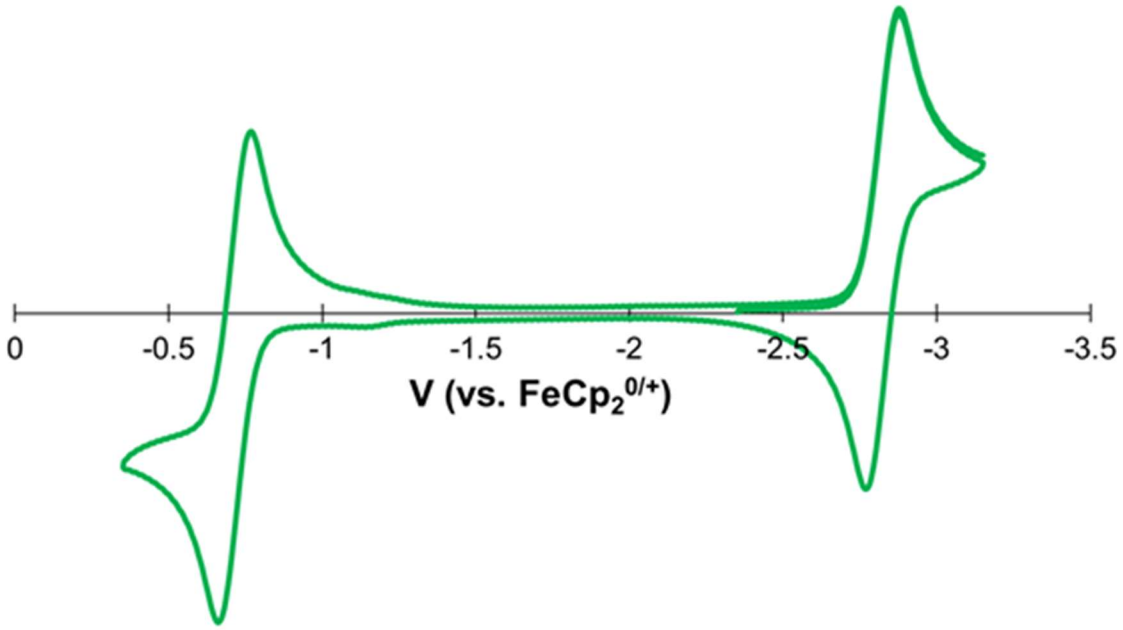

Figure A.1.9. Full cyclic voltammogram of **1** obtained in 0.4 M [TBA][PF_6] in THF at 50 mV/s. CV was re-collected because the reduction event was not originally reported.

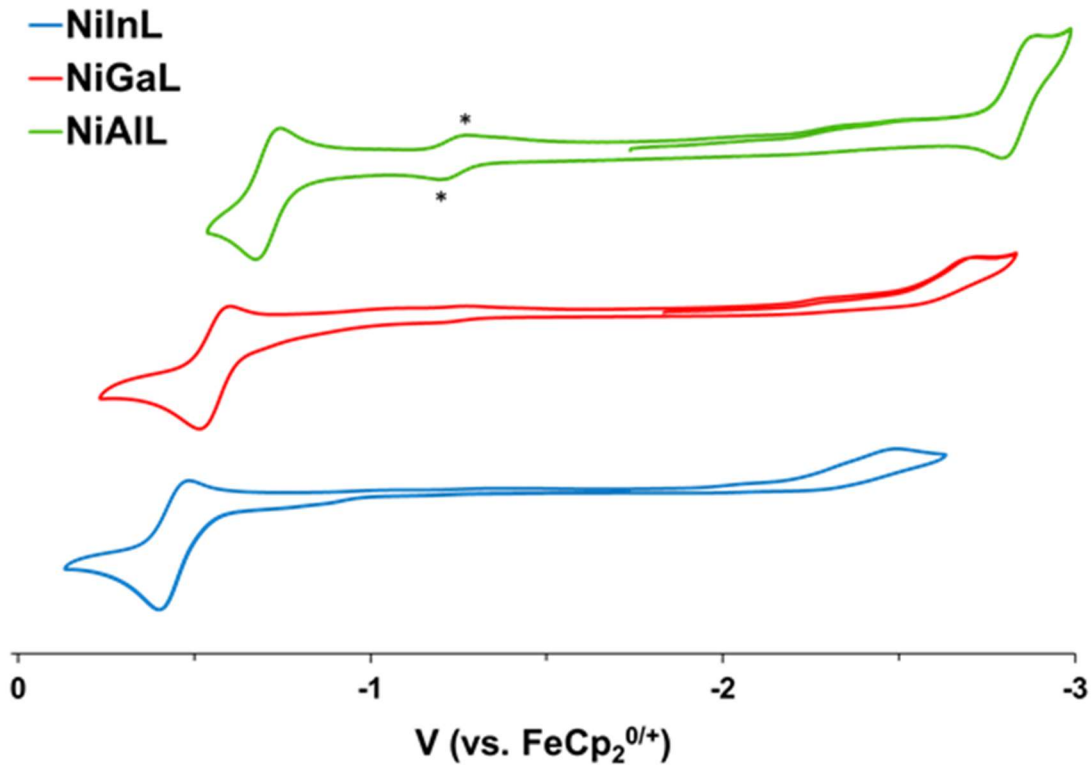

Figure A.1.10. Full cyclic voltammograms of **1**, **2**, and **3** obtained in 0.4 M [TBA][PF_6] in CH_3CN at 50 mV/s. An asterisk (*) indicates an impurity of **4**.

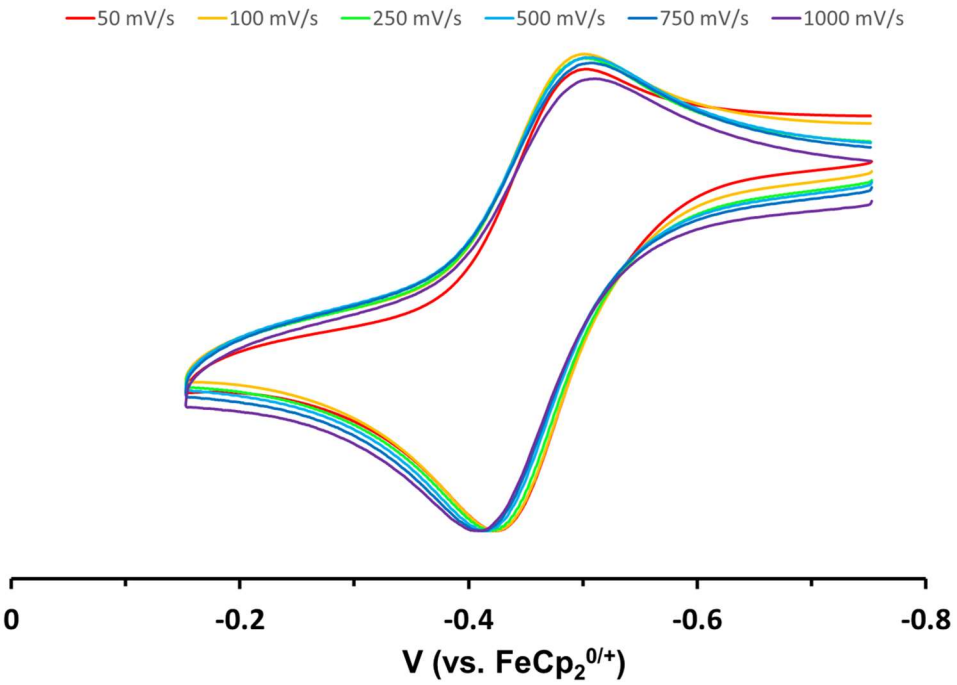

Figure A.1.11. Scan rate study for Ni(I/0) redox couple of **3** in 0.4 M [TBA][PF_6] in CH_3CN. Scan rates from 50 to 1000 mV/s were collected, with the peak remaining quasi-reversible at all scan rates examined. A similar relative insensitivity to scan rate was observed for the irreversible Ni(I/0) couple of **3** in THF.

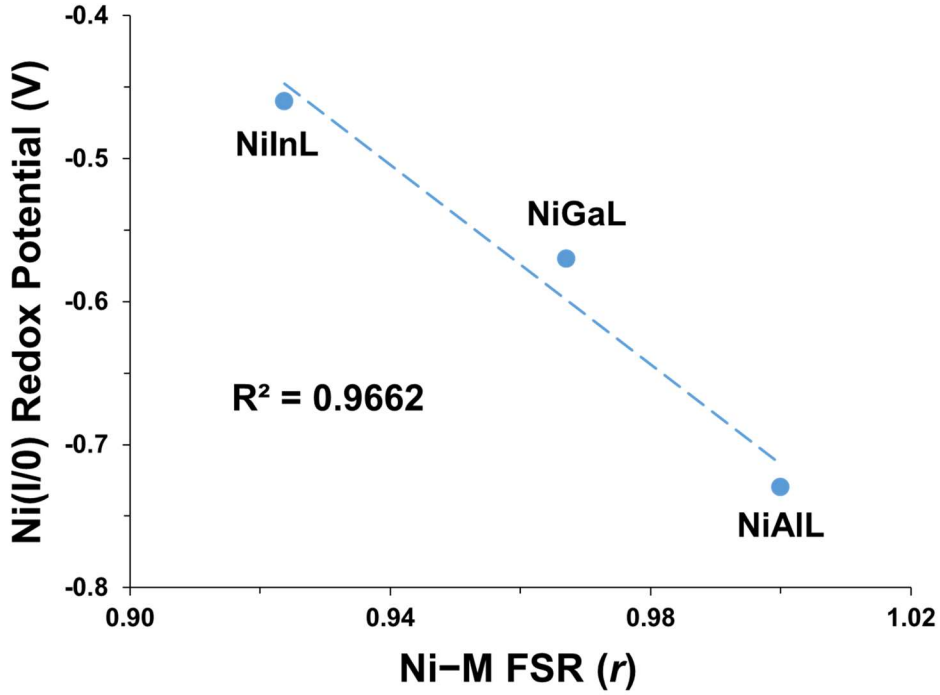

Figure A.1.12. Plot of Ni(I/0) redox potential in CH_3CN vs. Ni−M FSR ($r_{Alvarez}$). Note that the same plot for $r_{Pauling}$ values leads to a slightly worse correlation (R^2=0.896).

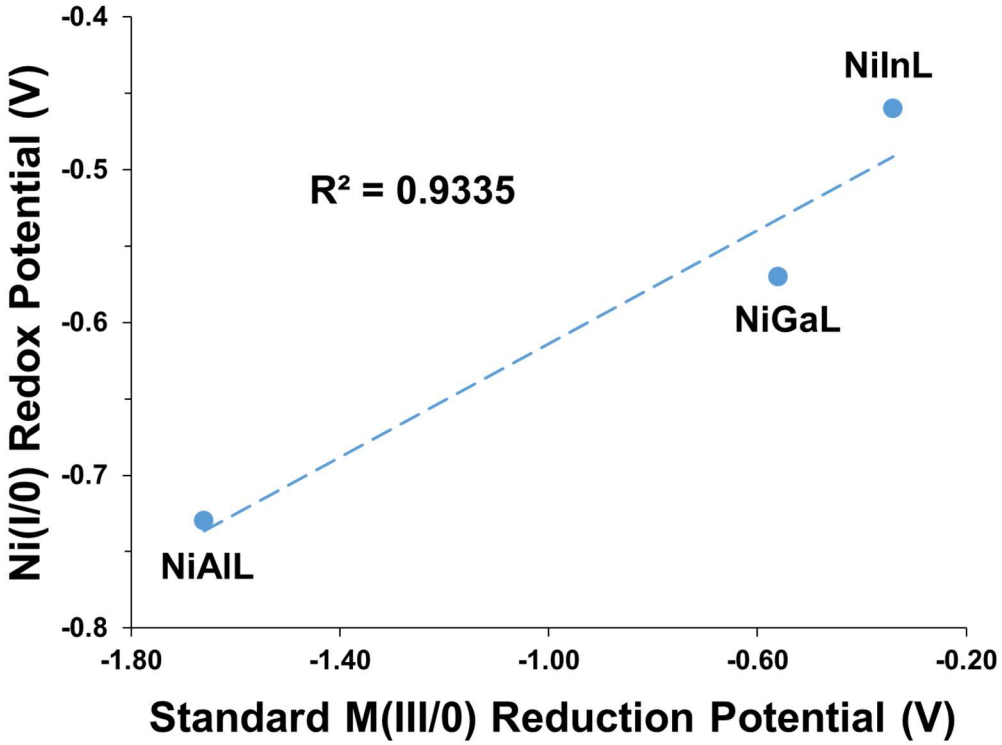

Figure A.1.13. Plot of Ni(I/0) redox potential in CH_3CN vs. standard M(III/0) reduction potential for group 13 M(III).

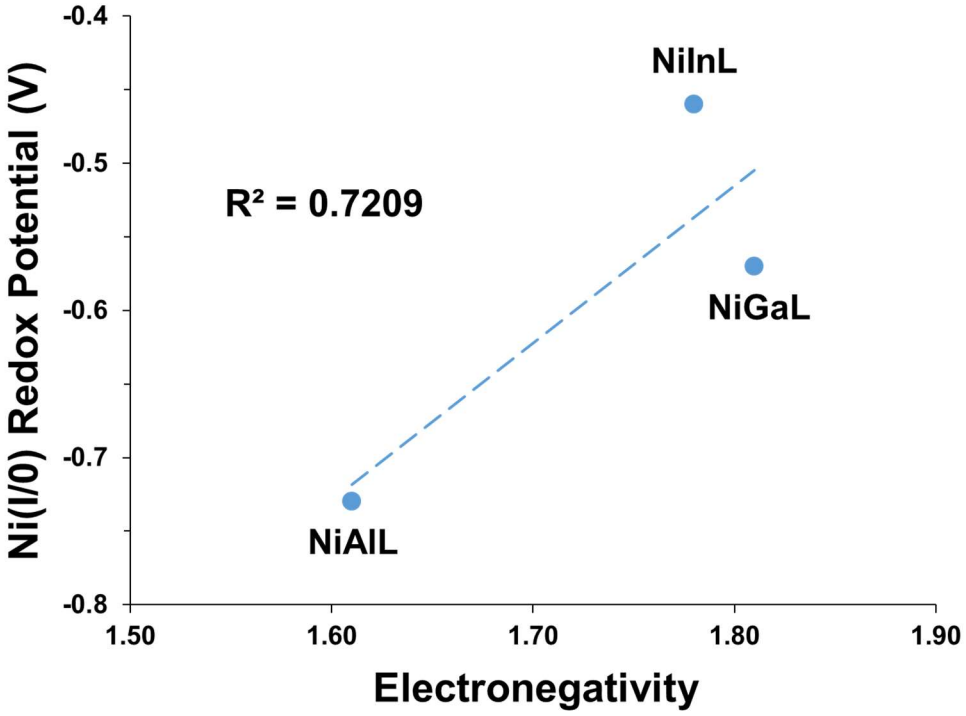

Figure A.1.14. Plot of Ni(I/0) redox potential in CH_3CN vs. electronegativity of group 13 M.

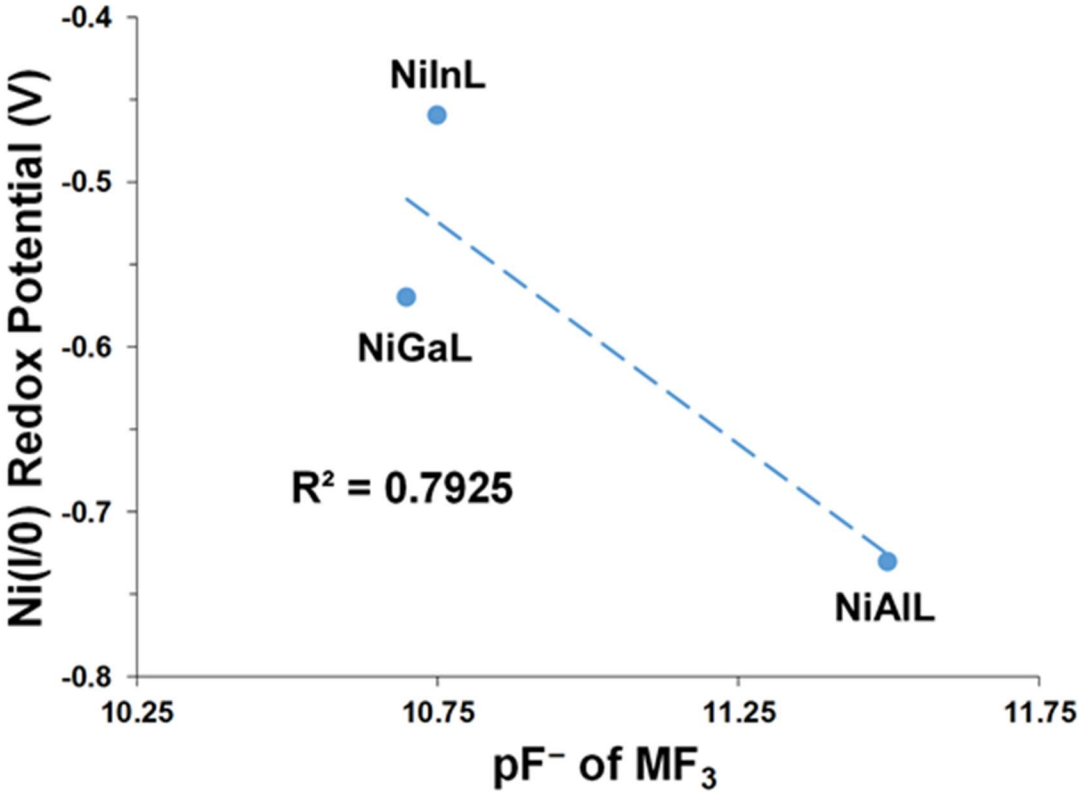

Figure A.1.15. Plot of Ni(I/0) redox potential in CH_3CN vs. pF^- of group 13 MF_3.

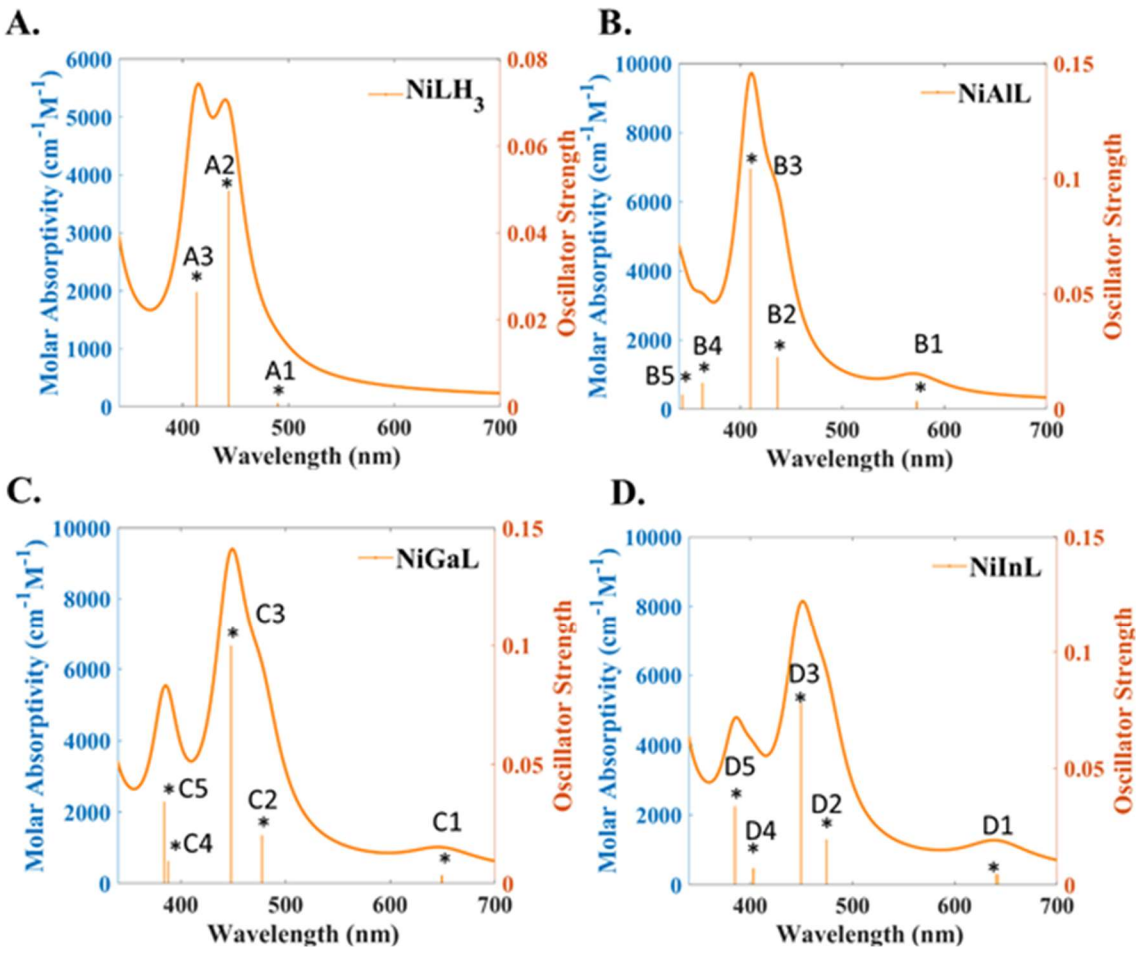

Figure A.1.16. Simulated UV-Vis spectrum of $NiLH_3$, NiAlL, NiGaL, and NiInL as calculated by TD-DFT with M06-D3 in THF (SMD). Transition labels (A1, A2, etc.) are assigned in Table A.1.1 on the following page.

Table A.1.1. M06-D3 TD-DFT transition assignments for $NiLH_3$, NiAlL, NiGaL, and NiInL complexes. Assignments refer to the simulated UV-vis spectra in Figure A.1.16.

Transition Types	M06-D3			expt.
$NiLH_3$	Index	nm	*f*	nm
$d_{xy}/d_{x^2-y^2} \rightarrow$ LUMO	A1	490	0.0008	
$d_{yz}/d_{xz} \rightarrow$ LUMO	A3	413	0.0264	497
$d_{z^2} \rightarrow$ LUMO	A2	443	0.0497	
NiAlL	Index	nm	*f*	nm
$d_{xy}/d_{x^2-y^2} \rightarrow$ LUMO	B1	573	0.0034	600
$d_{yz}/d_{xz} \rightarrow$ LUMO	B2	437	0.0225	490
Ligands N,C + $(d_{z^2}) \rightarrow$ LUMO	B3	410	0.1043	430
Ligands N,C + $d_{xz}/d_{yz} \rightarrow$ LUMO	B5	343	0.0063	
$d_{z^2} \rightarrow$ LUMO	B4	363	0.0114	
NiGaL	Index	nm	*f*	nm
$d_{xy}/d_{x^2-y^2} \rightarrow$ LUMO	C1	650	0.0034	638
$d_{yz}/d_{xz} \rightarrow$ LUMO	C2	478	0.0202	508
Ligands N,C + $d_{z^2} \rightarrow$ LUMO	C3	448	0.0999	464
Ligands N,C + $d_{xz}/d_{yz} \rightarrow$ LUMO	C4	388	0.0094	
$d_{z^2} \rightarrow$ LUMO	C5	384	0.0344	
NiInL	Index	nm	*f*	nm
$d_{xy}/d_{x^2-y^2} \rightarrow$ LUMO	D1	642	0.0046	699
$d_{yz}/d_{xz} \rightarrow$ LUMO	D2	475	0.0195	530
Ligands N,C + $(d_{z^2}) \rightarrow$ LUMO	D3	449	0.078	488
Ligands N,C + $d_{xz}/d_{yz} \rightarrow$ LUMO	D4	403	0.0071	
$d_{z^2} \rightarrow$ LUMO	D5	385	0.0337	

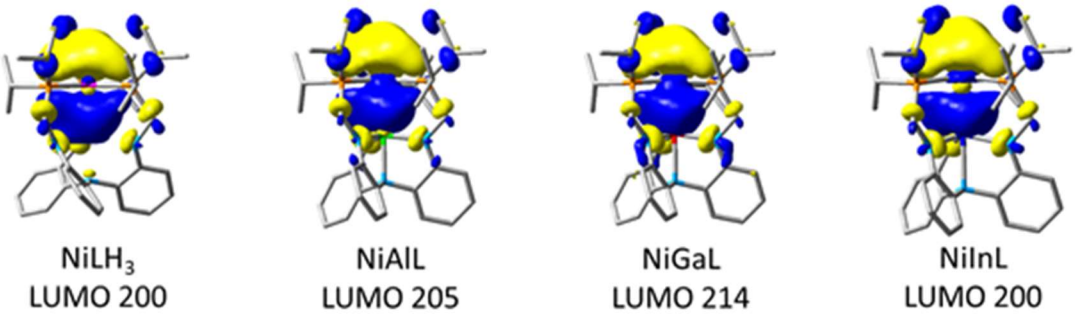

Figure A.1.17. LUMOs of $NiLH_3$ and NiML complexes, as calculated with M06-D3/bs4. Note that the analogous orbitals given by M06-L/bs1 have the same appearance.

Table A.1.2. Molecular orbital composition analysis of the LUMOs of $NiLH_3$ and NiML complexes. Pictures of the LUMOs are displayed in Figure A.1.17.

M06-D3/bs4			**Ni**			**M**		**P**
No.		# Orb	d	s	p	s	p	p
$NiLH_3$	LUMO	200						0.90
NiAlL	LUMO	205	0.05	0.11		0.10	0.16	0.50
NiGaL	LUMO	214	0.08	0.12		0.14	0.12	0.42
NiInL	LUMO	200	0.09	0.15		0.13	0.08	0.50

M06-L/bs1			**Ni**			**M**		**P**
MO	No.		d	s	p	s	p	p
$NiLH_3$	LUMO	200			0.23			0.30
NiAlL	LUMO	205	0.06		0.14	0.16	0.10	0.18
NiGaL	LUMO	214	0.09		0.16	0.17	0.08	0.18
NiInL	LUMO	200	0.08	0.07	0.11	0.21	0.12	0.23

Appendix 2: Supplemental Figures for Chapter 3

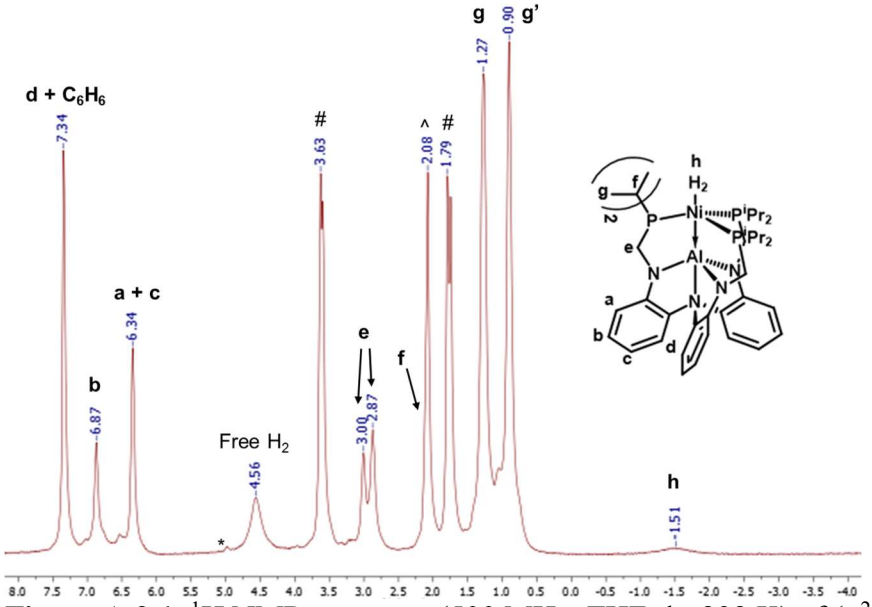

Figure A.2.1. ^{1}H NMR spectrum (500 MHz, THF-d_8, 232 K) of (η^2-H_2)NiAlL (**1**−H_2) generated *in-situ* from binding equilibrium of **1** (~50 mM) under 34 atm H_2. Low T and elevated H_2 pressure are needed to drive the binding equilibrium toward **1**−H_2. However, it should be noted that the binding equilibrium only converges to near complete binding at very low T (200 K). Residual solvent peaks of THF (#), toluene (^), and C_6H_6 are denoted, and a small N*H* peak of the $NiLH_3$ ^{31}P chemical shift standard (4.99 ppm) are denoted (*).

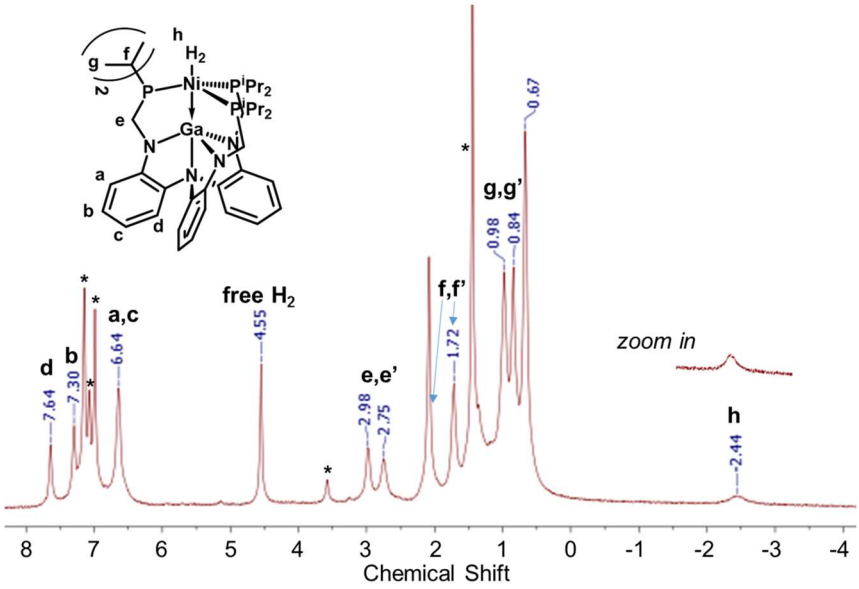

Figure A.2.2. ^{1}H NMR spectrum (500 MHz, toluene-d^8) of (η^2-H_2)NiGaL (**2**−H_2) at 200 K under 13.6 atm H_2. Peaks are labelled with their assignments, and a close-up of the hydride region is shown for visual clarity. Residual solvent peaks indicated by asterisks (*).

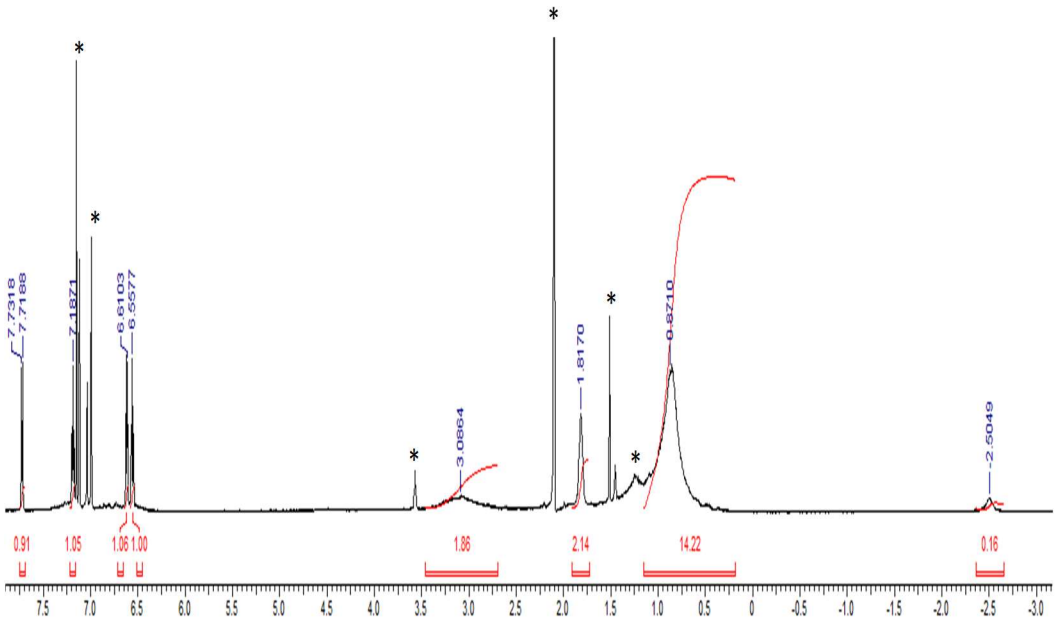

Figure A.2.3. ^{1}H NMR spectrum (600 MHz, toluene-d^{8}) of (η^{2}-H$_2$)NiInL (**3**−H$_2$) at 281 K under 1 atm H$_2$. Residual solvent peaks indicated by *.

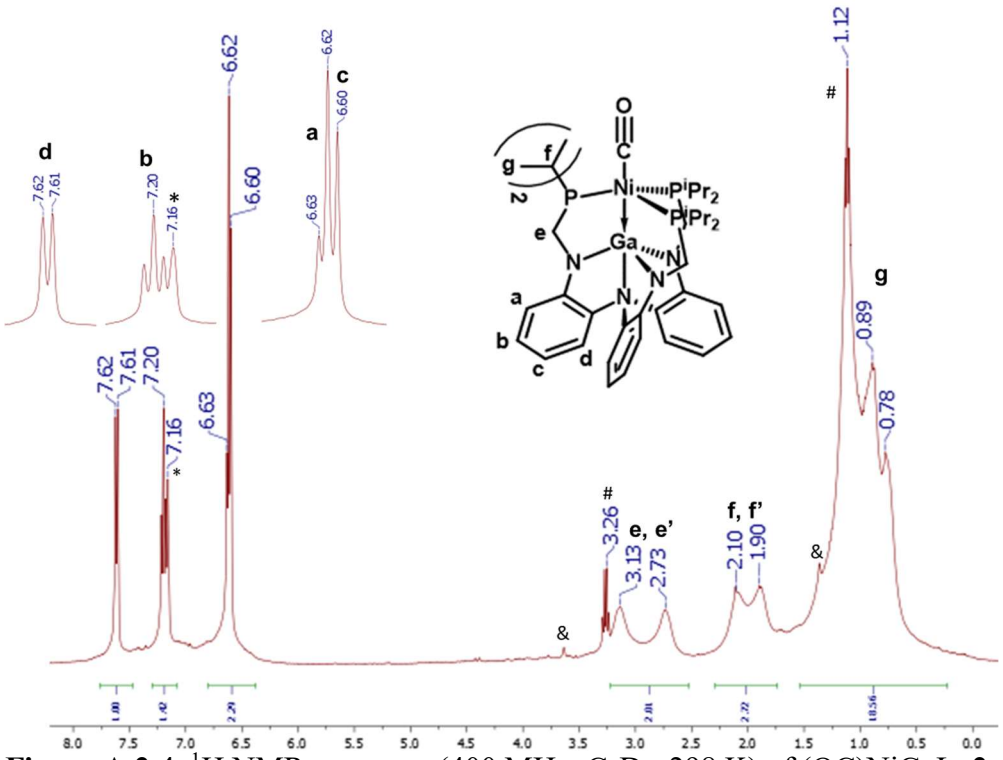

Figure A.2.4. ^{1}H NMR spectrum (400 MHz, C$_6$D$_6$, 298 K) of (OC)NiGaL, **2**−CO. Residual solvent peaks of benzene (*), THF (&), diethyl ether (#) are denoted. Inset shows a zoom in of the aryl region showing resolved coupling (*top left*).

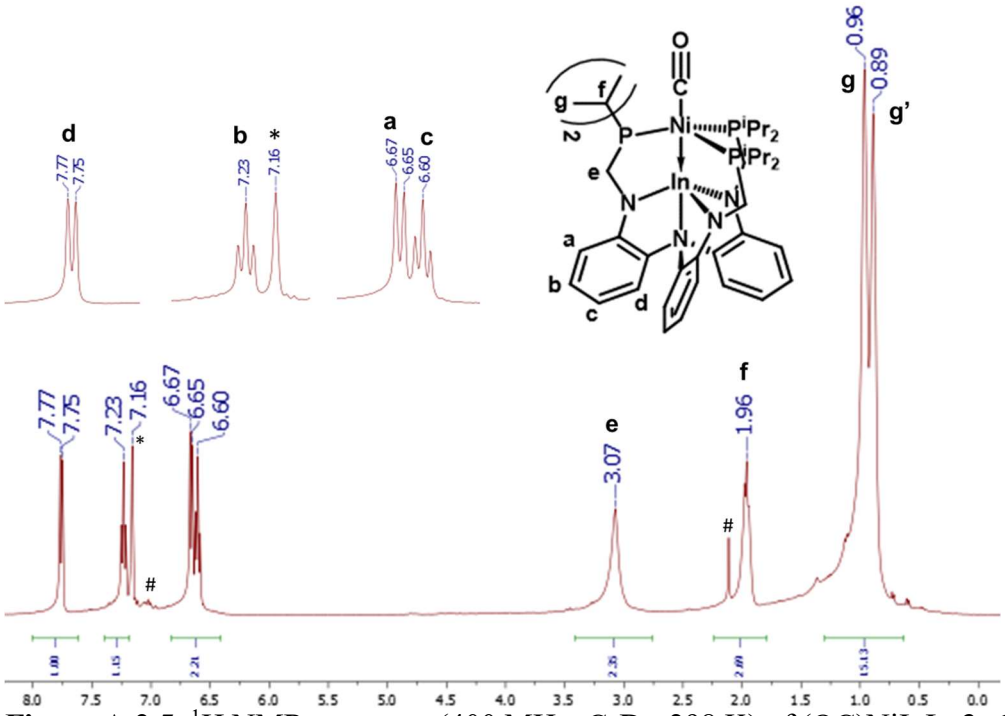

Figure A.2.5. ^{1}H NMR spectrum (400 MHz, C_6D_6, 298 K) of (OC)NiInL, **3**−CO. Residual solvent peaks of benzene (*) and toluene (#) are denoted. Inset shows a zoom in of the aryl region showing resolved coupling (*top left*).

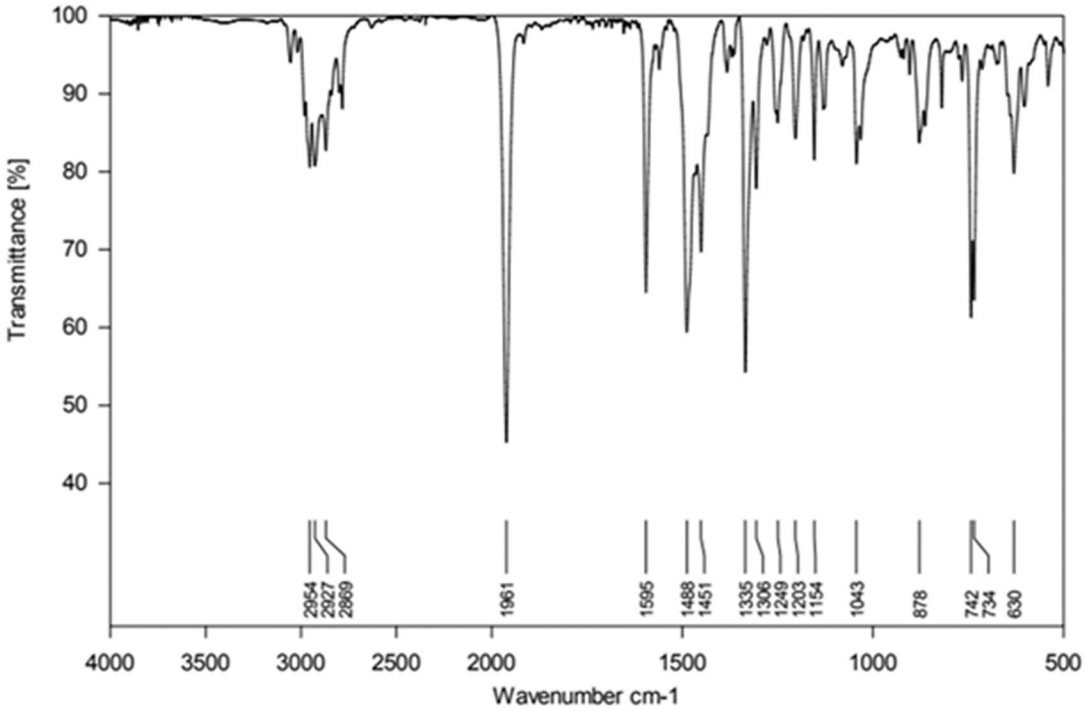

Figure A.2.6. IR spectrum (KBr pellet) of (OC)NiGaL (**2**−CO), showing ν(C≡O)=1961 cm^{-1}.

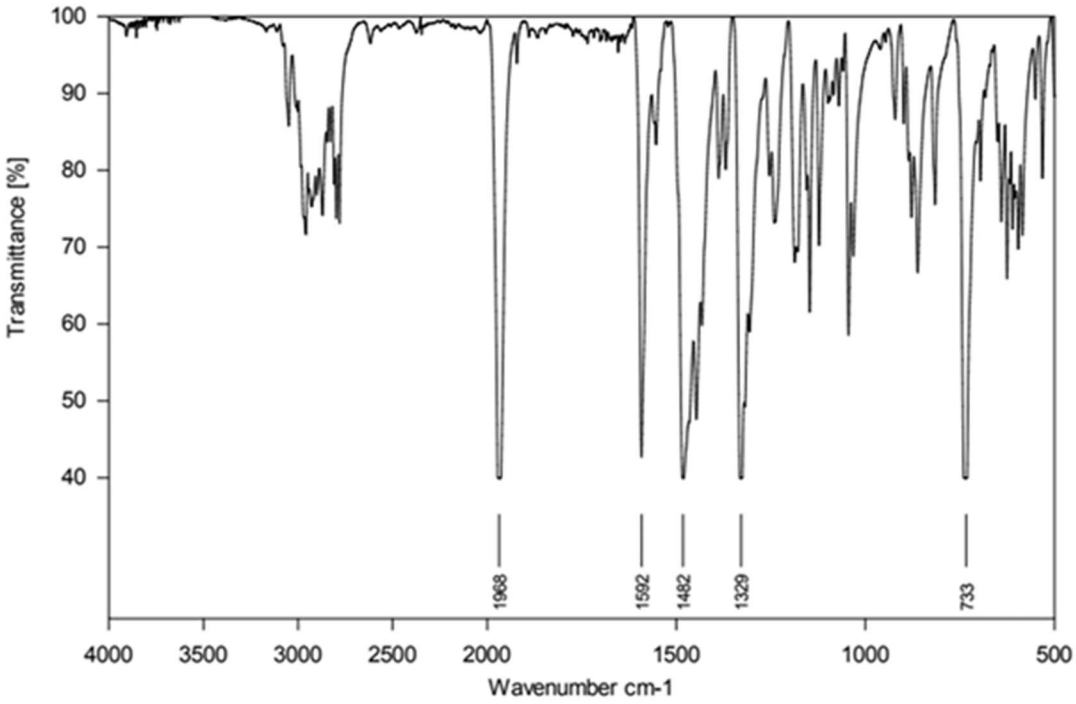

Figure A.2.7. IR spectrum (KBr pellet) of (OC)NiInL (**3**−CO), showing ν(C≡O)=1968 cm^{-1}.

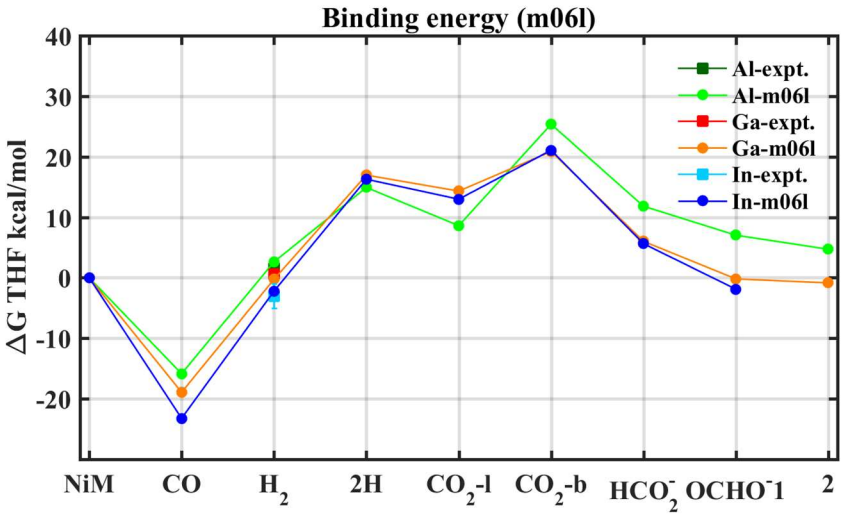

Figure A.2.8. DFT-calculated binding energies (M06-L/bs1) for NiML complexes showing that the relative order of ligand binding is: CO >> H_2 >> CO_2 for all complexes. Relative energies of linear (CO_2-l) and bent (CO_2-b) binding modes for CO_2 are shown (see Figure A.2.9 for optimized structures of different binding modes). Also shown are relative energies of $(H)_2$NiML ("2H") and two different modes of formate binding, H-bound (HCO_2^-) and O-bound ($OCHO^-$), which are not relevant here, but will be discussed in chapters 4-5. Also, note that THF is the solvent for these calculations, but minimal differences in binding energies for THF vs. toluene was subsequently calculated. Note that this figure is courtesy of Dr. Jing Xie.

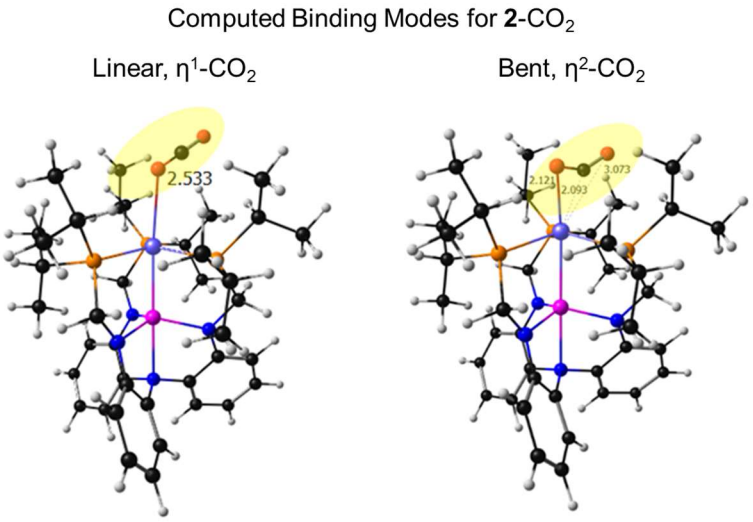

Figure A.2.9. DFT-calculated (M06-L/bs1) binding modes for CO_2 to complex **2**. The linear binding mode, where CO_2 is coordinated η^1 through oxygen, is calculated to be more stable by 5.6 kcal/mol than the bent mode, where CO_2 is coordinated side-on, η^2, presumably through one of CO_2 π bonds. Similar CO_2 binding modes and relative stabilities were also predicted for complexes **1** and **3**. Note that this figure has been adapted from that provided by Dr. Jing Xie.

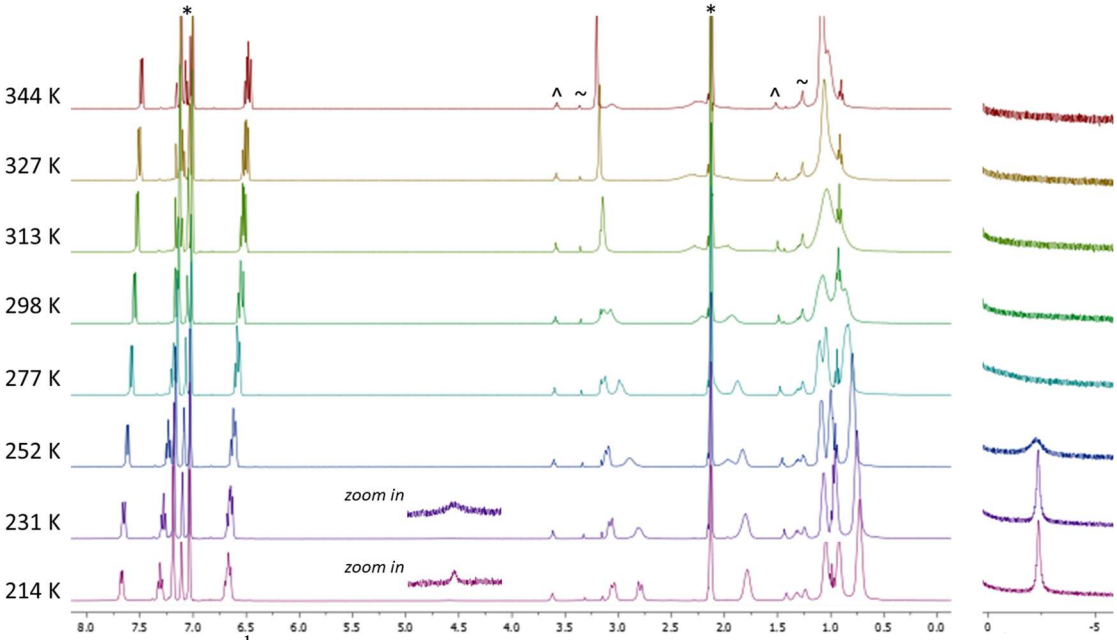

Figure A.2.10. VT ^{1}H NMR (toluene-d_8, 162 MHz) of **2** (~7.5 mM in 0.70 mL) under 1 atm H_2. Residual solvent peaks for toluene (*), THF (^), and diethyl ether (~) are denoted. Peaks for both free H_2 and bound H_2 are observable at T < 240 K, indicating that the binding equilibrium between free H_2 and Ni-bound H_2 becomes slow on the ^{1}H NMR timescale at low T (allowing both peaks to be observable). The free and bound H_2 resonances sharpen as T decreases from 252 K to 214 K. The methylene CH_2 protons (~3.14 ppm) are seen to be equivalent at T > 300 K, and observed to become inequivalent diastereotopic protons at 298 K and below.

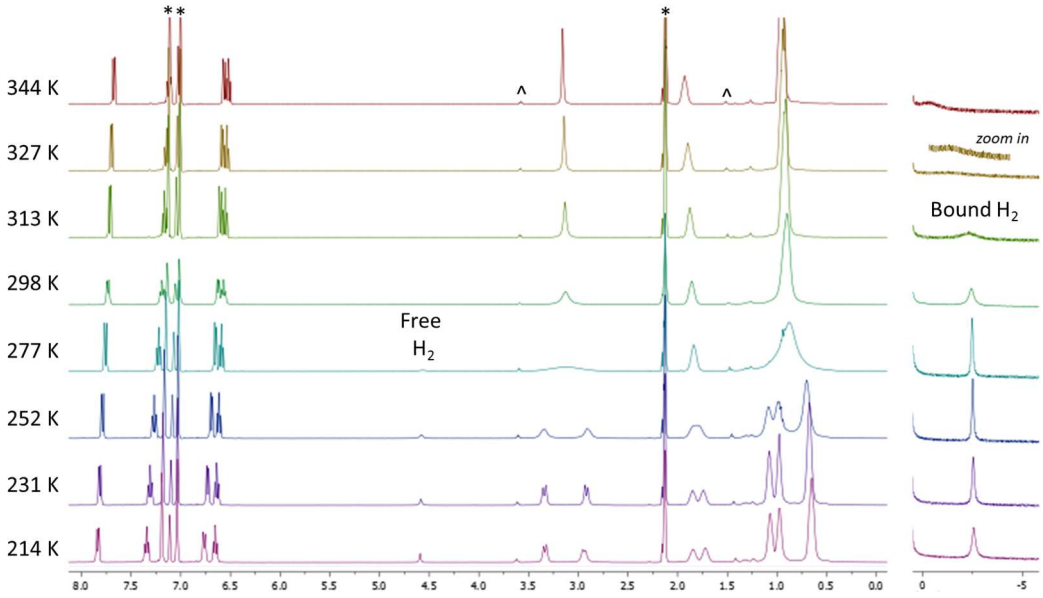

Figure A.2.11. VT ^{1}H NMR (toluene-d$_8$, 162 MHz) of **3** (~7.5 mM in 0.70 mL) under 1 atm H_2. Residual solvent peaks for toluene (*) and THF (#) are denoted. Peaks for both free H_2 and bound H_2 are observable at T < 300 K, indicating that the binding equilibrium between free H_2 and Ni-bound H_2 is slowing on the NMR timescale as T decreases (allowing both peaks to be observable). The bound H_2 resonance sharpens as T decreases from 313 K to 252 K, before broadening again with further decreases in T to 214 K. The methylene C*H*$_2$ protons (~3.15 ppm) are seen to be equivalent at T > 277 K, and observed to become inequivalent diastereotopic protons at lower T.

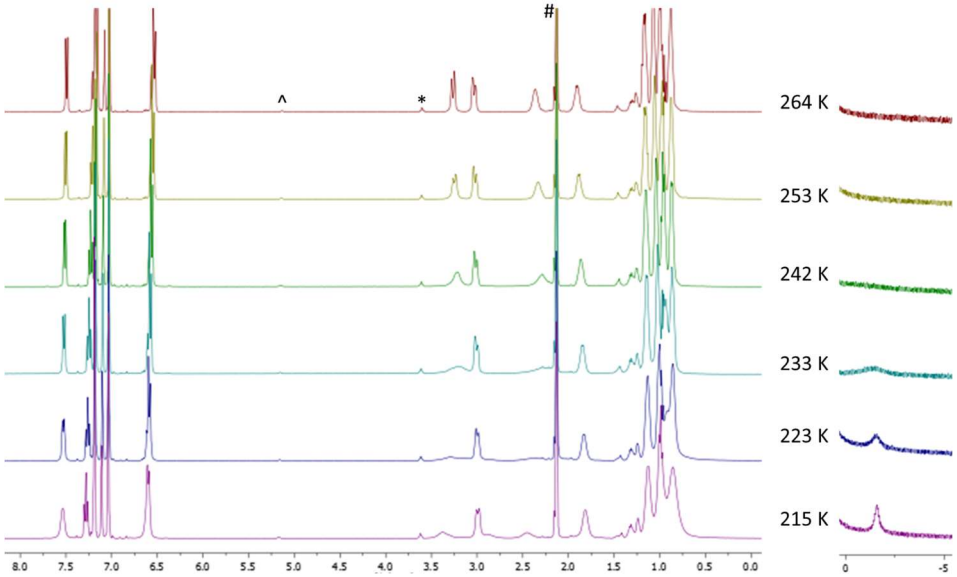

Figure A.2.12. VT ^{1}H NMR (toluene-d$_8$, 162 MHz) of **1** (~7.5 mM in 0.70 mL) under 1 atm H_2. (from 264 K to 215 K). Residual solvent peaks for toluene (#) and THF (*) are denoted, along with the N*H* peak (^) of the $NiLH_3$ chemical shift standard for ^{31}P NMR. A peak for Ni-bound H_2 is observable at ~ −1.6 ppm, with its lineshape sharpening upon cooling.

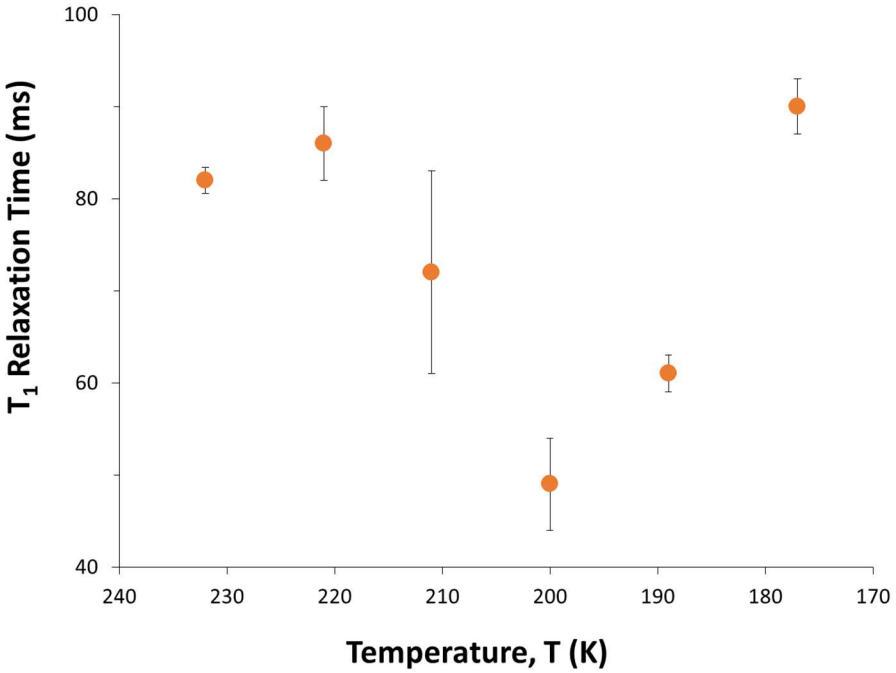

Figure A.2.13. Plot of T_1 relaxation time (in ms) of the bound H_2 resonance of **1**−H_2 vs. T (K) for **1** (~50 mM) under 34 atm H_2. T_1(min) was found to be 49 (±5) ms at 200 K, with the short T_1 value suggesting an intact H_2 ligand.

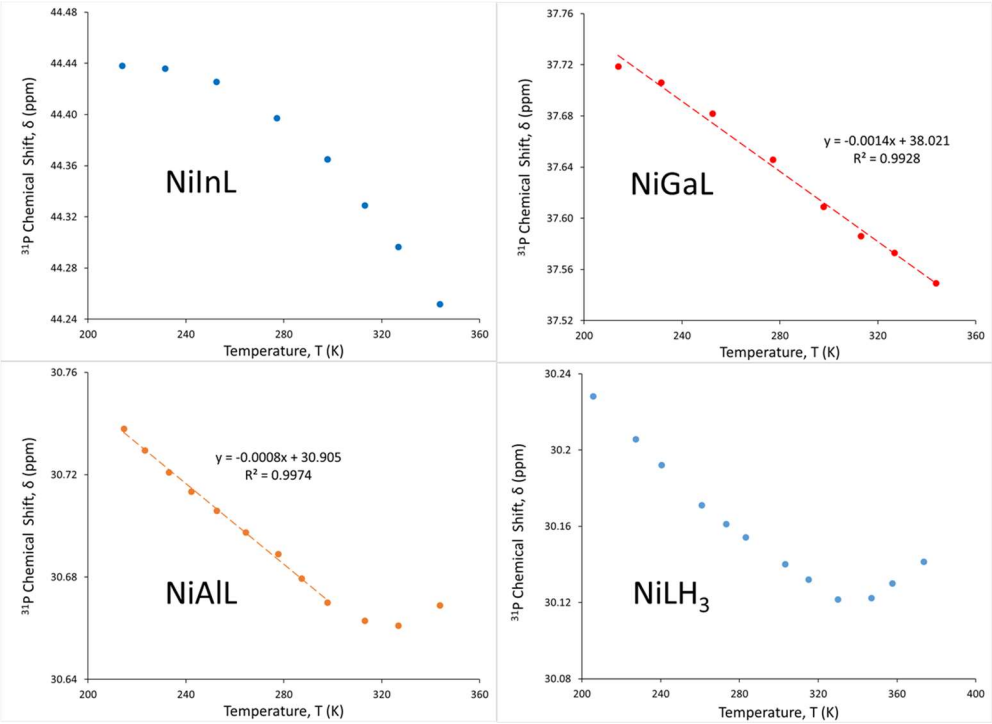

Figure A.2.14. ^{31}PNMR chemical shift dependence on T for complexes **1-4** in toluene-d_8 under 1 atm Argon from 213 K to 344 K. The observed chemical shift changes by <0.08, <0.18, <0.20, and <0.12 ppm over this T range for NiAlL (**1**), NiGaL (**2**), NiInL (**3**), and $NiLH_3$ (**4**), respectively.

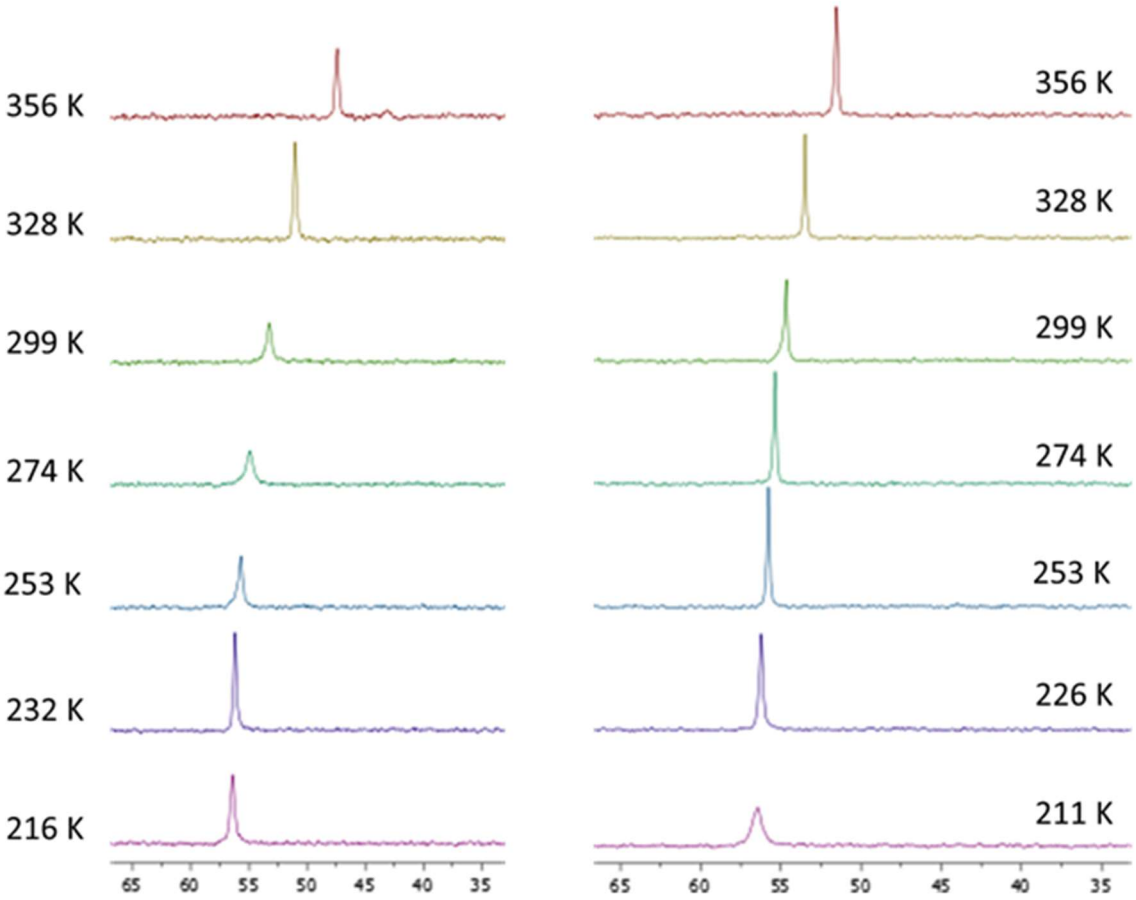

Figure A.2.15. VT ^{31}P NMR (toluene-d_8, 202.4 MHz) of **2** (~15 mM in 0.30 mL) under 13.6 atm H_2 (left) and 34.0 atm H_2 (right) obtained over the range from 210 K to 360 K. A fast equilibrium on the ^{31}P NMR timescale (202.4 MHz) is observable over the entire T range for both pressures. Due to the larger sampling of the equilibrium (ie. greater variance of δ), the data at 13.6 atm H_2 was used to obtain a van't Hoff plot (Figure A.2.16). Averaging the results obtained at 6.8 atm and 13.6 atm H_2 gives the final results for the H_2 binding parameters to **2** (Table 3.5). Also note that the ^{31}P resonance under 34 atm H_2 begins to broaden as T decreases from 226 K to 211 K, which is due to a process involving the loss of symmetry of the three phosphine donors, which is seen more clearly for (OC)NiML at low T.

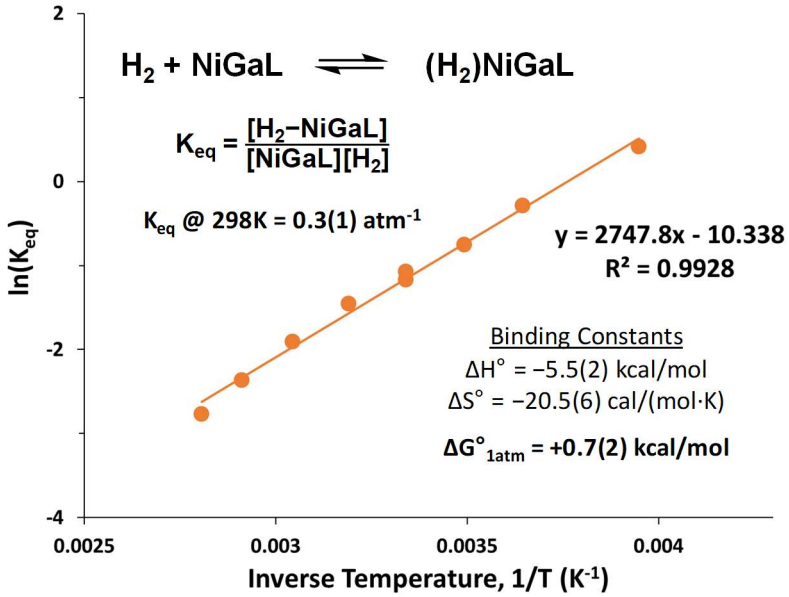

Figure A.2.16. Van't Hoff plot of $\ln(K_{H_2})$ vs. 1/T for H_2 binding equilibrium to **2**, based on VT ^{31}P NMR data displayed in Figure A.2.15 (collected under 13.6 atm H_2 for 9 data points from 250 K to 356 K). The thermodynamic binding constants ($\Delta H°$, $\Delta S°$, and $\Delta G°$) and the associated uncertainties obtained from linear regression of the van't Hoff plot are also displayed above (standard conditions: 298 K, 1 atm H_2, 1 M of all other species, toluene-d_8). Rigorously fast chemical exchange was able to be observed at all T >240 K, facilitating analysis of K_{H_2} at each T based on the observed chemical shift. The free energy value obtained at 13.6 atm H_2 of +0.7(2) kcal/mol was averaged with that obtained at 6.8 atm H_2 (+0.5(2) kcal/mol) to give the final value of +0.6(2) kcal/mol for H_2 binding to **2**.

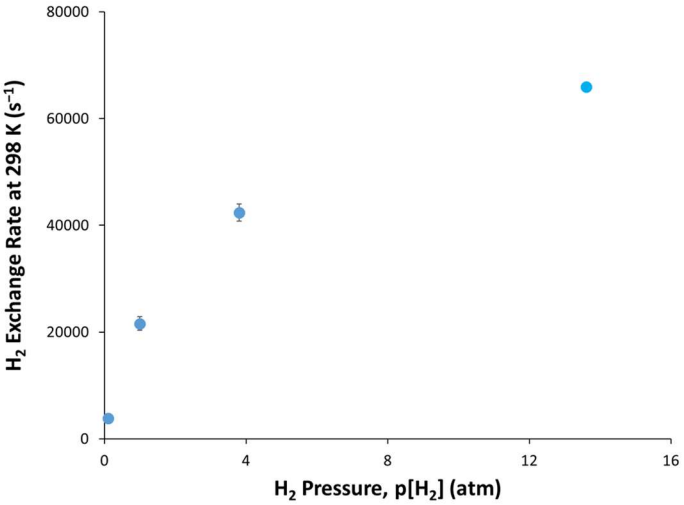

Figure A.2.17. Plot of H_2 self-exchange rate for **2** at 298 K (~7.5 mM in 0.70 mL toluene-d_8) vs. H_2 gas pressure. As the H_2 pressure increases, the exchange of free and bound H_2 takes place more rapidly, from 3.8(2) x 10^3 s^{-1} at 0.1 atm H_2 (remaining 0.9 atm Ar), to 2.2(2) x 10^4 s^{-1} at 1 atm H_2, to 4.2(2) x 10^4 s^{-1} at 3.8 atm H_2. At 13.6 atm H_2, the exchange rate was estimated to be ~6.6 x 10^4 s^{-1}.

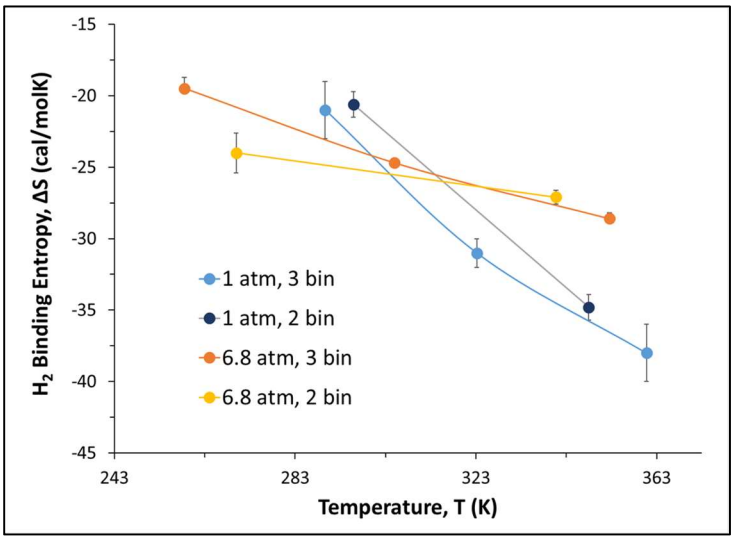

Figure A.2.18. Plot of $\Delta S°$ (cal/[mol·K]) for H_2 binding to **2** vs. average T of the T regime from which van't Hoff analyses were conducted on subsets of the full dataset. At 1.0 atm, $\Delta S°$ was found to be −35(1) and −21(1) kcal/mol for high and intermediate/low T regimes, respectively. Clearly these values are not constant and their significant temperature-dependence can be attributed to the breakdown of the assumption of fast exchange at 1.0 atm H_2. At 6.8 atm H_2, $\Delta S°$ was found to be more constant, with values of −27.1(5) and −24(1.4) kcal/mol for high and intermediate/low T regimes, respectively.

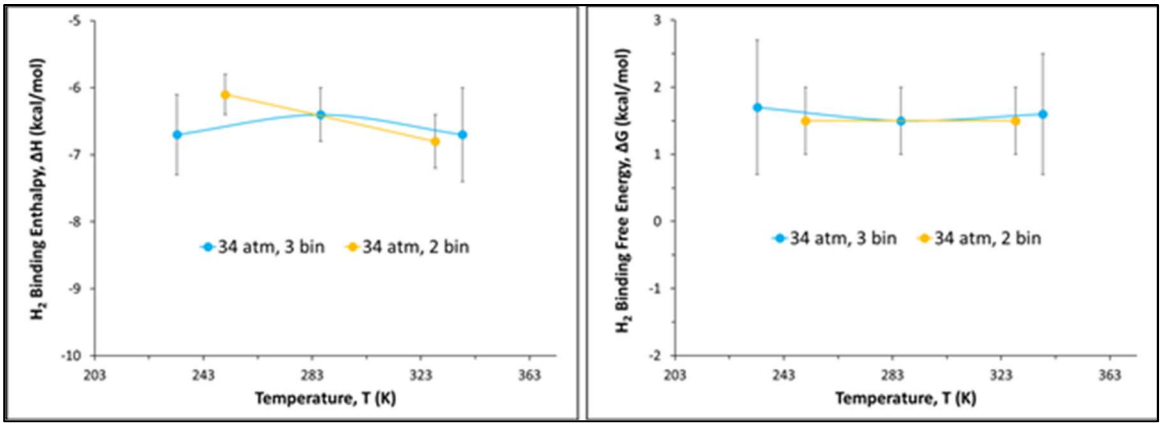

Figure A.2.19. Plot of $\Delta H°$ (left) and $\Delta G°$ (right) for H_2 binding to **1** vs. average T of the T regime for which the van't Hoff analysis was conducted. $\Delta H°$ was found to be −6.7(7), −6.4(4), −6.7(6) kcal/mol for high, intermediate, and low T regimes, respectively. $\Delta S°$ was found to be −28(2), −27(1), −28(3) cal/(mol·K) for high, intermediate, and low T regimes, respectively. Lastly, $\Delta G°$ was found to be +1.6(9), +1.5(5), +1.7(1.0) kcal/mol for high, intermediate, and low T regimes, respectively. All values are seen to be within experimental error of one another for all T ranges; similar results were found for $\Delta S°$ and $\Delta H°$, which is why the former plot was not shown. Note that the larger errors compared with the full dataset are because fewer data points are included in each van't Hoff analysis upon dividing the full dataset into different T regimes.

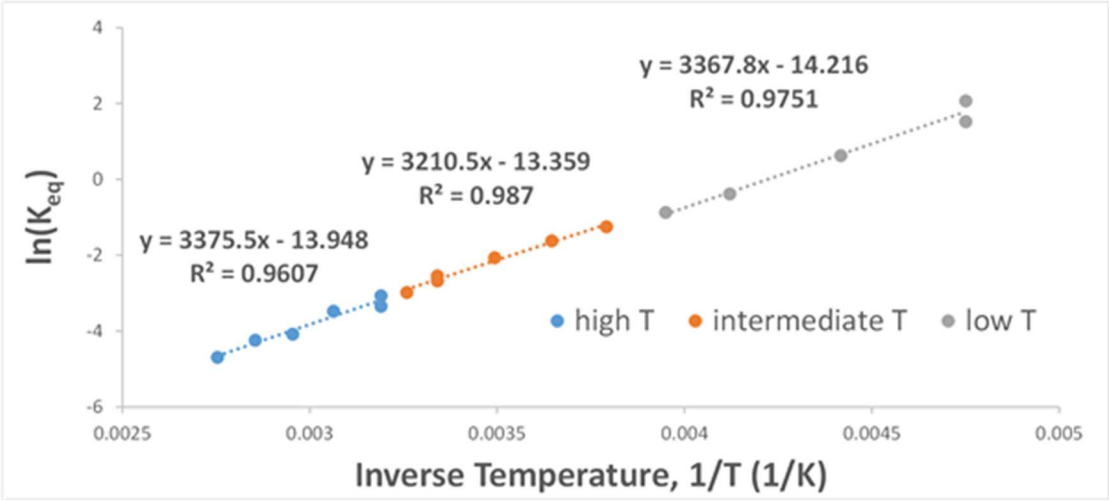

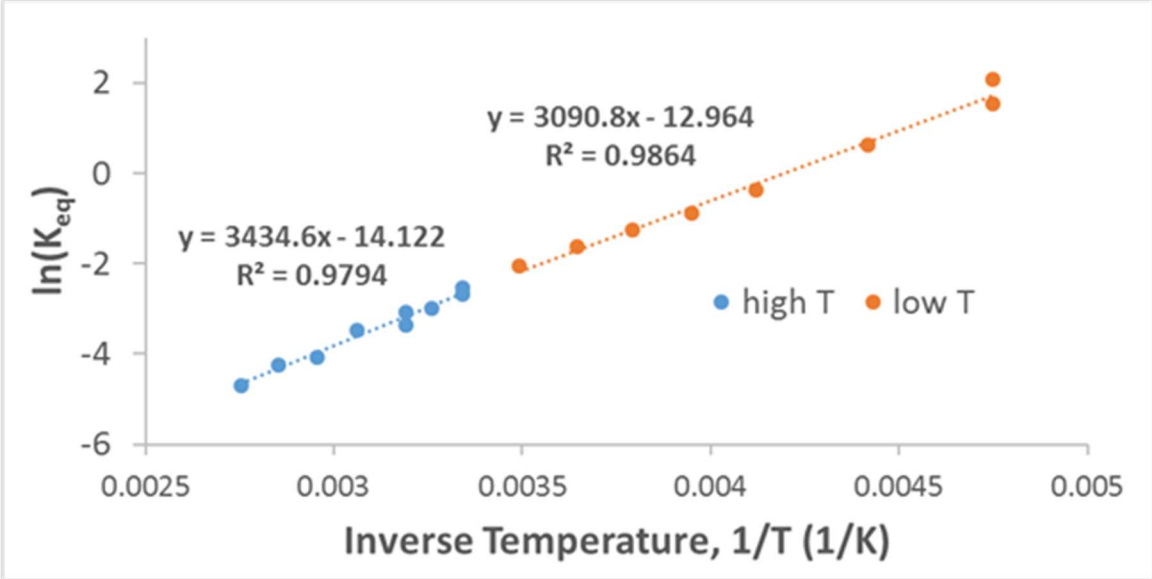

Figure A.2.20. Van't Hoff plot of $\ln(K_{H_2})$ vs. 1/T for H_2 binding equilibrium to **1** under 34.0 atm H_2, with the data broken up into T regimes in two different ways for analysis: (1) 3 "bins", with low T (210 K to 253 K), intermediate T (263 K to 307 K), high T (313 K to 368 K); and (2) 2 "bins", with low T (210 K to 287 K) and high T (298 K to 368 K). If fast exchange is a rigorously valid assumption at all T, then the binding parameters extracted from the slope and y-intercept of the van't Hoff plot should be essentially identical for all T regimes. This is seen to be the case, and Figure A.2.19 shows the invariance of $\Delta H°$ and $\Delta G°$ with T regime.

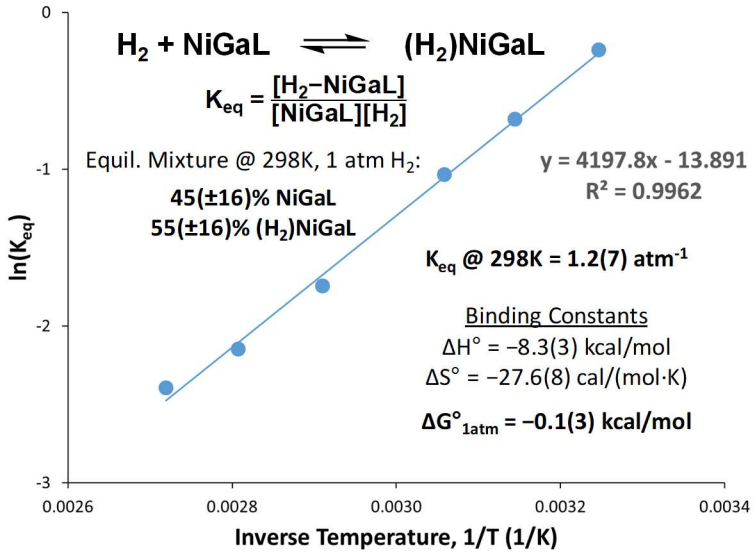

Figure A.2.21. Van't Hoff plot of $\ln(K_{H_2})$ vs. 1/T for H_2 binding equilibrium to **2**, based on VT ^{31}P NMR data collected under 0.1 atm H_2 from 300 K to 368 K. The thermodynamic binding parameters ($\Delta H°$, $\Delta S°$, and $\Delta G°$) and the associated uncertainties are displayed above (298 K, 1 atm H_2, 1 M of all other species, toluene-d_8). $\Delta G°$ was found to be −0.1(3) kcal/mol under 0.1 atm H_2 compared with +0.6(2) kcal/mol under the ideal fast exchange conditions at 6.8 and 13.6 atm H_2. Thus, a correction factor of +0.7 kcal/mol was applied to the value obtained for **3** under 0.1 atm H_2, giving a best estimate of $\Delta G°$ = −3.0(7) kcal/mol for the H_2 binding to **3**.

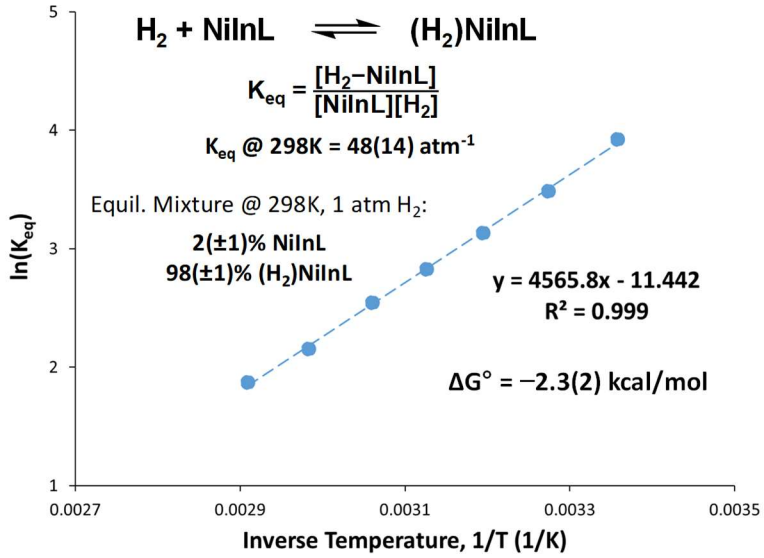

Figure A.2.22. Van't Hoff plot of $\ln(K_{H_2})$ vs. 1/T for H_2 binding equilibrium to **3**, based on relative concentrations of bound and unbound species from simulated VT ^{31}P NMR spectra (see Figure A.2.29). $\Delta G°$ and the associated uncertainty is displayed above (standard conditions: 298 K, 1 atm H_2, 1 M of all other species, toluene-d_8). Importantly, the $\Delta G°$ value from this plot (−2.3(2) kcal/mol) is within experimental error of the best estimate from the van't Hoff plot for 0.1 atm H_2 (−3.0(7) kcal/mol) after adjustment based on the control for **2** (Figure A.2.21).

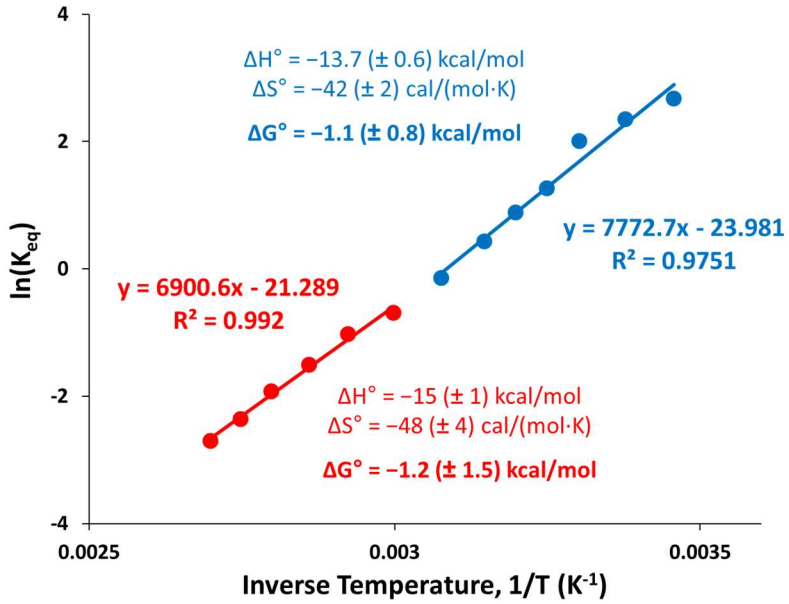

Figure A.2.23. Van't Hoff plot of $\ln(K_{N_2})$ vs. 1/T for N_2 binding equilibrium to **3**, based on VT ^{31}P NMR data collected under 1.0 atm N_2 for T range from 288 K to 370 K. To assess the validity of the fast exchange assumption, the data has been broken up into two different T regimes: high T (333 K to 370 K) and intermediate T (289 K to 325 K). All T < 288 K were not considered for van't Hoff analysis because exchange clearly slows. Fast exchange is a valid assumption at all T > 288 K, as evidenced by the fact that $\Delta H°$, $\Delta S°$, and $\Delta G°$ (displayed above) determined from data in different T regimes are within experimental error of one another.

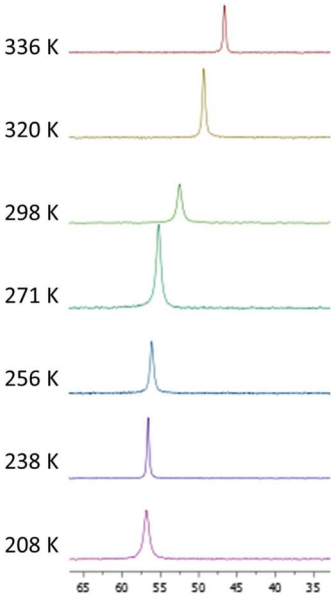

Figure A.2.24. VT ^{31}P NMR (THF, 161.9 MHz) of **2** (~12.2 mM in 0.62 mL) under 3.8 atm H_2 obtained over the range from 218 K to 336 K. The peak does not broaden significantly, indicating that the fast exchange assumption is valid for all T > 210 K, which were used to obtain a Van't Hoff plot (Figure A.2.26).

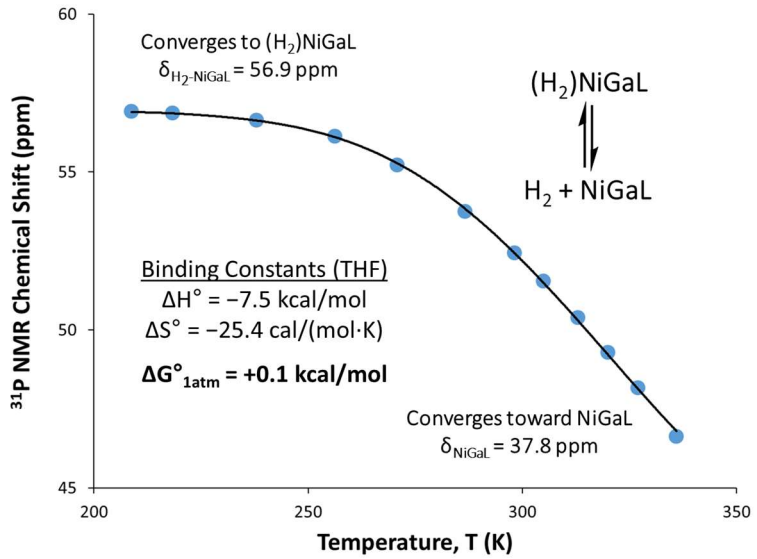

Figure A.2.25. Plot of ^{31}P NMR chemical shift vs. T for VT ^{31}P NMR data collected for **2** under 3.8 atm of H_2 in THF from 218 K to 336 K (Figure A.2.24), with both experimental (blue data points) and best-fit simulation profiles (black line) plotted. The best-fit simulation gave thermodynamic parameters that match those obtained from van't Hoff analysis (within the experimental error given by the van't Hoff plot regression; see Figure A.2.26).

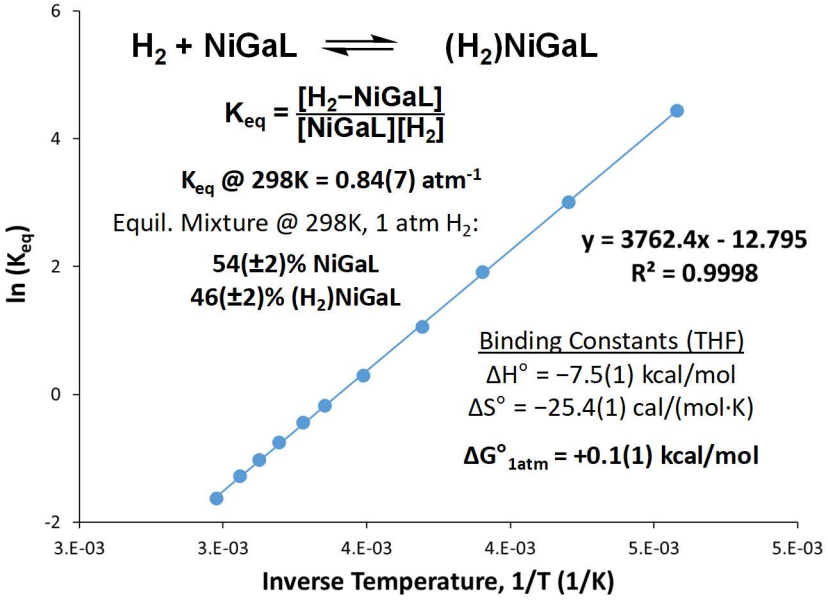

Figure A.2.26. Van't Hoff plot of $\ln(K_{H_2})$ vs. 1/T for H_2 binding equilibrium to **2** under 3.8 atm H_2 in THF. The thermodynamic binding constants ($\Delta H°$, $\Delta S°$, and $\Delta G°$) and the associated uncertainties obtained from linear regression of the van't Hoff plot are also displayed above (standard conditions: 298 K, 1 atm H_2, 1 M of all other species, THF). The free energy of H_2 binding to **2** ($\Delta G°$) was found to be slightly more favorable in THF than in toluene (by ~0.5 kcal/mol), albeit nearly within experimental error. H_2 binding being slightly more favorable in THF than in toluene was also predicted by DFT calculations (Table A.2.5).

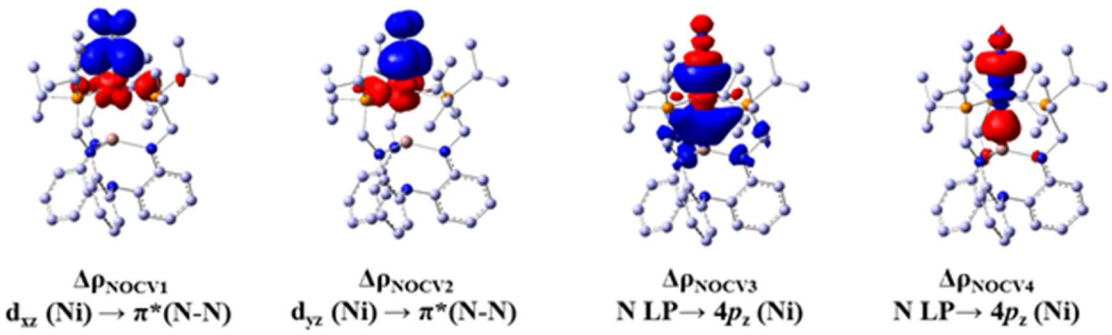

Figure A.2.27. Deformation density contributions ($\Delta\rho_{NOCVn}$, isovalue 0.04 a.u.) of NOCV pairs for N_2 binding to **3**, with hydrogen atoms omitted for clarity. Note that red indicates electron outflow, and blue indicates electron inflow. NOCV1 and NOCV2 show π-back-donation (Ni $3d_\pi \rightarrow N_2$ π*), while NOCV3 and NOCV4 show σ-donation (N_2 lone pair → Ni $4p_z$). Similar densities were computed for **1**–N_2 and **2**–N_2. Refer to Table A.2.11 for the relative energy contributions of each NOCV and for the overall π-back-donation vs. σ-donation contributions for N_2 binding to the NiML complexes.

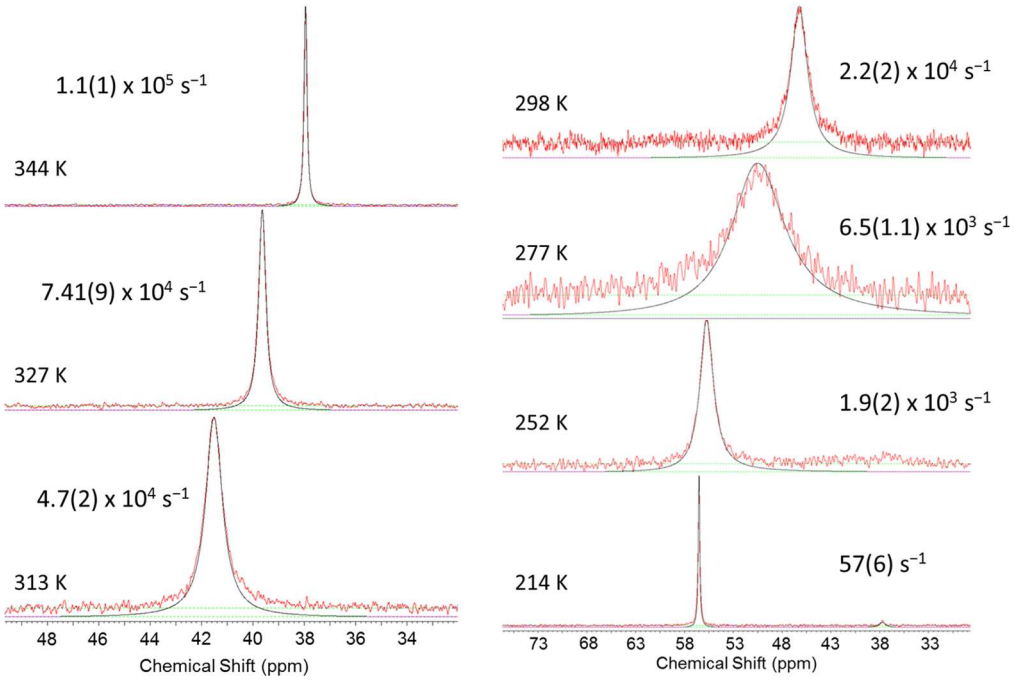

Figure A.2.28. Comparison of best fit simulations (black lines) and experimental VT ^{31}P NMR data (red lines, toluene-d_8, 162 MHz) for **2** (~7.5 mM in 0.70 mL) under 1 atm H_2 from 214 to 344 K. The exchange rates at each T and the associated uncertainty (displayed next to spectra) were determined by using gNMR version 5.0 to find the best fit for the experimental spectrum. Please refer to Figure A.2.31 for the Eyring plot from which the activation parameters for self-exchange were extracted. Note that low T broadening at 214 K due to loss of phosphine symmetry may interfere with the assumption that broadening not due to the intrinsic linewidth is attributable to chemical exchange broadening; as such, the simulated exchange rate at 214 K should be treated as an estimate.

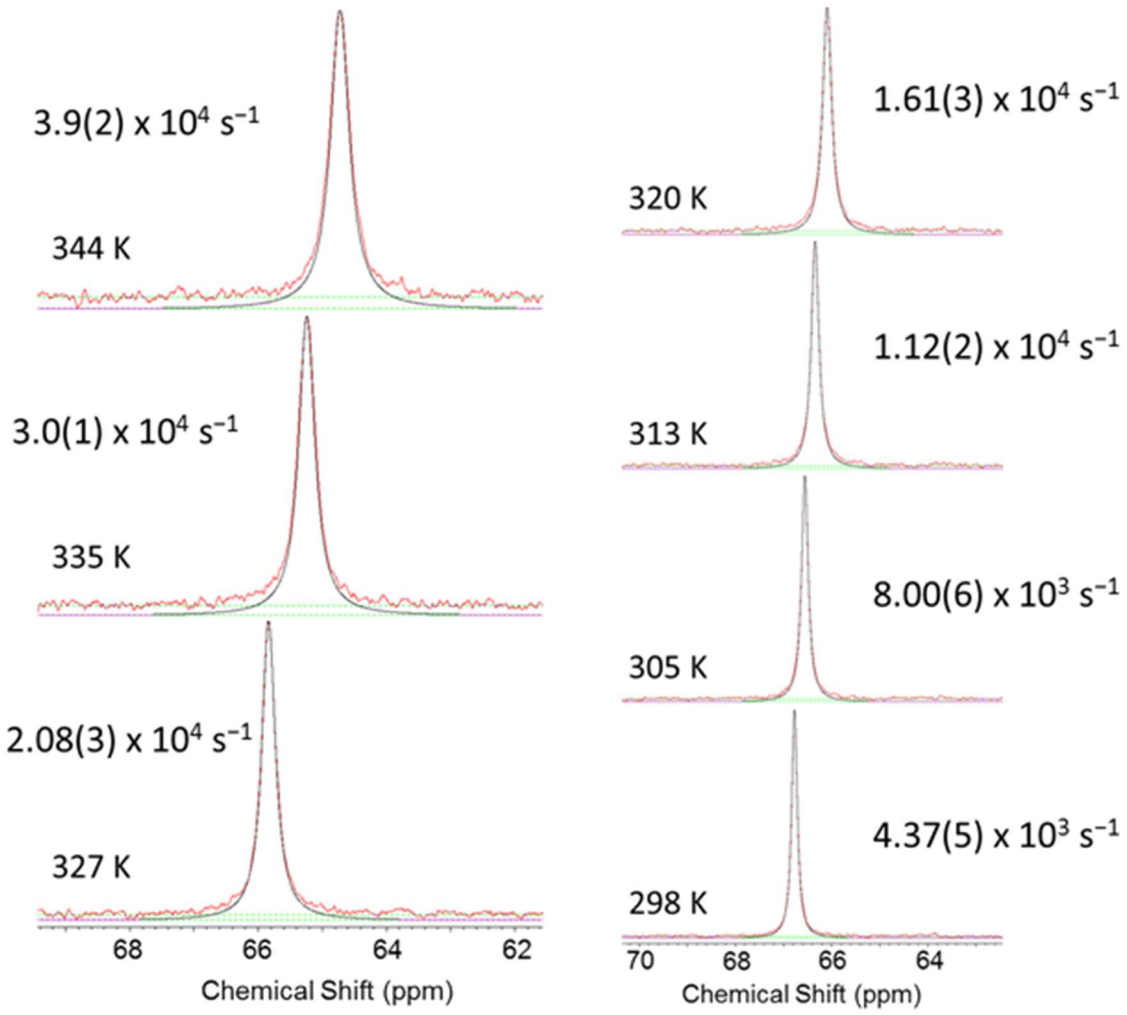

Figure A.2.29. Comparison of best fit simulations (black lines) and experimental VT ^{31}P NMR data (red lines, toluene-d_8, 162 MHz) for **3** (~7.5 mM in 0.70 mL) under 1 atm H_2 from 298 to 344 K. The exchange rates at each T and the associated uncertainty (displayed next to spectra) were determined by using gNMR version 5.0 to find the best fit for the experimental spectrum. Please refer to Figure A.2.32 for the Eyring plot from which the activation parameters for self-exchange were extracted. Note that at T < 298 K, the equilibrium lies so far toward the bound species (>98%) that exchange rates could not be reliably determined, and so these T were not considered for simulation or Eyring analyses.

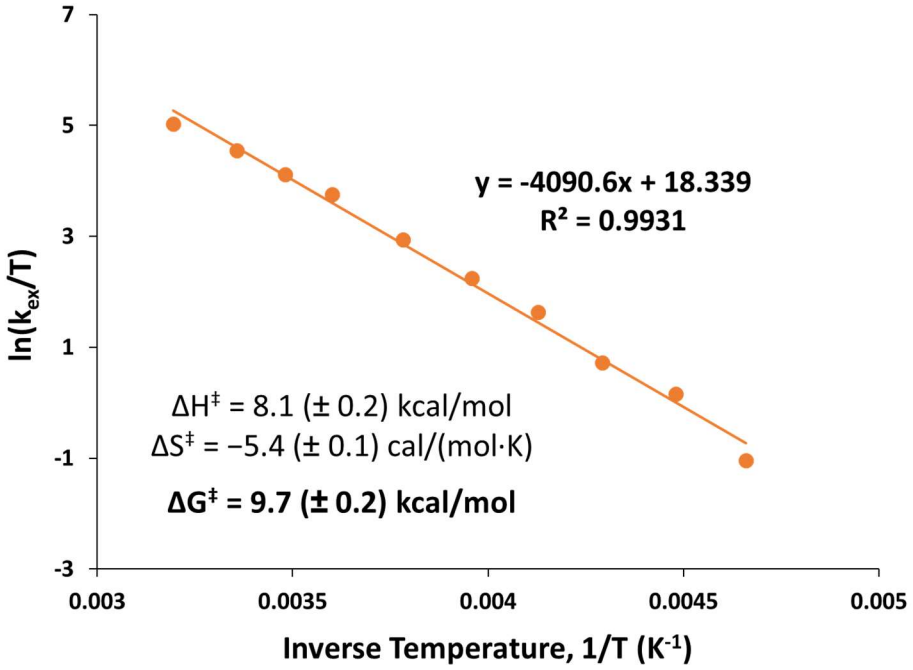

Figure A.2.30. Eyring plot of ln(rate$_{ex}$/T) vs. 1/T for H_2 binding to **1**, where rate$_{ex}$ is the exchange rate (in s^{-1}) extracted from lineshape analysis using gNMR to fit experimental VT ^{31}P NMR data. The activation parameters for H_2 self-exchange ($\Delta H^{\ddagger}_{ex}$, $\Delta S^{\ddagger}_{ex}$, and $\Delta G^{\ddagger}_{ex}$) and the associated uncertainties from linear regression are also displayed above.

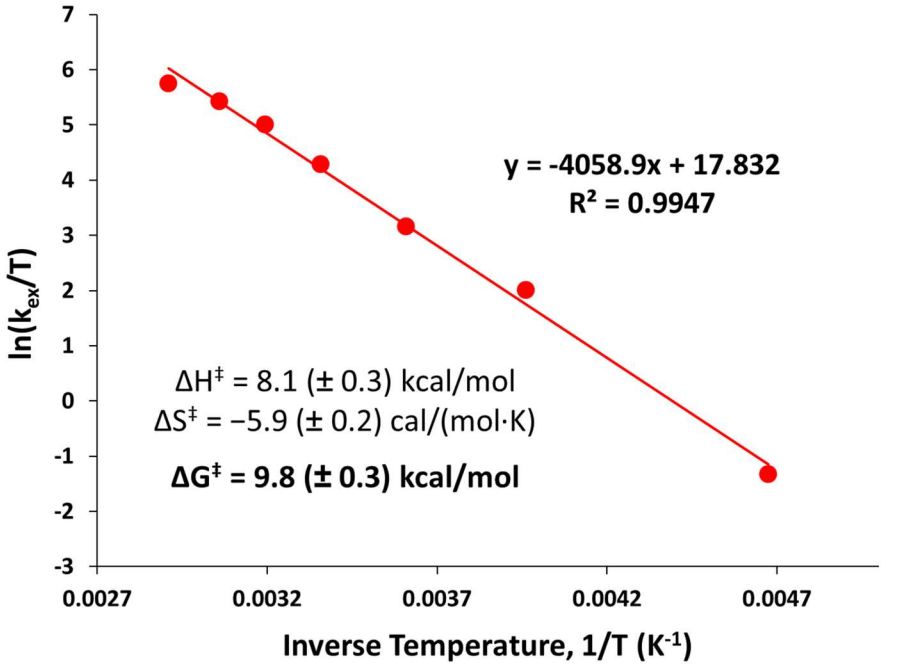

Figure A.2.31. Eyring plot of ln(rate$_{ex}$/T) vs. 1/T for H_2 binding to **2**, where rate$_{ex}$ is the exchange rate (in s^{-1}) extracted from lineshape analysis using gNMR to fit experimental VT ^{31}P NMR data. The activation parameters for H_2 self-exchange ($\Delta H^{\ddagger}_{ex}$, $\Delta S^{\ddagger}_{ex}$, and $\Delta G^{\ddagger}_{ex}$) and the associated uncertainties from linear regression are also displayed above.

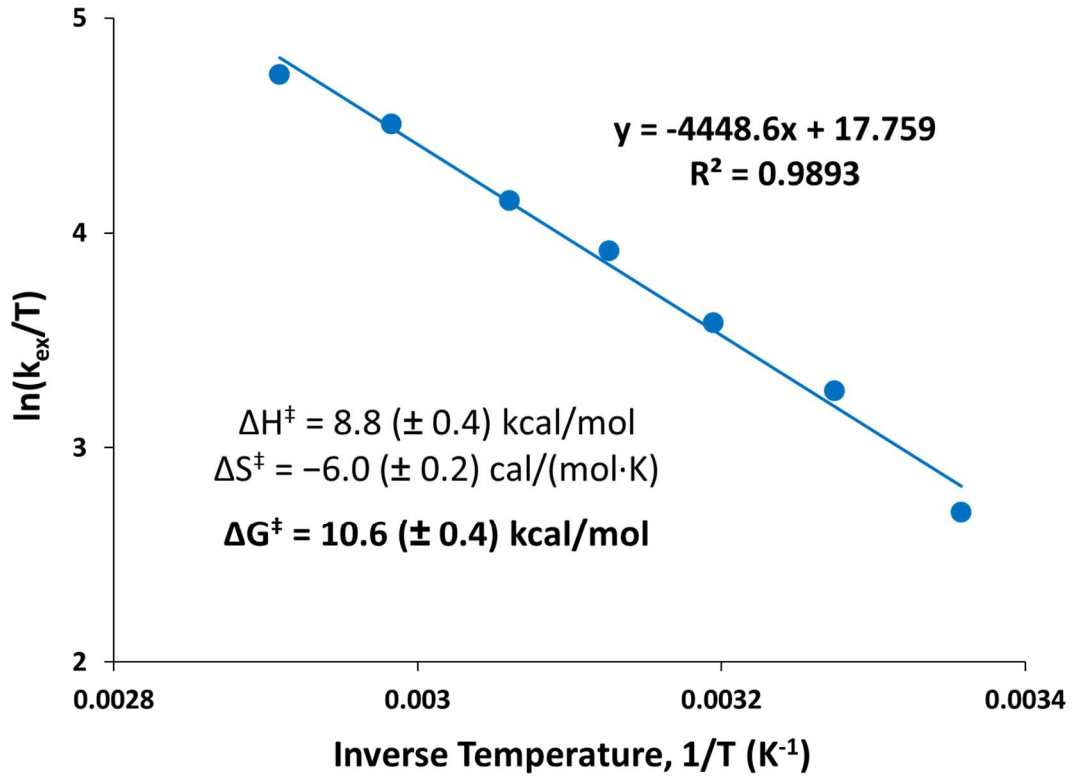

Figure A.2.32. Eyring plot of ln(rate$_{ex}$/T) vs. 1/T for H_2 binding to **3**, where rate$_{ex}$ is the exchange rate (in s^{-1}) extracted from lineshape analysis using gNMR to fit experimental VT ^{31}P NMR data. The activation parameters for H_2 self-exchange ($\Delta H^{\ddagger}_{ex}$, $\Delta S^{\ddagger}_{ex}$, and $\Delta G^{\ddagger}_{ex}$) and the associated uncertainties from linear regression are also displayed above. Note that at T <298 K, the equilibrium lies so far toward the bound species (>98%) that exchange rates could not be reliably determined, and so these T were not considered for Eyring analysis.

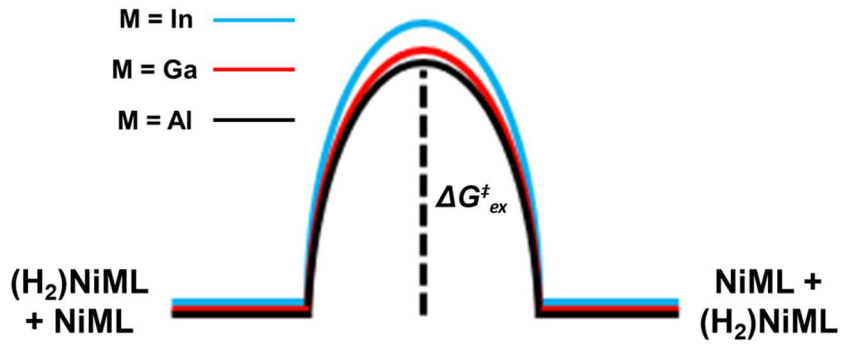

Figure A.2.33. Reaction coordinate diagram for H_2 self-exchange at NiML. Note that although the diagram is not rigorously to scale, it shows the trends in $\Delta G^{\ddagger}_{ex}$ (In = 10.6[4] > Ga = 9.8[3] ~ Al = 9.7[2]). The largest $\Delta G^{\ddagger}_{ex}$ barrier for NiInL is consistent with its exchange rate at 298 K being the slowest of the trio of complexes. The difference in $\Delta G^{\ddagger}_{ex}$ of ~0.9(5) kcal/mol between M=In and M=Al translates into a factor of 4.5(±3.6) difference in their relative exchange rates at 298 K, consistent with the observed factor of ~6.

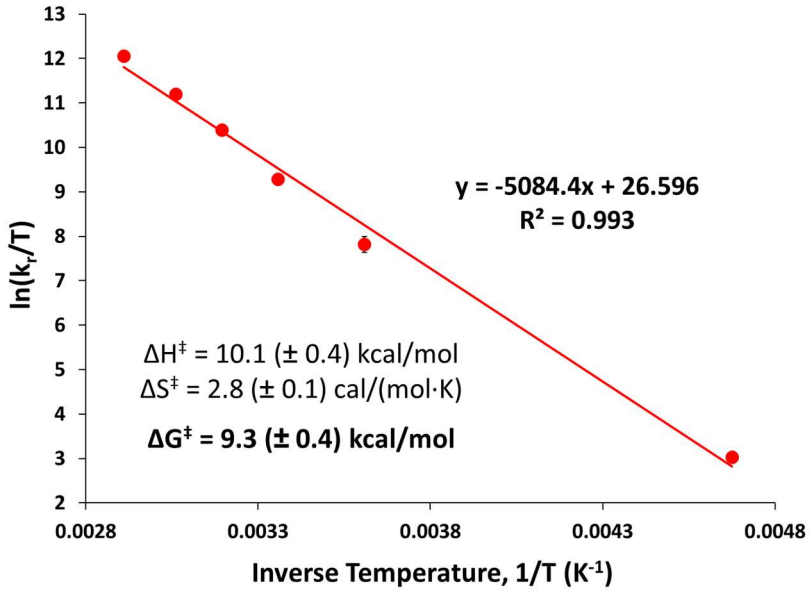

Figure A.2.34. Eyring plot of $\ln(k_{loss}/T)$ vs. 1/T for H_2 binding to **2**, where k_{loss} (or k_r) is the first-order rate constant for H_2 loss (in s^{-1}) extracted from the exchange rate from VT ^{31}PNMR data. The activation parameters for H_2 loss ($\Delta H^{\ddagger}_{loss}$, $\Delta S^{\ddagger}_{loss}$, and $\Delta G^{\ddagger}_{loss}$) and the associated uncertainties obtained from linear regression are also displayed above. The standard state was re-defined as 1 M H_2 in order to compare with literature values for the activation parameters of H_2 loss, all of which have been previously defined for 1 M H_2.

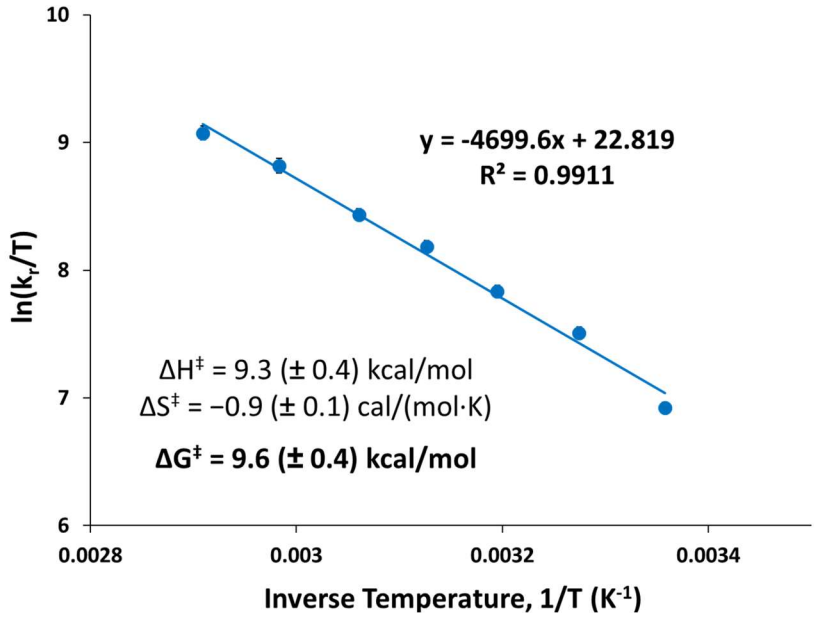

Figure A.2.35. Eyring plot of $\ln(k_{loss}/T)$ vs. 1/T for H_2 binding to **3**, where k_{loss} (or k_r) is the first-order rate constant for H_2 loss (in s^{-1}) extracted from the exchange rate from VT ^{31}PNMR data. The activation parameters for H_2 loss ($\Delta H^{\ddagger}_{loss}$, $\Delta S^{\ddagger}_{loss}$, and $\Delta G^{\ddagger}_{loss}$) and the associated uncertainties obtained from linear regression are also displayed above. The standard state was re-defined as 1 M H_2 in order to compare with literature values for the activation parameters of H_2 loss, all of which have been previously defined for 1 M H_2.

Table A.2.1. DFT-calculated structures for (η^2-H_2)NiML complexes computed using various functionals (with basis set 1, see Table 2.9, and A.2.11 for other methods). The H−H bond distances are predicted to increase in the order Al < Ga < In.

Metric	Functional (with basis set 1)			
	M06-L	PBE0	PBE0-D3	M06-D3
(η^2-H_2)NiAlL (**1**-H_2)				
Ni-Al	2.600	2.601	2.564	2.575
Ni-H	1.662	1.620	1.613	1.657
Ni-H	1.663	1.624	1.618	1.653
H-H	0.827	0.832	0.834	0.822
Ni-P	2.227	2.232	2.216	2.245
Al-N_{apical}	2.149	2.157	2.160	2.159
Al-N_{amide}	1.884	1.886	1.885	1.892
Ni to P_3-plane	0.29	0.28	0.28	0.28
Al to N_3-plane	0.29	0.29	0.30	0.29
(η^2-H_2)NiGaL (**2**-H_2)				
Ni-Ga	2.499	2.509	2.482	2.473
Ni-H	1.650	1.613	1.607	1.644
Ni-H	1.649	1.609	1.602	1.641
H-H	0.830	0.835	0.837	0.825
Ni-P	2.248	2.248	2.233	2.261
Ga-N_{apical}	2.291	2.281	2.281	2.287
Ga-N_{amide}	1.960	1.945	1.944	1.948
Ni to P_3-plane	0.30	0.27	0.28	0.27
Ga to N_3-plane	0.42	0.39	0.41	0.41
(η^2-)NiInL (**3**-H_2)				
Ni-In	2.603	2.564	2.542	2.579
Ni-H	1.639	1.603	1.598	1.645
Ni-H	1.633	1.599	1.593	1.641
H-H	0.835	0.839	0.841	0.825
Ni-P	2.287	2.286	2.269	2.302
In-N_{apical}	2.292	2.310	2.310	2.301
In-N_{amide}	2.051	2.060	2.059	2.050
Ni to P_3-plane	0.370	0.334	0.340	0.365
In to N_3-plane	0.425	0.438	0.450	0.429

Table A.2.2. Thermodynamic binding parameters for H_2 binding to **2**, categorized by which assumptions are made with respect to the interdependence of T and P, as well as which data set(s) are included (data collected under 6.8 atm, 13.6 atm H_2, or both) and whether the values were extracted via van't Hoff analysis or from non-linear ^{31}P δ vs. T fitting. "P α T" assumes that P is proportional to T as described by Guy Lussac's Law, whereas "const. P" assumes that P remains constant. The values highlighted in pink, obtained from taking the average of the van't Hoff results at 6.8 and 13.6 atm, are the final values reported for H_2 binding to **2** in Table 3.5.

H_2 Pressure (atm)	Fit Type	Assumption	Fit Quality	# pts	T Range (K)	ΔH° (kcal/mol)	ΔS° (cal/[mol·K])	ΔG° (kcal/mol)
6.8	van't Hoff	P α T	$R^2 = 0.992$	15	> 240 K	−6.6 (± 0.2)	−23.8 (± 0.6)	+0.5 (± 0.2)
6.8	non-linear	P α T	$Res^2/pt = 0.13$	17	200 to 370 K	−6.8	−24.5	+0.5
6.8	van't Hoff	const. P	$R^2 = 0.991$	15	> 240 K	−6.0 (± 0.2)	−21.7 (± 0.5)	+0.5 (± 0.2)
6.8	non-linear	const. P	$Res^2/pt = 0.12$	17	200 to 370 K	−6.2	−22.4	+0.5
13.6	van't Hoff	P α T	$R^2 = 0.993$	9	> 240 K	−5.5 (± 0.2)	−20.5 (± 0.6)	+0.7 (± 0.2)
13.6	non-linear	P α T	$Res^2/pt = 0.05$	12	200 to 360 K	−5.8	−21.7	+0.6
13.6	van't Hoff	const. P	$R^2 = 0.992$	9	> 240 K	−4.9 (± 0.2)	−18.5 (± 0.6)	+0.6 (± 0.2)
13.6	non-linear	const. P	$Res^2/pt = 0.05$	12	200 to 360 K	−5.2	−19.6	+0.6
6.8, 13.6 average	non-linear	P α T	–	29	200 to 370 K	−6.3	−23.1	+0.6
6.8, 13.6 average	non-linear	const. P	–	29	200 to 370 K	−5.7	−21.0	+0.6
6.8, 13.6 combined fitting	non-linear	P α T	–	29	200 to 370 K	−6.7	−24.2	+0.5
6.8, 13.6 average	van't Hoff	P α T	–	24	> 240 K	−6.0 (± 0.8)	−22 (± 2)	+0.6 (± 0.2)
6.8, 13.6 average	van't Hoff	const. P	–	24	> 240 K	−5.4 (± 0.8)	−20 (± 2)	+0.6 (± 0.2)
6.8, 13.6 combined regression	van't Hoff	P α T	–	24	> 240 K	−6.3 (± 0.2)	−23.0 (± 0.7)	+0.6 (± 0.3)

Table A.2.3. Comparison of H_2 thermodynamic binding parameters for **1**, **2**, and **3** obtained from van't Hoff analysis and non-linear fitting of ^{31}P δ vs. T plots.[a]

	1		**2**[b]		**3**[c]	
	van't Hoff	non-linear	van't Hoff	non-linear	van't Hoff	non-linear
$\Delta H°$	−6.3(1)	−6.7	−6.0(8)	−6.3	−14.8(6)	−14.1
$\Delta S°$	−26.4(4)	−27.6	−22(2)	−23.1	−37(2)	−35.4
$\Delta G°$	+1.6(2)	+1.6	+0.6(2)	+0.6	−3.7(7)	−3.6

[a]Note that $\Delta H°$ and $\Delta G°$ are given in kcal/mol, and $\Delta S°$ has units of cal/(mol·K). Standard deviation in the last digit is shown in parenthesis, as obtained from van't Hoff linear regression analyses. Standard state is defined as 1 atm H_2, and 1 M of all other species in toluene, at 298 K. [b]Average of values obtained under 6.8 and 13.6 atm H_2, with standard deviation given between the values from the two datasets. [c]Estimated values extracted from fast-intermediate exchange regime data. See text for discussion, but −3.0(7) kcal/mol is reasoned to be a better estimate for $\Delta G°$.

Table A.2.4. Comparison of N_2 thermodynamic binding parameters for **1**, **2**, and **3** obtained from van't Hoff analysis and non-linear fitting of ^{31}P δ vs. T plots.[a]

	1[b]		**2**[c]		**3**	
	van't Hoff	non-linear	van't Hoff	non-linear	van't Hoff	non-linear
$\Delta H°$	−4.7(2)	−4.4	−4.7(3)	–	−14.5(3)	−14.5
$\Delta S°$	−27.5(5)	−26.4	−23(1)	–	−45(1)	−44.6
$\Delta G°$	+3.5(3)	+3.5	+2.1(5)	–	−1.2(4)	−1.2

[a]Note that $\Delta H°$ and $\Delta G°$ are given in kcal/mol, and $\Delta S°$ has units of cal/(mol·K). Standard deviation in the last digit is shown in parenthesis, as obtained from van't Hoff linear regression analyses. Standard state is defined as 1 atm N_2, and 1 M of all other species in toluene, at 298 K. [b]Non-linear fit only includes 4 data points where fast exchange was observed (of the 7 data points from van't Hoff analysis). [c]A non-linear fit of ^{31}P δ vs. T was not possible because chemical exchange was slow for all T examined.

Table A.2.5. Comparison of experimental and calculated H_2 binding energies for NiML complexes. Various methods were tested, all of which utilized the SMD solvent model (with toluene, THF, or CH_3CN as the solvent). Table courtesy of Dr. Jing Xie with minor alterations.

H_2 binding $\Delta G°$ (kcal/mol)					
Complex	expt.	m06l/bs1	pbe0/bs1	pbe0-d3/bs1	m06-d3/bs4
Solvent = toluene (298 K, 1 atm)					
4	-	6.25	8.54	7.75	6.72
1	1.6 ± 0.2	2.76	4.14	2.9	3.93
2	0.6 ± 0.2	0.92	2.18	0.83	0.71
3	−3.0 ± 0.7	-1.85	-0.35	-1.75	-1.16
Solvent = THF (298 K, 1 atm)					
4		6.21	8.36	7.63	7.18
1		2.62	3.91	2.67	3.52
2	0.1 ± 0.1	-0.26	-0.26	1.66	0.33
3		-2.22	-2.22	-0.65	-2.01
Solvent = CH_3CN (298 K, 1 atm)					
4		6.23	8.31	7.59	7.31
1		2.65	3.87	2.64	3.44
2		-0.34	-0.34	1.46	0.19
3		-2.21	-2.21	-0.72	-2.04

Table A.2.6. Comparison of experimental and calculated N_2 binding energies for NiML complexes. Various methods were tested, all of which utilized the SMD solvent model (with toluene, THF, or CH_3CN as the solvent). Table courtesy of Dr. Jing Xie with minor alterations.

N_2 binding $\Delta G°$ (kcal/mol)					
M	expt.	m06l/bs1	pbe0/bs1	pbe0-d3/bs1	m06-d3/bs4
Solvent = toluene (298 K, 1 atm)					
4	-	5.86	15.36		8.02
1	3.5 ± 0.3	6.25	13.58	9.95	6.05
2	2.1 ± 0.5	3.61	12.23	9.42	3.82
3	-1.2 ± 0.4	0.15	8.75	5.75	-1.81
Solvent = THF (298 K, 1 atm)					
4		5.60	15.18		8.29
1		6.13	13.48	9.87	6.33
2		3.15	11.69	8.92	4.07
3		-0.74	8.32	5.38	0.17
Solvent = CH_3CN (298 K, 1 atm)					
4		5.64	15.15		8.59
1		6.14	13.51	9.88	6.24
2		3.13	11.59	8.84	3.32
3		-0.81	8.25	5.36	-0.01

Table A.2.7. Measured H_2 thermodynamic binding parameters for **1**, **2**, and **3** for 1 M H_2 standard state.[a]

	1[b]	**2**[b,c]	**3**[d]
$\Delta H°$ (kcal/mol)	−7.7 (0.1)	−7.4 (0.8)	−16.2 (0.6)
$\Delta S°$ (cal/mol•K)	−19.5 (0.4)	−15 (2)	−30 (2)
$\Delta G°$ (kcal/mol)	−1.9 (0.2)	−2.9 (0.2)	−7.1 (0.7)

[a]Entries in parentheses are the standard deviations obtained from van't Hoff linear regression analyses. Standard state is defined as 1 M of all species in toluene, and 298 K. [b]Assumes [H_2] in toluene is proportional to pressure even at high pressures. [c]Average of values obtained under 6.8 and 13.6 atm H_2, with standard deviation given between the two datasets. [d]Estimated values extracted from fast-intermediate exchange regime data. See main text for discussion, but −6.5(7) kcal/mol is reasoned to be a better estimate for $\Delta G°$.

Table A.2.8. Measured N_2 thermodynamic binding parameters for **1**, **2**, and **3** for 1 M N_2 standard state.[a]

	1[b]	**2**	**3**
$\Delta H°$ (kcal/mol)	−5.4 (0.1)	−5.5 (0.3)	−15.2 (0.3)
$\Delta S°$ (cal/mol•K)	−19.5 (0.4)	−14.9 (1.3)	−36.6 (1.0)
$\Delta G°$ (kcal/mol)	+0.4 (0.1)	−1.0 (0.5)	−4.3 (0.4)

[a]Standard deviations obtained from van't Hoff linear regression analyses are shown in parenthesis. Standard state is defined as 1 M of all species in toluene, and 298 K. [b]Assumes [N_2] in toluene is proportional to pressure even at high pressures.

Table A.2.9. Comparison of structural parameters for NiInL (**3**) and (η^2-H_2)NiInL (**3**−H_2) and binding energies, as determined by experiment and theory. Table courtesy of Dr. Jing Xie.

		expt.	calculation								
			M06-L					M06-D3		PBE0	PBE0-D3
	Metric		bs0	bs1	bs2	bs3	bs4	bs1	bs4	bs1	bs1
NiInL	**Ni-In**	**2.457**	**2.522**	**2.522**	**2.510**	**2.474**	**2.490**	**2.513**	**2.469**	**2.492**	**2.478**
	In-N_{apical}	2.308	2.245	2.245	2.262	2.290	2.281	2.247	2.279	2.264	2.263
	Ni-N_{apical}	4.765	4.766	4.766	4.772	4.764	4.771	4.759	4.747	4.756	4.741
	Ni-P	2.252	2.243	2.243	2.247	2.211	2.250	2.262	2.257	2.252	2.240
	M-N_{eq}	2.118	2.044	2.044	2.061	2.070	2.069	2.041	2.065	2.053	2.053
	∑(∠P−Ni−P)	357.0	356.8	356.8	356.7	357.3	357.1	356.9	357.6	357.4	356.9
	∑(∠N_{eq}-M-N_{eq})	345.3	350.9	350.9	350.0	348.7	349.1	351.0	349.5	350.1	349.5
	Ni to P_3-plane	0.227	0.234	0.234	0.238	0.213	0.224	0.233	0.203	0.212	0.228
	M to N_3-plane	0.477	0.360	0.360	0.381	0.407	0.400	0.357	0.390	0.377	0.389
(H_2)NiInL	**Ni-In**	**2.492**	**2.602**	**2.603**	**2.580**	**2.555**	**2.561**	**2.579**	**2.531**	**2.564**	**2.542**
	In-N_{apical}	2.366	2.293	2.292	2.312	2.320	2.318	2.301	2.322	2.310	2.310
	Ni-N_{apical}	4.844	4.895	4.895	4.892	4.874	4.878	4.880	4.853	4.874	4.852
	Ni-H	1.63	1.639	1.639	1.636	1.624	1.631	1.645	1.628	1.603	1.598
	Ni-H	1.62	1.639	1.633	1.635	1.622	1.626	1.641	1.624	1.599	1.593
	H-H	0.80	0.836	0.835	0.837	0.844	0.845	0.825	0.837	0.839	0.841
	Ni-P	2.268	2.288	2.287	2.293	2.243	2.282	2.302	2.292	2.286	2.269
	M-N_{eq}	2.116	2.051	2.051	2.068	2.080	2.081	2.050	2.079	2.060	2.059
	∑(∠P−Ni−P)	355.1	352.4	352.3	352.5	353.2	352.7	352.6	353.2	353.7	353.4
	∑(∠N_{eq}-M-N_{eq})	344.0	347.4	347.5	346.3	346.4	346.1	347.2	345.9	346.8	346.1
	Ni to P_3-plane	0.32	0.369	0.370	0.366	0.341	0.358	0.365	0.349	0.334	0.340
	M to N_3-plane	0.51	0.426	0.425	0.448	0.449	0.455	0.429	0.458	0.438	0.450
$\Delta G°_{H2}$	**kcal/mol**	**-3.0 ± 0.7**	**-2.3**	**-1.9**	**-2.7**	**-1.0**	**-3.4**	**1.4**	**-1.2**	**-0.4**	**-1.8**

Note that bond distances are in Å and angles are in degrees. Experimental parameters are from the x-ray structure (100 K), with Ni−H and H−H distances obtained from the neutron structure. Refer to Table 2.9 for basis set details.

Table A.2.10. Orbital interaction energy contributions from the top four NOCV pairs to H_2−Ni bonding. Table and ETS-NOCV calculations courtesy of Dr. Jing Xie.

NOCV	Type	$(H_2)NiLH_3$	$(H_2)NiAlL$	$(H_2)NiGaL$	$(H_2)NiInL$
1	$\sigma_{H2} \rightarrow 4p_z$ (Ni)	-18.3	-14.5	-14.8	-15.2
2	$3d_{xz}$(Ni) $\rightarrow \sigma^*_{H2}$	-14.6	-12.8	-13.0	-13.9
3	$\sigma_{H2} \rightarrow 4p_z$ (Ni)	-6.4	-6.9	-6.9	-7.3
4	$3d_{yz}$(Ni) $\rightarrow \sigma^*_{H2}$	-1.4	-1.8	-1.8	-1.8
1+3	**Total $\sigma_{H2} \rightarrow 4p_z$ (Ni)**	-24.7	-21.4	-21.7	-22.5
	σ-donation %	**61%**	**59%**	**59%**	**59%**
2+4	**Total $3d_{xz/yz}$(Ni) → σ^*_{H2}**	-15.9	-14.6	-14.8	-15.7
	π-back-donation %	**39%**	**39%**	**41%**	**41%**
sub-total[a]		-40.6	-36.0	-36.6	-38.1

[a]Note that the sub-total, the sum of the orbital interaction energies for NOCVs 1-4, is not equal to the total $\Delta E_{orbital}$ since other minor orbital interaction energies are not considered the sub-total.

Table A.2.11. Orbital interaction energy contributions from the top four NOCV pairs to N_2−Ni bonding. Table and ETS-NOCV calculations courtesy of Dr. Jing Xie.

NOCV	Type	$(N_2)NiLH_3$	$(N_2)NiAlL$	$(N_2)NiGaL$	$(N_2)NiInL$
1	$3d_{xz}$ (Ni) → π*(N-N)	-17.2	-16.8	-12.9	-14.6
2	$3d_{yz}$ (Ni) → π*(N-N)	-17.2	-12.7	-12.9	-14.6
3	N LP $\rightarrow 4p_z$ (Ni)	-20.5	-13.7	-15.7	-16.6
4	N LP $\rightarrow 4p_z$ (Ni)	-5.4	-5.1	-5.4	-5.9
1+2	**3d (Ni) → π*(N-N) π-back-donation %**	-34.4 **57%**	-29.5 **61%**	-25.8 **55%**	-29.1 **56%**
3+4	**N LP $\rightarrow 4p_z$ (Ni)**	-25.9	-18.8	-21.1	-22.5
	σ-donation %	**43%**	**39%**	**45%**	**44%**
sub-total[a]		-60.2	-48.3	-46.9	-51.6

[a]Note that the sub-total, the sum of the orbital interaction energies for NOCVs 1-4, is not equal to the total $\Delta E_{orbital}$ since other minor orbital interaction energies are not considered the sub-total.

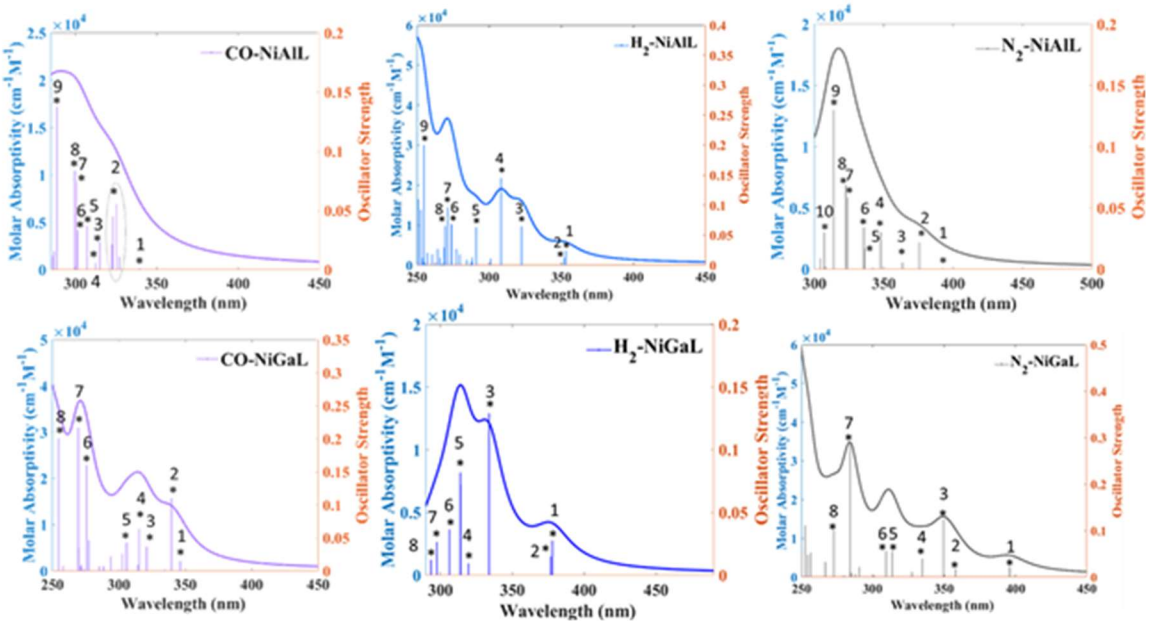

Figure A.2.33. Simulated UV-Vis spectra of N_2, H_2, and CO adducts of complexes **1** and **2**, as calculated by TD-DFT with M06-D3 in THF (SMD). Simulated UV-vis spectra for **3** are in Figure 3.31. Figure adapted from that provided by Dr. Jing Xie.

Table A.2.12. Transition assignments of first several excitations of N_2 adducts from TD-DFT calculations (M06-D3). Refer to Figure A.2.33. Table courtesy of Dr. Jing Xie.

(N_2)NiAlL	Transition (nm)	Description	
1	392	d_{xy} + Ligands P → N-N pi*	HOMO-1 → LUMO+1
2	376	d_{xy} + Ligands P → unocc. mix.	HOMO-1 → LUMO+4
3	364	d_{xy} + Ligands → N-N pi*	HOMO-1 → LUMO
4	348	$d_{x^2-y^2}$ + Ligands P,N,C → unocc. mix	HOMO-2,-4 → LUMO+4
5	336	d_{z^2},Ligands N, C→ N-N pi*	HOMO → LUMO+1
6	336	$d_{x^2-y^2}$ + Ligands P,N,C→ N-N pi*	HOMO-2 → LUMO+1
(N_2)NiGaL	Transition (nm)	Description	
1	396	$d_{xy}/d_{x^2-y^2}$ + Ligand P → unocc. mix.	HOMO-3,4 → LUMO+2
2	358	$d_{xy}/d_{x^2-y^2}$ + Ligand P → N-N pi*	HOMO-3,4 → LUMO, LUMO+1
3	350	Ligand N,C → unocc. mix.	HOMO → LUMO+2
4	335	$d_{xy}/d_{x^2-y^2}$ + Ligand P → N-N pi*	HOMO-3,4 → LUMO, LUMO+1
5	314	Ligand N,C → Ligands C, benzene	HOMO → LUMO+3,4
6	309	Ligand N,C → unocc. mix.	HOMO-1,2 → LUMO+2

Table A.2.13. Transition assignments of first several excitations of H_2 adducts from TD-DFT calculations (M06-D3). Refer to Figure A.2.33. Table courtesy of Dr. Jing Xie.

(H_2)NiAlL	Transition (nm)	Description	
1	353	$d_{x^2-y^2}$ → unocc. mix.	HOMO-1,3 → LUMO+3
2	352	d_{xy} → unocc. mix.	HOMO-2,4 → LUMO+3
3	323	Ligands N,C → Ligands C	HOMO → LUMO, LUMO+1
4	308	Ligands N,C → unocc. mix.	HOMO → LUMO+2
5	291	d_{xy/x^2-y^2} +Ligands N, C → Ligands C	HOMO-1,2 → LUMO, LUMO+1
6	274	Ligands N,C → Ligands C	HOMO → LUMO+4,+5
7	271	d_{z^2} → unocc. mix.	HOMO-5 → LUMO+2
8	270	$d_{x^2-y^2}$ + Ligands N,C → Ligands C, benzene	HOMO-3 → LUMO+1
9	255	Ligands N, C → Ligands C, benzene	HOMO → LUMO+6
(H_2)NiGaL	Transition (nm)	Description	
1	378	$d_{xy/}d_{x^2-y^2}$ → unocc. mix.	HOMO-3,-4 → LUMO
2	334	Ligands N, C → unocc. mix.	HOMO → LUMO
3	319	Ligands N,C → unocc. mix.	HOMO-7 → LUMO
4	314	Ligands N, C → Ligand C, benzene	HOMO → LUMO+1,+2
5	306	Ligands N,C → unocc. mix.	HOMO-1,2,8 → LUMO
6	297	Ligands N,C → unocc. mix.	HOMO-2 → LUMO
7	293	Ligands N,C → unocc. mix.	HOMO-8 → LUMO
8	286	Ligands N, C → Ligand C, benzene	HOMO-1 → LUMO+1

Table A.2.14. Transition assignments of first several excitations of CO adducts from TD-DFT calculations (M06-D3). Refer to Figure A.2.33. Table courtesy of Dr. Jing Xie.

(OC)NiAlL	Transition (nm)	Description	
1	340	$d_{x^2-y^2}$ + C-O pi & Ligands C →C-O pi*	HOMO-1,-3 → LUMO+2,3
2	327	Ligands C N, benzene → Ligands C, benzene	HOMO → LUMO,LUMO+1
	325		HOMO → LUMO
	323		HOMO → LUMO+1
	322		HOMO → LUMO+1
3	315	$d_{xy}/d_{x^2-y^2}$ + C-O pi→C-O pi*	HOMO-3,-4 → LUMO+2,+3
4	312	d_{z^2} + C-O sigma→C-O pi*	HOMO-5 → LUMO+2
5	307	$d_{x^2-y^2}$ + C-O pi & Ligands C N → unnoc. mix.	HOMO-1,-3 → LUMO+4
6	301	Ligands C N, benzene → unocc. mix.	HOMO → LUMO+4
7	301	d_{xy} + C-O pi & Ligands C N, benzene → unocc. mix	HOMO-4 → LUMO+4
8	300	d_{xy} + C-O pi→C-O pi*	HOMO-4 → LUMO+2,+3
(OC)NiGaL	Transition (nm)	Description	
1	346	$d_{x^2-y^2}$ + C-O pi → unocc. mix.	HOMO-3,-4 → LUMO
2	340	Ligands C, benzene → unocc. mix.	HOMO → LUMO
3	321	Ligands C, benzene → Ligands C, benzene	HOMO → LUMO+3,4
4	315	$d_{xy}/d_{x^2-y^2}$ + C-O pi → C-O pi*	HOMO-3,4 → LUMO+1,2
5	306	Ligands C, benzene → unocc. mix.	HOMO-1,2 → LUMO
6	276	Ligands C, benzene → Ligands C, benzene	HOMO → LUMO+5
7	270	d_{z^2} + C-O sigma→ unocc. mix.	HOMO-5 → LUMO

Appendix 3: Supplemental Figures for Chapter 4

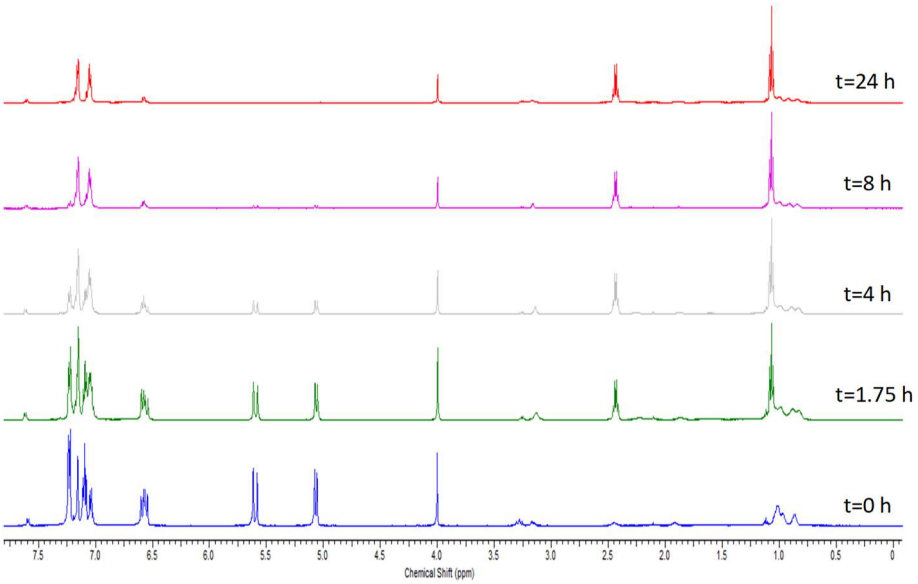

Figure A.3.1. Representative ^{1}H NMR spectra for various time points of the catalytic hydrogenation of styrene to ethyl benzene by NiGaL (**2**). The olefinic resonances of styrene (6.58 [m], 5.61 [d], 5.07 [d]) disappear over time, with concomitant appearance of ethyl benzene (2.44 [q], 1.08 [t]). The conversion over time was quantified by integration of the vinylic peaks of styrene against an internal ferrocene standard (4.00 [s]).

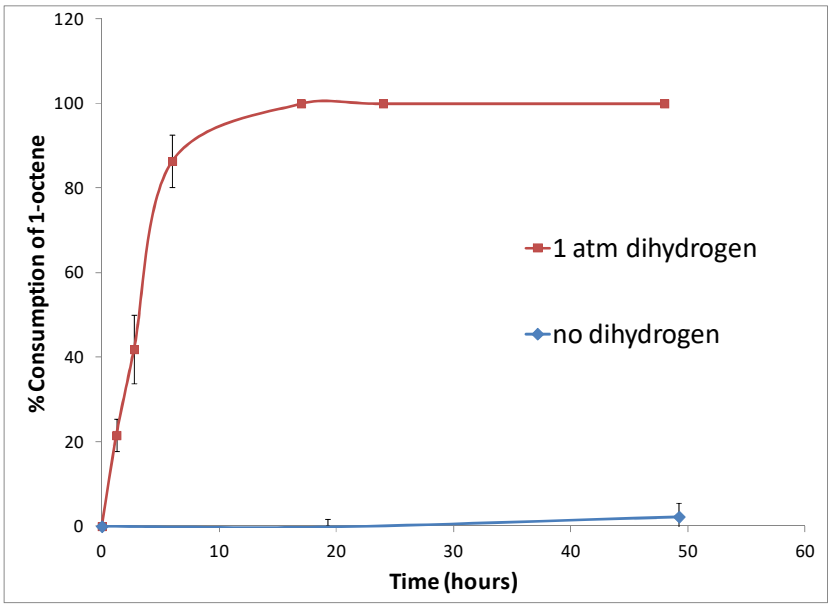

Figure A.3.2. Control reaction showing negligible (<2%) isomerization of 1-octene after 50 h in the absence of 1 atm H_2 under catalytic conditions with NiInL (**3**).

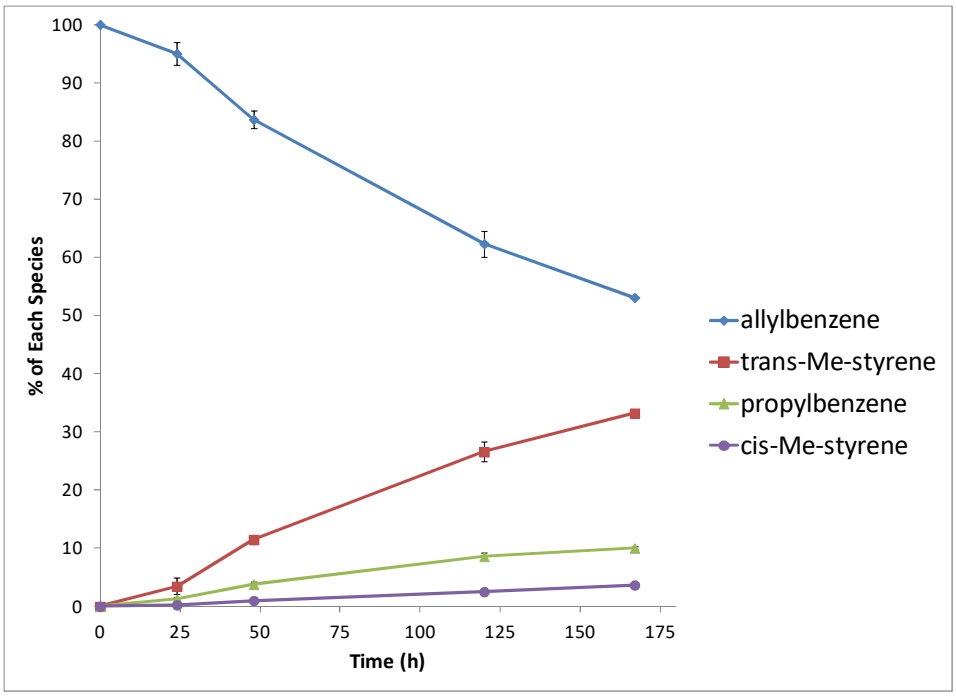

Figure A.3.3. Reaction profile of catalytic isomerization-hydrogenation of allylbenzene by NiInL (**3**).

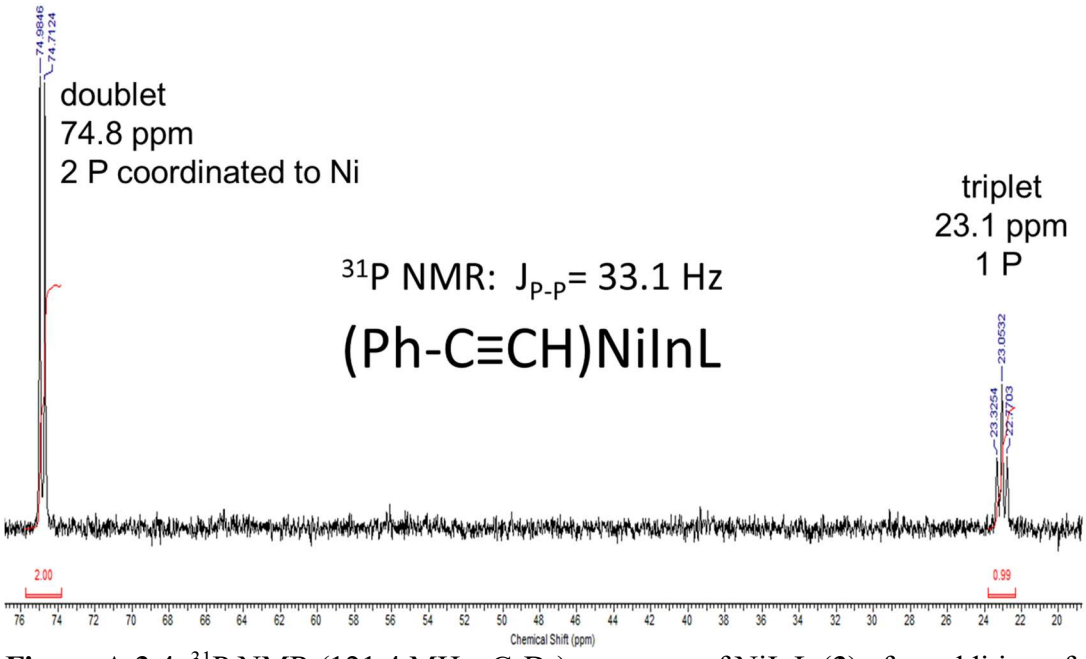

Figure A.3.4. ^{31}P NMR (121.4 MHz, C_6D_6) spectrum of NiInL (**3**) after addition of phenyl acetylene (1 equiv). A 2:1 ratio of ligand phosphines is observed with J_{PP} coupling resolved.

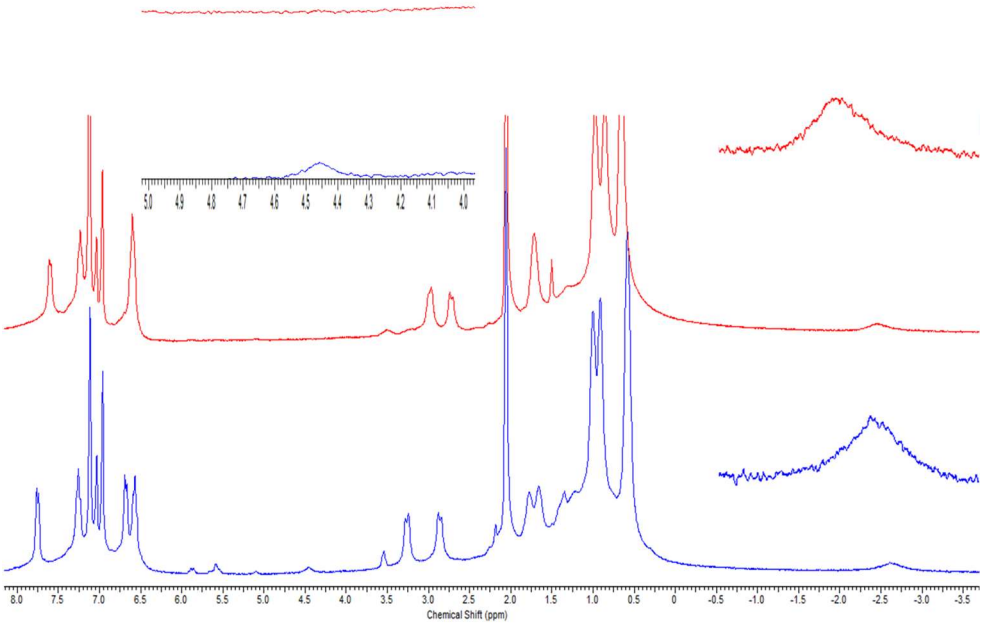

Figure A.3.5. ^{1}H NMR overlay of NiGaL (red) and NiInL (blue) at 223 K in toluene-d^{8} after addition of 1:1 H_2:D_2 mixture. Close-ups show the free H_2 region, which shows a small amount of free H_2 in the case of NiInL, but no HD (1:1:1 triplet at 4.5 ppm, with flanking peaks at 4.25 and 4.75 ppm) in either case. Likewise, close-ups of the bound (η^2-H_2)Ni resonance show that it does not split into a triplet in either case, as it would be expected to if HD were formed and then bound to NiML.

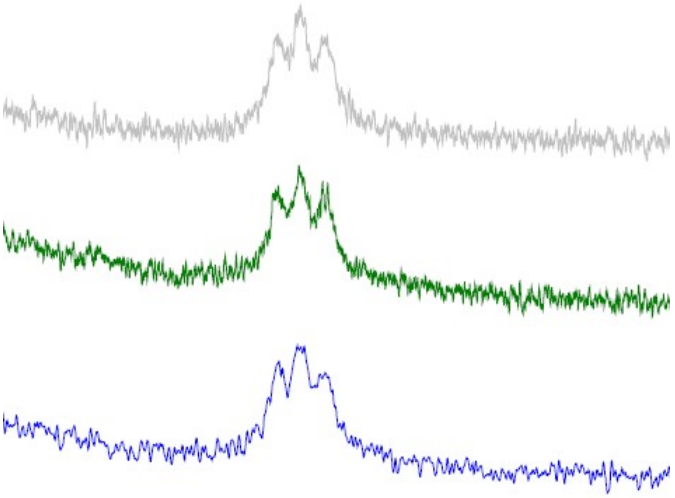

Figure A.3.6. ^{1}H NMR overlay of HD-NiGaL (**2**-HD) (peak is centered at -2.6 ppm in all spectra) in toluene-d^{8} at 213 K under 1 atm HD: after initial mixing (bottom), mixing for several days (middle), and after heating to 333 K for 1.5 days (top). No free H_2 or D_2 was observed. If HD was scrambled to H_2 and D_2, the center peak of the triplet should become significantly larger than the flanking peaks, which was not observed to any appreciable degree in this case.

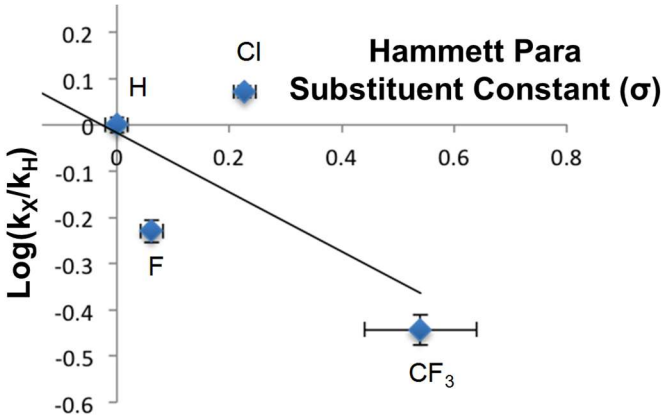

Figure A.3.7. Preliminary results for a Hammett plot, $\log(k_X/k_H)$ vs. Hammett para substituent constant (σ), for the rates of hydrogenation of para-substituted styrene derivatives catalyzed by **2**. Note that experiments conducted by former undergraduate student Nick Smith.

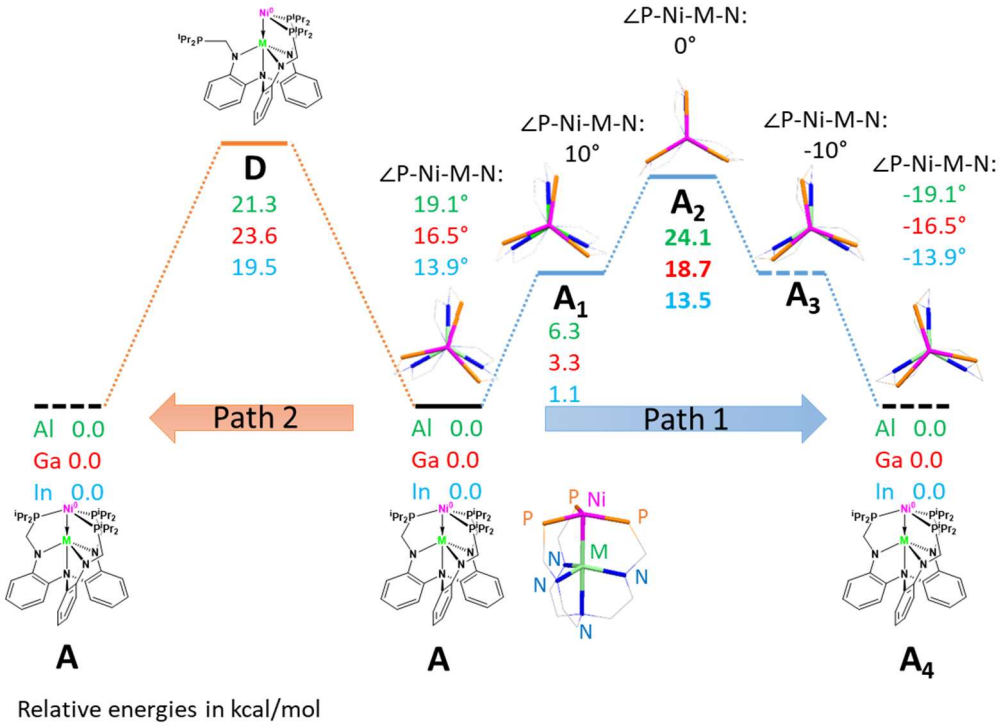

Figure A.3.8. Schematic profile of possible mechanisms for methylene coalescence behavior in NiML ^{1}H NMR experiment. ***Path 1***: **A**→**A**$_1$→**A**$_2$→**A**$_3$→**A**$_4$, conversion between pseudo-C_3 and pseudo-C_{3v} structure, via concerted "rocking" mechanism. Structure **A** is fully optimized in gas phase. To obtain structure **A**$_1$ and **A**$_2$, the positions of P atoms were modified to make ∠P−Ni−In−N$_{eq}$ dihedral angle to be 10° and 0°, respectively. Then the structures were partially optimized with all the Ni, M, N, and P atoms fixed, while carbon and hydrogen atoms could relax. ***Path 2***: **A**→**D**→**A**, one phosphine donor of ligand dissociates. For path 2, the relative free energies in toluene (SMD) under 298K and 1 atm were reported.

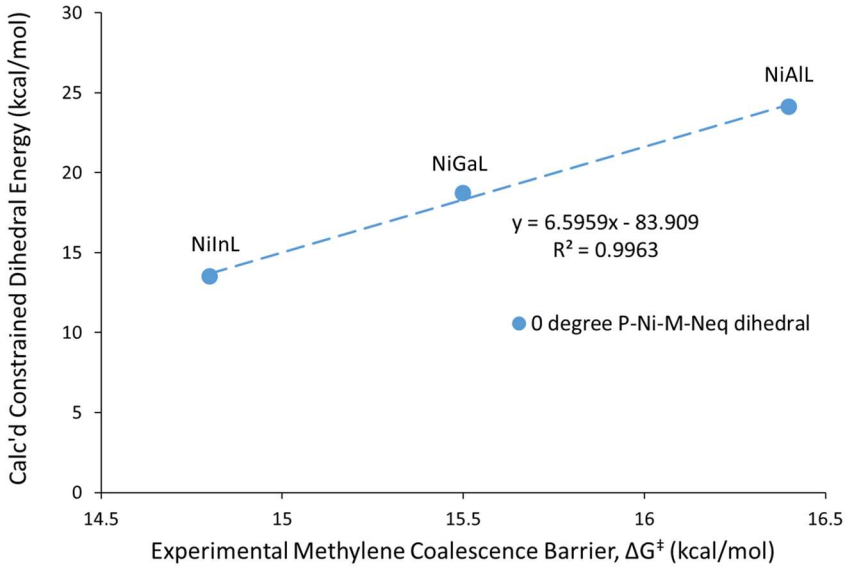

Figure A.3.9. Plot of DFT calculated energy of C_{3v} symmetric NiML complexes with constrained (0 degree) P–Ni–M–N_{eq} angles (relative to the energy of its natural angle) vs. experimental free energy barriers to methylene coalescence ($\Delta G^{\ddagger}_{MC}$) for NiML. The calculated energy for a dihedral angle of 0 degrees is meant to serve as a proxy for the transition state of the concerted "rocking" mechanism, which is shown pictorially in Figure A.3.8.

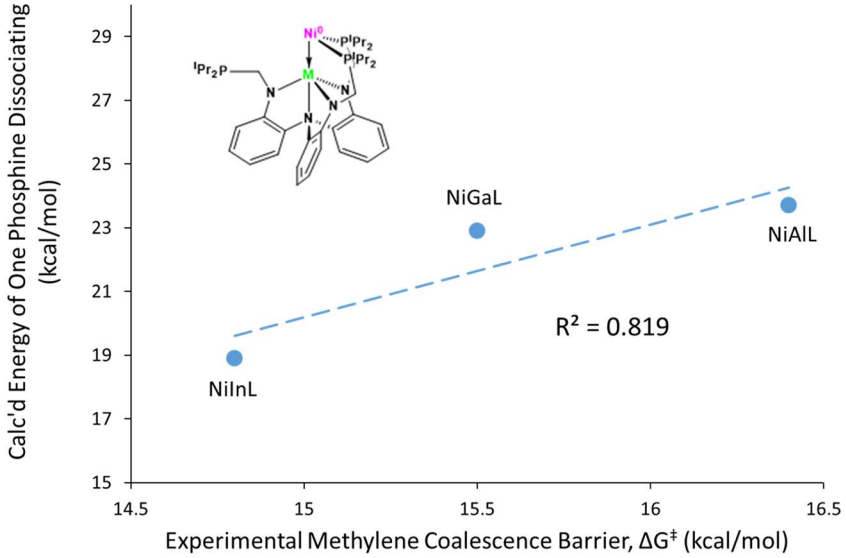

Figure A.3.10. Plot of DFT calculated energy of NiML with one of the phosphine arms dissociated (relative to the energy of that with all three phosphines coordinated to Ni) vs. experimental free energy barriers to methylene coalescence ($\Delta G^{\ddagger}_{MC}$) for NiML. The calculated energy of one of the phosphine arms dissociating (see picture above) is meant to serve as a proxy for the favorability of the methylene coalescence mechanism involving phosphine dissociation and re-coordination, the first step of which would require phosphine dissociation.

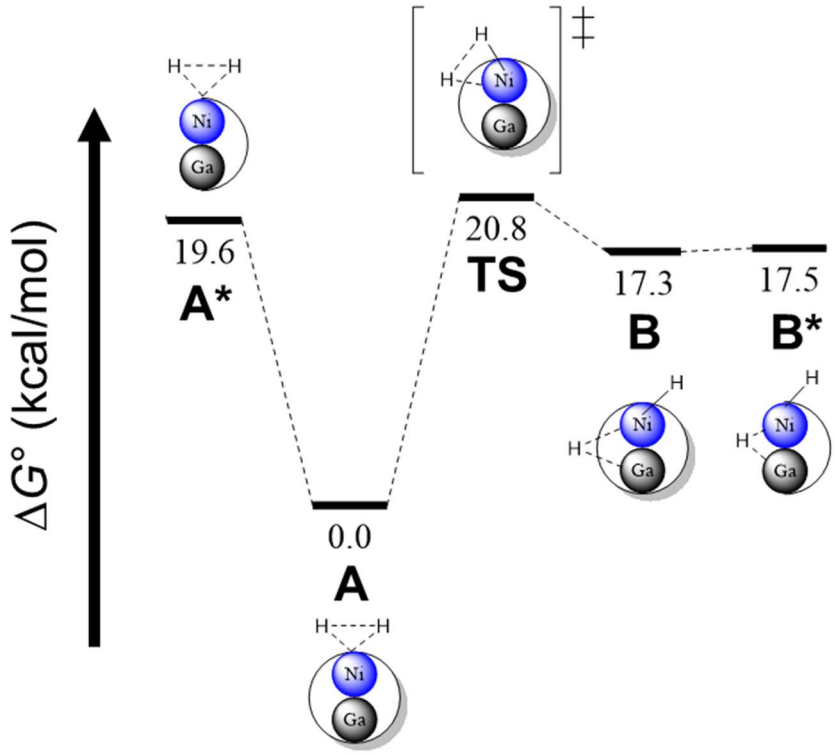

Figure A.3.11. DFT computed free energy profile in benzene for initial sequence of H_2 activation and phosphine dissociation, prior to olefin binding to intermediate **B***, as calculated using M06-L/bs1 with SMD solvent model (benzene). Please refer to computational details (section 4.4.3) and Table 2.9 for more details. Figure courtesy of Dr. Konstantinos Vogiatzis.

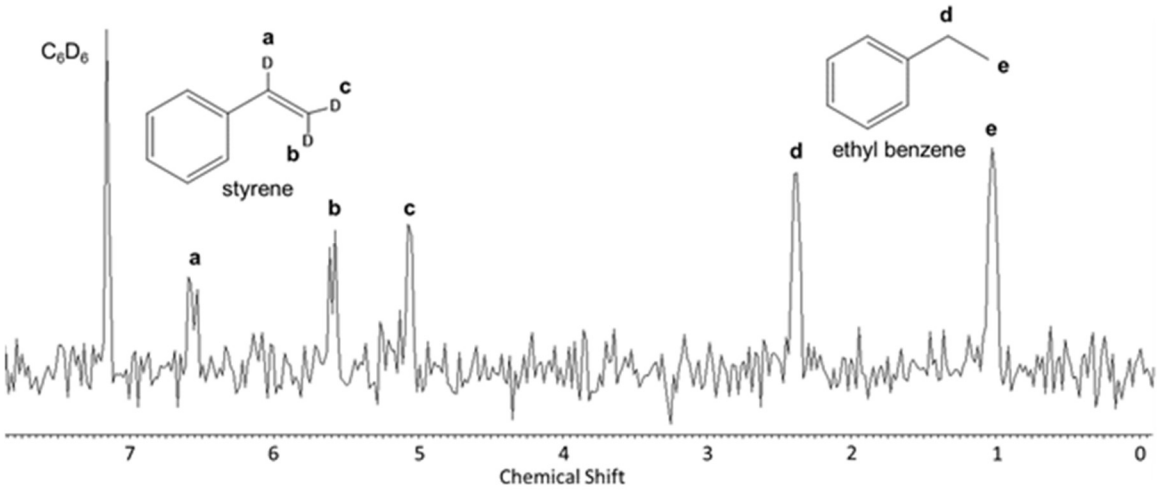

Figure A.3.12. ^{2}H NMR of styrene deuteration mediated by NiGaL (**2**). Deuterium was observed to have incorporated into all three olefinic positions of styrene, indicating that the insertion of styrene into Ni−H is reversible. Formation of deuterated ethyl benzene was also observed, as expected.

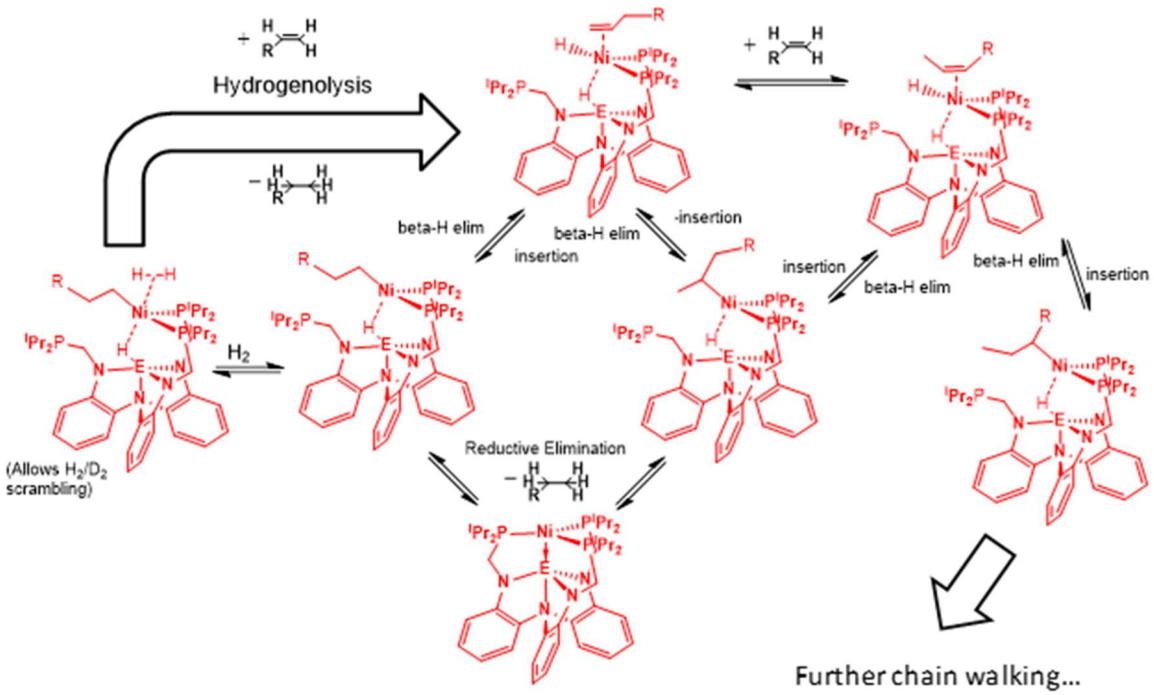

Figure A.3.13. Mechanistic scheme showing additional pathways for hydrogenolysis and further "chain-walking" via additional internal β-hydride elimination steps.

Table A.3.1. Comparison of hydrogenated product quantification by ^{1}H NMR and GC-MS analyses.[a]

Entry	catalyst	substrate	% hydrogenated yield[b]	
			^{1}H NMR	GC-MS
1	**3**	1-octene	>99	>99
2	**3**	styrene	>99	90(10)
3	**3**	*cis*-cyclooctene	93(3)	93(10)
5	**3**	allylbenzene[c]	7(3)	9(3)
6	**3**	phenyl acetylene[d]	trace	0.7(1)
7	**4**	styrene[e]	12(5)	13.4(8)
8	**4**	1-octene	47(7)	42(4)
9	**4**	*cis*-cyclooctene[f]	4(1)	3(1)
10	**4**	allylbenzene[c]	10.0(3)	8.7(8)

[a] see GC-MS calibration curves in the SI. [b]as determined after 24 h unless otherwise indicated. [c]after 168 h. [d]after 96 h. [e]after 48 h. [f]after 120 h.

Table A.3.2 Key bond distances (in Å) of intermediates and transition states of the hydrogenation of styrene, as optimized using M06-L/bs1 with SMD solvent model (C_6H_6). Please refer to computational details (section 4.4.3) and Table 2.9 for more details. Table courtesy of Dr. Konstantinos Vogiatzis.

	Intermediate	**Ni-Ga**	**Ni-H(1)**	**Ni-H(2)**	**Ga-H(2)**	**C(1)-C(2)**
	NiML	2.429	-	-	-	-
A	c-(η^2-H_2)NiGaL	2.499	1.654	1.652	-	-
TS1	Homolytic H_2 cleavage	2.463	1.564	1.470	2.662	-
B	c-(H)Ni(μ-H)GaL	2.536	1.511	1.503	1.831	-
B*	o-(H)Ni(μ-H)GaL	2.610	1.489	1.578	1.798	-
D	o-(sty)(H)Ni(μ-H)GaL	2.909	1.478	1.583	1.757	1.377
E	o-(CH_2CH_2Ph)(H)NiGaL	2.538	1.907	1.530	1.946	1.507
E'	o-(CH_3CHPh)(H)NiGaL	2.739	1.467	1.711	2.709	1.467
F*	o-NiGa(CH_3CH_2Ph)L	2.480	-	-	-	1.521

Note that c and o correspond to a closed (P_3Ni) and open ligand (P_2Ni), respectively.

Appendix 4: Supplemental Figures for Chapter 5

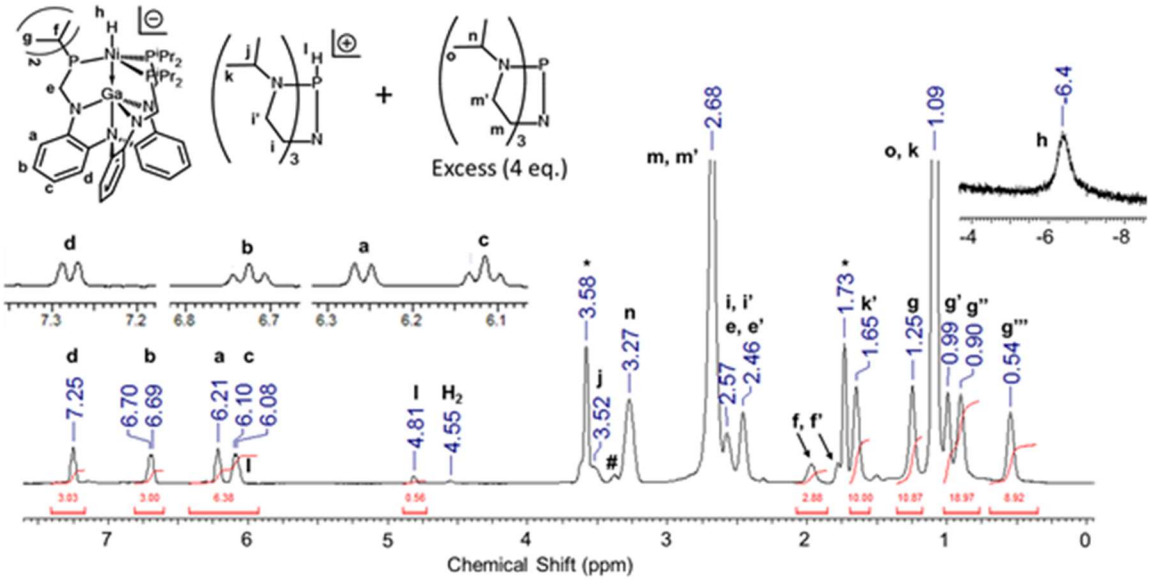

Figure A.4.1. ^{1}H NMR spectrum of [VkdH][**2**−H] (400 MHz, THF-d_8, 253 K), generated *in situ* by addition of 5 equiv. Vkd to **2** under 1 atm H_2. An excess of Vkd base is needed to drive the equilibrium and deprotonate **2**−H_2. Residual solvent peaks of THF (*) and diethyl ether (#) are denoted. Insets show close-ups of: aryl region at 298 K showing resolved coupling (top left), and hydride region (top right).

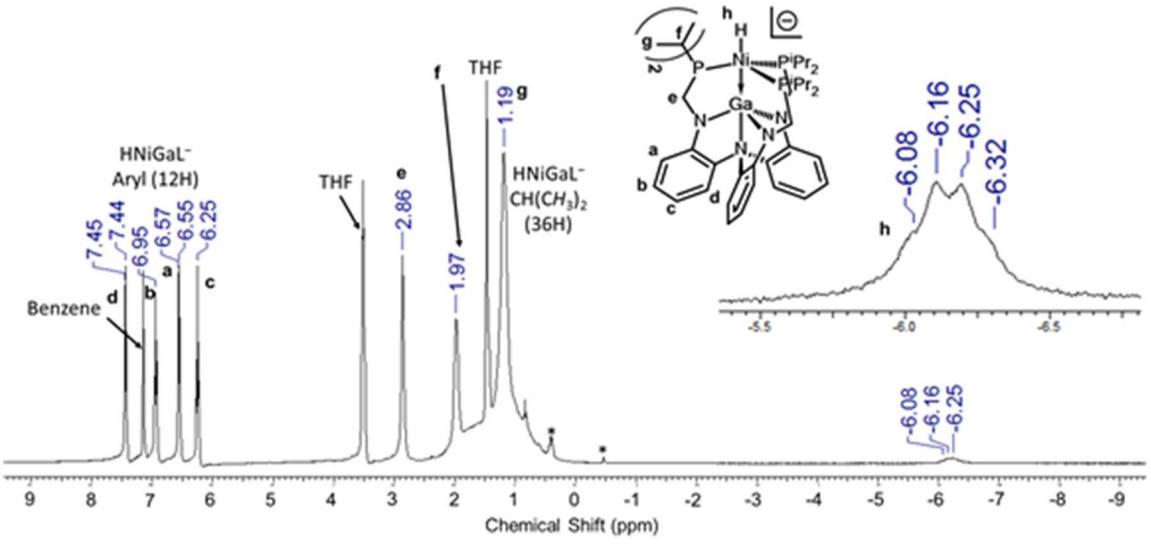

Figure A.4.2. ^{1}H NMR spectrum of [Na(THF)$_x$][**3**] (400 MHz, ~2:1 THF-d_8/C_6D_6). Residual solvent peaks of THF and benzene are labeled, and a trace impurity (presumably BEt_3) is denoted with an *. Inset shows a close-up of the hydride region. The hydride resonance was best resolved under these conditions as an apparent quartet with J_{HP}= 34.8 Hz, which is consistent with a terminal hydride coupled to three equivalent ^{31}P nuclei.

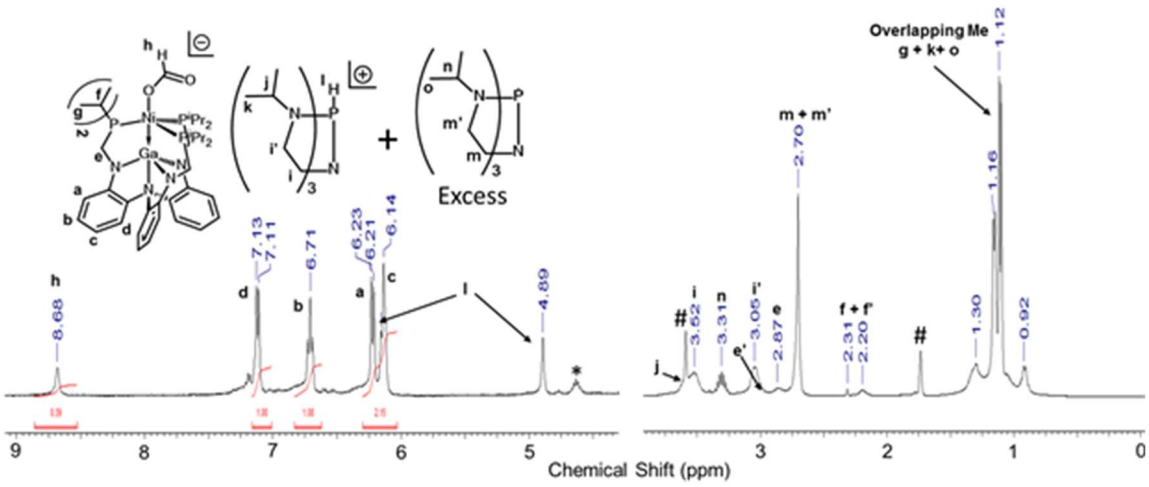

Figure A.4.3. ^{1}H NMR spectrum of [VkdH][**2**−O_2CH] (400 MHz, THF-d_8), generated *in situ* via addition of CO_2 (1 atm) to [VkdH][**2**−H]. The residual solvent peaks of THF (#) and residual H_2 (*) are denoted. A resonance at 8.68 ppm is attributed to coordinated formate in [VkdH][(*H*CO_2)NiGaL]. Due to extensive overlapping of the aliphatic proton resonances for [VkdH][**2**−O_2CH] and excess Vkd, the aliphatic peak assignments are tentative.

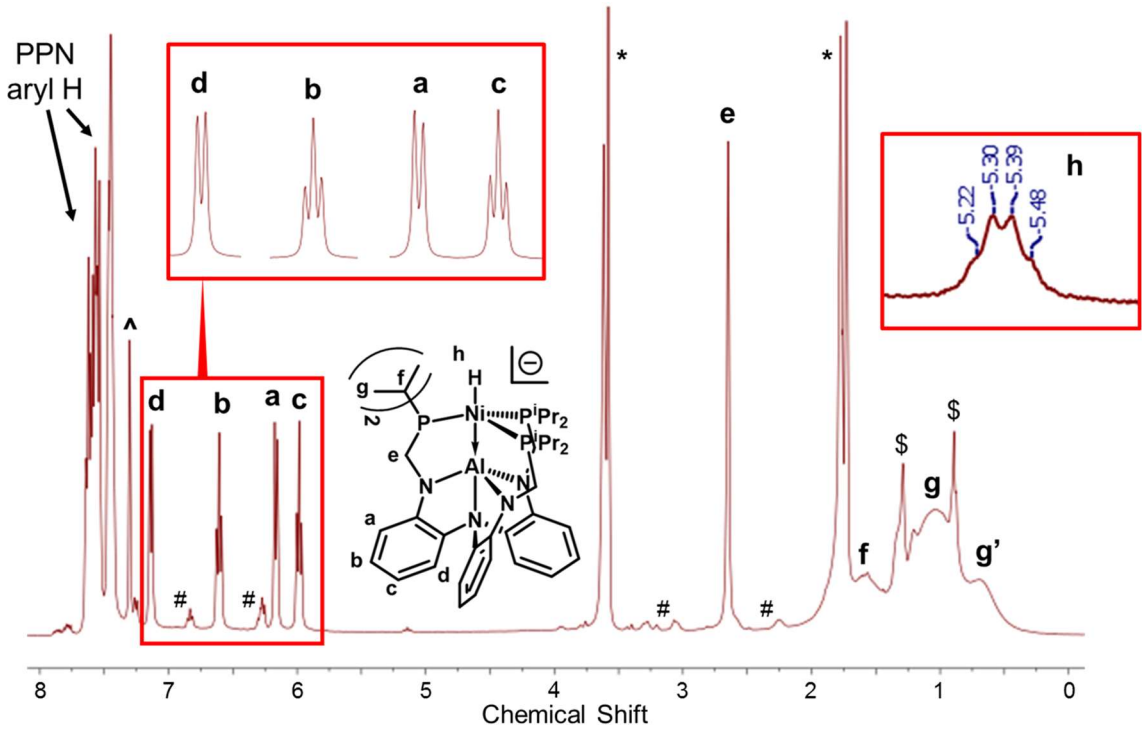

Figure A.4.4. ^{1}H NMR spectrum of [PPN][**1**−H] (400 MHz, THF-d_8, 298K). Residual solvent peaks of THF (*), benzene (^), and hexanes ($), along with a small amount of NiAlL (**1**, #) are denoted. Insets show close-ups of: the hydride region (top right), and resolved coupling in the aryl region at 298 K (top left).

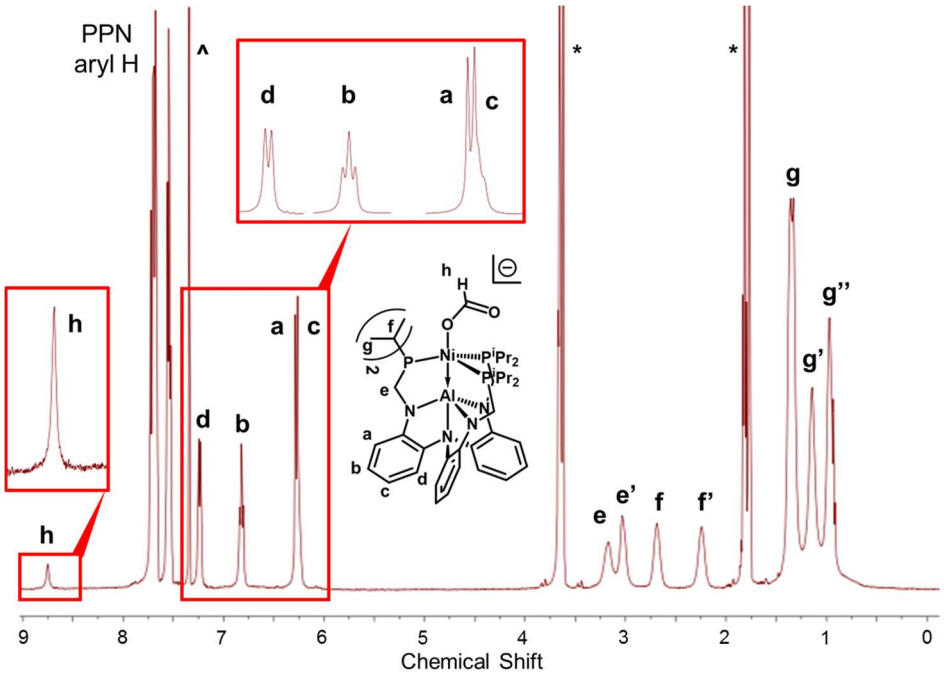

Figure A.4.5. ^{1}H NMR spectrum of [PPN][**1**−O_2CH] (400 MHz, THF-d_8). Residual solvent peaks of THF (*) and benzene (^) are denoted. Close-ups of the coordinated formate proton (top left) and of resolved coupling in the aryl region (top, center) are shown for visual clarity.

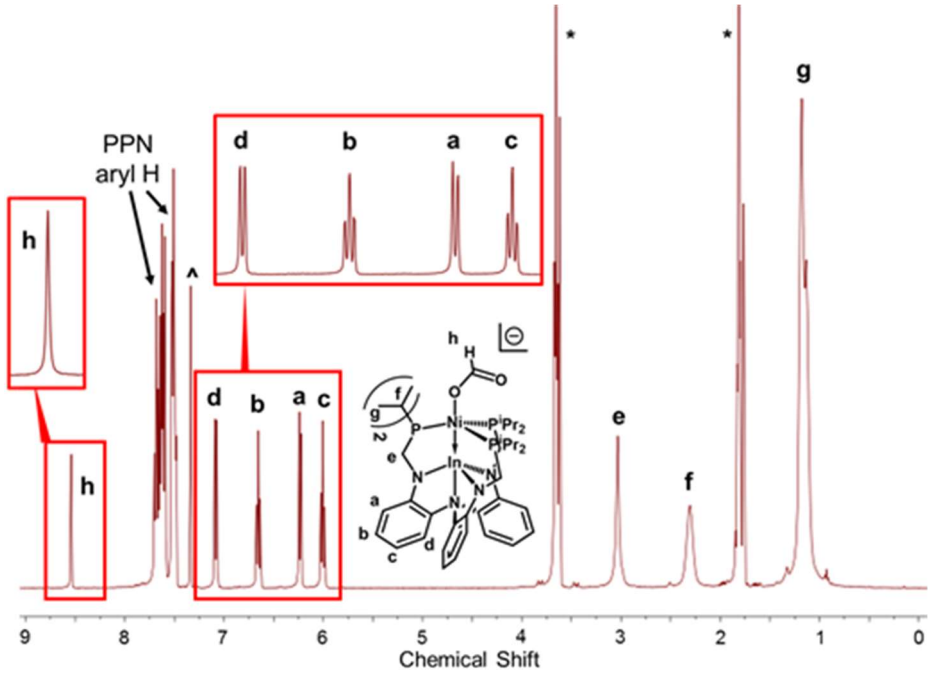

Figure A.4.6. ^{1}H NMR spectrum of [PPN][**3**−O_2CH] (400 MHz, THF-d_8). Residual solvent peaks of THF (*) and benzene (^) are denoted. Close-ups of the coordinated formate proton (top left) and of resolved coupling in the aryl region (top, center) are shown for visual clarity.

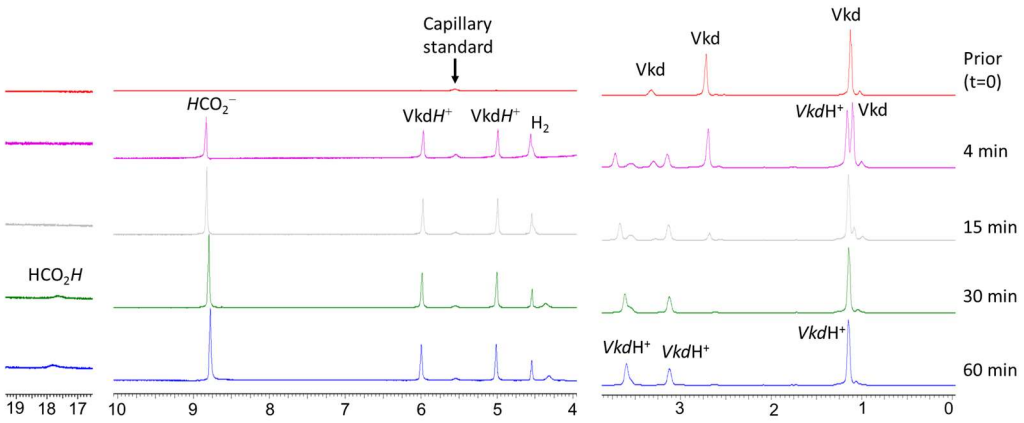

Figure A.4.7. Representative ^{1}H NMR spectra (500 MHz) for monitoring kinetics of catalytic trials. Catalytic conditions: [**2**]=0.25 mM, [Vkd]=800 mM, 0.30 mL THF-d_8, 34 atm of ~1:1 H_2/CO_2, and 298 K (Table 5.1, entry 3). Formate was quantified by integration of ^{1}H NMR resonance at 8.8 ppm against a capillary standard (broad peak at 5.5 ppm). The resulting formate yield based on this relative integration method closely matched the ratio of formate to protonated base, confirming the reliability of the method. Near the end of catalysis when [Vkd] is low, HCO_2H can be observed as a broad resonance at 17.8 ppm.

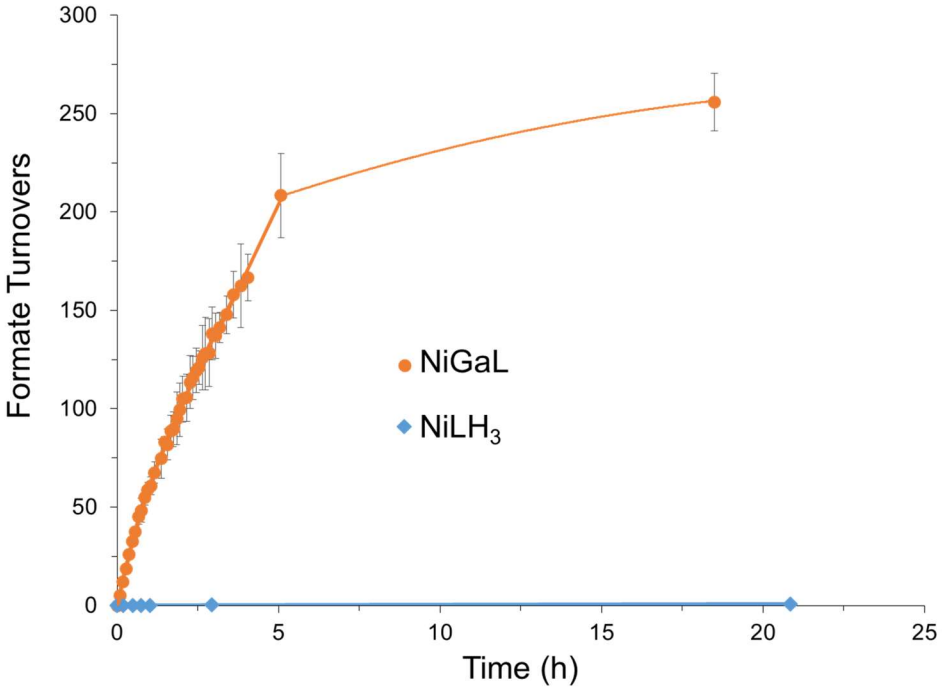

Figure A.4.8. Kinetic plot of formate turnovers versus time (hours) for catalytic trials corresponding to Table 5.1, entries 1 and 6. Error bars represent standard deviation in turnovers for duplicate trials. Catalytic conditions: 1 atm, 2.9 mM catalyst (NiGaL [**2**] or $NiLH_3$ [**4**]), 800 mM Vkd base in 0.40 mL THF-d_8 (maximum TON = 275).

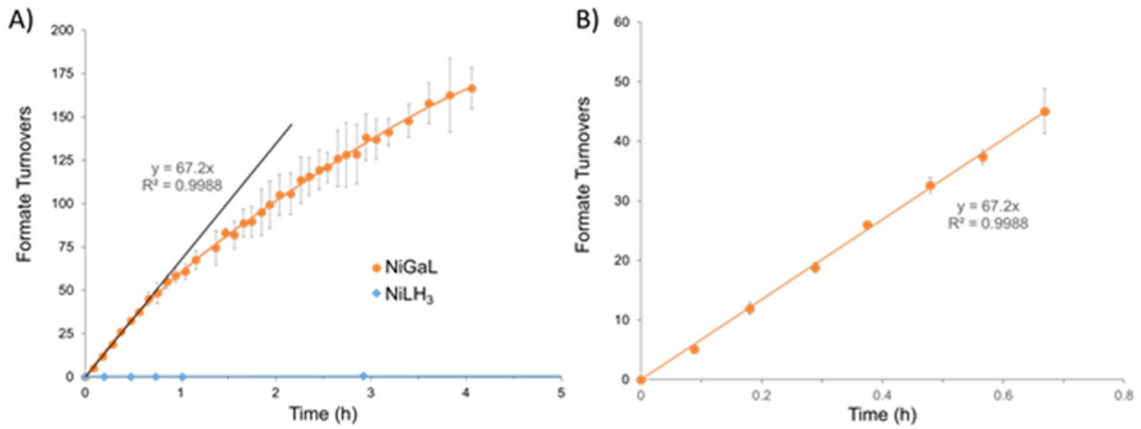

Figure A.4.9. Kinetic plot of formate turnovers versus time (hours) for catalytic trials corresponding to Table 5.1, entries 1 and 6, zooming in on: (A) first 5 hours and (B) first 40 minutes. In (B), the plot is linear, and the slope represents the initial rate for NiGaL (**2**, initial TOF = 67(±2) h^{-1}). The initial TOF for $NiLH_3$ (**4**, 0.14 (±0.02) h^{-1}) is taken to be over the first ~3 hours, as that is the first data point for which an appreciable amount of formate was formed in both duplicate trials.

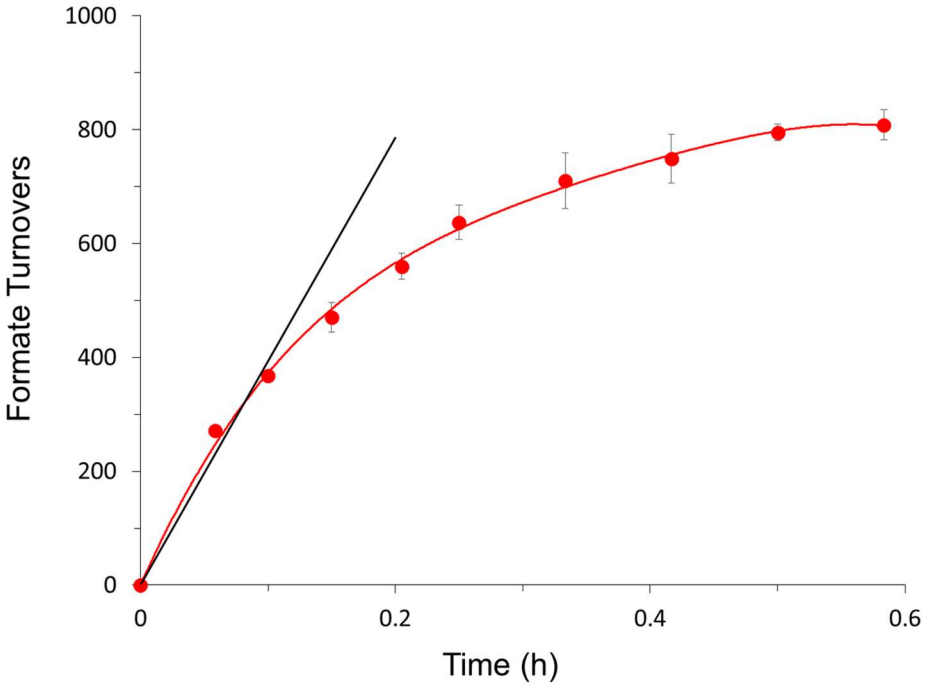

Figure A.4.10. Kinetic plot of formate turnovers versus time (hours) for catalytic trials corresponding to Table 5.1, entry 2. Catalytic conditions: 34 atm, 1.0 mM NiGaL (**2**), 800 mM Vkd in 0.30 mL THF-d_8 (maximum TON = 800). The initial TOF was taken to be the rate over the initial 6 minutes of the reaction (ie. the first two data points, turnovers/time after 6 minutes), giving initial TOF = 3680(±90) h^{-1}.

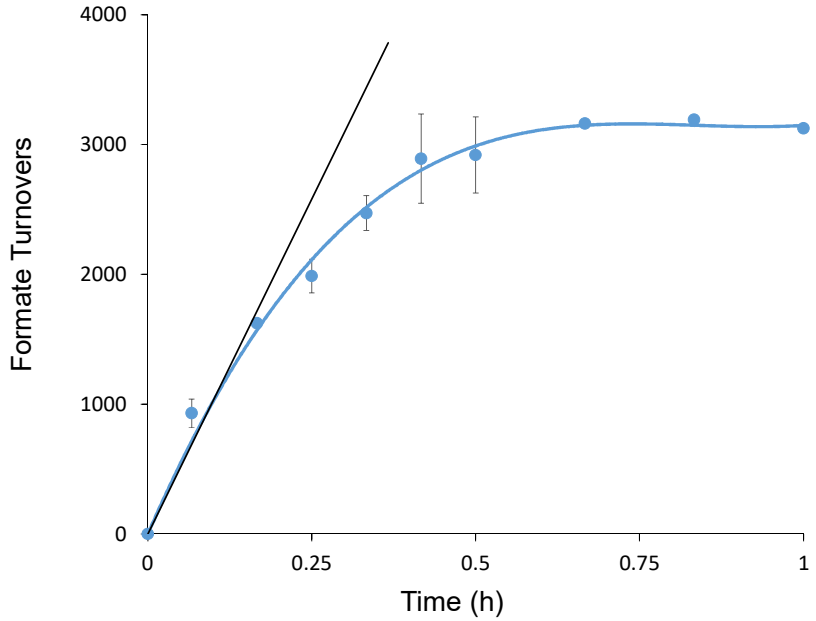

Figure A.4.11. Kinetic plot of formate turnovers versus time (hours) for catalytic trials corresponding to Table 5.1, entry 3. Catalytic conditions: 34 atm, 0.25 mM NiGaL (**2**), 800 mM Vkd in 0.30 mL THF-d_8 (maximum TON = 3200). The initial TOF was taken to be the reaction rate over the initial 10 minutes (ie. the first two data points, turnovers/time after 10 minutes), giving initial TOF = 9700(±400) h^{-1}.

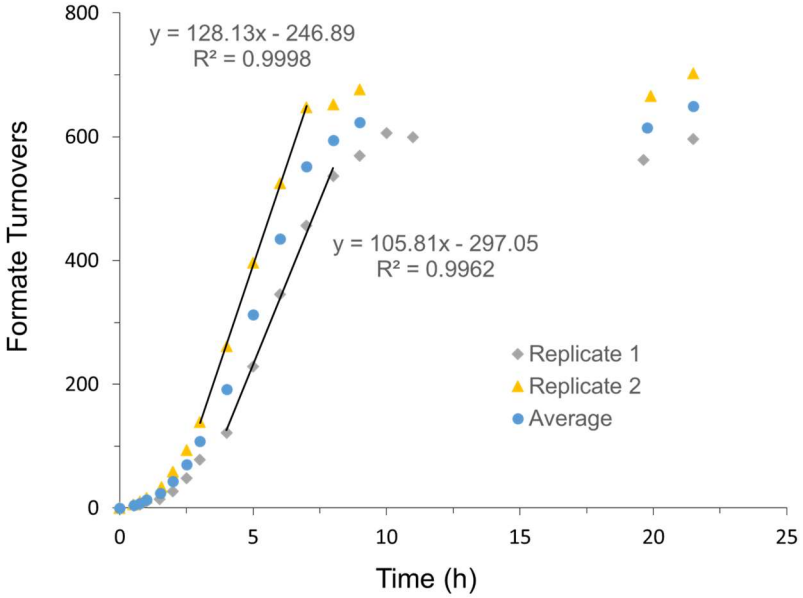

Figure A.4.12. Kinetic plot of formate turnovers versus time (hours) for catalytic trials using tBuTMG (Table 5.1, entry 4). Catalytic conditions: 34 atm, 1.0 mM NiGaL (**2**), 800 mM tBuTMG in 0.30 mL THF-d_8 (maximum TON = 800). The overall TOF accounts for the induction period (~3 h) and was defined as the overall time to reach >90% of the final formate yield. The initial TOF was taken to be the average slope of the linear region (after the induction period) from ~3.5 to 7.5 hours.

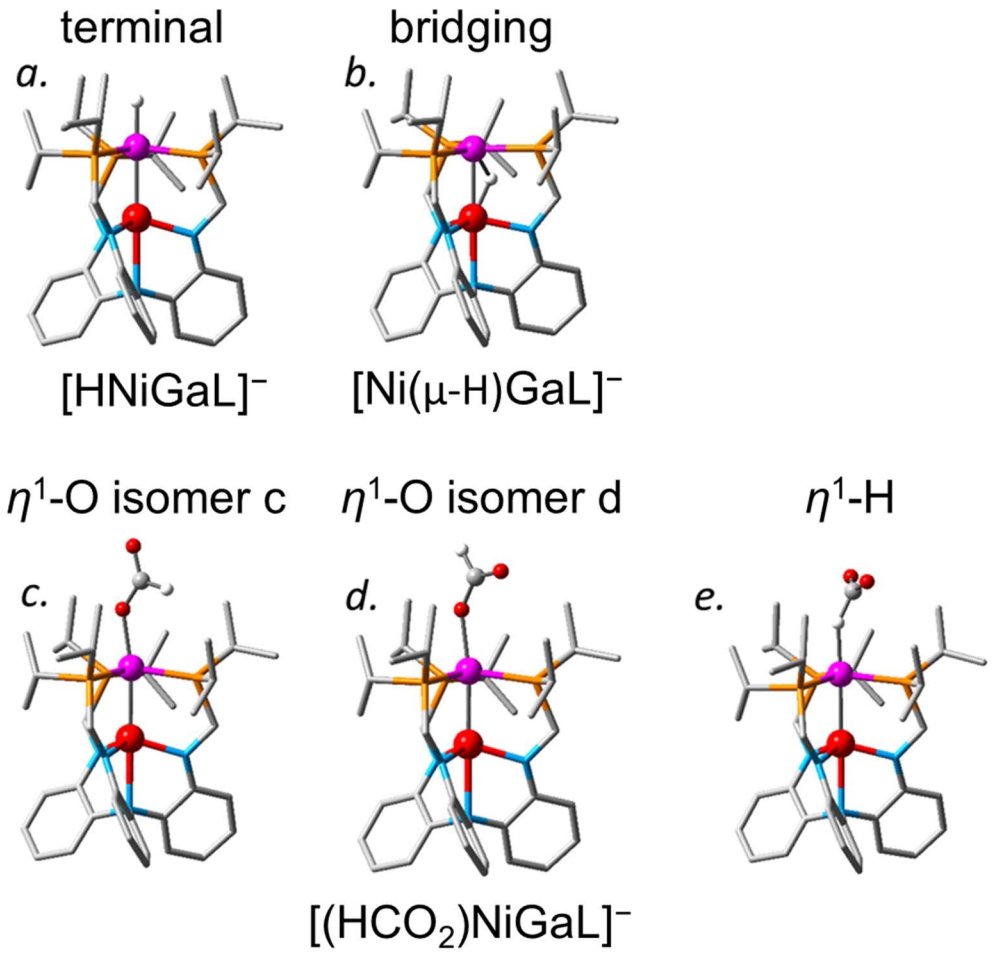

Figure A.4.13. DFT-optimized structures of potential isomers of $[HNiGaL]^-$ (*a, b*) and $[(HCO_2)NiGaL]^-$ (**4**: *c, d, e*). Color key: Ni, pink; Ga, red; P, orange; N, blue; C, grey; H, white. The H atoms of the ligand were omitted for clarity.

Table A.4.2. Energies of calculated isomers of $[HNiGaL]^-$ and $[(HCO_2)NiGaL]^-$. The most stable isomers are calculated to be the terminal hydride for $[HNiGaL]^-$ (isomer *a*, corresponding to figure above) and the η^1-O bound formate species (isomers *c* and *d*).

	$[HNiGaL]^-$		**$[(HCO_2)NiGaL]^-$**		
Isomer	***A***	***b***	***c***	***d***	***e***
Relative Energy (kcal/mol)	0	21.5	0	0.66	6.87

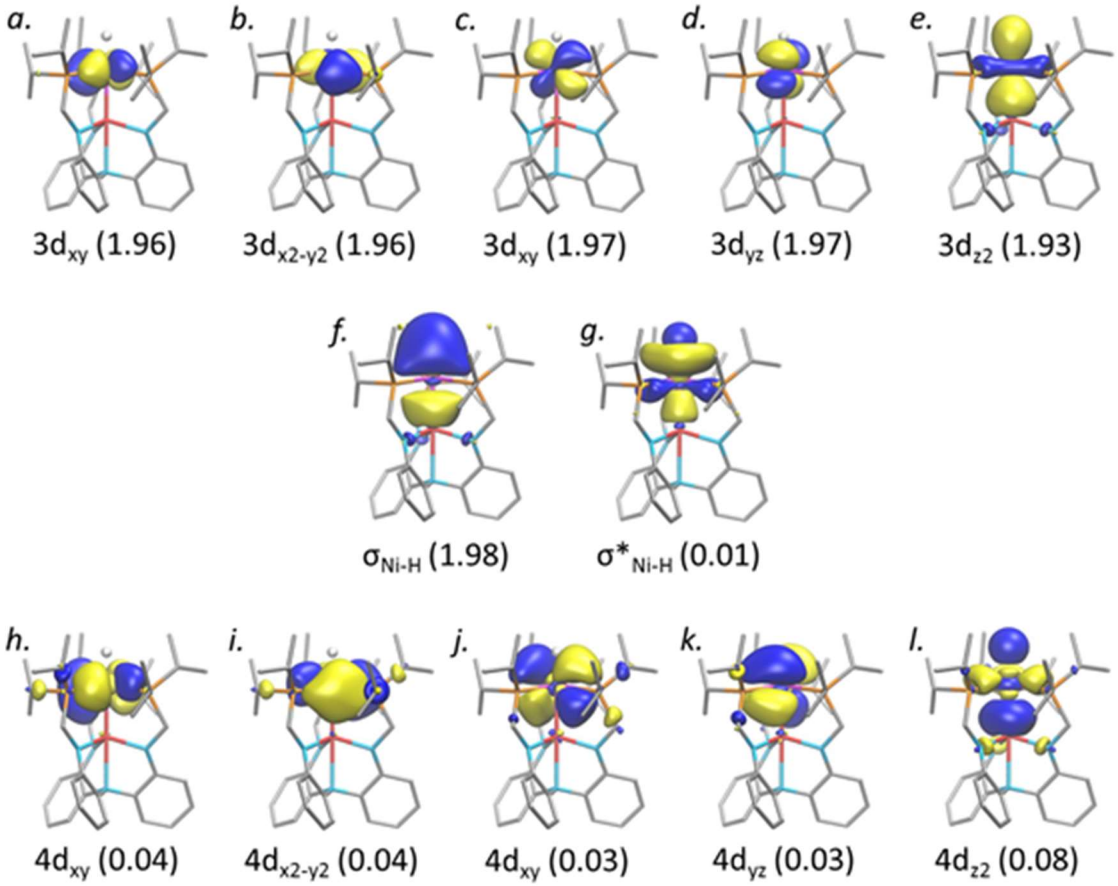

Figure A.4.14. Natural orbitals for the CAS(12,12) calculation of $[HNiGaL]^-$ ($[\mathbf{2}-H]^-$). The occupation number of each orbital is given in the parentheses. Singlet $[\mathbf{2}-H]^-$ is best described by a single-determinant wavefunction with five doubly occupied Ni 3d orbitals and one doubly occupied Ni−H σ-type orbital, which accounts for 88.9% of the total wavefunction.

Table A.4.3. Composition of the σ-symmetric natural orbitals (*e* – *g, l*) of $[HNiGaL]^-$ ($[\mathbf{2}-H]^-$) based on the CAS(12,12) calculation (Figure A.4.14). The contributions of various atomic orbitals centered on the hydride, Ni, and Ga are shown as percentages. The labels of the natural orbitals correspond to the figure shown above.

natural orbitals	H	Ni	Ga
e	8.8%	73.8% (3*d*)	10.7% (4*s*, 4*p*)
f	50.9%	29.0%(mainly 4*p*, minor 4*s*, 3*p*)	9.7% (4*s*, 4*p*)
g	29.4%	63.5%(mainly 4*s*, 4*p*, mimor 4*d*)	5.9% (4*s*, 4*p*)
l	18.6%	54.0% (mainly 3*d*, 4*d*, minor 4s,*p*)	15.0% (4*s*, 4*p*)

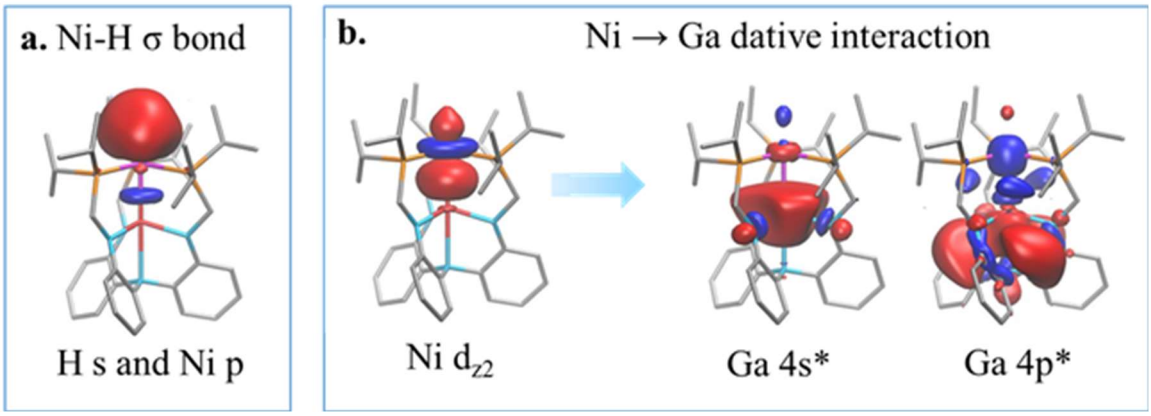

Figure A.4.15. Natural bond orbital (NBO) analysis for $[HNiGaL]^-$ ($[\mathbf{2}-H]^-$) focusing on (a) the Ni−H σ-bond and (b) the Ni→Ga donor-acceptor interaction between Ni ($3d_{z2}$) and Ga (4*s*, 4*p*). Color code, Ni, pink; Ga, red; P, orange; N, blue; C, grey; H, white. The ligand hydrogen atoms are omitted for clarity. The Ni−H σ-bond is composed of 42% Ni atomic orbitals (15% 4*s*, 79% 4*p*, 5% 3*d*) and 58% H 1*s* orbitals.

Table A.4.4. The donor-acceptor stabilization energy of the Ni→Ga dative interaction in NiGaL (**2**), and $[HNiGaL]^-$ ($[\mathbf{2}-H]^-$), as determined by natural bond orbital analysis.

	Donor-Acceptor Stabilization Energy (kcal/mol)	
Interaction type	**NiGaL**	**$[HNiGaL]^-$**
Ni ($3d_{z2}$) → Ga (4*s*)	71.66	83.24
Ni ($3d_{z2}$) → Ga (4*p*)	12.54	11.28
Total Ni → Ga interaction	84.20	94.52

Table A.4.5. Data obtained by monitoring H_2 heterolysis equilibrium for NiGaL (**2**) with Vkd base in THF, as described in synthetic procedure section. Reaction conditions for each trial are shown, with [Vkd] varied. Concentration ratios were obtained as described in the data analysis procedure section, with the reported error (one e.s.d.) representing the standard deviation across three or more time points once the system had converged to equilibrium.

Trial	Conditions			Equilibrated Concentration Ratios from Intgration		
	$p[H_2]$ (atm)	$[Ni]_{tot}$ (mM)	$[Base]_{tot}$ (mM)	$\frac{\{[(H_2)NiGaL] + [NiGaL]\}}{[HNiGaL^-]}$	$\frac{[(H_2)NiGaL]}{[NiGaL]}$	$[Vkd]/[VkdH^+]$
A	1	9.60	3.87	0.99 (± 0.13)	1.97 (± 0.01)	0.48 (± 0.01)
B	1	9.50	6.13	0.52 (± 0.04)	1.80 (± 0.06)	0.83 (± 0.06)

Table A.4.6. Thermodynamic data calculated from the equilibrium concentration ratios (Table A.4.4). Reported values are the average of trials A and B, with the error (one e.s.d.) propagated from deviations between and within trials.

Trial	Conditions			Thermodynamic Results (pKa)			Thermodynamic Results (ΔG_{H-})	
	$p[H_2]$ (atm)	$[Ni]_{tot}$ (mM)	$[Base]_{tot}$ (mM)	Measured K_{eq2}	pK_a {(H_2)NiGaL} THF	pK_a {(H_2)NiGaL} CH_3CN (est.)	Measured K_{eq1}	ΔG_{H-} {$HNiGaL^-$}
A	1	9.60	3.87	3.2 (± 1.6)	27.5 (± 0.2)	33.1 (± 0.2)	0.16 (± 0.14)	31.3 (± 0.6)
B	1	9.50	6.13	3.6 (± 2.3)	27.4 (± 0.3)	33.0 (± 0.3)	0.15 (± 0.17)	31.3 (± 0.7)
	Average			**3.4 (± 1.4)**	**27.5 (± 0.3)**	**33.1 (± 0.3)**	**0.16 (± 0.11)**	**31.3 (± 0.5)**

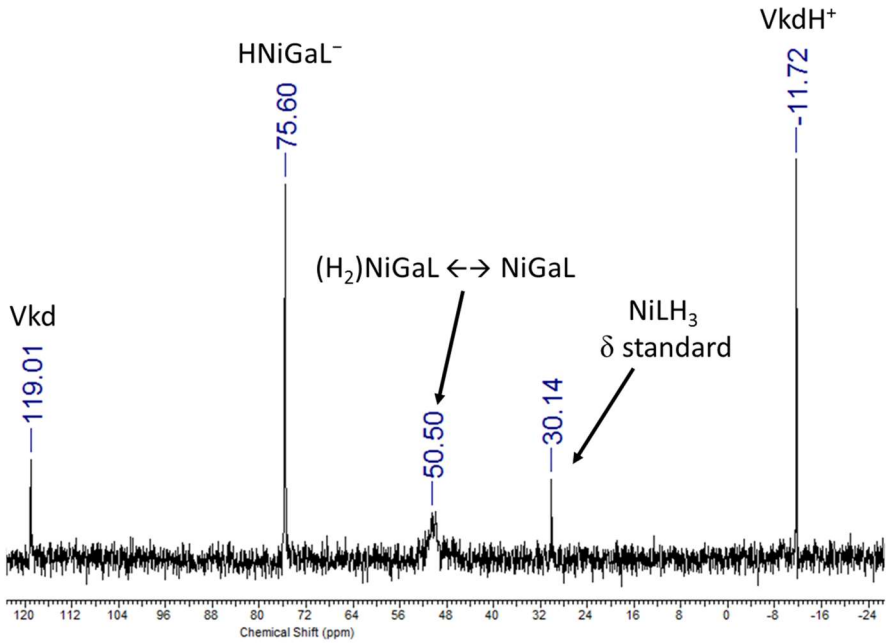

Figure A.4.16. Representative ^{31}P NMR (202.4 MHz, THF) for the H_2 heterolysis equilibrium of NiGaL (**2**) with Vkd base (taken for trial A after equilibrium had been reached at t=85 hours). Note that >100 scans were taken and improved signal-to-noise beyond what can be visualized here was achieved on the Varian NMR instrument itself on which integration was performed (using vNMRj software). Note that the bound and unbound species, **2** and **2**−H_2, are in fast-intermediate equilibrium on the ^{31}P NMR (202.4 MHz) timescale, giving rise to a broadened resonance.

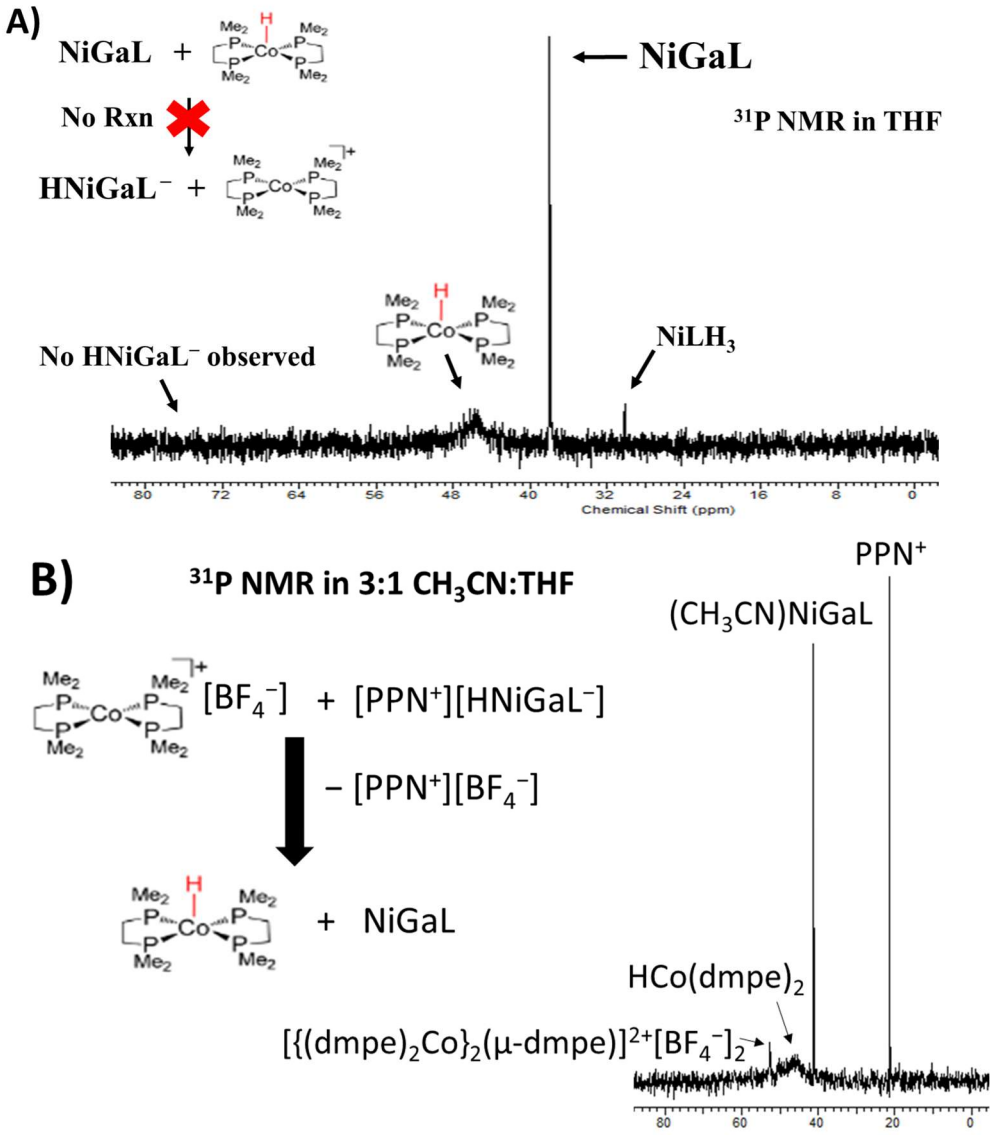

Figure A.4.17. ^{31}P NMR spectra (202.4 MHz, THF-d_8) for equimolar reactions of: (A) NiGaL (**2**) with $HCo(dmpe)_2$ and (B) [PPN][HNiGaL] with $[Co(dmpe)_2][BF_4]$. The experiment with $[\mathbf{2}–H]^-$ and $[Co(dmpe)_2]^+$ reacting to give $HCo(dmpe)_2$ and **2**-$NCCH_3$ was complicated by a small impurity of the dication dimer, $[\{(dmpe)_2Co\}_2(\mu\text{-}dmpe)_2][BF_4]_2$, which was present initially upon dissolution in CH_3CN (a very small peak at −14 ppm for μ-dmpe was also observed but not shown to allow the rest of the spectrum to be shown full scale), and grew in slightly over time as previously reported by Mock and co-workers (ref. 353).

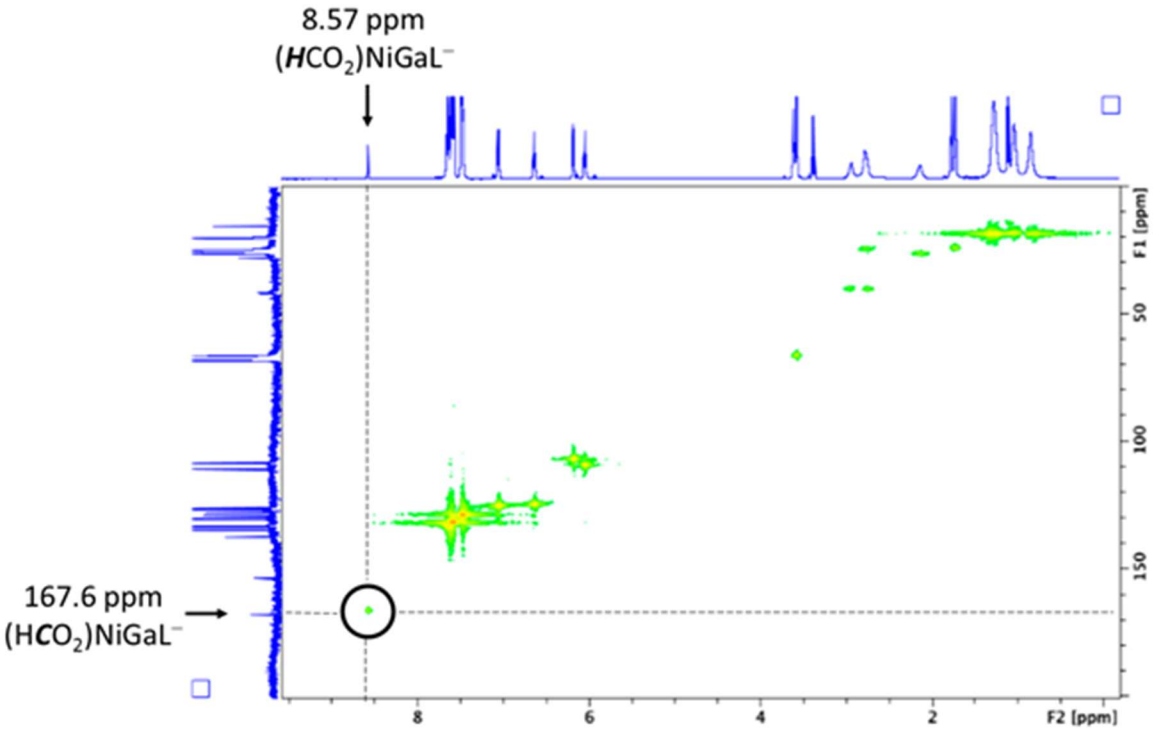

Figure A.4.18. ^{1}H-^{13}C HMQC NMR spectrum of [PPN][**2**−O_2CH] (500 MHz, THF-d_8). A cross-peak is observed between the coordinated formate 1H resonance (8.57 ppm) of [**2**−O_2CH]$^-$ and a ^{13}C resonance at 167.6 ppm, which has been attributed to the coordinated formate carbon atom.

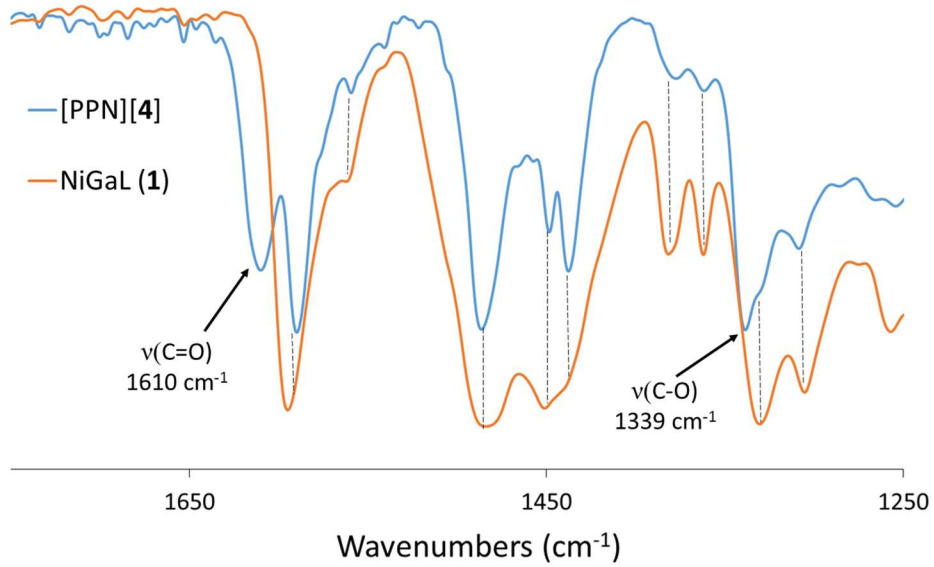

Figure A.4.19. IR spectra of [PPN][**2**−O_2CH] in comparison to **2** (KBr pellet). Assignments of the stretching modes associated with coordinated formate made based on the labeling study (Figure 5.11) are further validated by ruling out several peaks (1590, 1486, 1450, 1438 cm^{-1}) which match up well with the IR of **2**, and are therefore likely attributable to vibrational modes that are unrelated to the coordinated formate ligand.

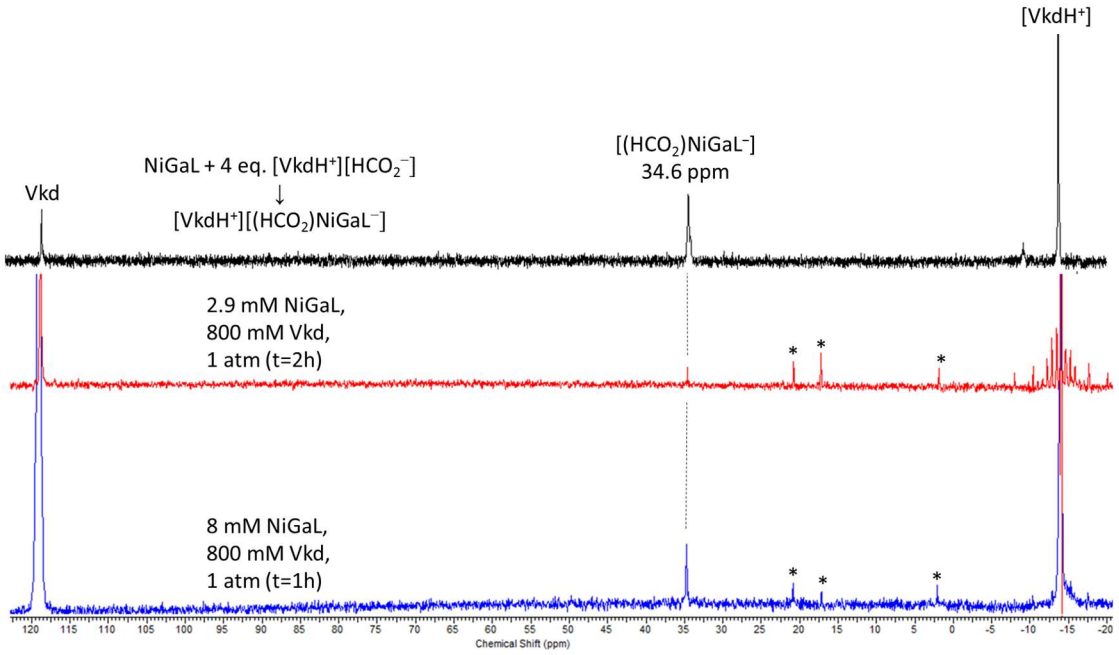

Figure A.4.20. ^{31}P NMR spectra taken during various catalytic trials in comparison to that of [VkdH][**2**−O_2CH] (202.4 MHz, THF-d_8). In all catalytic trials examined, the primary species which builds up during and throughout catalysis is [VkdH][**2**−O_2CH], as identified by the matching ^{31}P NMR resonance. Catalyst loadings below 2.9 mM did not have enough catalyst to observe the resting state by ^{31}P NMR. Small peaks for impurities in commercially purchased Vkd can also be seen (* at 20.7, 17.2, 2 ppm) due to the large excess of base employed.

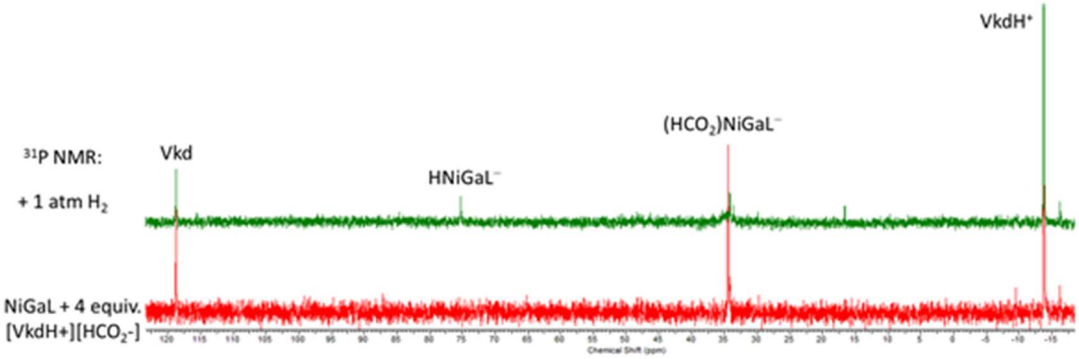

Figure A.4.21. Stacked ^{31}P NMR spectra (202.4 MHz, THF-d_8) for the addition of H_2 (1 atm) to [VkdH][**2**−O_2CH], which was generated *in situ* from addition of ~4 equiv of [VkdH][HCO_2] to **2**. Displacement of coordinated formate by H_2 was observed to occur, with subsequent deprotonation by a small amount of Vkd generating an equilibrium mixture of [VkdH][**2**−H] and [VkdH][**2**−O_2CH]. Thus, conversion to the active anionic Ni−H species from the catalytic resting state is seen to be feasible under H_2.

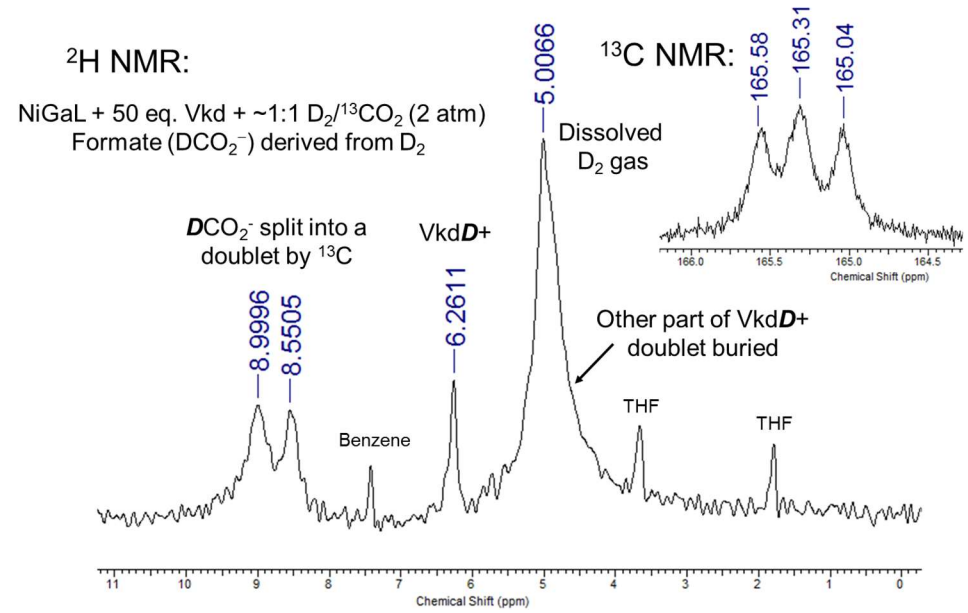

Figure A.4.22. Deuterium NMR spectrum after 2 h for catalytic trial with **2** (2 mol%), Vkd (50 equiv), and 2 atm of ~1:1 D_2/$^{13}CO_2$ (61.38 MHz, THF-d_8). The ^{2}H resonance for formate ($D^{13}CO_2^-$) is observed as a doublet, as expected due to coupling to ^{13}C ($J_{13C\text{-}2H}$ = 27 Hz). Deuterated base ($[VkdD]^+$) and dissolved D_2 gas were also observed. The corresponding $^{13}C\{^1H\}$ NMR spectrum (100.55 MHz, THF-d_8) is also shown (top right), and the ^{13}C resonance for formate ($D^{13}CO_2^-$) is split by deuterium (I=1) into the expected 1:1:1 triplet ($J_{13C\text{-}2H}$ = 27 Hz). On the basis of these labelling studies, formate is concluded to be derived from H_2 and CO_2 in typical trials using a ~1:1 H_2/CO_2 gas mixture.

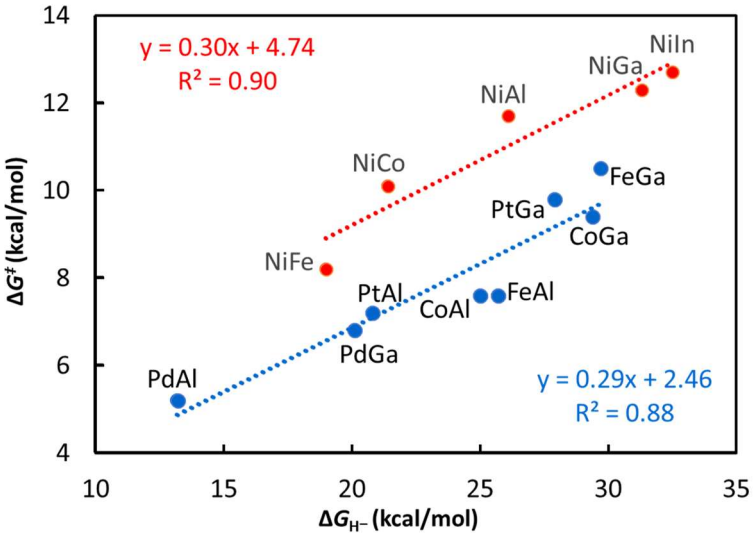

Figure A.4.23. Calculated $\Delta G^{\ddagger}$ for the outer-sphere hydride transfer to CO_2 from $[HM_1M_2L]^-$ as a function of the calculated $\Delta G°_{H-}$ in THF. Hydricity values were referenced to the experimentally determined $\Delta G°_{H-}$ value of 31.3 kcal/mol for $[HNiGaL]^-$ in CH_3CN.

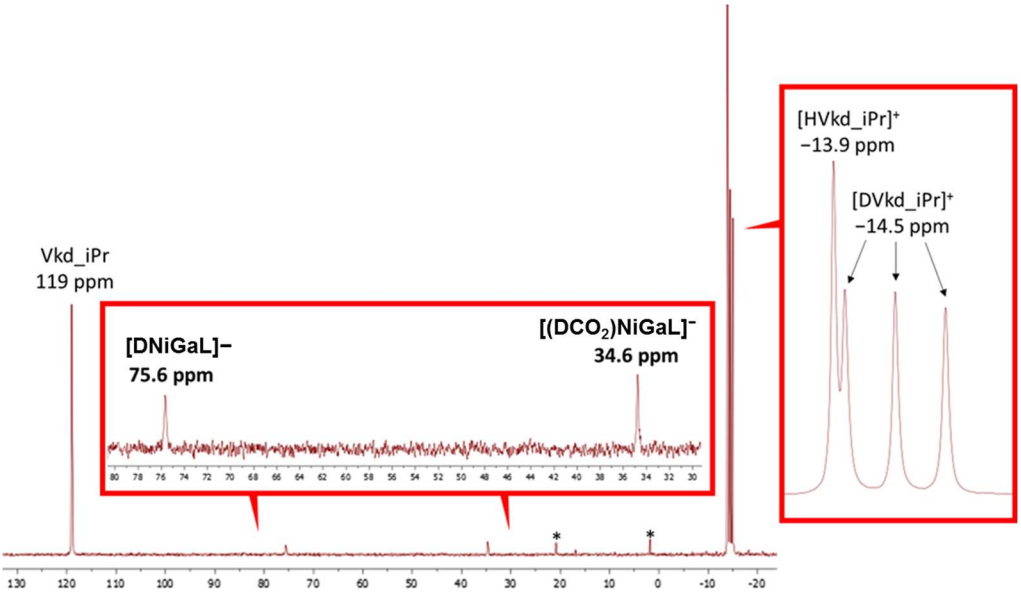

Figure A.2.24. ^{31}P NMR (161.9 MHz) obtained during CO_2 hydrogenation catalysis after 30 minutes (catalytic conditions: 2 mol% **2** (3.7 mM), ~180 mM Vkd, ~2 atm 1:1 $D_2/^{13}CO_2$, THF-d_8, 293 K). These labeling experiments were not conducted with the propylene glycol/water/dry ice bath to further dry the gas mixture, and as a result these studies contain greater residual water content than the catalytic trials with H_2/CO_2 gas. This can be seen in the protonation of a small amount of Vkd by residual water (~10%), whereas the rest of base was deuterated as expected from the use of D_2 (1:1:1 triplet, J_{DP}=75.4 Hz). Small impurities (*) in commercial Vkd are seen at 1.9 and 20.8 ppm (VkdP=O).

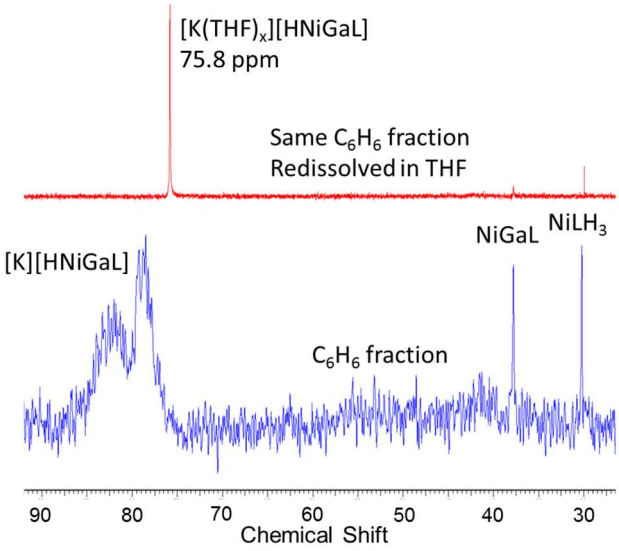

Figure A.4.25. Stacked ^{31}P NMR spectra of [K][HNiGaL] in THF (top) and benzene (bottom), showing the effect of chelation of $[K]^+$ by THF. A similar effect is observed upon adding 2,2,2-cryptand to [K][HNiGaL] in benzene.

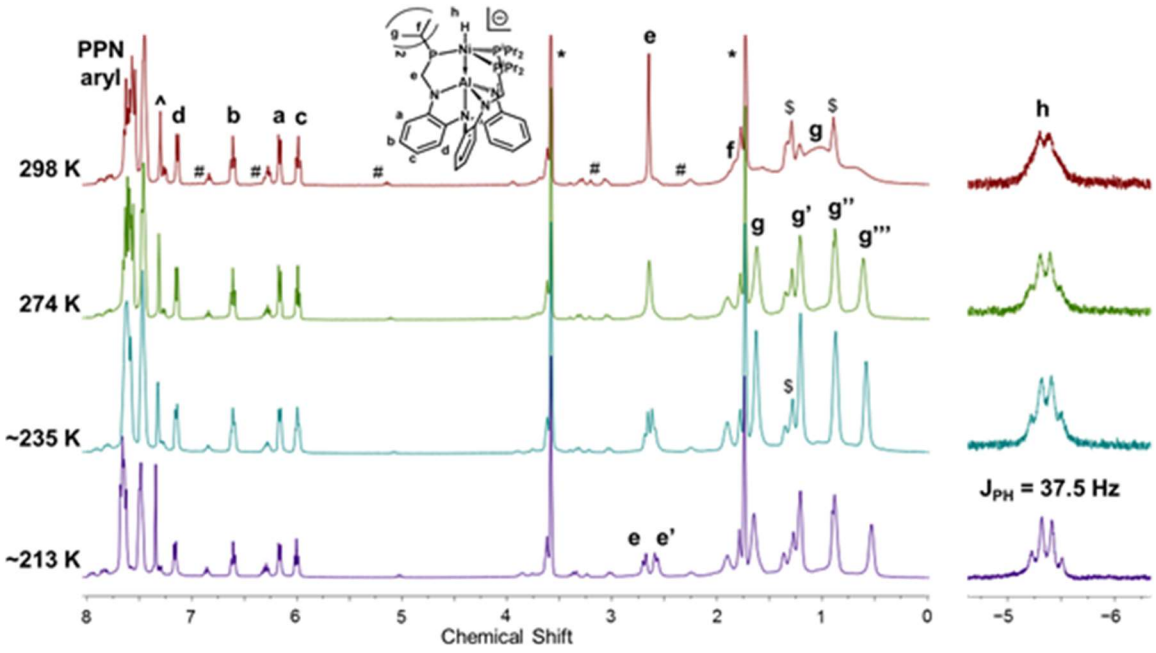

Figure A.4.26. VT ^{1}H NMR spectra of [PPN][**1**−H] (400 MHz, THF-d_8). Residual solvent peaks for THF (*), benzene (^), and hexanes ($) are denoted, along with a small amount of NiAlL (**1**, #). The hydride resonance is relatively sharp at 298 K, but further sharpens as with decreasing T, with J_{HP} coupling fully resolved at ~213 K. The methylene CH_2 protons (e) of the ligand are observed to become inequivalent (e,e') as T decreases, consistent with the molecule moving from C_{3v} symmetry at high T to C_3 symmetry at low T.

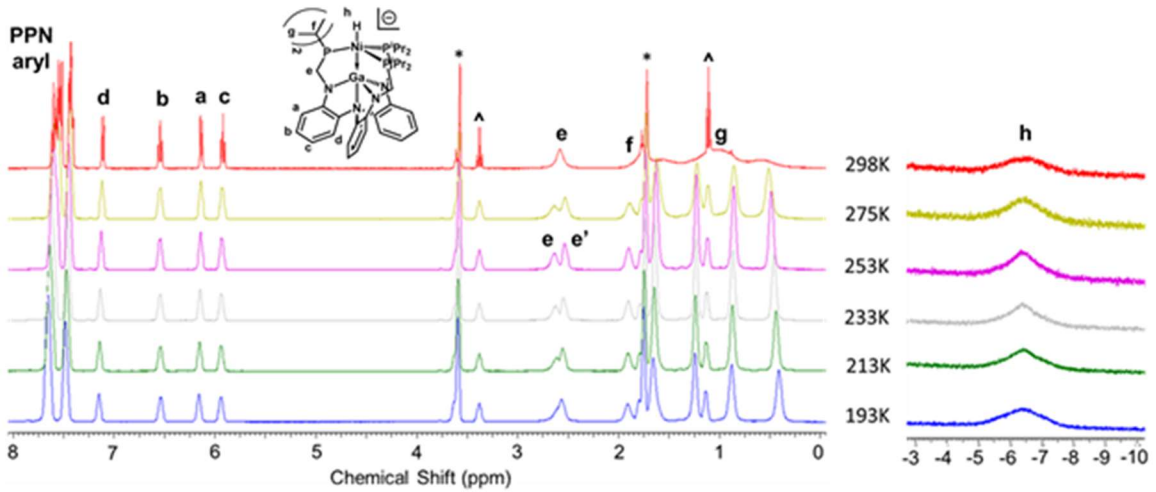

Figure A.2.27. VT ^{1}H NMR spectra of [PPN][**2**−H] (400 MHz, THF-d_8). Residual solvent peaks for THF (*) and diethyl ether (^) are denoted. The hydride resonance is very broad at 298 K, and sharpens slightly as T is decreased to 233 K, before beginning to broaden once again as T is further decreased to 193 K. The methylene CH_2 protons (e) of the ligand are observed to become inequivalent (e, e') as T decreases to 233 K. The methyl (g) and methine (f) protons also become inequivalent at lower T.

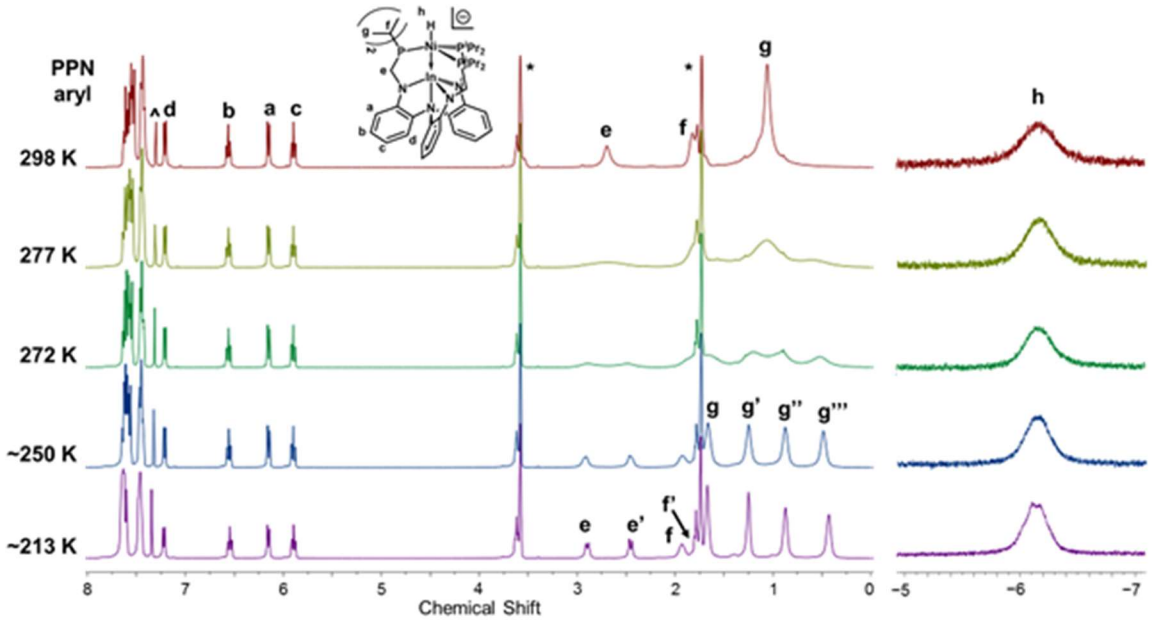

Figure A.2.28. VT ^{1}H NMR spectra of [PPN][**3**−H] (400 MHz, THF-d_8). Residual solvent peaks for THF (*) and benzene (^) are denoted. The hydride resonance is broad at 298 K, and only sharpens marginally as T is decreased, with JHP coupling just beginning to resolve at ~213 K. The methylene CH_2 protons (e) of the ligand are observed to become inequivalent (e, e') as T decreases to ~250 K, as are the methyl (g → g, g', g'', and g''') and methine (f → f, f') protons.

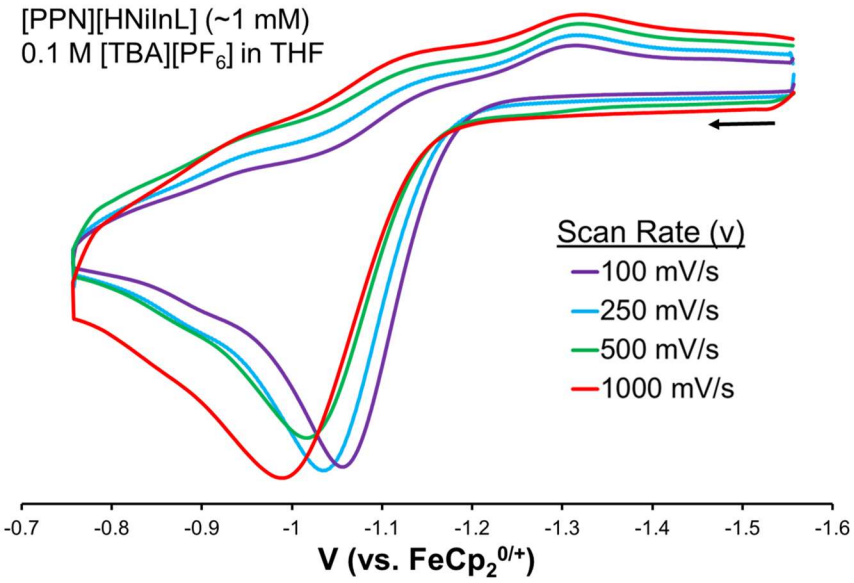

Figure A.2.29. CV scan rate study for [PPN][**3**−H] (~1 mM) with 0.1 M [TBA][PF_6] in THF, with the isolation of the irreversible Ni(0/I) oxidation event displayed. Current (*i*) has been corrected for scan rate (v) based on the proportionality of *i* to ($v^{0.5}$). The small E_{pc} current at −1.32 V is not believed to be related to the oxidation feature, as its potential does not shift as the E_{pa} shifts with varying scan rate.

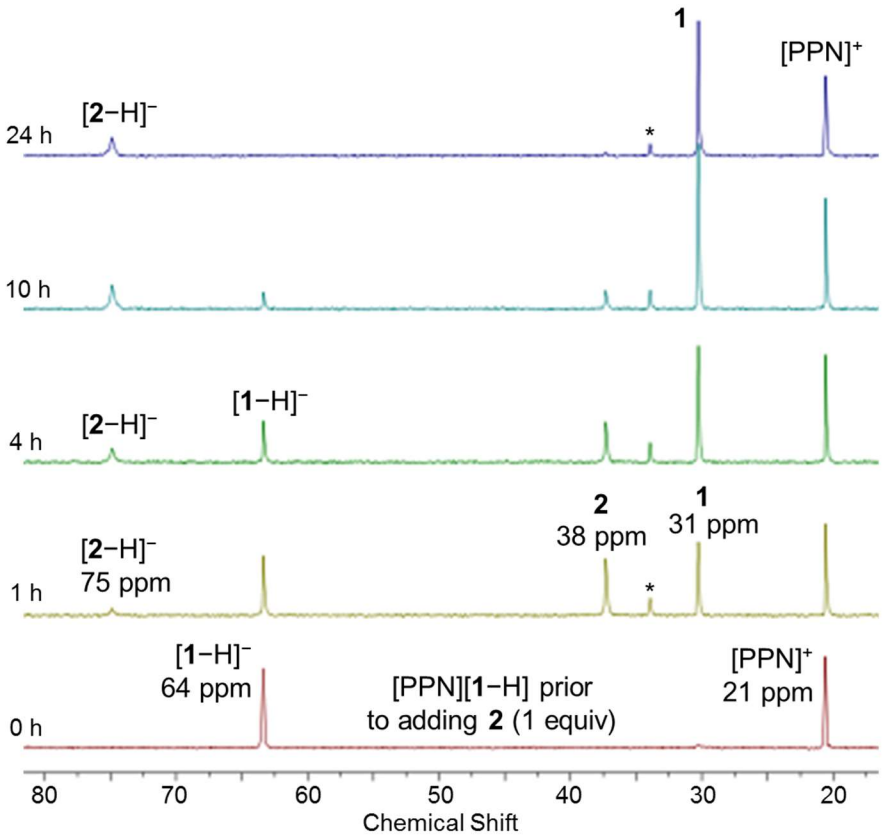

Figure A.4.30. Stacked ^{31}P NMR spectra (161.9 MHz) of hydride transfer from [PPN][**1**−H] to **2** in THF (~9.6 mM of each complex in 0.80 mL).

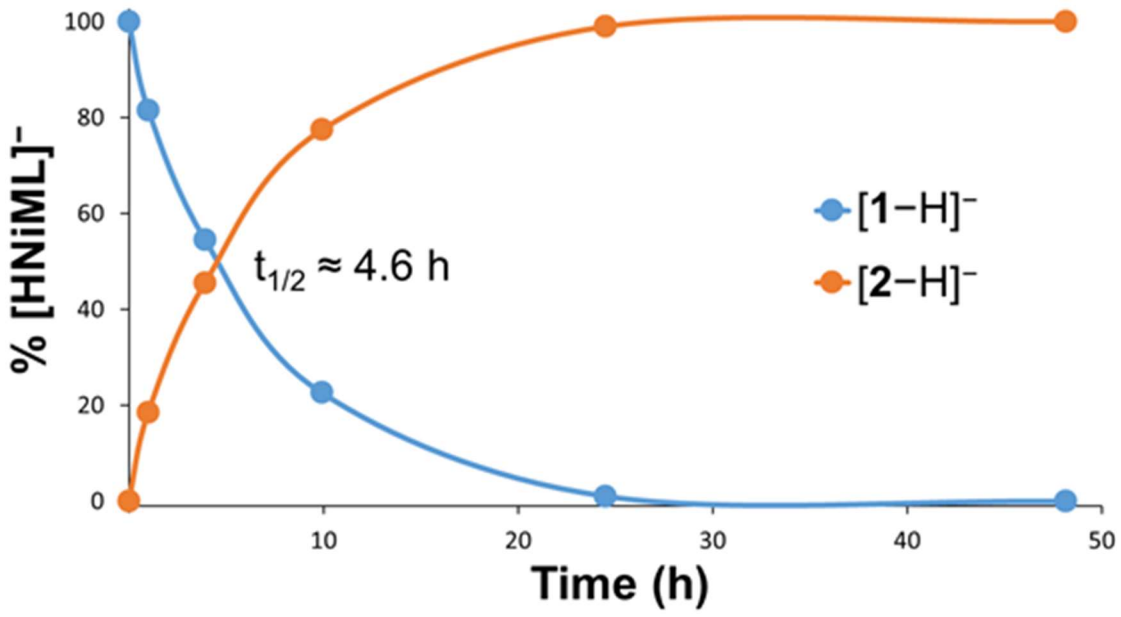

Figure A.4.31. Kinetic profile of hydride transfer from [PPN][**1**−H] to **2** in THF, based on quantitative integration of the ^{31}P NMR resonances shown in Figure A.4.30.

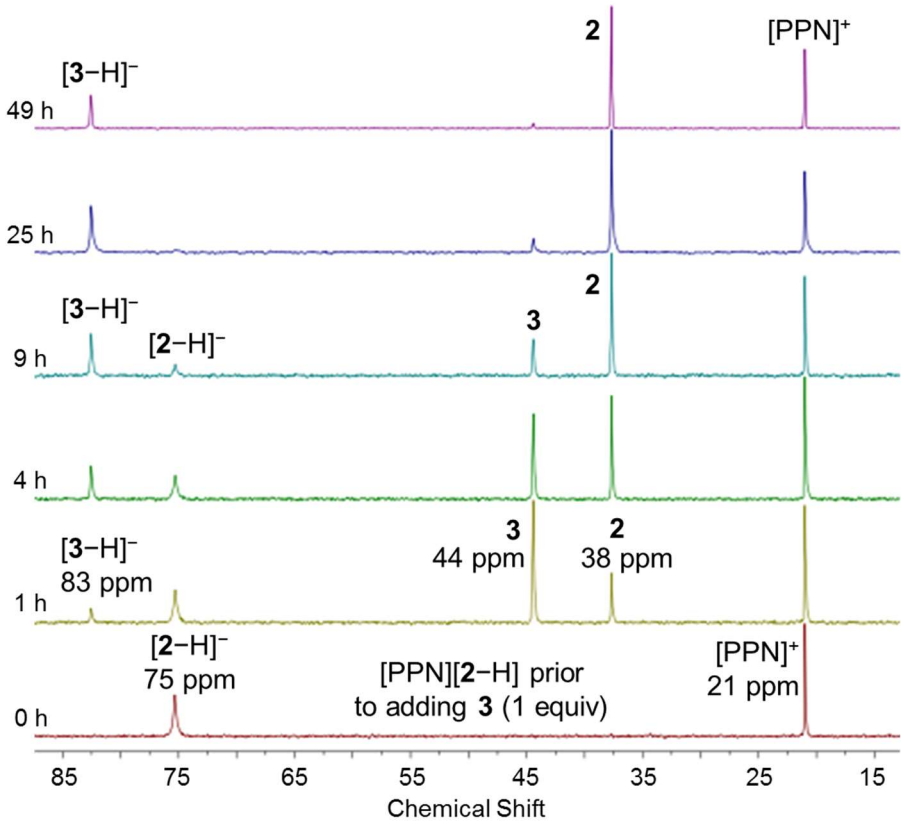

Figure A.4.32. Stacked ^{31}P NMR spectra (161.9 MHz) of hydride transfer from [PPN][**2**−H] to **3** in THF (~9.6 mM of each complex in 0.80 mL).

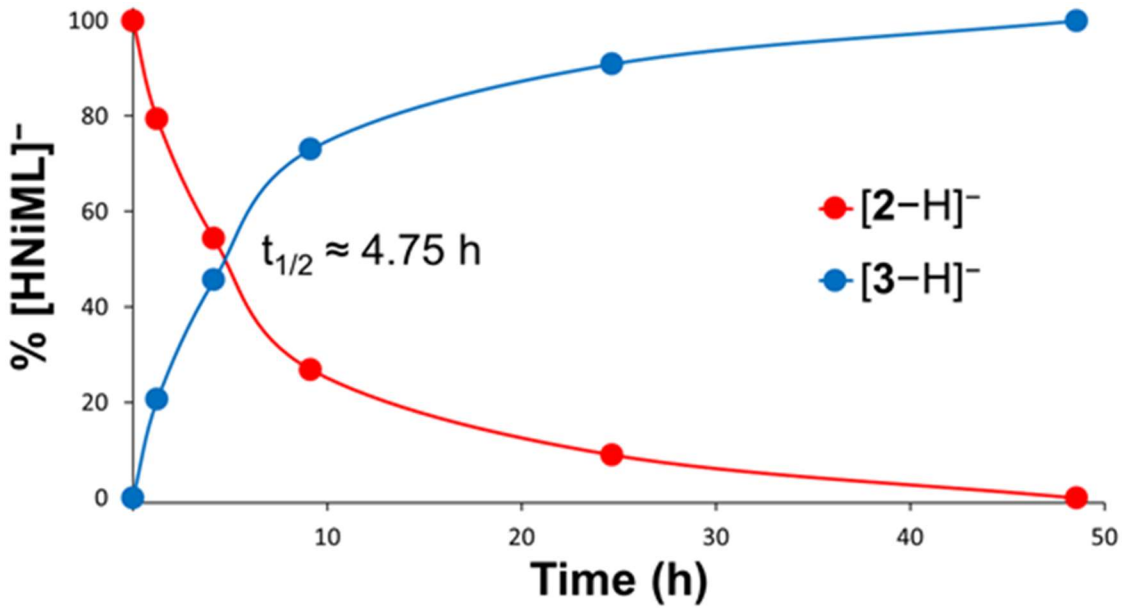

Figure A.4.33. Kinetic profile of hydride transfer from [PPN][**2**−H] to **3** in THF, based on quantitative integration of the ^{31}P NMR resonances shown in Figure A.4.32.

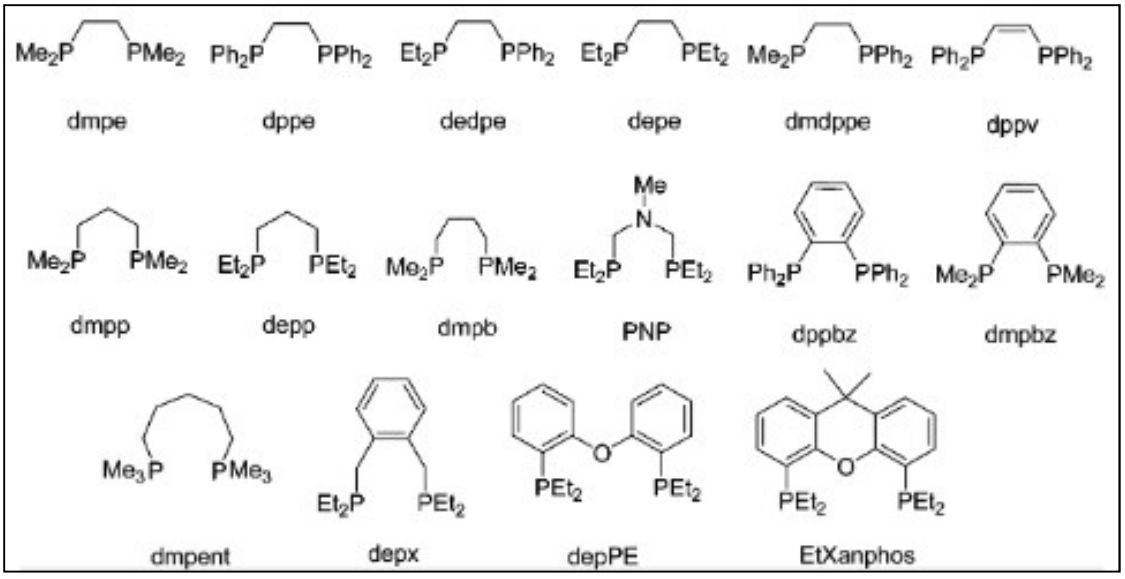

Figure A.4.34. Chart showing abbreviations and chemical structures of various diphosphine ligands, which are referred to in order to compare the NiML system to thermodynamic studies by Dubois and co-workers, as well as to catalytic studies by Linehan and co-workers. Abbreviations for the commonly used diphosphine ligands are also defined in the list of abbreviations.

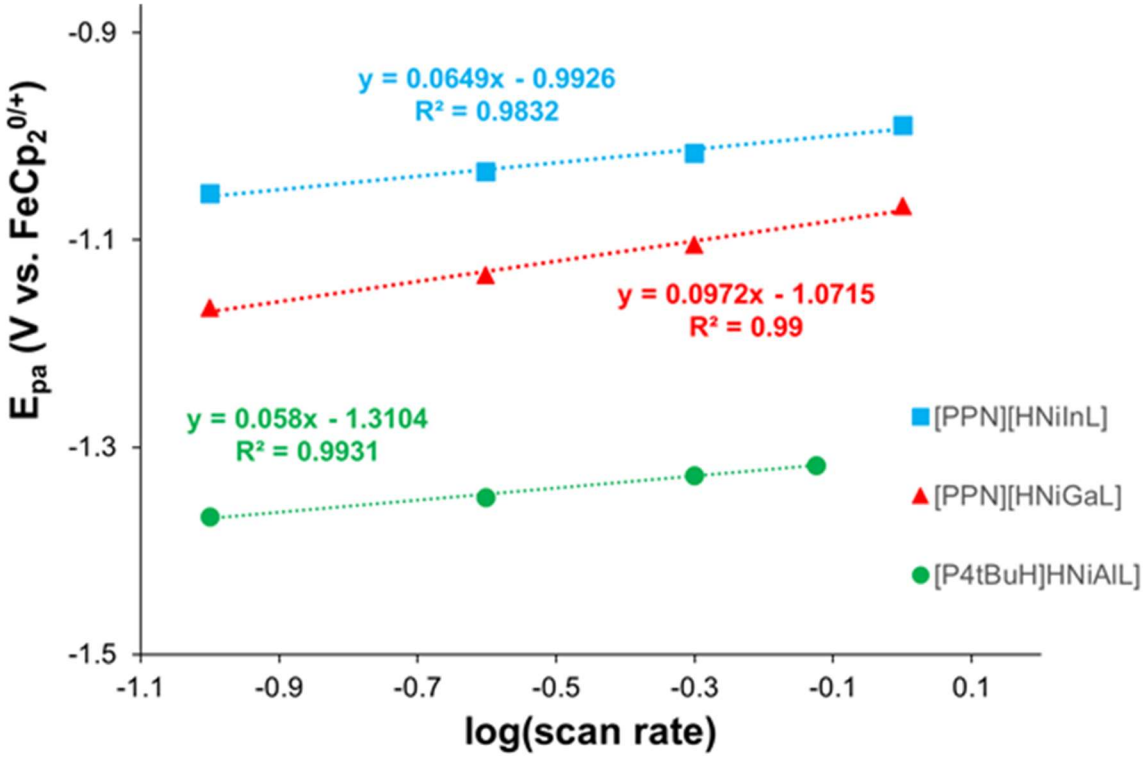

Figure A.4.35. Plot of E_{pa} potential vs. log(scan rate) for irreversible Ni(0/I) oxidation events in CVs of $[HNiML]^-$ complexes (~1 mM in THF, 0.1 M $[TBA][PF_6]$).

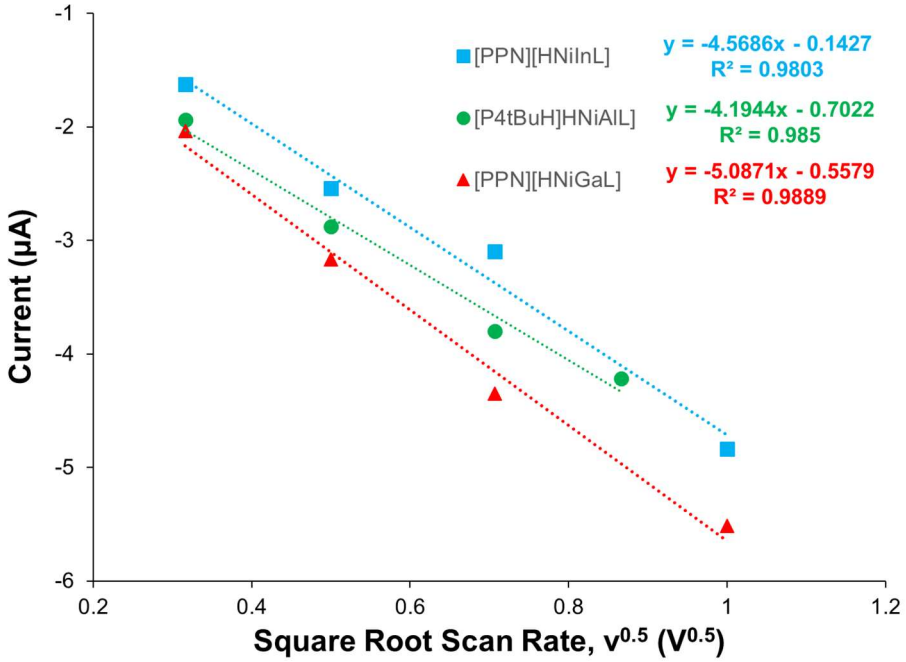

Figure A.4.36. Plot of current (i_{pa}) vs. (scan rate)$^{0.5}$ for irreversible Ni(0/I) oxidation events in CVs of $[HNiML]^-$ complexes (~1 mM in THF, 0.1 M [TBA][PF_6]).

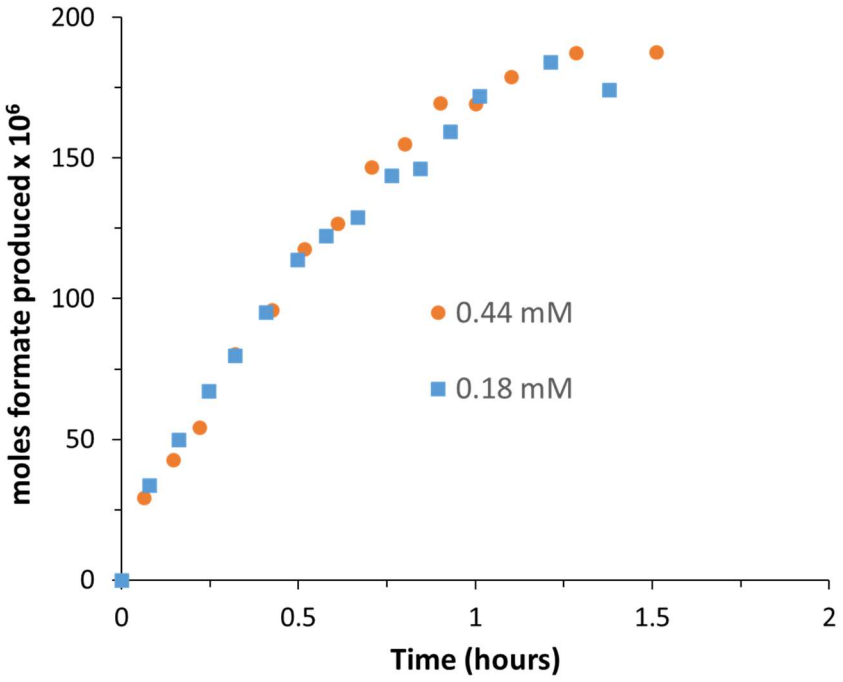

Figure A.4.37. Plot of moles formate produced vs. time (h) for different catalyst loadings of NiGaL (**2**). A clear dependence of the catalytic rate on [NiGaL] was observed (see Figure A.4.38), but the similarity of the rates shown here suggest that mass-transport limitations (ie. gas-liquid mixing) must also be considered as potentially limiting catalysis under certain conditions. Catalytic conditions: 880 mM Vkd, 34 atm of ~1:1 H_2/CO_2, 293 K, 0.30 mL THF-d_8.

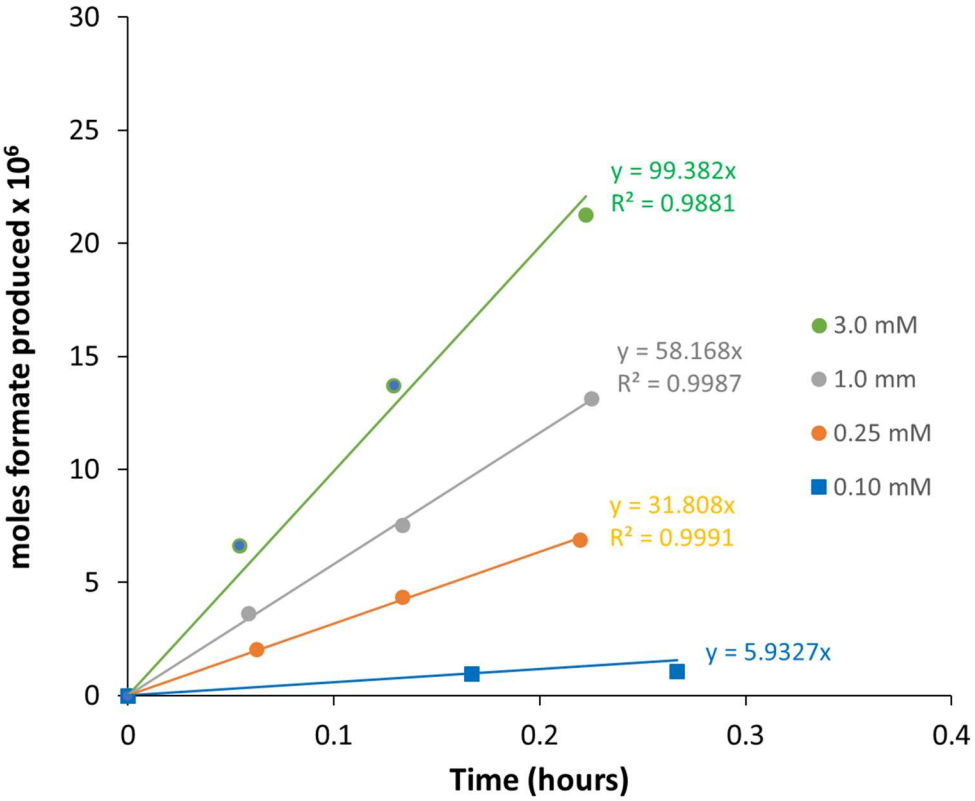

Figure A.4.38. Plot of moles formate produced (x 10^6) vs. time (h) for various catalyst loadings of NiGaL (**2**). The rate is seen to depend on [NiGaL] (ie. linear plot of initial TOF vs. [NiGaL]), but the rates at higher concentrations are slower than would be expected for first-order dependence. This is hypothesized to be the result of mass-transport limitations at higher catalyst loadings under these catalytic conditions (500 mM Vkd, 1 atm of ~1:1 H_2/CO_2, 293 K, 0.40 mL THF-d_8).

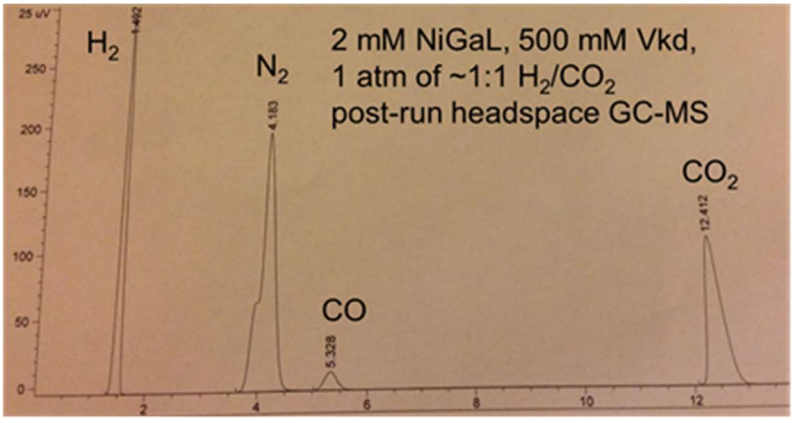

NiGaL mM	CO detected
0.25	none
0.50	0.7%
1.0	1.5%
2.0	0.8%
3.0	0.4%
4.2	trace
4.9	none

Figure A.4.39. Representative headpace GC-MS trace after a catalytic run (2 mM NiGaL, 500 mM Vkd, 1 atm of ~1:1 H_2/CO_2, 293 K, 0.40 mL THF-d_8) which shows a small amount of CO gas. The chart at the right shows the quantitative amount of CO found in the headspace for preliminary catalytic runs with various catalyst concentrations.

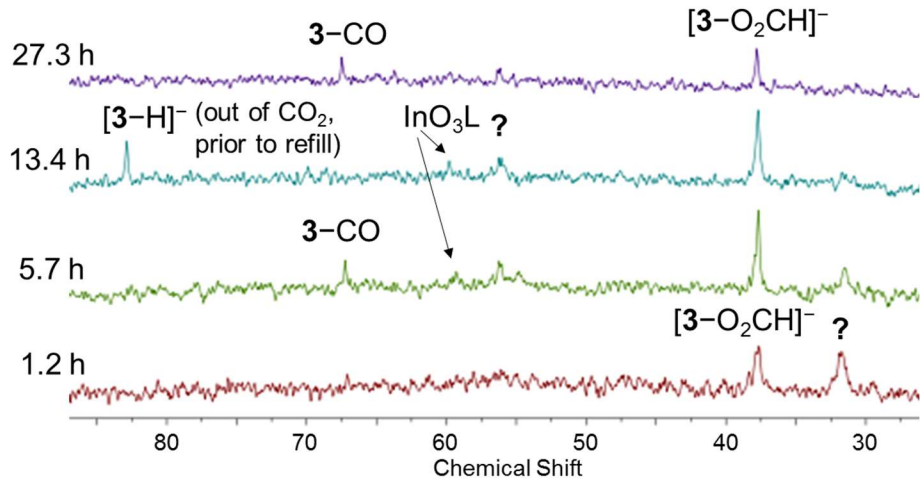

Figure A.4.40. *In situ* ^{31}P NMR spectra collected during catalysis under mild conditions (~1:1 H_2/CO_2 in 0.40 mL THF-d_8 at 293 K) for a second trial of 8 mM NiInL (**3**) and 800 mM Vkd base. ^{31}P resonances of the formate and CO adducts of **3** have been identified and labelled, with a few unidentified peaks also denoted (?). The anionic hydride, [**3**−H]$^-$, was also observed, presumably after CO_2 was completely consumed or highly depleted in the J. Young tube. A small amount of InO_3L was also observed at later time points. ^{31}P spectra are zoomed in to more clearly show the different catalyst species, so it should be noted that peaks for Vkd, [VkdH]$^+$ and impurities in the base are present in the spectra but not shown.

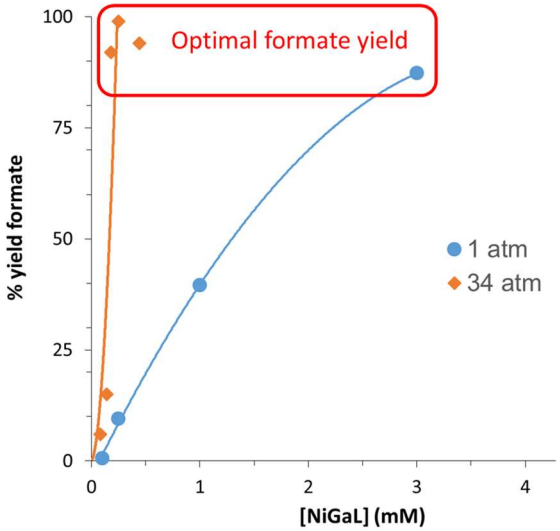

Figure A.4.41. Plot of formate % yield versus NiGaL catalyst loading for single catalytic trials with Vkd base at 1 and 34 atm of ~1:1 H_2/CO_2. Formate yields depend on both P(H_2/CO_2) and catalyst loading. Optimal catalytic conditions: [NiGaL] ≥ ~2.9 mM at 1 atm, and ~0.25 mM at 34 atm, which were the selected conditions for replicate trials in Table 5.1. Below these concentrations, the yield of formate decrease substantially, likely due to catalyst decomposition due to trace water and other impurities in the reaction mixture.

Table A.4.1. Comparison of activity for homogeneous Ni catalysts in the literature for CO_2 hydrogenation to formate (refs. X, Y, Z).

		Catalytic Conditions							Catalytic Results			
Catalyst	SI Ref. #	Solvent	Catalyst mM	Base (M)	Additive(s)	p(H_2)	p(CO_2)	T (°C)	Formate Turnovers	Time (h)	TOF[a] (h^{-1})	% yield
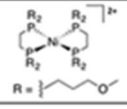 R =	45	H_2O[b]	29	$NaHCO_3$ (0.8)	none	17	17	40	1	100	0.022(2)	–[c]
								100	16	60	0.6(4)	–[c]
$NiCl_2$ + 1.5 eq. dcpe	46	DMSO	5	DBU (60)	none	40	160	50	4400	216	20.4[d]	37
			15	DBU (6)					330	21	15.7[d]	81
$Ni(dppe)_2$	47	C_6H_6	10	NEt_3 (5)	H_2O (50 M)	25	25	20	7	20	0.35[d]	1.4
NiGaL (**1**)	this work	THF	2.9	Vkd (0.8)	none	0.5	0.5	20	250	18	67	91
			0.25	Vkd (0.8)	none	17	17	20	3150	0.75	9700	99

[a]Initial TOF unless otherwise noted. [b]Buffered to pH = 9. [c]% yield complicated by equilibria with CO_2, H_2O, $NaHCO_3$. [d]Kinetics were not monitored, and as a result, TOF is an average TOF over the full reaction time.

Please refer to Appendix Figures A.4.13-A.4.16 for Tables A.4.2-A.4.6 which accompany them.

Table A.4.7. Experimental and theoretically calculated hydricity values ($\Delta G°_{H-}$, in kcal/mol) for selected complexes in CH_3CN using the C-PCM solvent model. The corresponding $\Delta G_{exchange/H-}$ energies are shown in parentheses. Note, all calculated $\Delta G°_{H-}$ values use $[HNi(dmpe)_2]^+$ as the reference complex, with $\Delta G°_{H-}$ = 50.7 kcal/mol (ref. 252). The choice of functional and basis set (see Table A.4.8) has a significant effect on the predicted hydricity values of the $[HNiGaL]^-$. The combination of M06-L/DEF2 and B3P86/BS2 levels of theory (method 2) gave the closest $\Delta G°_{H-}$ value (30.8 kcal/mol) compared to experimental value of 31.3(5) kcal/mol.

	$\Delta G°_{H-}$	calculated $\Delta G°_{H-}$					
	expt.	Method 1	Method 2	Method 3	Method 4	Method 5	Method 6
$HCo(dmpe)_2$	35.9[a]	40.2 (-10.5)	38.1 (-12.6)	37.2 (-13.5)	37.7 (-13.0)	36.8 (-13.9)	36.7 (-14.0)
$HRh(dmpe)_2$	23.2[a]	25.7 (-25.0)	28.3 (-22.4)	28.0 (-22.7)	27.2 (-23.5)	26.8 (-23.9)	26.0 (-24.7)
$[HNiGaL]^-$	31.3(5)[b]	38.9 (-11.8)	30.8 (-19.9)	28.8 (-22.0)	28.9 (-21.8)	28.1 (-22.6)	-

[a]refs. 323, 351-352. [b]ref. 128.

Table A.4.8. Six different computational methods used to calculate thermodynamic hydricity.

	geometry optimization in gas phase	single-point energy calculation in CH_3CN
Method 1	M06-L/DEF2	M06-L/DEF2
Method 2	M06-L/DEF2	B3P86/BS2
Method 3	M06-L/DEF2	B3P86/LANL2DZ+p
Method 4	B3P86/BS2	B3P86/BS2
Method 5	B3P86/BS2	B3P86/LANL2DZ+p
Method 6	B3P86/LANL2DZ+p	B3P86/LANL2DZ+p

Table A.4.9. Selected structural metrics for [PPN][HNiML] compared to the corresponding NiML complex for M=Al and In. Note that the crystal structures of the anionic hydrides were obtained by Matt Vollmer, and so the crystallographic details were not included in the experimental section.

Complex	NiAlL	[PPN][HNiAlL]	NiInL	[PPN][HNiInL]
distance (Å)				
Ni-Al	2.450(1)	2.4302(9)	2.457	2.4315(7)
Ni-P	2.204(1)	2.145(1)	2.252	2.212(2)
Al-N_{apical}	2.099(2)	2.296(2)	2.308	2.421(3)
Al-N_{eq} (avg)	1.876(1)	1.914(3)	2.118	2.141(5)
Ni-(P_3-plane)	0.13	0.196	0.23	0.282
Al-(N_3-plane)	0.26	0.428	0.48	0.587
Ni-H or Ni-O	–	1.48(4)	–	1.49(5)
Angle (°)				
Σ(P-Ni-P)	359.0	357.5	357	355.2
Σ(N_{eq}-M-N_{eq})	354.5	345.5	345	338.3